ISSN 0288-4534
CODEN: KPPJAD

KONA Powder and Particle Journal

No.36 (2019)

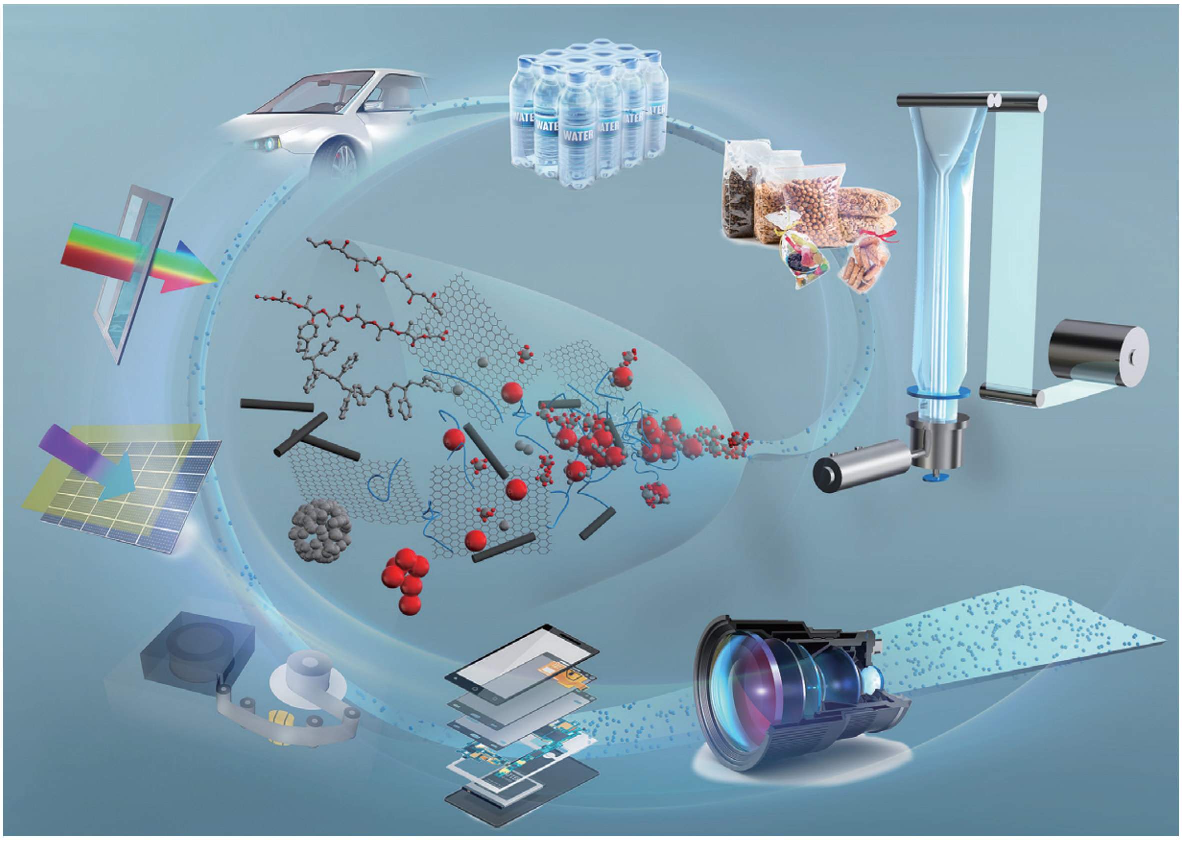

Hosokawa Powder Technology Foundation

About this Journal

KONA Powder and Particle Journal is a refereed scientific journal that publishes articles on powder and particle science and technology. This journal has been published annually since 1983 and is distributed free of charge to researchers, members of the scientific communities, universities and research libraries throughout the world, by Hosokawa Powder Technology Foundation (www.kona.or.jp/) established by Mr. Masuo Hosokawa in 1991.

The Chinese character "粉" in the cover is pronounced "KONA" in Japanese, and means "Powder". The hand written "粉" is after Mr. Eiichi Hosokawa, founder of the Hosokawa Micron Corporation (www.hosokawamicron.co.jp/en/global.html).

About the Cover

As an important part of modern devices and gadgets, polymer-based products have advanced through the introduction of nanoparticle fillers using several methods including blending, layer-by-layer, co-deposition and polymer infiltration, etc. Nanocomposites can improve significantly, for example, the mechanical, thermal, dielectric, conductive and magnetic performance of the polymer. However, manufacture constraints, cost and environmental/health concerns may hinder the quantity of admixed nanoparticles in the composite. Therefore, manufacturing and applications of nanocomposites should be considered wisely in order to balance the gains with possible drawbacks. This is discussed in detail on pp. 3–32.

Headquarters of Hosokawa Micron Corporation

Editorial Board

■ Publication Office
Hosokawa Powder Technology Foundation (www.kona.or.jp)
(in the headquarters building of Hosokawa Micron Corporation)
1-9, Shodaitajika, Hirakata-shi, Osaka 573-1132, Japan
E-mail: contact_zainq@hmc.hosokawa.com

■ Printing Office: Nakanishi Printing Co., Ltd., Japan

■ Publication Date: 10 January 2019

<Editorial>

<Review Papers>

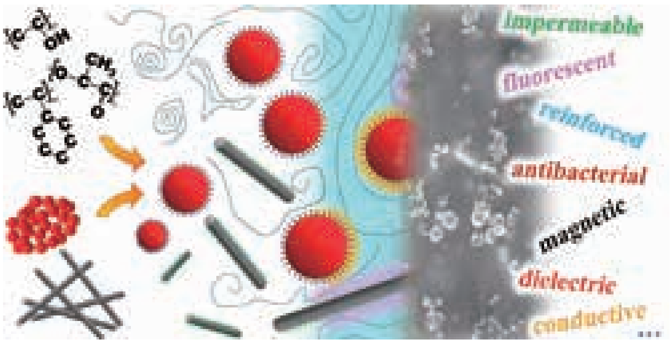
impermeable
fluorescent
reinforced
antibacterial
magnetic
dielectric
conductive
...

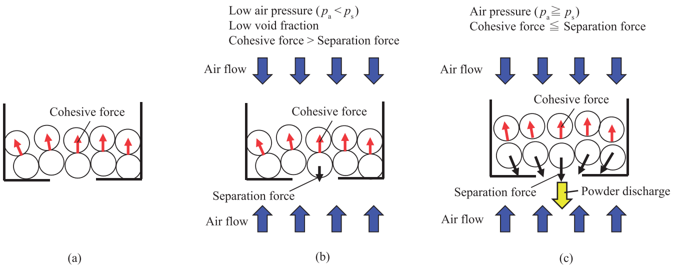
Cohesive force
(a)
Low air pressure ($p_a < p_s$)
Low void fraction
Cohesive force > Separation force
Air flow
Cohesive force
Separation force
Air flow
(b)
Air pressure ($p_a \geqq p_s$)
Cohesive force ≦ Separation force
Air flow
Cohesive force
Separation force
Powder discharge
Air flow
(c)

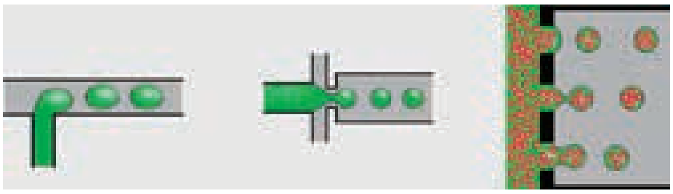

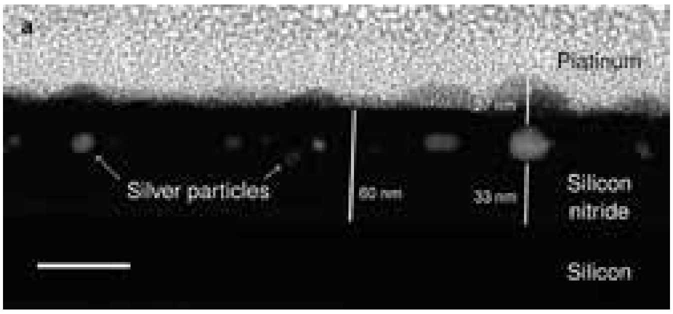
a
Platinum
Silver particles
60 nm
33 nm
Silicon nitride
Silicon

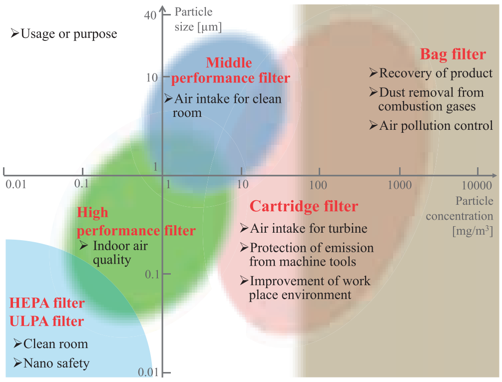
➢Usage or purpose
40
Particle size [μm]
10
1
0.1
0.01
Middle performance filter
➢Air intake for clean room
Bag filter
➢Recovery of product
➢Dust removal from combustion gases
➢Air pollution control
0.01
0.1
1
10
100
1000
10000
Particle concentration [mg/m³]
High performance filter
➢ Indoor air quality
Cartridge filter
➢Air intake for turbine
➢Protection of emission from machine tools
➢Improvement of work place environment
HEPA filter
ULPA filter
➢Clean room
➢Nano safety

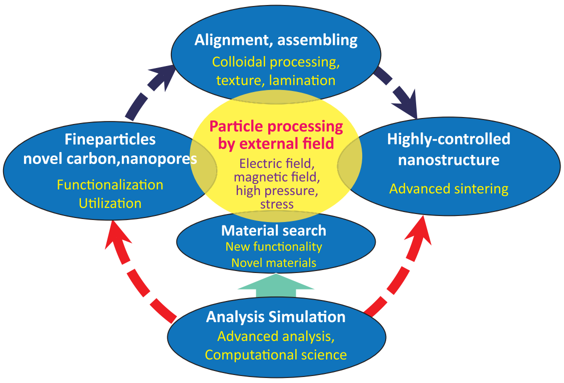
Alignment, assembling
Colloidal processing, texture, lamination
Fineparticles novel carbon,nanopores
Functionalization Utilization
Particle processing by external field
Electric field, magnetic field, high pressure, stress
Highly-controlled nanostructure
Advanced sintering
Material search
New functionality
Novel materials
Analysis Simulation
Advanced analysis, Computational science

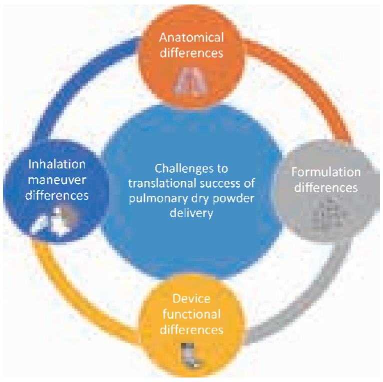
Anatomical differences
Inhalation maneuver differences
Challenges to translational success of pulmonary dry powder delivery
Formulation differences
Device functional differences

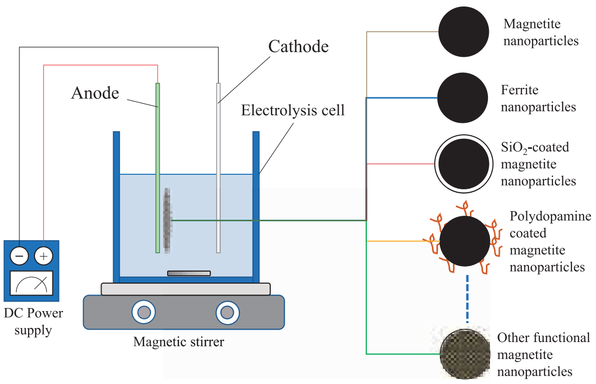
Cathode
Anode
Electrolysis cell
DC Power supply
Magnetic stirrer
Magnetite nanoparticles
Ferrite nanoparticles
SiO_2-coated magnetite nanoparticles
Polydopamine coated magnetite nanoparticles
Other functional magnetite nanoparticles

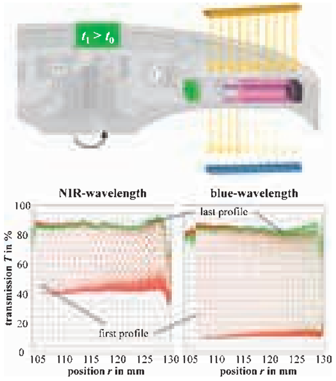
$t_1 > t_0$
NIR-wavelength
blue-wavelength
last profile
first profile
transmission T in %
100
80
60
40
20
0
105 110 115 120 125 130
position r in mm
105 110 115 120 125 130
position r in mm

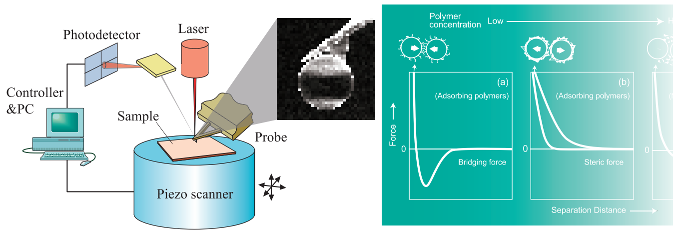
Photodetector
Laser
Controller &PC
Sample
Probe
Piezo scanner
Polymer concentration
Low
(a)
(Adsorbing polymers)
Bridging force
(b)
(Adsorbing polymers)
Steric force
Force
0
Separation Distance

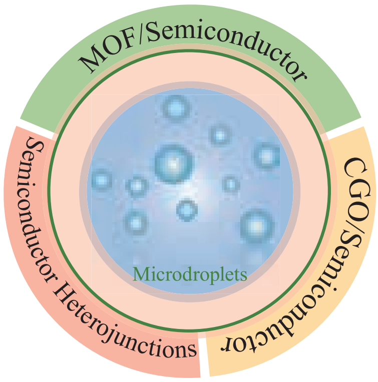
MOF/Semiconductor
CGO/Semiconductor
Semiconductor Heterojunctions
Microdroplets

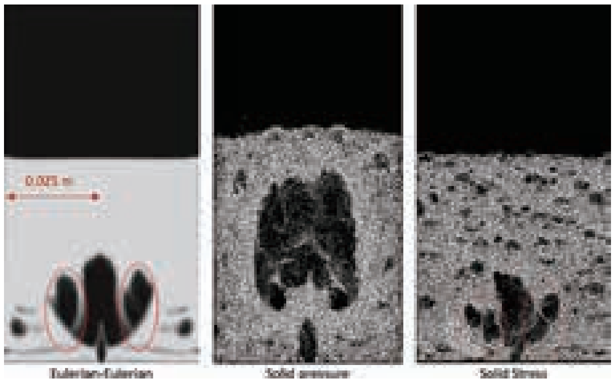
0.025 m
Eulerian-Eulerian
Solid pressure
Solid Stress

<Original Research Papers>

224 **Uniform Spherical Graphene/Monocrystal-Copper Powder Fabricated by the Low Wettability of Liquid/Solid Interface**

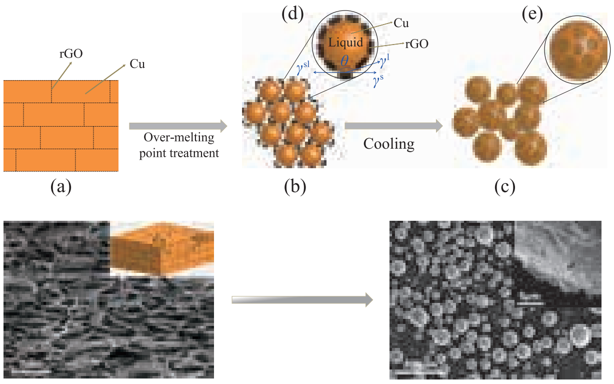

Jimin Lyu, Ding-Bang Xiong, Zhanqiu Tan, Genlian Fan, Qiang Guo, Cuiping Guo, Zhiqiang Li and Di Zhang

232 **Modified Ergun Equation for Airflow through Packed Bed of Loblolly Pine Grinds**

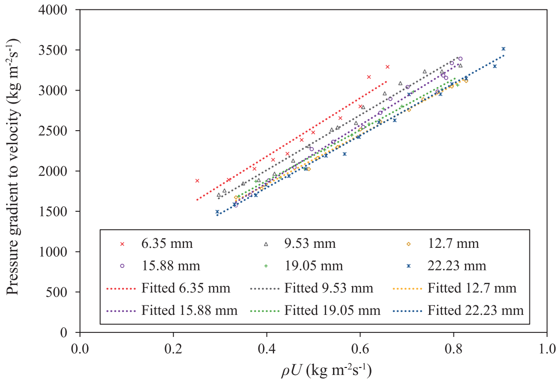

Gbenga Olatunde and Oladiran Fasina

241 **Effect of Moisture Content and Hammer Mill Screen Size on the Briquetting Characteristics of Woody and Herbaceous Biomass**

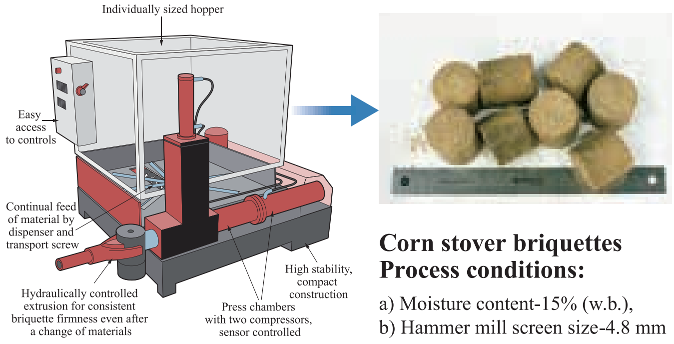

Corn stover briquettes
Process conditions:
a) Moisture content-15% (w.b.),
b) Hammer mill screen size-4.8 mm

Jaya Shankar Tumuluru

252 **Micromechanical Characterization of Particle-Particle Bond in Biomass Assemblies Formed at Different Applied Pressure and Temperature**

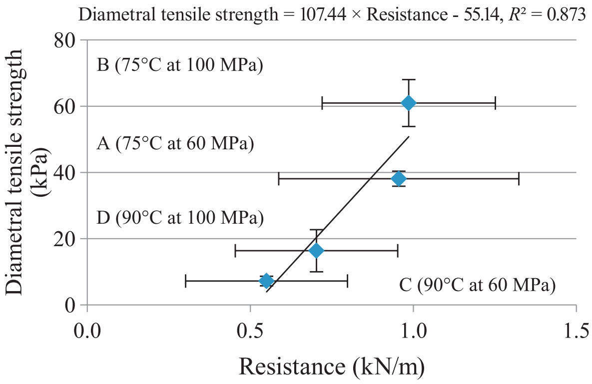

Apoorva Karamchandani, Hojae Yi and Virendra M. Puri

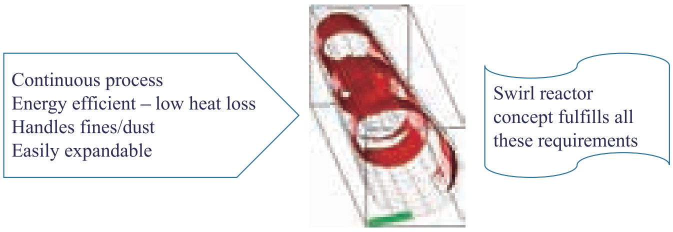

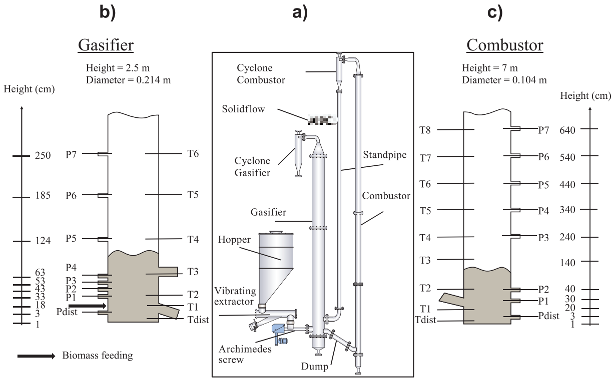

<Information Articles>

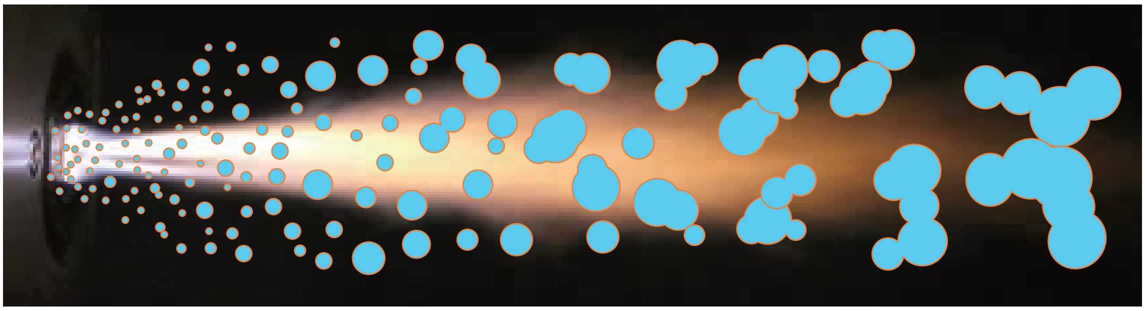

Selected research achievements for the 25th KONA Award: Flame aerosol synthesis of nanostructured materials with closely controlled characteristics. (p.296)

KONA Powder and Particle Journal No. 36 (2019) /Doi:10.14356/kona.2019019 Editorial

Reviewer Appreciation

Kikuo Okuyama, Editor-in-Chief
Hiroshima University, Japan

I would like to express my sincere gratitude to the reviewers for their hard work for the KONA Powder and Particle Journal. Thanks to the generous contributions of the volunteer reviewers as well as the interest of researchers in our journal, the number of submission to this journal is increasing after the registration on the major international journal platforms and its level is further improving. Because of the limited space of this annual journal, the number of papers published here is regrettably rather restricted. Therefore only the papers of good quality will be selected for the journal and further improved and refined by the reviewing process.

The editorial team of the KONA Journal would like to take this opportunity to gratefully acknowledge the reviewers here and deeply appreciate their valuable time and professional contributions to the KONA Journal. We apologize to any reviewers who may have been inadvertently omitted from this list. We are sincerely grateful to all who have been of any assistance to the publication of this journal.

BIRIS, Alexandru
BISCANS, Béatrice
BOURGEOIS, Florent
FUJIMOTO, Toshiyuki
FUKUI, Kunihiro
HICKEY, Anthony
HIGASHITANI, Ko
IIJIMA, Motoyuki
ISKANDAR, Ferry
KAGE, Hiroyuki
KUROSE, Ryoichi
LENGGORO, Wuled
MEESTERS, Gabriel
MILANI, Paolo
OGATA, Koichiro
OGI, Takashi
OKUYAMA, Kikuo
OTANI, Yoshio
PURI, Virendra
RASTEIRO, Maria da Graça
SAITO, Fumio
TSUJI, Takuya
WANG, Wei-Ning
YOKOYAMA, Toyokazu

Kikuo Okuyama

October 2018

KONA Powder and Particle Journal No. 36 (2019) 1–2/Doi:10.14356/kona.2019020 Editorial

Editor's Preface

Gabrie M.H. Meesters
Chairman of European/African Editorial Board
Delft University of Technology, The Netherlands

Dear KONA readers:

Before you lies the newest issue of the KONA journal. We can all be proud of the articles that are published in the printed version but even more papers can be found in the on-line version of KONA. What makes KONA special is the selection of the papers that we publish. For me as chairman of the European-African editorial group, we make a big effort to select and invite people to submit papers to the KONA editorial board. This sounds simple, but since we want high quality we need to select carefully, which does not make this task easy. Since the field of particle technology and solids handling is so wide and getting wider still, we try to select from this broad field, the best but also interesting papers possible.

The fact that we nowadays deal with particles in the nano range to over the centimeter range even makes the field broader, but even more challenging is that the areas where these different particles are applied spread over an even broader field. From medical to mining, from production of particles to environmental issues related to particle emissions, from nano particle production to large particle processing, from functionality development to bulk processing and from modelling to device and technologies development and applications. I studied particle technology in the late 1980s under the guidance of Prof. Brian Scarlett and at that time particle technology was an area mainly dominated by bulk processing, mainly researched from chemical or mechanical engineering groups. Today the broadness of the particle research has spread through almost all the disciplines. This makes it difficult to oversee the whole field of particle technology, but it gets the particle or solids technology into the place where we want them, next to gaseous and liquid systems. We are not there yet. We still need more knowledge and understanding. We need better models and sensors for proper particle process development. Models are getting much better due to the better computer systems, but also to the better understanding of particle behaviours and properties. Now sensor development needs to evolve to be better capable of controlling particulate systems, thus enabling better processing leading to higher quality of products and better economics of our processes. The next decades will be exciting.

KONA will continue to follow these developments. You will experience the broadness of particulate applications and technologies that are developed in different fields when reading the articles in the KONA Journal. We should benefit from the knowledge developed in a certain field to extend this to other fields. Applications or techniques used in the medical field, for example, can also be used in catalysis engineering, as long as we are capable and willing to interest ourselves in these different fields. Again that is why it is so exciting to read journals like KONA to find the similarities between our fields and explore the new ideas in another field.

Enjoy reading this edition of KONA and try to expand your knowledge by reading especially the articles from a completely other field of particle technology.

Gabrie M.H. Meesters
Chairman of European/African Editorial Board
Ass. Prof., Delft University of Technology
October 2018

KONA Powder and Particle Journal No. 36 (2019) 3–32/Doi:10.14356/kona.2019015 Review Paper

Nanoparticle Filler Content and Shape in Polymer Nanocomposites[†]

Christoph O. Blattmann and Sotiris E. Pratsinis[*]

[1] *Particle Technology Laboratory, Department of Mechanical and Process Engineering, ETH Zürich, Switzerland*

Abstract

Car tires, sealing caulk and high-voltage cable insulators are prime examples of commercially available and widely used composites of polymers containing nanostructured particles. In fact, myriads of applications can be realized but the usefulness of such nanocomposites depends heavily on composition, morphology, concentration and dispersion homogeneity of the nanoparticle filler in the polymer matrix. Optimizing these characteristics while ensuring economically feasible fabrication, determines the extent to which new products integrate nanocomposites. This review discusses challenges and manufacturing options of polymer nanocomposites and, in particular, which and how much nanoparticle fillers improve electrical/thermal conductivity, dielectric permittivity, gas permeability, magnetization and mechanical stability by critically reviewing and classifying over 280 peer-reviewed articles. Lastly, the economic, environmental and health implications associated with these materials are highlighted.

Keywords: filler content, aspect ratio, shape, polymer chain mobility, particle-polymer interface, nanocomposite composition

1. Introduction

The perfect grill party cannot pass without a delicious barbecue sauce: salt, pepper, mustard powder, a hint of allspice, some chili flakes and finely minced garlic mixed into a concoction of ketchup, oil and Worcester sauce. It is a composite, a particle composite that needs meticulous tuning to spread nicely on the roast without dripping right off into the smoldering embers. The ingredients are to be mixed evenly to avoid areas from becoming unbearably spicy from its chilies and others utterly dehydrating with saltiness. We crave for its addictive sweetness but when in excess (i.e. too much ketchup) it encourages charring whose taste we certainly dismay. Also the coarseness of the mustard powder should be properly chosen: Neither clumps nor grittiness is reason to praise.

Such barbecue sauce highlights how much science lays in a particle composite. Mixing viscosity, homogeneity, compound ratios and particle size are just some aspects indirectly referred to above that need critical assessment. Polymer composites, in contrast to delicious barbecue sauces, are composed of a polymer, the matrix material, and a filler (e.g., particles, molecules, or other polymers). In this review the focus is on those composites containing nanostructured particles or nanoparticles.

Car tires, silicone caulk, latex paint, tennis rackets, beverage containers and antimicrobial gloves are marketed commodities making use of them. While most of these examples profit from the filler's enhancement of mechanical strength and durability, the palette of characteristics that nanoparticles could give a polymer is exceedingly long. More precisely, frontline research has led to polymers with reduced gas permeability (Priolo M.A. et al., 2010), superior dielectric strength (Tang H. et al., 2012), high temperature stability (Moreno I. et al., 2013), strong magnetic actuation (Sotiriou G.A. et al., 2013), bright fluorescence (Jin F. et al., 2014) and improved thermal (Kuang Z. et al., 2015) and electrical (Mao Y. et al., 2016) conductivity just by adding the nanoparticle fillers. And with today's desire for multi-functionality (Sotiriou G.A. et al., 2013) and personalization, no wish seems too farfetched.

Although jaw-dropping how much polymer nanocomposites are capable of, they may not (yet) be the most attractive solution. A critical evaluation needs to be made to verify if anticipated specifications coincide with realistic ones. For this, filler composition (Yi P. et al., 2014), size (Schneider R. et al., 2015), shape (Bhanushali S. et al., 2017), surface chemistry (Niu Y. et al., 2015) and quantity (White S.I. et al., 2010) as well as choice of host

---

[†] Received 4 June 2018; Accepted 3 July 2018

[1] Sonneggstrasse 3, 8092 Zürich, Switzerland
[*] Corresponding author: Sotiris E. Pratsinis;
E-mail : pratsinis@ethz.ch
TEL: +41-44-632-31-80

polymer (Zhi C. et al., 2009) and manufacturing route (Slobodian P. et al., 2007) need to be considered.

This introduction is directly followed by a section comparing when nano-versus micro-particle fillers are the superior choice for nanocomposites. It also highlights how different these composites are depending on filler geometry. Thereafter, a short overview of manufacturing options is given. The subsequent section describes how strongly the nanoparticle–polymer interaction can influence the final composite performance. This gives motivation for multiple subsections that critically assess the influence of the nanoparticle filler on mechanical, thermal, dielectric, electrical, magnetic and gas permeation properties. A focus is placed on assessing which nanofiller composition, shape and quantity are realistic with current manufacturing technology and how much enhancement this can lead to. Before concluding, economic, environmental and health aspects are discussed.

2. Why “nano”

The reason for choosing nano- rather than micro-fillers for composites is not intuitive. Ease of processing, known hazards and lower price favor micro-fillers. But the more miniscule particles are attractive for polymer composites that exhibit small dimensions and require homogeneous filler distribution on the sub-micron scale (Suter M. et al., 2011a). Their incorporation also becomes indisputable when the pursued gain stems from the particle-polymer interface (Camenzind A. et al., 2010a) rather than the total filler volume or when the engineer envisions a bulk material with a property only exhibited by nanoparticles such as superparamagnetism (Zachariah M.R. et al., 1995). Furthermore, nano-sized fillers enable preparation of polymer composites with high transparency (Tao P. et al., 2013) that is quite attractive, for example, in today’s tremendous demand for transparent electronics and sensors (Langley D. et al., 2013). Also do not forget, the medical industry (in which esthetics matter!) also seeks such transparent nanoparticle fillers: The small primary particle size, their even distribution and high transparency of flame-made Ta_2O_5/SiO_2 in a dental adhesive are ideal for preparing radiopaque polymer nanocomposites (Schulz H. et al., 2008) that can facilitate early detection of secondary enamel caries.

These key reasons for selecting filler nanoparticles are schematically shown in **Fig. 1** by comparing composites of identical total volume (1000 μm^3). The microcomposite contains a single 5 μm diameter (d_p) particle corresponding to about 6.5 vol% filler content. Before becoming functional, however, such composites require further processing (e.g., drilling, milling, sanding). During processing, for example drilling a hole, this single particle is likely to be removed according to Murphy’s law (Matthews R.A.J., 1997) and thus creating a pure polymer devoid of any composite properties. By decreasing the filler size, it becomes increasingly difficult to remove all filler particles when drilling that same hole. More quantitatively, a *nano*composite with the same 6.5 vol% filler content would contain one billion (10^9) nanoparticles (d_p = 5 nm) which is equivalent to eight nanoparticles in each cubic subdomain (20 nm side length). This innumerous quantity can be distributed more evenly throughout the entire composite so that even after drilling multiple holes the original properties are preserved.

The exterior dimensions of the composite are just as critical: As depicted in **Fig. 1**, the microcomposite is a cube but a film with the same filler content may be preferred. But microparticle protrusion will occur for films with a thickness < 5 μm. Adding nanoparticles instead, circumvents this problem although surface roughening is common at high nanoparticle filler content (Suter M. et al., 2011a). More frequently, however, nanomaterials are added to polymers because of the particle-polymer interface (Camenzind A. et al., 2010b). A *single* microparticle has a larger surface area per particle but the nanoparticle has a far greater specific surface area (SSA, m^2 g^{-1}). So instead of only embedding a single 5 μm particle into the 1000 μm^3 composite (**Fig. 1**), one million (10^6) spherical nanoparticles (d_p = 5 nm) are incorporated having the same total surface area. This corresponds to adding 99.9 % less particle volume. Or bluntly stated, the materials engineer gets more “bang for the buck” for light-weight design.

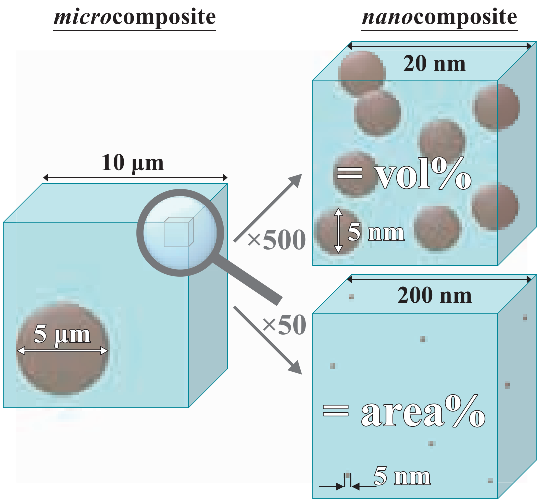

Fig. 1 Polymer micro- (left) and nanocomposites (right) containing fillers with particle size (d_p) = 5 μm and 5 nm, respectively. At same volume content (6.5 vol%) the 1000 μm^3 composite contains 1 billion nanoparticles instead of only one corresponding to eight for each 800 nm^3 subdomain. The same interfacial area is obtained with 1 million nanoparticles which is equal to adding 99.9 % less filler volume.

Nanoparticles come in myriads of shapes (**Fig. 2**) classified quite well by their aspect ratio (diameter per length or thickness, d_p/L): < 1 (platelet, sheets), = 1 (spheres, cubes) and > 1 (rods, tubes, fibers). Each of these typical shapes are more, or less, effective at introducing a novel property to a polymer. Spherical particles ($d_p/L = 1$), for example, are least effective for creating a percolating particle network (Norkhairunnisa M. et al., 2012). This is a drawback for electrical conductivity (Norkhairunnisa M. et al., 2012) but quite beneficial for preserving a higher breakdown strength in dielectrics (Feng Y. et al., 2015).

The aspect ratio unavoidably influences how many filler particles are required (**Fig. 2**). Their content in the polymer can be based on volume (vol%), weight (wt%) or area. Of these wt% is widely employed as it can be measured easily during preparation and confirmed afterwards (e.g., thermogravimetrically). Comparison based on interface area, on the other hand, is less straightforward as it requires knowledge of the particle SSA. Nanoparticle agglomeration and voids (Huang X. et al., 2012) contributes to significant deviation from the theoretical value. Therefore in practice, comparison based on interfacial area is not common for polymer nanocomposites.

Volumetric comparison is deduced from the filler weight under the assumption that nanoparticle density equals its known bulk value. This can be erroneous since significant size-dependence of the density, such as in carbon nanotubes (CNT) (Laurent C. et al., 2010) or also particle aggregates (Park K. et al., 2004), is quite likely. Density dependence on phase and crystallinity adds to the uncertainty as they may be complex (Fujiwara K. et al., 2014) or tedious (Ohtani B. et al., 1997) to determine. Nevertheless, volume-based comparison is most useful especially when drawing conclusions from different filler particle compositions. This is shown schematically in **Fig. 2** for carbon- and silver-based fillers and multiple particle aspect ratios. At equal filler dimensions (size and aspect ratio), volumetric comparison enables elimination of influence of the material density and therefore particle quantity in the polymer. This is not possible for a weight-based comparison misleading one to believe that far less carbon than silver nanoparticles are required in order to surpass a percolation threshold.

Selecting to report weight- or volume-based filler content can be a communication decision. It might be tempting to boast how much filler a novel synthesis technique is capable of incorporating; Then reporting values based on weight are quite attractive as they are usually larger. But alternatively, when presenting a functional light-weight nanocomposite it may be just as attractive to highlight with how little amount of filler nanoparticles (i.e. small numerical value) the sought property is obtained. Using a volume-based comparison is beneficial for this case.

3. Challenging manufacture

Fabrication of polymer nanocomposites is challenging due to particle surface effects and interparticle forces (Pyrgiotakis G. et al., 2013). Correspondingly, multiple manufacturing techniques have been developed. By far, the most common is by directly mixing the filler particles (Camenzind A. et al., 2010b) with the still unreacted monomer or the melted/dissolved polymer (**Fig. 3a**). This blend can be extruded, cast, sprayed or printed (just to name a few) and then dried, annealed or cured before further

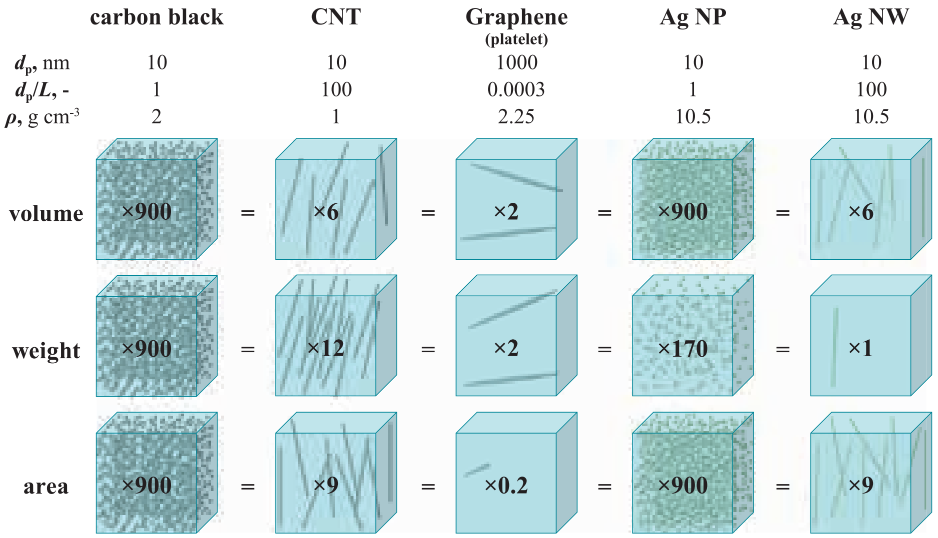

Fig. 2 Polymer nanocomposites (NC) of identical total volume containing fillers of different sizes, shapes and composition. The primary particle (or tube or disc) diameter (d_p), aspect ratio (d_p/L) and density (ρ) are noted for each. NCs in each row contain identical filler nanoparticle volume, weight and interface area (1st, 2nd and 3rd row, respectively). The particle count is overlaid onto each NC.

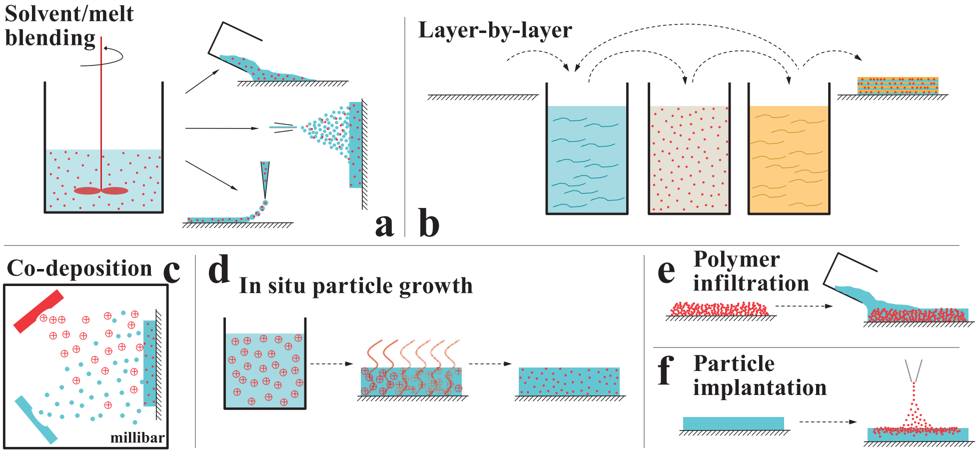

Fig. 3 Manufacturing of polymer nanocomposites is possible by solvent/melt blending (**a**), layer-by-layer adsorption (**b**), co-deposition (**c**), in situ particle growth (**d**), polymer infiltration (**e**) as well as particle implantation (**f**).

processing. The wide use of this approach stems from its employment of rather common equipment and applicability for various nanocomposite forms (bulk, films, fibers/filaments, microfabricated structures). These benefits are quite attractive in consideration of large scale fabrication and customized 3D-printed devices. Nevertheless, strong particle agglomeration (especially at the nanoscale) and high viscosity of the blend remain prominent hurdles that can lead to long processing (Chen Z. et al., 2015), inhomogeneities (Niu Y. et al., 2015), clogging of dispensing equipment (Lei Q. et al., 2016) and limitations of feasible nanocomposite dimensions (Suter M. et al., 2011a) and filler content (Schneider R. et al., 2015). Altering the nanoparticle surface chemistry (Bruno T.J. and Svoronos P.D., 2005, Iijima M. and Kamiya H., 2009) can mitigate these effects but requires additional, possibly tedious and lengthy processing (Wang D. et al., 2014).

The limitations have spurred the development of manufacturing alternatives such as layer-by-layer (LbL) adsorption (Hua F. et al., 2004) where films are obtained (**Fig. 3b**) by repeatedly exposing a substrate alternatingly to polymer and nanoparticle solutions (e.g., by dip- or drop-coating). The different components progressively deposit on top of each other by electrostatic adsorption requiring that compounds in subsequent layers have opposite charge. Thus LbL adsorption is a slow/lengthy process (about 20 nm per polymer-nanoparticle-polymer layer (Jiang C.Y. et al., 2004)) that depends on the charge difference of the compounds. Finding suitable material combinations (Hua F. et al., 2004) may be challenging. Nonetheless, homogeneous filler particle dispersion at high content is a key benefit.

The LbL adsorption is well suited for preparing thin gas barriers with high optical transparency (Priolo M.A. et al., 2010). This is achieved, for example, by the multi-layered structures of tunable thickness and nanoparticle filler quantity. Such gas barriers (oxygen transmission rate $< 10^{-5}$ cm^3 (m^2 day atm)$^{-1}$) are essential for prolonging the longevity of organic electronics where oxygen exposure is detrimental.

Co-deposition (**Fig. 3c**) is an alternative technique where simultaneous deposition of polymer and nanoparticle constituents (e.g., vapor condensation or sputtering) onto a substrate takes place (Faupel F. et al., 2007). Nanocomposite formation is precise (thickness, filler content) thanks to the quartz microbalance but long processing times and costly vacuum fabrication equipment make it rather expensive. High nanoparticle content of evenly distributed and mostly spherical metals or metal-alloys distinguishes this technique from others. But the tunability of nanoparticle filler content unfortunately relates to their size as was shown for a silver-nylon nanocomposite (Faupel F. et al., 2010).

The desire to prepare nanocomposites at more scalable conditions with little infrastructure are key concerns that are addressed by *in situ* nanoparticle growth. As indicated by the name, the nanoparticles are created directly in the polymer matrix (**Fig. 3d**) by decomposition or reaction (e.g., thermally induced) of organometallic precursors (Southward R.E. et al., 1995). Polymer-compatible synthesis (e.g., maximal exposure temperature) and choice of precursor (miscibility, reactivity and compatibility) limit the final composition (Deshmukh R.D. and Composto R.J., 2007). Nonetheless, a high content and homogeneous distribution of the nanoparticles are indisputable benefits. Nanoparticle dimensions, however, strongly depend on precursor composition, concentration, synthesis conditions and glass transition temperature of the polymer so that experimental optimization of the material is a prerequisite (Roppolo I. et al., 2017). Furthermore, one must consider that unreacted precursor or by-products may remain in the nanocomposite after synthesis (Ramesh G.V.

et al., 2009).

Polymer nanocomposites for electric (Blattmann C.O. et al., 2015) or thermal (Bhanushali S. et al., 2017) conductors require a percolating (i.e. interconnected) nanoparticle network. Such films can be prepared by infiltration of a polymer or monomer solution into the pores of a preexisting nanoparticle layer (**Fig. 3e**) (Sotiriou G.A. et al., 2013). This technique facilitates high nanoparticle filler content (up to 10 vol%) and thin multi-layered, multi-component nanocomposite films (Sotiriou G.A. et al., 2013) attractive for light-weight and optically transparent conductors (Hu W. et al., 2012). Thermal or radiative welding of the adjoining nanoparticles (Bhanushali S. et al., 2017) further improves the performance by reducing contact resistances. However, too densely-packed nanoparticle films exhibit tight crevices or inaccessible pockets that prevent infiltration by the matrix material and thus lead to trapped air bubbles (Im H. and Kim J., 2012). These usually are undesired. Very porous and loosely-packed films, on the other hand, may collapse upon infiltration (Sotiriou G.A. et al., 2013). Filler content, therefore, becomes counterbalanced by particle film stability and thickness.

Nanoparticle implantation (**Fig. 3f**) stands in direct contrast to the just introduced infiltration. Here, a preexisting polymer is exposed to a stream of spherical nanoparticles that have a high momentum enabling their penetration into the polymer (Ravagnan L. et al., 2009). Penetration of the nanoparticles is eased by higher polymer chain movement facilitated by manufacture at inclined temperatures (e.g., > 80–120 °C for polystyrene and poly(methyl methacrylate)) and polymers with lower glass transition temperature (Blattmann C.O. and Pratsinis S.E., 2016). However, metallic filler nanoparticle coalescence to larger ones (Corbelli G. et al., 2011) is favored at such conditions requiring closer attention to avoid disrupting nanoparticle percolation when electrical conductivity is sought. The filler penetration depth is limited to few hundred nanometers and strongly relates to its content that unavoidably is highest at the polymer surface (Ravagnan L. et al., 2009). Nanocomposite electrodes prepared by supersonic cluster beam implantation are biocompatible (Marelli M. et al., 2011) making them suitable for mapping neurons in the brain (Viventi J. et al., 2011) or as sensor gauges (Totaro M. et al., 2017) in prosthetics. Lengthy fabrication (Corbelli G. et al., 2011), however, may hamper their acceptance by industry.

Most improvements for fabrication of nanoparticle-filled polymers are based upon tweaking an existing technique. However, the development of novel manufacturing methods for polymer nanocomposites has not yet ceased. Recently, for example, a true single-step manufacturing method was proposed by our laboratory (Blattmann C.O. and Pratsinis S.E., 2018). There the flame-synthesis of nanoparticles, their combination with polymer and deposition as a film on a substrate are conducted quasi simultaneously. In addition to exhibiting only a single processing step, the rapid manufacturing (within minutes) can accommodate high nanoparticle filler content (more than 24 vol%) while retaining high dispersion homogeneity (**Fig. 4**). The long list of claimed improvements extends further but as all new concepts, it must prove itself in practice for research partners and industry to just consider the uptake: A true challenge!

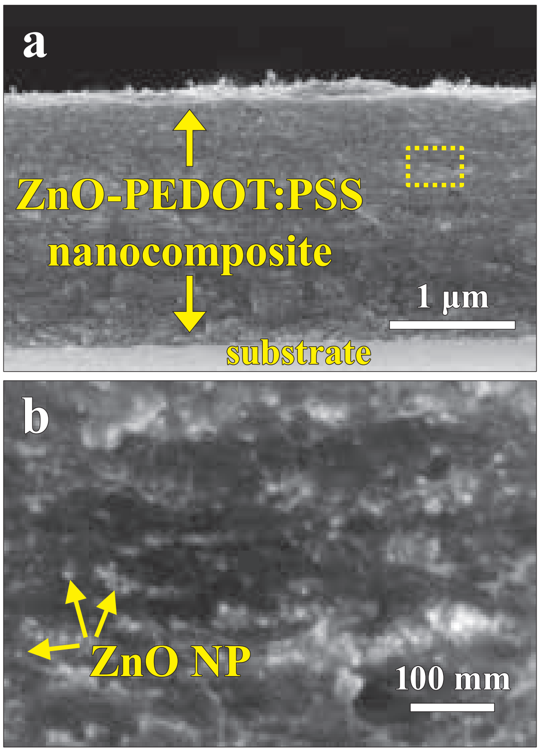

Fig. 4 Electron microscopy images of a flame-made ZnO nanoparticle-filled PEDOT:PSS film **a** prepared by simultaneous particle synthesis, combination with polymer and deposition on a substrate. **b** magnified section of that film with high nanoparticle content (bright spots) and homogeneous distribution in the polymer (dark areas).

4. Performance

The morphology (i.e. single or aggregated) and dispersion homogeneity of filler nanoparticles in a polymer can vary significantly leading directly to stark differences of nanocomposite performance. Prior to nanocomposite synthesis, the engineer must evaluate not only which particle size and shape to use but also its aggregation state (Camenzind A. et al., 2010a). In contrast to an agglomerate in which nanoparticles are only loosely bound by van der Waals and electrostatic forces (Iijima M. and Kamiya H., 2009), an aggregate consists of sintered, and therefore rigidly-connected, particles (Eggersdorfer M.L. and

Pratsinis S.E., 2014). Separating agglomerates to individual nanoparticles, e.g., by ultra-sonication (Schulz H. et al., 2008), makes them attractive for enabling high optical transparency (Chau J.L.H. et al., 2007) as their small size minimizes light scattering (Caseri W., 2000). Aggregated nanoparticles, on the other hand, can be better for enhancing the mechanical stability (Camenzind A. et al., 2010b) or facilitating the formation of a percolating network as needed for electrode preparation (Kovacs G. et al., 2009).

Unfortunately, overcoming agglomeration (**Fig. 5a**) of single and aggregated nanoparticles is challenging (Iijima M. and Kamiya H., 2009), even with ultra-sonication. They form primarily because of strong attraction between particles as well as incompatible surface chemistry with the polymer (Caseri W., 2000). Lengthier and more energy-intense processing can reduce agglomeration as has been shown during visibly transparent dental composite preparation (Schulz H. et al., 2008). This is of utmost importance due to their negative impact on performance. In Al_2O_3-PDMS nanocomposites (Yi P. et al., 2014), for example, the thermal conductivity reached saturation already at 5 wt% nanoparticle content. Also a carbon black filled acrylate (Bhawal P. et al., 2018) showed significant reduction in mechanical strength due to undesired particle agglomeration. Both of these studies highlight that lower filler content can mitigate agglomeration which, however, reduces the performance enhancement given by nanoparticles. For example, at 10 wt% the carbon black was dispersed evenly but was insufficient for enhancing the electrical conductivity (Bhawal P. et al., 2018). Similarly, agglomerating sheets of reduced graphene oxide in poly(methyl methacrylate) (PMMA) caused the tensile strength, Young's modulus and elongation-at-break to deteriorate significantly beyond 1 wt% nanoparticle content so that less had to be incorporated (Poddar M.K. et al., 2018).

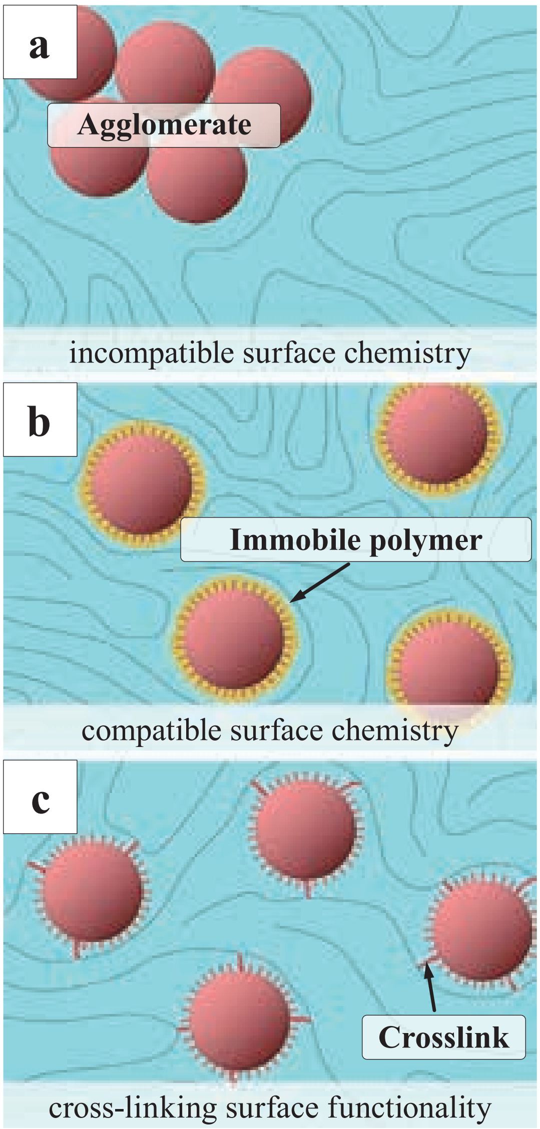

Fig. 5 The physical state of nanoparticles (red spheres) in polymer (blue) depends on their surface chemistry and affinity to polymer. Incompatible interface leads to agglomeration (**a**). Better surface chemistry of filler nanoparticle facilitates their dispersion homogeneity by forming a layer of immobilized polymer (**b**) or crosslinking (**c**).

Superior material homogeneity (i.e. less agglomeration) is obtained when the surface chemistry of nanoparticles is compatible (Wang Z. et al., 2014) with that of the polymer (**Fig. 5b**). Simple functional groups, such as hydroxyls (Liu S. et al., 2016), or more intricate oligomers (Wang G. et al., 2017) on the filler surface have shown effectiveness. However, this usually involves surface modification of the nanoparticle which can be rather tedious such as when encompassing multiple steps and polymerization (Chen Z. et al., 2015).

Compatible surface chemistry facilitates formation of a layer of immobilized polymer (yellow halo in **Fig. 5b**) around the filler nanoparticles (Camenzind A. et al., 2010a). In silicone rubber this layer is referred to as "bound rubber" (Litvinov V.M. et al., 2002). This layer of mechanically more rigid polymer ranges in thickness from a few (Camenzind A. et al., 2010b) to tens (Checchetto R. et al., 2014) of nanometers. Small nanoparticles are especially good candidates for obtaining proportionally large amount of immobilized polymer due to their high SSA (Camenzind A. et al., 2010a). In fact, this is reflected already during fabrication by the significant increase of blending solution viscosity at relatively low nanoparticle filler content (Camenzind A. et al., 2010b).

Even more rigid polymer-filler interface is formed by enabling crosslinking between them (**Fig. 5c**). It is rather uncommon, though, but has been realized, for example, in superparamagnetic hydrogels (Campbell S.B. et al., 2013) that crosslink upon mixing of modified poly(N-isoprpylacrylamide) with the functionalized filler nanoparticles. The hydrogel compressive strength and modulus increased significantly at moderate crosslinking density that was directly proportional to nanoparticle content. An increase in Young's modulus was observed also in crosslinked nanocomposites containing $BaTiO_3$ (Pu Z. et al., 2017). In contrast, there is little difference in dielectric performance compared to those nanocomposites without crosslinking (Niu Y. et al., 2015). Furthermore, the elasticity and tensile strength decreased with filler content (Pu Z. et al., 2017) making the nanocomposite inferior to conventional elastomers (Yue Y. et al., 2013). Similar doubts hold true for an epoxy - CNTs composite (Choi J.H. et al., 2017) because the claimed improvement of filler dispersion and thermal conductivity can be obtained without crosslinking (Yi P. et al., 2014).

Benefits obtained for adding nanoparticles to polymers depend on various factors briefly discussed in the preceding text. In the following, the influence of nanoparticle type and content in the polymer will be highlighted for different properties.

4.1 Mechanical

Nanoparticle addition to a polymer can be an excellent method for mechanical reinforcement of the polymer matrix (Yoshikai K. et al., 2002). This conclusion is drawn often from the increasing mechanical modulus with nanoparticle content (Camenzind A. et al., 2010b). This, however, is only partially true as it depends on polymer type that can be classified, for example, according to the temperature-dependent mechanical storage modulus (**Fig. 6**) obtained by dynamic mechanical analysis (DMA) (Hu X. et al., 2010). In such a thermoplastic analysis enables clear differentiation between three temperature-dependent physical states (red line in **Fig. 6**) separated by glass transition (T_g) and melting temperature (T_m) (Sperling L.H., 2005).

Below T_g (i.e. common employment range) the mechanical modulus is rather constant, around 10^9 Pa. Its magnitude for various polymers is quite similar as it originates from the intermolecular attractive forces between molecular chains and their individual covalent bonds (Sperling L.H., 2005). Accordingly, semi-crystalline polymers (blue line in **Fig. 6**) exhibit only slight increase of the modulus (Shieh Y.-T. et al., 2010).

At T_g the motion of molecular chains increases leading to a decay of the modulus by about three orders of magnitude for fully amorphous (glassy) polymers (red line). Semi-crystalline ones (blue line) exhibit a smaller reduction of the modulus as polymer crystallites restrict that motion (Shieh Y.-T. et al., 2010). The T_g varies from < 0 °C to > 100 °C (Mark J.E., 2009) and depends even on polymer molecular weight (Blattmann C.O. and Pratsinis S.E., 2016) and film thickness (Singh L. et al., 2004).

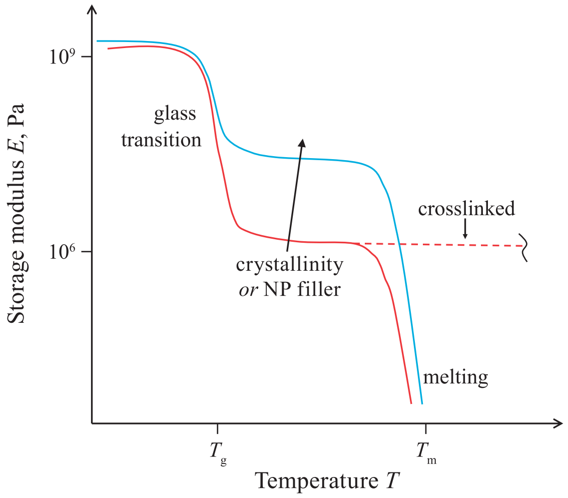

Fig. 6 The mechanical storage modulus of a polymer (nanocomposite) as a function of temperature as obtained through dynamic mechanical analysis (DMA). An amorphous polymer (red line) exhibits two temperature dependent modulus drops at the glass transition temperature (T_g) and towards the melting temperature (T_m). No T_m transition is seen for its crosslinked counterpart (broken red line). Increasing the polymer crystallinity or adding nanoparticles (blue line) increases the modulus between T_g and T_m.

Between T_g and T_m the mechanical modulus of glassy polymers plateaus (Sperling L.H., 2005) and decreases once more upon transiting to a melt (i.e. at T_m). This transition from a glassy state to a melt occurs more gradually for amorphous than semi-crystalline thermoplastics since crystallites remain intact up to T_m. In the presence of crosslinks (e.g., elastomers such as silicone rubber), this transition does not occur (dashed red line in **Fig. 6**) since polymer motion is kept restricted by the covalent bonds between chains (Sperling L.H., 2005). As a result, the mechanical modulus remains stable until polymer decomposition.

Mechanical stabilization of the polymer by addition of nanoparticles is analogous to semi-crystalline thermoplastics: Below T_g filler nanoparticles have a marginal effect (López D. et al., 2001). The T_g, however, may be shifted from that of the pure polymer depending on polymer-nanoparticle interactions (Pu Z. et al., 2017). Higher/lower T_g indicates better/worse compatibility (Zhu A. et al., 2008) due to formation of either immobilized polymer (**Fig. 5**) or free-volume (loosely organized polymer chains), respectively (Pu Z. et al., 2017). Loading poly(vinyl chloride) with 2 wt% of SiO_2 nanoparticles increased the T_g by 2.5 °C when good interfacial compatibility exists and decreased it by 1.5 °C for incompatible interfaces (Zhu A. et al., 2008). Increasing the T_g can be desirable as it may reduce polymer aging (Cangialosi D. et al., 2013). For poly(lactic acid) (PLA), for example, aging has detrimental effects on is mechanical stability (Ghazaryan G. et al., 2016). The addition of ZnO (Lizundia

E. et al., 2016) and CNTs (Lizundia E. and Sarasua J.R., 2012) improve PLA aging. This effect is reversed, however, upon nanoparticle agglomeration.

The largest effect of the nanoparticle filler on the modulus of the polymer (**Fig. 6**) occurs in the glassy state (i.e. between T_g and T_m). Analogous to semi-crystalline polymers, the modulus increases with nanoparticle content (Bhawal P. et al., 2018). Therefore, nanocomposites employed at temperatures above T_g profit most from addition of nanoparticles. This is exemplified by the storage modulus of ethylene methyl acrylate that improves by less than an order of magnitude below its T_g when adding 50 wt% (~37 vol%) carbon black (Bhawal P. et al., 2018). Above T_g, however, the modulus is increased by almost two orders of magnitude by such addition. A similar observation is made in silica-filled styrene-butadiene rubber (Yoshikai K. et al., 2002). There the modulus increases by 66 and 1200 % below and above T_g, respectively. In a semi-crystalline polymer nanocomposite the nanoparticles can stabilize the polymer directly (Camenzind A. et al., 2010b) and/or stimulate its crystallization (Cortes L.Q. et al., 2014).

Tensile stress-strain relations (**Fig. 7**) reveal the mechanical durability at a given temperature (usually 20–25 °C). **Fig. 7a** shows the general stress-strain curves of three thermoplastics of varying nanoparticle content below their T_g. The Young's modulus (i.e. linear slope at small strain) increases with nanoparticle content (Lizundia E. et al., 2016) in agreement with DMA (**Fig. 6**). In contrast, the strain-at-break (i.e. maximal strain before rupturing) decreases with particle content indicating that the nanocomposite becomes more brittle (Deshmukh K. et al., 2017). For low content of homogeneously dispersed nanoparticles (**Fig. 7a**: red solid line), a ductile behavior beyond the linear elastic region still can be observed before material failure (Luong N.D. et al., 2011). At high content (**Fig. 7a**: green broken line), strong agglomeration and/or poor interfacial compatibility (**Fig. 5a**), however, lead to material failure prior to surpassing the linear elastic region (Lizundia E. et al., 2016). For PLA strong embrittlement is already observed when filled with only 0.25 wt% (~0.6 vol%) of ZnO nanorods (Lizundia E. et al., 2016). This contrasts to nanocomposites with functionalized exfoliated graphite in PMMA (Wang J. et al., 2012) and polyimide (Luong N.D. et al., 2011) at 1 wt% (~0.54 vol%) and 0.75 wt% (~0.49 vol%), respectively, as they still possess some ductility beyond the linear elastic region. Their low nanoparticle contents indicate quite clearly, though, that strong embrittlement will set in already after adding rather little filler amount.

In contrast to this typical tensile stress-strain behavior shown in **Fig. 7a**, some studies report that embrittlement of the thermoplastic nanocomposite is preceded by a prior enhancement of the ductility. The strain-at-break of PLA, for example, increased by about 0.5 % when adding 0.18 vol% of Ag NWs (Doganay D. et al., 2016). More nanoparticles (0.24 vol%) led to common embrittlement. This improvement was attributed to the homogeneous filler dispersion achieved by the positive effect of the poly(vinylpyrrolidone) coating on the Ag NWs resulting in a compatible interface (Doganay D. et al., 2016).

Unlike earlier mentioned PMMA-graphite nanocomposites (Wang J. et al., 2012), the strain-at-break of PMMA filled with graphene oxide nanosheets increased by 4 % (Poddar M.K. et al., 2018). However, the latter contained merely 0.4 wt% (0.21 vol%) of fillers in contrast to the brittle PMMA-graphite nanocomposite (0.9 wt% exfoliated graphite) made by Wang J. et al. (2012). At comparable nanoparticle content (1 wt%), Poddar et al. (2018) reported a similar strong embrittlement by filler

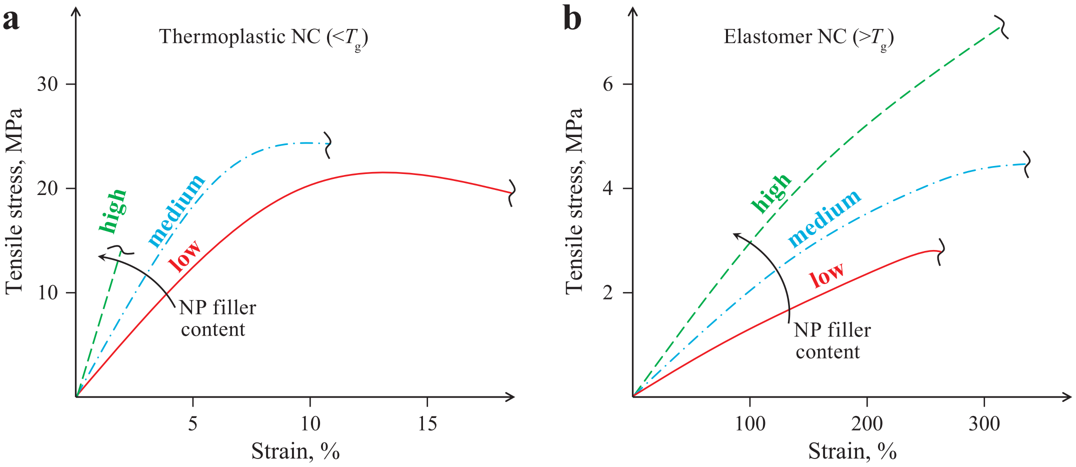

Fig. 7 Tensile stress-strain relations for thermoplastic (**a**) and elastomer (**b**) nanocomposites (NC) with increasing nanoparticle (NP) content. Thermoplastic NCs exhibit larger Young's modulus (steeper slope) but become more brittle (smaller maximal strain) with increasing NP content. Elastomer NCs exhibit higher Young's modulus and elasticity with the addition of NPs.

particle agglomeration.

Thermoplastic nanocomposites exhibit a characteristic increase of the yield strength (= maximal stress prior to plastic deformation) at low nanoparticle content (**Fig. 7a**: red solid line) (Deshmukh K. et al., 2017). However, agglomeration and poor polymer-nanoparticle compatibility lead to reduction of the yield strength (green broken line) (Zhu A. et al., 2008). The effect is, therefore, quite similar to the decreasing nanocomposite ductility (discussed above) with nanoparticle filler content.

Fig. 7b shows the general tensile stress-strain relation of silicone rubber nanocomposites (above T_g) containing different loadings of nanoparticles (Yue Y. et al., 2013). These crosslinked nanocomposites exhibit significant improvement in Young's modulus, yield strength and strain-at-break. In **Fig. 7b** this improvement is seen by comparing the solid red line with the blue dot-broken one. In quantitative terms, the strain at break of silicone rubber (Yue Y. et al., 2013) improves from ~160 to ~380 % by adding silica nanoparticles (~12.5 vol%). More silica (~19.3 vol%) leads to further increase of the elastic modulus but deteriorates the strain-at-break (330 %). This embrittlement is shown schematically in **Fig. 7b** (green broken line). Decreasing the nanoparticle size while maintaining the same volume loading increases the modulus and strain-at-break (Camenzind A. et al., 2010b). This arises from the increasing bound rubber fraction that forms when incorporating smaller filler nanoparticles.

Cross-linked polyurethane (PU) nanocomposites are similar to those containing silicone rubber as host polymer with respect to exhibiting an increasing modulus and ultimate strain with nanoparticle addition (Çakmakçı E. et al., 2014). However, they become less elastic upon nanoparticle addition. For example, the strain-at-break decreases by 540 % (= 286 %–826 %) when adding 8.7 vol% of $BaTiO_3$ (Yin G. et al., 2017) whereas the Young's modulus increases to 30.5 MPa (+ 50 %). Analogous observations are made in PU nanocomposites containing hexagonal boron nitride (Çakmakçı E. et al., 2014) and magnetite nanoparticles (Das B. et al., 2013).

4.2 Thermal

Polymers are poor heat conductors due to their low thermal conductivity k (usually < 0.4 W m^{-1} K^{-1}). But their flexibility and good conformability to uneven or rough surfaces as well as the ability to apply them to hard-to-reach areas make them attractive for heat conductors in electronics. Adding high-k nanoparticles (e.g., boron nitride, CNT, graphene, metals) to polymers improves their thermal conductivity. For example, adding Al_2O_3 nanoparticles (10 vol%) nearly doubles the k of an epoxy (Moreira D.C. et al., 2016). More alumina leads to entrapped air, nanoparticle agglomeration and poor interfacial contact between polymer and particles that restrict additional enhancement of k. Such upper limit of the k is also observed in PMMA containing BN nanosheets (Pullanchiyodan A. et al., 2017) and PDMS with Al_2O_3 nanoparticles (Yi P. et al., 2014) due to entrapped air and filler agglomeration, respectively. The importance of the nanoparticle-polymer interface for ensuring homogeneous dispersion and intimate contact with the matrix is shown nicely by CNT filled epoxy nanocomposites (Choi J.H. et al., 2017). That work clarifies that selecting the proper organic linker between polymer and CNT is crucial for a superior k.

Direct contact between high-k fillers diminishes the heat transfer resistance leading to an increase of the nanocomposite k. Such nanocomposites have been realized, for example, by infiltration of poly(styrene) (PS) into a porous BN nanotube film (Zhi C. et al., 2009). This improved the k of PS by more than 20 times. In fact, very high (> 1) and low (< 1) aspect ratio nanoparticles are best (White S.I. et al., 2010) for creating an interconnected nanoparticle network within a polymer. **Fig. 8a** shows the enhancement of thermal conductivity (Δk) as a function of nanoparticle aspect ratio from literature (according to symbol shape and color). Nitrides (squares) are most common due to high k and extensive availability of BN nanosheets/platelets. Oxides (diamonds) mainly consist of spherical Al_2O_3 or TiO_2 nanoparticles whereas high aspect ratio Ag and Cu NWs are the most frequently used metals (triangles). Carbon-based nanoparticles (circles) are mostly CNTs. Due to the slight correlation between nanoparticle aspect ratio and composition, this dataset (**Fig. 8**) may exhibit an unavoidable material bias that should be kept in mind when interpreting it.

In general, the least improvement of k is obtained in general with spherical nanoparticles with which the maximum reported Δk of the nanocomposite just barely surpasses 1 W m^{-1} K^{-1} (**Fig. 8a**). This agrees well with their inferior ability to form a percolating network (Rivière L. et al., 2016). According to **Fig. 8a** it is difficult to distinguish if nanoparticles with aspect ratios < 1 (platelets) or > 1 (wires) are better fillers for thermal conducting nanocomposites since their achievable Δk ranges are largely overlapping. Elongated carbon-based nanoparticles, however, seem to be the worst high aspect ratio fillers as inferred from their low Δk. Their characteristic high phonon scattering at the nanoparticle interface is a likely cause (Marconnet A.M. et al., 2011).

Reduction of the heat transport resistance is controlled not only by aspect ratio but also by the quantity of nanoparticle-nanoparticle and nanoparticle-polymer junctions. Minimizing these junctions, such as by nanoparticle filler alignment in the direction of heat transfer, is ideal for increasing Δk (Zhang X. et al., 2017). For example, randomly embedded BN nanosheets (12.5 vol%) in PDMS tripled the k of the polymer to 0.53 W m^{-1} K^{-1}

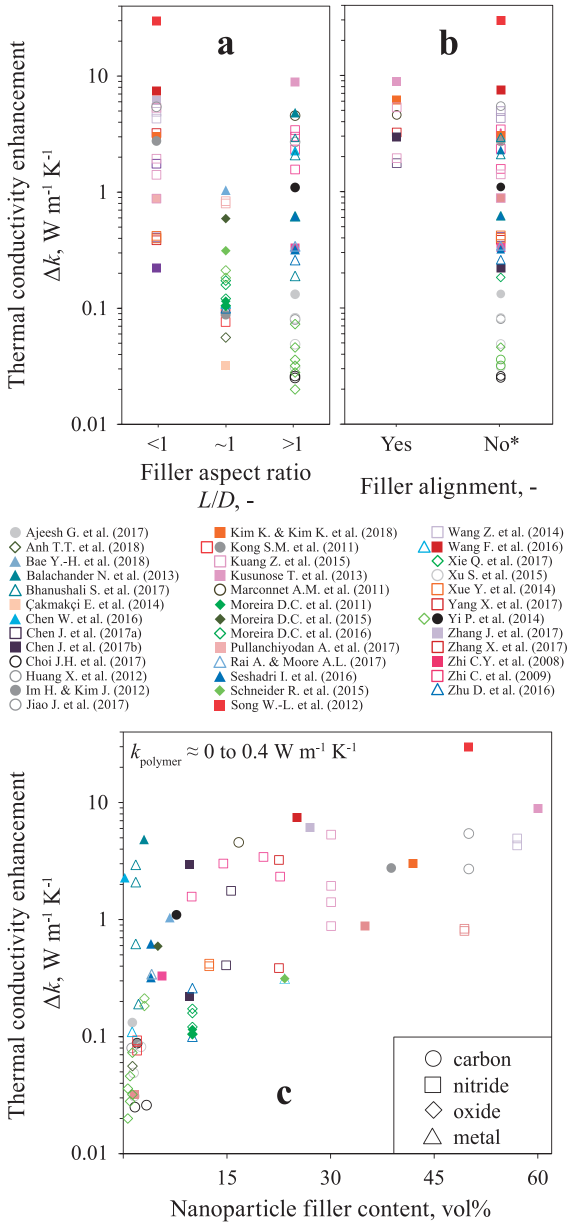

Fig. 8 The thermal conductivity of a polymer k_P is enhanced when adding nanoparticles to it (k_{NC}). The thermal conductivity enhancement Δk (k_{NC}-k_P) extracted from literature (according to symbol shape and color) as a function of nanoparticle filler aspect ratio (**a**), alignment (**b**) and content (**c**). Symbols differentiate between carbon (circles), nitride (squares), oxide (diamonds) and metallic (triangles) nanoparticle fillers. Spherical nanoparticles ($L/D = 1$) are not included in (**b**). Detailed listing of all data is in Blattmann C.O. (2019).
*: Includes nanocomposites with aligned nanoparticles *not* sought or aimed for by author(s).

(Chen J. et al., 2017a). By aligning these nanosheets, Chen et al. (2017a) additionally improved this k by more than three times (1.75 W m^{-1} K^{-1}) in the anticipated heat transfer direction. Perpendicular to the alignment direction, the k was similar to that of the nanocomposite with randomly dispersed BN. This suggests that enhancement of k through alignment of the nanoparticles does not deteriorate the corresponding perpendicular heat transfer.

A greater overview concerning the effect of filler alignment on Δk is shown in **Fig. 8b**. The data do not consider polymer nanocomposites with spherical nanoparticle fillers as they cannot be aligned. A consistently high Δk (> 1 W m^{-1} K^{-1}) is obtained for polymer nanocomposites with aligned nanoparticles (**Fig. 8b**). However, unaligned fillers are capable of promoting similar high Δk which may question the efficacy. A possible explanation is that nanoparticle alignment is not anticipated but can occur freely due to the filler aspect ratio, high viscosity of the mixing solution and/or polymer nanocomposite manufacturing method (Zhang X. et al., 2017). Unnoticed and/or not reported nanoparticle alignment (indicated by asterisk) remains disguised even for attentive readers of those manuscripts.

Figs. 8a, b neglect a crucial aspect that is expected to lead to strong variation and discrepancy: Nanoparticle content. In fact, most researchers increase the nanoparticle content as much as possible (Yi P. et al., 2014) to encourage high thermal conductivity. **Fig. 8c** shows Δk as a function of nanoparticle filler content. Differentiation is made between the material categories shown in **Fig. 8a**.

Fig. 8c clearly shows that obtaining single-digit Δk by adding nanoparticles is realistic. But the amount of nanoparticles for achieving this increase varies dramatically. For example, a BN nanosheet-loaded poly(phenylene sulfide) (~49 vol%) increased the k by 0.84 W m^{-1} K^{-1} (Yang X. et al., 2017) whereas poly(vinyl butyral) required only 9.9 vol% of BN nanotubes (Zhi C. et al., 2009) to obtain greater Δk (1.57 W m^{-1} K^{-1}). But a PDMS filled with Au NWs (Balachander N. et al., 2013) surpassed this value ($\Delta k = 4.84$ W m^{-1} K^{-1}) with even less nanoparticles (3 vol%). This underlines the strong variation among nanocomposites that can be reduced, in some instances substantially, by selection of a different nanoparticle filler material.

Metallic nanoparticles (frequently high aspect ratio ones, **Fig. 8a**) are added only in small quantities (< 10 vol%) to obtain a $\Delta k > 1$ W m^{-1} K^{-1}. In fact, metals seem to be the best choice for obtaining a high k with the least nanoparticle volume content. When plotting Δk as a function of weight-based filler content, i.e. wt%, no differentiation between the material types can be recognized (Blattmann, C.O., 2019).

Metal oxides (mostly spherical, see **Fig. 8a**) are added up to a similar volume content as metals (generally < 10 vol%). The obtained enhancement in the k, however, is significantly lower (Δk < 0.6 W m^{-1} K^{-1}). On the one hand, this may be caused by their inferior nanoparticle aspect ratio (usually $L/D = 1$) discussed in connection with **Fig. 8a**. However, just as decisive is the difference in thermal conductivity of the nanoparticle materials: The k of silver and copper (430 and 400 W m^{-1} K^{-1}, respectively) is more than ten times higher than that of alumina or titania (35 and 10 W m^{-1} K^{-1}, respectively) (Rumble J.R., 2018). In fact, this deviation by about an order of magnitude agrees quite well with the similarly lower Δk of the corresponding polymer nanocomposites (**Fig. 8c**).

Carbon- and nitride-based nanoparticles lead to similar Δk that generally level off below 5 W m^{-1} K^{-1} at around 10–20 vol% filler content. This content threshold is approximately equal to the amount up to which metals and oxides are added (**Fig. 8c**): Coincidence? It could suggest an ideal range up to which the greatest gain is obtained before being counterbalanced by deteriorating effects such as the difficulty to compound, filler agglomeration and nanocomposite embrittlement (Schneider R. et al., 2015).

Hexagonal boron nitride (most common nitride in **Fig. 8**) has an in-plane thermal conductivity (~ 400 W m^{-1} K^{-1} (Jo I. et al., 2013)) similar to silver and copper (2018). This is mirrored in **Fig. 8c** by the Δk of the nanocomposites since both metal and nitride filled polymers reach values of similar maxima (1 to 10 W m^{-1} K^{-1}). Accordingly, it is expected that polymers with CNTs (3000 W m^{-1} K^{-1} (Kim P. et al., 2001)) or graphite (1950 W m^{-1} K^{-1} (2018)) exhibit higher k. However, these carbon containing polymer nanocomposites do not excel in performance. Even in thin nanocomposite films containing 16.7 vol% of aligned CNTs the k barely reaches 5 W m^{-1} K^{-1} in the in-plane direction (Marconnet A.M. et al., 2011). The authors reason the deviation from theory with the imperfection of the CNTs, e.g., those with defects, inhomogeneous conductivity and imprecise morphology, that largely reflects the challenging manufacture of these nanoparticles in pristine quality (Nessim G.D., 2010). Additional deterioration in nanocarbon filled polymers stems from the heat transfer mechanism that leads to proportionally more grave losses at the polymer-filled junctions between nanoparticles (Kim P. et al., 2001).

4.3 Dielectric

Conventional capacitive energy storage is realized by a ceramic sandwiched between two electrodes. High dielectric constant ceramics are most attractive since these increase the theoretical energy density of the capacitors that are used in light-weight and rapidly accessible electricity storage. Their low breakdown field strength (i.e. low breakdown voltage), however, prevents the realization of these high energy densities (Barber P. et al., 2009). In contrast, polymer dielectrics have a rather low dielectric permittivity but offer high breakdown strength. By merging polymer and ceramics into a nanocomposite it is anticipated to make use of the benefits of the individual constituent. It is important to highlight, here in specific, that *nano*composites are more attractive than *micro*composites since thinner dielectric films should enable higher energy densities.

Fig. 9a shows the permittivity enhancement, i.e. permittivity of the nanocomposite (ε_{NC}) normalized to that of the polymer (ε_P), as a function of nanoparticle filler content (evaluated at 1 kHz). The data shown in **Fig. 9** were extracted from literature (symbol shape and color) that comprises primarily of barium titanate ($BaTiO_3$) nanoparticles in poly(vinylidene fluoride) (PVDF). The unavoidable composition bias stems from the high dielectric permittivity of the constituents, their commercial availability and the ability to manufacture these nanocomposites by solvent blending. To identify possible effects resulting from the nanoparticle aspect ratio, differentiation is made between spheres (circles, $L/D = 1$) and wires/rods (squares, $L/D > 1$). Platelets/sheets ($L/D < 1$) are not considered in **Fig. 9** as they are uncommon for this application.

The permittivity enhancement increases with nanoparticle content (**Fig. 9a**). This increase is lower for polymer nanocomposites filled with spherical than elongated ($L/D > 1$) nanoparticles. At 20 vol% nanoparticle content, for example, $\varepsilon_{NC}/\varepsilon_P$ ranges from 1.5 to 5.2 for spheres and from 2.6 to 34.3 for wires/rods. The spread of $\varepsilon_{NC}/\varepsilon_P$ becomes even more obvious at 40 vol%: 2.2–12.0 and 2.2–71.8 for spheres and wires/rods, respectively. The differing data spread is most likely the effect of filler source since spherical nanoparticles (frequently $d_p = 100$ nm) are often from the same commercial suppliers whereas elongated ones are synthesized by small entities or individual laboratories. The latter possess greater leverage for tuning/optimizing the particles according to method, infrastructure and skill of the engineer and, therefore, leading to more significant variability. Although wires/rods exhibit greater spread of $\varepsilon_{NC}/\varepsilon_P$ than spheres, marginal differences are observed between these nanoparticle shapes (**Fig. 9**). This is seen from the strong overlap of squares and spheres. Only few published reports give reason to believe that elongated nanoparticles are superior fillers for dielectric nanocomposites. And these are difficult to assimilate as they exhibit different filler aspect ratios L/D (= 13.7 to 2000), nanocomposite compositions, preparation techniques and nanoparticle alignment direction.

However, some researchers explicitly investigated the effect of nanoparticle aspect ratio such as the solution blended $BaTiO_3$ (3.6 vol%) - PVDF nanocomposite (Pan Z. et al., 2017). In that work $\varepsilon_{NC}/\varepsilon_P$ increases from 1.3 to 1.8 to 2.1 with increasing nanoparticle aspect ratio ($L/D = 1$, 30 or 100). In fact, similar findings are shown also for a nanocomposite with 10 vol% $BaTiO_3$ nanoparticles in a PVDF co-polymer where $\varepsilon_{NC}/\varepsilon_P$ improves from 1.7 to 2.9

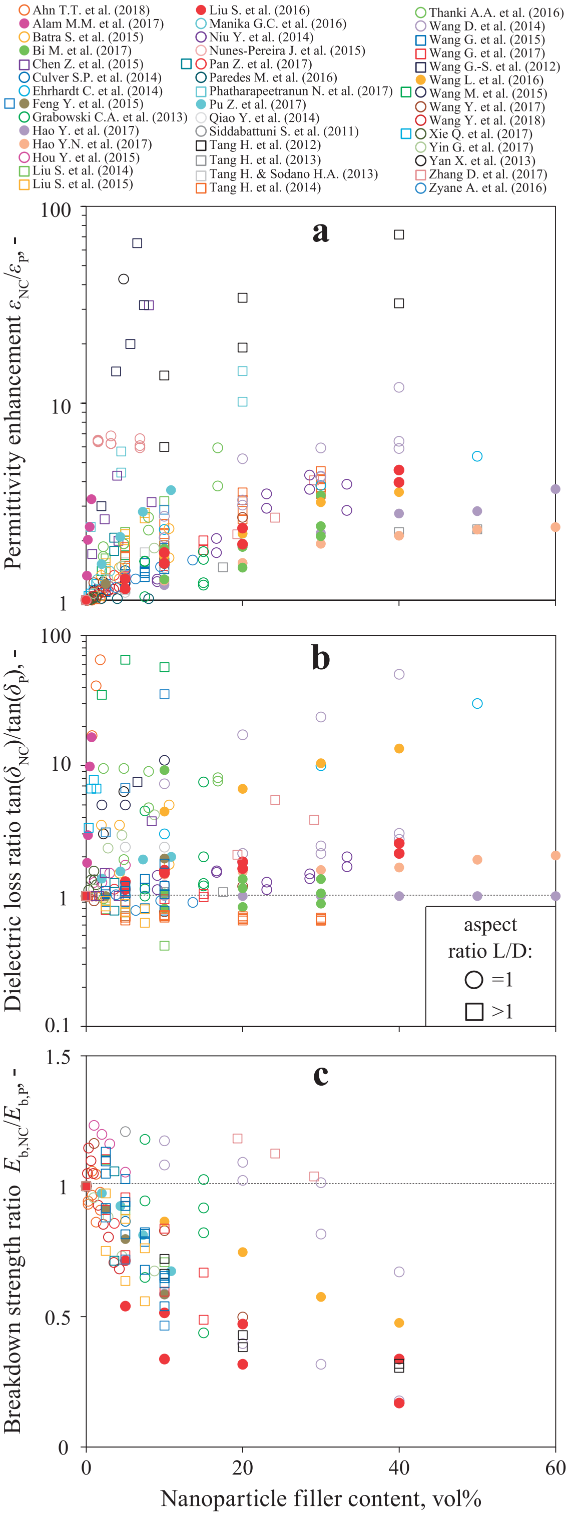

Fig. 9 Relative enhancement of dielectric polymer nanocomposite (**a**) permittivity (ε_{NC}), (**b**) dielectric loss ($\tan(\delta_{NC})$) and (**c**) breakdown strength ($E_{b,NC}$) as a function of filler nanoparticle content. Differentiation is made between spherical (circle, *L*/*D* = 1) and elongated (square, *L*/*D* > 1) nanoparticles. Improved dielectric performance is characterized by numerical values > 1 in **a** and **c** and < 1 in **b**. All data are extracted from literature (according to symbol shape and color) at 1 kHz frequency. Detailed listing of all data is in Blattmann C.O. (2019).

upon increasing the nanoparticle filler aspect ratio from 1 to 25 (Feng Y. et al., 2015). A rather small improvement of $\varepsilon_{NC}/\varepsilon_P$ (1.03 versus 1.20), however, is observed in an epoxy filled with 1.3 vol% of TiO_2 when increasing the L/D of the nanoparticles from 1 to 100 (Xie Q. et al., 2017). In that case, the comparatively lower permittivity enhancement may stem from the absence of nanoparticle surface functionalization. In fact, the effect of nanoparticle surface functionalization is just as important (Niu Y. et al., 2015), if not even more crucial (Wang D. et al., 2014) than the aspect ratio: Adding an organic coating around the nanoparticles reduces agglomeration in the polymer but can induce a lower dielectric permittivity in comparison to when using the pristine (i.e. untreated) counterpart (Niu Y. et al., 2015). A thin coating layer (e.g., fluorination (Liu S. et al., 2015), hydroxylation (Liu S. et al., 2016)) may be most desirable to minimize lowering of the ε_{NC} (Wang D. et al., 2014) while still encouraging the formation of a good polymer-nanoparticle interface (Wang L. et al., 2016) and minimal agglomeration.

The composition of filler nanoparticles effects in substantial variation of $\varepsilon_{NC}/\varepsilon_P$. The ε_{NC} of polymer containing silica (Paredes M. et al., 2016), titania (Xie Q. et al., 2017) and $BaTiO_3$ (Pan Z. et al., 2017) increases in this sequence due to the identically increasing dielectric constant (Barber P. et al., 2009) of these oxides. More easily overlooked, however, is that each phase of $BaTiO_3$ (Schädli G.N. et al., 2017) exhibits a unique dielectric permittivity. This is investigated, on the one hand, with a polycarbonate filled with 16.8 vol% cubic $BaTiO_3$ nanoparticles that leads to a permittivity enhancement of 3.8 (Thanki A.A. and Goyal R.K., 2016). Exchanging the cubic with tetragonal $BaTiO_3$ nanoparticles improves the $\varepsilon_{NC}/\varepsilon_P$ to 5.9.

In addition to the dielectric permittivity, the performance of a composite capacitor is determined by its losses due to conduction of charges and material heating (Thanki A.A. and Goyal R.K., 2016). This is characterized by the dielectric loss ($\tan(\delta)$) that should be as low as possible. **Fig. 9b** shows the dielectric loss ratio $\tan(\delta_{NC})/\tan(\delta_P)$ as a function of nanoparticle content in the polymer (evaluated at 1 kHz). Frequently, the $\tan(\delta_{NC})$ is larger than $\tan(\delta_P)$ so that the dielectric loss ratio becomes greater than 1. This, however, is undesired as it reflects a deterioration in comparison to pristine polymer (Barber P. et al., 2009). Although significant spread of data is observed in **Fig. 9b**, most of the ratios are < 10 and increase with nanoparticle content.

The $\tan(\delta_{NC})/\tan(\delta_P)$ inferred loss occurs for one part due to electrical charge dissipation through the nanocomposite (Xie Q. et al., 2017). The formation of a percolating nanoparticle network is the leading factor that increases the charge transfer (Norkhairunnisa M. et al., 2012). As a countermeasure, multilayered dielectrics exhibiting lower nanoparticle content in the direct vicinity of the electrodes have been proposed (Hu P. et al., 2013). These electrode-adjacent layers act as charge transfer barriers which effectively retain the dielectric loss nearly identical to that of the polymer.

Dielectric losses also stem from poor interfacial interaction between nanoparticle and polymer as this prevents immobilized polymer formation (Tanaka T. et al., 2005), facilitates agglomeration (Hou Y. et al., 2015) and can lead to entrapped air (Liu S. et al., 2014). This highlights, once again, that chemical modification of the nanoparticle surface must be well tuned: Here, to balance the desired reduction of the dielectric loss with the undesired inferior permittivity (Wang D. et al., 2014).

Depending on nanoparticle fabrication (Tohma T. et al., 2002), the dielectric loss of the filler may be smaller than that of the polymer. This results in $\tan(\delta_{\mathrm{NC}})/\tan(\delta_{\mathrm{P}})$ being less than unity and decreasing with nanoparticle content. This is obtained, for instance, in a nanocomposite filled with alumina-encapsulated $BaTiO_3$ nanofibers (Pan Z. et al., 2017). The authors claim that the alumina coating reduces the interfacial polarization at the nanoparticle interface, acts as electrical insulator and facilitates homogeneous nanoparticle dispersion. All of these supposedly lead to the lower dielectric loss. The effect on $\tan(\delta_{\mathrm{NC}})/\tan(\delta_{\mathrm{P}}) < 1$, however, is likely to stem primarily from the $BaTiO_3$ nanofiber core as it improves the dielectric loss ratio most significantly.

In contrast to coating individual filler nanoparticles, Hu et al. (2013) could reduce the dielectric loss by preparing multilayered nanocomposite films. There the outer layers contain TiO_2 nanoparticles while the central one is filled with Mn-doped $Ba_{0.3}Sr_{0.7}TiO_3$. This assembly enables a gradual increase of permittivity towards the central nanocomposite layer due to the lower ε of TiO_2 than that of Mn-doped $Ba_{0.3}Sr_{0.7}TiO_3$. The permittivity gradient is considered beneficial for reducing the losses that originate from polarization at interfaces of materials with starkly different ε (i.e. polymer and ceramic).

Fig. 9b shows that polymers containing high aspect ratio nanoparticles can be divided according to their dielectric loss: $\tan(\delta_{\mathrm{nc}})/\tan(\delta_{\mathrm{p}}) > 1$ or ≤ 1. The former is expected since high aspect ratio nanoparticles more readily form a percolating network (Wang M. et al., 2015) that facilitates charge transfer especially when aligned (Zhang D. et al., 2017). Nanowire alignment, however, may also be a probable reason why some polymer nanocomposites exhibit a $\tan(\delta_{\mathrm{NC}})/\tan(\delta_{\mathrm{P}}) \leq 1$. It was observed, for example, that solvent cast films with nanowires exhibited a preferential orientation (Hu P. et al., 2013) in the in-plane direction, i.e. perpendicular to charge transfer. That is effective in lowering the dielectric loss. In fact, all nanocomposites in **Fig. 9b** that contain nanowires and exhibit a $\tan(\delta_{\mathrm{NC}})/\tan(\delta_{\mathrm{P}}) \leq 1$, were prepared by casting from solutions of polymer (PVDF-based) in dimethylformamide (DMF). In fact, only Feng Y. et al. (2015) (included in **Fig. 9b**) employed this approach and obtained nanocomposites with $\tan(\delta_{\mathrm{NC}})/\tan(\delta_{\mathrm{P}}) > 1$. This work also happens to be the only one that refrained from nanoparticle surface modification: A predicament of filler agglomeration (Wang G. et al., 2017).

This subsection began with mentioning that an undeniable reason for selecting a polymer nanocomposite as a dielectric over the pure ceramic is because of the low breakdown strength (E_{b}) of the latter. This intrinsic property of the ceramic unfortunately cannot be masked with a polymer but it can be subdued. **Fig. 9c** shows the breakdown strength ratio of the nanocomposite to the unfilled polymer ($E_{\mathrm{b,NC}}/E_{\mathrm{b,P}}$). This ratio decreases with filler content so that quite frequently the $E_{\mathrm{b,NC}}$ is less than half of the $E_{\mathrm{b,P}}$ when 20 vol% nanoparticles are added. Although significantly lower than the pure polymer (PVDF: $E_{\mathrm{b,P}} \approx 300\text{–}400\ \mathrm{V\ \mu m^{-1}}$), this is still reasonably higher than the pure ceramic ($BaTiO_3$: $E_{\mathrm{b}} \approx 10\ \mathrm{V\ \mu m^{-1}}$). **Fig. 9c** indicates that the decreasing E_{b}-ratio is independent of nanoparticle aspect ratio as can be inferred from the strongly overlapping symbols.

Especially below 10 vol% nanoparticle content (**Fig. 9c**), some authors claim an increase of E_{b}. This is the case, for example, in multilayered nanocomposites containing a concentration gradient of $BaTiO_3$ nanoparticles (Wang Y. et al., 2018). There the low nanoparticle content in the outermost nanocomposite layers were found to effectively scatter, absorb and/or dissipate the kinetic energy of passing electrons enabling $E_{\mathrm{b,NC}}/E_{\mathrm{b,P}}$ to become > 1. In the absence of the gradient, the nanoparticle agglomerates facilitated charge transfer and decreased the breakdown strength as in most dielectric polymer nanocomposites. Consistent with Wang Y. et al. (2018), a $BaTiO_3$-poly(styrene) nanocomposite also exhibited an increasing breakdown strength up to about 10 vol% nanoparticle content but only when nanoparticle fillers were dispersed homogeneously in the polymer (Wang D. et al., 2014). This improved E_{b} was attributed to the efficient scattering and trapping of electrons by nanoparticles that mitigates charge transfer.

4.4 Electrical conductivity

Dielectric polymer nanocomposites aim to block charge transfer (see subsection 4.3) as electrical conductivity leads to losses. An electrically conductive path in nanocomposites for heat dissipation (see subsection 4.2) in electronics can be undesirable as well, as it can lead to shorts in the device circuitry. This subsection, however, focuses explicitly on making polymers electrically conductive by adding nanoparticle fillers.

Electron propagation through a polymer relies on a conductive path (Blattmann C.O. et al., 2015). Upon adding a sufficient amount of nanoparticles, i.e. the percolation threshold (p_c), they form paths of interconnected particles (Mutiso R.M. and Winey K.I., 2012). Quite frequently, though, these path-forming particles are just barely touching or still are separated by a thin polymer gap. The only means for electrical conductivity is by tunneling (Mutiso R.M. and Winey K.I., 2012) of the electrons through this resistive polymer. Electron tunneling leads to a characteristic S-shaped curve of the conductivity as a function of nanoparticle content (Karttunen M. et al., 2008): Higher filler content induces narrowing of the tunneling gaps and more directly contacting nanoparticles (Norkhairunnisa M. et al., 2012) and thus gradually increasing the conductivity.

The electrical conductivity of the polymer nanocomposite relies on nanoparticle composition. **Fig. 10a** shows the saturated electrical conductivity (σ) of the polymer nanocomposite reported in literature (symbol shape, color and fill) categorized according to nanoparticle filler type. The electrical conductivity in **Fig. 10** ranges from 10^{-10} to 10^4 S cm^{-1} depending on nanoparticle filler type. However, significant variability is seen for each type separately so that pinpointing an optimal one is difficult. One recognizes, though, that silver-based nanoparticles are capable of inheriting the highest electrical conductivity to the polymer but still less than that of metallic copper.

The strong scatter of the σ in **Fig. 10a** stems from the variable filler quality (Almudever C.G. and Rubio A., 2015), manufacture difficulties (Mao Y. et al., 2016) and material/manufacture compromises that need to be undertaken (Mapkar J.A. et al., 2013). Synthesis of CNTs, for example, leads to a mixture of conducting and semiconducting nanoparticles whereas the conductivity of the former depends on doping, diameter, density and chirality (Almudever C.G. and Rubio A., 2015). Furthermore, in addition to agglomeration occurring with all nanoparticles, slender elongated ones (i.e. tubes, wires, fibers) can deform (Steinmann W. et al., 2013) or even fracture (Triambulo R.E. et al., 2014), for example during manufacturing (e.g., ultrasonication, compounding), possibly leading to conductivity reduction.

High conductivity variability in graphene-polymer nanocomposites can be due to the largely differing techniques applied for exfoliating and oxidizing the graphite powder: Hummer's method (Hummers W.S. and Offeman R.E., 1958) can lead to nanocomposites with reasonably high conductivity (Stankovich S. et al., 2006). Nanocomposites with similar electrical performance, however, can also be prepared with microwave exfoliated graphite (Kujawski M. et al., 2010). Most common, though, is graphite processing by a *modified* Hummer's method followed by thermal shock (Zheng W. and Wong S.-C., 2003). At about 3 vol% filler content in PMMA (Zheng W. and Wong S.-C., 2003) or poly(amide) (Pan Y.-X. et al., 2000) these nanocomposites (both containing oxidized graphene prepared by modified Hummer's method) exhibit an electrical conductivity of 20 µS cm^{-1} or 1 mS cm^{-1}, respectively: A rather big difference indicating how crucial is the nanoparticle filler quality.

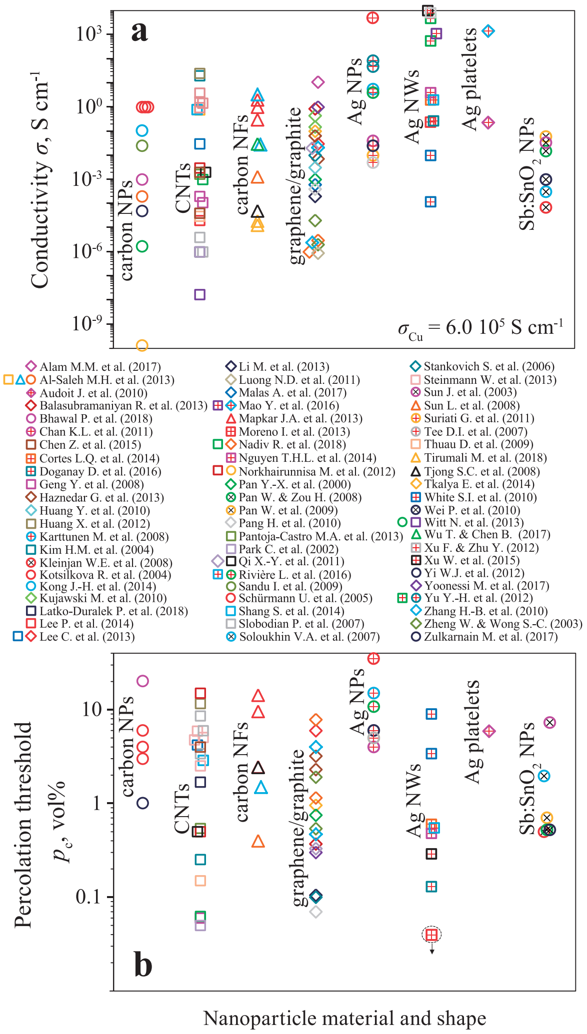

Fig. 10 **a**) Broad electrical conductivity range (σ) that can be obtained in polymers by adding conductive nanoparticle (NP) fillers. **b**) The required volume content of nanoparticle fillers to reach conductivity (percolation threshold p_c). Both σ and p_c are sorted according to composition and aspect ratio: carbon (open symbols), silver (symbols with red cross), Sb:SnO$_2$ (symbols with black X) and spheres (circle), rods/wires (square), fibers (triangle) and platelets/sheets (diamond). Data are extracted from literature. Detailed listing of all data is in Blattmann C.O. (2019).

The polyol process used for Ag NW synthesis (Coskun S. et al., 2013) leads to a thin polymer coating that encapsulates the nanowire. This coating inevitably acts as an insulator so that electron tunneling through it is unavoidable. Such organic layers, however, are required to prevent nanowire agglomeration in the polymer (Geng Y. et al., 2008). Generally, a compromise needs to be found with respect to adding a thin and yet effective coating to the conductive nanoparticles. For example, carbon nanofibers with surface treatment exhibit inferior electrical conductivity than pristine nanoparticles (Mapkar J.A. et al., 2013) but induce superior nanocomposite mechanical stability due to their more homogeneous dispersion. In a CNT-epoxy nanocomposite (Geng Y. et al., 2008), however, this unwanted reduction of the σ is diminished by selecting a non-covalently bound surfactant rather than a covalently-binding silane functionalization. Preparation of nanocomposites by polymer infiltration (**Fig. 3e**) allows one to circumvent the use of these organic coatings (Sotiriou G.A. et al., 2013) or, at least, remove them by thermal annealing the nanoparticle film before embedding. Annealing a Ag NW film (Coskun S. et al., 2013) not only removes the insulating coating but also sinters the nanoparticles at their junctions further enhancing electrical conductivity.

Nanoparticles of doped metal oxide semiconductors, such as Sb:SnO_2, are attractive fillers for preparing electrically conductive and transparent nanocomposites. The conductivity of these polymer nanocomposites depends largely on the amount of Sb doping in the nanoparticles (Kojima M. et al., 1993) and their synthesis technique. The latter determines, for example, the valence state of antimony (i.e. Sb^{3+}, Sb^{5+}) (Müller V. et al., 2009). With respect to doping content, it has been shown that sintered 4 at% Sb in SnO_2 nanoparticles prepared in solution leads to a film exhibiting a $\sigma > 100$ S cm^{-1} (Müller V. et al., 2009). When prepared by spray pyrolysis, however, σ is greatest when only adding 2 at% of Sb (Jain G. and Kumar R., 2004). But others (Kleinjan W.E. et al., 2008) use more heavily doped Sb:SnO_2 (~13 at%) according to the maximal conductivity (0.03 S cm^{-1}) obtained at that Sb content. These nanocomposites exemplify once more the origin of the σ variability.

According to **Fig. 10a** it is difficult to determine *a priori* from the nanoparticle materials how high the σ of the polymer nanocomposite will be. For electrostatic dissipation ($\sigma > 10^{-6}$ S cm^{-1}), however, most of these fillers are well suited (Mapkar J.A. et al., 2013). Electromagnetic interference shielding requires $\sigma > 0.1$ S cm^{-1} (Mapkar J.A. et al., 2013) whereas for high-end electronics the σ must be as high as possible to reduce ohmic heating. For the latter, Ag-based nanoparticles are usually the best filler for polymers (**Fig. 10a**).

In general, carbon-based and Sb:SnO_2 nanoparticle fillers are ideal for an electrical conductivity from 10^{-6} to 10 S cm^{-1}, whereas nanosilver-filled polymers are a reasonable choice for a σ between 10^{-3} and 10^4 S cm^{-1}. The required amount of nanoparticle fillers to reach this electrical conductivity range, however, varies significantly from below 0.1 to above 30 vol%. **Fig. 10b** shows the percolation threshold (p_c) of polymer nanocomposites separated according to nanoparticle type. Likewise to the polymer nanocomposite conductivity (**Fig. 10a**), the p_c deviates strongly between fillers. In contrast, though, rather than a material dependency, the p_c is determined by the nanoparticle shape: High and low aspect ratio nanoparticles (CNTs, graphene, Ag NWs) are superior when conductivity should be reached with addition of the least nanoparticle amount to the polymer. Filling polymers with spherical nanoparticles (Ag and carbon NPs) requires the highest filler content. This is in agreement with percolation theory that predicts facilitated percolation for elongated/flat particles over spherical ones (Mutiso R.M. and Winey K.I., 2012). The Ag NW content in poly(styrene), for instance, can be reduced from 9 to 3.4 vol% by increasing the aspect ratio from 8 to 31 (White S.I. et al., 2010). Even more dramatic difference in p_c is revealed in a nanocomposite of poly(ether etherketone) containing either spherical Ag NPs or Ag NWs ($L/D = 220$) (Rivière L. et al., 2016): The p_c decreases by more than 10 vol% to 0.55 vol% when using the higher aspect ratio nanoparticle fillers.

The low p_c of high aspect ratio nanoparticles has curbed the use of Ag NWs (He X. et al., 2014) and CNTs (Yu Z.B. et al., 2011) for preparing transparent electrodes. In fact, they have become prime candidates for replacing brittle indium tin oxide (Kumar A. and Zhou C.W., 2010) that many modern electronics (e.g., touchscreens) rely heavily on. Such polymer nanocomposites are always prepared as thin films since transparency is inversely proportional to thickness and nanoparticle filler content (Hu W. et al., 2012). Unfortunately, though, the conductivity is directly proportional to thickness and filler content so that a compromise (i.e. conductivity vs. transparency) becomes unavoidable.

Preparation of these nanowire- and nanotube-based (transparent) electrodes is done (Hu W. et al., 2012) predominantly by polymer infiltration (**Fig. 3e**). This ensures that the nanoparticles are touching or even sintered together (Coskun S. et al., 2013) before embedding in the polymer. A drawback of such electrodes, however, is the rather large fraction of nanocomposite surface area exhibiting no Ag NWs or CNTs for direct electron conduction (Noh Y.J. et al., 2013). These nanoparticle devoid areas are especially suboptimal for devices like photovoltaics (Noh Y.J. et al., 2013) and light emitting diodes (Triambulo R.E. et al., 2014) as they restrict efficient charge propagation from the semiconductor to the electrode.

4.5 Magnetic

A unique property of nano-sized ferromagnetic materials is their decreasing magnetic hysteresis with size (i.e. superparamagnetism) (Wiggers H., 2009). In other words, they are magnetic in the presence of a magnetic field but exhibit no remnant magnetization upon removing it (Nguyen D.T. and Kim K.-S., 2016). In contrast to dielectric and thermal/electric conductivity properties for which conventional bulk materials can be used, superparamagnetism is obtained only with nanoparticles (Nguyen D.T. and Kim K.-S., 2016) or nanocomposites made thereof (Sotiriou G.A. et al., 2013). **Fig. 11** shows the saturation magnetization ratio of the nanocomposite (M_{NC}) to that of the nanoparticle (M_{NP}) as a function of filler content. The data points are extracted from published work (symbol shape and color). Iron oxide (magnetite, maghemite) and iron oxide alloys are the most common nanoparticle fillers.

As expected the polymer nanocomposite becomes more magnetic with increasing nanoparticle content. What remains obscure in **Fig. 11** is that by adding nanoparticles with a higher M_{NP}, a nanocomposite with greater saturation magnetization is obtained for the same filler content. Or alternatively, less nanoparticles need to be added to the polymer for reaching the same final M_{NC}. This explains why magnetite ($M_{\mathrm{NP}} = 92$ emu g^{-1} (Dallas P. et al., 2006)) is more attractive than maghemite ($M_{\mathrm{NP}} = 65$ emu g^{-1} (Li D. et al., 2007)). Metal nanoparticles have a superior M_{NP} over oxides but a protective coating to avoid rapid oxidation is required (Grass R.N. and Stark W.J., 2006). Such a coating, or for that sake, any surface modification, reduces the overall nanoparticle M_{NP}.

Similar to composition, nanoparticle size plays a crucial role since too small nanoparticles exhibit inferior saturation magnetization (Li D. et al., 2007). Li D. et al. (2007) determined that flame-made γ-$\mathrm{Fe_2O_3}$ reached the maximal M_{NP} when $d_{\mathrm{p}} = 13$ nm. At half the size ($d_{\mathrm{p}} = 6$ nm), the M_{NP} reduced to a third.

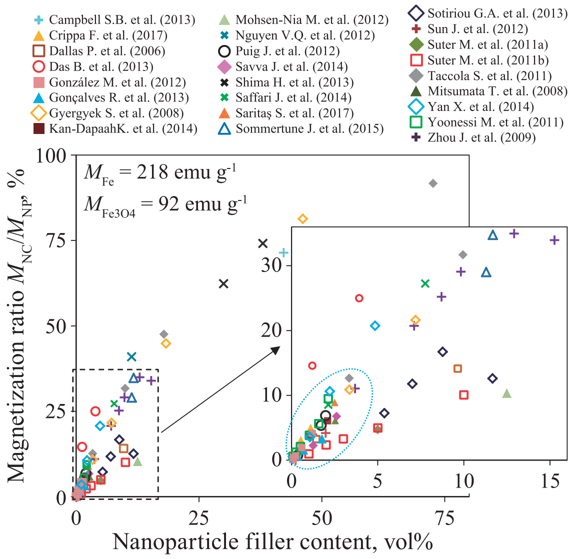

Fig. 11 Superparamagnetic nanocomposites can only be obtained by admixing such nanoparticles to the polymer. The saturation magnetization ratio of the polymer nanocomposites (M_{NC}) to that of nanoparticles (M_{NP}) as a function nanoparticle filler content. Data points are extracted from literature (according to symbol shape and color). Detailed listing of all data is in Blattmann C.O. (2019).

Fig. 11 shows that up to about 25 vol% nanoparticle content in a polymer the magnetization ratio already reaches 50 %. This non-linearity is removed, however when presented as a function of weight (Blattmann C.O., 2019) rather than volume content. Indifferent of this non-linearity, it can be recognized that most data are shown for nanoparticle contents below 15 vol% (enlarged area). The range < 5 vol% (encircled) is researched most often. This indicates the realistic upper content limit of superparamagnetic nanoparticles that can be added to the polymer. It agrees well with that of similarly sized ($d_{\mathrm{p}} < 20$ nm) silica nanoparticle in silicone rubber (Camenzind A. et al., 2010b): Above 6.2 vol% nanoparticle content, manufacture becomes difficult due to the accompanying high viscosity of the blending solution. It should be noted, though, that these superparamagnetic nanoparticles are prepared most often via wet-chemistry leading to separate spheres (Sahoo Y. et al., 2005). These are more easily dispersed than fractal-like aggregates like fumed silica (Camenzind A. et al., 2010a). Thus, a higher content of nanoparticle fillers theoretically can be added to the polymer. However, by wise selection of nanocomposite processing, a higher filler content can be achieved also with fractal-like nanoparticles. For example, Sotiriou G.A. et al. (2013) prepared micrometer-thin superparamagnetic PMMA nanocomposite cantilevers with over 10 vol% of flame-made γ-$\mathrm{Fe_2O_3}$ nanoparticle fillers by polymer infiltration into a stabilized particle film (**Fig. 3e**).

4.6 Gas permeability

Developing and improving organic electronics for photovoltaics (Gaume J. et al., 2012) and light emitting diodes (Coskun S. et al., 2013) is pursued for the assembly of lightweight, flexible, inexpensive and more environmentally friendly devices. However, some of their components are extremely sensitive to oxygen or water so that under ambient conditions degradation occurs rapidly. To prolong the device life expectancy, their development needs to go hand-in-hand with that of thin transparent gas barriers (Gaume J. et al., 2012).

A completely different field, food packaging, relies just as heavily on inexpensive, consumer-appealing, non-toxic and protective polymers to enable long shelf-life (Duncan T.V., 2011). Restricting gas exchange is a key function of such polymeric films. Produce ripening or fouling during transport and at the grocery store, for example, can be reduced with adequate packaging materials.

Pure polymer films offer some protection against gas molecule penetration that, however, can be improved by adding nanoparticles (Duncan T.V., 2011). **Fig. 12a** shows the relative gas permeability (permeability of the nanocomposite P_{NC} to that of the unfilled polymer P_P) as a function of nanoparticle filler content. The data, extracted from published work (symbol shape and color), differentiates according to nanoparticle aspect ratio: spheres (circles) and platelets (diamonds). A P_{NC}/P_P less than unity (< 1) corresponds to an enhanced barrier effect, i.e. reduced gas permeability.

Fig. 12a clearly shows that the addition of nanoparticles most often reduces the relative gas permeability. Nanoplatelets are seemingly more effective than spherical nanoparticles according to the nanocomposite P_{NC}/P_P that rarely exceeds unity when adding nanoplatelets. So they are preferred by most researchers as is reflected by the indisputable greater quantity of diamonds than circles in **Fig. 12a**. This is attributed to the popularity to use natural clay nanoparticles (e.g., montmorillonite, saponite, bentonite) as they are non-toxic, transparent, lightweight and inexpensive (Chang J.-H. et al., 2014). Common employment of clay nanoplatelets also stems from the notion that the impermeable nanoparticle fillers create a tortuous (i.e. indirect) path for the passing gas molecule (Feldman D., 2013). For in-plane aligned platelets this barrier mechanism indisputably occurs but it does not reflect the entire picture. **Fig. 12b** schematically shows the major influences of nanoparticle fillers on the gas permeability of a nanocomposite. Those that reduce or increase the permeability are labeled with a green downward- or red upward-pointing arrow, respectively. Most of these effects are related to nanoparticle's influence on the polymer chain mobility: In essence, decreasing the chain mobility reduces P_{NC}/P_P.

The addition of 2.2 vol% of exfoliated graphene oxide nanoplatelets to polyethylene was sufficient to reduce the nitrogen permeability to more than half of the pure polymer (Checchetto R. et al., 2014). This reduction of gas permeability is related to the 20 nm thick immobilized polymer that engulfs the nanoparticles and impedes gas molecules from passing. Quite surprising is that the immobilized polymer was formed even though no surface treatment was conducted to encourage nanoparticle-polymer interactions. The opposite effect (i.e. increasing permeability) was shown (Chen Y. et al., 2011) for spherical titania nanoparticles (5.2 vol%) in a thermoplastic PU. Poor interaction between particle and polymer increased the fraction of polymer free-volume, and therefore also the molecular chain mobility, leading to an increase of the nitrogen permeability ratio to > 3.3. After improving the nanocomposite manufacturing, however, the polymer-nanoparticle interaction could be enhanced improving the nanocomposite N_2 barrier properties ($P_{NC}/P_P < 0.9$).

Similar to immobilized polymer surrounding nanoparticle fillers (Checchetto R. et al., 2014), polymer crystallites restrict chain mobility suppressing the gas flow. In fact, pure semi-crystalline poly(ethylene terephthalate) (Hu Y.S. et al., 2005) is used on a standard basis for carbonated beverage bottles. Adding nanoparticles to those polymers, however, can influence crystallite formation.

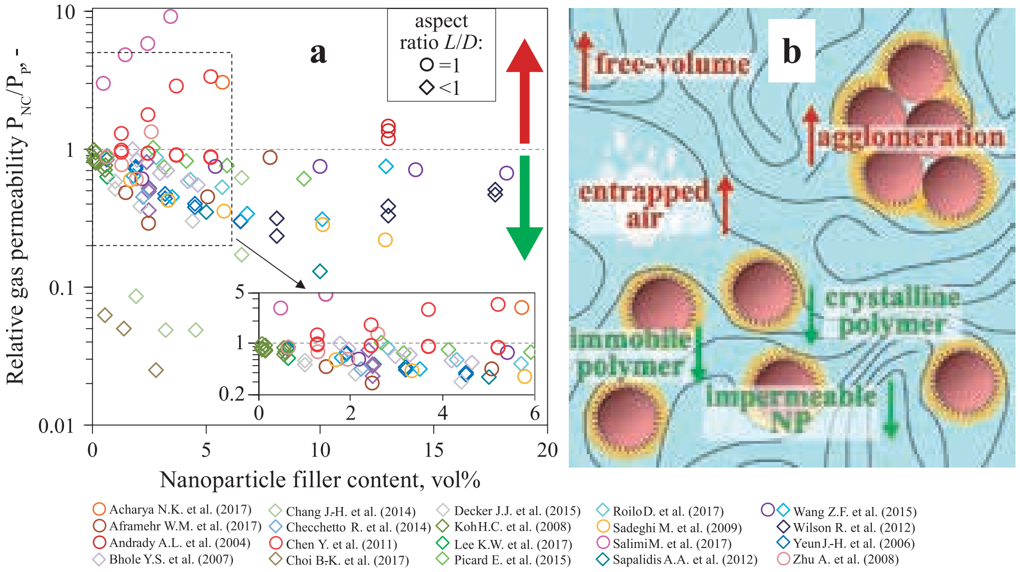

Fig. 12 Nanoparticle addition to polymers alters gas permeability. **a)** The relative gas (O_2 and N_2) permeability of nanocomposite (P_{NC}) to that of unfilled polymer (P_P) as a function of nanoparticle filler content. The data from literature (symbol shape and color) differentiate between spherical nanoparticles (circles, $L/D = 1$) and flat nanoplatelets/-sheets (diamonds, $L/D < 1$). Improved gas barriers have a $P_{NC}/P_P < 1$. **b)** Schematic summary of positive (green downward-pointing arrow) and negative (red upward-pointing arrow) effect of nanoparticles on the polymer with respect to restricting gas passage. Detailed listing of all data is in Blattmann C.O. (2019).

For example, the crystallinity of crosslinked poly(vinyl alcohol) (PVA) is increased (Choi B.-K. et al., 2017) by adding graphene oxide nanoparticles because of their crystal nucleating effect on the polymer. This had enabled a steady decrease of the oxygen permeability with filler content. In carbon black filled PLA the nanoparticle nucleating effect also promoted higher polymer crystallinity making subsequent thermal annealing superfluous (Delgado P.A. et al., 2016). There, the enhanced crystallinity was considered to be the primary reason for increasing the mechanical stability.

It cannot be generalized, though, that adding nanoparticles leads to a more crystalline polymer: Well dispersed carbon nanoparticles in PLA enhanced the crystallization rate but had little effect on final crystallinity (Sobkowicz M.J. et al., 2011). There the polymer crystallites were smaller but more numerous. In contrast, a significant reduction of polymer crystallinity was observed in a nanoclay-PVA composite (Sapalidis A.A. et al., 2012). This reduction was attributed to the strong nanoparticle-polymer interfacial interaction that encouraged amorphous immobilized PVA to form rather than polymer crystallites. Nevertheless, this reduced the $P_{\mathrm{NC}}/P_{\mathrm{P}}$ of the nanocomposite to 0.13 at 10 vol% nanoparticle filler content.

Fig. 12a shows that most work reports nanocomposites with a nanoparticle filler content < 10 vol%. In fact, this happens to be the range up to which the greatest reduction of permeability is observed. At higher contents the benefits are outweighed due to nanoparticle agglomeration (Picard E. et al., 2015), entrapped air (Salimi M. et al., 2017) and highly mobile polymer free-volume (Wilson R. et al., 2012). These unwanted effects frequently occur simultaneously to one another due to impeded nanocomposite processing at high nanoparticle contents.

5. Pros and cons: A delicate balance

Society has diverse expectations that can be challenging to meet. It will not refrain from action when ideas, regulations or products do not meet its standards which can lead to uproar in public rallies, hefty disputes on online platforms or boycotts of goods and services. This may be the graveyard of a costly innovation (Hudson J. and Orviska M., 2009) irrespective on how unjust the public's verdict is.

"Nano", as in polymer *nano*composite, is a term the general public finds difficult to judge (Schwarz-Plaschg C., 2016). It can be associated with both fancy, new and improved technology as well as an invisible and uncontrollable danger to health and environment. It is therefore the task of industry to integrate nanoparticles wisely into its products to avoid a loss-of-face (rightfully or not). The benefits, costs and risks need to be analyzed carefully.

The term "polymer nanocomposite" awakens the idea that an inexpensive polymer is upgraded by either improving it or adding a functionality. Unavoidably, their addition leads to greater cost due to the nanoparticle fillers as well as additional or more tedious processing. Fumed silica, titania, alumina and carbon black are prepared on large industrial scale so that no exorbitant cost increase due to material can be expected. Abundant and naturally occurring nanoclays are no overwhelming cost burden either. Quite frequently, though, high-quality nanocomposites contain elongated Ag NWs (Yu Y.-H. et al., 2012), well-exfoliated and oxidized graphene nanosheets (Pang H. et al., 2010), mono-dispersed quantum dots (Wang X. et al., 2011) or doped metal oxides (Kleinjan W.E. et al., 2008). Their fabrication in relatively small batches in liquid solutions with significant waste and possibly even low yield are sure signs of a costly product.

Now comes the evaluation: Is there an alternative? Highly conductive polymer nanocomposites made of Ag NWs, for example, can be replaced by less expensive carbon NPs like carbon black (**Fig. 10**). The electrical conductivity will be lower and the nanocomposite electrode unavoidably will become black. If either of these are detrimental, one can possibly resort to CNTs or even a commercially available pure polymer alternative such as poly(ethylenedioxythiophene):poly(styrene sulfonate) (PEDOT:PSS) (Ghosh S. et al., 1998). It may be just as lucrative to consider the use of various types of fillers simultaneously (Im H. and Kim J., 2012) or combining conductive polymers with the expensive nanoparticles (Kim Y.-S. et al., 2014) in order to obtain a compromise in price and quality.

Nanocomposite price needs to be kept low but just as critical is the minimization of health risks associated with manufacture and use. Non-biased risk assessments at realistic conditions are required and should be openly available to public. Only this way it is possible to properly inform the public and avoid the rising and spreading of misconceptions (Schwarz-Plaschg C., 2016) that could lead to boycotts and hamper one's reputation. In fact, the formation of misconceptions may not be too farfetched since ion release (Sotiriou G.A. et al., 2012b), radical formation (Long T.C. et al., 2006), obstruction of the respiratory system (Sotiriou G.A. et al., 2012a) and compositions of toxic heavy metals (Mao M. et al., 2013) are known drawbacks of certain nanoparticles. Once embedded in a polymer, however, these may be minimized or even eliminated but requires careful evaluation in advance.

Additionally, the public is developing an awareness to select sustainable materials/sources and considers their afterlife. Degradation during use or in landfills or decomposition via incineration may lead to environmental exposure of the previously confined nanoparticles (Singh D. et al., 2016). A prime example: Antibacterial clothing from which nanosilver can be removed during regular washing may lead to nanosilver accumulation in sewage sludge (Blaser S.A. et al., 2008). If such risks do exist, it may be quite wise and less costly on the long run if the manufacturer implements a recycling strategy for users to return old materials/devices as already is common practice for laser printer cartridges. Designing a polymer nanocomposite that was made to last, however, may be extremely difficult to separate into its individual constituents as done during true recycling. Nevertheless, closing the full life-cycle (from mining to manufacture to use to recycling) is a goal that should be envisioned also for polymer nanocomposites.

6. Concluding remarks

The presence of particles in polymer creates amazing nanocomposites with multitude of functionalities. Unfortunately, just as long is the list of challenges that accompanies the preparation of nanocomposites. The most prominent are achieving agglomerate-free and evenly distributed nanoparticles without entrapping air bubbles and still realizing the target performance. Nevertheless, a chest full of manufacturing techniques is available to realize the envisioned nanocomposite. However, only few of these may surpass the requirements for large-scale fabrication. This does not necessarily only mean high output quantity but also customization as is inferred from industry's increasing adoption of 3D-printing: A manufacturing technique that, by the way, is well suited for preparing complex polymer nanocomposites at various scales and shapes.

One must not forget, though, that the particle crucially influences the polymer characteristics. Without good knowledge of the characteristics of the particles, improving the polymer by their addition unavoidably becomes a difficult task. It can be as simple as particle size and their specific surface area (SSA) that determine how much immobilized polymer can form or their tendency to cluster into agglomerates or the ability to refrain from scattering light. In monocrystalline nanoparticles, for example, the crystal size is proportional to the SSA that is required for interaction with the polymer. But in polycrystalline nanoparticles as well as non-exfoliated platelets (e.g., graphite, nanoclay, boron nitride) this dimension can mislead a novice to believe that more area is accessible for particle-polymer interaction. Also surface chemistry needs to be well understood: The hydroxyl groups on the surface, for example, frequently link metal oxide particles and the host polymer. Slightly modifying their surface, such as by adding a functional group or silica coating, may be the key to improving particle filler dispersion as this enables the binding of surface functional groups. However, such surface functional groups as well as undesired residual organics on the surface of particles from their synthesis, can also hamper the composite performance (e.g., electrical conductivity). A particle expert, therefore, always will be a step (or two!) ahead when selecting the right fillers.

It is not uncommon that higher nanoparticle filler content is considered to lead to better performance. That may be true when stubbornly focusing on a *single* property but when stepping back and viewing the entire picture, it becomes clear that higher nanoparticle content is not always better: Higher permittivity in dielectric nanocomposites by adding more nanoparticle fillers comes at the cost of greater loss and lower breakdown strength (**Fig. 9**). And a more magnetic thermoplastic nanocomposite (i.e. greater nanoparticle content, **Fig. 11**) can lead to embrittlement. And do not neglect: mechanical mixing of the nanoparticles and polymer may become impossible at high filler content due to rising viscosity or inability to achieve the dimension specifications of the final nanocomposite. So, preparing a polymer nanocomposite requires a holistic approach that simultaneously considers the constituents, process and product.

Acknowledgements

Financial support from the ETH Zürich (# ETH-08 14-2) and Swiss National Science Foundation (#205320_163243 and 206021_170729) are kindly acknowledged.

Nomenclature

CNT	carbon nanotube
d_p	primary particle (or: tube, disc) diameter (nm)
D	nanoparticle diameter (nm)
Δk	thermal conductivity enhancement(W m^{-1} K^{-1})
E	mechanical modulus (Pa)
E_b	breakdown strength (V m^{-1})
$E_{b,NC}$, $E_{b,P}$	breakdown strength of nanocomposite/ polymer (V m^{-1})
L	nanoparticle length (tubes, wires) or thickness (platelets, sheets) (nm)
L/D	nanoparticle aspect ratio (nm nm^{-1})
M_{NC}, M_{NP}	saturation magnetization of nanocomposite/ nanoparticle (emu g^{-1})
NC	nanocomposite
NF	nanofiber
NP	nanoparticle
NW	nanowire

p_c	percolation threshold (vol%)
PDMS	poly(dimethylsiloxane), silicone rubber
PLA	poly(lactic acid)
PMMA	poly(methyl methacrylate)
P_NC, P_P	gas permeability of nanocomposite/polymer (mol cm cm^{-2} s^{-1} Pa^{-1})
PU	poly(urethane)
PVA	poly(vinyl alcohol)
PVDF	poly(vinylidene fluoride)
SSA	specific surface area (m^2 g^{-1})
T	temperature (K)
tan(δ_NC), tan(δ_P)	dielectric loss of nanocomposite/polymer (-)
T_g	glass transition temperature (K)
T_m	melting temperature (K)
ε_NC, ε_P	permittivity of nanocomposite/polymer (-)
ρ	density (kg m^{-3})
σ	electrical conductivity (S cm^{-1})

References

Acharya N.K., Temperature-dependent gas transport and its correlation with kinetic diameter in polymer nanocomposite membrane, Bull Mat Sci, 40 (2017) 537–543.

Aframehr W.M., Molki B., Heidarian P., Behzad T., Sadeghi M., Bagheri R., Effect of calcium carbonate nanoparticles on barrier properties and biodegradability of polylactic acid, Fibers Polym, 18 (2017) 2041–2048.

Ajeesh G., Bhowmik S., Sivakumar V., Varshney L., Kumar V., Abraham M., Influence of surface activated carbon nano fiber on thermo-mechanical properties of high performance polymeric nanocomposites, J Compos Mater, 51 (2017) 1057–1072.

Al-Saleh M.H., Gelves G.A., Sundararaj U., Carbon nanofiber/polyethylene nanocomposite: Processing behavior, microstructure and electrical properties, Mater Design, 52 (2013) 128–133.

Alam F., Yu J., Shen D., Dai W., Li H., Zeng X., Yao Y., Du S., Jiang N., Lin C.-T., Highly conductive 3D segregated graphene architecture in polypropylene composite with efficient EMI shielding, Polymers, 9 (2017) 662. DOI:10.3390/polym9120662

Alam M.M., Ghosh S.K., Sarkar D., Sen S., Mandal D., Improved dielectric constant and breakdown strength of γ-phase dominant super toughened polyvinylidene fluoride/TiO_2 nanocomposite film: an excellent material for energy storage applications and piezoelectric throughput, Nanotechnology, 28 (2017) 015503. http://stacks.iop.org/0957-4484/28/i=1/a=015503

Almudever C.G., Rubio A., Variability and reliability analysis of CNFET technology: Impact of manufacturing imperfections, Microelectron Reliab, 55 (2015) 358–366.

Andrady A.L., Merkel T.C., Toy L.G., Effect of particle size on gas permeability of filled superglassy polymers, Macromolecules, 37 (2004) 4329–4331.

Anh T.T., Fréchette M., David É., Veillette R., Moraille P., Effect of POSS-grafted titanium dioxide on the electrical and thermal properties of LDPE/TiO_2 polymer nanocomposite, J Appl Polym Sci, 135 (2018) 46095. DOI:10.1002/app.46095

Audoit J., Laffont L., Lonjon A., Dantras E., Lacabanne C., Percolative silver nanoplates/PVDF nanocomposites: Bulk and surface electrical conduction, Polymer, 78 (2015) 104–110.

Bae Y.-H., Yu M.-J., Vu M.C., Choi W.K., Kim S.-R., Synergistic effects of segregated network by polymethylmethacrylate beads and sintering of copper nanoparticles on thermal and electrical properties of epoxy composites, Compos Sci Technol, 155 (2018) 144–150.

Balachander N., Seshadri I., Mehta R.J., Schadler L.S., Borca-Tasciuc T., Keblinski P., Ramanath G., Nanowire-filled polymer composites with ultrahigh thermal conductivity, Appl Phys Lett, 102 (2013) 093117. DOI: 10.1063/1.4793419

Balasubramaniyan R., Pham V.H., Jang J., Hur S.H., Chung J.S., A one pot solution blending method for highly conductive poly (methyl methacrylate)-highly reduced graphene nanocomposites, Electron Mater Lett, 9 (2013) 837–839.

Barber P., Balasubramanian S., Anguchamy Y., Gong S., Wibowo A., Gao H., Ploehn H., Zur Loye H.-C., Polymer composite and nanocomposite dielectric materials for pulse power energy storage, Materials, 2 (2009) 1697–1733. DOI:10.3390/ma2041697

Batra S., Cakmak M., Ultra-capacitor flexible films with tailored dielectric constants using electric field assisted assembly of nanoparticles, Nanoscale, 7 (2015) 20571–20583.

Bhanushali S., Ghosh P.C., Simon G.P., Cheng W., Copper nanowire-filled soft elastomer composites for applications as thermal interface materials, Adv Mater Interfaces, 4 (2017) 1700387. DOI: 10.1002/admi.201700387

Bhawal P., Ganguly S., Das T.K., Mondal S., Das N.C., Mechanically robust conductive carbon clusters confined ethylene methyl acrylate–based flexible composites for superior shielding effectiveness, Polym Adv Technol, 29 (2018) 95–110.

Bhole Y.S., Wanjale S.D., Kharul U.K., Jog J.P., Assessing feasibility of polyarylate–clay nanocomposites towards improvement of gas selectivity, J Membr Sci, 306 (2007) 277–286.

Bi M., Hao Y., Zhang J., Lei M., Bi K., Particle size effect of $BaTiO_3$ nanofillers on the energy storage performance of polymer nanocomposites, Nanoscale, 9 (2017) 16386–16395.

Blaser S.A., Scheringer M., MacLeod M., Hungerbühler K., Estimation of cumulative aquatic exposure and risk due to silver: Contribution of nano-functionalized plastics and textiles, Sci Total Environ, 390 (2008) 396–409.

Blattmann, C.O., Application and Synthesis of Polymer Nanocomposites, Dr.sc. PhD thesis, ETH Zürich (2019).

Blattmann C.O., Pratsinis S.E., *In situ* measurement of conductivity during nanocomposite film deposition, Appl Surf Sci, 371 (2016) 329–336.

Blattmann C.O., Pratsinis S.E., Single-step fabrication of polymer nanocomposite films, Materials, 11 (2018) 1177. DOI:

10.3390/ma11071177

Blattmann C.O., Sotiriou G.A., Pratsinis S.E., Rapid synthesis of flexible conductive polymer nanocomposite films, Nanotechnology, 26 (2015) 125601(6pp). http://stacks.iop.org/0957-4484/26/i=12/a=125601

Bruno T.J., Svoronos P.D., CRC Handbook of Fundamental Spectroscopic Correlation Charts, CRC Press, 2005.

Çakmakçı E., Koçyiğit Ç., Çakır S., Durmus A., Kahraman M.V., Preparation and characterization of thermally conductive thermoplastic polyurethane/h-BN nanocomposites, Polym Compos, 35 (2014) 530–538.

Camenzind A., Caseri W.R., Pratsinis S.E., Flame-made nanoparticles for nanocomposites, Nano Today, 5 (2010a) 48–65.

Camenzind A., Schweizer T., Sztucki M., Pratsinis S.E., Structure & strength of silica-PDMS nanocomposites, Polymer, 51 (2010b) 1796–1804.

Campbell S.B., Patenaude M., Hoare T., Injectable superparamagnets: Highly elastic and degradable poly(N-isopropylacrylamide)–superparamagnetic iron oxide nanoparticle (SPION) composite hydrogels, Biomacromolecules, 14 (2013) 644–653.

Cangialosi D., Boucher V.M., Alegria A., Colmenero J., Physical aging in polymers and polymer nanocomposites: Recent results and open questions, Soft Matter, 9 (2013) 8619–8630.

Caseri W., Nanocomposites of polymers and metals or semiconductors: Historical background and optical properties, Macromol Rapid Comm, 21 (2000) 705–722.

Chan K.L., Mariatti M., Lockman Z., Sim L.C., Effects of the size and filler loading on the properties of copper- and silver-nanoparticle-filled epoxy composites, J Appl Polym Sci, 121 (2011) 3145–3152.

Chang J.-H., Ham M., Kim J.-C., Comparison of properties of poly(vinyl alcohol) nanocomposites containing two different clays, J Nanosci Nanotechno, 14 (2014) 8783–8791.

Chau J.L.H., Lin Y.-M., Li A.-K., Su W.-F., Chang K.-S., Hsu S.L.-C., Li T.-L., Transparent high refractive index nanocomposite thin films, Mater Lett, 61 (2007) 2908–2910.

Checchetto R., Miotello A., Nicolais L., Carotenuto G., Gas transport through nanocomposite membrane composed by polyethylene with dispersed graphite nanoplatelets, J Membr Sci, 463 (2014) 196–204.

Chen J., Huang X., Sun B., Wang Y., Zhu Y., Jiang P., Vertically aligned and interconnected boron nitride nanosheets for advanced flexible nanocomposite thermal interface materials, ACS Appl Mater Interfaces, 9 (2017a) 30909–30917.

Chen J., Huang X., Zhu Y., Jiang P., Cellulose nanofiber supported 3D interconnected BN nanosheets for epoxy nanocomposites with ultrahigh thermal management capability, Adv Funct Mater, 27 (2017b) 1604754. DOI:10.1002/adfm.201604754

Chen W., Wang Z., Zhi C., Zhang W., High thermal conductivity and temperature probing of copper nanowire/upconversion nanoparticles/epoxy composite, Compos Sci Technol, 130 (2016) 63–69.

Chen Y., Wang R., Zhou J., Fan H., Shi B., Membrane formation temperature-dependent gas transport through thermo-sensitive polyurethane containing in situ-generated TiO_2 nanoparticles, Polymer, 52 (2011) 1856–1867.

Chen Z., Xie L., Huang X., Li S., Jiang P., Achieving large dielectric property improvement in polymer/carbon nanotube composites by engineering the nanotube surface via atom transfer radical polymerization, Carbon, 95 (2015) 895–903.

Choi B.-K., Park S.-J., Seo M.-K., Effect of graphene oxide on thermal, optical, and gas permeability of graphene oxide/poly(vinyl alcohol) hybrid films using the boric acid, J Nanosci Nanotechno, 17 (2017) 7368–7372.

Choi J.H., Song H.J., Jung J., Yu J.W., You N.-H., Goh M., Effect of crosslink density on thermal conductivity of epoxy/carbon nanotube nanocomposites, J Appl Polym Sci, 134 (2017) 44253. DOI: 10.1002/app.44253

Corbelli G., Ghisleri C., Marelli M., Milani P., Ravagnan L., Highly deformable nanostructured elastomeric electrodes with improving conductivity upon cyclical stretching, Adv Mater, 23 (2011) 4504–4508.

Cortes L.Q., Lonjon A., Dantras E., Lacabanne C., High-performance thermoplastic composites poly(ether ketone ketone)/silver nanowires: Morphological, mechanical and electrical properties, J Non-Cryst Solids, 391 (2014) 106–111.

Coskun S., Ates E.S., Unalan H.E., Optimization of silver nanowire networks for polymer light emitting diode electrodes, Nanotechnology, 24 (2013) 125202(8pp). http://stacks.iop.org/0957-4484/24/i=12/a=125202

Crippa F., Moore T.L., Mortato M., Geers C., Haeni L., Hirt A.M., Rothen-Rutishauser B., Petri-Fink A., Dynamic and biocompatible thermo-responsive magnetic hydrogels that respond to an alternating magnetic field, J Magn Magn Mater, 427 (2017) 212–219.

Culver S.P., Beier C.W., Rafson J.P., Brutchey R.L., Surface modification of $BaTiO_3$ inclusions in polydicyclopentadiene nanocomposites for energy storage, J Appl Polym Sci, 131 (2014) 40290. DOI: 10.1002/app.40290

Dallas P., Georgakilas V., Niarchos D., Komninou P., Kehagias T., Petridis D., Synthesis, characterization and thermal properties of polymer/magnetite nanocomposites, Nanotechnology, 17 (2006) 2046–2053.

Das B., Mandal M., Upadhyay A., Chattopadhyay P., Karak N., Bio-based hyperbranched polyurethane/Fe_3O_4 nanocomposites: smart antibacterial biomaterials for biomedical devices and implants, Biomed Mater, 8 (2013) 035003. http://stacks.iop.org/1748-605X/8/i=3/a=035003

Decker J.J., Meyers K.P., Paul D.R., Schiraldi D.A., Hiltner A., Nazarenko S., Polyethylene-based nanocomposites containing organoclay: A new approach to enhance gas barrier via multilayer coextrusion and interdiffusion, Polymer, 61 (2015) 42–54.

Delgado P.A., Brutman J.P., Masica K., Molde J., Wood B., Hillmyer M.A., High surface area carbon black (BP-2000) as a reinforcing agent for poly[(−)-lactide], J Appl Polym Sci, 133 (2016) 43926. DOI: 10.1002/app.43926

Deshmukh K., Ahamed M.B., Sadasivuni K.K., Ponnamma D., AlMaadeed M.A.-A., Deshmukh R.R., Pasha S.K.K., Polu A.R., Chidambaram K., Fumed SiO_2 nanoparticle reinforced biopolymer blend nanocomposites with high dielectric constant and low dielectric loss for flexible organic electronics, J Appl Polym Sci, 134 (2017) 44427. DOI: 10.1002/app.44427

Deshmukh R.D., Composto R.J., Surface segregation and formation of silver nanoparticles created in situ in poly(methyl methacrylate) films, Chem Mater, 19 (2007) 745–754.

Doganay D., Coskun S., Kaynak C., Unalan H.E., Electrical, mechanical and thermal properties of aligned silver nanowire/polylactide nanocomposite films, Compos Pt B-Eng, 99 (2016) 288–296.

Duncan T.V., Applications of nanotechnology in food packaging and food safety: Barrier materials, antimicrobials and sensors, J Colloid Interf Sci, 363 (2011) 1–24.

Eggersdorfer M.L., Pratsinis S.E., Agglomerates and aggregates of nanoparticles made in the gas phase, Adv Powder Technol, 25 (2014) 71–90.

Ehrhardt C., Fettkenhauer C., Glenneberg J., Munchgesang W., Leipner H.S., Diestelhorst M., Lemm S., Beige H., Ebbinghaus S.G., A solution-based approach to composite dielectric films of surface functionalized $CaCu_3Ti_4O_{12}$ and P(VDF-HFP), J Mater Chem A, 2 (2014) 2266–2274.

Faupel F., Zaporojtchenko V., Greve H., Schuermann U., Chakravadhanula V.S.K., Hanisch C., Kulkarni A., Gerber A., Quandt E., Podschun R., Deposition of nanocomposites by plasmas, Contrib Plasma Phys, 47 (2007) 537–544.

Faupel F., Zaporojtchenko V., Strunskus T., Elbahri M., Metal-polymer nanocomposites for functional applications, Adv Eng Mater, 12 (2010) 1177–1190.

Feldman D., Polymer Nanocomposite Barriers, J Macromol Sci Part A-Pure Appl Chem, 50 (2013) 441–448.

Feng Y., Li W.L., Hou Y.F., Yu Y., Cao W.P., Zhang T.D., Fei W.D., Enhanced dielectric properties of PVDF-HFP/$BaTiO_3$-nanowire composites induced by interfacial polarization and wire-shape, J Mater Chem C, 3 (2015) 1250–1260.

Fujiwara K., Deligiannakis Y., Skoutelis C.G., Pratsinis S.E., Visible-light active black TiO_2-Ag/TiO_x particles, Appl Catal B-Environ, 154 (2014) 9–15.

Gaume J., Taviot-Gueho C., Cros S., Rivaton A., Thérias S., Gardette J.-L., Optimization of PVA clay nanocomposite for ultra-barrier multilayer encapsulation of organic solar cells, Sol Energ Mat Sol C, 99 (2012) 240–249.

Geng Y., Liu M.Y., Li J., Shi X.M., Kim J.K., Effects of surfactant treatment on mechanical and electrical properties of CNT/epoxy nanocomposites, Compos Pt A-Appl Sci Manuf, 39 (2008) 1876–1883.

Ghazaryan G., Schaller R., Feldman K., Tervoort T.A., Rejuvenation of PLLA: Effect of plastic deformation and orientation on physical ageing in poly(l-lactic acid) films, J Polym Sci B Polym Phys, 54 (2016) 2233–2244.

Ghosh S., Rasmusson J., Inganäs O., Supramolecular self-assembly for enhanced conductivity in conjugated polymer blends: Ionic crosslinking in blends of poly(3,4-ethylenedioxythiophene)-poly(styrenesulfonate) and poly (vinylpyrrolidone), Adv Mater, 10 (1998) 1097–1099.

Gonçalves R., Martins P.M., Caparrós C., Martins P., Benelmekki M., Botelho G., Lanceros-Mendez S., Lasheras A., Gutiérrez J., Barandiarán J.M., Nucleation of the electroactive β-phase, dielectric and magnetic response of poly(vinylidene fluoride) composites with Fe_2O_3 nanoparticles, J Non-Cryst Solids, 361 (2013) 93–99.

González M., Martín-Fabiani I., Baselga J., Pozuelo J., Magnetic nanocomposites based on hydrogenated epoxy resin, Mater Chem Phys, 132 (2012) 618–624.

Grabowski C.A., Fillery S.P., Westing N.M., Chi C., Meth J.S., Durstock M.F., Vaia R.A., Dielectric breakdown in silica–amorphous polymer nanocomposite films: The role of the polymer matrix, ACS Appl Mater Interfaces, 5 (2013) 5486–5492.

Grass R.N., Stark W.J., Gas phase synthesis of fcc-cobalt nanoparticles, J Mater Chem, 16 (2006) 1825–1830.

Gyergyek S., Huskić M., Makovec D., Drofenik M., Superparamagnetic nanocomposites of iron oxide in a polymethyl methacrylate matrix synthesized by in situ polymerization, Colloids Surf A Physicochem Eng Asp, 317 (2008) 49–55.

Hao Y., Wang X., Bi K., Zhang J., Huang Y., Wu L., Zhao P., Xu K., Lei M., Li L., Significantly enhanced energy storage performance promoted by ultimate sized ferroelectric $BaTiO_3$ fillers in nanocomposite films, Nano Energy, 31 (2017) 49–56.

Hao Y.N., Bi K., O'Brien S., Wang X.X., Lombardi J., Pearsall F., Li W.L., Lei M., Wu Y., Li L.T., Interface structure, precursor rheology and dielectric properties of $BaTiO_3$/PVDF-hfp nanocomposite films prepared from colloidal perovskite nanoparticles, RSC Adv, 7 (2017) 32886–32892.

Haznedar G., Cravanzola S., Zanetti M., Scarano D., Zecchina A., Cesano F., Graphite nanoplatelets and carbon nanotubes based polyethylene composites: Electrical conductivity and morphology, Mater Chem Phys, 143 (2013) 47–52.

He X., He R., Liu A.l., Chen X., Zhao Z., Feng S., Chen N., Zhang M., A highly conductive, flexible, transparent composite electrode based on the lamination of silver nanowires and polyvinyl alcohol, J Mater Chem C, 2 (2014) 9737–9745.

Hou Y., Deng Y., Wang Y., Gao H., Uniform distribution of low content $BaTiO_3$ nanoparticles in poly(vinylidene fluoride) nanocomposite: Toward high dielectric breakdown strength and energy storage density, RSC Adv, 5 (2015) 72090–72098.

Hu P., Wang J., Shen Y., Guan Y., Lin Y., Nan C.-W., Highly enhanced energy density induced by hetero-interface in sandwich-structured polymer nanocomposites, J Mater Chem A, 1 (2013) 12321–12326.

Hu W., Niu X., Li L., Yun S., Yu Z., Pei Q., Intrinsically stretchable transparent electrodes based on silver-nanowire-cross-linked-polyacrylate composites, Nanotechnology, 23 (2012) 344002. http://stacks.iop.org/0957-4484/23/i=34/a=344002

Hu X., Johnson R.B., Schlea M.R., Kaur J., Shofner M.L., The effect of matrix morphology on nanocomposite properties, Polymer, 51 (2010) 748–754.

Hu Y.S., Prattipati V., Mehta S., Schiraldi D.A., Hiltner A., Baer E., Improving gas barrier of PET by blending with aromatic polyamides, Polymer, 46 (2005) 2685–2698.

Hua F., Cui T.H., Lvov Y.M., Ultrathin cantilevers based on polymer-ceramic nanocomposite assembled through layer-by-layer adsorption, Nano Lett, 4 (2004) 823–825.

Huang X., Zhi C., Jiang P., Toward effective synergetic effects from graphene nanoplatelets and carbon nanotubes on thermal conductivity of ultrahigh volume fraction nanocarbon epoxy composites, J Phys Chem C, 116 (2012) 23812–23820.

Huang Y., Qin Y., Zhou Y., Niu H., Yu Z.-Z., Dong J.-Y., Polypropylene/graphene oxide nanocomposites prepared by in situ ziegler−natta polymerization, Chem Mater, 22 (2010) 4096–4102.

Hudson J., Orviska M., European public opinion warms to nanotechnology, Nano Today, 4 (2009) 455–457.

Hummers W.S., Offeman R.E., Preparation of graphitic oxide, J Amer Chem Soc, 80 (1958) 1339–1339.

Iijima M., Kamiya H., Surface modification for improving the stability of nanoparticles in liquid media, KONA Powder Part J, 27 (2009) 119–129.

Im H., Kim J., Thermal conductivity of a graphene oxide–carbon nanotube hybrid/epoxy composite, Carbon, 50 (2012) 5429–5440.

Jain G., Kumar R., Electrical and optical properties of tin oxide and antimony doped tin oxide films, Opt Mater, 26 (2004) 27–31.

Jiang C.Y., Markutsya S., Tsukruk V.V., Collective and individual plasmon resonances in nanoparticle films obtained by spin-assisted layer-by-layer assembly, Langmuir, 20 (2004) 882–890.

Jiao J., Cui Y., Xia Y., Improved thermal conductivity of epoxy composites prepared with a mixed filler of multiwalled carbon nanotubes and aluminum nitride particles, High Perform Polym, 29 (2017) 484–492.

Jin F., Zheng M.-L., Zhang M.-L., Zhao Z.-S., Duan X.-M., A facile layer-by-layer assembly method for the fabrication of fluorescent polymer/quantum dot nanocomposite thin films, RSC Adv, 4 (2014) 33206–33214.

Jo I., Pettes M.T., Kim J., Watanabe K., Taniguchi T., Yao Z., Shi L., Thermal conductivity and phonon transport in suspended few-layer hexagonal boron nitride, Nano Lett, 13 (2013) 550–554.

Kan-Dapaah K., Rahbar N., Soboyejo W., Implantable magnetic nanocomposites for the localized treatment of breast cancer, J Appl Phys, 116 (2014) 233505(11pp). DOI:10.1063/1.4903736

Karttunen M., Ruuskanen P., Pitkänen V., Albers W.M., Electrically conductive metal polymer nanocomposites for electronics applications, J Electron Mater, 37 (2008) 951–954.

Kim H.M., Kim K., Lee C.Y., Joo J., Cho S.J., Yoon H.S., Pejakovic D.A., Yoo J.W., Epstein A.J., Electrical conductivity and electromagnetic interference shielding of multiwalled carbon nanotube composites containing Fe catalyst, Appl Phys Lett, 84 (2004) 589–591.

Kim K., Kim J., Exfoliated boron nitride nanosheet/MWCNT hybrid composite for thermal conductive material via epoxy wetting, Compos Pt B-Eng, 140 (2018) 9–15.

Kim P., Shi L., Majumdar A., McEuen P.L., Thermal transport measurements of individual multiwalled nanotubes, Phys Rev Lett, 87 (2001) 215502(4pp). DOI:10.1103/PhysRevLett.87.215502

Kim Y.-S., Chang M.-H., Lee E.-J., Ihm D.-W., Kim J.-Y., Improved electrical conductivity of PEDOT-based electrode films hybridized with silver nanowires, Synth Met, 195 (2014) 69–74.

Kleinjan W.E., Brokken-Zijp J.C.M., van de Belt R., Chen Z., de With G., Antimony-doped tin oxide nanoparticles for conductive polymer nanocomposites, J Mater Res, 23 (2008) 869–880.

Koh H.C., Park J.S., Jeong M.A., Hwang H.Y., Hong Y.T., Ha S.Y., Nam S.Y., Preparation and gas permeation properties of biodegradable polymer/layered silicate nanocomposite membranes, Desalination, 233 (2008) 201–209.

Kojima M., Kato H., Gatto M., Blackening of tin oxide thin-films heavily-doped with antimony, Philos Mag B, 68 (1993) 215–222.

Kong J.-H., Jang N.-S., Kim S.-H., Kim J.-M., Simple and rapid micropatterning of conductive carbon composites and its application to elastic strain sensors, Carbon, 77 (2014) 199–207.

Kong S.M., Mariatti M., Busfield J.J.C., Effects of types of fillers and filler loading on the properties of silicone rubber composites, J Reinf Plast Compos, 30 (2011) 1087–1096.

Kotsilkova R., Nesheva D., Nedkov I., Krusteva E., Stavrev S., Rheological, electrical, and microwave properties of polymers with nanosized carbon particles, J Appl Polym Sci, 92 (2004) 2220–2227.

Kovacs G., Düring L., Michel S., Terrasi G., Stacked dielectric elastomer actuator for tensile force transmission, Sens Actuator A-Phys, 155 (2009) 299–307.

Kuang Z., Chen Y., Lu Y., Liu L., Hu S., Wen S., Mao Y., Zhang L., Fabrication of highly oriented hexagonal boron nitride nanosheet/elastomer nanocomposites with high thermal conductivity, Small, 11 (2015) 1655–1659.

Kujawski M., Pearse J., Smela E., PDMS/graphite stretchable electrodes for dielectric elastomer actuators, in: Bar-Cohen Y. (Ed.), Electroactive Polymer Actuators and Devices, (2010) pp.76420R 76421–76429.

Kumar A., Zhou C.W., The race to replace tin-doped indium oxide: Which material will win?, ACS Nano, 4 (2010) 11–14.

Kusunose T., Yagi T., Firoz S.H., Sekino T., Fabrication of epoxy/silicon nitride nanowire composites and evaluation of their thermal conductivity, J Mater Chem A, 1 (2013) 3440–3445.

Langley D., Giusti G., Mayousse C., Celle C., Bellet D., Simonato J.-P., Flexible transparent conductive materials based on silver nanowire networks: A review, Nanotechnology, 24 (2013) 452001. http://stacks.iop.org/0957-4484/24/i=45/a=452001

Latko-Durałek P., Macutkevic J., Kay C., Boczkowska A., McNally T., Hot-melt adhesives based on co-polyamide and multiwalled carbon nanotubes, J Appl Polym Sci, 135 (2018) 45999. DOI:10.1002/app.45999

Laurent C., Flahaut E., Peigney A., The weight and density of carbon nanotubes versus the number of walls and diameter, Carbon, 48 (2010) 2994–2996.

Lee C., Jug L., Meng E., High strain biocompatible polydimethylsiloxane-based conductive graphene and multiwalled carbon nanotube nanocomposite strain sensors, Appl Phys

Lett, 102 (2013) 183511(5pp). DOI:10.1063/1.4804580

Lee K.W., Chung J.W., Kwak S.-Y., Flexible poly(vinyl chloride) nanocomposites reinforced with hyperbranched polyglycerol–functionalized graphene oxide for enhanced gas barrier performance, ACS Appl Mater Interfaces, 9 (2017) 33149-33158.

Lee P., Ham J., Lee J., Hong S., Han S., Suh Y.D., Lee S.E., Yeo J., Lee S.S., Lee D., Ko S.H., Highly stretchable or transparent conductor fabrication by a hierarchical multiscale hybrid nanocomposite, Adv Funct Mater, 24 (2014) 5671–5678.

Lei Q., Dancer C.E.J., Grovenor C.R.M., Grant P.S., Preparation, microstructure and microwave dielectric properties of sprayed PFA/barium titanate composite films, Compos Sci Technol, 129 (2016) 198–204.

Li D., Teoh W.Y., Selomulya C., Woodward R.C., Munroe P., Amal R., Insight into microstructural and magnetic properties of flame-made γ-Fe_2O_3 nanoparticles, J Mater Chem, 17 (2007) 4876–4884.

Li M., Gao C., Hu H., Zhao Z., Electrical conductivity of thermally reduced graphene oxide/polymer composites with a segregated structure, Carbon, 65 (2013) 371–373.

Litvinov V.M., Barthel H., Weis J., Structure of a PDMS layer grafted onto a silica surface studied by means of DSC and solid-state NMR, Macromolecules, 35 (2002) 4356–4364.

Liu S., Xiao S., Xiu S., Shen B., Zhai J., An Z., Poly(vinylidene fluoride) nanocomposite capacitors with a significantly enhanced dielectric constant and energy density by filling with surface-fluorinated $Ba_{0.6}Sr_{0.4}TiO_3$ nanofibers, RSC Adv, 5 (2015) 40692–40699.

Liu S., Xiu S., Shen B., Zhai J., Kong L., Dielectric properties and energy storage densities of poly(vinylidenefluoride) nanocomposite with surface hydroxylated cube shaped $Ba_{0.6}Sr_{0.4}TiO_3$ nanoparticles, Polymers, 8 (2016) 45(11pp). DOI:10.3390/polym8020045

Liu S., Zhai J., Wang J., Xue S., Zhang W., Enhanced energy storage density in poly(vinylidene fluoride) nanocomposites by a small loading of surface-hydroxylated $Ba_{0.6}Sr_{0.4}TiO_3$ nanofibers, ACS Appl Mater Interfaces, 6 (2014) 1533–1540.

Lizundia E., Pérez-Álvarez L., Sáenz-Pérez M., Patrocinio D., Vilas J.L., León L.M., Physical aging and mechanical performance of poly(L-lactide)/ZnO nanocomposites, J Appl Polym Sci, 133 (2016) 43619. DOI: 10.1002/app.43619

Lizundia E., Sarasua J.R., Physical aging in poly(L-lactide) and its multi-wall carbon nanotube nanocomposites, Macromol Symp, 321-322 (2012) 118–123.

Long T.C., Saleh N., Tilton R.D., Lowry G.V., Veronesi B., Titanium dioxide (P25) produces reactive oxygen species in immortalized brain microglia (BV2): Implications for nanoparticle neurotoxicity, Environ Sci Technol, 40 (2006) 4346–4352.

López D., Cendoya I., Torres F., Tejada J., Mijangos C., Preparation and characterization of polystyrene-based magnetic nanocomposites. Thermal, mechanical and magnetic properties, Polym Eng Sci, 41 (2001) 1845–1852.

Luong N.D., Hippi U., Korhonen J.T., Soininen A.J., Ruokolainen J., Johansson L.-S., Nam J.-D., Sinh L.H., Seppälä J., Enhanced mechanical and electrical properties of polyimide film by graphene sheets via in situ polymerization, Polymer, 52 (2011) 5237–5242.

Malas A., Bharati A., Verkinderen O., Goderis B., Moldenaers P., Cardinaels R., Effect of the GO reduction method on the dielectric properties, electrical conductivity and crystalline behavior of PEO/rGO nanocomposites, Polymers, 9 (2017) 613(21pp). DIO:10.3390/polym9110613

Manika G.C., Psarras G.C., Energy storage and harvesting in $BaTiO_3$ epoxy nanodielectrics, High Voltage, 1 (2016) 151–157.

Mao M., Zhou C., Shen H., Wang H., Wang S., Li L.S., Bright, transparent, and light-emitting films using fluorescent QDs–polystyrene composite microspheres, Mater Lett, 111 (2013) 97–100.

Mao Y., Guo J., Hu C., Yang H., Yang Y., Chen S., A low-cost, highly-conductive polyvinyl alcohol flexible film with Ag-microsheets and AgNWs as fillers, RSC Adv, 6 (2016) 80905–80909.

Mapkar J.A., Belashi A., Berhan L.M., Coleman M.R., Formation of high loading flexible carbon nanofiber network composites, Compos Sci Technol, 75 (2013) 1–6.

Marconnet A.M., Yamamoto N., Panzer M.A., Wardle B.L., Goodson K.E., Thermal conduction in aligned carbon nanotube–polymer nanocomposites with high packing density, ACS Nano, 5 (2011) 4818–4825.

Marelli M., Divitini G., Collini C., Ravagnan L., Corbelli G., Ghisleri C., Gianfelice A., Lenardi C., Milani P., Lorenzelli L., Flexible and biocompatible microelectrode arrays fabricated by supersonic cluster beam deposition on SU-8, J Micromech Microeng, 21 (2011) 45013(16pp). http://stacks.iop.org/0960-1317/21/i=4/a=045013

Mark J.E., Polymer Data Handbook, Oxford University Press, New York, NY (USA), 2009.

Matthews R.A.J., The science of Murphy's law, Sci Am, 276 (1997) 88–91.

Mitsumata T., Horikoshi Y., Negami K., High-power actuators made of two-phase magnetic gels, Jap J Appl Phys, 47 (2008) 7257. http://stacks.iop.org/1347-4065/47/i=9R/a=7257

Mohsen-Nia M., Mohammad Doulabi F.S., Preparation and characterization of $CoFe_2O_4$/Polyvinyl acetate nanocomposite, Polym-Plast Technol Eng, 51 (2012) 1122–1126.

Moreira D.C., Braga Junior N.R., Benevides R.O., Sphaier L.A., Nunes L.C.S., Temperature-dependent thermal conductivity of silicone-Al_2O_3 nanocomposites, Appl Phys A-Mater Sci Process, 121 (2015) 1227–1234.

Moreira D.C., Braga N.R.J., Sphaier L.A., Nunes L.C., Size effect on the thermal intensification of alumina-filled nanocomposites, J Compos Mater 50 (2016) 3699–3707.

Moreira D.C., Sphaier L.A., Reis J.M.L., Nunes L.C.S., Experimental investigation of heat conduction in polyester–Al_2O_3 and polyester–CuO nanocomposites, Exp Therm Fluid Sci, 35 (2011) 1458–1462.

Moreno I., Navascues N., Arruebo M., Irusta S., Santamaria J., Facile preparation of transparent and conductive polymer films based on silver nanowire/polycarbonate nanocomposites, Nanotechnology, 24 (2013) 275603. http://stacks.iop.org/0957-4484/24/i=27/a=275603

Müller V., Rasp M., Štefanić G., Ba J., Günther S., Rathousky J., Niederberger M., Fattakhova-Rohlfing D., Highly conducting nanosized monodispersed antimony-doped tin oxide particles synthesized via nonaqueous sol−gel procedure, Chem Mater, 21 (2009) 5229–5236.

Mutiso R.M., Winey K.I., Electrical Conductivity of Polymer Nanocomposites, in: Matyjaszewski K., Möller M. (Eds.), Polymer Science: A Comprehensive Reference, Elsevier, Amsterdam (2012) pp.327–344.

Nadiv R., Shachar G., Peretz-Damari S., Varenik M., Levy I., Buzaglo M., Ruse E., Regev O., Performance of nanocarbon loaded polymer composites: Dimensionality matters, Carbon, 126 (2018) 410–418.

Nessim G.D., Properties, synthesis, and growth mechanisms of carbon nanotubes with special focus on thermal chemical vapor deposition, Nanoscale, 2 (2010) 1306–1323.

Nguyen D.T., Kim K.-S., Controlled magnetic properties of iron oxide-based nanoparticles for smart therapy, KONA Powder Part J, 33 (2016) 33–47.

Nguyen T.H.L., Quiroga Cortes L., Lonjon A., Dantras E., Lacabanne C., High conductive Ag nanowire–polyimide composites: Charge transport mechanism in thermoplastic thermostable materials, J Non-Cryst Solids, 385 (2014) 34–39.

Nguyen V.Q., Ahmed A.S., Ramanujan R.V., Morphing soft magnetic composites, Adv Mater, 24 (2012) 4041–4054.

Niu Y., Bai Y., Yu K., Wang Y., Xiang F., Wang H., Effect of the modifier structure on the performance of barium titanate/poly(vinylidene fluoride) nanocomposites for energy storage applications, ACS Appl Mater Interfaces, 7 (2015) 24168–24176.

Noh Y.J., Kim S.S., Kim T.W., Na S.I., Effect of sheet resistance of Ag-nanowire-based electrodes on cell-performances of ITO-free organic solar cells, Semicond Sci Technol, 28 (2013) 125008. http://stacks.iop.org/0268-1242/28/i=12/a=125008

Norkhairunnisa M., Azizan A., Mariatti M., Ismail H., Sim L.C., Thermal stability and electrical behavior of polydimethylsiloxane nanocomposites with carbon nanotubes and carbon black fillers, J Compos Mater, 46 (2012) 903–910.

Nunes-Pereira J., Sencadas V., Correia V., Cardoso V.F., Han W., Rocha J.G., Lanceros-Méndez S., Energy harvesting performance of $BaTiO_3$/poly(vinylidene fluoride–trifluoroethylene) spin coated nanocomposites, Compos Pt B-Eng, 72 (2015) 130–136.

Ohtani B., Ogawa Y., Nishimoto S.-i., Photocatalytic activity of amorphous−anatase mixture of titanium(IV) oxide particles suspended in aqueous solutions, J Phys Chem B, 101 (1997) 3746–3752.

Pan W., Zhang H., Chen Y., Electrical and Mechanical Properties of PMMA/nano-ATO Composites, J Mater Sci Technol, 25 (2009) 247–250.

Pan W., Zou H., Characterization of PAN/ATO nanocomposites prepared by solution blending, Bull Mater Sci, 31 (2008) 807–811.

Pan Y.-X., Yu Z.-Z., Ou Y.-C., Hu G.-H., A new process of fabricating electrically conducting nylon 6/graphite nanocomposites via intercalation polymerization, J Polym Sci Pt B-Polym Phys, 38 (2000) 1626–1633.

Pan Z., Yao L., Zhai J., Yang K., Shen B., Wang H., Ultrafast discharge and high-energy-density of polymer nanocomposites achieved via optimizing the structure design of barium titanates, ACS Sustain Chem Eng, 5 (2017) 4707–4717.

Pang H., Chen T., Zhang G., Zeng B., Li Z.-M., An electrically conducting polymer/graphene composite with a very low percolation threshold, Mater Lett, 64 (2010) 2226–2229.

Pantoja-Castro M.A., Perez-Robles J.F., Gonzalez-Rodriguez H., Vorobiev-Vasilievitch Y., Martinez-Tejada H.V., Velasco-Santos C., Synthesis and investigation of PMMA films with homogeneously dispersed multiwalled carbon nanotubes, Mater Chem Phys, 140 (2013) 458–464.

Paredes M., Angammana C.J., Jayaram S.H., Experimental study of dielectric properties of fumed silica/silicone composites, IEEE Conf Electr Insul Dielectr Phenom (CEIDP), (2016) 683–686. DOI: 10.1109/CEIDP.2016.7785689

Park C., Ounaies Z., Watson K.A., Crooks R.E., Smith J., Lowther S.E., Connell J.W., Siochi E.J., Harrison J.S., Clair T.L.S., Dispersion of single wall carbon nanotubes by in situ polymerization under sonication, Chem Phys Lett, 364 (2002) 303–308.

Park K., Kittelson D.B., Zachariah M.R., McMurry P.H., Measurement of inherent material density of nanoparticle agglomerates, J Nanopart Res, 6 (2004) 267–272.

Phatharapeetranun N., Ksapabutr B., Marani D., Bowen J.R., Esposito V., 3D-printed barium titanate/poly(vinylidene fluoride) nano-hybrids with anisotropic dielectric properties, J Mater Chem C, 5 (2017) 12430–12440.

Picard E., Gerard J.F., Espuche E., Reinforcement of the gas barrier properties of polyethylene and polyamide through the nanocomposite approach: Key factors and limitations, Oil Gas Sci Technol, 70 (2015) 237–249.

Poddar M.K., Pradhan S., Moholkar V.S., Arjmand M., Sundararaj U., Ultrasound–assisted synthesis and characterization of polymethyl methacrylate/reduced graphene oxide nanocomposites, AIChE J, 64 (2018) 673–687.

Priolo M.A., Gamboa D., Holder K.M., Grunlan J.C., Super gas barrier of transparent polymer−clay multilayer ultrathin films, Nano Lett, 10 (2010) 4970–4974.

Pu Z., Zheng X., Tian Y., Hu L., Zhong J., Flexible ultra-high-temperature polymer-based dielectrics with high permittivity for film capacitor applications, Polymers, 9 (2017) 596(12pp). DOI:10.3390/polym9110596

Puig J., Hoppe C.E., Fasce L.A., Pérez C.J., Piñeiro-Redondo Y., Bañobre-López M., López-Quintela M.A., Rivas J., Williams R.J.J., Superparamagnetic Nanocomposites based on the dispersion of oleic acid-stabilized magnetite nanoparticles in a diglycidylether of bisphenol A-based epoxy matrix: Magnetic, hyperthermia and shape memory, J Phys Chem C, 116 (2012) 13421–13428.

Pullanchiyodan A., S. Nair K., Surendran K.P., Silver-decorated boron nitride nanosheets as an effective hybrid filler in PMMA for high-thermal-conductivity electronic substrates, ACS Omega, 2 (2017) 8825–8835.

Pyrgiotakis G., Blattmann C.O., Pratsinis S., Demokritou P., Nanoparticle–nanoparticle interactions in biological media by atomic force microscopy, Langmuir, 29 (2013) 11385–11395.

Qi X.-Y., Yan D., Jiang Z., Cao Y.-K., Yu Z.-Z., Yavari F., Koratkar N., Enhanced electrical conductivity in polystyrene nanocomposites at ultra-low graphene content, ACS Appl Mater Interfaces, 3 (2011) 3130–3133.

Qiao Y., Islam M.S., Wang L., Yan Y., Zhang J., Benicewicz B.C., Ploehn H.J., Tang C., Thiophene polymer-grafted barium titanate nanoparticles toward nanodielectric composites, Chem Mater, 26 (2014) 5319–5326.

Rai A., Moore A.L., Enhanced thermal conduction and influence of interfacial resistance within flexible high aspect ratio copper nanowire/polymer composites, Compos Sci Technol, 144 (2017) 70–78.

Ramesh G.V., Porel S., Radhakrishnan T.P., Polymer thin films embedded with in situ grown metal nanoparticles, Chem Soc Rev, 38 (2009) 2646–2656.

Ravagnan L., Divitini G., Rebasti S., Marelli M., Piseri P., Milani P., Poly(methyl methacrylate)-palladium clusters nanocomposite formation by supersonic cluster beam deposition: a method for microstructured metallization of polymer surfaces, J Phys D Appl Phys, 42 (2009) 82002(11pp). http://stacks.iop.org/0022-3727/42/i=8/a=082002

Rivière L., Lonjon A., Dantras E., Lacabanne C., Olivier P., Gleizes N.R., Silver fillers aspect ratio influence on electrical and thermal conductivity in PEEK/Ag nanocomposites, Eur Polym J, 85 (2016) 115–125.

Roilo D., Patil P.N., Brusa R.S., Miotello A., Aghion S., Ferragut R., Checchetto R., Polymer rigidification in graphene based nanocomposites: Gas barrier effects and free volume reduction, Polymer, 121 (2017) 17–25.

Roppolo I., Castellino M., Bejtka K., Rizza G., Perrone D., Coulon P.-E., Chiappone A., Rajan K., Bocchini S., Ricciardi C., Pirri C.F., Chiolerio A., Resistive switching in polymer nanocomposites by matrix-controlled in situ nanoparticles generation, J Phys Chem C, 121 (2017) 14285–14295.

Rumble J.R. ed., CRC Handbook of Chemistry and Physics, 98th Edition (Internet Version), CRC Press/Taylor & Francis, Boca Raton, Florida, 2018.

Sadeghi M., Semsarzadeh M.A., Moadel H., Enhancement of the gas separation properties of polybenzimidazole (PBI) membrane by incorporation of silica nano particles, J Membr Sci, 331 (2009) 21–30.

Saffari J., Ghanbari D., Mir N., Khandan-Barani K., Sonochemical synthesis of $CoFe_2O_4$ nanoparticles and their application in magnetic polystyrene nanocomposites, J Ind Eng Chem, 20 (2014) 4119–4123.

Sahoo Y., Goodarzi A., Swihart M.T., Ohulchanskyy T.Y., Kaur N., Furlani E.P., Prasad P.N., Aqueous ferrofluid of magnetite nanoparticles: Fluorescence labeling and magnetophoretic control, J Phys Chem B, 109 (2005) 3879–3885.

Salimi M., Pirouzfar V., Kianfar E., Enhanced gas transport properties in silica nanoparticle filler-polystyrene nanocomposite membranes, Colloid Polym Sci, 295 (2017) 215–226.

Sandu I., Florescu L.G., Fleaca C., Dragomirescu A., Nanocarbon film as a percolation network for nanocarbon/polymer composites, J Reinf Plast Compos, 28 (2009) 2397–2404.

Sapalidis A.A., Katsaros F.K., Steriotis T.A., Kanellopoulos N.K., Properties of poly(vinyl alcohol)—bentonite clay nanocomposite films in relation to polymer–clay interactions, J Appl Polym Sci, 123 (2012) 1812–1821.

Sarıtaş S., Eşsiz S., Sarı B., Synthesis and characterization of foldable and magnetic field-sensitive, freestanding poly(vinyl acetate)/poly(vinyl chloride)/polyfuran composite and nanocomposite films, J Magn Magn Mater, 433 (2017) 120–130.

Savva I., Constantinou D., Marinica O., Vasile E., Vekas L., Krasia-Christoforou T., Fabrication and characterization of superparamagnetic poly(vinyl pyrrolidone)/poly(L-lactide)/Fe_3O_4 electrospun membranes, J Magn Magn Mater, 352 (2014) 30–35.

Schädli G.N., Büchel R., Pratsinis S.E., Nanogenerator power output: influence of particle size and crystallinity of $BaTiO_3$, Nanotechnology, 28 (2017) 275705. http://stacks.iop.org/0957-4484/28/i=27/a=275705

Schneider R., Lüthi S.R., Albrecht K., Brülisauer M., Bernard A., Geiger T., Transparent silicone calcium fluoride nanocomposite with improved thermal conductivity, Macromol Mater Eng, 300 (2015) 80–85.

Schulz H., Schimmöller B., Pratsinis S.E., Salz U., Bock T., Radiopaque dental adhesives: Dispersion of flame-made Ta_2O_5/SiO_2 nanoparticles in methacrylic matrices, J Dent, 36 (2008) 579–587.

Schürmann U., Hartung W., Takele H., Zaporojtchenko V., Faupel F., Controlled syntheses of Ag-polytetrafluoroethylene nanocomposite thin films by co-sputtering from two magnetron sources, Nanotechnology, 16 (2005) 1078–1082.

Schwarz-Plaschg C., Nanotechnology is like… The rhetorical roles of analogies in public engagement, Public Underst Sci, 27 (2016) 153–167.

Seshadri I., Esquenazi G.L., Cardinal T., Borca-Tasciuc T., Ramanath G., Microwave synthesis of branched silver nanowires and their use as fillers for high thermal conductivity polymer composites, Nanotechnology, 27 (2016) 175601. http://stacks.iop.org/0957-4484/27/i=17/a=175601

Shang S., Gan L., Yuen M.C.-W., Jiang S.-X., Mei Luo N., Carbon nanotubes based high temperature vulcanized silicone rubber nanocomposite with excellent elasticity and electrical properties, Comp Pt A-Appl Sci Manuf, 66 (2014) 135–141.

Shieh Y.-T., Lin Y.-S., Twu Y.-K., Tsai H.-B., Lin R.-H., Effect of crystallinity on enthalpy recovery peaks and cold-crystallization peaks in PET via TMDSC and DMA studies, J Appl Polym Sci, 116 (2010) 1334–1341.

Shima H., Kawai T., Matsushima Y., Unuma H., Kawamura K., Li Z., Kawashita M., Magnetite fine particles highly loaded PMMA microspheres for hyperthermia of deep-seated cancer, J Ceram Soc Jap, 121 (2013) 802–806.

Shimazaki Y., Hojo F., Takezawa Y., Highly thermoconductive polymer nanocomposite with a nanoporous α-alumina sheet, ACS Appl Mater Inter, 1 (2009) 225–227.

Siddabattuni S., Schuman T.P., Dogan F., Improved polymer nanocomposite dielectric breakdown performance through barium titanate to epoxy interface control, Mater Sci Eng B, 176 (2011) 1422–1429.

Singh D., Sotiriou G.A., Zhang F., Mead J., Bello D., Wohlleben W., Demokritou P., End-of-life thermal decomposition of nano-enabled polymers: effect of nanofiller loading and polymer matrix on by-products, Environ-Sci Nano, 3 (2016) 1293–1305.

Singh L., Ludovice P.J., Henderson C.L., Influence of molecular weight and film thickness on the glass transition temperature and coefficient of thermal expansion of supported ultrathin polymer films, Thin Solid Films, 449 (2004) 231–241.

Slobodian P., Lengálová A., Sáha P., Šlouf M., Poly(methyl methacrylate)/multi-wall carbon nanotubes composites prepared by solvent cast technique: Composites electrical percolation threshold, J Reinf Plast Compos, 26 (2007) 1705–1712.

Sobkowicz M.J., Sosa R., Dorgan J.R., Supramolecular bionanocomposites, part 2: Effects of carbon nanoparticle surface functionality on polylactide crystallization, J Appl Polym Sci, 121 (2011) 2029–2038.

Soloukhin V.A., Brokken-Zijp J.C.M., de with G., Conductive ATO-acrylate nanocomposite hybrid coatings: Experimental results and modeling, J Polym Sci Pt B-Polym Phys, 45 (2007) 2147–2160.

Sommertune J., Sugunan A., Ahniyaz A., Bejhed R.S., Sarwe A., Johansson C., Balceris C., Ludwig F., Posth O., Fornara A., Polymer/iron oxide nanoparticle composites- A straight forward and scalable synthesis approach, Int J Mol Sci, 16 (2015) 19752–19768.

Song W.-L., Wang P., Cao L., Anderson A., Meziani M.J., Farr A.J., Sun Y.-P., Polymer/boron nitride nanocomposite materials for superior thermal transport performance, Angew Chem-Int Edit, 51 (2012) 6498–6501.

Sotiriou G.A., Blattmann C.O., Pratsinis S.E., Flexible, multifunctional, magnetically actuated nanocomposite films, Adv Funct Mater, 23 (2013) 34–41.

Sotiriou G.A., Diaz E., Long M.S., Godleski J., Brain J., Pratsinis S.E., Demokritou P., A novel platform for pulmonary and cardiovascular toxicological characterization of inhaled engineered nanomaterials, Nanotoxicology, 6 (2012a) 680–690.

Sotiriou G.A., Meyer A., Knijnenburg J.T.N., Panke S., Pratsinis S.E., Quantifying the origin of released Ag^+ ions from nanosilver, Langmuir, 28 (2012b) 15929–15936.

Southward R.E., Thompson D.S., Thompson D.W., Caplan M.L., St. Clair A.K., Synthesis of reflective polyimide films via in situ silver(I) reduction, Chem Mater, 7 (1995) 2171–2180.

Sperling L.H., Glass-rubber transition behavior, Introduction to Physical Polymer Science, John Wiley & Sons, Inc., (2005) pp.349–425.

Stankovich S., Dikin D.A., Dommett G.H.B., Kohlhaas K.M., Zimney E.J., Stach E.A., Piner R.D., Nguyen S.T., Ruoff R.S., Graphene-based composite materials, Nature, 442 (2006) 282–286. DOI: 10.1038/nature04969

Steinmann W., Vad T., Weise B., Wulfhorst J., Seide G., Gries T., Heidelmann M., Weirich T., Extrusion of CNT-modified polymers with low viscosity—Influence of crystallization and CNT orientation on the electrical property, Polym Polym Compos, 21 (2013) 473–482.

Sun J., Gerberich W.W., Francis L.F., Electrical and optical properties of ceramic-polymer nanocomposite coatings, J Polym Sci Pt B-Polym Phys, 41 (2003) 1744–1761.

Sun J., Zhang Q., Guo F., Gu J., Zhang J., Preparation and characterization of magnetic polyimide hybrid thin films, J Appl Polym Sci, 125 (2012) 725–730.

Sun L., O'Reilly J.Y., Tien C.-W., Sue H.-J., Preparation of electrically conductive polystyrene/carbon nanofiber nanocomposite films, J Chem Educ, 85 (2008) 1105. DOI: 10.1021/ed085p1105

Suriati G., Mariatti M., Azizan A., Effects of filler shape and size on the properties of silver filled epoxy composite for electronic applications, J Mater Sci -Mater Electron, 22 (2011) 56–63.

Suter M., Ergeneman O., Zurcher J., Moitzi C., Pane S., Rudin T., Pratsinis S.E., Nelson B.J., Hierold C., A photopatternable superparamagnetic nanocomposite: Material characterization and fabrication of microstructures, Sens Actuator B-Chem, 156 (2011a) 433–443.

Suter M., Ergeneman O., Zürcher J., Schmid S., Camenzind A., Nelson B.J., Hierold C., Superparamagnetic photocurable nanocomposite for the fabrication of microcantilevers, J Micromech Microeng, 21 (2011b) 25023(9pp). http://stacks.iop.org/0960-1317/21/i=2/a=025023

Taccola S., Desii A., Pensabene V., Fujie T., Saito A., Takeoka S., Dario P., Menciassi A., Mattoli V., Free-standing poly(L-lactic acid) nanofilms loaded with superparamagnetic nanoparticles, Langmuir, 27 (2011) 5589–5595.

Tanaka T., Kozako M., Fuse N., Ohki Y., Proposal of a multicore model for polymer nanocomposite dielectrics, IEEE Trns Dielectr Electr Insul, 12 (2005) 669–681.

Tang H., Lin Y., Sodano H.A., Enhanced energy storage in nanocomposite capacitors through aligned PZT nanowires by uniaxial strain assembly, Adv Energy Mater, 2 (2012) 469–476.

Tang H., Lin Y., Sodano H.A., Synthesis of high aspect ratio $BaTiO_3$ nanowires for high energy density nanocomposite capacitors, Adv Energy Mater, 3 (2013) 451–456.

Tang H., Sodano H.A., Ultra high energy density nanocomposite capacitors with fast discharge using $Ba_{0.2}Sr_{0.8}TiO_3$ nanowires, Nano Lett, 13 (2013) 1373–1379.

Tang H., Zhou Z., Sodano H.A., Relationship between $BaTiO_3$ Nanowire Aspect Ratio and the Dielectric Permittivity of Nanocomposites, ACS Appl Mater Interfaces, 6 (2014) 5450–5455.

Tao P., Viswanath A., Li Y., Siegel R.W., Benicewicz B.C., Schadler L.S., Bulk transparent epoxy nanocomposites filled with poly(glycidyl methacrylate) brush-grafted TiO_2 nanoparticles, Polymer, 54 (2013) 1639–1646.

Tee D.I., Mariatti M., Azizan A., See C.H., Chong K.F., Effect of silane-based coupling agent on the properties of silver nanoparticles filled epoxy composites, Compos Sci Technol, 67 (2007) 2584–2591.

Thanki A.A., Goyal R.K., Study on effect of cubic- and tetragonal phased $BaTiO_3$ on the electrical and thermal properties of polymeric nanocomposites, Mater Chem Phys, 183 (2016) 447–456.

Thuau D., Koutsos V., Cheung R., Electrical and mechanical properties of carbon nanotube-polyimide composites, J Vac Sci Technol B Microelectron Nanometer Struct Process Meas Phenom, 27 (2009) 3139–3144.

Tirumali M., Kandasubramanian B., Kumaraswamy A., Subramani N.K., B S., Fabrication, physicochemical characterizations and electrical conductivity studies of modified carbon nanofiber-reinforced epoxy composites: Effect of 1-butyl-3-methylimidazolium tetrafluoroborate ionic liquid, Polym-Plast Technol Eng, 57 (2018) 218–228.

Tjong S.C., Liang G.D., Bao S.P., Effects of crystallization on dispersion of carbon nanofibers and electrical properties of polymer nanocomposites, Polym Eng Sci, 48 (2008) 177–183.

Tkalya E., Ghislandi M., Otten R., Lotya M., Alekseev A., van der Schoot P., Coleman J., de With G., Koning C., Experimental and theoretical study of the influence of the state of dispersion of graphene on the percolation threshold of conductive graphene/polystyrene nanocomposites, ACS Appl Mater Interfaces, 6 (2014) 15113–15121.

Tohma T., Masumoto H., Goto T., Microstructure and dielectric properties of barium titanate film prepared by MOCVD, Mater Trans, 43 (2002) 2880–2884.

Totaro M., Mondini A., Bellacicca A., Milani P., Beccai L., Integrated simultaneous detection of tactile and bending cues for soft robotics, Soft Robot, 4 (2017) 400–410.

Triambulo R.E., Cheong H.-G., Park J.-W., All-solution-processed foldable transparent electrodes of Ag nanowire mesh and metal matrix films for flexible electronics, Org Electron, 15 (2014) 2685–2695.

Viventi J., Kim D.-H., Vigeland L., Frechette E.S., Blanco J.A., Kim Y.-S., Avrin A.E., Tiruvadi V.R., Hwang S.-W., Vanleer A.C., Wulsin D.F., Davis K., Gelber C.E., Palmer L., Van der Spiegel J., Wu J., Xiao J., Huang Y., Contreras D., Rogers J.A., Litt B., Flexible, foldable, actively multiplexed, high-density electrode array for mapping brain activity in vivo, Nat Neurosci, 14 (2011) 1599–1605.

Wang D., Huang M., Zha J.W., Zhao J., Dang Z.M., Cheng Z., Dielectric properties of polystyrene based composites filled with core-shell $BaTiO_3$ polystyrene hybrid nanoparticles, IEEE Trans Dielectr Electr Insul, 21 (2014) 1438–1445.

Wang F., Yao Y., Zeng X., Huang T., Sun R., Xu J., Wong C.-P., Highly thermally conductive polymer nanocomposites based on boron nitride nanosheets decorated with silver nanoparticles, RSC Adv, 6 (2016) 41630–41636.

Wang G.-S., Nie L.-Z., Yu S.-H., Tunable wave absorption properties of β-MnO_2 nanorods and their application in dielectric composites, RSC Adv, 2 (2012) 6216–6221.

Wang G., Huang X., Jiang P., Tailoring dielectric properties and energy density of ferroelectric polymer nanocomposites by high-k nanowires, ACS Appl Mater Interfaces, 7 (2015) 18017–18027.

Wang G., Huang X., Jiang P., Bio-Inspired fluoro-polydopamine meets barium titanate nanowires: A perfect combination to enhance energy storage capability of polymer nanocomposites, ACS Appl Mater Interfaces, 9 (2017) 7547–7555.

Wang J., Shi Z., Ge Y., Wang Y., Fan J., Yin J., Solvent exfoliated graphene for reinforcement of PMMA composites prepared by in situ polymerization, Mater Chem Phys, 136 (2012) 43–50.

Wang L., Gao F., Xu F., Zhang K., Wang M., Qin M., Fabrication, characterisation and dielectric properties of KH550 modified BST/PVDF nanocomposites with high dielectric strength, High Voltage, 1 (2016) 158–165.

Wang M., Li W.L., Feng Y., Hou Y.F., Zhang T.D., Fei W.D., Yin J.H., Effect of $BaTiO_3$ nanowires on dielectric properties and energy storage density of polyimide composite films, Ceram Int, 41 (2015) 13582–13588.

Wang X., Li W., Sun K., Stable efficient CdSe/CdS/ZnS core/multi-shell nanophosphors fabricated through a phosphine-free route for white light-emitting-diodes with high color rendering properties, J Mater Chem, 21 (2011) 8558–8565.

Wang Y., Wang L., Yuan Q., Chen J., Niu Y., Xu X., Cheng Y., Yao B., Wang Q., Wang H., Ultrahigh energy density and greatly enhanced discharged efficiency of sandwich-structured polymer nanocomposites with optimized spatial organization, Nano Energy, 44 (2018) 364–370.

Wang Y., Wang L., Yuan Q., Niu Y., Chen J., Wang Q., Wang H., Ultrahigh electric displacement and energy density in gradient layer-structured $BaTiO_3$/PVDF nanocomposites with an interfacial barrier effect, J Mater Chem A, 5 (2017) 10849–10855.

Wang Z., Fu Y., Meng W., Zhi C., Solvent-free fabrication of thermally conductive insulating epoxy composites with boron nitride nanoplatelets as fillers, Nanoscale Res Lett, 9 (2014) 643(7pp). DOI:10.1186/1556-276X-9-643

Wang Z.F., Wang B., Qi N., Zhang H.F., Zhang L.Q., Influence of fillers on free volume and gas barrier properties in styrene-butadiene rubber studied by positrons, Polymer, 46 (2005) 719–724.

Wei P., Xiaowei H., Yan C., Preparation and characterization of poly(vinyl alcohol)/antimony-doped tin oxide nanocomposites, Int J Polym Mater Polym Biomat, 60 (2010) 223–232.

White S.I., Mutiso R.M., Vora P.M., Jahnke D., Hsu S., Kikkawa J.M., Li J., Fischer J.E., Winey K.I., Electrical percolation behavior in silver nanowire-polystyrene composites: Simulation and experiment, Adv Funct Mater, 20 (2010) 2709–2716.

Wiggers H., Novel material properties based on flame-synthesized nanomaterials, KONA Powder Part J, 27 (2009) 186–194.

Wilson R., Plivelic T.S., Aprem A.S., Ranganathaiagh C., Kumar S.A., Thomas S., Preparation and characterization of EVA/clay Nanocomposites with improved barrier performance, J Appl Polym Sci, 123 (2012) 3806–3818.

Witt N., Tang Y., Ye L., Fang L., Silicone rubber nanocomposites containing a small amount of hybrid fillers with enhanced electrical sensitivity, Mater Design, 45 (2013) 548–554.

Wu T., Chen B., Facile fabrication of porous conductive thermoplastic polyurethane nanocomposite films via solution casting, Sci Rep, 7 (2017) 17470(11pp). DOI:10.1038/s41598-017-17647-w

Xie Q., Cheng Y., Chen S., Wu G., Wang Z., Jia Z., Dielectric and thermal properties of epoxy resins with TiO_2 nanowires, J Mater Sci-Mater Electron, 28 (2017) 17871–17880.

Xu F., Zhu Y., Highly conductive and stretchable silver nanowire conductors, Adv Mater, 24 (2012) 5117–5122.

Xu S., Akchurin A., Liu T., Wood W., Tangpong X.W., Akhatov I.S., Zhong W.-H., Thermal properties of carbon nanofiber reinforced high-density polyethylene nanocomposites, J Compos Mater, 49 (2015) 795–805.

Xu W., Xu Q., Huang Q., Tan R., Shen W., Song W., Electrically conductive silver nanowires-filled methylcellulose composite transparent films with high mechanical properties, Mater Lett, 152 (2015) 173–176.

Xue Y., Jin X., Fan Y., Tian R., Xu X., Li J., Lin J., Zhang J., Hu L., Tang C., Large-scale synthesis of hexagonal boron nitride nanosheets and their improvement in thermal properties of epoxy composites, Polym Compos, 35 (2014) 1707–1715.

Yan X., He Q., Zhang X., Gu H., Chen H., Wang Q., Sun L., Wei S., Guo Z., Magnetic polystyrene nanocomposites reinforced with magnetite nanoparticles, Macromol Mater Eng, 299 (2014) 485–494.

Yang X., Tang L., Guo Y., Liang C., Zhang Q., Kou K., Gu J., Improvement of thermal conductivities for PPS dielectric nanocomposites via incorporating NH_2-POSS functionalized nBN fillers, Compos Pt A-Appl Sci Manuf, 101 (2017) 237–242.

Yeun J.-H., Bang G.-S., Park B.J., Ham S.K., Chang J.-H., Poly(vinyl alcohol) nanocomposite films: Thermooptical properties, morphology, and gas permeability, J Appl Polym Sci, 101 (2006) 591–596.

Yi P., Awang R.A., Rowe W.S.T., Kalantar-Zadeh K., Khoshmanesh K., PDMS nanocomposites for heat transfer enhancement in microfluidic platforms, Lab Chip, 14 (2014) 3419–3426.

Yi W.J., Wang Y.Y., Wang G.F., Tao X.M., Investigation of carbon black/silicone elastomer/dimethylsilicone oil composites for flexible strain sensors, Polym Test, 31 (2012) 677–684.

Yin G., Yang Y., Song F., Renard C., Dang Z.-M., Shi C.-Y., Wang D., Dielectric elastomer generator with improved energy density and conversion efficiency based on polyurethane composites, ACS Appl Mater Interfaces, 9 (2017) 5237–5243.

Yoonessi M., Gaier J.R., Sahimi M., Daulton T.L., Kaner R.B., Meador M.A., Fabrication of graphene–polyimide nanocomposites with superior electrical conductivity, ACS Appl Mater Interfaces, 9 (2017) 43230–43238.

Yoonessi M., Peck J.A., Bail J.L., Rogers R.B., Lerch B.A., Meador M.A., Transparent large-strain thermoplastic polyurethane magnetoactive nanocomposites, ACS Appl Mater Inter, 3 (2011) 2686–2693.

Yoshikai K., Ohsaki T., Furukawa M., Silica reinforcement of synthetic diene rubbers by sol–gel process in the latex, J Appl Polym Sci, 85 (2002) 2053–2063.

Yu Y.-H., Ma C.-C.M., Teng C.-C., Huang Y.-L., Lee S.-H., Wang I., Wei M.-H., Electrical, morphological, and electromagnetic interference shielding properties of silver nanowires and nanoparticles conductive composites, Mater Chem Phys, 136 (2012) 334–340.

Yu Z.B., Niu X.F., Liu Z.T., Pei Q.B., Intrinsically stretchable polymer light-emitting devices using carbon nanotube-polymer composite electrodes, Adv Mater, 23 (2011) 3989–3994.

Yue Y., Zhang H., Zhang Z., Chen Y., Tensile properties of fumed silica filled polydimethylsiloxane networks, Compos Pt A-Appl Sci Manuf, 54 (2013) 20–27.

Zachariah M.R., Aquino M.I., Shull R.D., Steel E.B., Formation of superparamagnetic nanocomposites from vapor phase condensation in a flame, Nanostruct Mater, 5 (1995) 383–392.

Zhang D., Liu W., Tang L., Zhou K., Luo H., High performance capacitors via aligned TiO_2 nanowire array, Appl Phys Lett, 110 (2017) 133902(6pp). DOI:10.1063/1.4979407

Zhang H.-B., Zheng W.-G., Yan Q., Yang Y., Wang J.-W., Lu Z.-H., Ji G.-Y., Yu Z.-Z., Electrically conductive polyethylene terephthalate/graphene nanocomposites prepared by melt compounding, Polymer, 51 (2010) 1191–1196.

Zhang J., Wang X., Yu C., Li Q., Li Z., Li C., Lu H., Zhang Q., Zhao J., Hu M., Yao Y., A facile method to prepare flexible boron nitride/poly(vinyl alcohol) composites with enhanced thermal conductivity, Compos Sci Technol, 149 (2017) 41–47.

Zhang X., Zhang J., Xia L., Li C., Wang J., Xu F., Zhang X., Wu H., Guo S., Simple and consecutive Melt extrusion method to fabricate thermally conductive composites with highly oriented boron nitrides, ACS Appl Mater Interfaces, 9 (2017) 22977–22984.

Zheng W., Wong S.-C., Electrical conductivity and dielectric properties of PMMA/expanded graphite composites, Compos Sci Technol, 63 (2003) 225–235.

Zhi C., Bando Y., Terao T., Tang C., Kuwahara H., Golberg D., Towards thermoconductive, electrically insulating polymeric composites with boron nitride nanotubes as fillers, Adv Funct Mater, 19 (2009) 1857–1862.

Zhi C.Y., Bando Y., Wang W.L., Tang C.C., Kuwahara H., Golberg D., Mechanical and thermal properties of polymethyl methacrylate-BN nanotube composites, J Nanomater, 2008 (2008) 642036(5pp). DOI:10.1155/2008/642036

Zhou J., Li R., Liu S., Li Q., Zhang L., Zhang L., Guan J., Structure and magnetic properties of regenerated cellulose/Fe_3O_4 nanocomposite films, J Appl Polym Sci, 111 (2009) 2477–2484.

Zhu A., Cai A., Zhang J., Jia H., Wang J., PMMA-grafted-silica/PVC nanocomposites: Mechanical performance and barrier properties, J Appl Polym Sci, 108 (2008) 2189–2196.

Zhu D., Yu W., Du H., Chen L., Li Y., Xie H., Thermal conductivity of composite materials containing copper nanowires, J Nanomater, 2016 (2016) 3089716(6pp) DOI:10.1155/2016/3089716

Zulkarnain M., Fadzil M.A., Mariatti M., Azid I.A., Effects of silver microparticles and nanoparticles on thermal and electrical characteristics of electrically conductive adhesives, J Electron Mater, 46 (2017) 6727–6735.

Zyane A., Belfkira A., Brouillette F., Marchet P., Lucas R., $BaTiO_3$ incorporation effect on the dielectric properties of polymer from aqueous emulsion: An enhanced dispersion technique, J Appl Polym Sci, 133 (2016) 44333. DOI:10.1002/app.44333

Authors' Short Biographies

Christoph O. Blattmann

Christoph O. Blattmann is a PhD candidate in the Particle Technology Laboratory (PTL) at the Swiss Institute of Technology in Zürich (ETH Zürich). He focuses primarily on flame synthesis of functional nanoparticles and their incorporation with a host polymer. His education as mechanical and process engineer (BSc and MSc degrees from ETH Zürich), research internships at Harvard University School of Public Health and the many projects he has done at PTL lend him a sturdy foundation for advancing the manufacturing of sophisticated polymer nanocomposites.

Sotiris E. Pratsinis

Sotiris E. Pratsinis is Professor of Process Engineering and Materials Science in ETH Zurich, Switzerland and Director of its Particle Technology Laboratory. He has Diploma (Chem.Eng.) from Aristotle University of Thessaloniki, Greece and PhD from UCLA, USA. His research focuses on particle dynamics (coagulation, flocculation of agg(reg/lomer)ates) with emphasis on aerosol synthesis of materials for industrial (pigment, photo/catalyst, gas sensor) and life science (breath analysis, biomaterials, nutrition) applications. His research was recognized by a U.S. NSF *Presidential Young Investigator Award*, the AIChE *Thomas Baron Award*, a *Humboldt Award* from Germany and a 2009 *Advanced Investigator Grant* from the European Research Council. Since 2012 he is member of the Swiss *Academy of Engineering*.

KONA Powder and Particle Journal No. 36 (2019) 33–49/Doi:10.14356/kona.2019002 Review Paper

A Review: Recent Progress on Evaluation of Flowability and Floodability of Powder [†]

Koichiro Ogata

[1] *Department of Mechanical Engineering, National Institute of Technology, Oita College, Japan*

Abstract

Recent studies evaluating the flowability and floodability of cohesive powder under conditions of consolidation, mechanical force, vibrating force, fluid force, and floodability are reviewed. The ball indentation test is an effective method for evaluating the flowability of a small amount of cohesive powder at very low stress under consolidation conditions. The environmental conditions such as temperature and humidity play an important role in the flow of cohesive powder. With regard to cohesive powder flowing under mechanical force, the FT4 powder rheometer can evaluate the powder flowability using the total energy which is related to the shear stress on the impeller blade. The vibrating capillary method and the vibrating shear tube method are effective for the measurement of the flowability of strongly cohesive powder. The test using powder discharge by air flow can assess the flowability of cohesive powder which Carr's flowability index is an equivalent level by using mass flow rate and interstitial air pressure. Finally, the flushing of cohesive powder occurs when the interstitial air pressure and the void fraction are high. The pressure difference between the interstitial air pressure and the outside of an orifice are the dominant factors in the spouting of powder.

Keywords: ball indentation, caking, rheometer, vibration, air pressure, flushing

1. Introduction

Powders and bulk solids are widely used in various industries such as material production, food processing and pharmaceutical development. When using these powders, they will go through several handling processes such as storage, discharge, transportation, mixing, filling, milling and separation. Recently, cohesive powder used in these processes is substantially increasing because it has many advantages, for instance, having a superior reaction potential due to a large specific surface area (Naito M. and Makino H., 2011). On the other hand, the handling of cohesive powder in air becomes extremely difficult because of cohesive forces arising from van der Waals force, electrostatic force and liquid bridge force. Cohesive forces also become stronger relative to gravity force as the particle size decreases (SPTJ, 2006). Therefore, adhesion and cohesion forces give rise to problems with powder handling equipment such as the stable operation of powder handling processes and the quality control of product material. Additionally, rat hole and bridge would occur upon discharge from storage and pipeline transportation if cohesive forces are strong. Unexpected discharge of cohesive powder from a small gap would also occur when cohesive powder is released from a hopper exit. These phenomena are known to cause trouble in the powder handling equipment and it is necessary to avoid them.

The typical flowing form of powder in equipment is classified by gravity flow, compression flow, mechanical flow, vibrating flow and fluid flow. This classification arises from the dynamic behaviour and it is deeply linked with the dynamic properties of powder flow. Furthermore, cohesive powder flow is influenced by the particle properties, for instance, size and shape, and by external factors such as external forces and the surrounding environment. As mentioned above, the understanding of cohesive powder flow is strongly connected with the operation of powder handling equipment. It is therefore necessary to evaluate flowability and floodability of powder in conditions as close as possible to the actual behaviour and operating conditions.

Carr (1965a, 1965b, 1969) suggested powder flow could be evaluated by using some powder properties. According to this method, the flowability is evaluated through angle of repose, compressibility, angle of spatula, and cohesiveness or uniformity, whilst the floodability is evaluated through by angle of fall, angle of difference, dispersibility, and flowability index. In general, Carr's method may

---

[†] Received 4 October 2017; Accepted 15 December 2017
J-STAGE Advance published online 17 March 2018

[1] 1666 Maki, Oita 870-0152, Japan
E-mail: k-ogata@oita-ct.ac.jp
TEL: +81-975-552-6927 FAX: +81-975-552-6927

be validated under static condition of bulk solids. However, this method is not suitable for the dynamic condition of powder because the evaluation of flowability and floodability is carried out using the above mentioned parameters. Therefore, a direct evaluation of flowability and floodability of powders is necessary, and there are many instruments for this purpose. Based on these backgrounds, this review introduces recent works for the evaluation of flowability and floodability by the classification of powder flowing in compressed flow, mechanical forced flow, vibrating flow, fluid flow, and flooding. It focuses on the dynamic measurement, flow mechanism, and the critical point of powder flow because they are important factors in the understanding of powder flow.

2. Powder flow under consolidation

Powders are often subjected to compressive forces in scenarios such as discharge to storage, compression moulding and tableting shoes. In these processes, the understanding of the yield strength is important for equipment design. If the powder has experienced normal and shear stresses from an external force then it would be possible to carry out an evaluation based on a shear test and consolidation test. With regard to the evaluation, Schwedes (2003) reported that there are many testers to measure the flowability of powders such as the Jenike shear cell (Jenike, 1967), Schulze ring shear tester (Schulze, 2008) and others. Amongst these testers, the shear cell is the most commonly used and there are many studies and reviews. Therefore, a detailed explanation for evaluation of flowability by shear cells is not given in this article. On the other hand, these testers need to improve the evaluation of the bulk cohesion and the tensile strength caused by indirect measurements. Some researchers pointed out the tensile strength is determined by extrapolating yield locus on the tensile region (Schulze, 2008), and is overestimated (Vasilenko et al., 2013). Zafar et al. (2015) mentioned the measurement of flowability of cohesive powders at low stress is difficult because the inter-particle contact forces have a strong effect. For these reasons, there is a request for a direct measurement of tensile strength and an evaluation method that can measure at a low stress level. In this section, the review focuses on new tests for the evaluation of flowability of cohesive powder under low stress conditions.

Hassanpour and Ghadiri (2007) proposed the ball indentation method on a powder bed. This method can be performed on small amounts of loosely compacted powders. They examined the flowability of bulk powders using an indentation test and an unconfined compression test, where a small assembly of powders was compacted at low pressure levels. Sample powders of about 5 g were formed as weak tablets, and they were consolidated into a cylinder by piston. The given piston pressure was from 3 to 20 kPa and the loading speed was 1 mm/min. The formed tablet was indented by using a spherical indenter of a glass sphere of 1.588 mm in diameter. **Fig. 1** shows how the hardness calculation is carried out. The hardness of consolidated powder H_D is calculated by the penetration depth and load during a test cycle.

$$H_D = \frac{F_{\max}}{A_{\rm i}} \tag{1}$$

where $F_{\max}$ is the maximum indentation load. $A_{\rm i}$ is the projected area of the impression as follows:

$$A_{\rm i} = \pi\left(d_{\rm b}h_{\rm c} - h_{\rm c}^2\right) \tag{2}$$

where $d_{\rm b}$ is the diameter of indenter and $h_{\rm c}$ is the critical indentation depth which is estimated through the interception of the tangent with the unloading curve as shown in **Fig. 1**.

Hassanpour and Ghadiri (2007) reported the yield stress obtained from indentation was similar to that of unconfined compression for the cases of α-lactose and mag-

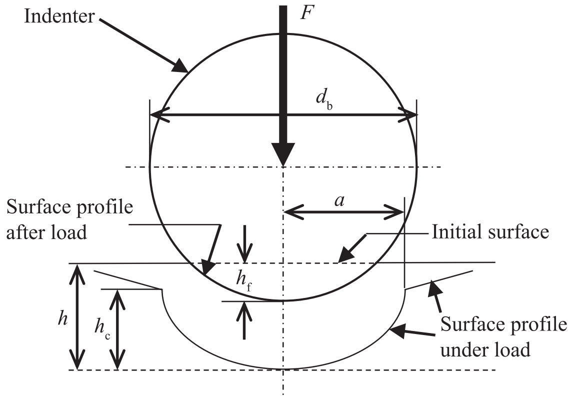

(a) Schematic of ball indentation test

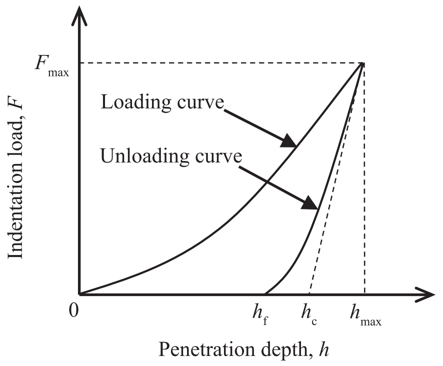

(b) Loading and unloading curve

Fig. 1 Geometry for measurement of indentation hardness of week powder compacts. Reprinted with permission from Ref. (Zafar et al., 2015). Copyright: (2015) Elsevier B.V.

nesium carbonate, whilst the indentation results for the cohesive glass beads differed from those of unconfined compression. They speculated this difference might be attributed to constraint factor, which is affected by particle shape and inter-particle friction. Furthermore, through comparison between Distinct Element Method (DEM) simulation and experiments, they found a linear correlation between the unconfined yield stress and the consolidation pressure.

Wang et al. (2008) also experimentally investigated the indentation hardness of α-lactose monohydrate, microcrystalline cellulose and starch powder. They found the constraint factor for a powder bed is not a single value, and concluded the constraint factor would depend on single particle properties such as particle shape, roughness and friction coefficient. Drawing on Hassanpour and Ghadiri (2007) and Wang et al. (2008), Pasha et al. (2013) carried out numerical analysis of the ball indentation method using DEM simulation. Their analysis results mainly revealed a minimum bed height of 20 particle diameters is required in order to achieve reliable hardness values, and small indenters with diameters smaller than 16 particle diameters exhibit fluctuations in hardness measurements. They also noted if the indenter size is too close to the die size, the walls provide confinement and increase the measured hardness.

Zafar et al. (2017a) analysed the operating conditions of the ball indentation method. In this study, five kinds of powders (three silanised cohesive spherical glass beads, limestone, and Durcal 15) were used. They showed a sieved method gave a uniform packing with minimum void fraction. They revealed the dimensionless penetration depth at a given consolidation pressure must exceed 0.4 and the minimum indenter size should be larger than 16 times the mean particle diameter as well as Pasha et al. (2013). The upper limit of the indenter to the bed diameter should be also smaller than 0.65. As a conclusion, they defined minimum indenter size, bed height, and bed volume as shown in **Table 1**.

Zafar et al. (2015) stated that it becomes difficult to obtain reliable values of the unconfined yield strength when the applied stresses were below 1 kPa. They experimentally examined the tensile strength and hardness of bulk cohesive powders by using the Raining bed method, the Sevilla powder tester, and the Ball indentation method, and compared them with the results obtained from the Schulze ring shear tester. From the relationship between tensile strength and applied stress, they reported the results of a shear cell and the Sevilla powder tester were in approximate agreement. They also found the measurement results of the hardness by the ball indentation method and the unconfined yield stress by the shear cell method increased linearly with the applied stress. This result shows clearly the hardness measurement of the powder bed by the ball indentation method is linked to the tensile strength. Based on these results, the ball indentation method can evaluate the flowability on a small quantity of cohesive powders at low stress levels.

Table 1 Minimum indenter and sample size requirement for ball indentation. Reprinted with permission from Ref. (Zafar et al., 2017a). Copyright: (2017) Elsevier B.V.

Size x_p (μm)	Minimum diameter (mm)		Bed height (mm)	Bed Volume (mm^3)
	Indenter	Bed		
50	0.85	1.7	2	5
100	1.7	3.4	4	40
200	3.4	6.8	8	300
500	8.5	17	20	4500

In addition, the assessing of caking behaviour such as the consolidation flow of cohesive powders is important. Zafar et al. (2017b) undertook a comprehensive review on the mechanism and the testers of bulk powder caking. Recently, there have been new methods for measuring caking characterization, for example, the environmental caking tester (Calvert et al., 2013) and the Edinburgh powder tester (Thakur et al., 2014). Calvert et al. (2013) have introduced the environmental uniaxial caking tester which can control the temperature and relative humidity at the inlet and exit of the powder bed as shown in **Fig. 2**. The experiments were performed under 14 different conditions where the applied uniaxial stress, the temperature, the relative humidity and the consolidation time were varied. The sample powder had a mean particle diameter of 0.92 mm. They measured the stress and strain during the consolidation test and the maximum stress was taken as the cake strength. They found the cake strength increased with increasing consolidation stress, consolidation time, temperature and relative humidity. These results revealed the cake strength was related to the environmental and mechanical conditions to which the sample powder was exposed.

Thakur et al. (2014) have also studied the caking behaviour of spray-dried detergent powders using the Edinburgh powder tester. The tested powder had the same solid density and different moisture content and size ranges. They examined the relationship between unconfined strength and axial consolidation stress. As a result, a sample of higher moisture content displayed higher unconfined strength under the same conditions of consolidation stress. They surmised this was because the moisture increased the stickiness and plasticity of contact. A larger particle size also showed higher unconfined strength compared to a smaller one. Consequently, Thakur et al (2014) argued the coarse particles have higher moisture content and have more plastic deformation compared to small size

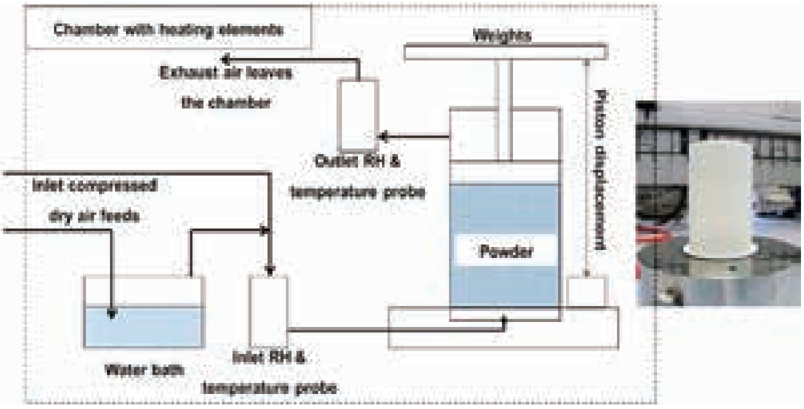

Fig. 2 A schematic illustration of environmental caking rig set up. Reprinted with permission from Ref. (Zafar et al., 2017b). Copyright: (2017) Elsevier B.V.

particles. They also pointed out the possibility of higher contact area and higher adhesion in case of the coarse particles.

Chen et al. (2017) have experimentally investigated caking behaviour by adopting the ball indentation method. In this study, they examined the effect of relative humidity, temperature and time against the hardness of the powder bed. The sample powders used were three pharmaceutical excipient powders (PVP, HPC and $CaHPO_4$) with different hygroscopicity. They discovered that due to the coupled effect of the increase in relative humidity and temperature on powder caking, the hardness of all the powders increased. They also found the glass transition of PVP appeared when the relative humidity was the higher value. This means that the state of the powder bed of PVP changed from “bonded” to “transformed” on adsorption of moisture. Furthermore, when the relative humidity of HPC changed, the samples transformed from a glassy state into a rubbery state, and then the particles fused together and the volume of the powder bed decreased significantly. These results show the change of cohesive forces between particles depend on the surrounding environment, and that indicates the environmental conditions and the particle properties are important parameters for evaluating the consolidation flow.

3. Powder flow by mechanical force

There are many equipments that mix powders by mechanical force, such as mixers, screw feeders, and rotary valves. The flow of powder in the equipment is a dynamic phenomenon, and dynamic flowability tests have been developed: the rheological properties of the powder are evaluated by the measurement of the stirring torque of the impeller and the blade in the powder bed (Satoh et al., 1994 and Bruni et al., 2005). In recent years, the powder rheometer method has been applied to evaluate the dynamic behaviour of powder, and one of the well-known tester is the FT4 powder rheometer (Freeman, 2007). This method evaluates the powder flowability by a total energy E, which is calculated with Eq. (3) using the measured force and torque on a rotating blade in the powder bed.

$$E = \int_0^h \left(\frac{T}{R\tan B} + F \right) \mathrm{d}h \tag{3}$$

where T is the torque on the impeller, F is the vertical force on the base, R is the impeller radius, β is the helix angle and h is the penetration depth.

However, the understanding of the flow mechanism of the powder rheometer has been requested, and many researchers have experimentally and numerically examined the flowability of powder in the FT4 (Bharadwaj et al. 2010 and others).

Bharadwaj et al. (2010) have investigated the flow of non-cohesive particles in the FT4 using DEM simulation. They examined the effect of particle properties such as size, shape and friction by the simulated force and torque on the impeller blade in the particle bed. The particles used were spherical glass beads ranging from 1 to 3 mm, and the aspect ratio was also varied from 1.0 to 2.0. There were also glass beads of an irregular shape. They reported the particle size and size distribution have a minimal effect on the mixing torque and force, whilst the particle shape was an important factor because the force and torque increases for non-spherical particles as compared to spherical particles. Furthermore, they noted the sliding and rolling friction coefficients were also important factors to determine the force and torque on the blade.

Hare et al. (2015, 2017) have explored the flow mechanism of cohesive powder in the powder rheometer. They carried out direct measurements of DEM parameters such as the surface energy and the elastic and plastic stiffness, and analysed the dynamic behaviour of silanised cohesive glass beads ranging from 1.7 to 2.1 mm by DEM. **Fig. 3** shows the relation of total flow energy and coefficient of

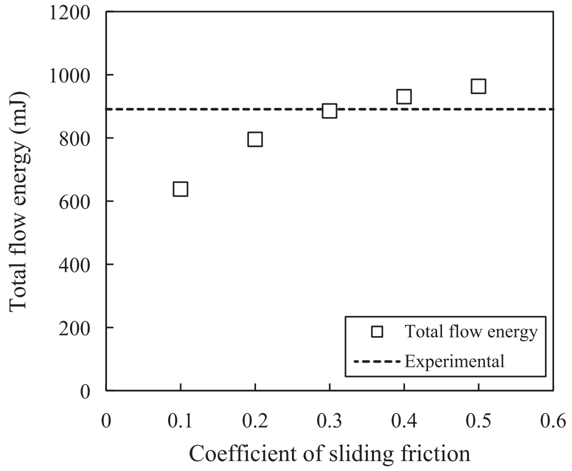

Fig. 3 Influence of sliding friction coefficient on total flow energy. Reprinted with permission from Ref. (Hare et al., 2015). Copyright: (2015) Elsevier B.V.

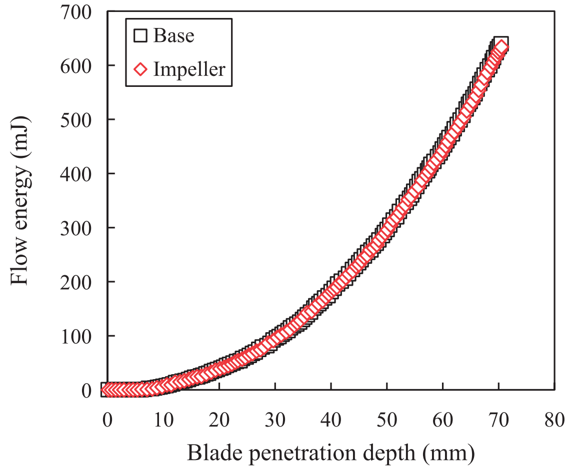

Fig. 4 The flow energies calculated using the vertical forces acting on the base and the impeller. Reprinted with permission from Ref. (Hare et al., 2015). Copyright: (2015) Elsevier B.V.

sliding friction, and they pointed out the flow energy receives the influence of the coefficient of sliding friction between particles. **Fig. 4** shows a comparison with the flow energy calculated using the vertical forces acting on the base and the impeller. It shows that the flow energies using the force acting on the impeller and the base were almost same. They mentioned the resistance to flow was predominantly rotational, i.e. $T/R \tan \beta >> F$.

Furthermore, the stresses in front of the blade were also calculated by the DEM. They indicated both average compressive stress and deviatoric stress increased almost linearly with the blade penetration depth. Therefore, they suggested a characteristic shear stress can be determined for a powder under a given test condition in the FT4.

Wilkinson et al. (2017) analysed the flowability of powder in the FT4 using DEM and varied five input parameters (the static and rolling friction coefficients, coefficient of restitution, Young's modulus, and the cohesion energy density). They confirmed the findings of Bharadwaj et al. (2010) and Hare et al. (2015, 2017), and found the static and rolling friction parameters play a critical role in the determination of the basic flow energy (BFE) and the specific energy (SE) of the powder bed. In addition, the cohesion energy density between particles also played a significant role in the change of BFE. This means that the cohesiveness of the powder will influence the flowability of the powder.

Yan et al. (2016) have examined the mixing and segregation in the FT4 by using DEM simulation. They used the binary mixtures with the different particle size ratio and volume fraction. To evaluate mixing and segregation during the blade movement, the number of contact particles in the mixture of two particles were evaluated by the segregation index. They found the segregation index and the flow energy decreased with increasing the number of test cycles in case of layered particles. On the other hand, when the initial filling state was mixed, the segregation index and the flow energy increased. Furthermore, a large particle size ratio led to a higher segregation and flow energy rate. They also showed the size ratio and the volume fraction were influenced by the change of flow energy gradient. These results suggested the FT4 could compare and rank the segregation tendency for particulate materials.

Pantaleev et al. (2017) have also performed an analysis on powder mixing in the paddle blade mixer by using DEM. They used the measurement result of flow energy in the FT4 for the optimization of the model parameters in DEM simulation. The powder used was the zeolite powder with cohesiveness which varied depending on the moisture content and the bulk density. The measurement result by the standard BFE test in the FT4 showed the flow energy increased markedly when the moisture content had a high value. To this result, they argued this trend was related to the significant contribution of inter-particle cohesive forces such as liquid bridging. However, the difference in flow energy was not clear at the range with the intermediate moisture content powders. From these results, it might be necessary to improve the sensitivity of the measurements in the FT4.

Nan et al. (2017) have analysed the dynamic behaviour of the non-cohesive particle bed under aeration conditions in the FT4 by using both experiments and numerical simulations. They carried out the standard downward test and the permeability test. The particles used were polyethylene particles and the simulations were performed in the same geometry as the FT4 experiments. They simulated the flow energy, the strain rate and the stresses when the tip speed and the superficial gas velocity were varied. As a result, they found both flow energy and shear stress increased linearly with increasing strain rate and also decreased with the increase in gas velocity. Furthermore, they indicated the relationship between the flow energy and the shear stress was clearly correlated. This result suggested the shear stress could determine the flow energy in the FT4 as also outlined by Hare et al. (2015, 2017).

Nagashima and Ishikura (2015) have experimentally examined the influences of blade speed, consolidation and aeration on the total energy in the dynamic test of the FT4. They also measured the compressibility in the bulk test which carried out the volume reduction by applying a normal stress to the sample powder. In the experiment, ten kinds of powders which belonged to the classification of Geldart A, B and C were used. They showed the total energy could be evaluated by the compressibility and the cohesiveness when the blade speed and the gas flow were changed. Furthermore, the difference in total energy of the Geldart A, B and C particles clearly varied. In the aeration tests with the Geldart C particle, they observed agglomeration of particles and channelling into the powder bed. This result indicated the Geldart A and B particles were easily fluidized by aeration test and the total energy could evaluate the flowability of powder of the different particle sizes. Additionally, Bruni et al. (2007a, b) and Tomasetta et al. (2012) have also examined the rheological properties under aeration and fluidization by using a mechanically stirred fluid-bed rheometer.

Leturia et al. (2014) focused on the effect of the state of compaction and void fraction on bulk solids for the evaluation of powder flowability. They carried out the experiment of the rotational shear cell test, the consolidation test, the dynamic test and the aeration test by using the FT4, and also performed a tap density volumeter and the fluidization tests. In this study, five materials from nanoparticles to group B particle were selected and two binary mixtures were also used. They arranged the relationship between the flow index of the shear cell measurements and the compressibility of the consolidation tests under packed bed conditions. This result indicated the powder flow can be divided in three main regions such as easy/free flowing powders, cohesive powders, and intermediate behaviour. They also compared the Hausner ratio measurements with the flow rate index (FRI) of the dynamic test under the free surface conditions. From this result, the powder flow can be classified in two regions and the dynamic test was a quick way to evaluate flow properties of free flowing to relatively cohesive powders. Furthermore, under the aeration conditions, the aeration test was also a quick way to evaluate the effect of aeration on powder flow properties. This method can be used to evaluate if a powder is likely to be fluidized. On the other hand, they pointed out a more detailed understanding of the physical phenomena on the powder rheometer measurements is still needed, and the connection of several characterization methods is required to ensure a complete understanding of the powder flow properties over a wide range of conditions.

Recently, Li et al. (2018) have performed the standard dynamic test by using the FT4, where cohesive powders such as three kinds of $CaCO_3$ and ZrO_2 were used. They compared the results of BFE and FRI, and pointed out these values were difficult to distinguish between very similar materials. Therefore, they aimed to develop a new dynamic testing method which was based on the autocorrelation analysis of the torque measurements on the FT4. In the experiment, six powders belonging to Geldart group A, B and C were tested. They observed the powder behaviour during testing, and analysed the raw data of normal force and torque measurements. The results of cohesive powders found an empty space based on the particle agglomeration appeared behind the blade, and the torque oscillations such as a periodic behaviour occurred. They argued this oscillation was significant in the cohesive powder compared to a free-flowing powder, and an autocorrelation analysis was applied to evaluate the flowability of powder. The results showed the oscillation amplitude and the cycle time increased with increasing the powder cohesiveness. On the other hand, a free-flowing powder exhibited a liquid-like behaviour and showed almost no periodic motion. From these studies of the FT4, this method could be available to evaluate the flowability of powders, whilst it seems to need the improvement of the evaluating flowability of cohesive powders.

4. Powder flow under vibration force

With regard to the powder handling by using the vibration field, there are a large number of options such as feeder, drying, and powder blocking prevention. These operations induce complex powder flow which depends on vibration amplitude and frequency. It is therefore important to understand the mechanism of powder flow in this field. In general, the feeding of smaller particles becomes difficult because of the effect of their cohesiveness, and intermittent powder flow will occur (Matsusaka et al., 1995a, 1996). These phenomena are because fine particles will agglomerate by the effect of cohesiveness. Therefore, in order to achieve reliable fine powder handling, vibration is applied to cohesive powder and flowability of powders under a vibrating field is an important subject.

Matsusaka et al. (1995a, 1996) have developed microfeeding of fine powders by using a vibrating capillary tube. Their powder feeder consists of a powder discharge hopper, a glass tube, a capillary tube, where the inside diameter of the capillary tube ranges from 0.4 to 1.6 mm. This feeder had horizontal vibration which was smaller than 760 Hz in frequency. In the experiment, three alumina powders and a fly ash powder were used where the

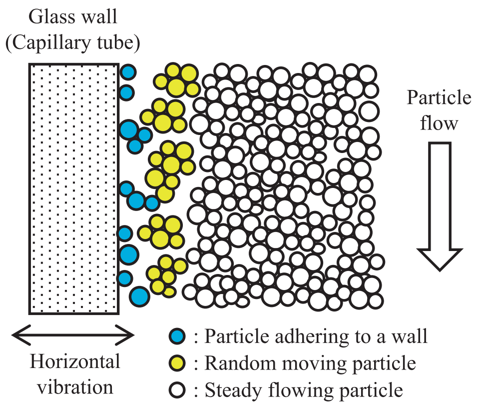

Fig. 5 Schematic particle flow near inside wall at cross-sectional view in the vibrating capillary tube method. Reprinted with permission from Ref. (Matsusaka et al., 1995a). Copyright: (1995) J. Soc. Powder Tech, Japan.

size range was from 6 to 20 μm. They revealed the discharged mass from the vibrating capillary tube for all the powder can be strictly controlled with this system. **Fig. 5** shows the schematic particle flow near the inside wall under the horizontal vibration. It was found only the particles near the inside wall of the capillary tube were flowing randomly by the effect of cohesive forces, and the other particles inside the tube were transported downwards as a lump of powder. In addition, they indicated the critical condition of the powder discharge was related to the vibration acceleration, and a high frequency will be necessary to discharge the cohesive powder. Furthermore, Matsusaka et al. (1995b) have achieved the discharge of fine powder as small as 0.4 μm by using a capillary tube along with ultrasonic vibration applied by using a piezoelectric transducer of 20 kHz. They observed fine powder passed through the vibrating capillary tube, and the powder movement was approximated by plug flow with a thin boundary layer near the inner wall. They also found the continuous discharge for fine powder by using this method was possible.

Building on the former results, Jiang et al. (2006) have proposed the evaluation method of flowability of powder based on the vibrating capillary method. Jiang et al. (2009) have explored the performance of this system, in which a capillary tube was vibrated horizontally by a piezoelectric vibrator. The range of sample powders was from 5.2 to 58.2 μm. They examined the dynamic powder flowability by the relationship between the mass flow rate of powder and the vibration acceleration. According to their result, when the vibration acceleration exceeded a critical value, the powder flow began. The critical vibration acceleration was determined as the value where the powder flow rate exceeds 2 mg/s. They also observed the voids in the particle layer at a capillary tube by the CT images, and found the packing structure distribution transitioned from inhomogeneous to homogeneous when the vibration acceleration increased. Furthermore, Jiang et al. (2009) analysed the relationship between the critical vibration acceleration and the angle of repose to evaluate the powder flowability. The result found both the critical vibration acceleration and the angle of repose decreased with increasing mass median diameter. Furthermore, the variation of the critical vibration amplitude was sufficiently larger than that of angle of repose. This result showed the vibrating capillary method can have a high resolution in the flowability analysis.

Ishii et al. (2011a) have experimentally investigated the flowability of ZrO_2 and WO_3 particles by using the vibrating tube method. These particles had different concentrations, with mixtures made by coarse particles from 106 to 250 μm and fine particles under 45 μm. In this study, they evaluated the powder flowability by the two characteristic mass flow rates: the maximum mass flow rate for the increase in the vibration acceleration and the mass flow rate for the decrease in the vibration acceleration. They found the two characteristic mass flow rates were capable of evaluating the flowability because these experimental curves against the concentration of fine particles were similar to the results of Carr's flowability index. Furthermore, they showed the relationship between the Carr's flowability index and the two characteristic mass flow rates, and argued the sensitivity of the vibrating tube method was higher than that of the Carr's flowability index. Additionally, Ishii et al. (2011b) have challenged to reduce the sample amount required for the measurement and evaluation of flowability. As a result, they concluded the flowability can be measured using 10 g or less of particles, and the vibrating tube method is suitable for measuring the flowability of a small amount of particles.

In light of the results reviewed above, measurement of the flowability by vibrating capillary tube turns out to be a simple method, because the powder being discharged only from a capillary. However, if the adhesion forces between particles are too large, bridging will occur in the capillary, hence the measurement of powder discharge will be difficult even though the vibration is increased. To solve the problem of the capillary method, Zainuddin et al. (2012) have developed an evaluation method for powder flowability by using the vibration shear tube method. In this system, the powder can be discharged through a narrow gap between a vibrating tube edge and a flat bottom surface, since the particles receive high shear forces to overcome the adhesion and friction forces. **Fig. 6** summarizes the schematic mechanism of powder flow in the vibration shear tube method. To evaluate the static properties of the powder flowability, they proposed the critical vibration acceleration which was determined by a threshold of mass flow rate at the beginning of particle discharge. On the other hand, to evaluate the dynamic properties related to the dynamic friction of particles, a

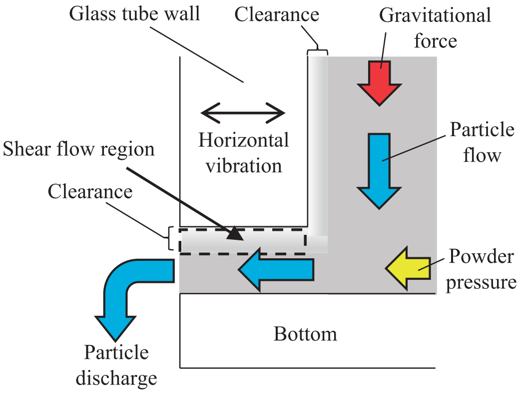

Fig. 6 Schematic mechanism of powder flow in the vibration shear tube method. Reprinted with permission from Ref. (Zainuddin et al., 2012). Copyright: (2012) Elsevier B.V.

characteristic mass flow rate at a vibration acceleration of 300 m/s^2 was introduced, because a stable powder flow was observed for all the samples on this acceleration. As a result, they found the flowability depends on the mass median diameter, and high vibration was required to disintegrate the agglomerates into small pieces, and to flow through the gap. Furthermore, they stated that with this method, an improvement of the measurement efficiency can be expected by reducing the measurement time and sample amount.

Horio et al. (2014) have also examined the effect of particle shape on the powder flowability by using the vibration shear tube method. In this research, microcrystalline cellulose particles were used, and the variation of the aspect ratio was from 1.8 to 6.4. The critical acceleration and the characteristic mass flow rate were determined in the same way as Zainuddin et al. (2012). They showed the angle of repose and the compressibility of powders were related to the critical acceleration and the characteristic mass flow rate. Furthermore, they indicated higher aspect ratios resulted in higher static and dynamic friction forces. This means the vibrating shear tube method can detect the effect of particle aspect ratio in powder flowability. From these results, the vibrating capillary method and the vibrating shear tube method can be recognized effective in the evaluation of flowability of the cohesive powders.

5. Powder flow by fluid force

With respect to powder flow by fluid force, the fluidization and aeration of powder are widely used in operations such as a reaction, drying, and transportation. This is because good gas-solid contacts and heat transfer characteristics can be obtained. Furthermore, the blow tanks and the air slides are classified as the powder supply equipment of the fluidization type. In these apparatuses, the fluidized air is applied into the powder, and the influences of inter-particle force and particle-wall surface force are reduced. Based on this operation, the flowability of powder is improved, and a smooth supply of the powder is achieved. In general operation of fluidization and aeration, the permeability air is supplied through the gas distributor at the bottom of the powder bed in a vessel. Geldart (1973) explored that the group A and B particles can be fluidized easily by permeated air, and the group D particle is possible to fluidize by large inertia force. On the other hand, it mentioned the fluidization of the group C particle was extremely difficult, because of the influence of an increased cohesion force. Therefore, the evaluation of cohesive powder flow using fluidization and aeration operations is highly important. To this issue, the powder discharge from an orifice by fluidization and aeration is well known, and there are so many researches such as the examples below.

De Jong et al. (1969/70, 1975a, b) have investigated the discharge characteristics of the group B particle from an orifice at the bottom of a vessel, where air was supplied from the bottom of the powder bed or both the bottom and the top of the bed. They proposed an empirical correlation of the mass flow rate m_p as a function of pressure difference between powder bed and outside of orifice p_a, particle density ρ_p, initial void fraction ε_i, orifice diameter D and particle diameter x_p.

$$m_\mathrm{p} = C_\mathrm{d}\frac{\pi}{4}\left(D - k_\mathrm{p}x_\mathrm{p}\right)^2\sqrt{2\left(1-\varepsilon_\mathrm{i}\right)\rho_\mathrm{p}p_\mathrm{a}} \tag{4}$$

where C_d is discharge coefficient and k_p is particle shape factor.

Meanwhile they referred the supply position of air was not important. Geldart and Haesebrouck (1983) also experimentally examined the spouting of powder from an orifice at the bottom of the powder bed by using the groups A, B, C and D particles. They compared between the experimental results and a correlation as well as De Jong (1969/70). Furthermore, Martin and Davidson (1983) carried out the discharge experiments of the group A particle from the side of the vessel. The result revealed the mass flow rate of powder was proportional to the square root of pressure difference as the results of previous researchers.

On the other hand, when fluidization and aeration are applied to cohesive powder such as the group A and C particles in Geldart classification, the control of powder flow would be difficult. This means the cohesive forces between particles (such as van der Waals force, electro static force, and liquid bridge force) and the particle-fluid interaction forces have a strong influence on the powder flow. Therefore, the evaluation of flow for cohesive powder under the same operating conditions is important. Regarding this issue, Donsi et al. (2003) and Barletta et al. (2007) have investigated the discharge properties of powder from an orifice by using air of aeration and fluidization, which was introduced at the bottom of the powder bed of the group C particle (such as magnesium carbonate, silica, etc.). According to their results, the fluidization of the cohesive powder in the vessel by giving air flow was possible, whilst large agglomerates and cracks occurred in the powder bed. They also observed the aggregate diameter of discharged powder from an orifice was in the range from 1 to 6 mm. These results can be understood the group C particles couldn't maintain the primary particle size by the influence in cohesive forces. Donsi et al. (2004) also reported the rat hole and funnel flows were arising when the given air velocity was lower. Meanwhile, they found the mass flow phenomenon of cohesive powder bed was exhibited when the air velocity was over the minimum fluidizing velocity. Furthermore, Cannavacciuolo et al. (2009) have challenged the fluidized discharge using cohesive powders of the range of micron and submicron sizes. They revealed a high air velocity was needed in order to eliminate the phenomena of piping and bridging of the powder bed. The result indicated the air velocity given to the powder bed was an important factor to suppress the unsteady flow of the cohesive powder.

Additionally, Ogata (2008, 2009) has experimentally examined the spouting phenomenon of cohesive powder bed through a circular orifice at the bottom of a vessel by using air flow. The powder used was a soft wheat flour of 46 µm with a particle density of 1493 kg/m^3. This powder belongs to the group A particle, and the powder discharge from an orifice by gravity force was difficult. In this study, the air was supplied with three ways such as only the top of the powder bed, only the bottom, and both the top and bottom. As a result, when the same flow rate of air was simultaneously introduced both the top and bottom of the powder bed, the steady flow of cohesive powder was obtained. They also revealed critical conditions for the continuous spouting of the powder from an orifice existed. Ogata et al. (2013) have also attempted the discharge of silica powder which belongs to the group C particle. They found the flow pattern of the powder bed in a vessel became mass flow. They also referred the interstitial air pressure on the powder bed and the initial void fraction were strongly related with the beginning of the powder discharge and the mass flow rate of the powder. From the above results, the cohesive powder in group A and C particles can be smoothly discharged by using this method. However, these studies did not focus on the evaluation of flowability of cohesive powder.

Based on the previous studies, Ogata et al. (2015) have explored the evaluation of flowability of cohesive powder by using the test of the powder discharge from an orifice by air flow. The powders used were three kinds of Calcium hydroxide from 9.6 to 41 µm with the same particle density. In this study, they determined the beginning conditions of powder discharge by the relation of the continuous powder discharge through an orifice and the interstitial air pressure on the powder bed. They also explained the flow mechanism of cohesive powder using air flow as shown in **Fig. 7**. On the initial condition in **Fig. 7(a)**, the free-flowing of cohesive powder through an orifice at the bottom of the powder bed was difficult to achieve because of the effect of cohesiveness between particles. When the air was supplied from both the top and the bottom of the powder bed, they observed the cohesive powder flow did not occur as shown in **Fig. 7(b)**. This conditions were the low interstitial air pressure and the low initial void fraction.

On the other hand, as shown in **Fig. 7(c)**, when the interstitial air pressure was increased, the cohesive powder was discharged through an orifice at the bottom of the powder bed. They concluded the difference in the powder flow was deeply linked to the relation between the cohe-

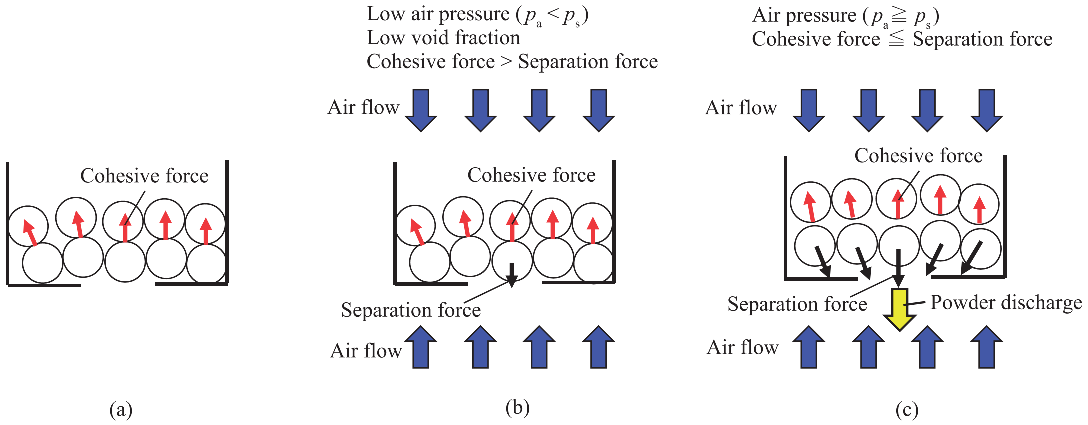

Fig. 7 Schematic of mechanism of powder flow in the test of powder discharge by air flow. Reprinted with permission from Ref. (Ogata et al., 2015). Copyright: (2015) J. Soc. Powder Tech, Japan.

sive force and the separation force on the particles. As for this flow mechanism, in order to start of powder flow, the separation force caused by the air pressure should overcome the cohesive forces on the powder in a stationary state.

Furthermore, Ogata et al. (2017) estimated the separation force on a particle in the powder bed based on Rumpf equation (Rumpf, 1970 and Tsubaki, 1984) as follows.

$$H = \frac{\pi p_s x_p^2}{k_c (1 - \varepsilon_i)} \tag{5}$$

where H is the separation force, p_s is the interstitial air pressure at the beginning of powder discharge, x_p is the mean particle diameter, ε_i is the initial void fraction of the powder bed, and k_c is the coordination number by Ridgway-Tarbuck correlation (1967).

They also expressed the cohesiveness on the powder by the ratio of separation force H and gravity force F_g as following equation.

$$\frac{H}{F_g} = \frac{6 p_s}{\rho_p g x_p (1 - \varepsilon_i)\left(13.8 - \sqrt{175 - 232(1 - \varepsilon_i)}\right)} \tag{6}$$

In addition, they evaluated the flowability of cohesive powder using the relationship between the mass flow rate of powder and the averaged interstitial air pressure at the top of the powder bed. In this study, three kinds of calcium hydroxide with different particle diameters were used. The mean particle diameter of an original powder, $Ca(OH)_2$-A, was 13.1 μm and other particle diameters, i.e. $Ca(OH)_2$-B and $Ca(OH)_2$-C, were 14.1 μm and 2.5 μm, respectively. Flowabilities of these powders using Carr's method were in order: $Ca(OH)_2$-A = $Ca(OH)_2$-C < $Ca(OH)_2$-B.

As for experimental conditions, the initial void fraction and the interstitial air pressure were varied. **Fig. 8** shows the relationship between the mass flow rate and the averaged interstitial air pressure under the natural packing. The result showed the mass flow rate of the smallest powder, $Ca(OH)_2$-C, was lower than the other two powders, and unsteady flow was arising. They also confirmed the mass flow rate of $Ca(OH)_2$-A decreased slightly compared to that of $Ca(OH)_2$-B. Based on these results, they revealed flowabilities of three powders were in order; $Ca(OH)_2$-C < $Ca(OH)_2$-A < $Ca(OH)_2$-B. Furthermore, as the result in **Fig. 9**, they found the cohesiveness of these powders was classified by $Ca(OH)_2$-B < $Ca(OH)_2$-A <

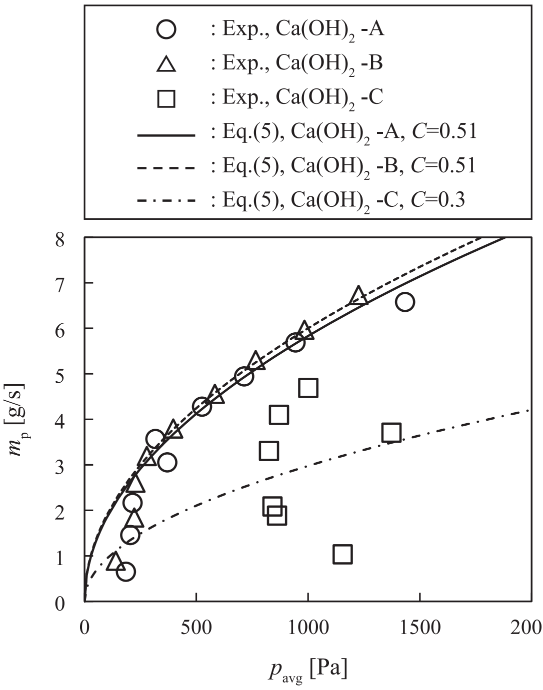

Fig. 8 Relationship between the mass flow rate and the average interstitial air pressure as the natural packing where $Ca(OH)_2$-A: $\varepsilon_i = 0.811–0.815$, $Ca(OH)_2$-B: $\varepsilon_i = 0.796–0.804$, $Ca(OH)_2$-C: $\varepsilon_i = 0.860$. Reprinted with permission from Ref. (Ogata et al., 2017). Copyright: (2017) J. Soc. Powder Tech, Japan.

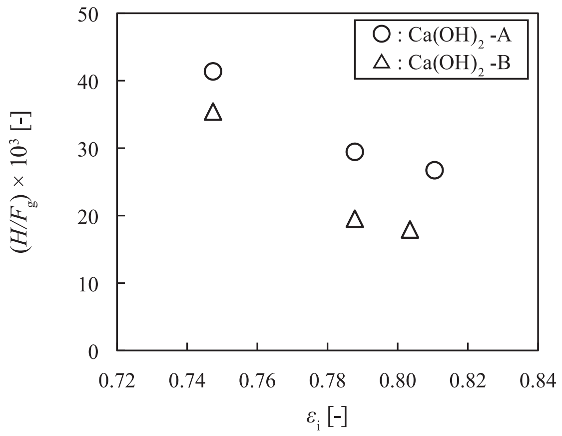

(a) $Ca(OH)_2$ -A and B

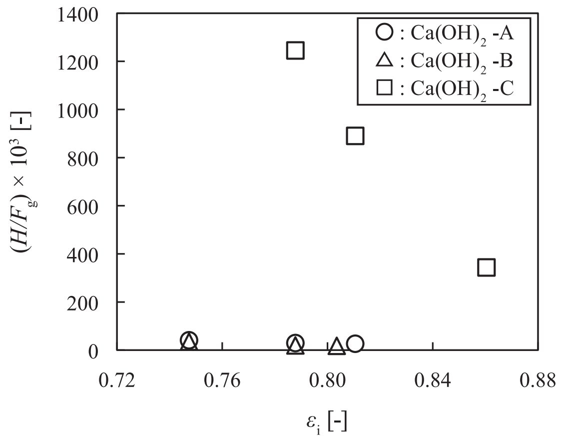

(b) $Ca(OH)_2$ -A, B and C

Fig. 9 Relationship between the ratio of separation force to gravity force and the initial void fraction (a) $Ca(OH)_2$-A and B (b) $Ca(OH)_2$-A, B and C. Reprinted with permission from Ref. (Ogata et al., 2017). Copyright: (2017) J. Soc. Powder Tech, Japan.

$Ca(OH)_2$-C. This was because the ratio of separation force to gravity force increased with the decrease in the particle diameter. In addition, they inferred a main factor of cohesive force in this study was van der Waals force. From these results, this method can be applied in the evaluation of the flowability and the cohesiveness of the powder.

6. Flooding phenomenon of powder

If the cohesive powder in a hopper contains a large amount of air, the powder flows out suddenly from a hopper exit. In general, this phenomenon is called the flooding or the flushing of powder, and can induce serious trouble in powder handling equipment such as rotary feeders, mono pumps, and silos. Therefore, the understanding of the flow mechanism of flooding is necessary. With regard to this subject, Schwedes (2003) explained flooding of powder as a fluid-like behaviour of fine particles which are fluidized by the gas flow. The author quoted the results of the flooding tendencies by Geldart and Williams (1985), and described the tendencies were classified by Geldart diagram (Geldart, 1973). As a result of the review, the flooding of the group D particles cannot occur, and the group B particles indicate only a low flooding tendency. Furthermore, the group A particles are easily fluidized and they have a remarkable flooding tendency. On the other hand, the group C particles are very cohesive, and their flooding tendency is lower. Additionally, author mentioned the flooding tendencies cannot be investigated in shear testers. Regarding the measurement of powder flooding, some studies are available. Carr (1965a, 1965b, 1969) proposed the prediction method of the floodability of powder. This method needs to measure four kinds of powder properties such as angle of fall, angle of difference, dispersibility and flowability index. However, this method could not predict occasionally an exact flooding phenomenon when a fine powder of the group C particle was used. It is therefore necessary to understand the flow mechanism of flooding.

Flooding phenomenon is deeply related to aeration and deaeration of the powder bed. Therefore, there are former studies based on this point. Bruff (1969) has focused on the aerated powder which induces the flooding, and proposed a simple tester as an indicator of flooding. This study experimentally investigated the trend of flooding which was measured by the state of a forming pile of discharged powder from a glass tube. In the experiment, the powder was filled in a tube installed vertically, and was deaerated by using the vertical vibration. As the measurement, the shape of pile of powder on the flat plane was observed. It was concluded the flooding was arising when an angle of pile of powder was small. Lloyd et al. (1987) have also examined the deaeration of powder, and developed an annular shear cell of the Couette type to study in detail the flooding phenomenon for alumina powder. They found the shear stress was larger reduced when small quantities of air entrainment were introduced. They also revealed the transition from normal Coulomb-solid flow to liquid-like flow at high shear rates. Furthermore, their results suggested the addition of fine particles under 40 μm in diameter were greatly influencing the flooding of powder. Rathbone et al. (1987a, b) theoretically and experimentally analysed the aeration, the deaeration, and the flooding of fine powder, and referred the deaeration was a most effective factor for the prevention of flooding. However, the above researchers have focused merely on aeration and deaeration of powder bed. In a practical process, this phenomenon will induce an unstable mass flow rate and the powder leakage from an exit of the discharge equipment, and there is not an accurate evaluation method for the flooding phenomenon. On this subject, there are some works about the flow mechanism of the flushing by using an external loading, vibrating, and other forces.

Tomita et al. (1994) have explored the threshold conditions of the flushing generation. The tested powders were eight kinds of materials from 14 to 99 μm which belong to the group A and C particles. The experiment was conducted with a powder discharge device using a piston pressure at the top surface of the powder bed in a cylindrical vessel which has a small side orifice between 2 and 4 mm near the bottom. **Fig. 10** shows an example of the flushing phenomenon, where an orifice diameter is 4 mm, piston pressure is 2.77 kPa and the initial void fraction is 0.73 (Kuchii, 1997). The powder used is calcium carbonate of 24.6 μm which has a particle density of 2690 kg/m^3. This powder belongs to the boundary of the group A and C particles in the Geldart diagram. From the figure, the powder spouts out of an orifice due to the piston pressure acting on the surface of the powder bed, and this flow

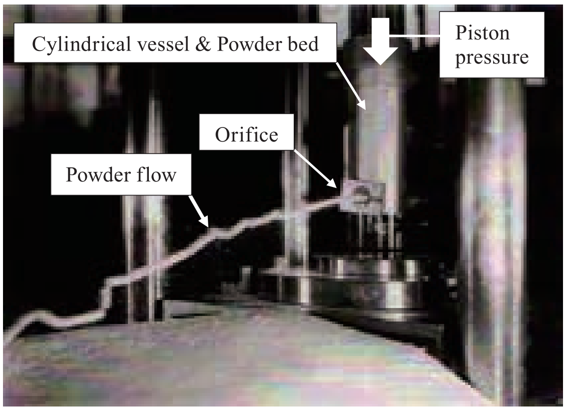

Fig. 10 Flow of calcium carbonate particles at the initial void fraction $\varepsilon_i = 0.73$. Reprinted with permission from Ref. (Kuchii, 1997). Copyright: (1997) Kyushu Institute of Technology Academic Repository.

seems like a liquid flow.

They defined mechanism of flushing as follows. The normal stress in a particulate material consists of interstitial fluid pressure and inter-particle or effective stress based on the particle contacts. When the void fraction of the powder is high, the load is mostly supported by the fluid pressure, since the number of particle contacts is relatively small. When an external load acts on the top surface of powder, the flushing of powder occurs through an orifice because the particle is dragged out by the fluid pressure. Based on this mechanism, they analysed the relationship between threshold void fraction and threshold piston pressure, and revealed the occurrence condition of the flushing depends on the initial void fraction and the interstitial fluid pressure.

Kuchii et al. (1996) have examined the relationship between the interstitial fluid pressure and the void fraction at the onset and end of flushing. They used seventeen test particles which belong to the group A, B and C particles. In this study, they compared the Carr's index and their results are shown in **Fig. 11**, where *FW* is the flowability index and *FL* is the floodability index. According to Carr's method (1965a), flushing arises easily if the floodability index has a higher measured value. However, Kuchii et al. (1996) pointed out that powders having a high floodability are not always occurring to flushing as shown in **Fig. 11**. Based on this results, they suggested the flushing occurs when the floodability index of the powder is larger than the flowability index, i.e. $FL \geq FW$. Furthermore, the results of the occurrence of flushing were plotted on the Geldart diagram, and it was confirmed flushing occurred in the group A and C particles agreeing with the result of Geldart et al. (1985). In addition, they referred the void fraction is an important factor governing the flushing phenomenon.

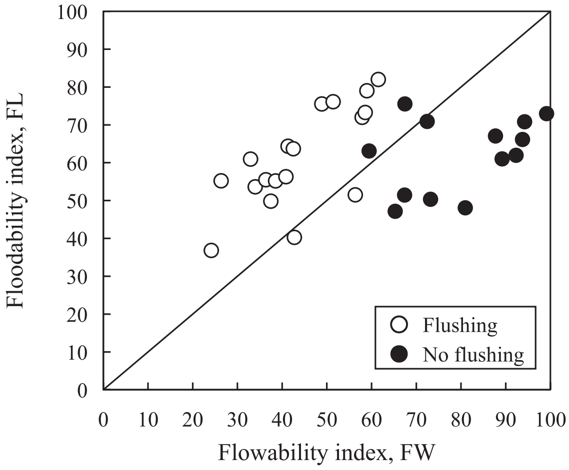

Fig. 11 Flowability index versus floodability index by the powder tester. Open symbols, flushing; closed symbols, no flushing. Reprinted with permission from Ref. (Kuchii, 1997). Copyright: (1997) Kyushu Institute of Technology Academic Repository.

Furthermore, Kuchii and Tomita (2002) have defined the flushing phenomenon as follows; when an external load is applied to the powder, the spurting of powder is generated by an increase in interstitial gas pressure in the powder bed. They carried out the experiments by using a rectangular vessel which has a slit at the bottom. They also numerically simulated by gas-solid two-phase flow model using Darcy's law. In this study, the tested particles were soft wheat flour and FCC catalyst which belong to the group A particle. They analysed the flow pattern during the flushing and the velocity distribution on the powder bed. The results showed the particle flow began near the slit at the bottom of vessel when the piston load was applied, and the velocity of particles is larger than that of free-flowing under gravitational acceleration. They also mentioned an increase in the interstitial fluid pressure appeared near the slit. This result indicated the interstitial air pressure greatly influences the flushing of powder.

Harada et al. (2002) have experimentally and numerically investigated the spouting of fine powder from a side orifice on a vessel by using the vertical vibration. The result showed both the intermittent powder flow and the continuous powder flow in response to vertical vibration. They found the powder spouted out like a plug when the vibration amplitude was comparatively small. Furthermore, when the vibration amplitude was large, they confirmed the powder flowed out like an intermittent dilute jet and dense flow. Furthermore, they also proposed the mechanism of the spouting of powder by vertical vibration as follows; (1) the relative motion of the powder bed to the vessel is induced by the vibration, (2) the pressure fluctuation is generated in response to the change in the gap between the bed and the vessel base, (3) the pressure difference between the vessel and the outside leads to periodic in- and out-flow of air through the orifice, and (4) the particles near the orifice spout out intermittently. **Fig. 12** shows the schematic mechanism of motion of powder bed and percolation fluid by using the vertical vibration (Harada, 2004). Additionally, they examined the dependence of the mass flow rate on the vibration and the particle properties by using dimensional analysis. The results showed the mass flow rate of powder was in proportion to the generated air pressure and in inverse proportion to the vibration frequency. They concluded the generated air flow influences the spouting of powder.

Tashiro et al. (2006a) have explored the onset condition of flushing from an orifice at the bottom of a flushing vessel by using the impact force of free falling of the fluidized soft wheat flour, where the particle properties were a mean particle size of 69.8 μm, a particle density of 1417 kg/m^3, and the moisture content between 11.9 and 13.4 %. The equipment consists of an upper hopper and a

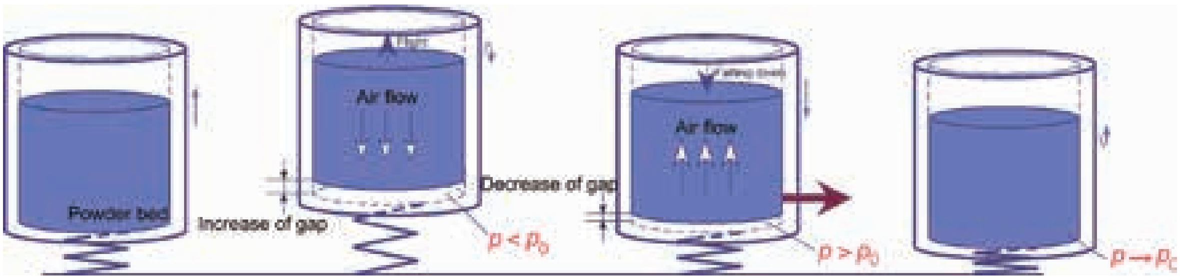

Fig. 12 Schematic of motion of powder bed and percolation fluid by using the vertically vibration of cohesive powder. Reprinted with permission from Ref. (Harada, 2004). Copyright: (2004) Journal of Jet Flow Engineering.

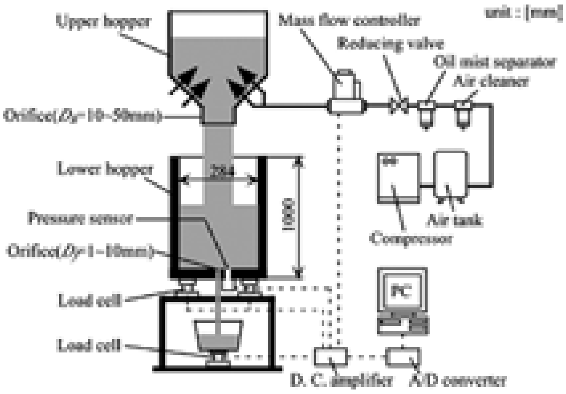

Fig. 13 Experimental apparatus for flushing by using the impact force of free falling powder. Reprinted with permission from Ref. (Tashiro et al., 2006a). Copyright: (2006) American Institute of Chemical Engineers.

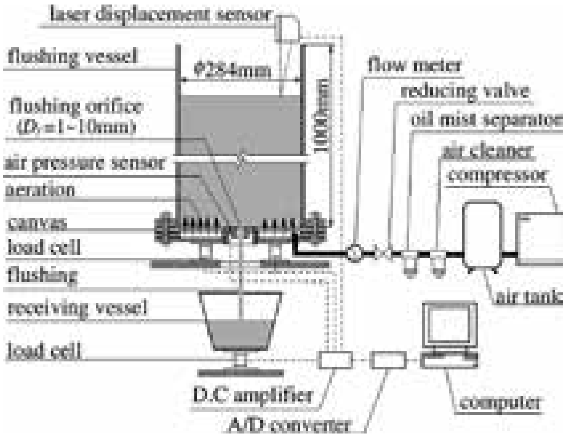

Fig. 14 Experimental apparatus for flushing by using the fluidized powder. Reprinted with permission from Ref. (Tashiro et al., 2006b).

flushing vessel which was arranged below an upper hopper as shown in **Fig. 13**. In the experiment, the mass flow rate of powder from an upper hopper was changed to give different impact forces on the powder in a flushing vessel. To measure the mass flow rate of flushing powder from a flushing vessel, the orifice diameter at the bottom of the flushing vessel was also varied. They showed the flushing occurs when the interstitial air pressure at the bottom of the flushing vessel was larger than 300 Pa, the initial void fraction was more than 0.54, and the mass flow rate of powder from an upper hopper exceeded 500 g/s.

Tashiro et al. (2006b) have also investigated the effect of the interstitial air pressure, the void fraction, the fluidized powder head and the orifice diameter of flushing vessel. In this study, a flushing vessel was directly fluidized, and the powder spouted out of an orifice at the bottom of the vessel as shown in **Fig. 14**. They found the interstitial air pressure at the bottom of the fluidized bed was proportional to the powder head, and its slope depended on the void fraction of powder. Furthermore, the liquid like characteristic was lost with the decrease in the void fraction of the powder bed. They also revealed the mass flow rate during the flushing was proportional to the square root of interstitial air pressure, and decreased with the orifice diameter.

From the above studies on the flushing phenomenon, it can be concluded that the interstitial fluid pressure and the void fraction greatly influence the flushing phenomenon, and the spouting of powder is dependent on the pressure difference between the interstitial air pressure and the outside of an orifice. Consequently, it can be understood the void fraction of the powder bed and the interstitial fluid pressure generated inside the bed are the dominant factors in the flushing of cohesive powder.

7. Conclusion

Recent progress in research on the evaluation of the flowability and floodability of cohesive powder has been reviewed. The contents have been classified by actual powder handling processes such as consolidation, mechanical force, vibration force, fluid force, and flooding.

The ball indentation test is available as an effective method because it can assess the flowability of a small amount of cohesive powder at very low stress compared to shear cell. The environmental conditions such as temperature and humidity will influence the particle properties, and these parameters play an important role on the flow of cohesive power. It is therefore necessary to use the evaluating equipment of powder flowability accounting for these parameters such as the environmental caking tester.

FT4 powder rheometer can evaluate the powder flowability using the total energy which is estimated from the torque on the impeller and the vertical force on the base. From the results of investigation of flow mechanism in this tester, shear stress can determine the flow energy for a powder under given test conditions in the FT4. On the other hand, it is necessary to note the results are influenced by particle properties such as particle shape and cohesiveness.

Regarding the evaluation of flowability of cohesive powder using vibration, the vibrating capillary method and the vibrating shear tube method have been developed. These systems can evaluate the flowability by using the mass flow rate and the vibration acceleration. These are effective operations to evaluate the flowability of strongly cohesive powder.

Evaluation method of flowability using cohesive powder discharge from an orifice by air pressure has also been introduced. This method can evaluate flowability based on the relationship between mass flow rate of powder and average interstitial air pressure at the top of the powder bed. Additionally, cohesiveness of powder can be also studied by using the ratio of separation force and gravity force on a particle.

To understand the mechanism of flushing, several methods such as external loading, vertical vibration, and the fluidized powder flow have been introduced. The results revealed the flushing occurred for high interstitial air pressure and void fraction, and the spouting of powder from an orifice is strongly related with the pressure difference between the interstitial air pressure and the outside of an orifice.

Acknowledgements

A part of this work of author was supported by JSPS Grant-in-Aid for Young Scientists (B) (Grant Number 16760143), and by a research grants of Hosokawa Powder Technology Foundation.

Nomenclature

a	real contact radius during the indentation (m)
A_i	projected area of the impression (m^2)
C_d	discharge coefficient (–)
d_b	diameter of indenter (m)
D	orifice diameter (m)
E	total energy (J)
F	vertical force acting on the base (N)
F_g	gravity force on a particle (N)
F_{max}	maximum indentation load (N)
FL	Carr's floodability index (–)
FW	Carr's flowability index (–)
g	gravitational acceleration (m s^{-2})
h	penetration depth (m)
h_c	critical indentation depth (m)
h_f	residual indentation depth (m)
h_{max}	maximum indentation depth (m)
H	separation force (N)
H_D	hardness of the consolidated powder (Pa)
k_c	coordination number (–)
k_p	particle shape factor (–)
m_p	mass flow rate (kg s^{-1})
p	pressure inside vessel (Pa)
p_a	pressure difference (Pa)
p_{avg}	average interstitial air pressure (Pa)
p_o	pressure at outside of an orifice (Pa)
p_s	interstitial air pressure at the beginning of powder discharge (Pa)
R	impeller radius (m)
T	torque acting on the impeller (N m)
x_p	mean particle diameter (m)
β	helix angle (degree)
ρ_p	particle density (kg m^{-3})
ε_i	initial void fraction (–)

References

Barletta D., Donsi G., Ferrari G., Poletto M., Russo P., Solid flow rate prediction in silo discharge of aerated cohesive powders, AIChE Journal, 53 (2007) 2240–2253.

Bharadwaj R., Ketterhagen W.R., Hancock B.C., Discrete element simulation study of a Freeman powder rheometer, Chemical Engineering Science, 65 (2010) 5747–5765.

Bruff W., Some characteristic qualities of powder materials, Journal of Engineering for Industry, Transactions of the ASME, 91 (1969) 323–328.

Bruni G., Colafigli A., Lettieri P., Elson T., Torque measurement in aerated powders using a mechanically stirred fluidized bed rheometer (msFBR), Chemical Engineering Research and Design, 83 (A11) (2005) 1311–1318.

Bruni G., Lettieri P., Newton D., Barletta D., An investigation of the effect of the interparticle forces on the fluidization behaviour of fine powders linked with rheological studies, Chemical Engineering Science, 62 (2007a) 387–396.

Bruni G., Barletta D., Poletto M., Lettieri P., A rheological model for the flowability of aerated fine powders, Chemical Engineering Science, 62 (2007b) 397–407.

Calvert G., Curcic N., Redhead C., Ahmadian H., Owen C., Beckett D., Ghadiri M., A new environmental bulk powder caking tester, Powder Technology, 249 (2013) 323–329.

Cannavacciuolo A., Barletta D., Donsi G., Ferrari G., Poletto M., Arch-free flow in aerated silo discharge of cohesive powders, Powder Technology, 191 (2009) 272–279.

Carr R.L., Evaluating flow properties of solids, Chemical Engineering, 72 (1965a) 163–168.

Carr R.L., Classifying flow properties of solids, Chemical Engineering, 72 (1965b) 69–72.

Carr R.L., Properties of solids, Chemical Engineering, 13 (1969) 7–16.

Chen Q., Zafer U., Ghadiri M., Bi J., Assessment of surface caking of powders using the ball indentation method, International Journal of Pharmaceutics, 521 (2017) 61–68.

De Jong J.A.H., Vertical air-controlled particle flow from a bunker through circular orifices, Powder Technology, 3 (1969/70) 279–286.

De Jong J.A.H., Aerated solids flow through a vertical standpipe below a pneumatically discharged bunker, Powder Technology, 12 (1975a) 197–200.

De Jong J.A.H., Hoelen Q.E.J.J.M., Cocurrent gas and particle flow during pneumatic discharge from a bunker through an orifice, Powder Technology, 12 (1975b) 201–208.

Donsi G., Ferrari G., Poletto M., Russo P., Aggregative behavior of cohesive magnesium carbonate powders during fluidization and aerated discharge, KONA Powder and Particle Journal, 21 (2003) 54–65.

Donsi G., Ferrari G., Poletto M., Russo P., Gas pressure measurement inside an aerated hopper, Chemical Engineering Research and Design, 82 (2004) 72–84.

Freeman R., Measuring the flow properties of consolidation, conditioned and aerated powders—A comparative study using a powder rheometer and a rotational shear cell, Powder Technology, 174 (2007) 25–33.

Geldart D., Types of gas fluidization, Powder Technology, 7 (1973) 285–292.

Geldart D., Haesebrouck M., Studies on the intermittent discharge of coarse solids from fluidised beds, Chemical Engineering Research and Design, 61 (1983) 162–166.

Geldart D., Williams, J.C., Flooding from hoppers: identifying powder likely to give problem, aeration, Powder Technology, 43 (1985) 181–183.

Harada S., Li H., Funatsu K., Tomita Y., Spouting of fine powder from vertically vibrated bed, Chemical Engineering Science, 57 (2002) 779–787.

Harada S., Particle jet generated by an external force, Journal of Jet Flow Engineering, 21 (2004) 13–18.

Hare C., Zafer U., Ghadiri M, Freeman T., Clayton J., Murtagh M., Analysis of the dynamic of the FT4 powder rheometer, Powder Technology, 285 (2015) 123–127.

Hare C., Zafer U., Ghadiri M, Freeman T., Clayton J. Murtagh M., Correction to "Analysis of the dynamic of the FT4 powder rheometer" [Powder Technol. 285 (2015) 123–127], Powder Technology, 315 (2017) 37–38.

Hassanpour A., Ghadiri M., Characterisation of flowability of loosely compacted cohesive powders by indentation, Particle & Particle Systems Characterization, 24 (2007) 117–123.

Horio T., Yasuda M., Matsusaka S., Effect of particle shape on powder flowability of microcrystalline cellulose as determined using the vibration shear tube method, International Journal of Pharmaceutics, 473 (2014) 572–578.

Ishii K., Suzuki M., Segawa T., Kihara Y., Yasuda M., Matsusaka S., Flowability measurement of pulverized and granulated materials using vibrating tube method, Advanced Powder Technology, 22 (2011a) 319–323.

Ishii K., Suzuki M., Segawa T., Kihara Y., Yasuda M., Matsusaka S., A vibrating tube method for evaluating flowability of a small amount of sample particles, Advanced Powder Technology, 22 (2011b) 522–525.

Jenike A.W., Quantitative design of mass-flow bins, Powder Technology, 1 (1967) 237–244.

Jiang Y., Matsusaka S., Masuda H., Yokoyama T., Evaluation of flowability of composite particles and powder mixtures by a vibrating capillary method, Journal of Chemical Engineering of Japan, 39 (2006) 14–21.

Jiang Y., Matsusaka S., Masuda H., Qian Y., Development of measurement system for powder flowability based on vibrating capillary method, Powder Technology, 188 (2009) 242–247.

Kuchii S., Tsutsumiya M., Funatsu K., Tomita Y., Interstitial fluid pressure and voidage in flushing phenomenon of fine powders, Advanced Powder Technology, 7 (1996) 41–49.

Kuchii S., Research on flushing phenomenon of powder, Ph.D. Thesis, Kyushu Institute of Technology, 1997.

Kuchii S, Tomita Y., Flushing phenomenon of fine powder, Powder Technology, 126 (2002) 275–282.

Leturia M., Benali M., Lagarde S., Ronga I, Saleh K., Characterization of flow properties of cohesive powders: A comparative study of traditional and new testing methods, Powder Technology, 253 (2014) 406–423.

Li M., Leturia M., Saleh K., Analysis of the periodic motion in a powder rheometer and development of a new flowability testing method, KONA Powder and Particle Journal, 35 (2018) 160–171. Doi:10.14356/kona.2018002.

Lloyd P.J., Webb P.J., The flooding of a powder—the importance of particle size distribution, Powder Technology, 51 (1987) 125–133.

Martin P.D., Davidson J.F., Flow of powder through an orifice from a fluidized bed, Chemical Engineering Research and Design, 61 (1983) 225–232.

Matsusaka S., Yamamoto K., Masuda H., Micro-feeding of a fine powder using a vibrating capillary tube, Journal of the Society of Powder Technology, Japan, 32 (1995a) 83–88.

Matsusaka S., Urakawa M., Masuda H., Micro-feeding of fine powders using a capillary tube with ultrasonic vibration, Advanced Powder Technology, 6 (1995b) 283–293.

Matsusaka S., Yamamoto K., Masuda H., Micro-feeding of a fine powder using a vibrating capillary tube, Advanced Powder Technology, 7 (1996) 141–151.

Nagashima H., Ishikura T., Identification of flow properties of fine powders based on dynamic flow characteristics obtained by stirring and aerating, Journal of the Society of Powder Technology, Japan, 52 (2015) 576–584.

Naito M. and Makino H., Shoho Kara Manabu Funtaigizyutsu (in Japanese), Morikita Shuppan, 2011. ISBN: 978-4-627-24181-7

Nan W., Ghadiri M., Wang Y., Analysis of powder rheometry of FT4: Effect of air flow, Chemical Engineering Science, 162 (2017) 141–151.

Ogata K., Spouting phenomenon of fluidized fine cohesive powder, Journal of the Society of Powder Technology, Japan, 45 (2008) 844–851.

Ogata K., Effect of initial void fraction and fluidized air flow on spouting of fine powder through an orifice, Journal of the Society of Powder Technology, Japan, 46 (2009) 187–196.

Ogata K., Miura S., Experimental investigation of cohesive fine powder discharge from an orifice using air flow, Proceedings of the 8th International Conference on Multiphase Flow 2013 (CD-ROM), Paper No.620 (2013) 1–5.

Ogata K., Miura S., Ouchi K., Utsunomiya Y., Ninomiya Y., Study on evaluation of flowability of cohesive powder using test of powder discharge by air flow, Journal of the Society of Powder Technology, Japan, 52 (2015) 714–722.

Ogata K., Ouchi K., Evaluation of flowability of cohesive powder using test of powder discharge by air flow, Journal of the Society of Powder Technology, Japan, 54 (2017) 460–469.

Pantaleev S., Yordanova S., Janda A., Marigo M., Ooi J.Y., An experimentally validated DEM study of powder mixing in a paddle blade mixer, Powder Technology, 311 (2017) 287–302.

Pasha M., Hare C., Hassanpour A., Ghadiri M., Analysis of ball indentation on cohesive powder beds using distinct element modelling, Powder Technology, 233 (2013) 80–90.

Rumpf H.C.H., Zur theorie der zugfestigkeit von agglomeraten bei kraftübertragung an kontaktpunkten, Chemie Ingenieur Technik, 42 (1970) 538–540.

Ridgway H., Tarbuck K.J., The random packing of spheres, British Chemical Engineering, 12 (1967) 384–388.

Rathbone T., Nedderman R.M., The deaeration of fine powders, Powder Technology, 51 (1987a) 115–124.

Rathbone T., Nedderman R.M., Devidson J.F., Aeration, deaeration, and flooding of the particles, Chemical Engineering Science, 42 (1987b) 725–736.

Satoh M., Kondo N., Iwasaki T., Miyanami K., Okudaira Y., Ando H., The development of a rotary-intrusion-type rheometer for a powder bed and the measurement of the dynamic physical properties of powders, Journal of the Society of Powder Technology, Japan, 11 (1994) 783–788.

Schulze D., Discussion of testers and test procedures, in: Powders and Bulk Solids: Behavior, Characterization, Storage and Flow, Springer Berlin Heidelberg, Berlin, Heidelberg (2008) pp. 163–198.

Schwedes J., Review on testers for measuring flow properties of bulk solids, Granular Matter, 5 (2003) 1–45.

Tashiro H., Ogata K., Wakamizu Y., Funatsu K., Tomita Y., Flushing phenomenon due to the impact force on the powder surface by free falling of particles, Proceedings of World Congress on Particle Technology 5 (CD-ROM), Paper No. 40a (2006a) 1–7.

Tashiro H., Ogata K., Wakamizu Y., Funatsu K., Tomita Y., Flushing phenomenon of fine powder due to the head, Proceeding of the 5th International Conference for Conveying and Handling of Particulate Solids (CD-ROM), Paper No. 96 (2006b) 1–6.

Thakur S.C., Ahmadian H, Sun J., Ooi J.Y., An experimental and numerical study of packing, compression, and caking behaviour of detergent powders, Particuology, 12 (2014) 2–12.

SPTJ (The Society of Powder Technology, Japan), Kisoutyuu no Ryuushi Bunsan Bunkyuu Bunri Sousa (in Japanese), Nikkan Kogyo Shinbunsha, Tokyo, 2006. ISBN: 978-4-526-05580-5

Tomita Y., Ikeuchi H., Kuchii S., Funatsu K., Flooding (“flushing”) of powder through a small orifice by an external load, Journal of Rheology, 38 (1994) 231–240.

Tomasetta I., Barletta D., Lettieri P., Poletto M., The measurement of powder flow properties with a mechanically stirred aerated bed, Chemical Engineering Science, 69 (2012) 373–381.

Tsubaki J., New interpretation and application of Rumpf equation, Journal of the Society of Powder Technology, Japan, 21 (1984) 30–39.

Vasilenko A., Koynov S., Glasser B.J., Muzzio F.J., Role of consolidation state in the measurement of bulk density and cohesion, Powder Technology, 239 (2013) 366–373

Wang C., Hassanpour A., Ghadiri M., Characterization of flowability cohesive powders by testing small quantities of weak compacts, Particuology, 6 (2008) 282–285.

Wilkinson S.K., Turnbull S.A., Yan Z., Stitt E.H., Morigo M., A parametric evaluation of powder flowability using a Freeman rheometer through statistical and sensitivity analysis: A discrete element method (DEM) study, Computers and Chemical Engineering, 97 (2017) 161–174.

Yan Z., Wilkinson S.K., Stitt E.H., Marigo M., Investigating mixing and segregation using discrete element modelling (DEM) in the Freeman FT4 rheometer, International Journal of Pharmaceutics, 513 (2016) 38–48.

Zainuddin M.I., Yasuda M., Liu Y., Maruyama H., Matsusaka S., Development of vibration shear tube method for powder flowability evaluation, Powder Technology, 217 (2012) 548–553.

Zafar U., Hare C., Calvert G., Ghadiri M., Girimonte R., Formisani B., Quintanilla M.A.S., Velverde J.M., Comparison of cohesive powder flowability measured by Schuzle shear cell, Raining bed method, Sevilla powder tester and new Ball indentation method, Powder Technology, 286 (2015) 807–816.

Zafar U., Hare C., Hassanpour A., Ghadiri M., Ball indentation on powder beds for assessing powder flowability: Analysis of operation window, Powder Technology, 310 (2017a) 300–306.

Zafar U., Vivacqua V., Calvert G., Ghadiri M., Cleaver J.A.S., A review of bulk powder caking, Powder Technology, 313 (2017b) 389–401.

Author’s Short Biography

Koichiro Ogata

Koichiro Ogata is an Associate Professor of mechanical engineering at the National Institute of Technology (NIT), Oita College. He received his PhD degree in 2001 from the Kyushu Institute of Technology (KIT). He was a research fellow until 2003 at the KIT and worked until 2012 at the NIT, Oshima College. He is a visiting researcher in school of Chemical and Process Engineering at the University of Leeds in 2017–2018. He is focusing on the study of dry powder handling such as evaluation of flowability of cohesive powder, dense phase pneumatic conveying, dispersion of cohesive powder, and the heating characteristics of waste gypsum.

KONA Powder and Particle Journal No. 36 (2019) 50–71/Doi:10.14356/kona.2019004 Review Paper

Droplet Microfluidics as a Tool for the Generation of Granular Matters and Functional Emulsions[†]

Adam S. Opalski, Tomasz S. Kaminski and Piotr Garstecki[*]

[1] *Institute of Physical Chemistry, Polish Academy of Sciences, Poland*

Abstract

Emulsion—a liquid dispersed in another liquid—is in many respects very similar to granular matter. In the early 2000s a new technology—droplet microfluidics—began emerging from the wider field of microfluidics. Droplet microfluidics was quickly established as a discipline of science and engineering and has been used for the generation of highly uniform emulsions. The last few years have brought significant advances to the field, directed towards a wide range of applications in material sciences—from synthesis of nanoparticles in droplets to assembling complex droplets and using droplets as templates for ordered materials, with applications in food, cosmetic and diagnostic industries. Droplet microfluidic platforms are also successfully used as analytical tools in molecular biology and biochemistry, in e.g. high-throughput screening, digital assays, encapsulation of single cells, sequencing technologies, and in point-of-care diagnostic applications. This article provides an accessible overview of the physical phenomena observed in multiphase flow at the microscale and the techniques in droplet microfluidics systems. We also present the most interesting applications and potential further directions of research in this fascinating young field of science and engineering.

Keywords: emulsions, microfabrication, microdroplets, microfluidics, double emulsions, material sciences

1. Introduction

Granular materials are interesting from the physical point of view as they can be considered both as unusual solids and as unusual fluids. For example, despite being large conglomerates of discrete macroscopic particles, granular materials can flow like fluids (Hinrichsen and Wolf, 2004). These materials comprise discrete pieces of solid materials immersed in an interstitial fluid, e.g. air, just like emulsions in which discrete volumes of liquid are dispersed in another liquid (Everett, 1972). Similarly to the physicochemical methods of production of monodisperse particles and granules, microfluidics provides an approach to generate monodisperse functional emulsions—fluidic equivalents of granular materials (**Fig. 1**). Droplet microfluidics is a young and dynamic field of research that focuses on precise manipulations of microdroplets with volumes ranging from femto- to microliters—i.e. covering the range of three orders of magnitude in the length scale (here measured by the diameter of the droplet) between a micrometer and a millimeter (Leman et al., 2015).

2. General introduction to microfluidics

Microfluidics is an interdisciplinary field of research intersecting engineering, physics, chemistry, nanotechnology, biology and material sciences (Joensson and Andersson Svahn, 2012). Microfluidics studies the properties of fluids at the microscale and develops systems relevant to both academic and industrial applications. Microfluidic techniques are based on the precise handling of small volumes of fluids confined to miniature channels with typical dimensions from one to hundreds of microns. The small dimensions guarantee the laminar flow of liquids and provide for precise control over the transport of fluids (Jeon et al., 2000; Reyes et al., 2002). The channels are usually microfabricated on small polymeric (thermoplastic or elastomer) or glass plates and are typically inexpensive and disposable (Berthier et al., 2012; Unger et al., 2000).

2.1 Single-phase microfluidics

In the first years of the microfluidic era, the research focused only on the single-phase continuous-flow systems which controlled the flow of miscible liquids in the networks of microfluidic channels (Squires and Quake, 2005). In these systems small portions of fluids are delivered to a chip in a specified order and are next mixed and

---

[†] Received 30 June 2017; Accepted 17 August 2017
J-STAGE Advance published online 17 March 2018

[1] Kasprzaka 44/52, 01-224 Warsaw, Poland
[*] Corresponding author: Piotr Garstecki;
E-mail: garst@ichf.edu.pl
TEL: +48-22-343-2233 FAX: +48-22-343-3333

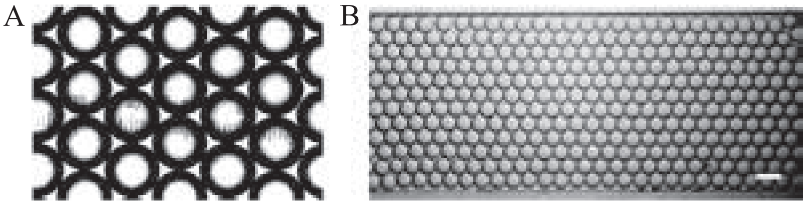

Fig. 1 (**A**): Array sizing of monodisperse close-packed polystyrene particles observed by microscopy. Image used in compliance with Creative Commons BY 4.0 (Mitchell, 2000). (**B**): Collection of monodisperse water droplets submerged in oil and stored in a microfluidic chamber (Holtze et al., 2008). Reproduced from (Holtze et al., 2008) with permission of The Royal Society of Chemistry.

incubated under various conditions (Sackmann et al., 2014). Flow is usually applied and controlled via the use of pneumatic microvalves (pressure-driven flow), pumps (displacement-driven flow) (Harrison et al., 1993) or with the use of specific physical phenomena such as, e.g. electro-wetting or electrokinetic flow (Persat et al., 2009a, b). The breakthrough point for single-phase microfluidics was development of the microfluidic large-scale integration—a fluidic equivalent of a technology routinely used in the electronic industry that allowed for massive parallelization in the execution of biological assays and chemical reactions in complex microscopic hydraulic architectures (Melin and Quake, 2007; Thorsen et al., 2002).

2.2 Limitations of continuous flow microfluidics

Despite many unique characteristics that led to powerful and robust applications, single-phase microfluidics has limitations. First drawback is the parabolic profile of flow with faster velocity of the fluid at the center of the channel (phenomenon known as Taylor-Aris dispersion) that results in unequal residence times of substrates in single-phase microfluidic reactors (Aris, 1960; Taylor, 1953). Additionally, mixing is slow due to the laminar regime of flow typical at the microscale, and this problem is further amplified in the case of viscous fluids (Casadevall i Solvas and deMello, 2011; Song et al., 2006; Squires and Quake, 2005). Moreover, the solid substrate is in direct contact with the solution and as a consequence, chemical compounds and biological objects (biomacromolecules, proteins, nucleic acids, cells, etc.) can foul the surface of the channel, thus leading to cross-contamination or, in extreme cases, to clogging of the channel (Schneider et al., 2013). And vice versa—bulk material of the chip can release chemical compounds influencing the process in the microfluidic reactor—e.g. monomers of uncured polymer poly(dimethylsiloxane), PDMS, can be toxic for cells growing in a single-phase microfluidic chamber (Regehr et al., 2009). Another challenge lies in the demanding fabrication of multilayer devices that contain a relatively large number of flow inputs and outputs providing complete control over the transport of the fluid, yet the entire system is characterized by slow actuation of the integrated valves (Thorsen et al., 2002).

3. Droplet microfluidics

3.1 Introduction to droplet microfluidics

Microdroplets possess several unique properties that justify the research on multiphase flows at the microscale and their use as an attractive alternative to the classic macroscale reactors or continuous-flow microfluidic systems. Droplet microfluidics is a technique in which multiple immiscible fluids are confined in microchannels whose size is typically in a range from one to hundreds of micrometers. Discrete volumes of liquids or gases (i.e. droplets or bubbles) are transported, manipulated and investigated in the network of microscopic channels. The common and main function of microfluidic multiphase systems is the generation of highly monodisperse emulsions. Microdroplet emulsions are denoted as water-in-oil (or W/O), if an aqueous phase is dispersed in an organic phase, or oil-in-water (O/W), if the phases are inversed (Xu et al., 2006). There are other combinations of fluids used in microdroplet systems, including i) water-in-water emulsion (Esquena, 2016); ii) oil in another oil, (Klapper et al., 2008) or iii) emulsions that comprise more than two phases (highly ordered emulsions, e.g. double-emulsion W/O/W or O/W/O, triple-emulsion W/O/W/O, etc.) (Abate and Weitz, 2009; Vladisavljević et al., 2017).

Droplets dispersed in the immiscible continuous phase offer the advantage of large numbers of isolated microvolumes—without the need to build solid wall enclosures for each of the microvolumes (Agresti et al., 2010). Spatial isolation of fluidic microcompartments limits the risk of cross-contamination and completely prevents dispersion of the time of residence of analytes in the flow-through system (Temiz et al., 2015). Good heat and mass transfer and fast mixing also occur thanks to the chaotic advection (Gu et al., 2011; Tice et al., 2003, 2004). Microfluidic systems are used to perform typical laboratory operations using a fraction of the volume of the reagents and overall in a shorter time when compared to batch methods (Teh et al., 2008). The droplet microfluidic systems can be automated and operated at extremely high throughputs of up to thousands of operations per second (e.g. generation or sorting of droplets in the microfluidic device) (Guzowski et al., 2011; Leman et al., 2015; Sciambi and Abate, 2015).

3.2 Basics of physics of microdroplet systems

3.2.1 Surface forces

The fundamental force in the generation and stability of emulsions is that stemming from the energy of interfaces. Liquid molecules are held together by cohesive forces and each molecule is pulled in every direction equally by its neighbors. At the interface between two immiscible fluids, molecules are pulled only by their neighbors from the inside of the droplet, creating additional internal pressure, called Laplace pressure (ΔP). In the equilibrium state, this pressure is balanced by the surface tension—a tendency to curve the interface to minimize the surface area. Balance of forces is described by the Young-Laplace equation:

$$\Delta P = P_{\text{inside}} - P_{\text{outside}} = \gamma (1/R_1 + 1/R_2) \quad (1)$$

ΔP–Laplace pressure [Pa];

P_{inside}–pressure inside the curved interface [Pa];

P_{outside}–pressure outside the curved interface [Pa];

γ–surface tension [J·m^{-2}];

R_1 and R_2–principal radii of curvature. (Tadros, 2013; de Gennes et al., 2004)

Surface tension plays the critical role in the stability of droplets during their transport and the manipulation of them on a chip (Joensson and Andersson Svahn, 2012). Emulsions are metastable and with time they degrade via the coalescence and Ostwald ripening—a process within which the droplets merge with each other (Leal-Calderon and Poulin, 1999). The lifetime of droplets (and the emulsion) may vary from milliseconds to years depending on the stabilizing characteristics of a surfactant, physical conditions of the environment and the index of polydispersity—i.e. the breadth of the distribution of volumes of the droplets (Baret, 2012). The most common composition of continuous phase used in droplet microfluidics comprises fluorinated liquid and a biocompatible fluorosurfactant which ensures stability of the emulsions (Holtze et al., 2008). For other liquids one must use a suitable surfactant which is often a challenge (Baret, 2012; Holtze et al., 2008).

Novel and promising approaches to stabilizing emulsions are based on the use of nanoparticles in the so-called Pickering emulsions (Pan et al., 2014, 2015), or surfactant-free emulsions (Sakai, 2008). In complex emulsions, such as double emulsions in which the droplets encapsulate yet more droplets in themselves, it is important to use proper sets of additives for each phase (surfactants, osmotic agents) in order to balance all types of forces in the system, including osmotic pressure, Laplace pressure and interfacial forces (Deng et al., 2016; Kanouni et al., 2002; Zinchenko et al., 2014).

3.2.2 Wetting

In droplet microfluidic systems, a phenomenon of utmost importance is wetting, i.e. the ability of the solid surface to maintain contact with a continuous liquid due to molecular interactions (Tarazona, 1987). Wetting can be defined as the function of the surface tension and contact angle between the fluid and the solid and is schematically presented in **Fig. 2**. In general, for contact angles $\theta < 90°$, wetting of the surface by the liquid is favorable. For contact angles $\theta > 90°$, wetting is unfavorable—fluid minimizes the contact area with solid. When $\theta \sim 90°$, then liquid partially wets the solid substrate and makes the precise control over liquid very challenging, which is highly undesirable in droplet microfluidics. For the droplet microfluidic systems to work reproducibly and controllably, it is a critical requirement that the droplet phase does not wet the walls of the channels and is always separated from these walls by at least a thin wetting film of

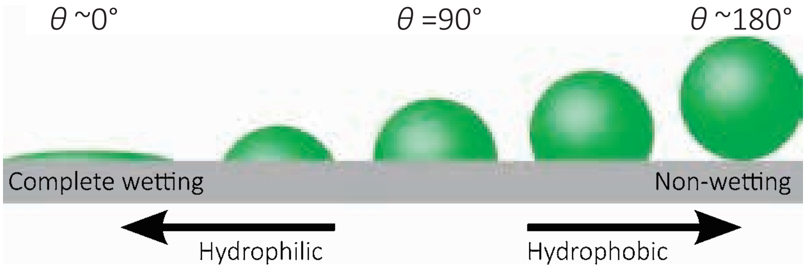

Fig. 2 Schematic illustration of the phenomena of hydrophilicity and hydrophobicity and partial wetting of the surface as a function of the static contact angle of the aqueous droplet phase on the solid substrate.

the continuous liquid. In droplet microfluidic systems, wetting of the channel walls by both phases must be perfectly controlled in order for the system to work in a stable and predictable manner. Preferential wetting of the walls by one of the phases determines which phase is the continuous phase (the one that wets walls) and which one will be dispersed (does not wet the walls). W/O emulsions, or any multiple emulsion with oil as the outer phase, are made in hydrophobic devices (Jankowski et al., 2011). O/W or any multiple emulsions with an aqueous outer phase are formed in hydrophilic devices (Derzsi et al., 2011; Jankowski et al., 2013).

3.2.3 Capillary number

The capillary number (*Ca*) is a dimensionless quantity that is used to define the mechanism of droplet formation in each of the following methods of droplet generation: i) in co-axial capillaries (Huang et al., 2014), ii) T-junction (Christopher et al., 2008; De Menech et al., 2008; Garstecki et al., 2006; Van Steijn et al., 2009), iii) flow-focusing junction (Dollet et al., 2008; Garstecki et al., 2005b; Nie et al., 2008) and iv) step-emulsification systems (Hein et al., 2015a, b). *Ca* represents the ratio of viscous forces versus interfacial tension forces and is defined as

$$Ca = \mu U / \gamma \tag{2}$$

μ–dynamic viscosity of the fluid [Pa·s];

U–characteristic velocity of the fluid [$\text{m}\cdot\text{s}^{-1}$];

γ–surface tension [$\text{J}\cdot\text{m}^{-2}$].

For low values of *Ca* ($Ca <\sim 10^{-2}$), droplet formation is driven by interfacial forces in the so-called squeezing regime (Garstecki et al., 2005b, 2006). The tip of the stream of the droplet phase advances to the junction and blocks the flow of the continuous liquid. The viscous shear exerted by the flow of the continuous liquid is too weak to deform the growing droplet. At the same time, the droplet obstructs the flow of the continuous liquid through the junction and the pressure upstream of the droplet increases and causes squeezing of the neck connecting the growing droplet with the inflow of the droplet phase. This process gradually leads to collapse of the neck of the liquid to be dispersed and release of a discrete volume of the liquid as a droplet. Within the squeezing regime, the volume of the droplet depends predominantly on the ratio of flow velocities of both immiscible phases and does not significantly depend on the viscosities of the liquids or the interfacial tension between them.

The predominating force changes from interfacial to shear stress at higher values of *Ca* in the dripping regime. During this process, the droplet is formed before the phase to be dispersed fills the cross-section of the microchannel, which results in much higher droplet formation rates than in the squeezing regime. At very high flow rates of fluids which result in high shear forces and high values of *Ca*, the droplets are produced in a jetting regime in which an unstable jet of fluid is formed and droplets are pinched-off far downstream of the junction (Utada et al., 2007; Zhu and Wang, 2017).

In some cases, besides *Ca*, other dimensionless numbers can also be used for the description of the process of droplet formation—e.g. Weber number (*We*), Péclet number (*Pe*), and Bond number (*Bo*). However, their significance in the description of phenomena in microfluidic systems is usually much smaller than the role of *Ca* (Lagus and Edd, 2013).

3.3 Formation of droplets in microfluidic systems

3.3.1 Methods using co-flowing streams of immiscible phases

The formation of droplets is the primary functionality of droplet microfluidic systems. Currently, active microfluidic methods are mostly used for the generation of monodisperse droplets. We define active droplet formation as a process during which the droplets are sheared from the liquid thread by a stream of continuous phase. Such methods are characterized by the use of dedicated geometries for droplet formation, i.e. i) T-junction, introduced in the early 2000s (Thorsen et al., 2001) depicted in **Fig. 3A**; ii) flow-focusing junction introduced to the planar microfluidic devices by Anna et al. (Anna et al., 2003) shown in **Fig. 3B**; and iii) co-flowing geometry presented in **Fig. 3C** (Umbanhowar et al., 2000; Utada et al., 2005). The use of these geometries requires active control of the flow of all the phases, and results in the high-throughput production of droplets. During the active generation of droplets, significant volumes of outer phase liquids are used, in comparison to the volume of dispersed phase, resulting in quite sparse emulsions with a polydispersity index usually below 5 % in diameter (Zhu and Wang, 2017; Zinchenko et al., 2014).

3.3.2 Passive methods requiring the flow of only the dispersed phase

Microfluidic techniques exploiting interfacial phenomena rather than forces resulting from the flow of the continuous liquid are called passive methods and comprise microchannel emulsification (Sugiura et al., 2000), membrane emulsification (Spyropoulos et al., 2014), EDGE emulsification (van Dijke et al., 2010), and step emulsification (Dangla et al., 2013). Often they do not even require outer phase flow and yield highly monodisperse droplets (Dutka et al., 2016; Zhu and Wang, 2017). Step emulsification shares roots with microchannel emulsifica-

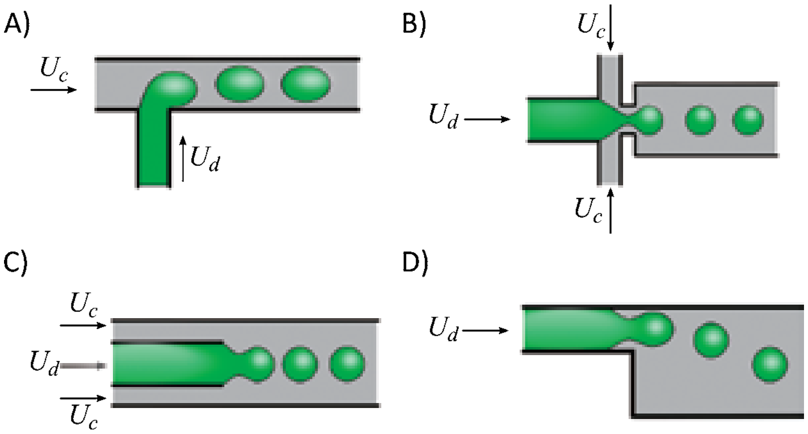

Fig. 3 Schematic diagrams depicting different geometries used for formation of droplets: **A**) T-junction, **B**) flow-focusing junction, **C**) co-axial capillaries, **D**) step-emulsification module. The volume of generated droplets is defined by several factors, including flow velocities of the dispersed phase (U_d) and continuous phase (U_c) and dimensions of microfluidic channels.

tion and is presented in **Fig. 3D** together with methods of active droplet formation (Dangla et al., 2013; Kobayashi et al., 2002).

3.3.3 Production of multiple emulsions

A very interesting section of droplet microfluidics is the formation of double emulsions (DE) that are defined as emulsions of complex droplets with an inner immiscible core liquid encapsulated in a liquid shell. The complex structure of the immiscible core and shell is suspended in yet another liquid of continuous phase. The innermost and outermost liquids may be the same fluid, e.g. water. Most commonly, double-emulsion droplets comprise aqueous droplets in an oil shell suspended in an aqueous environment (W/O/W), but emulsions of a higher order and different composition are also known and generated in microfluidic systems (Choi et al., 2016a; Garti, 1997). Ideally, the volume of the middle phase should be as low as possible since a reduction of the shell thickness makes double emulsions more stable against rupture, defined as a coalescence of the core droplet with the outer phase. The rupture of the double droplet occurs when the inner droplet moves towards the outer interface of the shell and breaks it. The hydrodynamic resistance that impedes movement of the inner droplet increases with the reduction in shell thickness—for sufficiently thin shells the hydrodynamic resistance allows only marginal fluid flows (Kim et al., 2011; Vian et al., 2016). Currently, the most advanced direct method of single-core DE production reports a 2.5-µm-thick shell in droplets 50 µm in diameter. The thickness of the shell can be further reduced by post-processing to submicron dimensions, i.e. squeezing the double emulsion through the narrow slit that causes the multiple emulsion to lose some shell volume (Akamatsu et al., 2015; Arriaga et al., 2015; Vian et al., 2016) or by dewetting of the shell phase which may lead to the formation of polymerosome (Deng et al., 2016; Ho et al., 2008; Kim et al., 2013).

Microfluidic systems for the generation of multiple droplets are similar to those used for the formation of single emulsions—they utilize one droplet generation junction located in proximity to another junction. Usually, systems for DE generation require chemical treatment of the surface to adjust the wettability of the channel walls (Abate et al., 2011).

Fig. 4 depicts selected and the most common methods for the generation of DE in microfluidic channels. For more information on double emulsion generation, the reader is encouraged to study excellent reviews on the subject (Chong et al., 2015; Vladisavljević et al., 2017; Zhu and Wang, 2017).

All the actively controlled methods provide users with a high degree of control over the process of formation and over the structure of double emulsions, comprising droplets either with single or with multiple cores. The microfluidic methods are truly unique in providing the ability to tune the volumes and number of the cores in multiple droplets. The methods shown in **Fig. 4A** and **4B** share the principle that at first an aqueous droplet is generated in oil in a hydrophobic junction. Next the droplet is transported within an oil thread to another junction of different (hydrophilic) wetting properties where a second aqueous phase shears off the (W/O) single droplet to form a double (W/O/W) droplet (Nisisako et al., 2005; Yan et al., 2013). The mechanism is different in the case of the liquids flowing co-axially in a glass capillary where the DE formation occurs in a single step (**Fig. 4C**). The device comprises two cylindrical glass capillary tubes nested within yet another glass capillary. The inner fluid is pumped through a tapered cylindrical capillary tube, and the middle fluid is

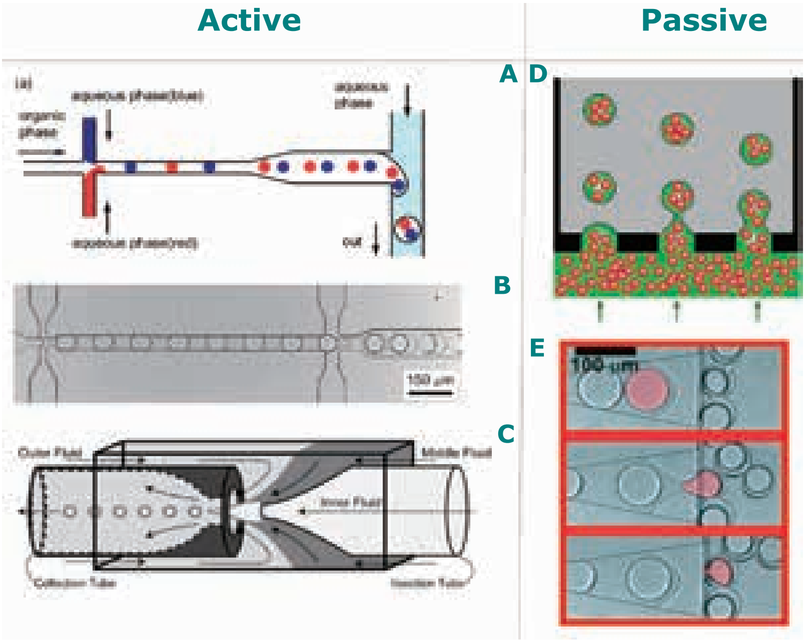

Fig. 4 Schematics of microfluidic technologies for the generation of double emulsions. **A–C** show methods in which the outer phase flow is controlled, **D** and **E** depict methods without the control over the outer phase. **A**—two consecutive T-junctions. Adapted from (Nisisako et al., 2005) with permission from The Royal Society of Chemistry; **B**—two consecutive flow-focusing junctions (Yan et al., 2013); **C**—co-axial microcapillary device that forms double emulsions—from (Utada et al., 2005). Reprinted with permission from AAAS; **D**—microchannel emulsification of a single emulsion into a double emulsion (Sugiura et al., 2004). The image was created exclusively for the purpose of this review. **E**—a single emulsion fed into a step-emulsification module to produce a double emulsion. Adapted from (Eggersdorfer et al., 2017) with permission of The Royal Society of Chemistry.

pumped through the outer coaxial region. Both fluids form a coaxial flow at the exit of the tapered tube where they meet the outermost fluid, supplied from the other direction through the outer coaxial region. As there is only one outlet from the device, all fluids are forced to flow through the exit orifice where they are hydrodynamically focused into a co-axial thread that eventually ruptures to form multiple droplets (Choi et al., 2016b; Utada et al., 2005).

Methods for the formation of double emulsions are considered passive ones if just the final emulsification step is passive. Firstly, the feed (single emulsion) is generated. Then, the single emulsion is passively split by an outer fluid to form a double emulsion. Passive processes provide a smaller degree of control over the droplet formation, because the operations are hard-wired into the geometries of the devices. Droplet formation also depends on the parameters of used fluids, however, to a smaller extent than on the geometry (Chong et al., 2015; Van Der Graaf et al., 2005). A first system for passive encapsulation of the precisely controlled number of cores inside a double-emulsion droplet has been shown just recently—the single emulsion is used as the feed. Core diameters in the feed emulsion are much smaller than the resultant double emulsions (Eggersdorfer et al., 2017). **Fig. 4** shows two systems for passive emulsification techniques: i) an approach by Eggersdorfer who developed the so-called ‘millipede’ device where multiple step-emulsification nozzles operate in parallel (**Fig. 4E**) (Eggersdorfer et al., 2017), and ii) a system by Sugiura et al., where the single emulsion is extruded from the microchannel through the orifices in the silicone membrane to the outer phase (**Fig. 4D**) (Sugiura et al., 2004).

An interesting method for the formation of a double emulsion utilizes automated droplet microfluidic systems. Such systems combine active and passive methods of droplet formation, enabling the custom tailoring of multiple droplets one by one (Guzowski et al., 2013). The system allows the formation of multiple emulsions that differ in many aspects—from the number of core droplets, the volume fractions (ratio of volume of inner droplet to the outer shell) to the shape of the formed multi-compartment system (Guzowski and Garstecki, 2015; Guzowski et al., 2012, 2013).

In automated microfluidic systems, the operator can use externally controlled valves to program the protocol to be executed, e.g. a sequence of single emulsion droplets to be produced at the first T-junction and then transported to the step at the entrance to the deep reservoir where it becomes engulfed passively in the outer phase—see **Fig. 5A** (Guzowski and Garstecki, 2015; Guzowski et al.,

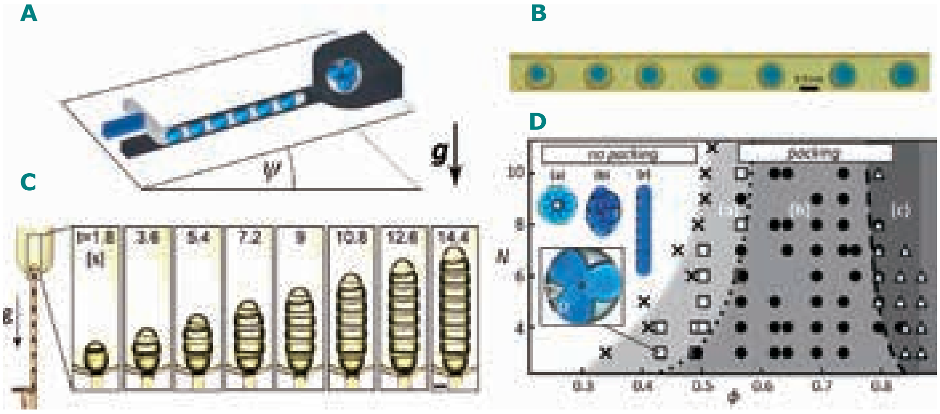

Fig. 5 Automated microfluidic systems for the production of multiple droplets. **A**—overview of the microfluidic device operated in the three phases (blue—aqueous, grey—hydrocarbon oil, dark grey—fluorinated oil), position at angle Ψ in relation to the ground. **B**—subsequent double droplets with various volume fractions, produced with the system depicted in frame **A**. **C**—snapshots of the formation of multiple droplets—a chain with the number of segments increasing in time. **D**—stability diagram for multiple droplets containing N cores in a shell in relation to the volume fractions of the cores (φ). The areas correspond to packing regimes of the cores: a) negligible deformation of the shell, b) strong deformation of the shell (> 5 % asphericity) and c) linear chains of droplets. The inset shows the equilibrium contact angle between the drops, 45° ± 5°. Panels **A** and **D** are reprinted from (Guzowski and Garstecki, 2015) under CC3.0, panel **B** is reprinted from (Guzowski et al. 2013), with permission from The Royal Society of Chemistry and panel **C** from (Guzowski et al. 2012) with permission from The Royal Society of Chemistry.

2012, 2013). Automated systems for the production of double emulsions offer precise control over the size and composition of complex droplets in multiple emulsions, as well as their shape and packing of the core droplets—see **Fig. 5B–5D**. The automated droplet microfluidic system allows tailored single-core double emulsions (**Fig. 5B**) to be obtained, as well as long, multi-compartment chains, stabilized by capillary bridges between the core droplets (**Fig. 5C**). Inner cores can be packed in a number of ways depending on the number of cores and their volume fraction, as presented in **Fig. 5D** (Guzowski and Garstecki, 2015).

3.4 Operations on droplets

The versatility of the droplet microfluidic techniques stems from the ability to first generate and then manipulate droplets on a chip. The droplets can be transported through the network of microchannels and then they can be merged, split, incubated, sorted and the outcome of the reaction can be detected using optical, electrochemical or other analytical methods (Haeberle et al., 2012). Each of the operations can be performed in a dedicated module—a building block of the whole microfluidic system, and these modules can be arranged to form complex devices with many functionalities integrated into a single microfluidic chip (Mair et al., 2017; Schuler et al., 2016).

4. Fabrication of the microfluidic devices for the production of microdroplets

4.1 Prototyping methods

Droplet microfluidic devices can be microfabricated from various materials, e.g. glass, elastomers, thermoplastics, metal, silicone or hybrids of glass and polymer. The choice of the material for fabrication of the chip depends on numerous factors such as: application, cost, material properties and feasibility of fabrication. Some of the most popular methods of prototyping are multi-layer soft lithography, etching, CNC milling, pulling glass capillaries and 3D printing of the microfluidic devices (Jeong et al., 2016).

Microchannels in glass and silicone plates can be fabricated using the deep reactive ion etching (DRIE) technique. The plate must be protected from etching everywhere except for the area of the desired pattern of channels, e.g. by Ni-electroplating or photoresist deposition. Bonding two glass plates with etched features requires a very precise alignment and this process is technically challenging (Harrison et al., 1993; Nisisako and Torii, 2008). Nowadays, glass or silicone plate microfluidic chips are rarely used. Other types of glass devices such as coaxially nested glass capillaries are very common for the production of multiple emulsions (Utada et al., 2005; Zhao et al., 2016). Poly(dimethylsiloxane), usually referred as PDMS, is a material that offers many advantages: it can be used for the reproduction of micron-sized features by replica molding, it is transparent to visible light, it cures at low temperature, it is non-toxic, biocompatible and gas-permeable, and its surface can be easily modified (Duffy et al., 1998; McDonald and Whitesides, 2002; McDonald et al., 2000). PDMS is a perfect material to complement lithographic techniques and gives a name to ‘soft’ lithography, and the elements of devices made of this elastomer can be easily bonded to one another and to a range of others materials, most importantly to glass, after activation of the surface, e.g. with oxygen plasma or corona discharge (Haubert et al., 2006). Soft lithography enables the monolithic fabrication of fluidic components within one piece of PDMS (e.g. inlets, outlets, connectors, valves, mixers), allowing large-scale integration of the microfluidic circuits (Nisisako and Torii, 2008; Thorsen et al., 2002). Poly(dimethylsiloxane) is highly biocompatible, gas-permeable, is an easy-to-work-with material and is the perfect choice for the fabrication of microfluidic devices for biomedical and biological experiments (Zhou et al., 2010). However, PDMS has some disadvantages such as low chemical compatibility—most importantly this material is not well suited to working with organic solvents as they swell the elastomer and the dimensions of the channels may be significantly distorted (Seemann et al., 2012).

A breakthrough in prototyping was the development of soft lithography by Xia and Whitesides presented in **Fig. 6** (Xia and Whitesides, 1998). In common microfabrication protocols, photoresist (e.g. SU-8) is first spin-coated on a glass or silicone slide and then exposed through a mask with a pattern of channels. The exposed resin hardens and the non-exposed photoresist is subsequently washed away. Such a master of the microfluidic device is chemically protected by the deposition of fluorosilanes. Liquid non-polymerized elastomer (PDMS with the curing agent) can be poured onto the matrix, cross-linked by baking at elevated temperatures and peeled off—yielding a perfect negative replica of the silicone-photoresist master. Such an elastomer element cast can then be used as a ready-made part of a microfluidic device and bonded to a glass slide or piece of solid PDMS by activating the surface with plasma. Aligning and bonding two or more layers of patterned PDMS is widely used and is known as multilayer soft lithography. The PDMS cast can be utilized in an alternative way: a chemically protected PDMS cast (by the deposition of fluorosilanes) can be used as a master for the further casting of PDMS. This allows limiting the use of fragile silicon wafers and speeds up the prototyping process, as many such masters can be prepared within a day while microfabricating photoresist on silicone is time-consuming.

Many thermoplastic materials are more rigid than PDMS and they are more robust in terms of mass production. Thermoplastics are also characterized by moderate thermal and chemical compatibility properties, e.g. inferior to properties of glass, but still acceptable for many applications (Jeong et al., 2016). The most common thermoplastics used for the fabrication of microfluidic chips are the following materials: polycarbonate (PC) (Ogończyk et al., 2010), polymethylmethacrylate (PMMA) (Conchouso et al., 2014), cyclic-olefin copolymers (COC) (Stachowiak et al., 2007), polystyrene (PS) (Li et al., 2012), polytetrafluoroethylene (PTFE, also known under the brand name Teflon®), fluorinated ethylene propylene (FEP) (Horka et al., 2016). Prototyping in thermoplastics is usually done by i) micromilling the channels in the plate and bonding it to another plate (Ogończyk et al., 2010); or by ii) 3D printing the appropriate polymer, e.g. methacrylate-based photoresist, in the shape of the microfluidic device (Femmer et al., 2015). These prototyping methods are fast, inexpensive and reliable, but fail to deliver large batches of microfluidic chips. For the mass production of thermoplastic devices, other methods are used, mainly injection molding and hot embossing (Jeong et al., 2016).

4.2 Surface chemistry

In order to maintain precise control over the transport of fluids in the microfluidic chip, the walls of channels have to be preferentially wet by the continuous phase and at the same time the droplet phase should be repelled (Derzsi et al., 2011). Some materials have intrinsically de-

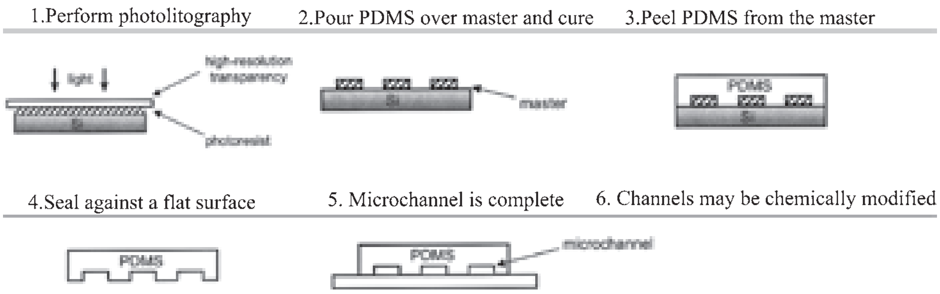

Fig. 6 Schematics presenting consecutive steps in a common soft lithography procedure. Adapted with permission from (McDonald and Whitesides 2002). Copyright 2002 American Chemical Society.

fined wetting properties: hydrophilic (e.g. glass) or hydrophobic (e.g. PDMS), but modification of the surface is still needed in order to i) further increase or decrease the contact angle between the solid of the channel walls and the working fluids (Jankowski et al., 2013); ii) pattern the device with hydrophobic (or hydrophilic) areas in order to, e.g. produce multiple droplets (Abate et al., 2010b; Kim S.C. et al., 2015); iii) shield the microchannel walls from the deposition of unwanted molecules and from the intake of swelling solvents (Abate et al., 2008; Lee et al., 2003; Zhou et al., 2012); or to iv) increase the adherence of the mammalian cells to the solid substrate (Zuchowska et al., 2016). Easy and durable methods for the modification of the microchannels in PDMS and hybrid PDMS glass devices are available. We can divide the methods into two categories: i) hydrophobic modification and ii) making the surface of channels more hydrophilic.

To make PDMS hydrophobic, a sol-gel method is frequently used. It relies on coating the PDMS and glass channels with a glass-like layer with tunable properties (Abate et al., 2008). Other methods are based on the deposition of hydrophobic (or fluorophilic) compounds on the surface of the channels via injection of a solution to the microchannel and evaporation of the solvent (Derzsi et al., 2016). The lifetime of such coatings differs—the sol-gel method is a very durable coating, while fluorosilanes can be washed away even after a few hours of usage of a microfluidic device, hence the modification agent is tailored to the application.

During bonding of the PDMS to the piece of glass/PDMS by oxygen plasma or corona discharge, the PDMS surface is rendered hydrophilic due to activation of the surface (Haubert et al. 2006, Jo et al. 2000). The easiest method to keep the device hydrophilic is to flood the microchannels with water—it will keep the surface hydrophilic as long as water is present. To maintain the hydrophilic surface for a longer period of time, polymers can be deposited on the activated PDMS surface (Kovach et al., 2014; Yan et al., 2013; Zhou et al., 2012).

Some methods allow for the patterning of the surface of the channels, making it possible to define hydrophilic and hydrophobic areas of the microfluidic network. This is possible due to a selective modification of the channel surface, e.g. flowing a modifying solution only to the desired regions of the channel network, e.g. hydrophilic modification by acrylic monomer that can bind to the glassy sol-gel coating (Abate et al., 2010b). Alternatively, the device can be patterned by treating parts of the microfluidic channel network with oxygen plasma or corona discharge—ionized oxygen species produced in those processes bombard the exposed PDMS surface and oxidize the surface, rendering the natively hydrophobic PDMS hydrophilic (Filla et al., 2011; Kim et al., 2015).

Other materials used in microfluidics such as thermoplastics (polycarbonate, PMMA or COC) can have their surface modified. Surface activation with, e.g. ionized oxygen species renders such polymers temporarily hydrophilic—after some time, the surface regains its original properties (Jokinen et al., 2012). To modify the thermoplastics permanently, the surface needs to be physically or chemically modified by, e.g. the layer-by-layer deposition of the polyanions and polycations on a polycarbonate (Derzsi et al., 2011), coating polycarbonate with either a hydrophilic or hydrophobic compound (Jankowski and Garstecki, 2016; Jankowski et al., 2012, 2013), sequential photografting of poly(ethylene glycol) on COC (Stachowiak et al., 2007), or by deposition of silica nanoparticles on PMMA (Ortiz et al., 2017).

5. Applications of droplet microfluidics

Droplet microfluidics is a perfect approach for executing simple protocols that involve handling a large number of small liquid microreactors. This feature makes the microdroplet technology extremely useful for biological applications including the high-throughput investigation of single cells and droplet digital polymerase chain reactions (ddPCR) (Agresti et al., 2010; Baker, 2012; Duncombe et al., 2015; Hindson et al., 2011; Rakszewska et al., 2014; Zinchenko et al., 2014). Droplet microfluidics is also useful for drug research (Sackmann et al., 2014; Vladisavljević et al., 2013), food industry (Neethirajan et al., 2011; Ushikubo et al., 2014; Zanatta et al., 2017), and material sciences for the synthesis and investigation of micro- and nanomaterials such as, e.g. quantum dots, polymeric and inorganic microparticles, capsules (Herranz-Blanco et al., 2014; Vannoy et al., 2011; Zhang L. et al., 2015).

5.1 Chemistry in droplets

The excellent heat and mass transfer in droplets is exploited in the performance of various organic chemistry reactions in microfluidic devices (Kreutzer et al., 2005; Sobieszuk and Napieralska, 2016). For many reactions, the yield is directly associated with the degree of mixing, and microchannel patterns provide the means for the rapid and controllable mixing of content of droplets (de Mello, 2006; Tice et al., 2003). There are also applications of microdroplets in green chemistry—energy consumption may be reduced compared to bulk synthesis (Pieber and Kappe, 2013), and a higher selectivity of reactions allows easier product clean-up (Wiles et al., 2006).

Microfluidic devices offer the capability of performing a wide range of reactions in droplets, e.g. catalysis using the Suzuki-Miyaura reaction (Theberge et al., 2009), hydrolysis of p-nitrotoluene (Ahmed et al., 2006), bromination of alkenes (Cygan et al., 2005), deacetylation of ouabain hexaacetate (Ac_6-OUA) (Hatakeyama et al., 2006) or synthesis of benzyl phenyl ester using PTC (Phase Transfer Catalysts) (Ji et al., 2012). Additionally, reactions at the microscale are safer since smaller volumes of dangerous and explosive substrates can be used, e.g. elemental fluorine for direct regioselective fluorination (Chambers et al., 2005), or preparation of radiolabeled probes (Lee et al., 2005). The high-throughput and spatial separation of samples make droplet microfluidics perfectly suitable for discovery chemistry—screening the libraries of compounds in search of, e.g. new catalysts (Goodell et al., 2009; Kreutz et al., 2010). Droplet microfluidics is also a perfect tool to investigate the chemical communication of compartments comprising chemical oscillators such as the Belousov-Zhabotinsky reaction (Guzowski et al., 2016). An excellent overview of the various reactions performed in microdroplets can be found in a review by Elvira (Elvira et al., 2013) as well as in more recent publications (Guardingo et al., 2016; Wleklinski et al., 2016).

5.2 Synthesis of nano- and microparticles

A wide range of nanoparticles (NPs) and microparticles can be synthesized and generated in microfluidic devices, including but not being limited to: metallic NPs, e.g. gold (Duraiswamy and Khan, 2009, Sebastian Cabeza et al., 2012), silver (Xu et al., 2016), core-shell NPs (Zhu and Guo, 2016), Janus microparticles (Maeda et al., 2012; Nisisako 2016), polymer microcapsules and microspheres (Chuah et al., 2009; Ekanem et al., 2017; He et al., 2011; Kumacheva and Garstecki, 2011a, b; Sugiura et al., 2001; Thiele and Seiffert, 2011), semiconductor NPs including quantum dots (Lignos et al., 2014; Vannoy et al., 2011), and silica NPs (Shirk et al., 2013; Wacker et al., 2012). **Fig. 7** shows an exemplary synthesis of quantum dots in the droplet microfluidic set-up. Double emulsions allow easy and efficient synthesis of capsules and beads, including particles carrying bioactive ingredients (Datta et al., 2014; Deng et al., 2016; Deshpande et al., 2016; Kim et al., 2011). Double emulsions can be efficiently combined with the technique of polymerization of the outer liquid layer in order to obtain various solid shells filled with desired compounds (Wang et al., 2013). DEs with thin shells are the most desirable in the process of fabrication of microcapsules (Datta et al., 2014). The polymerizing agent can be suspended in the shell yielding liquid drops with the solid shell. However, thick shells allow core droplets for movement within the shell so they are off center. After polymerization of such DEs, the shell thickness is not homogeneous and may hamper, e.g. control over the release kinetics of encapsulants (Datta et al., 2012). Thin oil shells may also serve as sacrificial templates for the production of aqueous-based microgels suspended in water—they can spontaneously de-wet upon polymerization of the core droplet (e.g. UV-initiated) to transfer freshly prepared microgels directly into the aqueous solution (Choi et al., 2016b). Another interesting feature of the thin-shelled DEs is that they can be stable until triggered. This unique feature enabled use of DEs in the controlled release of small hydrophilic molecules and can be developed for controlled drug application (Zhao et al., 2016).

5.3 Crystallization in droplets

One of the main applications of droplet microfluidics were the studies of crystallization processes, especially protein crystallization. Since there are no universal conditions for the crystallization of proteins or microparticles—the optimum parameters need to be found in multidimensional chemical space (e.g. pH, crystallizing agents, temperature) (Li and Ismagilov, 2010). Droplet microfluidics offers great control over heat and mass transfer and low sample volumes, providing at the same time the possibility executing high-throughput experiments. The synergy of these advantages resulted in development of systems that allow the automated determination of solubility dia-

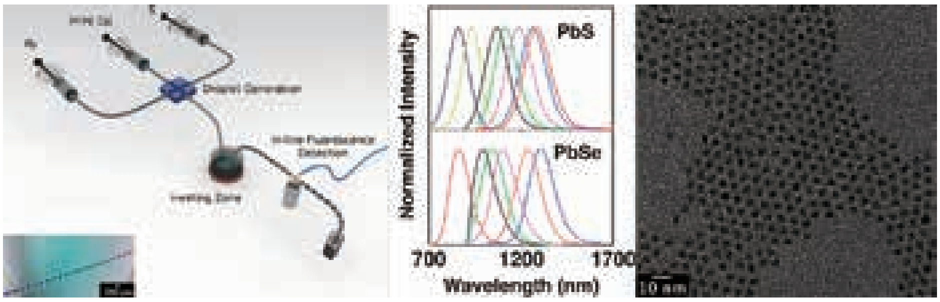

Fig. 7 Synthesis of PbS nanoparticles, adapted from (Lignos et al., 2014). Left panel shows how substrates, denoted as [Pb] and [S], are compartmentalized in the trains of droplets submerged in fluorinated oil and then heated. The fluorescence is detected in-line. The inset shows droplets with synthesized quantum dots. The middle panel shows the photoluminescence spectra of nanoparticles obtained under different conditions. Right panel shows TEM micrographs of PbS nanoparticles obtained in the presented system. Reprinted with permission from (Lignos et al., 2014). Copyright 2014 American Chemical Society.

grams of proteins (Dolega et al., 2012), and the control of the kinetic pathways in a phase diagram, and that give insight into nucleation and growth processes (Leng and Salmon, 2009; Shi et al., 2017). Detection systems could be coupled with droplet microfluidic devices for monitoring the course of crystallization reactions, e.g. using real-time spectroscopy analysis (Lignos et al., 2015, 2017) or Small-Angle X-ray Scattering (SAXS) (Pham et al., 2017; Rodríguez-Ruiz et al., 2017). In combination with a large number of droplets, new analytical methods make quantitative measurements of crystallization kinetics possible (Prileszky and Furst, 2016).

High-throughput droplet crystallization assays were developed to work with small volumes, which is invaluable for researchers working with precious materials or samples that are difficult to obtain. In particular, Rustem Ismagilov's group has been active in investigating and optimizing protein crystallization in nanoliter droplets (Hatakeyama et al., 2006; Li and Ismagilov, 2010; Zheng et al., 2003). The research group of Andrew deMello focused on the monitoring of crystallization phenomena of various particles, with special emphasis on nanocrystals (Lignos et al., 2015; Maceiczyk et al., 2016). An example of such research is the time-resolved measurement of the nucleation and growth of PbS crystals in droplets that enabled elucidation of the kinetics of colloid crystallization. Analysis of the kinetics indicated that there are two steps during the early stage of the reaction: in a first step (< 1 second), the nucleation of uniform particles occurs, and in the second one, the particles grow while their concentration decreases, which is consistent with the kinetic model of Ostwald Ripening (Lignos et al., 2015).

Crystals may have many forms characterized by polymorphism expressed by different physical, chemical and biological properties (Braga et al., 2009; Leng and Salmon, 2009). Differentiating between the polymorphs is crucial, especially for the pharmaceuticals industry—a chemical compound may exist in multiple possible crystalline structures, directly influencing the quality of the drug (Mangin et al., 2009). Droplet microfluidic methods allow partitioning the crystallization assay into the small volume of droplets, which may result in the encapsulation of a single crystal nucleus per droplet. As the nucleation process is stochastic, various forms can nucleate in neighboring droplets. With no competition from other nuclei, even highly unstable forms can persist and grow inside the droplet, yielding mononuclear crystals (Shi et al., 2017). Hence, droplet microfluidics allows, e.g. the screening of mononuclear crystals in order to find the most thermodynamically stable form of an active pharmaceutical ingredient. Consequently, the optimization of the crystallization conditions in droplets could be used for obtaining the desired polymorph (Leon et al., 2015; Wang et al., 2011; Yamaguchi et al., 2013).

5.4 Biological and biochemical assays in high throughput

A number of biological assays can be performed using droplet microfluidic chips. The methods for spatiotemporal control over the droplet position on a chip or the techniques for droplet barcoding (Macosko et al., 2015; Rotem et al., 2015; Zhang Y. et al., 2015) offer a way to link the outcome of the reaction with the chemical composition of a droplet (Abate et al., 2010a; Amselem et al., 2016; Jakiela et al., 2013). Well-developed methods for culturing bacteria and eukaryotic cells (Clausell-Tormos et al., 2008; Jakiela et al., 2013; Moffitt et al., 2012), allowed for rapid investigation on the level of single cells. Assays detecting single biomolecules (Hughes et al., 2004; Rissin et al., 2010; Shim et al., 2013) can be performed at a very high throughput (Agresti et al., 2010; Cheng et al., 2016; Lim and Abate, 2013; Lim et al., 2015; Terekhov et al., 2017).

Droplet microfluidics offers an astonishing number of applications in molecular biology, biochemistry, drug discovery, and cancer research. Here, we will mention just a few of the important achievements of droplet research in these fields: i) digitized diagnostic assays (Hindson et al., 2011; Rissin et al., 2010; Tang and Shum, 2016); ii) directed evolution towards the improvement of the catalytic functions of enzymes and microorganisms (Fischlechner et al., 2014; Levin and Aharoni, 2012; Zinchenko et al., 2014); iii) determination of optimum conditions for protein crystallization (Yamaguchi et al., 2013; Zheng et al., 2003; Zhu and Fang, 2013); iv) new experimental approaches useful in the next-generation sequencing of cell genomes (Ma et al., 2017; Macosko et al., 2015; Zhang K. et al., 2016); and v) analysis of larger model organisms such as *C. elegans* (Aubry et al., 2015).

5.5 Industrial applications

Microfluidic methods allow the production of emulsions that are highly monodisperse, with precisely determined diameters of the droplets, and tailored chemical composition of the interface. All these features allow tuning the emulsions for a particular application, yet the microfluidic methods are characterized by intrinsically low volumetric throughput, limiting their applicability (Amstad et al., 2016). Several attempts for parallelization to increase the throughput of the generation of droplets have been reported, e.g.: i) 144 T-junctions in an annular chip (Nisisako et al. 2012); ii) up to 512 flow-focusing junctions in a multilayer annular device, yielding up to a liter of emulsion per hour (ca. 200 μm in diameter, CV~6 %); iii) 28 flow-focusing junctions producing monodisperse droplets up to 3 l/h (ca. 500 μm in diameter); iv) parallel system comprising over 500 step-emulsification junctions to produce up to 150 ml/h of emulsion (ca. 20–160 μm in diameter, CV~3 %, 256–550 nozzles) (Amstad et al., 2016); v) numerous micropillars homogenizing the passing stream of fluid into millions of droplets per second with a level of dispersity higher than 5 %, which is sufficient for some applications (Akbari et al., 2017).

Microfluidic methods for the production of droplets have already found their use in certain industries, especially health-related ones, e.g. in the field of diagnostics and detection of pathogens, e.g. i) performing droplet digital PCR (Hindson et al., 2011); digital ELISA in droplets (Shim et al., 2013) for the detection of very low concentrations of DNA or proteins; ii) fast and precise quantitative detection of pathogenic bacteria in droplets of blood (Kang et al., 2014). Droplet microfluidic technologies can also be implemented in, e.g. food and pharmaceutical industries such as in the evaluation of food freshness (Itoh et al., 2012) or encapsulation of active ingredients for drug delivery (Mora-Huertas et al., 2010).

There is a number of university spin-offs and start-ups founded on droplet microfluidic technologies that have entered the market and might create new branches of industry (Neethirajan et al., 2011; Yetisen et al., 2015). Some of them, together with well-established companies, offer new products for researchers that work in the areas of molecular and cell biology, molecular diagnostics and drug development (Neethirajan et al., 2011; The Microfluidic Circle, 2017). Some of the microfluidic companies have already been acquired by bigger players such as Biorad (who acquired Raindance Technologies, Quantalife and GnuBio for their ddPCR and sequencing technologies). There are companies offering microfluidic solutions that are not directed at academia—for example Capsum (Capsum, 2017), a company offering the formulation of fine cosmetics or Calyxia, a start-up producing size-controlled micrometer capsules for application in the chemicals industry (Walters, 2016).

6. Outlook

Droplet microfluidics has already come a long way since the first demonstration of the formation of droplets on a planar microfluidic chip (Thorsen et al., 2001). Hundreds of researchers across the globe solved a diverse set of challenges and problems, especially in microfabrication, choice of materials and reagents and in the physics of multiphase flow at the microscale.

The progress in droplet microfluidics has also led to academic demonstrations of applications that could open new technological possibilities in such areas as:

i) **analytical sciences and diagnostics**, e.g. by providing users with an array of novel and unique assays such as digital PCR or single-cell sequencing (Hatch et al., 2011; Lan et al., 2017).
ii) **pharmacology**, e.g. by introducing novel methods of drug delivery using microcapsules formed with the use of microdroplets, and the highly selective synthesis of polymorphs of active pharmacological ingredients (Leon et al., 2015; Vladisavljević et al., 2013).
iii) **fluid mechanics**, e.g. by investigating the fundamental properties of fluid flow at the microscale (Garstecki et al., 2005a; Nabavi et al., 2015).
iv) **material sciences**, e.g. by overcoming the slow or non-uniform heat and mass transfer in chemical reactions (Song et al., 2006), developing new methods for the generation of highly monodisperse microparticles, capsules (Ekanem et al., 2017; Wang et al., 2011), and porous materials (Thurgood et al., 2017).

The highest impact, at least up till now, has been in biological sciences, listed very briefly in the previous section. Droplet microfluidics helps with detecting medical disorders and microfluidic technologies are already found in diagnostic systems for the detection of infectious, genetic and degenerative diseases. The most important applications of microdroplet technologies comprise the analysis of rare mutations associated with cancer (Pekin et al., 2011), detection of circulating tumor DNA (Garrigou et al., 2016), health monitoring after organ transplantation (Goh et al., 2017) and detection and quantification of pathogenic bacteria (Kang et al., 2014). As the basic physics behind microscale multiphase flows is already well known and the microfabrication techniques are at the level at which it is feasible to mass-produce inexpensive cartridges, we can expect further development of droplet microfluidic technologies for even more complex applications in biological research and medical diagnostics.

Droplet microfluidics is also used in synthetic and physical chemistry. The use of microdroplet reactors will be helpful in the optimization of reactions conditions (Abolhasani et al., 2015a, c) and determination of selected important properties of chemical compounds such as partitions coefficients (Abolhasani et al., 2015b). Droplet microfluidics can be useful in specific applications, as e.g. controlled synthesis at the liquid-liquid interface. The limited volume of the droplet microreactors restricts their use in the classic and large-scale synthesis of common chemical compounds. The situation is different in the case of synthesis and formulation of fine and expensive chemicals such as nanocrystals and microcapsules for which droplet microfluidic have already proved to be a very promising alternative to classic technologies (Ekanem et al., 2017; Nightingale et al., 2014; Phillips et al., 2014). Further studies on the crystallization will be carried out and they might reflect on the fundamental knowledge—e.g. deeper understanding of the nucleation process—as well as on the pharmaceuticals industry—e.g. reduction of time needed for the development of novel drugs by allowing early-stage screening of minimal amounts of crystals and co-crystals (Shi et al., 2017)

Microfluidics is still a rapidly developing field of research. The interest has slowly been shifting from the methods for droplet production or manipulation to the development of new applications of already known droplet microfluidic techniques and systems that now allow for high-throughput investigation on biological and chemical processes. High-throughput screening using droplet techniques can identify the most efficient reaction conditions, properties of materials, strains or variants of enzymes that can later be used either by microfluidic or bulk methods.

In terms of generation of new types of capsules, particles and materials for practical applications, currently the biggest challenge is to scale up the production rate, at least on the level of kilograms of materials per hour. This can be realized either by massive parallelization and/or by using new types of devices capable of sustaining very high pressures. We envisage that the current extensive research efforts will lead to substantial improvement and dissemination of droplet microfluidics which will become an important and widely known approach in the research of powders and microparticles.

Acknowledgements

This work was supported by the National Science Centre funding based on decisions number: DEC-2016/23/N/ST4/01020 (Preludium) and DEC-2014/12/W/NZ6/00454 (Symfonia) and the Foundation for Polish Science through the program TEAM TECH/2016-2/10. T.S.K. acknowledges the support from the Ministry of Science and Higher Education through the scholarship for outstanding young researchers (0722/E-64/STYP/10/295).

References

Abate A.R., Hung T., Mary P., Agresti J.J., Weitz D.A., High-throughput injection with microfluidics using picoinjectors, Proceedings of the National Academy of Sciences, 107 (2010a) 19163–19166. DOI: 10.1073/pnas.1006888107

Abate A.R., Lee D., Do T., Holtze C., Weitz D.A., Glass coating for PDMS microfluidic channels by sol–gel methods, Lab on a Chip, 8 (2008) 516–518. DOI: 10.1039/b800001h

Abate A.R., Thiele J., Weinhart M., Weitz D.A., Patterning microfluidic device wettability using flow confinement, Lab on a Chip, 10 (2010b) 1774–1776. DOI: 10.1039/c004124f

Abate A.R., Thiele J., Weitz D.A., One-step formation of multiple emulsions in microfluidics, Lab on a Chip, 11 (2011) 253–258. DOI: 10.1039/C0LC00236D

Abate A.R., Weitz D.A., High-order multiple emulsions formed in poly(dimethylsiloxane) microfluidics, Small, 5 (2009) 2030–2032. DOI: 10.1002/smll.200900569

Abolhasani M., Bruno N.C., Jensen K.F., Oscillatory three-phase flow reactor for studies of bi-phasic catalytic reactions, Chemical Communications, 51 (2015a) 8916–8919. DOI: 10.1039/C5CC02051D

Abolhasani M., Coley C.W., Jensen K.F., Multiphase oscillatory flow strategy for in situ measurement and screening of partition coefficients, Analytical Chemistry, 87 (2015b) 11130–11136. DOI: 10.1021/acs.analchem.5b03311

Abolhasani M., Coley C.W., Xie L., Chen O., Bawendi M.G., Jensen K.F., Oscillatory microprocessor for growth and in situ characterization of semiconductor nanocrystals, Chemistry of Materials, 27 (2015c) 6131–6138. DOI: 10.1021/acs.chemmater.5b02821

Agresti J.J., Antipov E., Abate A.R., Ahn K., Rowat A.C., Baret J.C., Marquez M., Klibanov A.M., Griffiths A.D., Weitz D.A., Ultrahigh-throughput screening in drop-based microfluidics for directed evolution, Proceedings of the National Academy of Sciences, 107 (2010) 4004–4009. DOI: 10.1073/pnas.0910781107

Ahmed B., Barrow D., Wirth T., Enhancement of reaction rates by segmented fluid flow in capillary scale reactors, Advanced Synthesis and Catalysis, 348 (2006) 1043–1048. DOI: 10.1002/adsc.200505480

Akamatsu K., Kanasugi S., Nakao S.I., Weitz D.A., Membrane-Integrated glass capillary device for preparing small-sized water-in-oil-in-water emulsion droplets, Langmuir, 31 (2015) 7166–7172. DOI: 10.1021/acs.langmuir.5b01514

Akbari S., Pirbodaghi T., Kamm R.D., Hammond P.T., A versatile microfluidic device for high throughput production of microparticles and cell microencapsulation, Lab on a Chip, 17 (2017) 2067–2075. DOI: 10.1039/C6LC01568A

Amselem G., Guermonprez C., Drogue B., Michelin S., Baroud C.N., Universal microfluidic platform for bioassays in anchored droplets, Lab on a Chip, 16 (2016) 4200–4211. DOI: 10.1039/C6LC00968A

Amstad E., Chemama M., Eggersdorfer M., Arriaga L.R., Brenner M.P., Weitz D.A., Robust scalable high throughput production of monodisperse drops, Lab on a Chip, 16 (2016) 4163–4172. DOI: 10.1039/C6LC01075J

Anna S.L., Bontoux N., Stone H.A., Formation of dispersions using “flow focusing” in microchannels, Applied Physics Letters, 82 (2003) 364–366. DOI: 10.1063/1.1537519

Aris R., On the dispersion of a solute in pulsating flow through a tube, Proceedings of the Royal Society A: Mathematical, Physical and Engineering Sciences, 259 (1960) 370–376. DOI: 10.1098/rspa.1960.0231

Arriaga L.R., Amstad E., Weitz D.A., Scalable single-step microfluidic production of single-core double emulsions with ultra-thin shells, Lab on a Chip, 15 (2015) 3335–3340. DOI: 10.1039/C5LC00631G

Aubry G., Zhan M., Lu H., Hydrogel-droplet microfluidic platform for high-resolution imaging and sorting of early larval Caenorhabditis elegans, Lab on a Chip, 15 (2015) 1424–1431. DOI: 10.1039/C4LC01384K

Baker M., Digital PCR hits its stride, Nature Methods, 9 (2012) 541–544. DOI: 10.1038/nmeth.2027

Baret J.-C., Surfactants in droplet-based microfluidics, Lab on a Chip, 12 (2012) 422–433. DOI: 10.1039/C1LC20582J

Braga D., Grepioni F., Maini L., Polito M., Crystal polymorphism and multiple crystal forms, Structure and Bonding, 132 (2009) 25–50. DOI: 10.1007/430_2008_7

Capsum, 2017, <http://capsum.net/en/collections> accessed 16.02.2018.

Casadevall i Solvas X., deMello A., Droplet microfluidics: recent developments and future applications, Chemical Communications, 47 (2011) 1936–1942. DOI: 10.1039/C0CC02474K

Chambers R.D., Fox M.A., Holling D., Nakano T., Okazoe T., Sandford G., Elemental fluorine. Part 16. Versatile thin-film gas-liquid multi-channel microreactors for effective scale-out, Lab on a Chip, 5 (2005) 191–198. DOI: 10.1039/b416400h

Cheng Y.-H., Chen Y.-C., Brien R., Yoon E., Scaling and automation of a high-throughput single-cell-derived tumor sphere assay chip, Lab on a Chip, 16 (2016) 3708–3717. DOI: 10.1039/C6LC00778C

Choi C.H., Lee H., Abbaspourrad A., Kim J.H., Fan J., Caggioni M., Wesner C., Zhu T., Weitz D.A., Triple emulsion drops with an ultrathin water layer: High encapsulation efficiency and enhanced cargo retention in microcapsules, Advanced Materials, 28 (2016a) 3340–3344. DOI: 10.1002/adma.201505801

Choi C.H., Wang H., Lee H., Kim J.H., Zhang L., Mao A., Mooney D.J., Weitz D.A., One-step generation of cell-laden microgels using double emulsion drops with a sacrificial ultra-thin oil shell, Lab on a Chip, 16 (2016b) 1549–1555. DOI: 10.1039/C6LC00261G

Chong D.T., Liu X.S., Ma H.J., Huang G.Y., Han Y.L., Cui X.Y., Yan J.J., Xu F., Advances in fabricating double-emulsion droplets and their biomedical applications, Microfluidics and Nanofluidics, 19 (2015) 1071–1090. DOI: 10.1007/s10404-015-1635-8

Christopher G.F., Noharuddin N.N., Taylor J.A., Anna S.L., Experimental observations of the squeezing-to-dripping transition in T-shaped microfluidic junctions, Physical Review E, 78 (2008) 1–12. DOI: 10.1103/PhysRevE.78.036317

Chuah A.M., Kuroiwa T., Kobayashi I., Zhang X., Nakajima M., Preparation of uniformly sized alginate microspheres using the novel combined methods of microchannel emulsification and external gelation, Colloids and Surfaces A: Physicochemical and Engineering Aspects, 351 (2009) 9–17. DOI: 10.1016/j.colsurfa.2009.09.005

Clausell-Tormos J., Lieber D., Baret J.C., El-Harrak A., Miller O.J., Frenz L., Blouwolff J., Humphry K.J., Köster S., Duan H., Holtze C., Weitz D.A., Griffiths A.D., Merten C.A., Droplet-based microfluidic platforms for the encapsulation and screening of mammalian cells and multicellular organisms, Chemistry and Biology, 15 (2008) 427–437. DOI: 10.1016/j.chembiol.2008.04.004

Conchouso D., Castro D., Khan S.A., Foulds I.G., Three-dimensional parallelization of microfluidic droplet generators for a litre per hour volume production of single emulsions, Lab on a Chip, 14 (2014) 3011–3020. DOI: 10.1039/C4LC00379A

Cygan Z.T., Cabral J.T., Beers K.L., Amis E.J., Microfluidic platform for the generation of organic-phase microreactors, Langmuir, 21 (2005) 3629–3634. DOI: 10.1021/la0471137

Dangla R., Fradet E., Lopez Y., Baroud C.N., The physical mechanisms of step emulsification, Journal of Physics D: Applied Physics, 46 (2013) 114003–114003. DOI: 10.1088/0022-3727/46/11/114003

Datta S.S., Abbaspourrad A., Amstad E., Fan J., Kim S.H., Romanowsky M., Shum H.C., Sun B., Utada A.S., Windbergs M., Zhou S., Weitz D.A., 25th anniversary article: Double emulsion templated solid microcapsules: Mechanics and controlled release, Advanced Materials, 26 (2014) 2205–2218. DOI: 10.1002/adma.201305119

Datta S.S., Kim S.H., Paulose J., Abbaspourrad A., Nelson D.R., Weitz D.A., Delayed buckling and guided folding of inhomogeneous capsules, Physical Review Letters, 109 (2012) 134302–134302. DOI: 10.1103/PhysRevLett.109.134302

de Mello A.J., Control and detection of chemical reactions in microfluidic systems, Nature, 442 (2006) 394–402. DOI: 10.1038/nature05062

De Menech M., Garstecki P., Jousse F., Stone H.A., Transition from squeezing to dripping in a microfluidic T-shaped junction, Journal of Fluid Mechanics, 595 (2008) 141–161. DOI: 10.1017/S002211200700910X

Deng N.N., Yelleswarapu M., Huck W.T.S., Monodisperse uni- and multicompartment liposomes, Journal of the American Chemical Society, 138 (2016) 7584–7591. DOI: 10.1021/jacs.6b02107

Derzsi L., Jankowski P., Lisowski W., Garstecki P., Hydrophilic polycarbonate for generation of oil in water emulsions in microfluidic devices, Lab on a Chip, 11 (2011) 1151–1156. DOI: 10.1039/c0lc00438c

Derzsi L., Kaminski T.S., Garstecki P., Antibiograms in five pipetting steps: precise dilution assays in sub-microliter volumes with a conventional pipette, Lab on a Chip, 16 (2016) 893–901. DOI: 10.1039/C5LC01151E

Deshpande S., Caspi Y., Meijering A.E.C., Dekker C., Octanol-assisted liposome assembly on chip, Nature Communications, 7 (2016) 10447–10447. DOI: 10.1038/ncomms10447

Dolega M.E., Jakiela S., Razew M., Rakszewska A., Cybulski O., Garstecki P., Iterative operations on microdroplets and continuous monitoring of processes within them; determination of solubility diagrams of proteins, Lab on a Chip, 12 (2012) 4022–4025. DOI: 10.1039/c2lc40174f

Dollet B., Van Hoeve W., Raven J.P., Marmottant P., Versluis M., Role of the channel geometry on the bubble pinch-off in flow-focusing devices, Physical Review Letters, 100 (2008) 034504–034504. DOI: 10.1103/PhysRevLett.100.034504

Duffy D.C., McDonald J.C., Schueller O.J.A., Whitesides G.M., Rapid prototyping of microfluidic systems in poly(dimethylsiloxane), Analytical Chemistry, 70 (1998) 4974–4984. DOI: 10.1021/ac980656z

Duncombe T.A., Tentori A.M., Herr A.E., Microfluidics: Reframing biological enquiry, Nature Reviews Molecular Cell Biology, 16 (2015) 554–567. DOI: 10.1038/nrm4041

Duraiswamy S., Khan S.A., Droplet-based microfluidic synthesis of anisotropic metal nanocrystals, Small, 5 (2009) 2828–2834. DOI: 10.1002/smll.200901453

Dutka F., Opalski A.S., Garstecki P., Nano-liter droplet libraries from a pipette: step-emulsificator that stabilizes droplet volume against variation in flow rate, Lab on a Chip, 16 (2016) 2044–2049. DOI: 10.1039/C6LC00265J

Eggersdorfer M.L., Zheng W., Nawar S., Mercandetti C., Ofner A., Leibacher I., Koehler S., Weitz D.A., Tandem emulsification for high-throughput production of double emulsions, Lab on a Chip, 17 (2017) 936–942. DOI: 10.1039/C6LC01553K

Ekanem E.E., Zhang Z., Vladisavljević G.T., Facile microfluidic production of composite polymer core-shell microcapsules and crescent-shaped microparticles, Journal of Colloid and Interface Science, 498 (2017) 387–394. DOI: 10.1016/j.jcis.2017.03.067

Elvira K.S., i Solvas X.C., Wootton R.C.R., de Mello A.J., The past, present and potential for microfluidic reactor technology in chemical synthesis, Nature Chemistry, 5 (2013) 905–915. DOI: 10.1038/nchem.1753

Esquena J., Water-in-water (W/W) emulsions, Current Opinion in Colloid and Interface Science, 25 (2016) 109–119. DOI: 10.1016/j.cocis.2016.09.010

Everett D.H., Manual of symbols and terminology for physicochemical quantities and units, Appendix II: definitions, terminology and symbols in colloid and surface chemistry, Pure and Applied Chemistry, 31 (1972) 577–638. DOI: 10.1351/pac197231040577

Femmer T., Jans A., Eswein R., Anwar N., Moeller M., Wessling M., Kuehne A.J.C., High-throughput generation of emulsions and microgels in parallelized microfluidic drop-makers prepared by rapid prototyping, ACS Applied Materials and Interfaces, 7 (2015) 12635–12638. DOI: 10.1021/acsami.5b03969

Filla L.A., Kirkpatrick D.C., Martin R.S., Use of a corona discharge to selectively pattern a hydrophilic/hydrophobic interface for integrating segmented flow with microchip electrophoresis and electrochemical detection, Analytical Chemistry, 83 (2011) 5996–6003. DOI: 10.1021/ac201007s

Fischlechner M., Schaerli Y., Mohamed M.F., Patil S., Abell C., Hollfelder F., Evolution of enzyme catalysts caged in biomimetic gel-shell beads, Nature Chemistry, 6 (2014) 791–796. DOI: 10.1038/nchem.1996

Garrigou S., Perkins G., Garlan F., Normand C., Didelot A., Le Corre D., Peyvandi S., Mulot C., Niarra R., Aucouturier P., et al., A study of hypermethylated circulating tumor DNA as a universal colorectal cancer biomarker, Clinical Chemistry, 62 (2016) 1129–1139. DOI: 10.1373/clinchem.2015.253609

Garstecki P., Fuerstman M.J., Stone H.A., Whitesides G.M., Formation of droplets and bubbles in a microfluidic T-junction—scaling and mechanism of break-up, Lab on a Chip, 6 (2006) 437–446. DOI: 10.1039/b510841a

Garstecki P., Fuerstman M.J., Whitesides G.M., Nonlinear dynamics of a flow-focusing bubble generator: An inverted dripping faucet, Physical Review Letters, 94 (2005a) 234502–234502. DOI: 10.1103/PhysRevLett.94.234502

Garstecki P., Stone H.A., Whitesides G.M., Mechanism for flow-rate controlled breakup in confined geometries: A route to monodisperse emulsions, Physical Review Letters, 94 (2005b) 164501–164501. DOI: 10.1103/PhysRevLett.94.164501

Garti N., Double emulsions—Scope, limitations and new achievements, Colloids and Surfaces A: Physicochemical and Engineering Aspects, 123–124 (1997) 233–246. DOI: 10.1016/S0927-7757(96)03809-5

Goh S.K., Muralidharan V., Christophi C., Do H., Dobrovic A., Probe-free digital PCR quantitative methodology to measure donor-specific cell-free DNA after solid-organ transplantation, Clinical Chemistry, 63 (2017) 742–750. DOI: 10.1373/clinchem.2016.264838

Goodell J.R., McMullen J.P., Zaborenko N., Maloney J.R., Ho C.X., Jensen K.F., Porco J.A., Beeler A.B., Development of an automated microfluidic reaction platform for multidimensional screening: Reaction discovery employing bicyclo[3.2.1]octanoid scaffolds, Journal of Organic Chemistry, 74 (2009) 6169–6180. DOI: 10.1021/jo901073v

Gu H., Duits M.H.G., Mugele F., Droplets formation and merging in two-phase flow microfluidics, International journal of molecular sciences, 12 (2011) 2572–2597. DOI: 10.3390/ijms12042572

Guardingo M., Busqué F., Ruiz-Molina D., Reactions in ultra-small droplets by tip-assisted chemistry, Chemical Communications, 52 (2016) 11617–11626. DOI: 10.1039/C6CC03504C

Guzowski J., Garstecki P., Droplet clusters: Exploring the phase space of soft mesoscale atoms, Physical Review Letters, 114 (2015) 188302–188302. DOI: 10.1103/PhysRevLett.114.188302

Guzowski J., Gizynski K., Gorecki J., Garstecki P., Microfluidic platform for reproducible self-assembly of chemically communicating droplet networks with predesigned number and type of the communicating compartments, Lab on a Chip, 16 (2016) 764–772. DOI: 10.1039/C5LC01526J

Guzowski J., Jakiela S., Korczyk P.M., Garstecki P., Custom tailoring multiple droplets one-by-one, Lab on a Chip, 13 (2013) 4308–4311. DOI: 10.1039/c3lc50841b

Guzowski J., Korczyk P.M., Jakiela S., Garstecki P., Automated high-throughput generation of droplets, Lab on a Chip, 11 (2011) 3593–3595. DOI: 10.1039/c1lc20595a

Guzowski J., Korczyk P.M., Jakiela S., Garstecki P., The structure and stability of multiple micro-droplets, Soft Matter, 8 (2012) 7269–7269. DOI: 10.1039/c2sm25838b

Haeberle S., Mark D., Von Stetten F., Zengerle R., Microfluidic platforms for lab-on-a-chip applications, Microsystems and Nanotechnology, 9783642182 (2012) 853–895. DOI: 10.1007/978-3-642-18293-8_22

Harrison D.J., Fluri K., Seiler K., Fan Z., Effenhauser C.S., Manz A., Micromachining a miniaturized capillary electrophoresis-based chemical analysis system on a chip, Science, 261 (1993) 895–897. DOI: 10.1126/science.261.5123.895

Hatakeyama T., Chen D.L., Ismagilov R.F., Microgram-scale testing of reaction conditions in solution using nanoliter plugs in microfluidics with detection by MALDI-MS, Journal of the American Chemical Society, 128 (2006) 2518–2519. DOI: 10.1021/ja057720w

Hatch A.C., Fisher J.S., Tovar A.R., Hsieh A.T., Lin R., Pentoney S.L., Yang D.L., Lee A.P., 1-Million droplet array with wide-field fluorescence imaging for digital PCR, Lab on a

Chip, 11 (2011) 3838–3845. DOI: 10.1039/c1lc20561g

Haubert K., Drier T., Beebe D., PDMS bonding by means of a portable, low-cost corona system, Lab on a Chip, 6 (2006) 1548–1549. DOI: 10.1039/b610567j

He T., Liang Q., Zhang K., Mu X., Luo T., Wang Y., Luo G., A modified microfluidic chip for fabrication of paclitaxel-loaded poly(l-lactic acid) microspheres, Microfluidics and Nanofluidics, 10 (2011) 1289–1298. DOI: 10.1007/s10404-010-0760-7

Hein M., Afkhami S., Seemann R., Kondic L., Capillary focusing close to a topographic step: shape and instability of confined liquid filaments, Microfluidics and Nanofluidics, 18 (2015a) 911–917. DOI: 10.1007/s10404-014-1481-0

Hein M., Fleury J.-B., Seemann R., Coexistence of different droplet generating instabilities: new breakup regimes of a liquid filament, Soft Matter, 11 (2015b) 5246–5252. DOI: 10.1039/C5SM00736D

Herranz-Blanco B., Arriaga L.R., Mäkilä E., Correia A., Shrestha N., Mirza S., Weitz D.A., Salonen J., Hirvonen J., Santos H.A., Microfluidic assembly of multistage porous silicon–lipid vesicles for controlled drug release, Lab on a Chip, 14 (2014) 1083–1086. DOI: 10.1039/C3LC51260F

Hindson B.J., Ness K.D., Masquelier D.A., Belgrader P., Heredia N.J., Makarewicz A.J., Bright I.J., Lucero M.Y., Hiddessen A.L., Legler T.C., et al., High-throughput droplet digital PCR system for absolute quantitation of DNA copy number, Analytical Chemistry, 83 (2011) 8604–8610. DOI: 10.1021/ac202028g

Hinrichsen H., Wolf D.E., Eds., The Physics of Granular Media, Wiley-VCH Verlag GmbH & Co. KGaA, Weinheim, 2004, ISBN: 9783527403738. DOI: 10.1002/352760362X

Ho C.S., Kim J.W., Weitz D.A., Microfluidic fabrication of monodisperse biocompatible and biodegradable polymersomes with controlled permeability, Journal of the American Chemical Society, 130 (2008) 9543–9549. DOI: 10.1021/ja802157y

Holtze C., Rowat A.C., Agresti J.J., Hutchison J.B., Angilè F.E., Schmitz C.H.J., Köster S., Duan H., Humphry K.J., Scanga R.A., Johnson J.S., Pisignano D., Weitz D.A., Biocompatible surfactants for water-in-fluorocarbon emulsions, Lab on a Chip, 8 (2008) 1632–1639. DOI: 10.1039/b806706f

Horka M., Sun S., Ruszczak A., Garstecki P., Mayr T., Lifetime of phosphorescence from nanoparticles yields accurate measurement of concentration of oxygen in microdroplets, Allowing one to monitor the metabolism of bacteria, Analytical Chemistry, 88 (2016) 12006–12012. DOI: 10.1021/acs.analchem.6b03758

Huang K.Y.S., Bento J.L., Stredney M.A., Napoli O.J., Adamson D.H., Robust coaxial capillary microfluidic device for the high throughput formation of polymersomes, Microfluidics and Nanofluidics, 18 (2014) 149–157. DOI: 10.1007/s10404-014-1415-x

Hughes I., Blasiole B., Huss D., Warchol M.E., Rath N.P., Hurle B., Ignatova E., David Dickman J., Thalmann R., Levenson R., Ornitz D.M., Otopetrin 1 is required for otolith formation in the zebrafish Danio rerio, Developmental Biology, 276 (2004) 391–402. DOI: 10.1016/j.ydbio.2004.09.001

Itoh D., Sassa F., Nishi T., Kani Y., Murata M., Suzuki H., Droplet-based microfluidic sensing system for rapid fish freshness determination, Sensors and Actuators, B: Chemical, 171–172 (2012) 619–626. DOI: 10.1016/j.snb.2012.05.043

Jakiela S., Kaminski T.S., Cybulski O., Weibel D.B., Garstecki P., Bacterial growth and adaptation in microdroplet chemostats, Angewandte Chemie—International Edition, 52 (2013) 8908–8911. DOI: 10.1002/anie.201301524

Jankowski P., Garstecki P., Stable hydrophilic surface of polycarbonate, Sensors and Actuators, B: Chemical, 226 (2016) 151–155. DOI: 10.1016/j.snb.2015.11.100

Jankowski P., Ogończyk D., Derzsi L., Lisowski W., Garstecki P., Hydrophilic polycarbonate chips for generation of oil-in-water (O/W) and water-in-oil-in-water (W/O/W) emulsions, Microfluidics and Nanofluidics, 14 (2013) 597–604. DOI: 10.1007/s10404-012-1078-4

Jankowski P., Ogonczyk D., Kosinski A., Lisowski W., Garstecki P., Hydrophobic modification of polycarbonate for reproducible and stable formation of biocompatible microparticles, Lab on a Chip, 11 (2011) 748–752. DOI: 10.1039/C0LC00360C

Jankowski P., Ogończyk D., Lisowski W., Garstecki P., Polyethyleneimine coating renders polycarbonate resistant to organic solvents, Lab on a Chip, 12 (2012) 2580–2584. DOI: 10.1039/c2lc21297h

Jeon N.L., Dertinger S.K.W., Chiu D.T., Choi I.S., Stroock A.D., Whitesides G.M., Generation of solution and surface gradients using microfluidic systems, Langmuir, 16 (2000) 8311–8316. DOI: 10.1021/la000600b

Jeong H.H., Issadore D., Lee D., Recent developments in scale-up of microfluidic emulsion generation via parallelization, Korean Journal of Chemical Engineering, 33 (2016) 1757–1766. DOI: 10.1007/s11814-016-0041-6

Ji J., Zhao Y., Guo L., Liu B., Ji C., Yang P., Interfacial organic synthesis in a simple droplet-based microfluidic system, Lab on a Chip, 12 (2012) 1373–1377. DOI: 10.1039/c2lc40052a

Jo B.H., van Lerberghe L.M., Motsegood K.M., Beebe D.J., Three-dimensional micro-channel fabrication in polydimethylsiloxane (PDMS) elastomer, Journal of Microelectromechanical Systems, 9 (2000) 76–81. DOI: 10.1109/84.825780

Joensson H.N., Andersson Svahn H., Droplet microfluidics-A tool for single-cell analysis, Angewandte Chemie—International Edition, 51 (2012) 12176–12192. DOI: 10.1002/anie.201200460

Jokinen V., Suvanto P., Franssila S., Oxygen and nitrogen plasma hydrophilization and hydrophobic recovery of polymers, Biomicrofluidics, 6 (2012) 1–10. DOI: 10.1063/1.3673251

Kang D.K., Ali M.M., Zhang K., Huang S.S., Peterson E., Digman M.A., Gratton E., Zhao W., Rapid detection of single bacteria in unprocessed blood using Integrated Comprehensive Droplet Digital Detection, Nature Communications, 5 (2014) 5427–5427. DOI: 10.1038/ncomms6427

Kanouni M., Rosano H.L., Naouli N., Preparation of a stable double emulsion (W1/O/W2): Role of the interfacial films on the stability of the system, Advances in Colloid and Interface Science, 99 (2002) 229–254. DOI: 10.1016/S0001-

8686(02)00079-9

Kim S.C., Sukovich D.J., Abate A.R., Patterning microfluidic device wettability with spatially-controlled plasma oxidation, Lab on a Chip, 15 (2015) 3163–3169. DOI: 10.1039/C5LC00626K

Kim S.H., Kim J.W., Kim D.H., Han S.H., Weitz D.A., Polymersomes containing a hydrogel network for high stability and controlled release, Small, 9 (2013) 124–131. DOI: 10.1002/smll.201201709

Kim S.-H., Kim J.W., Cho J.-C., Weitz D.A., Double-emulsion drops with ultra-thin shells for capsule templates, Lab on a Chip, 11 (2011) 3162–3166. DOI: 10.1039/c1lc20434c

Klapper M., Nenov S., Haschick R., Müller K., Müllen K., Oil-in-Oil emulsions: A unique tool for the formation of polymer nanoparticles, Accounts of Chemical Research, 41 (2008) 1190–1201. DOI: 10.1021/ar8001206

Kobayashi I., Nakajima M., Chun K., Kikuchi Y., Fujita H., Silicon array of elongated through-holes for monodisperse emulsion droplets, AIChE Journal, 48 (2002) 1639–1644. DOI: 10.1002/aic.690480807

Kovach K.M., Capadona J.R., Gupta A.S., Potkay J.A., The effects of PEG-based surface modification of PDMS microchannels on long-term hemocompatibility, Journal of Biomedical Materials Research—Part A, 102 (2014) 4195–4205. DOI: 10.1002/jbm.a.35090

Kreutz J.E., Shukhaev A., Du W., Druskin S., Daugulis O., Ismagilov R.F., Evolution of catalysts directed by genetic algorithms in a plug-based microfluidic device tested with oxidation of methane by oxygen, Journal of the American Chemical Society, 132 (2010) 3128–3132. DOI: 10.1021/ja909853x

Kreutzer M.T., Kapteijn F., Moulijn J.A., Heiszwolf J.J., Multiphase monolith reactors: Chemical reaction engineering of segmented flow in microchannels, Chemical Engineering Science, 60 (2005) 5895–5916. DOI: 10.1016/j.ces.2005.03.022

Kumacheva E., Garstecki P., Eds., Microfluidic Reactors for Polymer Particles, John Wiley & Sons, Ltd, 2011a, ISBN 9780470057735.

Kumacheva E., Garstecki P., Microfluidic Production of Hydrogel Particles, in: Kumacheva E., Garstecki P. (Eds.), Microfluidic Reactors for Polymer Particles, John Wiley & Sons, Ltd, 2011b, pp.146–169. DOI: 10.1002/9780470979228.ch8

Lagus T.P., Edd J.F., A review of the theory, methods and recent applications of high-throughput single-cell droplet microfluidics, Journal of Physics D: Applied Physics, 46 (2013) 114005. DOI: 10.1088/0022-3727/46/11/114005

Lan F., Demaree B., Ahmed N., Abate A.R., Single-cell genome sequencing at ultra-high-throughput with microfluidic droplet barcoding, Nature Biotechnology, 35 (2017) 640–646. DOI: 10.1038/nbt.3880

Leal-Calderon F., Poulin P., Progress in understanding emulsion metastability and surface forces, Current Opinion in Colloid and Interface Science, 4 (1999) 223–230. DOI: 10.1016/S1359-0294(99)00038-2

Lee C.-C., Sui G., Elizarov A., Shu C.J., Shin Y.-S., Dooley A.N., Huang J., Daridon A., Wyatt P.W., Stout D., et al., Multistep synthesis of a radiolabeled imaging probe using integrated microfluidics, Science, 310 (2005) 1793–1796. DOI: 10.1126/science.1118919

Lee J.N., Park C., Whitesides G.M., Solvent compatibility of poly(dimethylsiloxane)-based microfluidic devices, Analytical Chemistry, 75 (2003) 6544–6554. DOI: 10.1021/ac0346712

Leman M., Abouakil F., Griffiths A.D., Tabeling P., Droplet-based microfluidics at the femtolitre scale, Lab on a Chip, 15 (2015) 753–765. DOI: 10.1039/C4LC01122H

Leng J., Salmon J.-B., Microfluidic crystallization, Lab on a Chip, 9 (2009) 24–34. DOI: 10.1039/B807653G

Leon R.A.L., Badruddoza A.Z.M., Zheng L., Yeap E.W.Q., Toldy A.I., Wong K.Y., Hatton A.T., Khan S.A., Highly selective, kinetically driven polymorphic selection in microfluidic emulsion-based crystallization and formulation, Crystal Growth and Design, 15 (2015) 212–218. DOI: 10.1021/cg501222n

Levin I., Aharoni A., Evolution in microfluidic droplet, Chemistry and Biology, 19 (2012) 929–931. DOI: 10.1016/j.chembiol.2012.08.004

Li H., Fan Y., Kodzius R., Foulds I.G., Fabrication of polystyrene microfluidic devices using a pulsed CO_2 laser system, Microsystem Technologies, 18 (2012) 373–379. DOI: 10.1007/s00542-011-1410-z

Li L., Ismagilov R.F., Protein crystallization using microfluidic technologies based on valves, Droplets, and SlipChip, Annual Review of Biophysics, 39 (2010) 139–158. DOI: 10.1146/annurev.biophys.050708.133630

Lignos I., Maceiczyk R.M., de Mello A.J., Microfluidic technology: Uncovering the mechanisms of nanocrystal nucleation and growth, Accounts of Chemical Research, 50 (2017) 1248–1257. DOI: 10.1021/acs.accounts.7b00088

Lignos I., Protesescu L., Stavrakis S., Piveteau L., Speirs M.J., Loi M.a., Kovalenko M.V., Andrew J., Facile droplet-based microfluidic synthesis of monodisperse IV—VI semiconductor nanocrystals with coupled in-line NIR fluorescence detection, Chemistry of Materials, 26 (2014) 2975–2982. DOI: dx.doi.org/10.1021/cm500774p

Lignos I., Stavrakis S., Kilaj A., de Mello A.J., Millisecond-timescale monitoring of PbS nanoparticle nucleation and growth using droplet-based microfluidics, Small, 11 (2015) 4009–4017. DOI: 10.1002/smll.201500119

Lim J., Caen O., Vrignon J., Konrad M., Taly V., Baret J.C., Parallelized ultra-high throughput microfluidic emulsifier for multiplex kinetic assays, Biomicrofluidics, 9 (2015) 034101–034101. DOI: 10.1063/1.4919415

Lim S.W., Abate A.R., Ultrahigh-throughput sorting of microfluidic drops with flow cytometry, Lab on a Chip, 13 (2013) 4563–4572. DOI: 10.1039/c3lc50736j

Ma S., Murphy T.W., Lu C., Microfluidics for genome-wide studies involving next generation sequencing, Biomicrofluidics, 11 (2017) 021501. DOI: 10.1063/1.4978426

Maceiczyk R.M., Bezinge L., de Mello A.J., Kinetics of nanocrystal synthesis in a microfluidic reactor: theory and experiment, Reaction Chemistry & Engineering, 1 (2016) 261–271. DOI: 10.1039/C6RE00073H

Macosko E.Z., Basu A., Satija R., Nemesh J., Shekhar K., Goldman M., Tirosh I., Bialas A.R., Kamitaki N., Martersteck

E.M., et al., Highly parallel genome-wide expression profiling of individual cells using nanoliter droplets, Cell, 161 (2015) 1202–1214. DOI: 10.1016/j.cell.2015.05.002

Maeda K., Onoe H., Takinoue M., Takeuchi S., Controlled synthesis of 3D multi-compartmental particles with centrifuge-based microdroplet formation from a multi-barrelled capillary, Advanced Materials, 24 (2012) 1340–1346. DOI: 10.1002/adma.201102560

Mair P., Gielen F., Hollfelder F., Exploring sequence space in search of functional enzymes using microfluidic droplets, Current Opinion in Chemical Biology, 37 (2017) 137–144. DOI: 10.1016/j.cbpa.2017.02.018

Mangin D., Puel F., Veesler S., Polymorphism in processes of crystallization in solution: A practical review, Organic Process Research and Development, 13 (2009) 1241–1253. DOI: 10.1021/op900168f

McDonald J.C., Duffy D.C., Anderson J.R., Chiu D.T., Wu H., Schueller O.J.A., Whitesides G.M., Fabrication of microfluidic systems in poly(dimethylsiloxane), Electrophoresis, 21 (2000) 27–40. DOI: 10.1002/(SICI)1522-2683(20000101)21:1<27::AID-ELPS27>3.0.CO;2-C

McDonald J.C., Whitesides G.M., Poly(dimethylsiloxane) as a material for fabricating microfluidic devices, Accounts of Chemical Research, 35 (2002) 491–499. DOI: 10.1021/ar010110q

Melin J., Quake S.R., Microfluidic large-scale integration: The evolution of design rules for biological automation, Annual Review of Biophysics and Biomolecular Structure, 36 (2007) 213–231. DOI: 10.1146/annurev.biophys.36.040306.132646

Mitchell J.P., Particle standards: Their development and application, KONA Powder and Particle Journal, 18 (2000) 40–59.

Moffitt J.R., Lee J.B., Cluzel P., The single-cell chemostat: an agarose-based, microfluidic device for high-throughput, single-cell studies of bacteria and bacterial communities, Lab on a Chip, 12 (2012) 1487–1494. DOI: 10.1039/c2lc00009a

Mora-Huertas C.E., Fessi H., Elaissari A., Polymer-based nanocapsules for drug delivery, International Journal of Pharmaceutics, 385 (2010) 113–142. DOI: 10.1016/j.ijpharm.2009.10.018

Nabavi S.A., Gu S., Vladisavljević G.T., Ekanem E.E., Dynamics of double emulsion break-up in three phase glass capillary microfluidic devices, Journal of Colloid and Interface Science, 450 (2015) 279–287. DOI: 10.1016/j.jcis.2015.03.032

Neethirajan S., Kobayashi I., Nakajima M., Wu D., Nandagopal S., Lin F., Microfluidics for food, agriculture and biosystems industries, Lab on a Chip, 11 (2011) 1574–1586. DOI: 10.1039/c0lc00230e

Nie Z., Seo M.S., Xu S., Lewis P.C., Mok M., Kumacheva E., Whitesides G.M., Garstecki P., Stone H.A., Emulsification in a microfluidic flow-focusing device: Effect of the viscosities of the liquids, Microfluidics and Nanofluidics, 5 (2008) 585–594. DOI: 10.1007/s10404-008-0271-y

Nightingale A.M., Phillips T.W., Bannock J.H., de Mello J.C., Controlled multistep synthesis in a three-phase droplet reactor, Nature Communications, 5 (2014) 3777–3785. DOI: 10.1038/ncomms4777

Nisisako T., Recent advances in microfluidic production of Janus droplets and particles, Current Opinion in Colloid and Interface Science, 25 (2016) 1–12. DOI: 10.1016/j.cocis.2016.05.003

Nisisako T., Ando T., Hatsuzawa T., High-volume production of single and compound emulsions in a microfluidic parallelization arrangement coupled with coaxial annular world-to-chip interfaces, Lab on a Chip, 12 (2012) 3426–3435. DOI: 10.1039/c2lc40245a

Nisisako T., Okushima S., Torii T., Controlled formulation of monodisperse double emulsions in a multiple-phase microfluidic system, Soft Matter, 1 (2005) 23–27. DOI: 10.1039/b501972a

Nisisako T., Torii T., Microfluidic large-scale integration on a chip for mass production of monodisperse droplets and particles, Lab on a Chip, 8 (2008) 287–293. DOI: 10.1039/B713141K

Ogończyk D., Węgrzyn J., Jankowski P., Dąbrowski B., Garstecki P., Bonding of microfluidic devices fabricated in polycarbonate, Lab on a Chip, 10 (2010) 1324–1327. DOI: 10.1039/b924439e

Ortiz R., Chen J.L., Stuckey D.C., Steele T.W.J., Poly(methyl methacrylate) Surface modification for surfactant-free real-time toxicity assay on droplet microfluidic platform, ACS Applied Materials and Interfaces, 9 (2017) 13801–13811. DOI: 10.1021/acsami.7b02682

Pan M., Lyu F., Tang S.K.Y., Fluorinated pickering emulsions with nonadsorbing interfaces for droplet-based enzymatic assays, Analytical Chemistry, 87 (2015) 7938–7943. DOI: 10.1021/acs.analchem.5b01753

Pan M., Rosenfeld L., Kim M., Xu M., Lin E., Derda R., Tang S.K.Y., Fluorinated pickering emulsions impede interfacial transport and form rigid interface for the growth of anchorage-dependent cells, ACS Applied Materials and Interfaces, 6 (2014) 21446–21453. DOI: 10.1021/am506443e

Pekin D., Skhiri Y., Baret J.-C., Le Corre D., Mazutis L., Ben Salem C., Millot F., El Harrak A., Hutchison J.B., Larson J.W., Link D.R., Laurent-Puig P., Griffiths A.D., Taly V., Quantitative and sensitive detection of rare mutations using droplet-based microfluidics, Lab on a Chip, 11 (2011) 2156–2166. DOI: 10.1039/c1lc20128j

Persat A., Chambers R.D., Santiago J.G., Basic principles of electrolyte chemistry for microfluidic electrokinetics. Part I: Acid–base equilibria and pH buffers, Lab on a Chip, 9 (2009a) 2437–2453. DOI: 10.1039/b906465f

Persat A., Suss M.E., Santiago J.G., Basic principles of electrolyte chemistry for microfluidic electrokinetics. Part II: Coupling between ion mobility, electrolysis, and acid–base equilibria, Lab on a Chip, 9 (2009b) 2454–2469. DOI: 10.1039/b906468k

Pham N., Radajewski D., Round A., Brennich M., Pernot P., Biscans B., Bonneté F., Teychené S., Coupling High Throughput microfluidics and small-angle X-ray scattering to study protein crystallization from solution, Analytical Chemistry, 89 (2017) 2282–2287. DOI: 10.1021/acs.analchem.6b03492

Phillips T.W., Lignos I.G., Maceiczyk R.M., DeMello A.J., DeMello J.C., Nanocrystal synthesis in microfluidic reactors: where next?, Lab on a Chip, 14 (2014) 3172–3180. DOI: 10.1039/C4LC00429A

Pieber B., Kappe C.O., Direct aerobic oxidation of 2-benzylpyridines in a gas–liquid continuous-flow regime using propylene carbonate as a solvent, Green Chemistry, 15 (2013) 320–324. DOI: 10.1039/c2gc36896j

Prileszky T.s.A., Furst E.M., Crystallization Kinetics of partially crystalline emulsion droplets in a microfluidic device, Langmuir, 32 (2016) 5141–5146. DOI: 10.1021/acs.langmuir.6b00420

Rakszewska A., Tel J., Chokkalingam V., Huck W.T.S., One drop at a time: Toward droplet microfluidics as a versatile tool for single-cell analysis, NPG Asia Materials, 6 (2014) e133–e133. DOI: 10.1038/am.2014.86

Regehr K.J., Domenech M., Koepsel J.T., Carver K.C., Ellison-Zelski S.J., Murphy W.L., Schuler L.A., Alarid E.T., Beebe D.J., Biological implications of polydimethylsiloxane-based microfluidic cell culture, Lab on a Chip, 9 (2009) 2132–2139. DOI: 10.1039/b903043c

Reyes D.R., Iossifidis D., Auroux P.A., Manz A., Micro total analysis systems. 1. Introduction, theory, and technology, Analytical Chemistry, 74 (2002) 2623–2636. DOI: 10.1021/ac0202435

Rissin D.M., Kan C.W., Campbell T.G., Howes S.C., Fournier D.R., Song L., Piech T., Patel P.P., Chang L., Rivnak A.J., Ferrell E.P., Randall J.D., Provuncher G.K., Walt D.R., Duffy D.C., Single-molecule enzyme-linked immunosorbent assay detects serum proteins at subfemtomolar concentrations, Nature Biotechnology, 28 (2010) 595–599. DOI: 10.1038/nbt.1641

Rodríguez-Ruiz I., Radajewski D., Charton S., Phamvan N., Brennich M., Pernot P., Bonneté F., Teychené S., Innovative high-throughput SAXS methodologies based on photonic lab-on-a-chip sensors: Application to macromolecular studies, Sensors, 17 (2017) 1266–1266. DOI: 10.3390/s17061266

Rotem A., Ram O., Shoresh N., Sperling R.A., Goren A., Weitz D.A., Bernstein B.E., Single-cell ChIP-seq reveals cell subpopulations defined by chromatin state, Nature Biotechnology, 33 (2015) 1165–1172. DOI: 10.1038/nbt.3383

Sackmann E.K., Fulton A.L., Beebe D.J., The present and future role of microfluidics in biomedical research, Nature, 507 (2014) 181–189. DOI: 10.1038/nature13118

Sakai T., Surfactant-free emulsions, Current Opinion in Colloid and Interface Science, 13 (2008) 228–235. DOI: 10.1016/j.cocis.2007.11.013

Schneider T., Kreutz J., Chiu D.T., The potential impact of droplet microfluidics in biology, Analytical Chemistry, 85 (2013) 3476–3482. DOI: 10.1021/ac400257c

Schuler F., Trotter M., Geltman M., Schwemmer F., Wadle S., Domínguez-Garrido E., López M., Cervera-Acedo C., Santibáñez P., von Stetten F., Zengerle R., Paust N., Digital droplet PCR on disk, Lab on a Chip, 16 (2016) 208–216. DOI: 10.1039/C5LC01068C

Sciambi A., Abate A.R., Accurate microfluidic sorting of droplets at 30 kHz, Lab on a Chip, 15 (2015) 47–51. DOI: 10.1039/C4LC01194E

Sebastian Cabeza V., Kuhn S., Kulkarni A.A., Jensen K.F., Size-controlled flow synthesis of gold nanoparticles using a segmented flow microfluidic platform, Langmuir, 28 (2012) 7007–7013. DOI: 10.1021/la205131e

Seemann R., Brinkmann M., Pfohl T., Herminghaus S., Droplet based microfluidics, Reports on Progress in Physics, 75 (2012) 16601–16641. DOI: 10.1088/0034-4885/75/1/016601

Shi H.-h., Xiao Y., Ferguson S., Huang X., Wang N., Hao H.-X., Progress of crystallization in microfluidic devices, Lab on a Chip, 17 (2017) 2167–2185. DOI: 10.1039/C6LC01225F

Shim J.U., Ranasinghe R.T., Smith C.A., Ibrahim S.M., Hollfelder F., Huck W.T.S., Klenerman D., Abell C., Ultrarapid generation of femtoliter microfluidic droplets for single-molecule-counting immunoassays, ACS Nano, 7 (2013) 5955–5964. DOI: 10.1021/nn401661d

Shirk K., Steiner C., Kim J.W., Marquez M., Martinez C.J., Assembly of colloidal silica crystals inside double emulsion drops, Langmuir, 29 (2013) 11849–11857. DOI: 10.1021/la4019986

Sobieszuk P., Napieralska K., Investigations of mass transfer in annular gas-liquid flow in a microreactor, Chemical and Process Engineering—Inzynieria Chemiczna i Procesowa, 37 (2016) 55–64. DOI: 10.1515/cpe-2016-0006

Song H., Chen D.L., Ismagilov R.F., Reactions in droplets in microfluidic channels, Angewandte Chemie—International Edition, 45 (2006) 7336–7356. DOI: 10.1002/anie.200601554

Spyropoulos F., Lloyd D.M., Hancocks R.D., Pawlik A.K., Advances in membrane emulsification. Part B: Recent developments in modelling and scale-up approaches, Journal of the Science of Food and Agriculture, 94 (2014) 628–638. DOI: 10.1002/jsfa.6443

Squires T.M., Quake S.R., Microfluidics: Fluid physics at the nanoliter scale, Reviews of Modern Physics, 77 (2005) 977–1026. DOI: 10.1103/RevModPhys.77.977

Stachowiak T.B., Mair D.A., Holden T.G., Lee L.J., Svec F., Fréchet J.M.J., Hydrophilic surface modification of cyclic olefin copolymer microfluidic chips using sequential photografting, Journal of Separation Science, 30 (2007) 1088–1093. DOI: 10.1002/jssc.200600515

Sugiura S., Nakajima M., Itou H., Seki M., Synthesis of polymeric microspheres with narrow size distributions employing microchannel emulsification, Macromolecular Rapid Communications, 22 (2001) 773–778. DOI: 10.1002/1521-3927(20010701)22:10<773::AID-MARC773>3.0.CO;2-H

Sugiura S., Nakajima M., Tong J., Nabetani H., Seki M., Preparation of monodispersed solid lipid microspheres using a microchannel emulsification technique, Journal of Colloid and Interface Science, 227 (2000) 95–103. DOI: 10.1006/jcis.2000.6843

Sugiura S., Nakajima M., Yamamoto K., Iwamoto S., Oda T., Satake M., Seki M., Preparation characteristics of water-in-oil-in-water multiple emulsions using microchannel emulsification, Journal of Colloid and Interface Science, 270 (2004) 221–228. DOI: 10.1016/j.jcis.2003.08.021

Tadros T.F., Emulsion Formation, Stability, and Rheology, in: Tadros T.F. (Ed.), Emulsion Formation and Stability, Wiley-VCH Verlag GmbH & Co. KGaA, Weinheim, 2013, pp. 1–75. DOI: 10.1002/9783527647941.ch1

Tang M.Y.H., Shum H.C., One-step immunoassay of C-reactive protein using droplet microfluidics, Lab on a Chip, 16 (2016) 4359–4365. DOI: 10.1039/C6LC01121G

Tarazona P., Capillarity and wetting, Physica Scripta, 1987 (1987) 369–374. DOI: 10.1088/0031-8949/1987/T19B/008

Taylor G., Dispersion of soluble matter in solvent flowing slowly through a tube, Proceedings of the Royal Society A: Mathematical, Physical and Engineering Sciences, 219 (1953) 186–203. DOI: 10.1098/rspa.1953.0139

Teh S.-Y., Lin R., Hung L.-H., Lee A.P., Droplet microfluidics, Lab on a Chip, 8 (2008) 198–220. DOI: 10.1039/b715524g

Temiz Y., Lovchik R.D., Kaigala G.V., Delamarche E., Lab-on-a-chip devices: How to close and plug the lab?, Microelectronic Engineering, 132 (2015) 156–175. DOI: 10.1016/j.mee.2014.10.013

Terekhov S.S., Smirnov I.V., Stepanova A.V., Bobik T.V., Mokrushina Y.A., Ponomarenko N.A., Belogurov A.A., Rubtsova M.P., Kartseva O.V., Gomzikova M.O., et al., Microfluidic droplet platform for ultrahigh-throughput single-cell screening of biodiversity, Proceedings of the National Academy of Sciences, 114 (2017) 2550–2555. DOI: 10.1073/pnas.1621226114

The Microfluidic Circle, 2017, *Emerging Microfluidic Companies*, <http://circle.ufluidix.com/microfluidic-companies/> accessed 16.02.2018.

Theberge A.B., Whyte G., Frenzel M., Fidalgo L.M., Wootton R.C.R., Huck W.T.S., Suzuki–Miyaura coupling reactions in aqueous microdroplets with catalytically active fluorous interfaces, Chemical Communications, (2009) 6225–6225. DOI: 10.1039/b911594c

Thiele J., Seiffert S., Double emulsions with controlled morphology by microgel scaffolding, Lab on a Chip, 11 (2011) 3188–3192. DOI: 10.1039/c1lc20242a

Thorsen T., Maerkl S.J., Quake S.R., Microfluidic large-scale integration, Science, 298 (2002) 580–584. DOI: 10.1126/science.1076996

Thorsen T., Roberts R.W., Arnold F.H., Quake S.R., Dynamic pattern formation in a vesicle-generating microfluidic device, Physical Review Letters, 86 (2001) 4163–4166. DOI: 10.1103/PhysRevLett.86.4163

Thurgood P., Baratchi S., Szydzik C., Mitchell A., Khoshmanesh K., Porous PDMS structures for the storage and release of aqueous solutions into fluidic environments, Lab on a Chip, 17 (2017) 2517–2527. DOI: 10.1039/C7LC00350A

Tice J.D., Lyon A.D., Ismagilov R.F., Effects of viscosity on droplet formation and mixing in microfluidic channels, Analytica Chimica Acta, 507 (2004) 73–77. DOI: 10.1016/j.aca.2003.11.024

Tice J.D., Song H., Lyon A.D., Ismagilov R.F., Formation of droplets and mixing in multiphase microfluidics at low values of the reynolds and the capillary numbers, Langmuir, 19 (2003) 9127–9133. DOI: 10.1021/la030090w

Umbanhowar P.B., Prasad V., Weitz D.A., Monodisperse emulsion generation via drop break off in a coflowing stream, Langmuir, 16 (2000) 347–351. DOI: 10.1021/la990101e

Unger M.A., Chou H.-P., Thorsen T., Scherer A., Quake S.R., Monolithic microfabricated valves and pumps by multilayer soft lithography, Science, 288 (2000) 113–116. DOI: 10.1126/science.288.5463.113

Ushikubo F.Y., Oliveira D.R.B., Michelon M., Cunha R.L., Designing food structure using microfluidics, Food Engineering Reviews, 7 (2014) 393–416. DOI: 10.1007/s12393-014-9100-0

Utada A.S., Chu L.Y., Fernandez-Nieves A., Link D.R., Holtze C., Weitz D.A., Dripping, jetting, drops, and wetting: The magic of microfluidics, MRS Bulletin, 32 (2007) 702–708. DOI: 10.1557/mrs2007.145

Utada A.S., Lorenceau E., Link D.R., Kaplan P.D., Stone H.A., Weitz D.A., Monodisperse double emulsions generated from a microcapillary device, Science, 308 (2005) 537–541. DOI: 10.1126/science.1109164

Van Der Graaf S., Schroën C.G.P.H., Boom R.M., Preparation of double emulsions by membrane emulsification—A review, Journal of Membrane Science, 251 (2005) 7–15. DOI: 10.1016/j.memsci.2004.12.013

Van Dijke K., de Ruiter R., Schroën K., Boom R., The mechanism of droplet formation in microfluidic EDGE systems, Soft Matter, 6 (2010) 321–330. DOI: 10.1039/B916141D

Van Steijn V., Kleijn C.R., Kreutzer M.T., Flows around confined bubbles and their importance in triggering pinch-off, Physical Review Letters, 103 (2009) 214501–214501. DOI: 10.1103/PhysRevLett.103.214501

Vannoy C.H., Tavares A.J., Omair Noor M., Uddayasankar U., Krull U.J., Biosensing with quantum dots: A microfluidic approach, Sensors, 11 (2011) 9732–9763. DOI: 10.3390/s111009732

Vian A., Favrod V., Amstad E., Reducing the shell thickness of double emulsions using microfluidics, Microfluidics and Nanofluidics, 20 (2016) 159–159. DOI: 10.1007/s10404-016-1827-x

Vladisavljević G.T., Al Nuumani R., Nabavi S., Microfluidic production of multiple emulsions, Micromachines, 8 (2017) 75–75. DOI: 10.3390/mi8030075

Vladisavljević G.T., Khalid N., Neves M.A., Kuroiwa T., Nakajima M., Uemura K., Ichikawa S., Kobayashi I., Industrial lab-on-a-chip: Design, applications and scale-up for drug discovery and delivery, Advanced Drug Delivery Reviews, 65 (2013) 1626–1663. DOI: 10.1016/j.addr.2013.07.017

Wacker J.B., Lignos I., Parashar V.K., Gijs M.A.M., Controlled synthesis of fluorescent silica nanoparticles inside microfluidic droplets, Lab on a Chip, 12 (2012) 3111–3116. DOI: 10.1039/c2lc40300e

Walters J., Calyxia, 2016, <http://www.calyxia.fr/> accessed 14.02.2018.

Wang J.T., Wang J., Han J.J., Fabrication of advanced particles and particle-based materials assisted by droplet-based microfluidics, Small, 7 (2011) 1728–1754. DOI: 10.1002/smll.201001913

Wang W., Zhang M.J., Xie R., Ju X.J., Yang C., Mou C.L., Weitz D.A., Chu L.Y., Hole-shell microparticles from controllably evolved double emulsions, Angewandte Chemie—International Edition, 52 (2013) 8084–8087. DOI: 10.1002/anie.201301590

Wiles C., Watts P., Haswell S.J., Clean and selective oxidation of aromatic alcohols using silica-supported Jones' reagent in a pressure-driven flow reactor, Tetrahedron Letters, 47

(2006) 5261–5264. DOI: 10.1016/j.tetlet.2006.05.157

Wleklinski M., Falcone C.E., Loren B.P., Jaman Z., Iyer K., Ewan H.S., Hyun S.H., Thompson D.H., Cooks R.G., Can Accelerated Reactions in Droplets Guide Chemistry at Scale?, European Journal of Organic Chemistry, 2016 (2016) 5480–5484. DOI: 10.1002/ejoc.201601270

Xia Y., Whitesides G.M., Soft lithography, Angewandte Chemie—International Edition International Edition, 37 (1998) 550–575. DOI: 10.1002/(SICI)1521-3773(19980316)37:5<550::AID-ANIE550>3.0.CO;2-G

Xu J.H., Li S.W., Tan J., Wang Y.J., Luo G.S., Controllable preparation of monodisperse O/W and W/O emulsions in the same microfluidic device, Langmuir, 22 (2006) 7943–7946. DOI: 10.1021/la0605743

Xu L., Peng J., Yan M., Zhang D., Shen A.Q., Droplet synthesis of silver nanoparticles by a microfluidic device, Chemical Engineering and Processing: Process Intensification, 102 (2016) 186–193. DOI: 10.1016/j.cep.2016.01.017

Yamaguchi H., Maeki M., Yamashita K., Nakamura H., Miyazaki M., Maeda H., Controlling one protein crystal growth by droplet-based microfluidic system, Journal of Biochemistry, 153 (2013) 339–346. DOI: 10.1093/jb/mvt001

Yan J., Bauer W.A.C., Fischlechner M., Hollfelder F., Kaminski C.F., Huck W.T.S., Monodisperse water-in-oil-in-water (W/O/W) Double emulsion droplets as uniform compartments for high-throughput analysis via flow cytometry, Micromachines, 4 (2013) 402–413. DOI: 10.3390/mi4040402

Yetisen A.K., Volpatti L.R., Coskun A.F., Cho S., Kamrani E., Butt H., Khademhosseini A., Yun S.H., Entrepreneurship, Lab on a Chip, 15 (2015) 3638–3660. DOI: 10.1039/C5LC00577A

Zanatta V., Rezzadori K., Penha F.M., Zin G., Lemos-Senna E., Petrus J.C.C., Di Luccio M., Stability of oil-in-water emulsions produced by membrane emulsification with microporous ceramic membranes, Journal of Food Engineering, 195 (2017) 73–84. DOI: 10.1016/j.jfoodeng.2016.09.025

Zhang K., Gao M., Chong Z., Li Y., Han X., Chen R., Qin L., Single-cell isolation by a modular single-cell pipette for RNA-sequencing, Lab on a Chip, 16 (2016) 4742–4748. DOI: 10.1039/C6LC01241H

Zhang L., Feng Q., Wang J., Zhang S., Ding B., Wei Y., Dong M., Ryu J.Y., Yoon T.Y., Shi X., Sun J., Jiang X., Microfluidic synthesis of hybrid nanoparticles with controlled lipid layers: Understanding flexibility-regulated cell-nanoparticle interaction, ACS Nano, 9 (2015) 9912–9921. DOI: 10.1021/acsnano.5b05792

Zhang Y., Sun J., Zou Y., Chen W., Zhang W., Xi J.J., Jiang X., Barcoded microchips for biomolecular assays, Analytical Chemistry, 87 (2015) 900–906. DOI: 10.1021/ac5032379

Zhao C.X., Chen D., Hui Y., Weitz D.A., Middelberg A.P.J., Stable ultrathin-shell double emulsions for controlled release, ChemPhysChem, 17 (2016) 1553–1556. DOI: 10.1002/cphc.201600142

Zheng B., Roach L.S., Ismagilov R.F., Screening of protein crystallization conditions on a microfluidic chip using nanoliter-size droplets, Journal of the American Chemical Society, 125 (2003) 11170–11171. DOI: 10.1021/ja037166v

Zhou J., Ellis A.V., Voelcker N.H., Recent developments in PDMS surface modification for microfluidic devices, Electrophoresis, 31 (2010) 2–16. DOI: 10.1002/elps.200900475

Zhou J., Khodakov D.A., Ellis A.V., Voelcker N.H., Surface modification for PDMS-based microfluidic devices, Electrophoresis, 33 (2012) 89–104. DOI: 10.1002/elps.201100482

Zhu A.-d., Guo M.Y., Single emulsion microfluidic production of Janus and core-shell particles via off-chip polymerization, Chinese Journal of Polymer Science, 34 (2016) 367–377. DOI: 10.1007/s10118-016-1748-x

Zhu P., Wang L., Passive and active droplet generation with microfluidics: a review, Lab Chip, 17 (2017) 34–75. DOI: 10.1039/C6LC01018K

Zhu Y., Fang Q., Analytical detection techniques for droplet microfluidics-A review, Analytica Chimica Acta, 787 (2013) 24–35. DOI: 10.1016/j.aca.2013.04.064

Zinchenko A., Devenish S.R.A., Kintses B., Colin P.Y., Fischlechner M., Hollfelder F., One in a million: Flow cytometric sorting of single cell-lysate assays in monodisperse picolitre double emulsion droplets for directed evolution, Analytical Chemistry, 86 (2014) 2526–2533. DOI: 10.1021/ac403585p

Zuchowska A., Kwiatkowski P., Jastrzebska E., Chudy M., Dybko A., Brzozka Z., Adhesion of MRC-5 and A549 cells on poly(dimethylsiloxane) surface modified by proteins, Electrophoresis, 37 (2016) 536–544. DOI: 10.1002/elps.201500250

Authors' Short Biographies

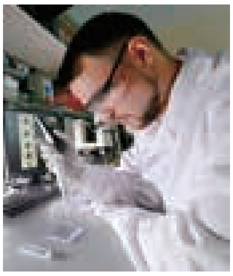

Adam S. Opalski

MSc Adam S. Opalski obtained his Bachelor's and Master's degree in biotechnology from the Faculty of Chemistry Warsaw University of Technology. He is currently pursuing a PhD in the field of microfluidics under the guidance of Prof. Garstecki at the Institute of Physical Chemistry of Polish Academy of Sciences. His research interests lie in investigation of the mechanism of double emulsion formation and use for biological research for which he has recently received a grant from the National Science Centre. Another topic of his studies are high-throughput techniques for droplet generation and manipulation.

Tomasz Kaminski

Tomasz Kaminski is a postdoctoral researcher in the group of Prof. Garstecki at the Institute of Physical Chemistry of the Polish Academy of Sciences in Warsaw. During his PhD studies, he was involved in the development of new micro-droplet technologies to a range of challenges in microbiology and biochemistry. He co-authored 18 publications and 21 patents and patent applications. He has conducted his research projects in collaboration with foreign research groups from Oxford University, University of Wisconsin-Madison, University of Tokyo and 3 spin-off companies: Scope Fluidics, Curiosity Diagnostics and Bacteromic that commercialize microfluidic technologies for medical diagnostics.

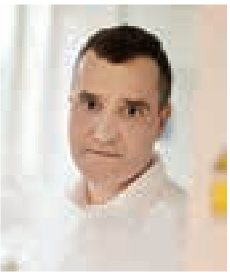

Piotr Garstecki

Piotr Garstecki is a full professor at the Institute of Physical Chemistry of the Polish Academy of Science, where he leads the Microfluidics and Complex Fluids Research Group. He obtained his MSc degree in theoretical physics from the College of Science in 1998 and his PhD in chemistry from the Institute of Physical Chemistry PAS. He later served as a postdoctoral fellow in the group of Prof. George Whitesides at Harvard University. He co-authored over a hundred scientific publications and multiple patent applications and co-founded multiple spin-out companies that use microfluidic technologies for the development of medical diagnostic systems.

KONA Powder and Particle Journal No. 36 (2019) 72–87/Doi:10.14356/kona.2019005 Review Paper

Using Nanoparticles as a Bottom-up Approach to Increase Solar Cell Efficiency[†]

Marcel Di Vece

[1] *CIMAINA and Department of Physics, University of Milan, Italy*

Abstract

Nanostructures in solar cells are used both for the active layers and for light management techniques. Particularly thin-film solar cells will benefit strongly from such nanoscale approaches as the light absorption needs to be improved. Nanoparticles produced by wet chemical techniques, sometimes in the form of quantum dots, are currently used to fabricate thin-film solar cells for research purposes. Light management studies use nanostructures that are often created by lithographic methods but which are too expensive for an industrial realisation. In this review paper, the opportunities for using nanoparticles as a bottom-up approach for both the active layer and light management nanostructures is discussed. Since both the wet chemical method and lithographic techniques have considerable limitations, the use of gas aggregation cluster sources is proposed as a promising method to advance the use of bottom-up nanoparticles for solar cells. Plasmonics, Mie scattering, quantum dots and new materials are reviewed with respect to the nanoparticle potential. The increase of solar cell efficiency by using ultra-clean and crystalline nanoparticles which are produced with a vacuum-compatible technique at low temperatures should be very interesting for science and technology, ultimately leading to industrial products.

Keywords: nanoparticle, solar cell, light management, plasmonics, Mie particles, quantum dots

1. Introduction

Solar cell technology is important for many reasons, of which the ecological sustainability is the most important. The first commercial solar cells based on silicon wafer technology have been around for many decades and their technology has shown incremental progress (**Fig. 1**). Currently, solar energy contributes to a bit more than 1 % of the global energy demand (in some countries up to 7 %), which clearly indicates that the price per kWh should be further reduced to become competitive (with conventional electricity sources) in more locations worldwide to obtain significantly higher market shares. Because the price of a solar cell is determined to a large extent by the module and installation costs, the efficiency of a solar cell determines its commercial success. This forms the basis of current ongoing solar cell research: the increase of photovoltaic efficiency. Research aims at higher efficiencies with cheap materials and using novel techniques (Green M.A., 2003; Conibeer G., 2007).

The efficiency of a solar cell has fundamental limits as determined by Shockley and Queisser (SQ), who calculated a maximum efficiency using a single p-n junction of 32 % for c-Si solar cells (Shockley W. and Queisser, 1961). With modern approaches such as tandem cells, the

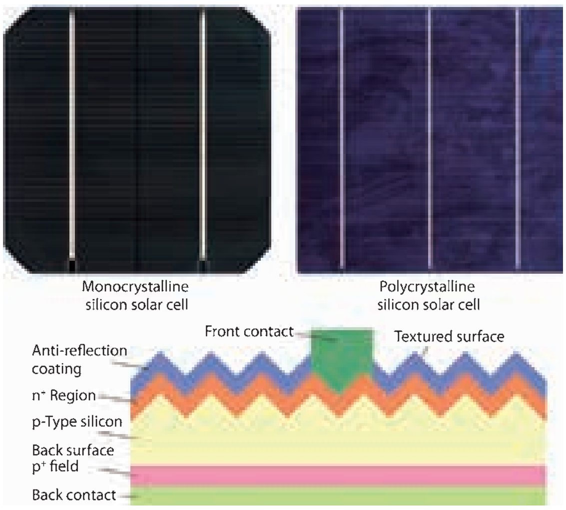

Fig. 1 Typical mono- and polycrystalline silicon solar cells (top), and simplified cross-section of a commercial monocrystalline silicon solar cell (bottom). Reprinted with permission of Saga T. (2010).

[†] Received 30 June 2017; Accepted 6 September 2017
J-STAGE Advance published online 31 March 2018

[1] via Celoria 16, 20133 Milano, Italy
E-mail: marcel.divece@unimi.it
TEL: +39-02503-17255

theoretical efficiency is 45 %. One of the most important processes to limit solar cell efficiency is the recombination of electrons and holes inside the active layer. Particularly for thick solar cells such as crystalline or multi-crystalline Si wafer solar cells, this reduces the efficiency very strongly. The obvious advantage of lower cost and lower energy consumption during fabrication forms a strong motivation for fabricating thin-film solar cells. It is clear that by reducing the thickness of the active layer in a solar cell, the optical absorption likely decreases as well. Therefore, the main aim in current thin-film solar cell development is the improvement of absorption by the choice of composition and with advanced light management. Several materials are currently being explored for thin-film solar cell technology, of which the a-Si, CdTe and CIGS are already commercially available (Lee A.U. and Ebong, 2017; Mints P., 2010), and the perovskites are knocking on the door (**Fig. 2**). Light management makes use of nanostructures which have intricate interactions with the incident light which can be used to stimulate optical absorption in thin-film solar cells (Yu E.T. and van de Lagemaat, 2011). Both the composition of a solar cell and light management with nanostructures form attractive possibilities for using nanoparticles. Light management can be achieved by light scattering on, for example metal particles, light in-coupling and local field enhancement (Atwater H.A. and Polman, 2010). Additionally, light in the UV and in the infra-red range is not harvested efficiently in solar cells. In the UV range, a considerable amount of energy is wasted by thermalisation of electrons, which are excited far beyond the band gap. In the infra-red range, the band gap is too large to be able to absorb the light. Therefore up- and down-converter materials are being investigated (Huang X. et al., 2013), which can be in the form of particles, to split the UV photons into two photons and combine the infra-red photons to a single photon, all resulting in an energy package comparable to that of the semiconductor band gap. Nanoparticles are particularly interesting as quantum dots which are semiconductor particles with a radius smaller than the Bohr radius and which enable the tuning of the band gap by changing the size (Jabbour G.E.and Doderer, 2010).

Most light management techniques currently being explored make use of lithography. Although this is very rewarding as a proof of principle, it is economically not viable. Therefore the use of nanoparticles forms an industrially interesting alternative because they can be deposited as a bottom-up method, making it fast and cheap. Nanoparticles can be fabricated by chemical or physical techniques, each of which have their advantages and disadvantages. The chemical route to nanoparticle fabrication and deposition is generally well known, as are the complications by matching it with existing solar cell fabrication techniques. Although the physical deposition of nanoparticles, particularly with cluster sources, has been around for several decades, the use in solar cell research and development has barely begun. This review paper is written to create awareness of the scientific and technological opportunities of the (physical) fabrication and implementation of nanoparticles for photovoltaics.

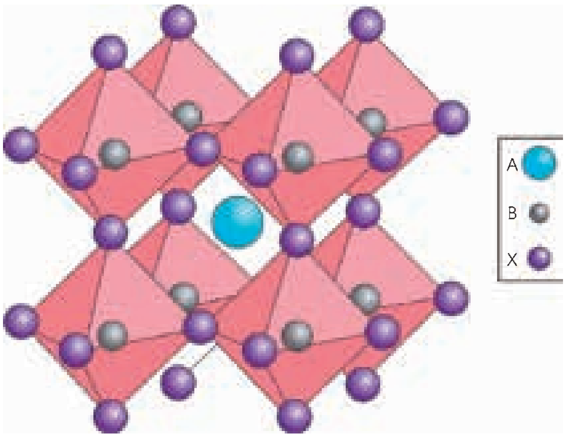

Fig. 2 Cubic perovskite crystal structure. For photovoltaically interesting perovskites, the large cation A is usually the methylammonium ion (CH_3NH_3), the small cation B is Pb and the anion X is a halogen ion (usually I, but both Cl and Br are also of interest). Reprinted with permission of Green M.A., et al. (2014).

2. Thin-film solar cells

Thin-film solar cells can be made of many possible materials which are all currently the object of research, and the thickness ranges from several μm to hundreds of nm. An overview of the most investigated, used and promising materials by Polman et al. (Polman A. et al., 2016), shows that the increase of efficiency due to research is the fastest for quantum dots, CZTS, CdTe, organic and perovskite solar cells. Except for Si (homojunction and heterojunction), GaAs and GaInP, most compositions are at least 25 % below their SQ limit, which implies that there is much room for improvement (**Fig. 3**).

The thin-film solar cell with a large market share is based on a-Si:H, which also forms an important research platform for light management studies. The advantages of a-Si:H based solar cells are its conformal growth, which creates many perspectives in combination with nanoscale approaches, and the possibility to form flexible solar cells. Unfortunately the efficiency of the a-Si:H thin-film solar cell did not improve much beyond 12 % for many years. The main reason is the abundant presence of defects which form recombination centres for the electrons and holes.

Although CdTe, and the chalcopyrite compound copper indium gallium diselenide (CIGS) are currently market

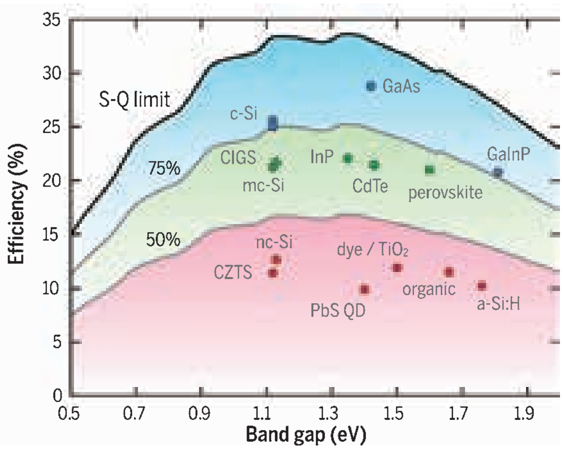

Fig. 3 Theoretical Shockley-Queisser detailed-balance limit as a function of band gap (black line) and 75 % and 50 % of the limit (gray lines). The record efficiencies for different materials are plotted for the corresponding band gaps. Reprinted with permission of Polman A., et al. (2016).

products as thin-film solar cells (Miles R.W. et al., 2007), research is increasing the laboratory efficiency which makes them more attractive.

Perovskites are currently being very intensively investigated, and impressive laboratory efficiencies of up to 22.1 % have been reported (**Fig. 2**). Although the advantages of perovskites include ease of fabrication, strong solar absorption and low non-radiative carrier recombination rates, the instability under ambient conditions and illumination due to the presence of organic compounds hinders commercial success. Replacement of the organic components is an important goal which will bring this material to the market. The low resistance of present perovskite technology to moist air and water vapour together with the inability to produce high-quality large surfaces forms a serious bottleneck. Although perovskites can be used as a thin-film solar cell, they can also be used as a dye particle in, for example a TiO_2 electrode.

3. Light management

In thick conventional crystalline silicon solar cells, light management techniques such as anti-reflection texture and coatings have been employed successfully for a long time. Because such an anti reflection texture has dimensions much larger than the thickness of thin-film solar cells they are not suitable. Therefore new light-trapping techniques at the nanoscale, which are compatible with the thin-film solar cell, have to be found (Brongersma M.L. et al., 2014; Chattopadhyay S. et al., 2010; Kuznetsov A.I. et al., 2016).

3.1 Plasmonics

Plasmonics, the electronic response of light interacting with metal nanostructures, is a promising novel concept in the quest for photovoltaic devices with high efficiencies and low-cost materials. The interest in plasmonics, which merges optics with electronics (Maier S.A. et al., 2001; Ozbay E., 2006) at very small scales, has increased considerably since about a decade. Five main effects are distinguished with the metal plasmon and optically active neighbouring materials (Maier S.A., 2007): 1) Plasmonic field enhancement (Atwater H.A. and Polman, 2010; Ferry V.E. et al., 2010; Pala R.A. et al., 2009; Pillai S. et al., 2007), (a near-field effect) increases the electromagnetic field close to the metal surface by orders of magnitude. This is the result of the (dipole) electric field around the metal nanoparticle in response to illumination. This is particularly interesting for thin-film solar cells as light concentration has a significant effect on the overall absorption. 2) Scattering at/by the metal nanoparticle (Bohren C.F. and Huffman, 2004) increases the light path length in a solar cell and is therefore an important mechanism to increase efficiency. Incident light is scattered off the metal object into a distribution of optical modes within the semiconductor. 3) Coupling of plasmon resonance to waveguide modes in thin semiconductor slabs. 4) The coupling of an (semiconductor) emitter to plasmon modes also affects both the radiative and non-radiative decay rates. This phenomenon is based on the principle that the strength with which an emitter couples with an electromagnetic field depends on its environment (Anger P. et al., 2006; Novotny L. and Hecht, 2006; Purcell E., 1946). 5) Energy transfer from the absorber/emitter to plasmon modes of a nearby nanoparticle or vice versa can occur by, for example Forster Energy Transfer (FRET) (Govorov A.O. et al., 2006). This energy will be partially dissipated or coupled to radiation (Clapp A.R. et al, 2006; Michalet X. et al., 2005). The balance between these effects depends strongly on the geometry, shape, size and distance (Haes A.J. et al., 2004). A schematic of some plasmonic interactions is shown in **Fig. 4**.

One of the first experimental investigations of plasmonic enhancement for photovoltaics involved silver nanoparticles in an organic solar cell (Stenzel O. et al., 1995; Westphalen M. et al., 2000). The first papers to explore the potential of localized surface plasmon resonance (LSPR) in solid-state photovoltaics were published in the late 1990s by Stuart and Hall (Stuart H.R. and Hall, 1996). Their device consisted of a thin silicon-on-insulator wafer, where the Si was 165 nm thick, and since the absorbing Si layer was separated from the Si substrate by a layer of SiO_2, it acts as a thin waveguide. Metal island formation was achieved by the deposition of a thin metallic film and annealing under N_2 so that the film coalesced

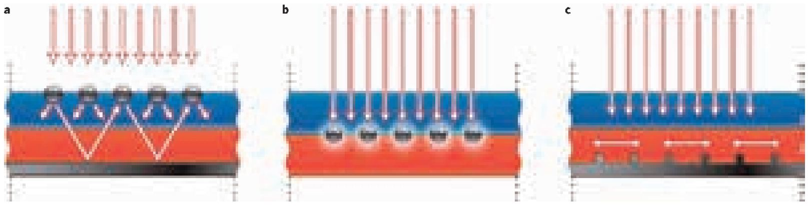

Fig. 4 Plasmonic light-trapping geometries for thin-film solar cells. **(a)** Light trapping by scattering from metal nanoparticles at the surface of the solar cell. Light is preferentially scattered and trapped into the semiconductor thin film by multiple and high-angle scattering, causing an increase in the effective optical path length in the cell. **(b)** Light trapping by the excitation of localized surface plasmons in metal nanoparticles embedded in the semiconductor. The near-field of the excited particles causes the creation of electron–hole pairs in the semiconductor. **(c)** Light trapping by the excitation of surface plasmon polaritons at the metal/semiconductor interface. A corrugated metal back surface couples light to surface plasmon polariton or photonic modes that propagate in the plane of the semiconductor layer. Reprinted with permission of Atwater H.A. and Polman A. (2010).

into discrete islands. Subsequent studies show that the local field enhancement and scattering of plasmonic nanostructures increases the solar cell performance (Atwater H.A. and Polman, 2010; Maier S. et al., 2001; Pala R.A. et al., 2009) (Ferry V.E. et al., 2010). Additionally, work by Barnard et al. (Barnard E.S. et al., 2011) shows the enhancing effect of silver nanostructures on the photocurrent in silicon. Underneath a metal nanoantenna, the field intensity is enhanced by a factor of 2.8 while locally, the field enhancement can be significantly higher (up to 20) in “hot spots” under the corners of the antenna. A theoretical study of plasmonic nanoparticles for solar cells shows that an absorption increase of 10–15 % is more than feasible (Akimov Y.A. et al., 2009).

To date, most research focused on noble metals (Hägglund C. et al., 2008; Nakayama K. et al., 2008) which have strong resonances in the visible part of the spectrum and have the advantage of being inert. However, the high price of noble metals makes them difficult for commercial solar cells. Although aluminium has its bulk plasmon resonance in the far UV range at around 150 nm, its plasmon resonance can be shifted, making it a cheap alternative. The plasmon resonance wavelength of aluminium nanoparticles can be shifted towards the visible range by selection of size, shape, configuration and dielectric environment (Ekinci Y. et al, 2008; Knight M.W. et al., 2012; Langhammer C. et al., 2008; Olson J. et al., 2014; Tan S.J. et al., 2014; Temple T.L. and Bagnall, 2011; van der Vliet T. and Di Vece, 2016). The electron collision frequency at a plasma frequency in the visible range in aluminium is in between that of gold and silver (Tassin P. et al., 2012), which make Ohmic losses acceptable. A theoretical study by Akimov at al. (Akimov Y.A. et al., 2009) has demonstrated that aluminium particles increase the optical absorption in a-Si:H over a wide wavelength range better than silver particles.

Nanoparticle plasmonics: although previous research on using plasmonics for solar cells included both nanoparticles and nanostructures formed by lithography as shown in **Fig. 5**, much work remains to be done as commercial applications are still not realized. Although lithography has been very rewarding as a proof of principle method, this top-down technique is economically not yet interesting. However, the roll-to-roll nano imprint lithography technique has been used in such studies and is industrially more interesting (Ferry V.E. et al., 2010; Kooy N. et al., 2014). The use of (plasmonic) nanoparticles from a bottom-up approach as demonstrated by Faraone G., et al. (2018) has many advantages such as speed and low cost, which brings these novel concepts within industrial reach.

3.2 Mie scatterers

A new approach to more efficiently coupling light into a thin-film solar cell is the use of Mie scatterers as shown in **Fig. 6**. In a Mie scatterer, usually a dielectric particle such as silicon (Spinelli P. and Polman, 2014) with the dimension of the wavelength of light (down to 10 %), the scattering of light often has a stronger intensity in the forward direction which is useful when a light absorbing material is placed beneath it. The forward scattering couples the light efficiently into the layers below it (Spinelli P. et al., 2012). Since a Mie scatterer is made out of a dielectric material and not a metal with electric resistance acting on the plasmonic resonance, its optical losses are minimal. When the Mie scatterer is large, the captured light will resonate at particular wavelengths, depending on the interference conditions, which enhances its optical cross-section for these wavelengths. The circulating light in this Mie scatterer can be coupled into a solar cell beneath it by leaking, which makes a more efficient and selective harvesting of light possible. Mie scattering can provide a broad-band optical absorption with, for example silicon nanocone arrays (Wang Z.Y. et al., 2015). The Mie scatterer is not limited to solar cells but can also be employed in solar fuel generation by light (Cheng Y.Y. et al.,

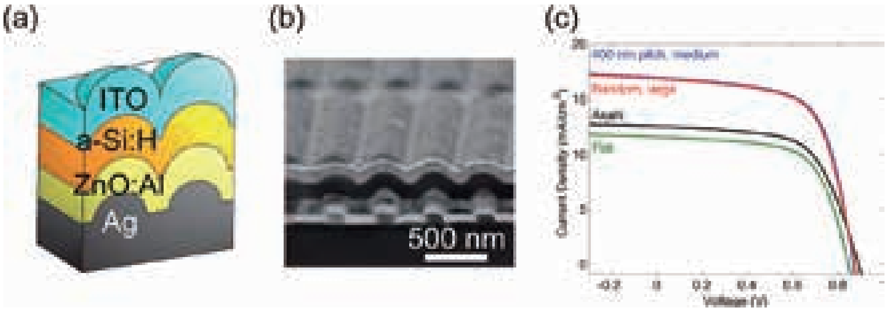

Fig. 5 Current–voltage characteristics of nanopatterned cells. The cells are conformally deposited over the patterned substrate, as shown schematically in **(a)** and in SEM cross-section in **(b)**. The maximum particle diameter in the backpattern was chosen so that nanostructures in the ITO top layer would touch without overlap. **(c)** Current density–voltage measurements for the best-efficiency cells on the substrate with 90 nm intrinsic layers. The optimized periodic pattern and the pseudorandom pattern have efficiencies of 9.6 and 9.4 %, respectively. Reprinted with permission of Ferry V.E., et al. (2011).

Fig. 6 Schematic showing how various optical resonances supported by a model cell structure can be excited to enhance light absorption in the active semiconductor material (green). The numbers 1–4 label four distinct coupling mechanisms. 1: Excitation of an optical (Mie) resonance of hexapolar symmetry in the NWs. This resonance is hybridized with a guided resonance in the underlying Si layer. 2: Fabry-Perot standing-wave resonance that results from the confinement of light between the reflecting top surface of the high-index Si film and the metallic back-reflector. 3: Guided resonance of the Si layer. 4: Excitation of diffracted modes. Such modes can be excited when incident light is redirected into the plane of the light-trapping layer, where they concentrate most of the field. These modes also extend into the underlying semiconductor layer where they can induce useful absorption. Reprinted with permission of Brongersma M.L., et al. (2014).

2012; Kim S.J. et al., 2014). The Mie scatterer composition can be chosen to obtain the desired optical properties as shown by using silicon carbide (Schuller J.A. et al., 2007), silica (Nunomura S. et al., 2010) and germanium (Cao L. et al. , 2010) particles.

In most of the current research of Mie scatterers for solar cells, top-down techniques such as lithography and laser printing (Zywietz U. et al., 2014) are used to create the desired nanostructures. As this is commercially not yet attractive, alternative methods (i.e. bottom-up) to fabricate Mie scatterers for solar cells need to be explored. Although wet chemical techniques are used to fabricate Mie scattering structures (Araújo A. et al., 2017; Karg M. et al., 2015), more industrially compatible techniques are desirable. A recent work by (Giannakoudakis and Di Vece, 2017) shows that TiO_2 Mie scatterers can be produced with a gas aggregation cluster source and combined with a-Si thin films. TiO_2 has also been used as a Mie scattering composite in dye-sensitized solar cells (Son S. et al., 2013) and as a scatterer for solar cells (Kang S.H. et al., 2008). Since thin a-Si films are used in solar cells, they function as a photovoltaic model system. TiO_2 Mie scatterers can easily be fabricated with a gas-phase aggregation cluster source (Barborini E. et al., 2003; Polonskyi O. et al., 2013), which is fast, cheap, vacuum-compatible and provides ultra-clean and well-defined particles. TiO_2 particles were also produced by a pulsed microplasma cluster source (Barborini E. et al., 2003), which demonstrates its versatility.

3.3 Quantum dots

Although commercial quantum dot solar cells are not available (Jabbour G.E. and Doderer, 2010), the quantum-dot-based emitting displays (QDOT) (Dai X. et al., 2017) demonstrate that this could become reality in the near future. Most of the current solar cell materials are used or could be used in a thin-film design. The inspiration for quantum dot solar cells is the tandem or multi junction cells in which more photons of different energy are harvested. Although such solar cells are commercially available and indeed have a higher efficiency (Law D.C. et al., 2010), they are, however, very expensive, leaving ample space for research towards economically viable materials.

The band gap of a semiconductor can be changed by reducing the size, typically well below 10 nm (Nebel C.E. et al., 1998; Nozik A.J., 2002) due to quantum confinement as illustrated in **Fig. 7**. These quantum dots (Alivisatos A.P., 1996; Murray C.B. et al., 2000) allow the use of a

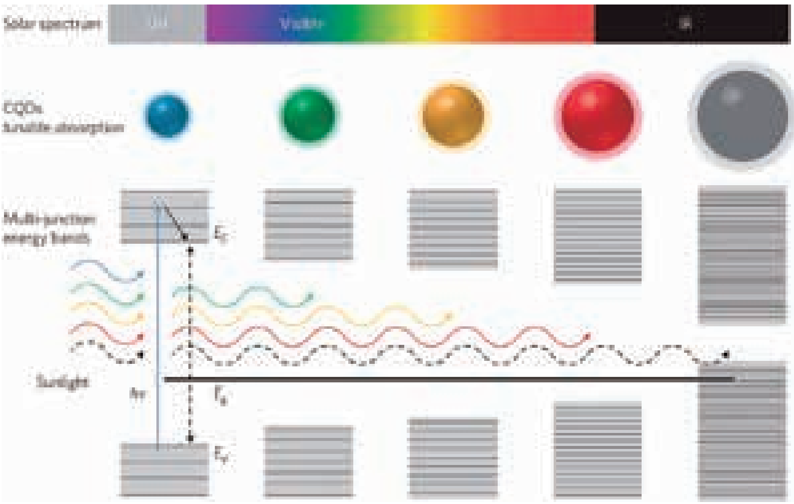

Fig. 7 Size-dependent absorption enables QDs to be tuned to absorb, sequentially, the constituent bands making up the sun's broad spectrum, paving the way for the construction of multi-junction solar cells that overcome the energy loss in single-junction cells resulting from thermalization. This is achieved by reducing the discrepancy between the energy of absorbed photons (*hv*) and the bandgap (e.g. dashed black arrow) of the material in which they are absorbed, so that the energy lost by the photoexcitations due to thermalization (solid black arrow) is minimized. E_C and E_V are the conduction and valence band edges, respectively. Reprinted with permission of Lan X. (2014).

single cheap semiconductor in a tandem solar cell. However, solar energy conversion to electricity in these quantum dot solar cells remains too low (below 10 % (Jabbour G.E. and Doderer, 2010)) and therefore requires fundamental improvements. One of the key factors is the efficient transport of charge carriers (electrons and holes) toward the opposing electrodes. The chemical properties of the quantum dot surface, the material between the quantum dots and the contact properties with the electrodes are all very important to obtain the best efficiency. One of the promising quantum dot compositions is PbS or PbSe, these are conveniently produced and have promising optical and electronic properties (Carey G.H. et al., 2015). A schematic of the different uses of quantum dots for solar cells is shown in **Fig. 8**.

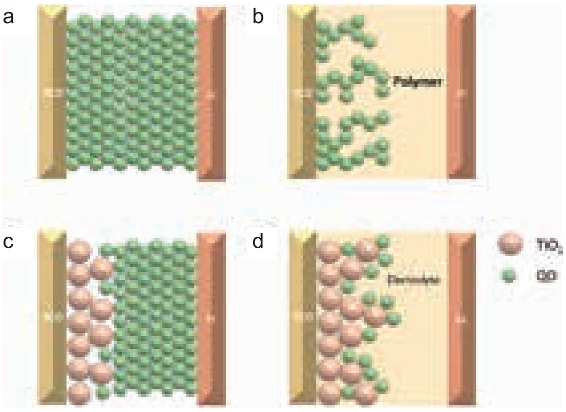

Fig. 8 Different QD-based photovoltaic cells. **(a)** Schottky cell; **(b)** hybrid polymer solar cells; **(c)** heterojunction cell and **(d)** QD-sensitized solar cell.

Silicon QD: although new concepts and materials are intensively investigated to further increase efficiencies, the "old work horse" silicon remains a very attractive photovoltaics (PV) material. Silicon as a quantum dot may lead to enhanced device performance (Conibeer G., 2007). Besides the possibility of silicon quantum dots to tune their band gap (Cullis A.G. and Canham, 1991) which can be employed in a tandem cell, a direct band gap may appear for the smallest sizes (de Boer W.D.A.M. et al., 2010). In principle a direct band gap increases absorption as compared with the indirect band gap of bulk crystalline silicon (Prokofiev A.A. et al., 2010). However, small quantum dots have a low density of states which in turn reduces their optical absorption.

The photoluminescence of silicon nanoparticles yielded a clear size dependence of the luminescence emission energy due to quantum confinement (Delerue C. et al., 1998; Ledoux G. et al., 2000; Takeoka S. et al, 2000; Tekin E. et al., 2008; Wilson W.L. et al., 1993). Photoluminescence on silicon particles which were fabricated by laser ablation showed radiative decay lifetimes of microseconds at room temperature which also depends on size and the available phonon contribution (Watanabe K. et al., 2002). Multiple exciton generation in silicon nanoparticles was observed by a step-like enhancement of the luminescence quantum yield (Timmerman D. et al., 2011). In a work by Trinh et al. (Trinh M.T. et al., 2012), the direct generation of multiple excitons was even possible in adjacent silicon nanoparticles.

The main reason why currently silicon quantum dot research is not very active is the inability to produce silicon quantum dots by wet chemical means. Various methods to fabricate silicon particles for solar cells have been studied with proof of principle devices. From silicon-rich silicon oxide or silicon carbide, nanoparticles are formed upon annealing whereby the silicon atoms aggregate to form particles (Conibeer G. et al., 2006). A similar process is possible by Si ion implantation (Shimizu-Iwayama T. et al., 1998). However, these silicon nanoparticles have a large size distribution and are often separated by large distances, which hinders electrical conductance. The large size distribution will prevent accurate tuning of the band gap and forms exciton-trapping centres. The fabrication of monodisperse silicon quantum dots with controllable separation distance is a prerequisite for successful application in a solar cell. Work by Mohan et al. (Mohan A. et al., 2017) shows that it is possible to obtain silicon nanoparticles by using a pulsed SiH_4/Ar plasma. In a recent work by Tang et al. (Tang W. et al., 2015), the silicon nanoparticles were fabricated with a gas aggregation cluster source, which is a promising route.

3.4 Spectral budgeting

Photons having an energy higher than twice that of the band gap (i.e. in the 280–400 nm spectral range) do not contribute efficiently to the energy conversion. To reduce the losses, photon conversion concepts have been proposed: down-shifting (where an ultraviolet (UV) photon is converted into a visible or infrared (IR) photon) (Hovel H.J. et al., 1979) and down-conversion (a UV photon is converted into two visible or IR photons) (Richards B.S., 2006; Trupke T. et al., 2002). Down-conversion is also often called singlet exciton fission (Lee J. et al., 2013). The advantage of down-shifting is that the reduced photon energy enables the photon to penetrate deeper into the active semiconductor layer while for down-conversion, the two photons are better absorbed. A schematic image to illustrate up- and down-conversion for a solar cell is shown in **Fig. 9**. To date, down-shifting and down-conversion have not led to significant improvements, and better systems need to be developed (Fix T. et al., 2015). Luminescence provides a good way to down-shift the photon (Švrček V. et al., 2004; van Sark W. G.J.H.M. et al., 2004).

Alternatively, the up-shifting (up-conversion) of IR photons, which means that multiple IR photons will be harvested by a nanoparticle and converted into a single photon in the visible range, can be used to increase the efficiency of a solar cell (Bloembergen N., 1959; De Wild J. et al., 2013). The commercially available up-converter, Gd_2O_2S:Yb^{3+}, Er^{3+}, in which Yb^{3+}absorbs light around 980 nm and Er^{3+} emits in the visible spectrum (400 to 700 nm) needs to be improved (de Wild J. et al., 2011; Haase M. and Schafer, 2011). For example, with nanocrystals of $NaYF_4$:Er^{3+}, Yb^{3+} also shows up-conversion. An advantage of using nanocrystals is that transparent solutions or transparent matrices with up-converting nanocrystals can be obtained.

3.5 Nanoparticles as a constituent

Many of the thin-film solar cells can also be fabricated by using nanoparticles as a constituent (Stolle C.J. et al., 2013). The dye-sensitized solar cells are famous and use TiO_2 particles as (dye) support (Gratzel M., 2001). Although the technology can be cheap, the dyes are often un-

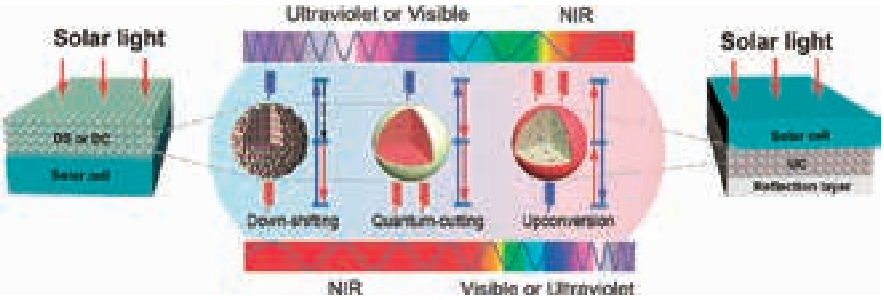

Fig. 9 Spectral conversion design for PV applications involving down-shifting (DS), quantum-cutting (QC), and upconversion (UC) of luminescent materials. In a typical downshifting process, upon excitation with a high-energy photon, non-radiative relaxation takes place followed by radiative relaxation, thereby resulting in the emission of a lower-energy photon. In contrast, two-step radiative relaxation occurs in the quantum-cutting process upon excitation with a high-energy photon, leading to the emission of two (or more) lower-energy photons. The upconversion process can convert two (or more) incident low-energy photons into a single higher-energy photon. The downshifting and quantum-cutting materials are generally placed on the front surface of a monofacial solar cell, allowing the downconverted photons to be absorbed by the solar cell. The upconversion material is typically placed in between a bifacial solar cell and a light-reflection layer to harvest the sub-bandgap spectrum of sunlight. Reprinted with permission of Huang X. (2013).

stable in sunlight and the presence of electrolytes makes it difficult to handle and seal. Additionally, the efficiencies have not surpassed 12 % during the last two decades of research. Nanoparticle precursors are used to fabricate CIGS (Kapur V.K. et al., 2003), CZTS (Lokhande A.C. et al., 2016) and CdTe (Anderson I.E. et al., 2009) solar cells. The particles are fabricated by wet chemical procedures and deposited from solution by spin-coating, ink-jet printing or spraying. The advantage is the relatively uncomplicated technique and the low temperatures. The disadvantages are the lack of crystallinity and presence of contaminants.

4. Nanoparticle sources for photovoltaics

4.1 Vacuum-compatible techniques

Colloidal nanoparticles have the advantage of large-volume production and ease of deposition by, for example, spin coating or electro spray. The main disadvantages are the stabilising chemicals in the solutions which form a source of contamination and some (crystalline) compositions are not easily synthesised by wet chemistry. The diverse fabrication methods of solar cells provide many opportunities for the different nanoparticle fabrication techniques. Thin-film a-Si:H is grown by plasma-enhanced chemical vapour deposition (PE-CVD) from Si- and H-containing precursors (Schropp R.E.I., 2015). Conductive electrodes and anti-reflection coatings are also applied in a vacuum environment. This makes physical deposition of particles with cluster sources very attractive. An example of embedding silver nanoparticles inside a-Si:H solar cells is given in **Fig. 10**. Although the reactor chamber of a cluster source can be at about 10^{-1} mbar, the deposition pressures of gas aggregation cluster sources are between 10^{-5} and 10^{-8} mbar, which leaves the solar cell (parts) undisturbed as the presence of reactive gaseous species is minimal. Along with the nanoparticles, a carrier gas is transported to the deposition chamber, usually argon and/or helium, both of which are noble gasses and therefore do not contaminate the solar cell.

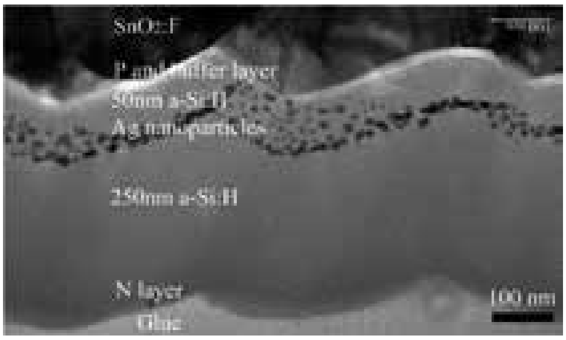

Fig. 10 TEM cross-section of an a-Si:H solar cell with silver nanoparticles embedded at a depth of 50 nm in the absorber layer. Reprinted with permission of Santbergen R. (2010).

Various cluster sources would be suitable for the fabrication of nanoparticles for PV. The different types of cluster sources are well described in literature (de Heer W.A., 1993; Popok V.N. et al., 2011; Wegner K. et al., 2006b). In the gas-aggregation source, metal is vaporized and introduced in a flow of cold inert gas. This causes the vapour to become highly supersaturated. Due to the low temperature of the inert gas, cluster production proceeds primarily by successive single-atom addition. The cluster size distribution is determined by the parameters of the source such as the metal-vapour density, gas flow rate, and dimensions of the various components. Gas-phase cluster sources work in either pulsed or continuous mode, both of which are suitable for optical layers. The term "cluster source" is slightly confusing as in the past, the device was often used to study few atom particles. Since many cluster sources are capable of producing nanoparticles of up to tens of nm, a new name would be appropriate.

The seeded supersonic nozzle source (SSNS) and the thermal gas aggregation source (TGAS) use thermal evaporation to produce nanoparticles at high yield, but is limited to the metals. The sputter gas aggregation source (SGAS) uses sputtering to replace Joule heating to vaporize the material. The strong advantage of this method is that any solid can be used: metals, semiconductors and insulators. In **Fig. 11**, silicon nanocrystals made with such a cluster source are shown. The laser ablation source

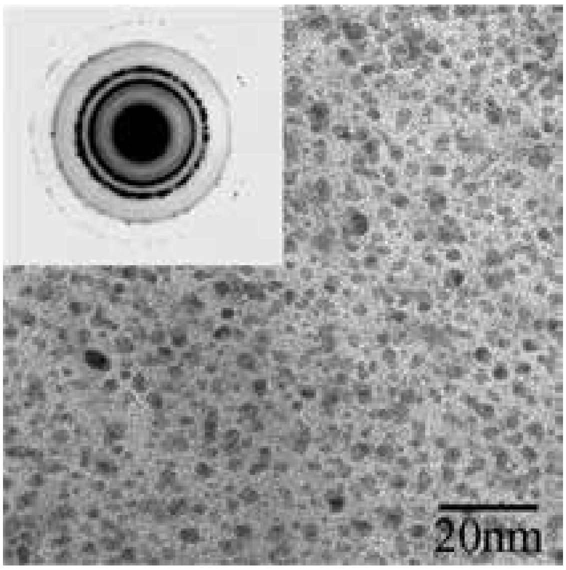

Fig. 11 TEM image showing the general morphology of the Si nanoparticles produced by a magnetron sputtering cluster source and the inset is the selected area electron diffraction pattern. Reprinted with permission of Wang L. (2008).

(LAS) also has the advantage of being able to ablate most solids and having a high yield. However, only small particles can be produced. Pulsed-arc cluster ion sources (PACIS) use an arc discharge between two metallic electrodes in combination with an inert gas burst. The yield is high but oxide particles can only be produced by the oxidation of metal particles, which is too complicated and time-consuming for optical coatings on semiconductor surfaces. Additionally, the particle sizes are very small. The pulsed microplasma cluster source (PMCS) combines the LAS and PACIS, resulting in high particle fluxes. However, only metal or highly doped semiconductor nanoparticles can be produced.

Cluster sources are excellently suited for producing light management structures with metal and dielectric particles. The particles can be deposited at any stage of the solar cell fabrication and the random distribution of particles may be advantageous. The most promising cluster source is the magnetron sputtering gas aggregation cluster source, which has the main advantage of being able to use all materials (metal, semiconductors and insulators). The main disadvantage is the production of excess material that deposits in the reactor chamber and which needs to be cleaned regularly. The magnetron sputter cluster source was developed by Haberland (Haberland H. et al., 1994) (**Fig. 12a**), and is now one of the few cluster sources which is commercially available ("Mantis", "Oxford Applied Research Inc."). Magnetron sputter cluster sources with multiple targets are currently also available which make it possible to produce complicated alloy or core shell nanoparticles.

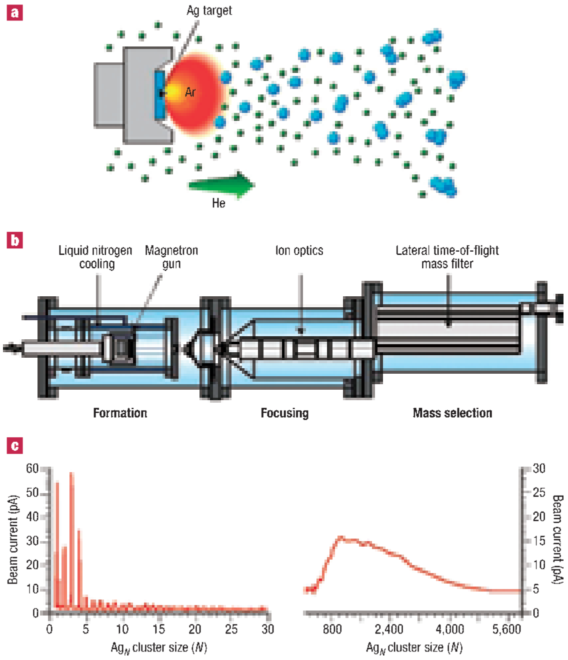

Fig. 12 Production of size-selected cluster beams. **(a)** Cluster formation by plasma sputtering and gas aggregation. **(b)** Overview of the complete cluster beam source. **(c)** Mass spectra of Ag clusters produced by the source. Reprinted with permission of Palmer R.E., et al. (2003).

The nanoparticle sizes from these cluster sources range from a few atoms to about 100 nm. The latter can usually be obtained using magnetron sputtering with a large aggregation distance. Considering, for example the Bohr radius of silicon and germanium, this allows the fabrication of quantum dots. With respect to plasmonic and Mie particles, this is clearly within range and compatible with thin-film solar cell dimensions. Complicated compositions such as perovskite particles are difficult to produce with gas aggregation cluster sources although multiple target magnetron sputtering is promising in this respect. A recent work by Palmer et al. demonstrates a high yield cluster source with the launch of a new type of cluster production: the "Matrix Assembly Cluster Source" (Palmer R.E. et al., 2016), in which large quantities of clusters are produced by use of an Ar matrix in which the cluster atoms aggregate and are subsequently sputtered out. Since the output has increased from nanoamps (in conventional cluster sources) to milliamps, this is indeed promising for industrial applications.

The mass selection of nanoparticles from a cluster source can be achieved by magnetic deflection (Gerlach W. and Stern, 1922), time of flight (de Heer W.A. and Milani, 1991; von Issendorff B. and Palmer, 1999), quadrupole mass filter (Paul W. and Steinwedel H., 2014), aerodynamic lenses (Piseri P. et al., 2004), the Wien filter (Wien W., 1902) and the magnetic sector. Although the disadvantage of all these systems is the loss of most of the particles produced by the cluster source and therefore a smaller amount will be deposited, the particle size can be easily tuned for optical purposes such as plasmonics or quantum dots. With some mass selectors, monolayers can be obtained in reasonable deposition times, such as the time of flight and quadrupole. This will often be good enough for light management structures. However, many cluster sources have a size distribution in the order of 10–20 % which is already sufficient for optical nanostructures. This does away with the necessity of a mass selector and increases the deposition time considerably. An example of a magnetron sputtering gas aggregation cluster source with time-of-flight mass selector is shown in **Fig. 12b**.

A laboratory gas aggregation cluster source can produce a monolayer of metal, insulator or semiconductor particles within about a minute. Up-scaling would increase this speed and enable the coverage of large areas. The produced nanoparticles are ultra clean and are therefore compatible with any solar cell fabrication stage. The easy and quick control over particle size, often by tuning parameters such as magnetron/laser power, gas flow and aggregation distance, provides versatility with respect to the desired configuration. The magnetron gas aggregation cluster source has the advantage of being able to produce metal, semiconductor and insulating particles by DC or RF sputtering. The nanoparticles from magnetron cluster sources are often highly crystalline, which is important for the plasmonic particles, Mie scatterers and quantum dots. Because the nanoparticle quantity required for solar cell applications ranges from sub-monolayers to about 50 monolayers, it is within the reach of most cluster sources. For example, silicon and germanium quantum dots have been very hard to fabricate with chemical methods, which provided limited research results. With gas aggregation cluster sources, it is possible to produce such quantum dots in optically thick layers. The formation of patterns made out of nanoparticles by using a hard mask may prove very useful to apply structures in the photovoltaic device (Wegner K. et al., 2006a). It is clear that this provides many research opportunities.

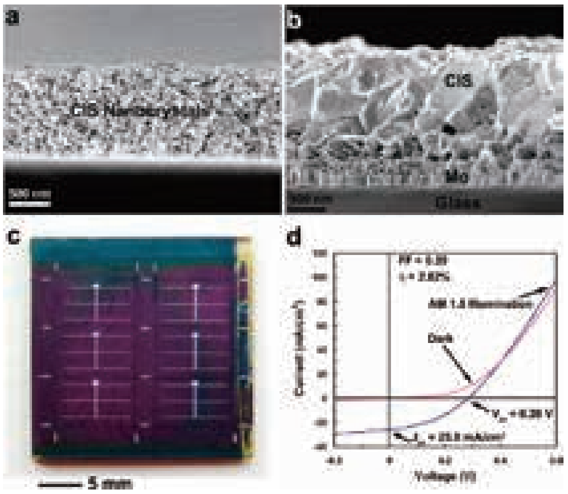

Fig. 13 CuInSe$_2$ solar cells fabricated from a nanocrystal ink. FESEM images of **(a)** CuInSe$_2$ nanocrystal thin film after casting and **(b)** after sintering in a Se/Ar atmosphere. **(c)** A photograph of the completed solar cells after chemical bath deposition of CdS, sputtering of i-ZnO and ITO, and evaporation of metal contacts. **(d)** The I–V characteristic of the finished device. Reprinted with permission of Guo Q. (2008).

4.2 Colloidal deposition

The colloidal deposition techniques are currently routinely used and could be easily up-scaled. The spin-coating of nanoparticles is probably the simplest method to deposit nanoparticles. For applying light management structures on solar cells, it has the disadvantage that the solution often interacts with the delicate solar cell surface, the solar cell needs to be exposed to the ambient and the size is limited due to the rotational motion. Spin-coating and layer-by-layer exchange lead to vast material waste: typically only 1–10 % of the consumed quantum dots are incorporated into the final film (Ning Z. et al., 2014). (Electro-) Spraying is a promising alternative which can cover very large scales reliably (Kramer I.J. et al., 2015; Salata O.V., 2005). The droplets containing particles are deposited on the desired substrate, after which the solvent evaporates. Although some molecules from the solution are also deposited, they may be able to evaporate or are considered to be harmless. A new development is the ink-jet deposition of colloidal quantum dots (Tekin E. et al., 2008), which even allows the creation of structures in the layers (Fischer A. et al., 2013; Kirmani A.R. et al., 2014). An example of a working solar cell produced by ink deposition is shown in **Fig. 13**.

A promising route by employing colloids is the aerosol deposition technique. The aerosol, in this case a liquid droplet containing the colloid particles, is sprayed on to the surface of interest, depositing metal, semiconductor and insulating nanoparticles (Gurav A. et al., 1993; Noor N. and Parkin, 2013; Palgrave R.G. and Parkin, 2006). Ultra-porous TiO$_2$ layers for perovskite solar cells are made by the flame pyrolysis of aerosols (Mayon Y.O., et al., 2016).

Colloidal particles have to be deposited from solutions, which makes it compatible with solar cell materials such as CIGS (Choi K.-H. et al., 2011), Perovskites or quantum dot solar cells. Both CIGS and CZTS solar cells can be fabricated by colloidal deposition (Akhavan V.A. et al., 2012). However, the solvents are often toxic and may not be compatible with vacuum techniques and reduce the possibility to hybridise the fabrication.

5. The future for nanoparticles and photovoltaics

Different scientific disciplines are often well separated and it is therefore important to create bridges between them, of which this review paper is an attempt. The photovoltaic community, including the novel concept work, is in general not familiar with nanoparticle research and vice versa. As described above, there are many aspects of novel concept solar cell development in which nanoparticles can play an important role. This is particularly interesting with respect to industrial feasibility, in contrast to lithographic techniques, which currently are limited to the proof of concept designs.

Two main nanoparticle and solar cell fabrication techniques can be distinguished: 1) the physical fabrication/deposition which often makes use of vacuum techniques, and 2) the chemical fabrication/deposition which involves the presence of liquids and is not necessarily compatible with physical fabrication/deposition. In contrast to conventional wafer-based solar cells, these fabrication processes can be performed at room temperature, which reduces the fabrication cost considerably.

The integration of cluster sources with research fields such as solar cells is currently not far beyond its conception. The maturation of using cluster sources for photovoltaics lies in the near future, which is stimulated by the commercial availability of gas aggregation cluster sources.

It is likely that nanoparticles will find their way into photovoltaics by different techniques and approaches. Light management remains interesting to increase the efficiency of thin-film solar cells for many years to come. The different compositions of thin-film solar cells, including the promising perovskites, will provide decades of research possibilities for nanoparticle implementation. From an industrial point of view, nanoparticles are cheap to produce and easy to combine with existing fabrication methods in PV technology. Not only do the separate scientific communities of PV and nanoparticles have to cross-fertilize, their industrial counterparts may significantly benefit from such an approach.

6. Conclusions

Using nanoparticles for photovoltaics is a promising bottom-up approach for various aspects of the thin-film solar cell. The nanoparticles can be used as a constituent such as CIGS or perovskite or as a quantum dot. Particularly the “traditional” materials such as silicon and GaAs are waiting for new fabrication techniques to be employed as quantum dots in solar cells. The nanoparticles can also be used as a light management structure in or on thin-film solar cells. Plasmonic particles can scatter light or the local field enhancement can increase absorption. Dielectric Mie scatterers can also scatter light or can function as light antennas to subsequently couple light into the active solar cell layer. Photon up- and down-conversion materials can also be fabricated as nanoparticles. Although wet chemical techniques can produce nanoparticles in large quantities, the disadvantage is the presence of unwanted chemicals from the fabrication procedure and a lack of crystallinity. Moreover, some compositions such as silicon and germanium turn out to be very difficult to fabricate chemically in the form of nanoparticles. The gas aggregation cluster source is proposed here as new fabrication technique for nanoparticles covering the compositional and light management parts in thin-film solar cells. Because thin-film solar cells require only one or several monolayers of particles, this is feasible. By merging two historically independent research fields, a bright future for nanoparticles and solar cells is on the horizon.

Acknowledgements

Discussions with Prof. Dr. Ruud E.I. Schropp are very much appreciated.

Nomenclature

CdTe	Cadmium telluride
CIGS	Copper indium gallium (di)selenide
CZTS	Copper zinc tin sulfide
FESEM	Field Emission Scanning Electron Microscopy
LAS	Laser ablation source
PACIS	Pulsed-arc cluster ion sources
PE-CVD	Plasma-enhanced chemical vapour deposition
PMCS	Pulsed microplasma cluster source
PV	Photovoltaics
QD	Quantum dot
SGAS	Sputter gas aggregation source
SQ	Shockley-Queisser
SSNS	Supersonic nozzle source
TEM	Transmission electron microscopy
TGAS	Thermal gas aggregation source

References

Akhavan V.A., Goodfellow B.W., Panthani M.G., Steinhagen C., Harvey T.B., Stolle C.J., Korgel B.A., Colloidal CIGS and CZTS nanocrystals: A precursor route to printed photovoltaics, Solution Processing Technology for Inorganic Films, Nanostructures and Functional Materials, Symposium JJ, 6th International Conference on Materials for Advanced Technologies, 26 June to 1 July 2011, Singapore, 189 (2012) 2–12. DOI: 10.1016/j.jssc.2011.11.002

Akimov Y.A., Koh W.S., Ostrikov K., Enhancement of optical absorption in thin-film solar cells through the excitation of higher-order nanoparticle plasmon modes, Optics Express, 17 (2009) 10195–10205. DOI: 10.1364/OE.17.010195

Alivisatos A.P., Perspectives on the physical chemistry of semiconductor nanocrystals, The Journal of Physical Chemistry, 100 (1996) 13226–13239. DOI: 10.1021/jp9535506

Anderson I.E., Breeze A.J., Olson J.D., Yang L., Sahoo Y., Carter S.A., All-inorganic spin-cast nanoparticle solar cells with nonselective electrodes, Applied Physics Letters, 94 (2009) 063101. DOI: 10.1063/1.3074368

Anger P., Bharadwaj P., Novotny L., Enhancement and quenching of single-molecule fluorescence, Physical Review Letters, 96 (2006) 113002. DOI: 10.1103/PhysRevLett.96.113002

Araújo A., Pimentel A., Oliveira M.J., Mendes M.J., Franco R., Fortunato E., Hugo Á., Martins R., Direct growth of plasmonic nanorod forests on paper substrates for low-cost flexible 3D SERS platforms, Flexible and Printed Electronics, 2 (2017) 014001.

Atwater H.A., Polman A., Plasmonics for improved photovoltaic devices, Nature Materials, 9 (2010) 205–213. DOI: 10.1038/nmat2629

Barborini E., Kholmanov I.N., Conti A.M., Piseri P., Vinati S., Milani P., Ducati C., Supersonic cluster beam deposition of nanostructured titania, The European Physical Journal D—Atomic, Molecular, Optical and Plasma Physics, 24 (2003) 277–282. DOI: 10.1140/epjd/e2003-00189-2

Barnard E.S., Pala R.A., Brongersma M.L., Photocurrent mapping of near-field optical antenna resonances, Nature Nanotechnology, 6 (2011) 588–593. DOI: 10.1038/nnano.2011.131

Bloembergen N., Solid state infrared quantum counters, Physical Review Letters, 2 (1959) 84–85. DOI: 10.1103/PhysRevLett.2.84

Bohren C.F., Huffman D.R., Eds., Absorption and Scattering of Light by Small Particles, Wiley-VCH, Weinheim, 2004, ISBN: 9780471293408.

Brongersma M.L., Cui Y., Fan S., Light management for photovoltaics using high-index nanostructures, Nature Materials, 13 (2014) 451–460. DOI:10.1038/nmat3921

Cao L., Park J.-S., Fan P., Clemens B., Brongersma M.L., Resonant Germanium Nanoantenna Photodetectors, Nano Letters, 10 (2010) 1229–1233. DOI: 10.1021/nl9037278

Carey G.H., Abdelhady A.L., Ning Z., Thon S.M., Bakr O.M., Sargent E.H., Colloidal quantum dot solar cells, Chemical Reviews, 115 (2015) 12732–12763. DOI: 10.1021/acs.chemrev.5b00063

Chattopadhyay S., Huang Y.F., Jen Y.J., Ganguly A., Chen K.H., Chen L.C., Anti-reflecting and photonic nanostructures, Materials Science and Engineering: R: Reports, 69 (2010) 1–35. DOI: https://doi.org/10.1016/j.mser.2010.04.001

Cheng Y.Y., Fuckel B., MacQueen R.W., Khoury T., Clady R.G.C.R., Schulze T.F., Ekins-Daukes N.J., Crossley M.J., Stannowski B., Lips K., Schmidt T.W., Improving the light-harvesting of amorphous silicon solar cells with photochemical upconversion, Energy & Environmental Science, 5 (2012) 6953–6959. DOI: 10.1039/C2EE21136J

Choi K.-H., Muhammad N.M., Dang H.-W., Lee A., Hwang J.-S., Nam J.W., Ryu B.-H., Electrospray deposition of thin copper-indium-diselenide films, International Journal of Materials Research, 102 (2011) 1252–1260. DOI: 10.3139/146.110581

Clapp A.R., Medintz I.L., Mattoussi H., Förster Resonance Energy Transfer Investigations Using Quantum-Dot Fluorophores, ChemPhysChem, 7 (2006) 47–57. DOI: 10.1002/cphc.200500217

Conibeer G., Third-generation photovoltaics, Materials Today, 10 (2007) 42–50. DOI: 10.1016/S1369-7021(07)70278-X

Conibeer G., Green M., Corkish R., Cho Y., Cho E.-C., Jiang C.-W., Fangsuwannarak T., Pink E., Huang Y., Puzzer T., Trupke T., Richards B., Shalav A., Lin K.-l., Silicon nanostructures for third generation photovoltaic solar cells, EMSR 2005—Proceedings of Symposium F on Thin Film and Nanostructured Materials for Photovoltaics, 511 (2006) 654–662. DOI: 10.1016/j.tsf.2005.12.119

Cullis A.G., Canham L.T., Visible light emission due to quantum size effects in highly porous crystalline silicon, Nature, 353 (1991) 335–338. DOI: 10.1038/353335a0

Dai X., Deng Y., Peng X., Jin Y., Quantum-Dot Light-Emitting Diodes for Large-Area Displays: Towards the Dawn of Commercialization, Advanced Materials, 29 (2017) 1607022-n/a. DOI: 10.1002/adma.201607022

De Boer W.D.A.M., Timmerman D., Dohnalová K., Yassievich I.N., Zhang H., Buma W.J., Gregorkiewicz T., Red spectral shift and enhanced quantum efficiency in phonon-free photoluminescence from silicon nanocrystals, Nature Nanotechnology, 5 (2010) 878–884. DOI: 10.1038/nnano.2010.236

De Heer W.A., The physics of simple metal clusters: experimental aspects and simple models, Reviews of Modern Physics, 65 (1993) 611–676. DOI: 10.1103/RevModPhys.65.611

De Heer W.A., Milani P., Large ion volume time-of-flight mass spectrometer with position- and velocity-sensitive detection capabilities for cluster beams, Review of Scientific Instruments, 62 (1991) 670–677. DOI: 10.1063/1.1142066

De Wild J., Duindam T.F., Rath J.K., Meijerink A., Van Sark W.G.J.H.M., Schropp R.E.I., Increased upconversion response in a-Si:H solar cells with broad band light, IEEE Journal of Photovoltaics, 3 (2013) DOI: 10.1109/JPHOTOV.2012.2213799

De Wild J., Meijerink A., Rath J.K., van Sark W.G.J.H.M., Schropp R.E.I., Upconverter solar cells: materials and applications, Energy & Environmental Science, 4 (2001) DOI: 10.1039/c1ee01659h

Delerue C., Allan G., Lannoo M., Optical band gap of Si nanoclusters, Journal of Luminescence, 80 (1998) 65–73. DOI: 10.1016/S0022-2313(98)00071-4

Ekinci Y., Solak H.H., Löffler J.F., Plasmon resonances of aluminum nanoparticles and nanorods, Journal of Applied Physics, 104 (2008) 083107. DOI: 10.1063/1.2999370

Faraone G., Modi R., Marom S., Podestà A., Di Vece M., Increasing the optical absorption in a-Si thin films by embedding gold nanoparticles, Optical Materials, 75 (2018) 204–210. DOI: 10.1016/j.optmat.2017.10.025

Ferry V.E., Munday J.N., Atwater H.A., Design Considerations for Plasmonic Photovoltaics, Advanced Materials, 22 (2010) 4794–4808. DOI: 10.1002/adma.201000488

Ferry V.E., Verschuuren M.A., Lare M.C.V., Schropp R.E.I., Atwater H.A., Polman A., Optimized spatial correlations for broadband light trapping nanopatterns in high efficiency ultrathin film a-Si:H solar cells, Nano Letters, 11 (2011) 4239–4245. DOI: 10.1021/nl202226r

Ferry V.E., Verschuuren M.A., Li H.B.T., Verhagen E., Walters R.J., Schropp R.E.I., Atwater H.A., Polman A., Light trapping in ultrathin plasmonic solar cells, Optics Express, 18 (2010) A237–A245. DOI: 10.1364/OE.18.00A237

Fischer A., Rollny L., Pan J., Carey G.H., Thon S.M., Hoogland S., Voznyy O., Zhitomirsky D., Kim J.Y., Bakr O.M., Sargent E.H., Directly deposited quantum dot solids using a colloidally stable nanoparticle ink, advanced materials, 25 (2013) 5742–5749. DOI: 10.1002/adma.201302147

Fix T., Ferblantier G., Rinnert H., Slaoui A., Evaluation of the effective quantum efficiency of photon conversion layers placed on solar cells, Solar Energy Materials and Solar

Cells, 132 (2015) 191–195. DOI: 10.1016/j.solmat.2014.09.009

Gerlach W., Stern O., Der experimentelle Nachweis der Richtungsquantelung im Magnetfeld, Zeitschrift für Physik, 9 (1922) 349–352. DOI: 10.1007/BF01326983

Giannakoudakis G., Di Vece M., Improving optical absorption in a-Si thin films with TiO_2 Mie scatterers, The European Physical Journal D, 71 (2017) 101. DOI: 10.1140/epjd/e2017-70570-7

Govorov A.O., Zhang W., Skeini T., Richardson H., Lee J., Kotov N.A., Gold nanoparticle ensembles as heaters and actuators: melting and collective plasmon resonances, Nanoscale Research Letters, 1 (2006) 84–90. DOI: 10.1007/s11671-006-9015-7

Gratzel M., Photoelectrochemical cells, Nature, 414 (2001) 338–344. DOI: 10.1038/35104607

Green M.A., Third Generation Photovoltaics: Advanced Solar Energy Conversion, Springer, Berlin, 2003, ISBN 978-3-540-26563-4.

Green M.A., Ho-Baillie A., Snaith H.J., The emergence of perovskite solar cells, Nature Photonics, 8 (2014) 506–514. DOI:10.1038/nphoton.2014.134

Guo Q., Kim S.J., Kar M., Shafarman W.N., Birkmire R.W., Stach E.A., Agrawal R., Hillhouse H.W., Development of $CuInSe_2$ nanocrystal and nanoring inks for low-cost solar cells, Nano Letters, 8 (2008) 2982–2987. DOI: 10.1021/nl802042g

Gurav A., Kodas T., Pluym T., Xiong Y., Aerosol processing of materials, Aerosol Science and Technology, 19 (1993) 411–452. DOI: 10.1080/02786829308959650

Haase M., Schafer H., Upconverting nanoparticles, Angewandte Chemie International Edition, 50 (2011) 5808–5829. DOI: 10.1002/anie.201005159

Haberland H., Mall M., Moseler M., Qiang Y., Reiners T., Thurner Y., Filling of micron-sized contact holes with copper by energetic cluster impact, Journal of Vacuum Science & Technology A: Vacuum, Surfaces, and Films, 12 (1994) 2925–2930. DOI: 10.1116/1.578967

Haes A.J., Zou S., Schatz G.C., Van Duyne R.P., A nanoscale optical biosensor: The long range distance dependence of the localized surface plasmon resonance of noble metal nanoparticles, The Journal of Physical Chemistry B, 108 (2004) 109–116. DOI: 10.1021/jp0361327

Hägglund C., Zäch M., Kasemo B., Enhanced charge carrier generation in dye sensitized solar cells by nanoparticle plasmons, Applied Physics Letters, 92 (2008) 013113. DOI: 10.1063/1.2830817

Hovel H.J., Hodgson R.T., Woodall J.M., The effect of fluorescent wavelength shifting on solar cell spectral response, Solar Energy Materials, 2 (1979) 19–29. DOI: 10.1016/0165-1633(79)90027-3

Huang X., Han S., Huang W., Liu X., Enhancing solar cell efficiency: the search for luminescent materials as spectral converters, Chemical Society Reviews, 42 (2013) 173–201. DOI: 10.1039/C2CS35288E

Jabbour G.E., Doderer D., Quantum dot solar cells: The best of both worlds, Nature Photonics, 4 (2010) 604–605. DOI: 10.1038/nphoton.2010.209

Kang S.H., Kim J.-Y., Kim H.S., Koh H.-D., Lee J.-S., Sung Y.-E., Influence of light scattering particles in the TiO_2 photoelectrode for solid-state dye-sensitized solar cell, Journal of Photochemistry and Photobiology A: Chemistry, 200 (2008) 294–300. DOI: 10.1016/j.jphotochem.2008.08.010

Kapur V.K., Bansal A., Le P., Asensio O.I., Non-vacuum processing of $CuIn_{1-x}Ga_xSe_2$ solar cells on rigid and flexible substrates using nanoparticle precursor inks, Proceedings of Symposium B, Thin Film Chalcogenide Photovoltaic Materials, E-MRS Spring Meeting, 431 (2003) 53–57. DOI: 10.1016/S0040-6090(03)00253-0

Karg M., König T.A.F., Retsch M., Stelling C., Reichstein P.M., Honold T., Thelakkat M., Fery A., Colloidal self-assembly concepts for light management in photovoltaics, Materials Today, 18 (2015) 185–205. DOI: 10.1016/j.mattod.2014.10.036

Kim S.J., Thomann I., Park J., Kang J.-H., Vasudev A.P., Brongersma M.L., Light trapping for solar fuel generation with Mie resonances, Nano Letters, 14 (2014) 1446–1452. DOI: 10.1021/nl404575e

Kirmani A.R., Carey G.H., Abdelsamie M., Yan B., Cha D., Rollny L.R., Cui X., Sargent E.H., Amassian A., Effect of solvent environment on colloidal-quantum-dot solar-cell manufacturability and performance, Advanced Materials, 26 (2014) 4717–4723. DOI: 10.1002/adma.201400577

Knight M.W., Liu L., Wang Y., Brown L., Mukherjee S., King N.S., Everitt H.O., Nordlander P., Halas N.J., Aluminum plasmonic nanoantennas, Nano Letters, 12 (2012) 6000–6004. DOI: 10.1021/nl303517v

Kooy N., Mohamed K., Pin L.T., Guan O.S., A review of roll-to-roll nanoimprint lithography, Nanoscale Research Letters, 9 (2014) 320. DOI: 10.1186/1556-276X-9-320

Kramer I.J., Minor J.C., Moreno-Bautista G., Rollny L., Kanjanaboos P., Kopilovic D., Thon S.M., Carey G.H., Chou K.W., Zhitomirsky D., Amassian A., Sargent E.H., Efficient spray-coated colloidal quantum dot solar cells, Advanced Materials, 27 (2015) 116–121. DOI: 10.1002/adma.201403281

Kuznetsov A.I., Miroshnichenko A.E., Brongersma M.L., Kivshar Y.S., Luk'yanchuk B., Optically resonant dielectric nanostructures, Science, 354 (2016) DOI: 10.1126/science.aag2472

Lan X., Masala S., Sargent E.H., Charge-extraction strategies for colloidal quantum dot photovoltaics, Nature Materials, 13 (2014) 233–240.

Langhammer C., Schwind M., Kasemo B., Zorić I., Localized surface plasmon resonances in Aluminum nanodisks, Nano Letters, 8 (2008) 1461–1471. DOI: 10.1021/nl080453i

Law D.C., King R.R., Yoon H., Archer M.J., Boca A., Fetzer C.M., Mesropian S., Isshiki T., Haddad M., Edmondson K.M., Bhusari D., Yen J., Sherif R.A., Atwater H.A., Karam N.H., Future technology pathways of terrestrial III–V multijunction solar cells for concentrator photovoltaic systems, Solar Energy Materials and Solar Cells, 94 (2010) DOI: 10.1016/j.solmat.2008.07.014

Ledoux G., Guillois O., Porterat D., Reynaud C., Huisken F., Kohn B., Paillard V., Photoluminescence properties of silicon nanocrystals as a function of their size, Physical Review B, 62 (2000) 15942–15951. DOI: 10.1103/PhysRevB.62.15942

Lee J., Jadhav P., Reusswig P.D., Yost S.R., Thompson N.J., Congreve D.N., Hontz E., Van Voorhis T., Baldo M.A., Singlet exciton fission photovoltaics, Accounts of Chemical Research, 46 (2013) 1300–1311. DOI: 10.1021/ar300288e

Lee T.D., Ebong A.U., A review of thin film solar cell technologies and challenges, Renewable and Sustainable Energy Reviews, 70 (2017) 1286–1297. DOI: 10.1016/j.rser.2016.12.028

Lokhande A.C., Gurav K.V., Jo E., Lokhande C.D., Kim J.H., Chemical synthesis of Cu_2SnS_3 (CTS) nanoparticles: A status review, Journal of Alloys and Compounds, 656 (2016) 295–310. DOI: 10.1016/j.jallcom.2015.09.232

Maier S.A., Plasmonics Fundamentals and Applications, Springer, 2007, ISBN 978-0-387-37825-1.

Maier S.A., Brongersma M.L., Kik P.G., Meltzer S., Requicha A.A.G., Atwater H.A., Plasmonics—A route to nanoscale optical devices, Advanced Materials, 13 (2001) 1501–1505. DOI: 10.1002/1521-4095(200110)13:19<1501::AID-ADMA1501>3.0.CO;2-Z

Mantis (Mantis Deposition Ltd.), Retrieved from http://www.mantisdeposition.com

Mayon Y.O., Duong T., Nasiri N., White T.P., Tricoli A., Catchpole K.R., Flame-made ultra-porous TiO_2 layers for perovskite solar cells. Nanotechnology, 27 (2016) 505403.

Michalet X., Pinaud F.F., Bentolila L.A., Tsay J.M., Doose S., Li J.J., Sundaresan G., Wu A.M., Gambhir S.S., Weiss S., Quantum dots for live cells, in vivo imaging, and diagnostics, Science, 307 (2005) 538–544. DOI: 10.1126/science.1104274

Miles R.W., Zoppi G., Forbes I., Inorganic photovoltaic cells, Materials Today, 10 (2007) 20–27. DOI: 10.1016/S1369-7021(07)70275-4

Mints P., The commercialization of thin film technologies: Past, present and future, Photovoltaic Specialists Conference (PVSC), 2010 35th IEEE, (2010) 002400–002404. DOI: 10.1109/PVSC.2010.5614355

Mohan A., Kaiser M., Verheijen M.A., Schropp R.E.I., Rath J.K., Microscopic studies of polycrystalline nanoparticle growth in free space, Journal of Crystal Growth, 467 (2017) 137–144. DOI: 10.1016/j.jcrysgro.2017.03.044

Murray C.B., Kagan C.R., Bawendi M.G., Synthesis and characterization of monodisperse nanocrystals and close-packed nanocrystal assemblies, Annual Review of Materials Science, 30 (2000) 545–610. DOI: 10.1146/annurev.matsci.30.1.545

Nakayama K., Tanabe K., Atwater H.A., Plasmonic nanoparticle enhanced light absorption in GaAs solar cells, Applied Physics Letters, 93 (2008) 121904. DOI: 10.1063/1.2988288

Nebel C.E., Christiansen S., Strunk H.P., Dahlheimer B., Karrer U., Stutzmann M., Laser-Interference crystallization of amorphous silicon: Applications and properties, physica status solidi (a), 166 (1998) 667–674. DOI: 10.1002/(SICI)1521-396X(199804)166:2<667::AID-PSSA667>3.0.CO;2-Y

Noor N., Parkin I.P., Enhanced transparent-conducting fluorine-doped tin oxide films formed by Aerosol-Assisted Chemical Vapour Deposition, Journal of Materials Chemistry C, 1 (2013) 984–996. DOI: 10.1039/C2TC00400C

Novotny L., Hecht B., Principles of Nano-Optics, Cambridge University Press, 2006, ISBN: 9780511166525

Nozik A.J., Quantum dot solar cells, Physica E: Low-dimensional Systems and Nanostructures, 14 (2002) 115–120. DOI: 10.1016/S1386-9477(02)00374-0

Nunomura S., Minowa A., Sai H., Kondo M., Mie scattering enhanced near-infrared light response of thin-film silicon solar cells, Applied Physics Letters, 97 (2010) 063507. DOI: 10.1063/1.3478465

Olson J., Manjavacas A., Liu L., Chang W.-S., Foerster B., King N.S., Knight M.W., Nordlander P., Halas N.J., Link S., Vivid, full-color aluminum plasmonic pixels, Proceedings of the National Academy of Sciences, 111 (2014) 14348–14353. DOI: 10.1073/pnas.1415970111

Oxford Applied Research Inc. Retrieved from http://www.oaresearch.co.uk

Ozbay E., Plasmonics: Merging Photonics and Electronics at Nanoscale Dimensions, Science, 311 (2006) 189–193. DOI: 10.1126/science.1114849

Pala R.A., White J., Barnard E., Liu J., Brongersma M.L., Design of plasmonic thin-film solar cells with broadband absorption enhancements, Advanced Materials, 21 (2009) 3504–3509. DOI: 10.1002/adma.200900331

Palgrave R.G., Parkin I.P., Aerosol assisted chemical vapor deposition using nanoparticle precursors: A route to nanocomposite thin films, Journal of the American Chemical Society, 128 (2006) 1587–1597. DOI: 10.1021/ja055563v

Palmer R.E., Cao L., Yin F., Note: Proof of principle of a new type of cluster beam source with potential for scale-up, Review of Scientific Instruments, 87 (2016) 046103. DOI: 10.1063/1.4947229

Palmer R.E., Pratontep S., Boyen H.G., Nanostructured surfaces from size-selected clusters, Nature Materials, 2 (2003) 443–448. DOI: 10.1038/nmat897

Paul W., Steinwedel H., Notizen: Ein neues Massenspektrometer ohne Magnetfeld, Zeitschrift für Naturforschung A, 8 (2014) 448. DOI: 10.1515/zna-1953-0710

Pillai S., Catchpole K.R., Trupke T., Green M.A., Surface plasmon enhanced silicon solar cells, Journal of Applied Physics, 101 (2007) 093105. DOI: 10.1063/1.2734885

Piseri P., Tafreshi H.V., Milani P., Manipulation of nanoparticles in supersonic beams for the production of nanostructured materials, Current Opinion in Solid State and Materials Science, 8 (2004) 195–202. DOI: 10.1016/j.cossms.2004.08.002

Polman A., Knight M., Garnett E.C., Ehrler B., Sinke W.C., Photovoltaic materials: Present efficiencies and future challenges, Science, 352 (2016) DOI: 10.1126/science.aad4424

Polonskyi O., Peter T., Mohammad Ahadi A., Hinz A., Strunskus T., Zaporojtchenko V., Biederman H., Faupel F., Huge increase in gas phase nanoparticle generation by pulsed direct current sputtering in a reactive gas admixture, Applied Physics Letters, 103 (2013) 033118. DOI: 10.1063/1.4816036

Popok V.N., Barke I., Campbell E.E.B., Meiwes-Broer K.-H., Cluster–surface interaction: From soft landing to implantation, Surface Science Reports, 66 (2011) 347–377. DOI: 10.1016/j.surfrep.2011.05.002

Prokofiev A.A., Moskalenko A.S., Yassievich I.N., de Boer W.D.A.M., Timmerman D., Zhang H., Buma W.J., Gregorkiewicz T., Direct bandgap optical transitions in Si nanocrystals, JETP Letters, 90 (2010) 758–762. DOI: 10.1134/S0021364009240059

Purcell E., Spontaneous emission probabilities at radio frequencies, in: Burstein E., Weisbuch C. (Eds) Confined Electrons and Photons, NATO ASI Series (Series B: Physics), vol 340. Springer, Boston, ISBN 978-1-4613-5807-7.

Raza S., Kadkhodazadeh S., Christensen T., Di Vece M., Wubs M., Mortensen N.A., Stenger N., Multipole plasmons and their disappearance in few-nanometre silver nanoparticles, Nature Communications, 6 (2015) 8788. DOI: 10.1038/ncomms9788

Richards B.S., Luminescent layers for enhanced silicon solar cell performance: Down-conversion, Solar Energy Materials and Solar Cells, 90 (2006) 1189–1207. DOI: 10.1016/j.solmat.2005.07.001

Saga T., Advances in crystalline silicon solar cell technology for industrial mass production, NPG Asia Materials, 2 (2010) 96–102. DOI: 10.1038/asiamat.2010.82

Salata O.V., Tools of Nanotechnology: Electrospray, Current Nanoscience, 1 (2005) 25–33. DOI: 10.2174/1573413052953192

Santbergen R., Liang R., Zeman M., A-Si:H solar cells with embedded silver nanoparticles, 35th IEEE Photovoltaic Specialists Conference, (2010) 000748–000753. DOI: 10.1109/PVSC.2010.5617095

Schropp R.E.I., Industrialization of hot wire chemical vapor deposition for thin film applications, 8th International conference on hot-wire CVD (Cat-CVD) processes (HWCVD 8), 595, Part B (2015) 272–283. DOI: 10.1016/j.tsf.2015.07.054

Schuller J.A., Zia R., Taubner T., Brongersma M.L., Dielectric metamaterials based on electric and magnetic resonances of silicon carbide particles, Physical Review Letters, 99 (2007) 107401. DOI: 10.1103/PhysRevLett.99.107401

Shimizu-Iwayama T., Kurumado N., Hole D.E., Townsend P.D., Optical properties of silicon nanoclusters fabricated by ion implantation, Journal of Applied Physics, 83 (1998) 6018–6022. DOI: 10.1063/1.367469

Shockley W., Queisser H.J., Detailed balance limit of efficiency of p-n junction solar cells, Journal of Applied Physics, 32 (1961) DOI: 10.1063/1.1736034

Son S., Hwang S.H., Kim C., Yun J.Y., Jang J., Designed synthesis of SiO_2/TiO_2 core/shell structure as light scattering material for highly efficient dye-sensitized solar cells, ACS Applied Materials & Interfaces, 5 (2013) 4815–4820. DOI: 10.1021/am400441v

Spinelli P., Polman A., Prospects of near-field plasmonic absorption enhancement in semiconductor materials using embedded Ag nanoparticles, Optics Express, 20 (2012) A641–A654. DOI: 10.1364/OE.20.00A641

Spinelli P., Polman A., Light trapping in thin crystalline Si solar cells using surface Mie scatterers, IEEE Journal of Photovoltaics, 4 (2014) 554–559. DOI: 10.1109/JPHOTOV.2013.2292744

Spinelli P., Verschuuren M.A., Polman A., Broadband omnidirectional antireflection coating based on subwavelength surface Mie resonators, Nature Communications, 3 (2012) 692. DOI: 10.1038/ncomms1691

Stenzel O., Stendal A., Voigtsberger K., von Borczyskowski C., Enhancement of the photovoltaic conversion efficiency of copper phthalocyanine thin film devices by incorporation of metal clusters, Solar Energy Materials and Solar Cells, 37 (1995) 337–348. DOI: 10.1016/0927-0248(95)00027-5

Stolle C.J., Harvey T.B., Korgel B.A., Nanocrystal photovoltaics: a review of recent progress, Nanotechnology/Separation engineering, 2 (2013) 160–167. DOI: 10.1016/j.coche.2013.03.001

Stuart H.R., Hall D.G., Absorption enhancement in silicon-on-insulator waveguides using metal island films, Applied Physics Letters, 69 (1996) 2327–2329. DOI: 10.1063/1.117513

Švrček V., Slaoui A., Muller J.C., Silicon nanocrystals as light converter for solar cells, Proceedings of Symposium D on Thin Film and Nano-Structured Materials for Photovoltaics, of the E-MRS 2003 Spring Conference, 451–452 (2004) 384–388. DOI: 10.1016/j.tsf.2003.10.133

Takeoka S., Fujii M., Hayashi S., Size-dependent photoluminescence from surface-oxidized Si nanocrystals in a weak confinement regime, Physical Review B, 62 (2000) 16820–16825. DOI: 10.1103/PhysRevB.62.16820

Tan H., Santbergen R., Smets A.H.M., Zeman M., Plasmonic Light trapping in thin-film silicon solar cells with improved self-assembled silver nanoparticles, Nano Letters, 12 (2012) 4070–4076. DOI: 10.1021/nl301521z

Tang W., Eilers J.J., van Huis M.A., Wang D., Schropp R.E.I., Di Vece M., Formation and photoluminescence of “cauliflower” silicon nanoparticles, The Journal of Physical Chemistry C, 119 (2015) 11042–11047. DOI: 10.1021/jp511660h

Tassin P., Koschny T., Kafesaki M., Soukoulis C.M., A comparison of graphene, superconductors and metals as conductors for metamaterials and plasmonics, Nature Photonics, 6 (2012) 259–264. DOI: 10.1038/nphoton.2012.27

Tekin E., Smith P.J., Schubert U.S., Inkjet printing as a deposition and patterning tool for polymers and inorganic particles, Soft Matter, 4 (2008) 703–713. DOI: 10.1039/B711984D

Temple T.L., Bagnall D.M., Optical properties of gold and aluminium nanoparticles for silicon solar cell applications, Journal of Applied Physics, 109 (2011) 084343. DOI: 10.1063/1.3574657

Timmerman D, Valenta J, Dohnalova K, de Boer W.D.A.M., Gregorkiewicz T, Step-like enhancement of luminescence quantum yield of silicon nanocrystals, Nature Nanotechnology, 6 (2011) 710–713. DOI: 10.1038/nnano.2011.167

Trinh M.T., Limpens R., de Boer W.D.A.M., Schins J.M., Siebbeles L.D.A., Gregorkiewicz T., Direct generation of multiple excitons in adjacent silicon nanocrystals revealed by induced absorption, Nature Photonics, 6 (2012) 316–321. DOI: 10.1038/nphoton.2012.36

Trupke T., Green M.A., Würfel P., Improving solar cell efficiencies by down-conversion of high-energy photons, Journal of Applied Physics, 92 (2002) DOI: 10.1063/1.1492021

Van der Vliet T., Di Vece M., Shifting the aluminum nanoparticle plasmon resonance to the visible with SiN and a-Si thin films, Thin Solid Films, 603 (2016) 404–407. DOI: 10.1016/j.tsf.2016.02.061

Van Sark W.G.J.H.M., Meijerink A., Schropp R.E.I., van Roosmalen J.A.M., Lysen E.H., Modeling improvement of spectral response of solar cells by deployment of spectral converters containing semiconductor nanocrystals, Semiconductors, 38 (2004) 962–969. DOI: 10.1134/1.1787120

Von Issendorff B., Palmer R.E., A new high transmission infinite range mass selector for cluster and nanoparticle beams, Review of Scientific Instruments, 70 (1999) 4497–4501. DOI: 10.1063/1.1150102

Wang Z.Y., Zhang R.J., Wang S.Y., Lu M., Chen X., Zheng Y.X., Chen L.Y., Ye Z., Wang C.Z., Ho K.M., Broadband optical absorption by tunable Mie resonances in silicon nanocone arrays, Scientific Reports, 5 (2015) 7810. DOI:10.1038/srep07810

Watanabe K., Sawada K., Koshiba M., Fujii M., Hayashi S., Photoluminescence decay-dynamics of Si nanoparticles prepared by pulsed laser ablation, COLA'01 SI, 197–198 (2002) 635–638. DOI: 10.1016/S0169-4332(02)00431-2

Wegner K., Barborini E., Piseri P., Milani P., Gas-Phase Synthesis of nanostructured particulate films, KONA Powder and Particle Journal, 24 (2006a) 54–69. DOI: 10.14356/kona.2006009

Wegner K., Piseri P., Tafreshi H.V., Milani P., Cluster beam deposition: a tool for nanoscale science and technology, Journal of Physics D: Applied Physics, 39 (2006b) R439. https://doi.org/10.1088/0022-3727/39/22/R02

Westphalen M., Kreibig U., Rostalski J., Lüth H., Meissner D., Metal cluster enhanced organic solar cells, Solar Energy Materials and Solar Cells, 61 (2000) 97–105. DOI: 10.1016/S0927-0248(99)00100-2

Wien W., Untersuchungen über die elektrische Entladung in verdünnten Gasen, Annalen der Physik, 313 (1902) 244–266. DOI: 10.1002/andp.19023130603

Wilson W.L., Szajowski P.F., Brus L.E., Quantum confinement in size-selected, surface-oxidized silicon nanocrystals, Science, 262 (1993) 1242–1244. DOI: 10.1126/science.262.5137.1242

Yahuitl Osorio M., The D., Noushin N., Thomas P.W., Antonio T., Kylie R.C., Flame-made ultra-porous TiO_2 layers for perovskite solar cells, Nanotechnology, 27 (2016) 505403.

Yu E.T., van de Lagemaat J., Photon management for photovoltaics, MRS Bulletin, 36 (2011) 424–428. DOI: 10.1557/mrs.2011.109

Zywietz U., Evlyukhin A.B., Reinhardt C., Chichkov B.N., Laser printing of silicon nanoparticles with resonant optical electric and magnetic responses, Nature Communications, 5 (2014) 3402. DOI:10.1038/ncomms4402

Author's Short Biography

Marcel Di Vece

Marcel Di Vece is currently affiliated with CIMAINA and the Department of Physics at the University of Milan, Italy. He obtained his PhD at Utrecht University (Netherlands) in 2003 on the "Switchable mirror". Since 2003, he has been working on various topics related to nanoparticles fabricated with gas aggregation sources. Since 2010, he has combined nanoparticles from a magnetron sputter nanoparticle source with thin films to investigate their potential for solar cells.

KONA Powder and Particle Journal No. 36 (2019) 88–113/Doi:10.14356/kona.2019006 Review Paper

Fine Particle Filtration Technology Using Fiber as Dust Collection Medium [†]

Chikao Kanaoka

[1] *Kanazawa University, Japan*

Abstract

Researches relating dust collector using fiber as particle collection body i.e., air filter, cartridge filter and nonwoven bag filter, were reviewed. Their filtration process was classified into 3 stages, i.e., Stage 1.inner filtration I, Stage 2.inner filtration II and Stage 3.surface filtration. Collection mechanisms of fresh circular fiber have been well understood and so-called classic filtration theory is applicable except single nano-particle, where discussion about the possibility of thermal rebound is necessary. In Stage 1, effects of shape of both fiber and particle, and filter structure, non-uniformity are the important issues. In Stages 2 and 3, filtration process becomes very complicated because of many affecting parameters. Main target in Stage 2 is to develop effective scheme to describe the phenomena and to find filter structure having a large holding capacity. Most important issue in Stage 3 is to develop the effective cleaning technique to minimize the dust emission based on rational but not empirical scheme.

Keywords: dust collection by fiber, collection mechanism, thermal rebound, dust holding capacity, dust cleaning

1. Introduction

Air pollution by particulate matter, especially PM2.5 is still a big issue or it is getting even worse because of rapid industrialization of developing countries, especially Northeast Asia and generation of secondary particles in the atmosphere. Nano safety is also a big issue in the field of nano-particle production. Air quality of workplace environment is important from the point of view of workers' health control. All of these issues are closely related to the elimination of particulate matter from air. However, particle size and concentration ranges are too broad to handle by only one dust collector and thus various types of dust collectors have been used to solve these problems. Among them, "filters using fiber" such as air filter, bag filter and cartridge filters play very important role because of excellent collection performance and relatively low cost. They are common in using as a particle collection body, but are different at principal working principle, filter structure and the covering area and so on.

Particle collection by the use of filter is a kind of old technology and thus the number of studies has been done from various view points and subjects. Even so, they are still needed and area of demand is expanding. Hence it is inevitable to understand the filtration phenomena and their applications.

Hence in this paper, filtration phenomena and theoretical and experimental researches, and their practical applications will be reviewed.

2. Classification of filter and collection behaviour

Fig. 1 shows a rough sketch of covering area of those filters. As seen from the figure, the covering area of filters ranges broad in both particle size and concentration, i.e., particle size ranges from order of several ten micron meters to nano meters and particle concentration from more than several dozen g/m^3 to several particles/m^3 or less. In the figure, applicable area of each filter is shown by different colors and main usages or purposes of each filter are also written in individual area.

The area of air filters locates at lower concentration range. Covering particle size and concentration range of air filter depends on the filter performance, i.e., middle efficiency filter covers larger size and high particle concentration area, high efficiency filter locates at the middle, and high efficiency particulate air (HEPA) filter and Ultra low Penetration air (ULPA) filter, locate very fine size and low concentration area.

Most important feature of air filters is that they collect particles inside the medium. Once filter becomes dust

---

[†] Received 4 September 2017; Accepted 14 November 2017

[1] Kakuma-machi, Kanazawa, Ishikawa, 920-1192, Japan
E-mail : kanaoka-4215@mail.bbexcite.jp

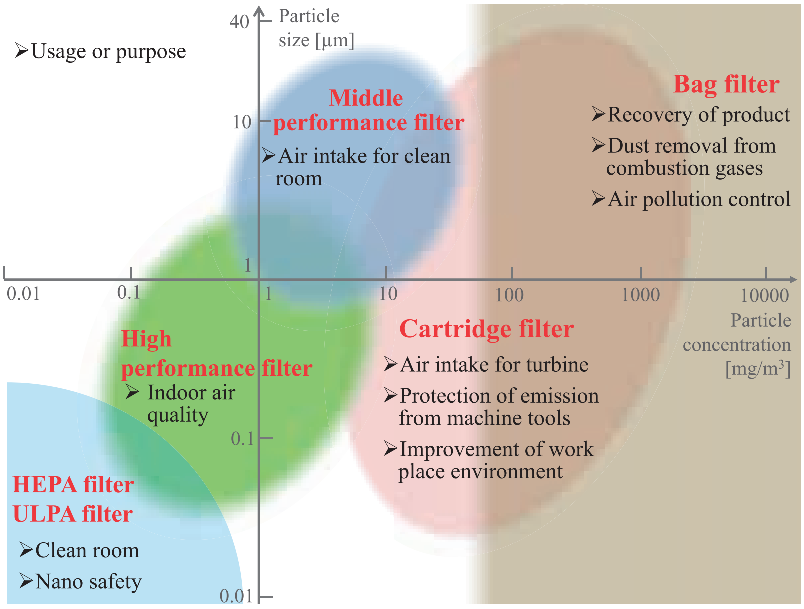

Fig. 1 Area map of filters against particle size and concentration.

loaded, especially for the case of solid particles, they stay and accumulate on the fiber. As a result, pressure drop across the filter rises with filtration time and particles accumulated inside the filter is too hard to remove them, i.e., regeneration of filter is extremely hard and thus air filter is usually discarded. Hence to increase the holding capacity of filter is an important issue. Collection of very fine particle like nano-size particle is another important issue for them.

Bag filter locates at the highest dust concentration range as high as ten g/m^3 or more, and cover whole particle size range. Cartridge filter is a kind of new type of filter and its coverage area overlaps almost but a little lower concentration compared with bag filter. Different from air filters, they are used at high particle concentration area, especially to recover powder products from industrial processes to suppress particulate emission of flue gas. Of course initial particle collection by a fresh filter takes place inside the filter, but it soon shifts to surface collection. Captured particles form a dust layer and it plays the actual collection medium, which collect particles almost perfectly regardless of particle size. Since dust layer becomes thicker with time and increases the flow resistance, it has to be removed occasionally to maintain continual operation. This also requires the filter medium to have sufficient mechanical strength against pressure drop.

Although two types of bag filter such as nonwoven and woven bag filters have been used for dust collection, nonwoven type bag filter is popularly used so that it increases practical importance now. Hence, discussion about woven type bag filter is eliminated in this article.

Table 1 compares the indices of 3 typical filters. They are different in many items like fiber size, thickness, packing density and etc. But they are still similar in using independent fibers to collect particles. Hence, they can be regarded as “air filters”.

If a fresh air filter is operated for a long time, its collection behavior changes to 3 stages with time as,

Stage 1: Particles are collected by any fibers in the filter (inner filtration I). Rigorously, this stage is the period until first particle is collected but in practice, it is regarded as the period when pressure drop and/or collection efficiency of the filter stay almost the same.

Stage 2: Particles are collected by both fresh and dust loaded fibers in the filter (inner filtration). In this stage, gas flow pattern near the dust loaded fiber changes due to the change of apparent fiber shape and thus filter collection efficiency and pressure drop increase rapidly.

This stage can be defined as the period between the starting time of pressure drop and filter efficiency increase, to the time before clogging of the filter.

Stage 3; Particles are collected on the filter surface and forms porous dust cake, pore size of which is about same size with incoming particles (surface filtration). In this stage, particles arrived to the filter are collected by the dust cake almost perfectly regardless of particle size and pressure drop increases linearly.

Air filters used at Stages 1 and 2 are middle and high performance filters, and HEPA and ULPA filters. Main purpose of the usage of air filter, especially HEPA and ULPA filter, is to make clean air into much cleaner air. To achieve this, it uses fine fibers to enhance fine particle collection. Although it can use for a long time because of low inlet particle concentration, it cannot use no longer than the holding capacity of the filter, which is unknown but does not exceed its void. Hence to increase the hold-

Table 1 Comparison of indices of filters.

Item	HEPA filter	Cartridge filter	Nonwoven bag filter
Fiber material	Glass, polymer	Polymer	Polymer
Fiber length	Short	Long (filament)	Short, long
Fiber size	Fine (< 2 µm)	Coarse (10~20 µm)	Coarse (10~20 µm)
Thickness	Thin (< 0.2 mm)	Middle (0.4~0.7 mm)	Thick (> 1 mm)
Packing density	Low (< 0.15)	High (> 0.25)	High (> 0.25)
Fiber mass per area	Low (< 100 g/m^2)	Middle (100~300 g/m^2)	High (300~900 g/m^2)
Process	Paper making	Thermal-compression	Needle punching
Shape	Sheet (pleated)	Sheet (pleated)	Cylinder, envelop
Principal mechanism of particle collection	Depth filtration	Surface filtration	Surface filtration
Re-generation	Non cleanable, discard	Cleanable, Re-use	Cleanable, Re-use

ing capacity is one of important subjects for air filter. Nano-size particle removal is another important issue for air filter, too.

Cartridge and bag filters are used at higher dust concentration. Important issue for them is how to reduce the amount of emission accompanying to cleaning process of dust cake from filter surface.

By the injection of cleaning air, most dust cake is removed to the dirty side of filter but small amount of dust is emitted from the clean side of the filter, by the back flow of cleaning air and dirty gas because almost no dust remains on and in the filter, i.e., emitted amount strongly depends on the collection performance of the filter itself. Furthermore some dust remains and forms firm deposit in the filter. Finally it effects on the life time of the filter.

2.1 Particle collection at Stage 1

This stage can be defined as the period when particle collection takes place on a clean fiber, i.e., no particle is collected on the fiber. Hence strictly speaking, this situation holds only at the point of the usage of the filter, but practically it is considered as the time duration no significant changes in filter efficiency and pressure drop are raised due to captured particles in the filter.

Capturing dynamics of particles is the basic of air filtration and thus it has been investigated from various view point. Hence many books and reviews have been published (Fuchs N.A., 1964; Davies C.N., 1966; Yeh H.-C. and Liu B.Y.H., 1974a, b; Kirsch A.A. and Stechkina I.B., 1978; Brown R.C., 1993; Friedlander S.K., 1977, 2000; Hinds W.C., 1999).

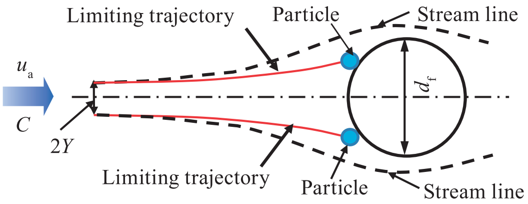

Fig. 2 Definition of single fiber collection efficiency.

2.1.1 Filter efficiency *E* and single fiber collection efficiency *η*

When a fresh air filter is composed of same size circular fibers and they are arranged perpendicular to the mean gas flow and are packed uniformly, filter efficiency is expressed by Eqn. (1) (Davies C.N., 1952)

$$E = 1 - \exp\left(-\frac{4}{\pi}\frac{\alpha}{1-\alpha}\frac{L}{d_\mathrm{f}}\eta\right) \tag{1}$$

In Eqn. (1), parameters other than η are related to filter itself. Hence, filter efficiency E can be estimated only by knowing the value of η for given filtration condition.

Single fiber collection efficiency η is defined as the mass ratio between particles captured on the fiber and total income particles in the projection area of the fiber in a unit time. Hence when the limiting particle trajectory is uniquely determined by solving the motion equation of particle such as collection by inertia, interception and gravity and so on, η is determined by Eqn. (2) by finding the inlet height of limiting trajectories, shown in **Fig. 2**.

$$\eta = (Cu_\mathrm{a} \cdot 2Y)/(Cu_\mathrm{a} d_\mathrm{f}) = Y/(d_\mathrm{f}/2) \tag{2}$$

u_a in Eqn. (2) is the approaching velocity of particle to the fiber and is $1/(1-\alpha)$ times of filtration velocity u.

For the case of diffusion, deposition rate is calculated by knowing the concentration profile of particle near the fiber surface by solving convective diffusion equation or Langevin equation.

From the previous studies, it is known that single fiber collection efficiency is a function of following dimensionless parameters.

$$\text{Reynolds number: } Re = \frac{\rho_g d_f u}{\mu} \tag{3}$$

$$\text{Stokes number: } Stk = \frac{C_C \rho_p d_p^2 u}{9 \mu d_f} \tag{4}$$

$$\text{Peclet number: } Pe = \frac{d_f u}{D_{BM}} \tag{5}$$

$$\text{Gravitational parameter: } G = \frac{\rho_p d_p^2 g}{18 \mu u} \tag{6}$$

$$\text{Interception parameter: } R = \frac{d_p}{d_f} \tag{7}$$

$$\eta = \eta(Re, Stk, Pe, G, R) \tag{8}$$

Eqns. (3) to (7) express the degree of influence of flow field near the fiber, particle inertia, diffusion, gravity and interception, respectively.

2.2 Single fiber collection efficiency by mechanical effect

2.2.1 Inertia and inertia-interception η_I, η_{IR}

Collection efficiency is calculated from limiting trajectory for a given set of *Stk*, *R* and *Re*. Early studies were performed for the impingement of mass particle to the fiber at potential and viscous flow fields (Landahl H.D. and Hermann R.G., 1949; Davies C.N. and Peetz C.V., 1956; Yoshioka, N. 1967a).

Davies C.N., (1952) also gave an approximate expression for $Re = 0.2$ as,

$$\eta_{IR} = 0.16\{R + (0.25 + 0.5R)Stk - 0.0263R \cdot Stk\} \tag{9}$$

However, flow field changes significantly by neighboring fibers, i.e., fiber packing density α (Kuwabara S., 1959; Happle, J., 1959). Fuchs N.A. and Stechikina I.B. (1963) first used Kuwabara flow model. Then flow calculation based on so-called “Kuwabara cell” became popular. Brown R.C. (1984, 1986) solved a flow through fibers in parallel by Fourie series analysis at low *Re*. Yoshioka N. (1969a), Emi H. et al. (1973, 1977) discussed the effect of α on η_{IR} in broad *Re* region.

Fig. 3 compares calculated inertia-interception efficiencies η_{IR} for $R = 0.1$ but different α such as 0 and 0.1. Clearly seen from the figure, difference of η_{IR} at small *Re* is large but decreases with *Re*.

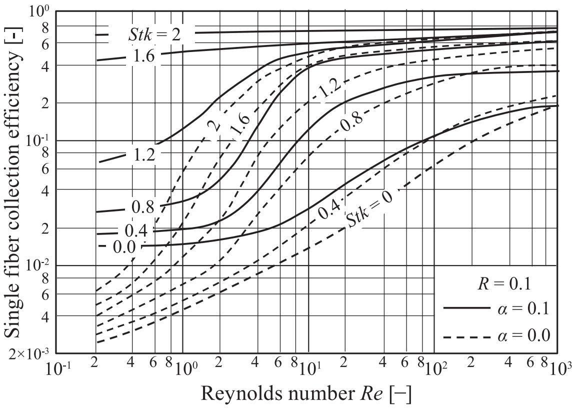

Fig. 3 Inertia-interception efficiency vs. *Re*. (Modified from Emi H. et al., 1977)

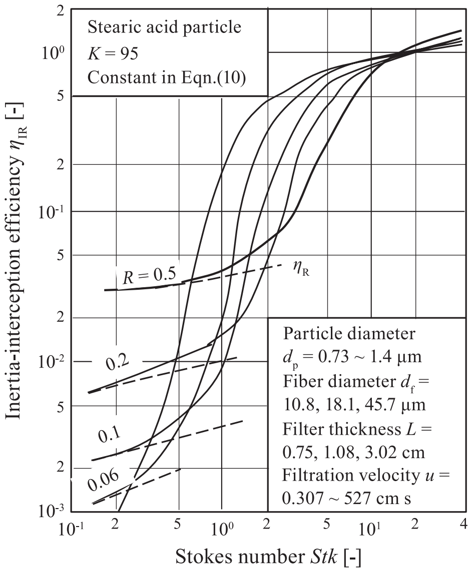

Fig. 4 Theoretical change of η_{IR} with *Stk*. (Modified from Yoshioka N. et al., 1969a).

Wong J.B. et al. (1956) measured collection efficiency of 0.4–1.3 µm sulfuric acid particle by a glass mat and compared with their theory. Friedlander S.K. (1957, 1958) correlated η with *Stk*, *R* and *Re*. Effect of fiber diameter, packing density and etc. on η_{IR} was discussed by Iinoya K. et al. (1965, 1970), Kimura N. and Iinoya K. (1965), Kimura N. (1969b), Makino K. and Iinoya K. (1969b), Lee K.W. and Liu B.Y.H. (1981). Yoshioka N. et al, (1967a, c, 1969a), Nguyen X. and Beeckmans J.M. (1975), Emi H. et al. (1973, 1977) calculated η_{IR} for various *Stk*, *R* and *Re*, and compared their experimental efficiency in **Fig. 4**.

Clearly seen form the figure, increasing trend of η_{IR} looks little unusual at small and large *Stk*, i.e., η_{IR} is large for large *R* but at intermediate *Stk*, η_{IR} for small *R* is larger than that for larger *Stk*. This unusual change is explained by considering that *Stk* is the product of *Re* and R^2 as shown in the following equation, i.e., changing *Stk* in the experiment also changes the flow, i.e., *Re* simultaneously. Significant contribution of each parameter appears at different and thus this is the reason of the inversion in η_{IR} in intermediate *Stk*.

$$Stk = \frac{C_{\mathrm{c}}}{9}\frac{\rho_{\mathrm{p}}}{\rho_{\mathrm{g}}}\frac{d_{\mathrm{f}}u\rho_{\mathrm{g}}}{\mu}\left(\frac{d_{\mathrm{p}}}{d_{\mathrm{g}}}\right)^2 = K\cdot Re\cdot R^2 \tag{10}$$

2.2.2 Interception η_{R} and gravity η_{GR}

When particles do not have inertia, they move along with gas stream and are collected on a fiber by interception. Collection efficiency in this situation was solved analytically by Langmuir I. (1942) for viscous flow (Lamb H., 1932) and potential flow, given by Eqns. (11) and (13), respectively.

Viscous flow $Re = 0$

$$\eta_{\mathrm{R}} = \frac{1}{2h}\left[2(1+R)\ln(1+R) + \frac{1}{1+R} - (1+R)\right] \tag{11}$$

Here, h is hydrodynamic factor for an isolated fiber and is expressive as,

$$h_{\mathrm{L}} = 2 - \ln Re \ \text{(Lamb's factor)} \tag{12}$$

Potential flow $Re = \infty$

$$\eta_{\mathrm{R}} = (1+R) - \frac{1}{1+R} \tag{13}$$

Stechkina I.B. and Fuchs N.A. (1966) obtained Eqn. (11) by using Kuwabara's hydrodynamic factor h_{K} in a group of parallel fibers (Kuwabara S., 1959).

$$h_{\mathrm{K}} = -\frac{1}{2}\ln\alpha + \alpha - \alpha^2/4 - 3/4 \tag{14}$$

Yoshioka N. and Emi, H. (1967b) also derived an approximate expression of Eqn. (11) as,

$$\eta_{\mathrm{R}} \cong \frac{1.25}{2h}R^{1.82} \tag{15}$$

Lee K.W. and Liu B.Y.H. (1981) also derived a similar expression as

$$\eta_{\mathrm{R}} = \frac{1}{2h}R^2 \tag{16}$$

Kimura and Iinoya (1965) obtained Eqn. (17) from velocity distribution in the boundary layer on a cylinder.

$$\eta_{\mathrm{R}} \cong \frac{1}{3}Re^{1/2}R^2 \tag{17}$$

Kirsh A.A. et al. (1975), Brown R.C. and Wake D. (1991) and Hubbard J.A. et al. (2012) studied interception efficiency at different conditions. For the case of interception-gravity, efficiency also depends on flow direction, Yoshioka et al. (1972) obtained analytical expressions by taking account of orientation of filter and flow as shown below,

Viscous flow $Re = 0$

Horizontal flow (filter is placed vertical)

$$\eta_{\mathrm{GR}} = \frac{1+R}{\sqrt{1+G^2\sqrt{1+\left(R^2/hG\right)^2}}} \times \left\{\frac{R^2\left[1/(1+R)^2 - 1 + \ln(1+R)^2\right]}{2h^2G}\right\} + G \tag{18}$$

Vertical down flow

$$\eta_{\mathrm{GR}} = \frac{1+R}{1+G}\left\{\frac{1}{2h}\left[\frac{1}{(1+R)^2} - 1 + \ln(1+R)^2\right] + G\right\} \tag{19}$$

Potential flow $Re = \infty$
Horizontal flow

$$\eta_{\mathrm{GR}} = \frac{\sqrt{(1+R)^4G^2 + \left[(1+R)^2 - 1\right]^2}}{(1+R)\sqrt{1+G^2}} \tag{20}$$

Vertical down flow

$$\eta_{\mathrm{GR}} = \frac{1}{1+G}\left[G(1+R) - \frac{1}{1+R} + (1+R)\right] \tag{21}$$

When $G = 0$, Eqns. (18) and (19) become Eqn. (11) and Eqns. (20) and (21) become Eqn. (13). Thomas J.W. et al. (1971) also discussed the effect of gravity.

2.2.3 Diffusion, diffusion-interception η_{D}, η_{DR}

Particle collection by diffusion and diffusion-interception effect is important for very fine particles, especially nanosize particles.

For mass point particles, most of analytical expressions obtained for viscous flow are proportion to $Pe^{-2/3}$ as (Langmuir I., 1942; Friedlander S.K., 1957; Natanson G.L., 1957b; Stechkina I.B. and Fuchs N.A., 1966; Kirsch A.A. and Fuchs N.A., 1968; Lee K.W. and Liu B.Y.H., 1981).

$$\eta_{\mathrm{D}} = Ah^{1/3}Pe^{-2/3} \tag{22}$$

(Langmuir, Friedlander, Natanson, Lee and Liu)

$$\eta_{\mathrm{D}} = 2.9{h_{\mathrm{K}}}^{1/3}Pe^{-2/3} + 0.62Pe^{-1} \tag{23}$$

(Stechkina and Fuchs)

Natanson derived the following expression for potential

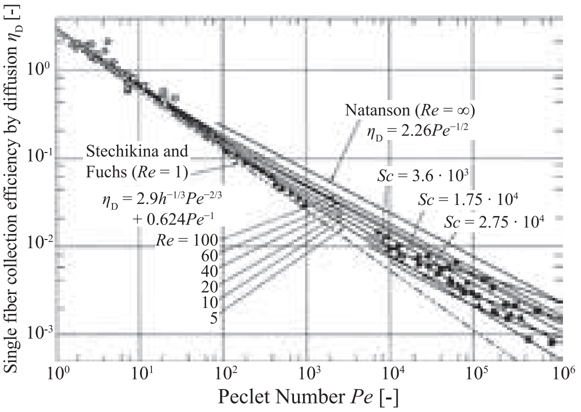

Fig. 5 Single fiber collection efficiency by diffusion. (Modified from Emi H. et al., 1982a)

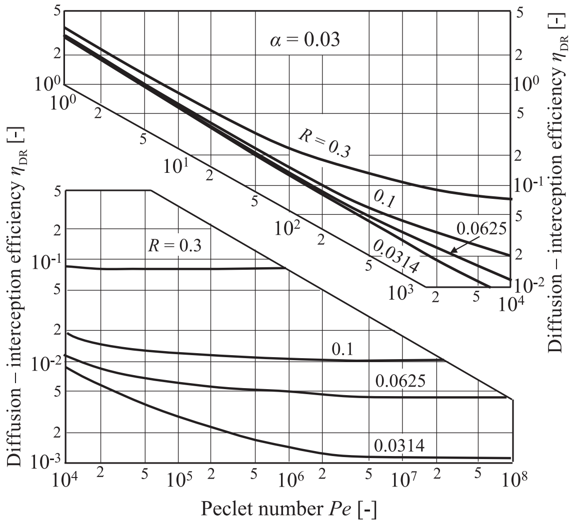

Fig. 6 Single fiber collection efficiency by diffusion-interception. (Modified from Kanaoka C., 1988)

flow (Natanson G. L., 1957b)

$$\eta_D = 2.26Pe^{-1/2} \tag{24}$$

Emi H. et al. (1982a) numerically calculated η_D at different Re and Sc shown in **Fig. 5**. It is remarkable that exponent of Pe changes from –2/3 to –1/2 as Re increases from 0 to infinity, which coincides with exponents in Eqns. (21) and (23). Ingham D.B., (1981) also obtained similar result.

Collection efficiency for $R \neq 0$, η_{DR} is very different from η_D (Lee K.W. and Liu B.Y.H., 1982; Kanaoka C., 1988). **Fig. 6** shows the calculated η_{DR} for various R (Kanaoka C., 1988). As seen from the figure, η_{DR} increases with decreasing Pe and becomes constant for each R at large Pe. Pich J. (1966), Smutek M. (1972), Kirsh A.A. et al. (1973), Van Osdell D. et al. (1990), Shapiro M. et al. (1991) discussed the effect of gas slip near a fiber.

Dahneke B. (1971) suggested the possibility of thermal rebound of nanoparticles. Wang H. and Kasper G. (1991) have developed a theory predicting a thermal rebound of particles smaller than 10 nm, it has been examined theoretically and experimentally.

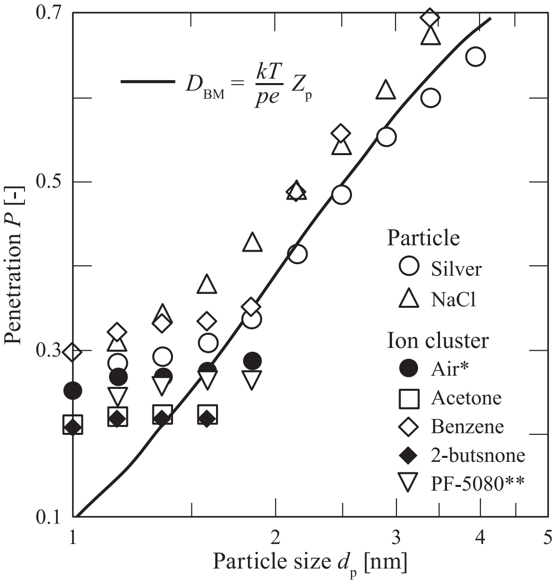

Fig. 7 Penetration of ultrafine particles and ion clusters through wire screens. (Modified from Ichitsubo H. et al., 1996)
* "air" refers the ions generated when no organic impurity was added to the air;
** PF-5800 is a mix of perfluoro compounds, comprising primarily compounds with 8 carbons, manufactured by 3M.

Theoretically, it has been discussed from coefficient of restitution and adhesion energy (Sato S. et al., 2007; Mouret G. et al., 2011) and Givehchi R. and Tan Z. (2014) discussed the effect of capillary force and existence of a thermal rebound but it has not been clearly demonstrated the existence of a thermal rebound.

Experimentally it has been examined by various combinations of particles (material and size), collection media (material, fiber diameter) and operation conditions many researchers such as Scheibel H.G. and Porstendörfer J. (1984), Van Osdell D.W. et al. (1990), Otani Y. et al. (1995), Skaptsov A.S. et al. (1996), Ichitsubo H. et al. (1996), Wang H.-C. (1996), Alonso et al. (1997), Kim C.S. et al. (2006), Kim S.C. et al. (2007), Japuntich D.A. et al. (2007), Steffens J. and Coury J.R. (2007a, b), Wang J. et al. (2007), Heim M. et al. (2005, 2010), Podgórski A. et al. (2006), Huang S. et al. (2007), Rengasamy S. et al. (2008), Shin W.G. et al. (2008), Golanski L. et al. (2009), Van Gulijk C. et al. (2009), Yamada S. et al. (2011). Reduction of efficiency was observed below 2 nm by only a few experiments. **Fig. 7** shows the experimental penetration by Ichitsubo et al. (1996). Givehchi R. and Tan Z. (2014, 2015) precisely reviewed the thermal rebound.

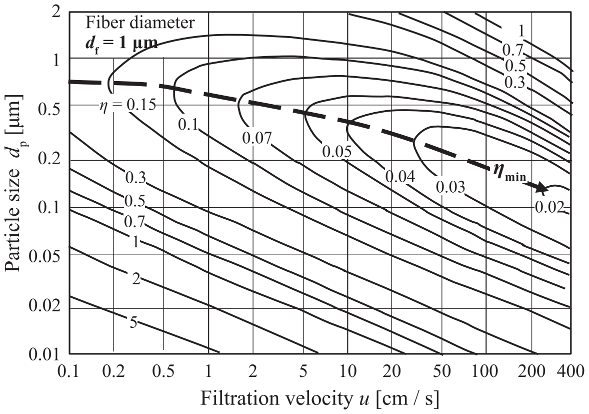

(a) η_{IDGR} for fiber diameter of 1 µm, α = 0

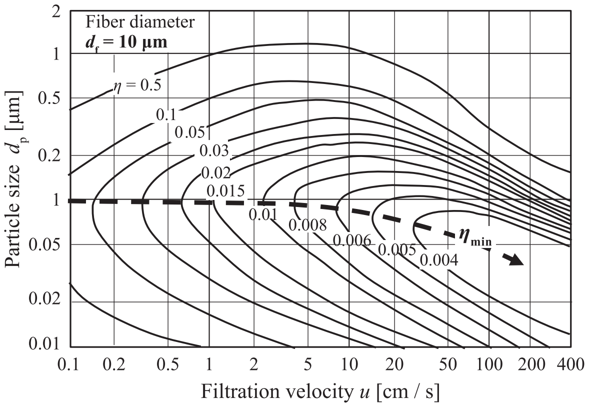

(b) η_{IDGR} for fiber diameter of 10 µm, α = 0

Fig. 8 Contour chart of total collection efficiency. (Modified from Emi H. et al., 1973)

2.2.4 Total collection efficiency by mechanical effects η_{IDGR}

In the actual filtration, every mechanism contributes to the capture of particle simultaneously. Hence collection efficiency taken account of all mechanisms has to be used for the estimation of actual filtration. Emi et al. estimated η_{IDGR} for an isolated fiber by taking account of the contribution of individual efficiency at given filtration condition.

Fig. 8(a) and **(b)** shows the predicted contour charts for fiber diameter of 1 and 10 µm (Emi H. et al., 1973). In the figure, each line is the line of equal collection efficiency and efficiency of contour line gets small from outside to inside. Furthermore, η_{IDGR} has a minimum efficiency η_{min} against filtration velocity u and particle size, d_p by keeping d_p and u constant, respectively. η_{min} appears at the transition region of two collection mechanisms and shifts to higher u and lower d_p, shown by the dashed arrow lines in both figures.

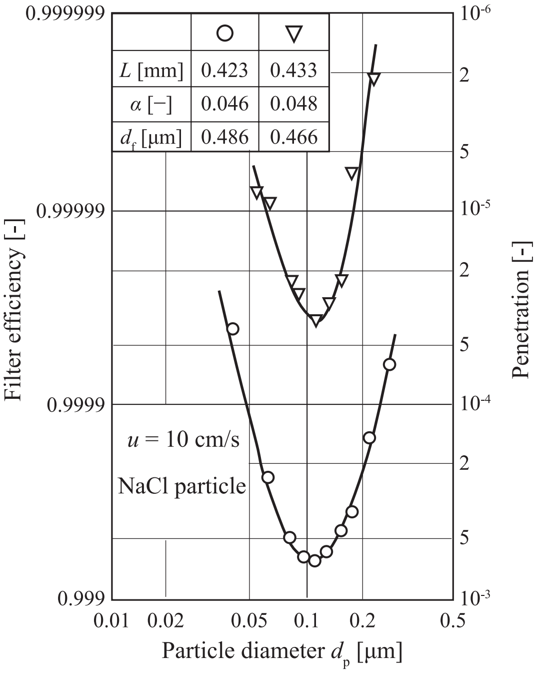

Fig. 9 Filter efficiency and penetration of HEPA filter. (Modified from Emi H. and Kanaoka C., 1981; Emi H. et al., 1982b)

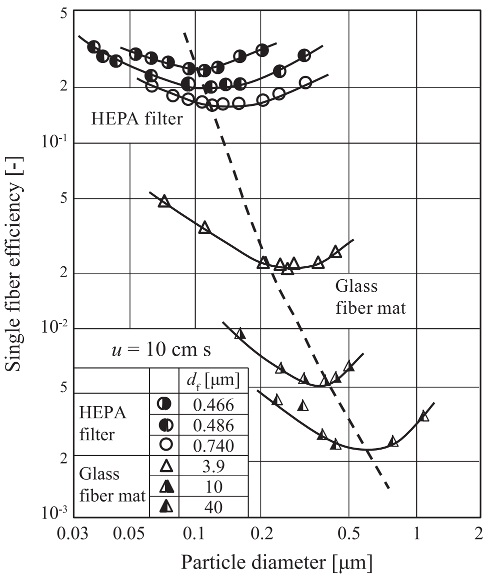

Fig. 10 Experimental single fiber collection efficiency ($\alpha_f \cong$ 0.05). (Modified from Emi H. et al., 1982b)

2.3 Filter efficiency

2.3.1. Particle size at minimum collection efficiency (MPPS)

As described above, η has minimum at certain filtration condition. This is especially important for high performance air filter like HEPA and ULPA filter. **Fig. 9** shows filter efficiency of two HEPA filters against particle size (Emi H. and Kanaoka C. 1981; Emi H. et al., 1982b). In

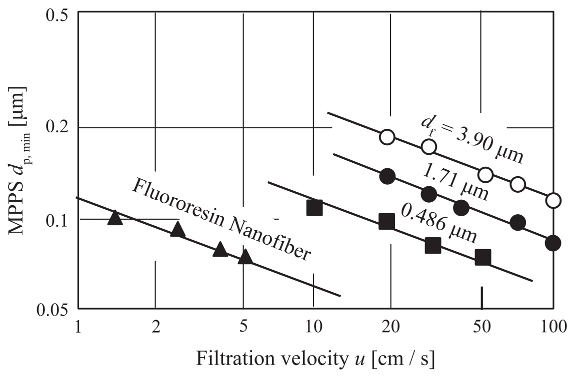

Fig. 11 Correlation of MPPS with filtration velocity. (Data from Emi H. et al., 1982b and Bao L. et al., 2015)

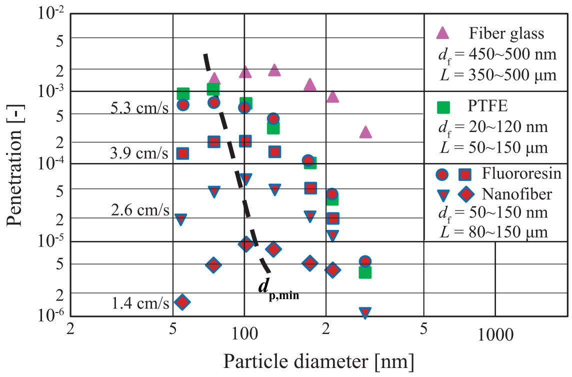

Fig. 12 Penetrations of nanofiber and ordinary HEPA filters. (Modified from Bao L. et al., 2015)

the figure, collection efficiency is higher than 99.9 % at any particle size and minimum efficiency appears around 0.1 μm and both penetrations differs more than an order of magnitude. Particle size at minimum collection efficiency (MPPS) is an important indicator of air filter since single fiber efficiency at MPPS is the lowest and thus the filter efficiency is higher than that at MPPS. **Fig. 10** shows behaviour of collection efficiency near MPPS of HEPA and fibrous mat filters (Emi H. et al., 1982b) and **Fig. 11** is an experimental correlation of MPPS with filtration velocity and fiber diameter. As seen from the figures, MPPS decreases as filtration velocity and fiber diameter decrease. Stechkina I.B et al. (1969), Wake D. (1989), Dhaniyala S. and Liu B.Y.H. (1999a, b), Podgórski A. et al. (2006) reported MPPS by different type of filters and particles.

Nanoparticle collection is an important issue. Hunt B. et al. (2014) calculated a single fiber collection efficiency of nanoparticles based on a mean first-passage time method. Wang J. et al. (2008a, b) demonstrated the superiority of a single layer nano-fiber filter against ordinary filter below 100 nm because of slip flow. Gopal R. et al.(2006), Yoon K. et al.(2006), Yun K.M. et al.(2007), Ma H. et al. (2010), Podgorski. A. et al. (2011), Kuo Y.Y. et al. (2014), Kao T.-H. et al. (2016) tested by spunbond nano filters. Bao L. et al. (2015) compared the penetrations of nanofiber filter and HEPA filters shown in **Fig. 12**. Their MPPS is also plotted in **Fig. 11** appearing smaller than ordinary filter. It decreases with filtration velocity and is almost parallel with previous result.

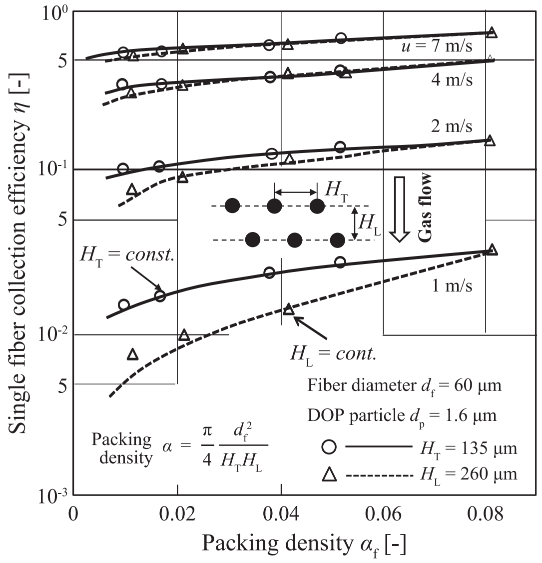

Fig. 13 Effect of inter-fiber distance on single fiber collection efficiency. (Kanaoka C. et al., 1984a)
Test filter PTFE non-circular fiber, $d_f = 13.7$ μm, mean fiber, Test particle: Atmospheric particle d_p = 0.3~0.5 μm, mass 700 ± 70 g/m^2, mean permeability 15 ± 5 cm/s
Dust concentration measurement by Digital dust counter
Size of one cell in the figure: 7 cm × 7 cm

2.4 Effects of filter structure, particle shape, fiber shape on filter performance

In actual filtration, filter and particles are very different from ideal. Effects of fiber size distribution were studied by Kirsh A.A. et al. (1975, 1978), Brown R.C. et al. (1987), Brown R.C. and Thorpe A. (2001). Concerning the effect of fiber orientation and packing was done by Overcamp T.J. (1985), Otani Y. et al. (1998), Bao L. et al. (1998), Dhaniyala S. and Liu B.Y.H. (2001), Endo Y. et al. (2001), Steffens J. and Coury J.R. (2007b), Mouret G. et al. (2009), Podgorski A. et al. (2009, 2011), Hunag S.-H. et al. (2010), Fotovati E. et al. (2010), Yamada S. et al. (2011), Eryu K. et al. (2011), Soltani P. et al. (2014), Shou D. et al. (2015), Kanaoka C. et al. (1984a, 2016, 2017).

Fig. 13 shows the effect of neighboring fiber on η in a parallel arrayed model filter by Kanaoka C. et al. (1984a). η for constant H_T is higher than that for constant H_L, suggesting H_T affects efficiency more than longitudinal interval.

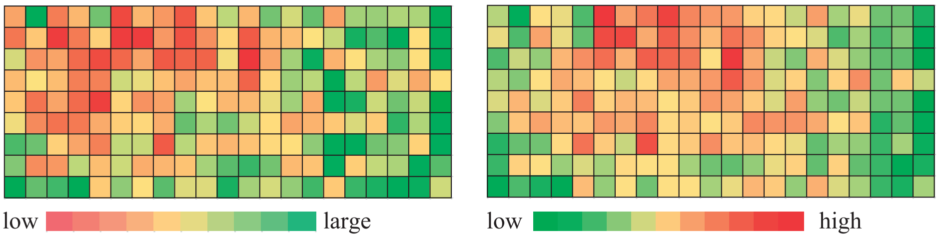

(a) Mass distribution (b) Permeability distribution

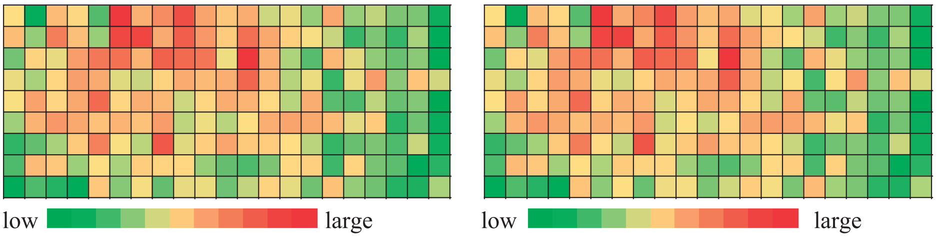

(c) Emission for u = 1 m/min (d) Emission for u = 2 m/min

Fig. 14 Distributions of fiber mass, permeability and particle emission from fibrous filter with 63 cm × 147 cm. (Kanaoka C. et al., 2016, 2017)

Fig. 14 shows the experimental distribution of fiber mass, permeability and particle emission at filtration velocities of 1 and 2 m/min of PTFE filter media with 63 cm × 147 cm. They were measured 7 cm × 7 cm cells. In the figure **(a)**, cell with reddish color indicates smaller fiber mass and greenish larger mass. Contrarily reddish color in figures **(b)**, **(c)** and **(d)** indicates high or large and greenish low or small. Their color distribution coincides with each other. This means that smaller is the fiber mass, higher and larger are permeability and particle emission from the filter.

On the influence of fiber shape, Kimura N. and Iinoya K.(1969a), Inagaki M. et al. (2001), Wang W. et al. (2012), Wang K. and Zhao H. (2015), Zhu C. et al.(2000). Boskovic L. et al. (2005, 2007, 2008), Jin X. et al. (2017) investigated for various shapes of fibers.

2.5 Single fiber collection efficiency by electrostatic effect

Collection performance by electrostatic effects depends on the charging states of particle and fiber and existence of external electric field.

For no external electric field, collection of charged particles by charged fibers was studied by Kraemer H.F. and Johnstone H.F. (1955), Yang S. and Lee’ G.W.M.(2005), and charged particles by uncharged fiber by Natanson G.L.(1957a), Lundgren D.A. and Whitby K.T. (1965), Yoshioka N. et al. (1968), Takahashi T. and Kanagawa A. (1975).

For the case of existence of electric field, collection of uncharged particles was studied by Zebel G. (1965), Iinoya K. et al. (1965), Kirsch A.A. (1972), Takahashi T. and Kanagawa A. (1978), Makino K. and Iinoya K. (1968, 1969a), and charged particles by Zebel G. (1965), Takahashi T. and Kanagawa A. (1978), Zhao Z.-M. (1991), Pnueli D. et al., (2000) and Sanchez A.L. et al. (2013).

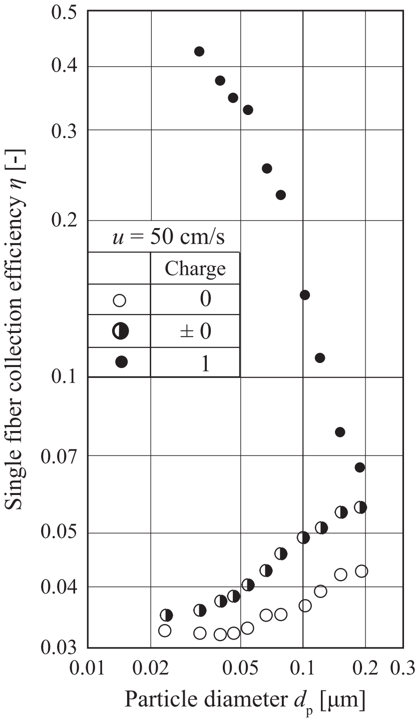

Fig. 15 Single fiber collection efficiency of particles at different charging state by an electret fiber (Modified from Emi H. et al., 1987)

After Turnhout J.V. (1976) invented an manufacturing method of electret filter, electret fibrous filter has been used popularly as a high performance air filter. Investigation about its collection mechanisms has been carried out from various view points such as collection mechanisms by Emi H. et al. (1987), Pich J. et al. (1987), Romay F.J. et al (1998), filtration performance of various particles by Baumgartner H.-P. and Löffler F. (1986), Kanaoka C. et al., (1987), Otani Y. et al. (1992, 1993), Kim J. et al. (2009), Chazelet S. et al. (2011), effect of charging process and collection performance by Nifuku M., et al. (2001), Kawabe M. et al. (2009), Choi H.-J. et al. (2015), Kilic A. et al. (2015). Time change of electret fiber was investigated by Kanaoka C. et al. (1984b), Lee M., et al. (2002), Choi H.-J. et al. (2014, 2015) and electrification method and process was by Kawabe M. et al. (2009), Kilic A. et al. (2015).

Fig. 15 shows η at different charging states by a rectangular electret fiber (Emi H. et al., 1987). As seen from the figure, since charged particle is captured by Coulomb force, η is very high at small particle and decreases with particle size becomes large. For non-charged and Boltzmann equilibrium particles, they are collected by induced force so that η is low at small size and increases with particle size.

3. Particle collection at Stage 2

Once particle is captured, gas flow in the vicinity of the fiber changes and thus filter performance such as filter efficiency and pressure drop changes with time.

This type of particle collection is utilized mainly in the field of air filtration such as for the creation of highly purified space, ventilation of air and intake air cleaning for internal combustion air and so on.

For the case of collection of solid particles by a fibrous filter, Yoshioka N. et al. (1969b), Kimura N. et al. (1969b, c, 1970, 1985, 1989), Davies C.N. (1970), Kanaoka C. et al. (1980a), Hinds W.C. and Kadrichu N.P. (1997), Bémer D. and Callé S. (2000), Sakano T. et al. (2000), Wang Q. et al. (2016), Hasolli N. et al. (2013a, b) measured evolution of filter performance and analyzed the phenomena based on the measurements.

Yoshioka N. et al. (1969b) applied analysis method of clarifying filtration and obtained analytical expressions for filter efficiency and dust load as,

$$E = 1 - \frac{\exp(-\lambda A C_{\mathrm{in}} u t)}{\exp(-\lambda A C_{\mathrm{in}} u t) + \exp(AL) - 1} \tag{25}$$

$$m = -\frac{1}{A}\frac{\exp(-\lambda A C_{\mathrm{in}} u t)}{\exp(-\lambda A C_{\mathrm{in}} u t) + \exp(AL) - 1} \tag{26}$$

$$A = \frac{4\alpha\eta_{\mathrm{m}}}{\pi(1-\alpha)d_{\mathrm{f}}} \tag{27}$$

In the derivation, they assumed collection efficiency of dust loaded fiber η_{m} as,

$$\eta_{\mathrm{m}} = \eta_0(1+\lambda m) \tag{28}$$

Their experimental result was explained by Eqns. (25) and (26) assuming $\lambda = 5\ \mathrm{m^3/kg}$.

Clogging of nano-size particles in HEPA filter was carried out concerning effect of gas slip (Leung W.W.-F. and Hung C.-H. 2008, 2009), particle distribution (Brourrous S. et al., 2014), structure and loading capacity (Contal P. et al., 2004; Kim S.C. et al., 2009), liquid and humidity, hygroscopicity (Payet S. et al.,1992; Contal P. et al., 2004; Gupta A. et al., 1993; Joubert A. et al., 2010; Agranovski I.E. and Shapiro M., 2001) and etc.

Measurements for the case of electret filter were carried out by Baumgartner H.-P. and Löffler F. (1986, 1987), Brown R.C. et al. (1988), Hiragi S. et al. (1990b), Stenhouse J.I.T. et al. (1992), Walsh D.C. and Stenhouse J.I.T. (1996, 1997a, b), Janssen L.L. et al. (2003), Ji J.H. et al. (2003), Yang S. et al. (2005), Yang S. and Lee G.W.M. (2005), Huang B. et al. (2006), Yang S. et al. (2007), Ardkapan S.R. et al. (2014), Xiao H. et al. (2014). They found a unique collection behavior relating to deterioration of electrostatic effect with dust load and recovery of collection efficiency afterwards, and discussed influences by various parameters.

At very initial stage, collected particles form dendritic

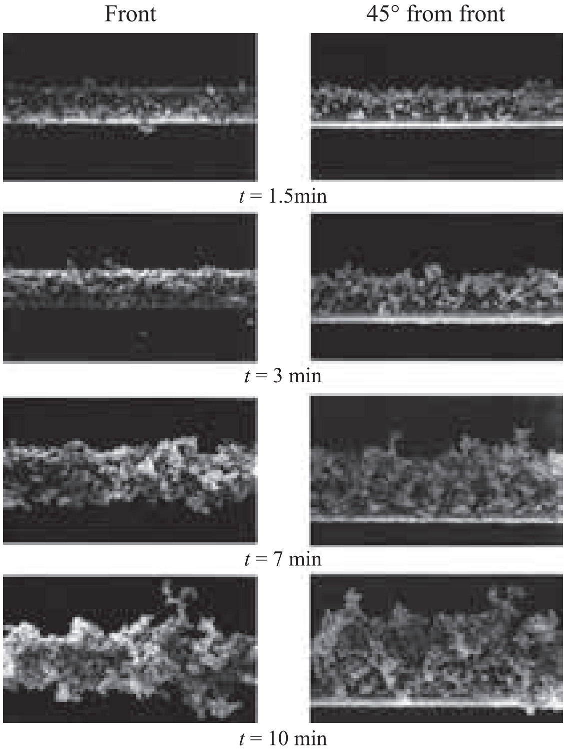

Fig. 16 Time change of particle deposit on a fiber. $d_{\mathrm{f}} = 10\ \mu\mathrm{m}$, $d_{\mathrm{p}} = 1\ \mu\mathrm{m}$, $\rho_{\mathrm{p}} = 11.34\ \mathrm{g/m^3}$ $u = 50\ \mathrm{cm/s}$, $Stk = 3.5$, $R = 0.1$ (Kanaoka C. et al., 1986).

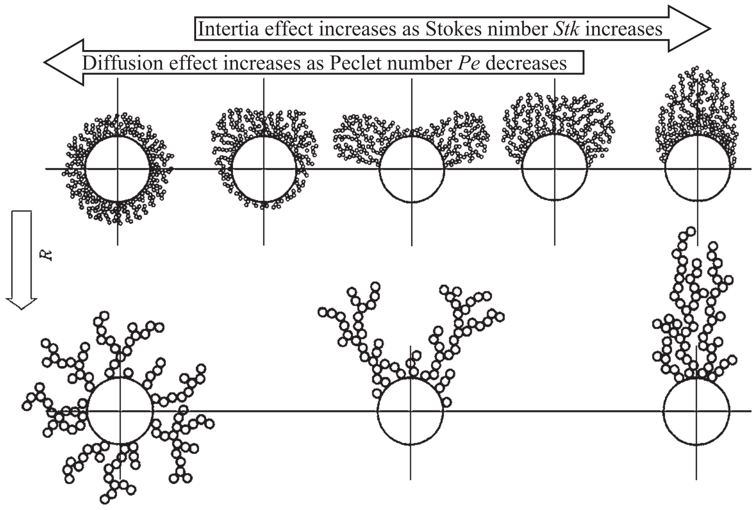

Fig. 17 Morphology of particle deposit by mechanical effects. (Modified from Kanaoka C. et al., 1982)

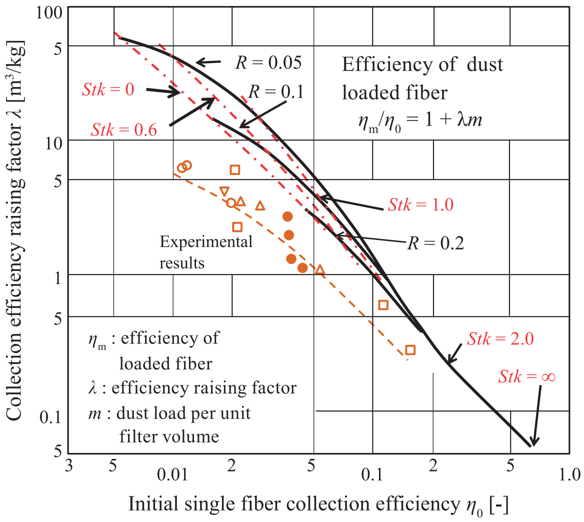

Fig. 18 Simulated and experimental collection efficiency raising factor (Modified from Myojo T. et al., 1984)

deposit on a fiber because of hindering effect. Accumulation of solid particles on a fiber was observed by Billings C.E. (1966), Bhutra S. and Payatakes A.C. (1979), Kanaoka C. et al. (1982) observed dendritic growth, Myojo T. et al. (1984), Kanaoka C. et al. (1982, 1986, 1990), Hiragi S. et al. (1990a, b), Song C.B. et al. (2006), Kasper G. et al. (2010), Müller T.K. et al. (2014a, b) observed and discussed the effect of re-entrainment of particles.

Fig. 16 shows the time change of accumulation of 1 μm particles collected on a 10 μm cylindrical tungsten wire. As seen from the figure, amount of collected particles increases with time so rapidly. Although particles are collected by very strong inertia effect such as $Stk = 3.5$ and then particles accumulated on the front surface, morphology of particle deposit changes with filtration condition as shown in **Fig. 17**. In the figure, deposition pattern at $Pe = 0$ and $Stk = \infty$ is drawn from theoretical consideration such as distributed uniformly around the fiber for $Pe = 0$ and sine curve shape in the front side of the fiber for $Stk = \infty$, respectively.

When particles are captured by inertia and/or interception effect, they accumulate on the front side of the fiber but for the case of diffusion, some of them will be collected in the rear side of the fiber. In general, collected particles form porous accumulates and they become coarser with *R*.

Payatakes A.C. (1976a, 1977), Payatakes A.C. and Tien C. (1976b), Payatakes A.C. and Gradoń L. (1980), Payatakes A.C. and Okuyama K. (1982) proposed a deterministic model of the formation of chain-like particle agglomerates on a fiber by interception and inertia effects.

Kanaoka C. et al. proposed a stochastic model of the formation of dendrites by interception (1978), inertia (1980b), diffusion (1982, 1983) and electrostatic force (2001). Bahners T. and Schollmeyer (1986), Cai J. and Peterson F. (1989a, b), Wongsri M. et al. (1991), El-shobokshy M.S. et al. (1994), Tanthapanichakoon W. et al. (2003), Sae-lim W. et al. (2006) also simulated the filtration process by different collection mechanism and different fiber property and structure by Monte Carlo simulation method. Schmidt E. (1996) simulated 3D dust structures formation, Karadimos A. and Ocone R. (2003) took into account the effect of change of the flow field by dust loading and develop CFD simulation code, Wang H. et al. (2013) and Przekop R. et al. (2003) used Lattice-Boltzmann two-phase flow model for simulation. Li S.Q. and Marshall J.S. (2007) simulated by DEM based on JKR theory for adhesive elastic contacts, Qian, F. et al. (2013) used CFD–DEM, Dunnett S.J. and Clement C.F. (2006, 2012) used boundary element model (BEM).

Kanaoka C. et al. (1978, 1982, 1983) obtained linear expression same as Eqn. (28) from simulation and experiments but value of λ was found as a function of filtration condition as shown in **Fig. 18**.

Kasper G. et al. (2009) proposed a power law expression for packing density $\alpha < 0.04$ as,

$$\eta_{\mathrm{m}} = \eta_0 \left(1 + bm^c\right) \tag{29}$$

In the above equation, b and c are empirical fit coefficients. The exponent c is on the order of 0.7 ± 0.05 and approaches to 1 for isolated fiber.

Evolution of pressure drop and holding capacity of particles in the filter is practically important. Medjimorec V. et al. (1981), Japuntich D.A. et al. (1994) estimated the drag forces acting on particle dendrites, Hiragi, S. (1990a), Kanaoka C. and Hiragi S. (1990b) proposed a model to predict pressure drop of dust loaded filter based on the observation of dust captured on parallel arrayed model filter at different times. Joubert A. et al. (2011) proposed a model for the pressure drop across HEPA filters during cake filtration in the presence of humidity. Thomas D. et al. (2014) and Bourrous et al. (2016) derived a model of clogging process of nano-size particles based on precise measurement of porosity and thickness of deposit and deposit distribution in the filter as,

$$\beta(x) = \frac{m}{S} \cdot \frac{k\exp(-kx)}{\rho_{\mathrm{p}}\{1 - \exp(-kx)\}} \tag{30}$$

Kanaoka C. and Hiragi S. (1990) and Hiragi S. (1990a) proposed to estimate the evolution of pressure drop by a drag theory.

$$F_{\mathrm{m}} = C_{\mathrm{Dm}} d_{\mathrm{fm}} \frac{1}{2} \rho_g u^2 = \frac{C_{\mathrm{Dm}}}{C_{D0}} \cdot \frac{d_{\mathrm{fm}}}{d_{\mathrm{f}}} \cdot F_0 \tag{31}$$

They determined the evolution of effective fiber diameter d_{fm} and drag coefficient C_{Dm} of a fiber by the accumulation of 0.33 μm and 0.8–0.84 μm on a fiber in a parallel arrayed model filter. Then they confirmed it by the experiments using a fan model filter and glass fibrous mat.

By using their proposal, evolution of filter efficiency, pressure drop and dust load distribution for a uniform filter and a gradient filter having packing gradient in flow direction was calculated. Packing density of both filters was assumed to be $\alpha_{\mathrm{f,av}} = 0.04$ for uniform filter and $\alpha_{\mathrm{f}}(x) = 0.07(x/L) + 0.01$ for gradient filter. Fiber diameter and particle size were set the same as Kanaoka et al. (1990). Non-consolidation of loaded dust due to the pressure drop of filter was assumed. Calculation conditions are listed in **Table 2**.

Table 2 Calculation conditions

Filter thickness	L	50 mm
Fiber diameter	d_{f}	30 μm
Mean packing density	$\alpha_{\mathrm{f,av}}$	0.04
Particle size	d_{p}	0.84 μm
Particle concentration	C_i	100 mg/m^3
Filtration velocity	u	50 cm/s

Fig. 19 shows the calculated evolution of filter efficiency, E and pressure drop, Δp_{m} of two filters, and loaded mass distributions in **Fig. 20**.

As seen from **Fig. 19**, E and Δp_{m} of both filters increase with *Cut* but E and Δp_{m} of the gradient filter are higher than those of uniform filter from the beginning and reaches 100 % collection efficiency faster. In the figure, pressure drop curve of the uniform filter stops the middle of the graph but that of the gradient filter continues much longer. In this case, gradient filter can operate about 3

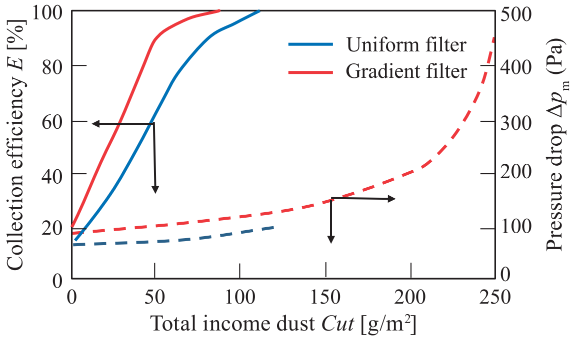

Fig. 19 Comparison of filter efficiency and pressure drop of uniform and gradient filters.

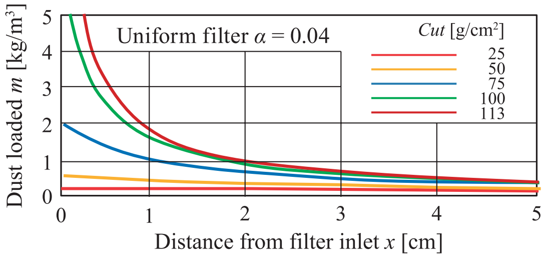

(a) Uniform filter

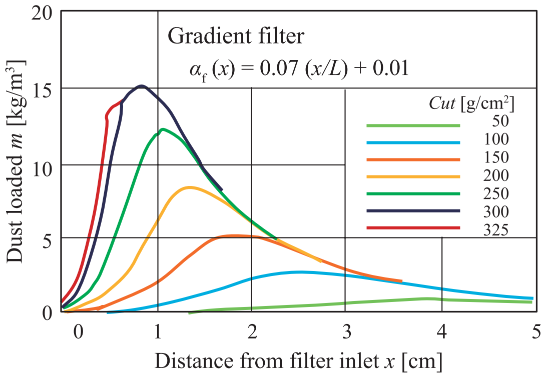

(b) Gradient filter

Fig. 20 Change of dust load distribution of uniform and gradient filters.

times of the uniform filter. This difference is explained by the difference in dust load distribution in the filter, for the case of uniform filter, dust accumulates mainly inlet part, but for the case of gradient filter, maximum load appears at rear part of the filter at beginning and it increases and shifts to front direction with time. Dust holding capacity of the filter can be predicted from distribution curve and expected maximum dust load shown by black and red curves in **Fig. 20(b)**. In this case, holding capacity of the gradient filter is about 3 times larger than the uniform filter. Same change of dust load distribution takes place when fiber has a size distribution in the depth direction. Hence, it can be said that holding capacity and service life time of air filter must be controllable by giving appropriate distribution in fiber packing density and/or size.

4. Particle collection at Stage 3

In this stage, particles are at dust cake formed on the filter media almost perfectly, i.e., forthcoming particles will be collected almost perfectly. Bag and cartridge filtration is the technology to utilize this situation. Bag filter is an important technology in the industrial sector. Hence, practical handbook and books have been published such as Billings C.E. and Wider J. (1970), Leith D. et al. (1978), Donovan R.P. (1985), Turner J.H. et al. (1987a, b), Löffler F. et al. (1988), Mukhopadhyay A. (2009a, b).

4.1 Dust cake formation and related phenomena

As described above, particles are removed perfectly at dust cake. However, the practical bag filtration is the repetition of filtration and cleaning of dust cake. As a result, grade efficiency $\eta(d_\mathrm{p})$ of filter changes as shown in **Fig. 21**. As seen from the figure, $\eta(d_\mathrm{p})$ is fairly low when the filter is fresh, i.e., never used before, but it becomes 100 % regardless of particle size just before dust cleaning, i.e., filter is covered with dust cake. Furthermore, the filter experienced 5 cleaning operations, $\eta(d_\mathrm{p})$ just after 5 cleanings is much higher than that of fresh filter at any particle size. This means $\eta(d_\mathrm{p})$ just after cleaning operation rises a little by the cleaning because of formation of primary dust layer.

After the cleaning operation, large amount of particles are emitted from the filter. **Fig. 22** (Yoneda T., 2001) is an example of the time change of exhausted dust concentration from a pilot scale bag filter system. As seen from the figure dust concentration impulsively jumps up and down more than 2 orders of magnitude from basement concentration just after the injection of cleaning pulse air.

Mori Y. et al. (1979) tested 9 different fabrics (fresh and used for each fabric) with 3 different particles and found pressure drop is expressive by the form of $\Delta p \propto u^n$, $n > 1$.

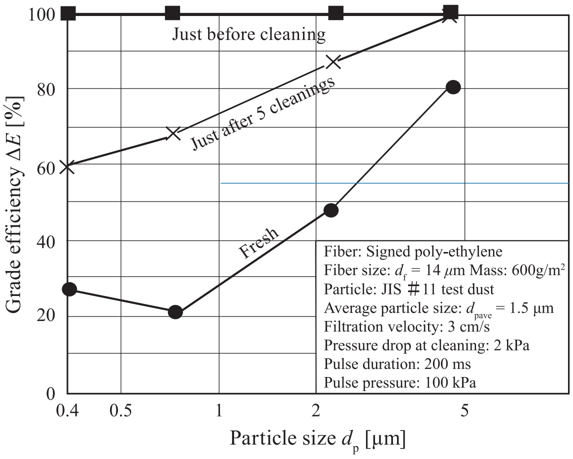

Fig. 21 Grade efficiency of bag filter medium. (Modified from Shin-Kogaiboushi no gijutsutohouki, 2015)

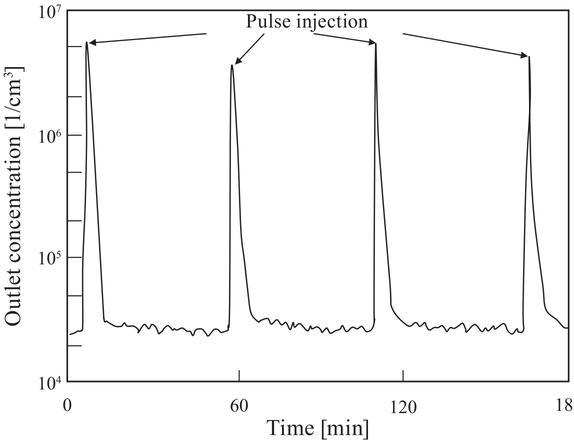

Fig. 22 Time change of emitted dust concentration from a bag filter. (Modified from Yoneda, T., 2001)

Pressure drop and filtration velocity show a hysteresis behavior at same dust load. Leith D.H. et al. (1977a, b) investigated recapturing of removed particles due to the strong back flow phenomenon. Hirota M. et al. (1985, 1987) discussed dust collection from the flowability of dust and Ikeno H. et al. (2009) from pressure drop and filter medium. Koch M. and Krammer G. (2008) discussed the effect of permeability distribution on the filter media characterization.

Yamada M. et al. (1987) estimated the mechanical strength of the dust Layer on bag fabric. Schmidt E. and Löffler F. (1990) observed the cross sectional structure of dust cakes by microscopic examination. Saleem M. et al. (2012) discussed the influence of operating parameters on the cake formation.

Ellenbecker M.J. and Leith D. (1980) obtained the effect of dust retention on pressure drop in a high velocity filter, and Cheng Y.-H. and Tsai C.-J. (1998) investigated factors influencing pressure drop through a dust cake during filtration. Silva C.R.N. et al. (1999) estimated cake/

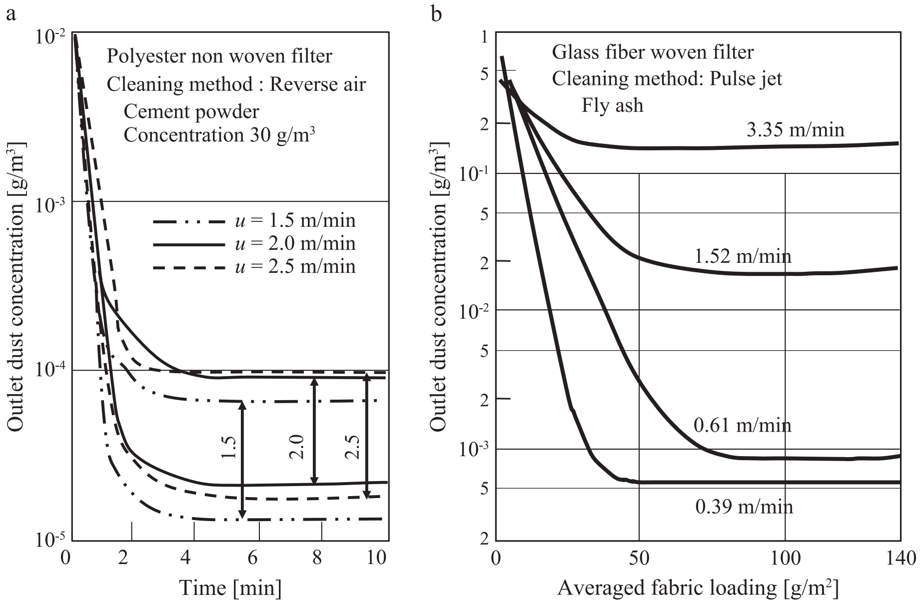

Fig. 23 Outlet dust concentration after cleaning process. **(a)** Nonwoven filter by reverse air; **(b)** Woven filter by pulsejet air. (Modified from Yoneda T., 1989; Dennis R. and Klemm H.A., 1979a, b)

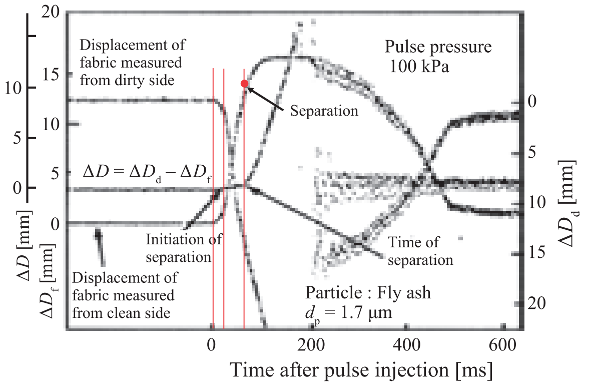

Fig. 24 Initiation and termination of the separation of dust layer. (Modified from Kanaoka C. et al., 1994)

fabric adhesion force from filtration and cleaning measurements.

Fig. 23 shows the detail change of outlet dust concentration after cleaning process at different filtration velocity studied by Yoneda T. (1989) for nonwoven filter and Dennis R. and Klemm H.A. (1979a, b) for woven filter. As seen from the figure, decreasing trends of both filters coincide with each other against time and filtration velocity, i.e., outlet concentration decreases steeply at the beginning and slows down and becomes stable in short time. Furthermore, stabilized concentration is lower as filtration velocity is low, despite of the different weaving and cleaning methods.

Leith D. and Ellenbecker M.J. (1982) measured dust emission characteristics of pulse-jet-cleaned fabric filters. Simon X. et al. (2014) also measured downstream particle puffs emitted during pulse-jet cleaning and investigated the influence of operating conditions and filter surface treatment, Fang C. et al. (2015) studied experimental investigation on particle entrainment behavior near a nozzle in gas–particle coaxial jets.

4.2 Cleaning of dust cake on the filter medium

Cleaning of dust cake is one of the most important processes. During filtration period, filter is pressed toward inside. When high pressure compressed gas is injected from the open end of the filter bag for a short time, it expands toward outside.

According to this filter movement, dust cake moves with filter but it is removed just before filter full expanded state of filter. This situation is shown in **Fig. 24** observed by the plane type fabric test rig (Kanaoka C. et al., 1994). In the figure, ΔD_f and ΔD_d stand, displacements measured from clean side and dirty side, respectively. ΔD is defined as $\Delta D = \Delta D_\mathrm{d} - \Delta D_\mathrm{f}$ and means the relative displacement of dust cake, i.e., when $\Delta D = 0$, dust cake moves with filter but $\Delta D > 0$, dust cake movement is different form filter motion, i.e., dust cake is removed from the filter. In the figure, after cleaning air is injected, ΔD_f increases and ΔD_d decreases. This means filter expands outward and filter and dust cake move together at very beginning (between left to middle red lines). Then dust cake moves slightly different from filter with time (between middle to right red lines). Finally, ΔD becomes large rapidly showing the separation of dust cake, which happens at red circle in the figure.

Dennis R. and Klemm H.A. (1980) and Dennis. R. et al. (1981) gave modelling concepts for pulse jet filtration and then analysed the pressure loss for pulse jet filters from the relationship between dust adhesion to the fabric and the opposing force. Leith D. and Ellenbecker M.J. (1980) also presented a theory for pressure drop in a pulse-jet cleaned fabric filter.

Iinoya K. et al. (1979) measured dust dislodging performance of a pulse-jet fabric filter. Humphries W. (1981) investigated the influence of cloth structure on dust dislodgement from fabric filters and discussed the relationship between residual dust load and the structure of filter medium. Kanaoka C. et al. (1994) investigated dust cleaning mechanism of a pulse jet type bag filter. Kanaoka C. and Yao Y. (2003) studied time dependency of the pressure drop in a flat type pulse jet fabric filter. Ikeno H. et al. (2004) studied pressure drop in bag filter based on patched cleaning model, Simon X. et al. (2007) experimentaly studied parameters affecting pulse-jet cleaning of bag filters supported by rigid rings. Binnig J. et al. (2011) analysed the cleaning pulse intensity in a surface filter test rig by dimensionless analysis method. Yao Y. et al. (2008) and Mao N. et al. (2008) compared the filter cleaning performance between VDI and JIS testing rigs for cleanable fabric filter. Qian Y. et al. (2015) investigated the effect of filtration operation and surface treatment on pulse-jet cleaning performance of filter bags. Ellenbecker M.J. and Leith D. (1983) measured dust removal characteristics of 3 fabrics with different surface treatment. Makino K. et al. (1976) and Ikazaki F. et al. (1978) studied dislodgement of dust cake by electrostatic effect. Tsubaki J. et al. (1982) and Naito, M. et al. (1984) studied dislodgement of deposited dust layer by applying normal stress. Park B.H. et al. (2010) proposed a preparation and characterization method of porous composite filter medium by polytetrafluoroethylene foam coating to improve separation performance.

4.3 Improvement of system performance

Since bag filter system is composed of many filter elements, its performance depends not only on the performance of individual filter but also on the system design and operation mode.

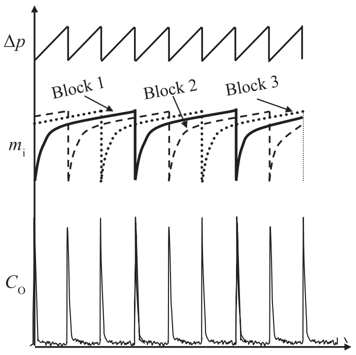

(a) Time changes of pressure drop, dust load and outlet dust concentration

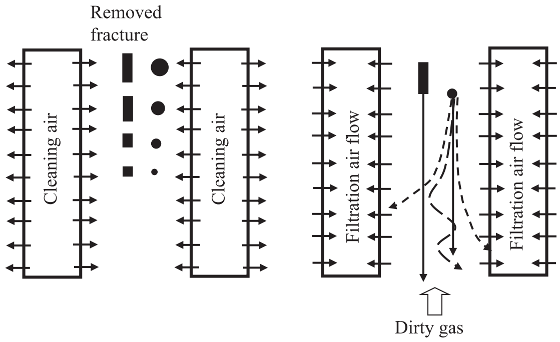

(b) Just after cleaning (c) Restart of filtration

Fig. 25 Conceptional expression of system parameters.

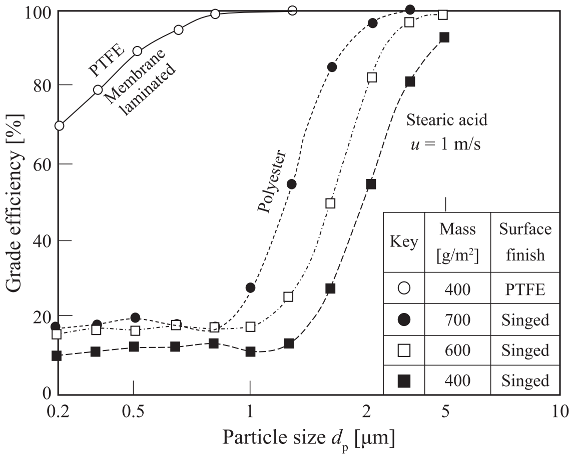

Fig. 26 Comparison of filter efficiency of different fiber mass and surface treatment for polyester filter media. (Modified from Hakamata T. et al., 1993)

Fig. 25 schematically shows **(a)** the changes of system parameters and **(b)** phenomena taking place in a bag filter system with 3 pulse cleaning blocks. **(a)** shows the time changes of parameters such as pressure drop of filter system Δp, dust load on a bag filter element in within each cleaning block m_i and emitted dust concentration from the filter system C_o, respectively. Pressure drop of the system drops when cleaning pulse is injected and increases with time until next cleaning operation so that it changes in zig zag shape with time but does not change so much. Concerning dust load m_i, by the cleaning operation at block 1, m_1 immediately drop down to almost zero but m_2 and m_3 stay fairly high values and then flow resistance of bag filters in block 1 decreases by the clean operation, m_1 increases quickly because of the concentration of gas flow to block 1 but dust load of other two blocks $\boldsymbol{m_2}$ and $\boldsymbol{m_3}$ do not change so much. Outlet is concerned, it jumps up at every cleaning process but drops down to very low level quickly and keeps almost the same level until next cleaning operation. **(b)** and **(c)** show the phenomena taking place in the filter system accompanying to the cleaning process, i.e., **(b)** shows the phenomena when cleaning compressed air is injected and **(c)** represents the situation just after filtration restarted. Since time interval between cleaning operation and restart of filtration is very short, removed dust has to fall down to the dust hopper against dirty gas flow and thus it has to have settling velocity. In another words, shape and size of fractures determine whether or not fractures drop down to the dust hopper or are recaptured by filter again.

Lu H.-C. and Tsai C.-J. (1998) studied to find the optimum design and operation parameters of a pulse-jet baghouse, and Ju J. et al. (2001) proposed a model to estimate the relation between filtration velocity and dust load in each cleaning cycle until reaching steady operation mode.

Improvement of collection performance of filter media is another important issue to improve the system performance. **Fig. 26** is the comparison of filter collection efficiency by the difference of fiber mass and surface treatment. As seen from the figure, collection efficiency increases fiber mass from 400 to 700 g/m$^{2.}$ However, collection efficiency of membrane laminated filter shows very high efficiency at any particle size despite that fiber mass of the basement filter is only 400 g/m^2.

4.4 Particle collection by cartridge filter

Cartridge filter was first developed as an air intake filter for vehicle engine and has been now used popularly even at high particle concentration region. Because of pleated and compact structure, filtration area per system volume can be larger than an ordinary cylindrical filter media and thus filter system size becomes small. However, cartridge filter has many problems relating to its structure.

Chen D.R. et al. (1995) and Chen D.R. and Pui D.Y.H. (1996) tried to optimize pleated filter designs by using a finite-element numerical model. Wakeman R.J. et al. (2005) analyzed the effects of medium compression, pleat deformation and pleat crowding are analyzed. Ming L. et al. (2010) experimentally studied 6 pleated fabric cartridges with different base media and geometrical dimensions in a pulse-jet cleaned dust collector. Then they evaluated the effect of cleaning methods and concluded that clean-on-demand mode performed better for filters with a low pleat ratio (< 4.0). Lo L. et al. (2010a, b) numerically and experimentally studied pleated fabric cartridges during pulse-jet cleaning. Joubert A. et al. (2010) evaluated the influence of humidity on the clogging pleated HEPA filters. Park B.H. et al. (2012) studied the influence of pleat geometry on filter cleaning in PTFE/glass composite filter. Bemer D. et al. (2013) studied clogging and cleaning cycles of a pleated cartridge filter by ultrafine particles. Hasolli N. et al. (2013a, b) evaluated the filtration performance of depth filter media cartridges as function of layer structure and pleat count. Bourrous S. et al. (2014) measured the nano-particles distribution in the pleated filters during clogging. Li J. et al. (2015) studied the improvement of dust cleaning effect by the installation of cone in a pleated filter cartridge during pulse-jet cleaning. Feng Z. and Long Z. (2016) simulated unsteady filtration. Kim J.-U. et al. (2017) evaluated the effective filtration area of a pleated filter bag in a pulse-jet bag house and found that effective filtration area decreases considerably due to its geometric configuration and dust clogging between pleat. Chen S. et al. (2017) studied the effect of pleat shape on reverse pulsed-jet cleaning of filter cartridges by CDF analysis and concluded that the shape of pleats has its effect on the pressure drop across pleated cartridges and pleat tip opening improves the uniformity of pressure on inner surfaces of pleats. Finally, they concluded trapezoidal pleat shape is a better candidate for pleating filter cartridges.

5. Summary

In this article, researches relating to dust collector using fiber as particle collection body, i.e., air filter, cartridge filter and nonwoven bag filter, were reviewed.

Particle collection process of air filter can be classified into 3 stages, i.e., Stage 1 (inner filtration I: collection by a fresh fiber), Stage 2 (inner filtration II: collection by both fresh and dust loaded fiber) and Stage 3 (surface filtration: collection by dust cake on the filter surface).

Particle collection in Stage 1 is practically applicable as far as collection efficiency and pressure drop of filter are stable. Collection behaviour of this stage is well understood and established for circular cylinder except in single nano-particles. However, effects of filter structure, inhomogeneity in fiber size and shape, and non-uniformity of fiber packing are not well understood.

Particle collection by fresh and dust loaded fiber take place in Stage 2. Due to the stochastic nature of particle collection, analysing method has not been established but analysing techniques using CDF are progressing. However, there are many parameters and issue remained in this stage. Especially, to find the suitable filter structure having large dust holding capacity is the important issue in this stage.

Particle collection Stage 3 is practically very important but due to the complicated phenomena, it is not well understood. Hence, most of dust collectors are designed on empirical basis. Hence, fundamental study in this stage is still needed.

Nomenclature

A	constant defined by Eqn. (27) [1/m]
b	empirical coefficient in Eqn. (29) [(kg/m^3)$^{-c}$]
C	particle concentration [kg/m^3]
C_C	Cunningham correction factor [–]
C_D	Drag coefficient of a fiber [–]
c	empirical exponent in Eqn. (29) [–]
ΔD	displacement of dust cake from filter surface
D_BM	diffusion constant [m^2/s]
ΔD_d	displacement of surface of dust cake measured from dirty side [m]
ΔD_f	displacement of filter surface measured from clean side [m]
d	size [m]
E	filter efficiency [–]
G	Gravitational parameter ($= \rho_\mathrm{p} d_\mathrm{p}^2 g/18\mu u$) [–]
g	acceleration of gravity (m/s^2)
H	distance between neighboring fibers
h	hydrodynamic factor [–]
k	constant in Eqn. (30)
L	filter thickness [m]
m	dust load per unit filter volume [kg/m^3]
R	Interception parameter ($= d_\mathrm{p}/d_\mathrm{f}$) [–]
Re	Reynolds number ($= \rho_\mathrm{g} d_\mathrm{f} u/\mu$) [–]
P	penetration [–]
pe	number of elementary charges in particle [–]
Pe	Peclet number ($= d_\mathrm{f} u/D_\mathrm{BM}$) [–]
S	filtration area [m^2]
Sc	Schmidt number ($= \mu/(\rho_\mathrm{g} D_\mathrm{BM})$) [–]
Stk	Stokes number ($= C_\mathrm{c} \rho_\mathrm{p} d_\mathrm{p}^2 u/9\mu d_\mathrm{f}$) [–]
T	temperature [K]
u	particle velocity or filtration velocity [m/s]
u_a	approaching velocity to a fiber [m/s]
x	distance from filter inlet [m]
z_p	electrical mobility [m^2/(V·s)]
α	packing density [–]
$\beta(x)$	deposition distribution function given in Eqn. (30) [–]
ε	porosity of filter [–]
η	single fiber collection efficiency [–]
κ	Boltzmann constant ($= 1.38064852 \times 10^{-23}$) [J/K]
λ	collection raising factor [-]
μ	gas viscosity [Pa·s]
ρ	density [kg/m^3]

Subscript

av	average
D	diffusion
f	fiber
g	gas
G	gravity
I	inertia
K	Kuwabara
L	Lamb
m	dust loaded
p	particle
R	interception
0	without dust load

References

Agranovski I.E., Shapiro M., Clogging of wet filters by dust particles, Journal of Aerosol Science, 32 (2001) 1009–1020.

Alonso M., Kousaka Y., Hashimoto T., Hashimoto N., Penetration of nanometer-sized aerosol particles through wire screen and laminar flow tube, Aerosol Science and Technology, 27 (1997) 471–480.

Ardkapan S.R., Johnson M.S., Yazdi S., Afshari A., Bergsøe N.C., Filtration efficiency of an electrostatic fibrous filter: Studying filtration dependency on ultrafine particle exposure and composition, Journal of Aerosol Science, 72 (2014) 14–20.

Bahners T., Schollmeyer E., Computer simulation of the filtration process in a fibrous filter collecting polydisperse dust, Journal of Aerosol Science, 17 (1986) 191–197, 199–200.

Bao L., Otani Y., Namiki N., Mori J., Emi H., Prediction of HEPA filter collection efficiency with a bimodal fiber size distribution, Kagaku Kogaku Ronbunshu, 24 (1998) 766–771.

Bao L., Kobayashi M., Aomi H., Matsuzaki H., Kiyotani H., Shibuya Y., Chaen S., Inui K., Kuo C.C., Siang D.K., Bin Z., Wei N.C., Balgis R., Ogi T., Okuyama K., Otani Y., Lin Z., Performance evaluation of the HEPA filter made of depth filtration nano-fiber media, 33rd Annual Tech. Meeting on Air Cleaning and Contamination Control proceeding, JACA (Japan Air Cleaning Association), 2015, pp. 90–93.

Baumgartner H.-P., Löffler F., The collection performance of electret filters in the particle size range 10 nm–10 µm, Journal of Aerosol Science, 17 (1986) 438–445.

Baumgartner H., Löffler F., Three-dimensional numerical simulation of the deposition of polydisperse aerosol particles on filter fibres—extended concept and preliminary results, Journal of Aerosol Science, 18 (1987) 885–888.

Bémer D., Callé S., Evolution of the efficiency and pressure drop of a filter media with loading, Aerosol Science and Technology, 33 (2000) 427–439.

Bemer D., Regnier R., Morele Y., Grippari F., Appert-collin J.C., Thoms D., Study of clogging and cleaning cycles of a pleated cartridge filter used in a thermal spraying process to filter ultrafine particles, Powder Technology, 234 (2013) 1–6.

Bhutra S., Payatakes A.C., Experimental investigation of dendritic deposition of aerosol particles, Journal of Aerosol Science, 10 (1979) 445–464.

Billings C.E., Effects of particle accumulation in aerosol filtration, W. M. Keck Laboratory of Environmental Health Engineering Report, California Institute of Technology, Pasadena, 1966.

Billings C.E., Wilder J., Handbook of fabric filter technology, Vol. 1: fabric filter systems study, GCA-TR-70-17-G, GCA Corporation, 1970.

Binnig J., Bredin A., Meyer J., Kasper G., Dimensional analysis of the cleaning pulse intensity in a surface filter test rig, Powder Technology, 211 (2011) 275–279.

Boskovic L., Altman I.S., Agranovski I.E., Braddock R.D., Myojo T., Choi M., Influence of particle shape on filtration processes. Aerosol Science and Technology, 39 (2005) 1184–1190.

Boskovic L. Agranovski I.E., Braddock R.D., Filtration of nanosized particles with different shape on oil coated fibres, Journal of Aerosol Science, 38 (2007) 1220–1229.

Boskovic L., Agranovski I.E., Altman I.S., Braddock, R.D., Filter efficiency as a function of nanoparticle velocity and shape, Journal of Aerosol Science, 39 (2008) 635–644.

Bourrous S., Bouilloux L., Ouf F.X., Appert-Collin J.C., Thomas D., Tampère L., Morele Y., Measurement of the nanoparticles distribution in flat and pleated filters during clogging, Aerosol Science and Technology, 48 (2014) 392–400.

Bourrous S., Bouilloux L., Ouf F.-X., Lemaitre P., Nerisson P., Thomas D., A.-Collin J.C., Measurement and modeling of pressure drop of HEPA filters clogged with ultrafine particles, Powder Technology, 289 (2016) 109–117.

Brown R.C., A many-fibre theory of airflow through a fibrous filter, Journal of Aerosol Science, 15 (1984) 583–593.

Brown R.C., A many-fibre theory of airflow through a fibrous filter—II: fluid inertia and fibre proximity, Journal of Aerosol Science, 17 (1986) 685–697.

Brown R.C., Davies J.K.W., Wake D., Penetration of test aerosols through filters described in terms of a gamma distribution of layer efficiencies, Journal of Aerosol Science, 18 (1987) 499–509.

Brown R.C., Wake D., Gray R., Blackford D.B., Bostock G.J., Effect of industrial aerosols on the performance of electrically charged filter material, The Annals of Occupational Hygiene, 32 (1988) 271–294.

Brown R.C., Wake D., Air filtration by interception-theory and experiment, Journal of Aerosol Science, 22 (1991) 181–186.

Brown R.C., Air Filtration, Pergamon Press, Oxford, 1993.

Brown R.C., Thorpe A., Glass-fibre filters with bimodal fibre size distributions, Powder Technology, 118 (2001) 3–9.

Cai J., Peterson F., Efficiency for monodisperse particles in instationary filtration, Journal of Aerosol Science, 20 (1989a) 955–958.

Cai J., Some remarks on efficiency due to dendrite formation, Journal of Aerosol Science, 20 (1989b) 959–962.

Chen D.R., Pui D.Y.H., Liu B.Y.H., Optimization of pleated filter designs using a finite-element numerical model, Aerosol Science and Technology, 23 (1995) 579–590.

Chen D.R., Pui D.Y.H., Optimization of pleated filter designs, Journal of Aerosol Science, 27 (1996) 654–655.

Chen S., Wang Q., Chen D.-R., Effect of pleat shape on reverse pulsed-jet cleaning of filter cartridges, Powder Technology, 305 (2017) 1–11.

Cheng Y.-H., Tsai C.-J., Factors influencing pressure drop through a dust cake during filtration, Aerosol Science and Technology, 29 (1998) 315–328.

Chazelet S., Bemer D., Grippari F., Effect of the test aerosol charge on the penetration through electret filter, Separation and Purification Technology, 79 (2011) 352–356.

Choi H.-J., Kim S.-B., Kim S. H., Lee M.-H., Preparation of electrospun polyurethane filter media and their collection mechanisms for ultrafine particles, Journal of the Air & Waste Management Association, 64 (2014) 322–329.

Choi H.-J., Park E.-S., Kim J.-U., Kim S.H., Lee M.-H., Experimental study on charge decay of electret filter due to organic solvent exposure, Aerosol Science and Technology, 49 (2015) 977–983.

Contal P., Simao J., Thomas D., Frising T., Callé S., Appert-Collin, J.C., Bémer D., Clogging of fibre filters by submicron droplets, Phenomena and influence of operating conditions, Journal of Aerosol Science, 35 (2004) 263–278.

Dahneke B., The capture of aerosol particles by surfaces, Journal of Colloid and Interface Science, 37 (1971) 342–353.

Davies C.N., The Separation of airborne dust and particles, Proceedings of the Institution of Mechanical Engineers, Part B: Management and engineering manufacture, 1 (1953) 185–213.

Davies C.N., Peetz C.V., Impingement of particles on a transverse cylinder, Proceedings of the Royal Society of London Series A, Mathematical and Physical Sciences, 234 (1956) 269–295.

Davies C.N., Aerosol Science, Academic Press, New York, 1966.

Davies C.N., The clogging of fibrous aerosol filters, Journal of Aerosol Science, 1 (1970) 35–39.

Dennis R., Klemm H.A., Fabric filter model format change. Vol. I. detailed technical report, Vol. II. user's guide, U.S. Environmental Protection Agency, Industrial Environmental Research Laboratory, Research Triangle Park, NC, EPA-600/7-79-043a, EPA-600/7-79-043b, 1979a.

Dennis R., Klemm H.A., A model for coal fly ash filtration, JAPCA (Journal of the Air Pollution Control Association), 29 (1979b) 230–234.

Dennis R., Klemm H.A., Modeling concepts for pulse jet filtration, JAPCA (Journal of the Air Pollution Control Association), 30 (1980) 38–43.

Dennis R., Wilder J.E., Harmon D.L., Predicting pressure loss for pulse jet filters, Journal of the Air Pollution Control Association, 31 (1981) 987–992.

Dhaniyala S., Liu B.Y.H., Investigations of particle penetration in fibrous filters: Part I. Experimental, Journal of the IEST, 42 (1999a) 32–40.

Dhaniyala S., Liu B.Y.H., Investigations of particle penetration in fibrous filters: Part II. theoretical, Journal of the IEST, 42 (1999b) 40–46.

Dhaniyala S., Liu B.Y.H., Theoretical modeling of filtration by nonuniform fibrous filters, Aerosol Science and Technology, 34 (2001)170–178.

Donovan R.P., Fabric filtration for combustion sources: fundamentals and basic technology, Marcel Dekker, 1985.

Dunnett S.J., Clement C.F., A numerical study of the effects of loading from diffusive deposition on the efficiency of fibrous filters, Journal of Aerosol Science, 37 (2006) 1116–1139.

Dunnett S.J., Clement, C.F., Numerical investigation into the loading behaviour of filters operating in the diffusional and interception deposition regimes, Journal of Aerosol Science, 53 (2012) 85–99.

Ellenbecker M.J., Leith D., The effect of dust retention on pressure drop in a high velocity pulse-jet fabric filter, Powder Technology, 25 (1980) 147–154.

Ellenbecker M.J., Leith D., Dust removal characteristics of fabrics used in pulse-jet filters, Powder Technology, 36 (1983) 13–19.

El-shobokshy M.S., Al-Sanea S.A., Adnan A.M., Computer simulation of monodisperse aerosol collection in fibrous filters, Aerosol Science and Technology, 20 (1994) 149–160.

Emi H., Okuyama K., Yoshioka N., Prediction of collection efficiency of aerosols by high-porosity fibrous filter, Journal of Chemical Engineering of Japan, 6 (1973) 349–354.

Emi H., Okuyama K., Adachi M., The effect of neighbouring fibers on the single fiber inertia-interception efficiency of aerosols, Journal of Chemical Engineering of Japan, 10 (1977) 148–153.

Emi H., Kanaoka C., Collection efficiency of high efficiency particulate air filter, Proceeding of International Symposium on Powder Technology ‘81, 1981, pp. 517–524.

Emi H., Kanaoka C., Kuwabara Y., The diffusion collection efficiency of fibers for aerosol over a wide range of Reynolds numbers, Journal of Aerosol Science, 13 (1982a) 403–413.

Emi H., Kanaoka C., Ishiguro T., Collection performance of high efficiency air filters, 6th Int. Sympo. Cont. Control, Tokyo, (1982b) 219–222.

Emi H., Kanaoka C., Otani Y., Ishiguro T., Collection mechanisms of electret filter, Particulate Science and Technology, 5 (1987) 161–171.

Endo Y., Chen D.-R., Pui D.Y.H., Air and water permeation resistance across dust cakes on filters—effects of particle polydispersity and shape factor, Powder Technology, 118 (2001) 24–31.

Eryu K., Seto T. Furuuchi M., Otani Y., Tajima N., Kato T., Effects of filter packing density and particle deposit on classification performance of inertial filter for sampling of $PM_{0.1,}$ Journal of Chemical Engineering of Japan, 44 (2011) 609–615.

Fang C., Xu J., Zhao H., Li W., Liu H., Experimental investigation on particle entrainment behaviors near a nozzle in gas–particle coaxial jets, Powder Technology, 286 (2015) 55–63.

Feng Z., Long Z., Modeling unsteady filtration performance of pleated filter, Aerosol Science and Technology, 50 (2016) 626–637.

Fotovati S., Vahedi Tafreshi H., Pourdeyhimi B., Influence of fiber orientation distribution on performance of aerosol filtration media, Chemical Engineering Science, 65 (2010) 5285–5293.

Friedlander S.K., Mass and heat transfer to single spheres and cylinders at low Reynolds numbers. AIChE Journal, 3 (1957) 43–48.

Friedlander S.K., Theory of aerosol filtration, Industrial & Engineering Chemistry, 50 (1958) 1161–1164.

Friedlander S.K., Smoke, dust and haze: Fundamentals of aerosol behavior, New York: Wiley, 1977.

Friedlander S.K., Smoke, Dust, and Haze: Fundamentals of Aerosol Dynamics, Oxford University Press, New York, 2000.

Fuchs N.A., Stechkina I.B., A note on the theory of fibrous aerosol filters, The Annals of Occupational Hygiene, 6 (1963) 27–30.

Fuchs N.A., The mechanics of aerosols, ed. by C.N. Davies, Oxford : Pergamon Press, 1964.

Givehchi R., Tan Z., An overview of airborne nano-particle filtration and thermal rebound theory, Aerosol and Air Quality Research, 14 (2014) 45–63.

Givehchi R., Tan Z., The effect of capillary force on airborne nanoparticle filtration, Journal of Aerosol Science, 83 (2015) 12–24.

Golanski L., Guiot A., Rouillon F., Pocachard J., Tardif F., Experimental evaluation of personal protection devices against graphite nanoaerosols: fibrous filter media, masks, protective clothing, and gloves, Human & Experimental Toxicology, 28 (2009) 353–359.

Gopal R., Kaur S., Ma Z., Chan C., Ramakrishna S., Matsuura T., Electrospun nanofibrous filtration membrane, Journal of Membrane Science, 281 (2006) 581–586.

Gupta A., Novick V.J., Biswas P., Monson P.R., Effect of humidity and particle hygroscopicity on the mass loading capacity of high efficiency particulate air (HEPA) Filters, Aerosol Science and Technology, 19 (1993) 94–107.

Hakamata T., Ushiroebisu K., Suzuki K., Yoneda T., Performance of pulse jet bag filter, 6th World Filtration Congress, (1993) 483–486.

Happel J., Viscous flow relative to arrays of cylinders, AIChE Journal, 5 (1959) 174–177.

Hasolli N., Park Y.O., Rhee Y.W., Filtration performance evaluation of depth filter media cartridges as function of layer structure and pleat count, Powder Technology, 237 (2013a) 24–31.

Hasolli N., Park Y.O., Rhee Y.W., Experimental study on filtration performance of flat sheet multiple-layer depth filter media for intake air filtration, Aerosol Science and Technology, 47 (2013b) 1334–1341.

Heim M., Mullins B.J., Wild M., Meyer J., Kasper G., Filtration efficiency of aerosol particles below 20 nanometers, Aerosol Science and Technology, 39 (2005) 782–789.

Heim M., Attoui M., Kasper G., The Efficiency of diffusional particle collection onto wire grids in the mobility equivalent size range of 1.2–8 nm, Journal of Aerosol Science, 41 (2010) 207–222.

Hinds W.C., Kadrichu N.P., The effect of dust loading on penetration and resistance of glass fiber filters, Aerosol Science and Technology, 27 (1997) 162–173.

Hinds W.C., Aerosol Technology: Properties, Behavior, and Measurement of Airborne Particles, 2nd Edition, John Wiley and Sons Inc., 1999, ISBN: 978-0-471-19410-1.

Hiragi S., Performance of dust loaded fibrous air filter, Ph.D. thesis, Kanazawa University, 1990a.

Hiragi S., Kanaoka C., Yamada K., Morphology of particle agglomerate on a fiber in air filter, Kagaku Kogaku Ronbunshu, 16 (1990b) 252–258.

Hirota M., Fudoh A., Mizuno Y., Oshima T., Effect of the flowability of dust on characteristics of dust collection by a filter cloth, Kagaku Kogaku Ronbunshu, 11 (1985) 7–12.

Hirota M., Shimizu Y., Oshima T., Effect of the flowability of dust on collection performance of repeatedly dislodged filter cloth, Kagaku Kogaku Ronbunshu, 13 (1987) 113–116.

Huang B., Yao Q., Li S.-Q., Zhao H.-L., Song Q., You C.-F., Experimental investigation on the particle capture by a single fiber using microscopic image technique, Powder Technology, 163 (2006) 125–133. DOI: https://doi.org/10.1016/j.powtec.2006.01.014

Huang S., Chen C., Chang C., Lai C., Chen C., Penetration of 4.5 nm to 10 μm aerosol particles through fibrous filters, Journal of Aerosol Science, 38 (2007) 719–727.

Hunag S.-H., Kuo Y.-M., Chang K.-N., Chen Y.-K.-Y., Lin W., Lin W.-Y., Chen C.-C., Experimental study on the effect of fiber orientation on filter quality, Aerosol Science and Technology, 44 (2010) 964–971.

Hubbard J.A., Brockmann J.E., Dellinger J., Lucero D.A., Sanchez A.L., Servantes B.L., Fibrous filter efficiency and pressure drop in the viscous-inertial transition flow regime, Aerosol Science and Technology, 46 (2012) 138–147. DOI: 10.1080/02786826.2011.616555

Humphries W., Influence of cloth structure on dust dislodgement from fabric filters, Powder Technology, 28 (1981) 189–194.

Hunt B., Thajudeen T., Hogan C.J., The single-fiber collision rate and filtration efficiency for nanoparticles I: The first-passage time calculation approach, Aerosol Science and Technology, 48 (2014) 875–885.

Ichitsubo H., Hashimoto T., Alonso M., Kousaka Y., Penetration of ultrafine particles and ion clusters through wire screens, Aerosol Science and Technology, 24 (1996) 119–127.

Iinoya K., Makino K, Kimura N., Experiments of dust collection by an electric charged fibrous filter, Chemical Engineering, 29 (1965) 574–578.

Iinoya K. Makino K., Inoue O., Imamura T., Dust collection performance of paper filters, Chemical Engineering, 34 (1970) 632–637.

Iinoya K., Mori Y., Makino K., Komatsu N., Ozaki M., Nagashima R., Dust dislodging performance of a pulse-jet fabric filter, Kagaku Kogaku Ronbunshu, 5 (1979) 500–505.

Ikazaki F., Toyama S., Makino K., Tada Y., Iinoya K., Mechanism of electrical dislodging of dust layer, Kagaku Kogaku Ronbunshu, 4 (1978) 117–122.

Ikeno H., Tada Y., Hiraoka S., Ikei M., Shuto Y., Study of pressure drop in bag filter based on patched cleaning model, Kagaku Kogaku Ronbunshu, 30 (2004) 14–21.

Ikeno H., Tada Y., Ishino T., Watanabe K., Effects of pressure drop and filter medium on the collection performance of bag filter, Journal of the Society of Powder Technology, Japan, 46 (2009) 598–604.

Inagaki M., Sakai K., Namiki N., Emi H., Otani Y., Effect of shape of fiber cross section on filter performance, Kagaku Kogaku Ronbunshu, 27 (2001) 113–120.

Ingham D.B., The diffusional deposition of aerosols in fibrous filters, Journal of Aerosol Science, 12 (1981) 357–365.

Janssen L.L., Bidwell J.O., Mullins H.E., Nelson T.J., Efficiency of degraded electret filters: part I—laboratory testing against NaCl and DOP before and after exposure to workplace Aerosols, Journal of the International Society for Respiratory Protection, 20 (2003) 71–80.

Japuntich D.A., Stenhouse J.I.T., Liu B.Y.H., Experimental results of solid monodisperse particle clogging of fibrous filters, Journal of Aerosol Science, 25 (1994) 385–393.

Japuntich D.A., Franklin L.M., Pui D.Y., Kuehn T.H., Kim S.C., Viner A.S., A comparison of two nano-sized particle air filtration tests in the diameter range of 10 to 400 nanometers, Journal of Nanoparticle Research, 9 (2007) 93–107.

Ji J.H., Bae G.N., Kang S.H., Hwang J., Effect of particle loading on the collection performance of an electret cabin air filter for submicron aerosols, Journal of Aerosol Science, 34 (2003) 1493–1504.

Jin X., Yang L., Du X., Yang Y., Modeling filtration performance of elliptical fibers with random distributions, Advanced Powder Technology, 28 (2017) 1193–1201.

Joubert A., Laborde J.C., Bouilloux L., Chazelet S., Thomas D., Influence of humidity on clogging of flat and pleated HEPA filters, Aerosol Science and Technology, 44 (2010) 1065–1076.

Joubert A., Laborde J.C., Bouilloux L., Chazelet S., Thomas D., Modelling the pressure drop across HEPA filters during cake filtration in the presence of humidity, Chemical Engineering Journal, 166 (2011) 616–623.

Ju J., Chiu M.-S., Tien C., Further work on pulse-jet fabric filtration modeling, Powder Technology, 118 (2001) 79–89.

Kanaoka C., Emi H., Myojo T., Simulation of deposition and growth of airbone particles on a fiber, Kagaku Kogaku Ronbunshu, 4 (1978) 535–537.

Kanaoka C., Emi H., Myojo T., Ohta M., Estimation of collection efficiency of an air filter with dust load, I.CHEM. E. Smpo. Series. No.59, (1980a) pp. 3:4/1–3:6/15.

Kanaoka C., Emi H., Myojo T., Simulation of the growing process of a particle dendrite and evaluation of a single fiber collection efficiency with dust load, Journal of Aerosol Science, 11 (1980b) 377–389.

Kanaoka C., Emi H., Ohta M., Performance of loaded air filters, 3rd Smpo. The transfer and utilization of particulate control technology, vol.III, EPA-600/9-82-005c, (1982) 280–289.

Kanaoka C., Emi H., Tanthapanichakoon W., Convective diffusional deposition and collection efficiency of aerosol on a dust-loaded fiber, AIChE Journal, 29 (1983) 895–902.

Kanaoka C., Emi H., Deguchi A., Effect of inter-fiber distance on collection efficiency of a single fiber in a model filter composed of parallel fibers in a row, in: Aerosols ed. by B.Y.H. Liu et al.(Elsevier), (1984a) pp. 536–536.

Kanaoka C., Emi H., Ishiguro T., Time dependency of collection performance of electret filter, in: Aerosols ed. by Liu et al.(Elsevier), 1984b pp. 613–616.

Kanaoka C., Emi H., Hiragi S., Myojo T., Morphology of particulate agglomerates on a cylindrical fiber and a collection efficiency of a dust loaded fiber, Aerosols-Formation and Reactivity, Pergamon Press, 1986, pp. 674–677.

Kanaoka C., Emi H., Otani Y., Iiyama T., Effect of charging state of particles on electret filtration. Aerosol Science and Technology, 7 (1987) 1–13.

Kanaoka C., Dust collection 2, Journal of the Society of Powder Technology, Japan, 25 (1988) 469–479.

Kanaoka C., Hiragi, S., Pressure drop of air filter with dust load, Journal of Aerosol Science, 21 (1990) 127–131.

Kanaoka C., Furuuchi M., Murai J., The dust cleaning mechanism of a pulse jet type bag filter, Journal of the Society of Powder Technology, Japan, 31 (1994) 424–429.

Kanaoka C., Hiragi S., Tanthapanichakoon T., Stochastic simulation of the agglomerative deposition process of aerosol particles on an electret fiber, Powder Technology, 118 (2001) 97–106.

Kanaoka C., Yao Y.P., Time dependency of the pressure drop in a flat type pulse jet fabric filter, Kagaku Kogaku Ronbunshu, 29 (2003) 267–271.

Kanaoka C., Bao L., Kobayashi M., Packing density distribution of fiber in a nonwoven filter media, 33rd Annual Tech. Meeting on Air Cleaning and Contamination Control proceeding, JACA (Japan Air Cleaning Association), 2016, pp. 96–99.

Kanaoka C., Bao L., Kobayashi M., Kimura I., Effect of surface structure on filter performance, 34th JACA (Japan Air Cleaning Association), 2017, pp. 121–124.

Kao T.-H., Su S.-K., Su C.-I., Lee A.-W., Chen J.-K., Polyacrylonitrile microscaffolds assembled from mesh structures of aligned electrospun nanofibers as high-efficiency particulate air filters, Aerosol Science and Technology, 50 (2016) 615–625.

Karadimos A., Ocone R.,' The effect of the flow field recalculation on fibrous filter loading: a numerical simulation, Powder Technology, 137 (2003) 109–119.

Kasper G., Schollmeter S., Meyer J., Hoferer J., The collection efficiency of a particle-loaded single filter fiber, Journal of Aerosol Science, 40 (2009) 993–1009.

Kasper G., Schollmeter S., Meyer J., Structure and density of deposits formed on filter fibers by inertial particle deposition and bounce, Journal of Aerosol Science, 41 (2010) 1167–1182.

Kawabe M., Iskandar F., Okuyama K., Corona charging process for polypropylene electret filter, Journal of the Institute of Electrostatics Japan, 33 (2009) 213–219.

Kilic A., Shim E.E., Pourdeyhimi B., Electrostatic capture efficiency enhancement of polypropylene electret filters with barium titanate, Aerosol Science and Technology, 49 (2015) 666–673.

Kim C.S., Bao L., Okuyama K., Shimada M., Niinuma, H., Filtration efficiency of a fibrous filter for nanoparticles, Journal of Nanoparticle Research, 8 (2006) 215–221.

Kim S.C., Harrington M.S., Pui D.Y.H., Experimental study of nanoparticles penetration through commercial filter media, Journal of Nanoparticle Research, 9 (2007) 117–125.

Kim J., Hinestroza J.P., Jasper W., Barker R.L., Effect of solvent exposure on the filtration performance of electrostatically charged polypropylene filter media, Textile Research Journal, 79 (2009) 343–350.

Kim J.-U., Hwang J., Choi H.-J., Lee M.-H., Effective filtration area of a pleated filter bag in a pulse-jet bag house, Powder Technology, 311 (2017) 522–527.

Kim S.C., Wang J., Shin W.G., Scheckman J.H., Pui D.Y.H., Structural properties and filter loading characteristics of soot agglomerates, Aerosol Science and Technology, 43 (2009) 1033–1041.

Kimura N., Iinoya K., Collection efficiency of single fiber mat filters, Chemical Engineering, 29 (1965) 538–546.

Kimura N., Iinoya K., Effect of fiber shape on performance of fiber mat filter, Chemical Engineering, 33 (1969a) 1008–1013.

Kimura N., Estimation for initial collection efficiency of a fibrous mat filters, Chemical Engineering, 33 (1969b) 1248–1254.

Kimura N., Iinoya K., Pressure drop of a fibrous mat filter with dust loading, Chemical Engineering, 33 (1969c) 1255–1260.

Kimura N., Shirato M., Collection efficiency of dry cloth-filter with dust loading, Chemical Engineering, 34 (1970) 984–990.

Kimura N., Iwata M., Komatsu, K., Collection efficiency of fibrous mat filters with dust loads, Kagaku Kogaku Ronbunshu, 11 (1985) 621–627.

Kimura N., Kanamori M., Mori H., Shirato M., Dust load distributions in fibrous mat and granular bed filters, Kagaku Kogaku Ronbunshu, 15 (1989) 119–125.

Kirsch A.A., Fuchs N.A., Studies on fibrous aerosol filters—iii diffusional deposition of aerosols in fibrous filters, The Annals of Occupational Hygiene, 11 (1968) 299–304. DOI: 10.1093/annhyg/11.4.299

Kirsch A.A., The influence of an external electric field on the deposition of aerosols in fibrous filters, Journal of Aerosol Science, 3 (1972) 25–29.

Kirsch A.A., Stechkina I.B., Fuchs N.A., Effect of gas slip on the pressure drop in fibrous filters, Journal of Aerosol Science, 4 (1973) 287–293. DOI: https://doi.org/10.1016/0021-8502(73)90089-X

Kirsh A.A., Stechkina I.B., Fuchs N.A., Efficiency of aerosol filters made of ultrafine polydisperse fibres, Journal of Aerosol Science, 6 (1975) 119–120.

Kirsch A.A., Stechkina I.B., The theory of aerosol filtration with fibrous filters, Section 4, in: Fundamentals of Aerosol Science, D.T. Shaw (Ed.), Wiley-InterScience, New York, (1978) pp. 170–252.

Koch M., Krammer G., The Permeability distribution (PD) method for filter media characterization, Aerosol Science and Technology, 42 (2008) 433–444.

Kraemer H.F., Johnstone H.F., Collection of aerosol particles in presence of electrostatic fields, Industrial & Engineering Chemistry, 47 (1955) 2426–2434. DOI: 10.1021/ie50552a020

Kuo Y.Y., Bruno F.C., Wang J., Filtration performance against nanoparticles by electrospun nylon-6 media containing ultrathin nanofibers, Aerosol Science and Technology, 48 (2014) 1332–1344.

Kuwabara S., The forces experienced by randomly distributed parallel circular cylinders or spheres in a viscous flow at small Reynolds numbers, Journal of the Physical Society of Japan, 14 (1959) 527–532. DOI: 10.1143/JPSJ.14.527

Lamb H., Hydrodynamics, Cambridge University Press, Cambridge, UK, 1932.

Landahl H.D., Herrmann R.G., Sampling of liquid aerosols by wires, cylinders, and slides, and the efficiency of impaction of the droplets, Journal of Colloid Science, 4 (1949) 103–136. DOI: 10.1016/0095-8522(49)90038-0

Langumuir I., Filtration of aerosols and the development of filter materials, OSRD, Report No.865, 1942.

Lee K.W., Liu B.Y.H., Experimental study of aerosol filtration by fibrous filters, Aerosol Science and Technology, 1 (1981) 35–46.

Lee K.W., Liu B.Y.H., Theoretical study of aerosol filtration by fibrous filters, Aerosol Science and Technology, 1 (1982) 147–161. DOI: 10.1080/02786828208958584

Lee M., Otani Y., Namiki N., Emi H., Prediction of collection efficiency of high-performance electret filters, Journal of Chemical Engineering of Japan, 35 (2002) 57–62. DOI: 10.1252/jcej.35.57

Leith D., First M.W., Performance of a pulse-jet filter at high filtration velocity I. Particle collection, Journal of the Air Pollution Control Association, 27 (1977a) 534–539. DOI: 10.1080/00022470.1977.10470452

Leith D., First M.W., Feldman H., Performance of a pulse-jet filter at high filtration velocity II. Filter cake redeposition, Journal of the Air Pollution Control Association, 27 (1977b) 636–642. DOI: 10.1080/00022470.1977.10470465

Leith D., First M.W., Gibson D.D., Performance of a high velocity pulse-jet filter, U.S. Environmental Protection Agency, Washington, D.C., EPA/600/7-78/131, 1978.

Leith D., Ellenbecker M.J., Theory for pressure drop in a pulse-jet cleaned fabric filter, Atmospheric Environment (1967), 14 (1980) 845–852. DOI: 10.1016/0004-6981(80)90141-9

Leith D., Ellenbecker M.J., Dust emission characteristics of pulse-jet-cleaned fabric filters, Aerosol Science and Technology, 1 (1982) 401–408. DOI: 10.1080/02786828208958604

Leung W.W.-F., Hung C.-H., Investigation on pressure drop evolution of fibrous filter operating in aerodynamic slip regime under continuous loading of sub-micron aerosols, Separation and Purification Technology, 63 (2008) 691–700. DOI: 10.1016/j.seppur.2008.07.015

Leung W.W.-F., Hung C.-H., Yuen P.-T., Experimental investigation on continuous filtration of sub-micron aerosol by filter composed of dual-layers including a nanofiber layer, Aerosol Science and Technology, 43 (2009) 1174–1183.

Li J., Li S., Zhou F., Effect of cone installation in a pleated filter cartridge during pulse-jet cleaning, Powder Technology, 284 (2015) 245–252.

Li S.Q., Marshall J.S., Discrete element simulation of micro-particle deposition on a cylindrical fiber in an array, Journal of Aerosol Science, 38 (2007) 1031–1046.

Lo L., Hu S., Chen D.R., Pui D.Y.H., Numerical study of pleated fabric cartridges during pulse-jet cleaning, Powder Technology, 198 (2010a) 75–81.

Lo L., Chen D.R., Pui D.Y.H., Experimental study of pleated fabric cartridges in a pulse-jet cleaned dust collector, Powder Technology, 197 (2010b) 141–149.

Löffler F., Dietrich H., Flatt W., Dust Collection with Bag Filters and Envelope Filters, Springer, 1988, ISBN 978-3-663-07900-2

Lu H.-C., Tsai C.-J., A Pilot-scale study of the design and operation parameters of a pulse-jet baghouse, Aerosol Science and Technology, 29 (1998) 510–524.

Lundgren D.A., Whitby K.T., Effect of particle electrostatic charge on filtration by fibrous filters, Industrial & Engineering Chemistry Process Design and Development, 4 (1965) 345–349. DOI: 10.1021/i260016a001

Ma H., Yoon K., Rong L., Mao Y., Mo Z., Fang D., Hollander Z., Gaiteri J., Hsiao B.S., Chu B., High-flux thin-film nanofibrous composite ultrafiltration membranes containing cellulose barrier layer, Journal of Materials Chemistry, 20 (2010) 4692–4704. DOI: 10.1039/B922536F

Makino K., Iinoya K., Experiments on collection efficiency of dielectric fiber mat filter, Chemical Engineering, 32 (1968) 99–104. DOI: 10.1252/kakoronbunshu1953.32.99

Makino K., Iinoya K., Estimation of collection efficiency of a dielectric fibrous filter, Chemical Engineering, 33 (1969a) 684–689. DOI: 10.1252/kakoronbunshu1953.33.684

Makino K., Iinoya K., Collection efficiency of a single fiber in a fibrous filter and in a porous medium filter, Chemical Engineering, 33 (1969b) 1261–1265. DOI: 10.1252/kakoronbunshu1953.33.1261

Makino K., Iinoya K., Shibamoto M., Toyama S., Ikazaki F., Experiments on electrical dislodging of dust layer, Kagaku Kogaku Ronbunshu, 2 (1976) 31–37. DOI: 10.1252/kakoronbunshu.2.31

Mao N., Yao Y., Hata M., Wada M., Kanaoka C., Comparison of filter cleaning performance between VDI and JIS testing rigs for cleanable fabric filter, Powder Technology, 180 (2008) 109–114.

Medjimorec V., Okuyama K., Payatakes A.C., Estimation of the drag forces acting on particle dendrites, Journal of Colloid and Interface Science, 82 (1981) 543–559. DOI: 10.1016/0021-9797(81)90396-9

Ming L., Chen D.R., Pui D.Y.H., Experimental study of pleated fabric cartridges in a pulse-jet cleaned dust collector, Powder Technology, 197 (2010) 141–149.

Mori Y., Kubori T., Ishizuka M., Makino K., Iinoya K., Fundamental experiments on the performance of dust filter fabrics, Kagaku Kougaku Ronbunshu, 5 (1979) 506–512.

Mouret G., Thomas D., Chazelet S., Collin J.-C.A., Bemer D., Penetration of nanoparticles through fibrous filters perforated with defined pinholes, Journal of Aerosol Science, 40 (2009) 762–775.

Mouret G., Chazelet S., Thomas D., Bemer D., Discussion about the thermal rebound of nanoparticles, Separation and Purification Technology, 78 (2011) 125–131. DOI: 10.1016/j.seppur.2011.01.016

Mukhopadhyay, A., Pulse-jet filtration: An effective way to control industrial pollution Part I: Theory, selection and design of pulse-jet filter, Textile Progress, 41 (2009a) 195–315.

Mukhopadhyay A., Pulse-jet filtration: An effective way to control industrial pollution Part II: Process characterization and evaluation of filter media, Textile Progress, 42 (2009b) 1–97.

Müller T., Meyer J., Kasper G., Low Reynolds number drag and particle collision efficiency of a cylindrical fiber within a parallel array, Journal of Aerosol Science, 77 (2014a) 50–66. DOI: 10.1016/j.jaerosci.2014.07.007

Müller T.K., Meyer J., Thébault E., Kasper G., Impact of an oil coating on particle deposition and dust holding capacity of fibrous filters, Powder Technology, 253 (2014b) 247–255.

Myojo T., Kanaoka, C., Emi H., Experimental observation of collection efficiency of a dust-loaded fiber, Journal of Aerosol Science, 15 (1984) 483–489.

Naito M., Tsubaki J., Jimb G., Shearing direction dislodgement of deposited dust layer on fabric filter-dislodgement by impaction acceleration-, Kagaku Kougaku Ronbunshu, 10 (1984) 744–749.

Natanson G.L., Diffusional deposition of aerosols on a flow-around cylinder impact of electrostatic attraction, Doklady Akademii Nauk SSSR, 112 (1957a) 696–699.

Natanson G.L., Diffusional precipitation of aerosols on a streamlined cylinder with a small capture coefficient, Proceedings of the Academy of Sciences of the USSR, 112 (1957b) 21–25.

Nguyen X., Beeckmans J.M., Single fibre capture efficiencies of aerosol particles in real and model filters in the inertial-interceptive domain, Journal of Aerosol Science, 6 (1975) 205–212.

Nifuku M., Zhou Y., Kiaiel A., Kobayashi T., Katoh H., Charging characteristics for electret filter materials, Journal of Aerosol Science, 51–52 (2001) 200–2005.

Otani Y., Emi H., Mori J., Initial collection efficiency of electret filter and its durability for solid and liquid particles, Kagaku Kougaku Ronbunshu, 18 (1992) 240–247.

Otani Y., Emi H., Mori J., Initial collection efficiency of electret filter and its durability for solid and liquid particles, KONA Powder and Particle Journal, 11 (1993) 207–214.

Otani Y., Emi H., Cho S.J., Namiki N., Generation of nanometer size particles and their removal from air, Advanced Powder Technology, 6 (1995) 271–281.

Otani Y., Bao L., Namiki N., Hosokawa M., Emi H., Influence of internal structure of fibrous filter on collection performance at low Peclet number, Kagaku Kougaku Ronbunshu, 24 (1998) 772–777.

Overcamp T.J., Filtration by randomly distributed fibers, Journal of Aerosol Science, 16 (1985) 473–475.

Park B.H., Lee M.-H., Kim S.B., Kim G.S., Jo Y.M., Preparation and characterization of porous composite filter medium by polytetrafluoroethylene foam coating, Journal of the Air & Waste Management Association, 60 (2010) 137–141.

Park B.H., Lee M.-H., Jo Y.M., Kim S.B., Influence of pleat geometry on filter cleaning in PTFE/glass composite filter, Journal of the Air & Waste Management Association, 62 (2012) 1257–1263.

Payatakes A.C., Model of the dynamic behavior of a fibrous filter. Application to case of pure interception during period of unhindered growth, Powder Technology, 14 (1976a) 267–278.

Payatakes A.C., Tien C., Particle deposition in fibrous media with dendrite-like pattern: A preliminary model, Journal of Aerosol Science, 7 (1976b) 85–94.

Payatakes A.C., Model of transient aerosol particle deposition in fibrous media with dendritic pattern, AIChE Journal, 23 (1977) 192–202.

Payatakes A.C., Gradoń L., Dendritic deposition of aerosol particles in fibrous media by inertial impaction and interception, Chemical Engineering Science, 35 (1980) 1083–1096. DOI: https://doi.org/10.1016/0009-2509(80)85097-4

Payatakes A.C., Okuyama K., Effects of aerosol particle deposition on the dynamic behavior of uniform or multilayer fibrous filters, Journal of Colloid and Interface Science, 88 (1982) 55–78. DOI: https://doi.org/10.1016/0021-9797(82)90155-2

Payet S., Boulaud D., Madelaine G., Renoux A., Penetration and pressure drop of a HEPA filter during loading with submicron liquid particles. Journal of Aerosol Science, 23 (1992) 723–735.

Pich J., Pressure drop of fibrous filters at small Knudsen numbers, The Annals of Occupational Hygiene, 9 (1966) 23–27. DOI: 10.1093/annhyg/9.1.23

Pich J., Emi H., Kanaoka C., Coulombic deposition mechanism in electret filters, Journal of Aerosol Science, 16 (1987) 29–35.

Pnueli D., Gutfinger C., Moldavsky L., Shuster K., Fichman M., Electrostatic porous filter with a blocking electrode, Journal of Aerosol Science, 31 (2000) 1371–1379.

Podgórski A., Bałazy A., Gradoń L., Application of nanofibers to improve the filtration efficiency of the most penetrating aerosol particles in fibrous filters, Chemical Engineering Science, 61 (2006) 6804–6815.

Podgórski A., Estimation of the upper limit of aerosol nanoparticles penetration through inhomogeneous fibrous filters, Journal of Nanoparticle Research, 11 (2009) 197–207. DOI: 10.1007/s11051-008-9472-2

Podgórski A., Maißer A., Szymanski W.W., Jackiewicz, A., Gradon, L., Singly charged nanoparticles through polydisperse fibrous filters, Journal of Aerosol Science and Technology, 45 (2011) 215–233.

Przekop R., Moskal A., Gradoń A., Lattice-Boltzmann approach for description of the structure of deposited particulate matter in fibrous filters, Journal of Aerosol Science, 34 (2003) 133–147.

Qian F., Huang N., Zhu X., Lu J., Numerical study of the gas–solid flow characteristic of fibrous media based on SEM using CFD–DEM, Powder Technology, 249 (2013) 63–70.

Qian Y., Bi Y., Zhang M., Chen H., Xu G., Effect of filtration operation and surface treatment on pulse-jet cleaning performance of filter bags, Powder Technology, 277 (2015) 82–88.

Rengasamy S., King W.P., Eimer B.C., Shaffer R.E., Filtration performance of NIOSH-approved N95 and P100 filtering facepiece respirators against 4 to 30 nanometer-size nanoparticles, Journal of Occupational and Environmental Hygiene, 5 (2008) 556–564. DOI: 10.1080/15459620802275387

Romay F.J., Liu B.Y.H., Chae S.-J., Experimental study of electrostatic capture mechanisms in commercial electret filters, Aerosol Science and Technology, 28 (1998) 224–234. DOI: 10.1080/02786829808965523

Sae-lim W., Tanthapanichakoon W., Kanaoka C., Correlation for the efficiency enhancement factor of a single electret fiber, Journal of Aerosol Science, 37 (2006) 228–240. DOI: 10.1016/j.jaerosci.2005.05.001

Sakano T., Otani Y., Namiki N., Emi H., Particle collection of medium performance air filters consisting of binary fibers under dust loaded conditions, Separation and Purification Technology, 19 (2000) 145–152. DOI: 10.1016/S1383-5866(99)00086-6

Saleem M., Krammer G., Khan R.U., Tahir M.S., Influence of operating parameters on cake formation in pilot scale pulse-jet bag filter, Powder Technology, 224 (2012) 28–35.

Sanchez A.L., Hubbard J.A., Dellinger J.G., Servantes B.L., Experimental study of electrostatic aerosol filtration at moderate filter face velocity, Aerosol Science and Technology, 47 (2013) 606–615.

Sato S., Chen D.R., Pui D.Y.H., Molecular dynamics study of nanoparticle collision with a surface–implication to nanoparticle filtration, Aerosol and Air Quality Research, 7 (2007) 278–303.

Scheibel H.G., Porstendörfer J., Penetration measurements for tube and screen-type diffusion batteries in the ultrafine particle size range, Journal of Aerosol Science, 15 (1984). 673–682.

Schmidt E., Löffler F., Preparation of dust cakes for microscopic examination, Powder Technology, 60 (1990) 173–177.

Schmidt E., Simulation of three-dimensional dust structures via particle trajectory calculations for cake-forming filtration, Powder Technology, 86 (1996) 113–117.

Shapiro, M., Kettner, I.J., Brenner, H., Transport mechanics and collection of submicrometer particles in fibrous filters. Journal of Aerosol Science, 22 (1991) 707–722.

Shin W.G., Mulholland G.W., Kim S.C., Pui D.Y.H., Experimental study of filtration efficiency of nanoparticles below 20 nm at elevated temperatures., Journal of Aerosol Science, 39 (2008) 488–499.

Shin-Kogaiboushi no gijutsutohouki 2015, Taiki-hen; Maruzen, 2015, p. 337, ISBN 978-4-86240-151-9.

Shou D., Fan J., Zhang H., Qian X., Ye L., Filtration efficiency of non-uniform fibrous filters, Aerosol Science and Technology, 49 (2015) 912–919.

Silva C.R.N., Negrini V.S., Aaguiar M.L., Coury J.R., Influence of gas velocity on cake formation and detachment, Power Technology, 101 (1999) 165–172.

Simon X., Chazelet S., Thomas D., Bémer D., Régnier R., Experimental study of pulse-jet cleaning of bag filters supported by rigid rings, Powder Technology, 172 (2007) 67–81.

Simon X., Bémer D., Chazelet S., Thomas D., Down-stream particle puffs emitted during pulse-jet cleaning of a baghouse wood dust collector: Influence of operating conditions and filter surface treatment, Powder Technology, 261 (2014) 61–70.

Skaptsov A.S., Baklanov A.M., Dubtsov S.N., Laulainen N.S., Sem G., Kaufman S., An experimental study of the thermal rebound effect of nanometer aerosol particles, Journal of Aerosol Science, 27 (1996) S145–S146.

Soltani P., Johari M.S., Zarrebini M., Effect of 3D fiber orientation on permeability of realistic fibrous porous networks, Powder Technology, 254 (2014) 44–56.

Song C.B., Park H.S., Lee K.W., Experimental study of filter clogging with monodisperse PSL particles, Powder Technology, 163 (2006) 152–159.

Stechkina I.B., Fuchs N.A., Studies on fibrous aerosol filters—I. Calculation of diffusional deposition of aerosols in fibrous filters, The Annals of Occupational Hygiene, 9 (1966) 59–64. DOI: 10.1093/annhyg/9.2.59

Stechkina I.B., Kirsch A.A., Fuchs N.A., Studies on fibrous aerosol filters—IV Calculation of aerosol deposition in model filters in the range of maximum penetration, The Annals of Occupational Hygiene, 12 (1969) 1–8. DOI: 10.1093/annhyg/12.1.1

Steffens J., Coury J.R., Collection efficiency of fiber filters operating on the removal of nano-sized aerosol particles: I—Homogeneous fibers, Separation and Purification Technology, 58 (2007a) 99–105. DOI: https://doi.org/10.1016/j.seppur.2007.07.011

Steffens J., Coury J.R., Collection efficiency of fiber filters operating on the removal of nano-sized aerosol particles: II. Heterogeneous fibers, Separation and Purification Technology, 58 (2007) 106–112. DOI: https://doi.org/10.1016/j.seppur.2007.07.012

Stenhouse J.I.T., Japuntich D., Liu B.Y.H., The behaviour of fibrous filters in the initial stages of filter loading, Journal of Aerosol Science, 23 (1992) 761–764.

Smutek M., On the separation of air-borne particles by diffusion, Journal of Aerosol Science, 3 (1972) 337–343. DOI: https://doi.org/10.1016/0021-8502(72)90088-2

Takahashi T., Kanagawa A., Effect of an external electric field on the filtration of aerosols by fibrous filters, Kagaku Kogaku Ronbunshu, 1 (1975) 644–649.

Takahashi T., Kanagawa A., Collection of charged aerosol particles by fibrous filters, Kagaku Kogaku Ronbunshu, 4 (1978) 446–451.

Tanthapanichakoon W., Maneeintr K., Charinpanitkul T., Kanaoka C., Estimation of collection efficiency enhancement factor for an electret fiber with dust load, Journal of Aerosol Science, 34 (2003) 1505–1522.

Thomas J.W., Rimberg D., Miller T.J., Gravity effect in air filtration, Journal of Aerosol Science, 2 (1971) 31–38.

Thomas D., Ouf F.X., Gensdarmes F., Bourrous S., Bouilloux L., Pressure drop model for nanostructured deposits, Separation and Purification Technology, 138 (2014) 144–152. DOI: 10.1016/j.seppur.2014.09.032

Tsubaki J., Naito M., Tagami H., Kousaka H., Jimbo G., Dislogdement of deposited dust layer on fabric filter by normal stress dislodgement by impaction acceleration, Kagaku Kogaku Ronbunshu, 8 (1982) 481–486.

Turner J.H., Viner A.S., McKenna J.D., Jenkins R.E., Vatavuk W.M., Sizing and costing of fabric filters, JAPCA (Journal of the Air Pollution Control Association), 37 (1987a) 749–759. DOI: 10.1080/08940630.1987.10466261

Turner J.H., Viner A.S., Jenkins R.E., Vatavuk W.M., McKenna J.D., Sizing and costing of fabric filters part II: Costing considerations, JAPCA (Journal of the Air Pollution Control Association), 37 (1987) 1105–1112. DOI: 10.1080/08940630.1987.10466306

Turnhout J.V., Method for the manufacture of an electret fibrous filter, U.S Patent, (1976) No.3998916.

Van Osdell D.W., Liu B.Y.H., Rubow K.L., Pui D.Y.H., Experimental study of sub-micrometer and ultrafine particle penetration and pressure drop for high efficiency filters, Aerosol Science and Technology, 12 (1990) 911– 925.

van Gulijk C., Bal E., Schmidt-Ott A., Experimental evidence of reduced sticking of nanoparticles on a metal grid, Journal of Aerosol Science, 40 (2009) 362–369. DOI: https://doi.org/10.1016/j.jaerosci.2008.12.005

Wake D., Anomalous effects in filter penetration measurements using the aerodynamic particle sizer (APS 3300), Journal of Aerosol Science, 20 (1989) 13–17.

Wakeman R.J., Hanspal N.S., Waghode A.N., Nassehi V., Analysis of pleat crowding and medium compression in pleated cartridge filters, Chemical Engineering Research and Design, 83 (2005) 1246–1255. DOI: https://doi.org/10.1205/cherd.04183

Walsh D.C., Stenhouse J.I.T., Scurrah K.L., Graef A., The effect of solid and liquid aerosol particle loading on fibrous filter material performance, Journal of Aerosol Science, 27 (1996) S617–S618.

Walsh D.C., Stenhouse J.I.T., Clogging of an electrically active fibrous filter material: experimental results and two-dimensional simulations, Powder Technology, 93 (1997a) 63–75.

Walsh D.C., Stenhouse J.I.T., The effect of particle size, charge, and composition on the loading characteristics of an electrically active fibrous filter material, Journal of Aerosol Science, 28 (1997) 307–321. DOI: https://doi.org/10.1016/S0021-8502(96)00434-X

Wang, H., Kasper, G., Filtration efficiency of nanometer-size aerosol particles, Journal of Aerosol Science, 22 (1991) 31–41.

Wang H., Zhao H., Wang K., He Y., Simulation of filtration process for multi-fiber filter using the Lattice-Boltzmann two-phase flow model, Journal of Aerosol Science, 66 (2013) 164–178.

Wang H.-C., Comparison of thermal rebound theory with penetration measurements of nanometer particles through wire screens, Aerosol Science and Technology, 24 (1996) 129–134.

Wang J., Chen D.R., Pui D.Y.H., Modeling of filtration efficiency of nanoparticles in standard filter media, in: Maynard A.D., Pui D.Y.H. (Eds.), Nanotechnology and Occupational Health, Springer Netherlands, Dordrecht, 2007, pp. 109–115, ISBN: 978-1-4020-5859-2.

Wang J., Kim S.C., Pui D.Y.H., Investigation of the figure of merit for filters with a single nanofiber layer on a substrate, Journal of Aerosol Science, 39 (2008a) 323–334.

Wang J., Kim S.C., Pui D.Y.H., Figure of merit of composite filters with micrometer and nanometer fibers, Aerosol Science and Technology, 42 (2008b) 722–728.

Wang K., Zhao H., The influence of fiber geometry and orientation angle on filtration performance, Aerosol Science and Technology, 49 (2015) 75–85. DOI: 10.1080/02786826.2014.1003278

Wang Q., Lin X., Chen D.-R., Effect of dust loading rate on the loading characteristics of high efficiency filter media, Powder Technology, 287 (2016) 20–28.

Wang W., Xie M., Wang L., An exact solution of interception efficiency over an elliptical fiber collector, Aerosol Science and Technology, 46 (2012) 843–851. DOI: 10.1080/02786826.2012.671559

Wong J.B., Ranz W.E., Johnstone H.F., Collection efficiency of aerosol particles and resistance to flow through fiber mats, Journal of Applied Physics, 27 (1956) 161–169. DOI: 10.1063/1.1722328

Wongsri M., Tanthapanichakoon W., Kanaoka C., Emi H., Convective diffusional collection of polydisperse aerosols on a dust loaded fiber, Advanced Powder Technology, 2 (1991) 11–23. DOI: https://doi.org/10.1016/S0921-8831(08)60717-7

Xiao H., Song Y., Chen G., Correlation between charge decay and solvent effect for melt-blown polypropylene electret filter fabrics., Journal of Electrostatics, 72 (2014) 311–314.

Yamada M., Kuramitsu K., Makino K., On estimation of the mechanical strength of the dust layer collected on bag filter cloths, Kagaku Kogaku Ronbunshu, 13 (1987) 13–19.

Yamada S., Seto T., Otani Y., Influence of filter inhomogeneity on sir filtration of nanoparticles, Aerosol and Air Quality Research, 11 (2011) 155–160.

Yang S., Lee G.W.M., Luo C.-H., Wu C.-C., Yu K.-P., Loading characteristics of filter pretreated with anionic surfactant for monodisperse solid particles, Powder Technology, 156 (2005) 52–60.

Yang S., Lee G.W.M., Filtration characteristics of a fibrous filter pretreated with anionic surfactants for monodisperse solid aerosols, Journal of Aerosol Science, 36 (2005) 419–437.

Yang S., Lee W.-M.G., Huang H.-L., Huang Y.-C., Luo C.-H., Wu C.-C., Yu K.-P., Aerosol penetration properties of an electret filter with submicron aerosols with various operating factors, Journal of Environmental Science and Health, Part A, 42 (2007) 51–57. DOI: 10.1080/10934520601015651

Yao Y., Hata M., Wada M., Kanaoka C., Comparison of filter cleaning performance between VDI and JIS testing rigs for cleanable fabric filter, Powder Technology, 180 (2008) 109–114.

Yoon K., Kim K., Wang X., Fang D., Hsiao B.S., Chu B., High flux ultrafiltration membranes based on electrospun nanofibrous PAN scaffolds and chitosan coating, Polymer, 47 (2006) 2434–2441. DOI: 10.1016/j.polymer.2006.01.042

Yeh H.-C., Liu B.Y.H., Aerosol filtration by fibrous filters—I. theoretical, Journal of Aerosol Science, 5 (1974a) 191–204.

Yeh H.-C., Liu B.Y.H., Aerosol filtration by fibrous filters—II.

experimental, Journal of Aerosol Science, 5 (1974b) 205–217.

Yoneda T., Present status of fabric filter technology, Earozoru Kenkyu, 4 (1989) 278–286. DOI: 10.11203/jar.4.278

Yoneda T., Dust collection technologies by fabric filters, Journal of the Society of Powder Technology, Japan, 38 (2001) 436–445. DOI: 10.4164/sptj.38.436

Yoshioka N., Emi H., Fukushima M., Filtration of aerosols by fibrous filters—Target efficiency at low Reynolds number, Chemical Engineering, 31 (1967a) 157–163. DOI: 10.1252/kakoronbunshu1953.31.157

Yoshioka N., Emi H., Development in air filtration theory, Chemical Engineering, 31 (1967b) 632–636. DOI: 10.1252/kakoronbunshu1953.31.632

Yoshioka N., Emi H., Sone H., Experimental examination of impaction efficiency of aerosol particles by means of the single cylinder, Chemical Engineering, 31 (1967c) 1011–1015. DOI: 10.1252/kakoronbunshu1953.31.1011

Yoshioka N., Emi H., Hattori M., Tamori I., Effect of electrostatic force on the filtration efficiency of aerosol, Chemical Engineering, 32 (1968) 815–820. DOI: 10.1252/kakoronbunshu1953.32.815

Yoshioka N., Emi H., Matsumura H., Yasunami M., Filtration of aerosols through the fibrous packed bed—On the collection efficiency over the whole range of Reynolds number—, Chemical Engineering, 33 (1969a) 381–386. DOI: 10.1252/kakoronbunshu1953.33.381

Yoshioka, N., Emi H., Yasunami M., Sato H., Filtration of aerosols through fibrous packed bed with dust loading, Chemical Engineering, 33 (1969b) 1013–1019. DOI:10.1252/kakoronbunshu1953.33.1013

Yoshioka N., Emi H., Kanaoka C, Yasunami M., Collection efficiency of aerosol by an isolated cylinder—Gravity and interception predominant region, Chemical Engineering, 36 (1972) 313–319. DOI:10.1252/kakoronbunshu1953.36.313

Yun K.M., Hogan C.J., Matsubayashi Y., Kawabe M., Iskandar F., Okuyama K., Nanoparticle filtration by electrospun polymer fibers, Chemical Engineering Science, 62 (2007) 4751–4759. DOI: https://doi.org/10.1016/j.ces.2007.06.007

Zebel G., Deposition of aerosol flowing past a cylindrical fiber in a uniform electric field, Journal of Colloid Science, 20 (1965) 522–543. DOI: https://doi.org/10.1016/0095-8522(65)90033-4

Zhao Z.-M., Tardos G.I., Pfeffer R., Separation of airborne dust in electrostatically enhanced fibrous filters, Chemical Engineering Communications, 108 (1991) 307–332. DOI: 10.1080/00986449108910964

Zhu C., Lin C.-H., Cheung C.S., Inertial impaction-dominated fibrous filtration with rectangular or cylindrical fibers, Powder Technology, 112 (2000) 149–162.

Author's Short Biography

Chikao Kanaoka

He earned Bachler, Master and Doctor degrees at Chemical Engineering, Kyoto University, 1966, 1968 and 1973, respectively.

He worked as research associate, lecturer (full time), Associate Professor and full Professor at Kanazawa University from 1971 to 2004. From 2004 to 2011, he worked at Ishikawa National College of Technology as a President.

He is now Professor Emeritus, Kanazawa University and Ishikawa National College of Technology.

His research interest is air filtration and bag filtration.

Fabrication of Ceramics with Highly Controlled Microstructures by Advanced Fine Powder Processing[†]

Yoshio Sakka

[1] National Institute for Materials Science, Japan

Abstract

Ceramics with highly controlled microstructures at all levels from micrometer to nanometer order are required to improve their properties. To realize such ceramics, advances in powder processing are indispensable. Powder processing involves the preparation of fine particles, surface modification, consolidation, and sintering. The colloidal processing using fine particles has received particular attention as a means of achieving ceramics with highly controlled microstructures. Here, the preparation of fine-grained ceramics through a well-dispersed suspension and the preparation of porous ceramics and nanocomposites through heterocoagulated suspensions are demonstrated. Then novel colloidal processing under an external field such as a strong magnetic field and/or an electric field and the fabrication of textured ceramics and laminated composites are demonstrated.

Keywords: colloidal processing, nanocomposite, heterocoagulation, porous ceramics, textured ceramics, electrophoretic deposition

1. Introduction

Precise control of the hierarchical, graded, laminated, and/or oriented microstructures at all levels from micrometer to nanometer order is required to add new functions and improve the performance of advanced ceramics. To satisfy the requirements for ceramics, advances in powder processing are indispensable (Sakka Y., 2006). Fine powder processing consists of the following processes: (1) preparation of fine particles, (2) surface modification of the fine particles, (3) consolidation, and (4) sintering. To obtain a fine microstructure after sintering, fine particles should be used as the starting material. However, as the particle size decreases, particles tend to agglomerate easily, leading to a nonuniform structure containing large pores caused by the agglomerates. To address this problem, colloidal processing, in which fine particles are dispersed in a solvent, formed, and consolidated, has been attracting attention (Lange F.F., 1989; Akasay I.A., 1991; Sakka Y., 2007).

If fine particles are densely packed in ceramic compacts and the distribution of the pore size is narrowed by controlling the dispersion of the fine particles, densification will occur at low temperatures, resulting in a dense and fine-grained microstructure. In addition, nanocomposites and ordered porous materials can be fabricated by the heterocoagulation of suspensions with well-dispersed fine particles having opposite charges. Furthermore, an electric field and a strong magnetic field applied externally during colloidal processing enable the high-level control of microstructures such as graded, laminated, and/or oriented microstructures.

As effective sintering methods for realizing a rapid temperature increase, microwave or millimeter-wave sintering and pulsed electric current sintering, in which pressure sintering is carried out while a pulsed current or voltage is applied to specimens (generally called spark plasma sintering (SPS), have been attracting attention (Grasso S. et al., 2009). In particular, SPS enables us to obtain compact and fine structures at a low temperature in a short time by applying pressure. Owing to the page limitation, novel sintering methods including SPS are not discussed in this review, but the understanding of the basic sintering mechanisms is very important (Maizza G. et al., 2007, 2009). Needless to say, for the development of high-performance ceramics, feedback from advanced analytical technology and simulations is crucial (Sakka Y., 2006).

This review discusses some merits of colloidal processing and demonstrates the fabrication of fine-grained ceramics using a well-dispersed suspension, and porous ceramics and nanocomposites through heterocoagulated suspensions. Then the fabrication of textured ceramics and laminated composites by novel colloidal processing

---

[†] Received 11 September 2017; Accepted 9 January 2018

[1] 1-2-1 Sengen, Tsukuba 305-0047, Japan
E-mail: sakka.yoshio@nims.go.jp
TEL: +81-29-859-2461 FAX: +81-29-859-2401

under external fields such as a strong magnetic field and/or electric field is described.

2. Fabrication of fine-grained ceramics by colloidal processing

In colloidal processing, fine particles are dispersed in a solution and consolidated to obtain a dense compact. **Table 1** shows typical colloidal processing accompanied by a drain step, in which the transport media and their driving forces are indicated (Nicholson P.S. et al., 1997; Sakka Y., 2007).

Slip casting (**Fig. 1(a)**) is the most widely used method of colloidal processing; a suspension is poured into in a porous mold and a consolidated layer is obtained. The consolidation rate is controlled by the drain rate at which the solvent is removed through the consolidated layer formed by the packed particles. Therefore, the consolidation rate is slower when using fine particles. Pressure casting, vacuum casting, or centrifugal casting is useful for the consolidation of fine particles. In these methods, the solvent is removed and a porous mold is necessary.

Table 1 Typical colloidal processing accompanied by a drain step. Revised by the table in Ref. (Nicholson P.S. et al., 1997), where the movers indicate moving species by each force and the watchers not moving ones.

Method	Force	Actors	
		Watchers	Movers
slip casting	capillarity	particles both ions	liquid
pressure/ vacuum casting	capillarity and/or pressure and/or suction	particles both ions	liquid
centrifugal force casting	centrifugal force	both ions	particles liquid
tape casting	mechanical	liquid particles both ions	-
EPD	electrohydrodynamics electrochemical	liquid	particles both ions

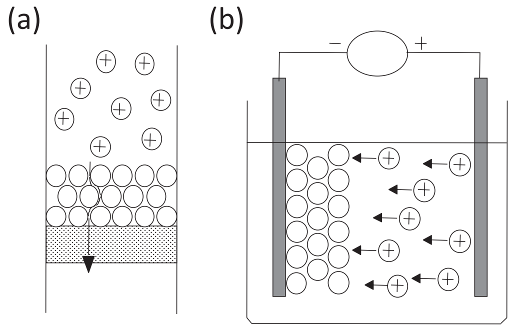

Fig. 1 Schematic of slip casting **(a)** and EPD **(b)**.

Tape casting is a method for forming a sheet film in which the suspension is poured onto a moving sheet via a knife edge, a so-called doctor blade. This process is widely used to form a laminated layer. In electrophoretic deposition (EPD), charged particles are moved and deposited on a substrate in an externally applied electric field. This method is suitable for the fabrication of ceramics with a highly controlled structure from fine particles because the deposition rate is high, regardless of the particle size, and the position and arrangement of the particles as well as the layer thickness can be controlled via the electric field (**Fig. 1(b)**) (Sarkar P. and Nicholson P.S., 1996; Besra L. and Liu M., 2007; Sakka Y. and Uchikoshi T., 2010).

As another colloidal processing without accompanying dehydration, gel casting and floc-casting have received increased attention because of isotropic shrinkage and precise dimensional accuracy (Young A.C. et al., 1991; Omatete O.O. et al., 1997; Santacruz I. et al., 2005; Bednarek P. et al., 2010). These methods are based on in-situ solidification by the polymerization of monomers or flocculation upon heating, etc., using a high-solid loading suspension. When using fine particles, such as a high-solid loading suspension cannot be prepared and a special technique is necessary for applying such a process.

The key to colloidal processing is to control the dispersion and the stabilization of fine particles in a solvent. Therefore, understanding of the characteristics of each particle in the solvent is essential. A ceramic particle is charged in a solvent, particularly in an aqueous suspension, owing to the particle surface (or surface adsorbed species) and solvent. During practical processing, systems where the particle dispersion can be controlled by the pH are limited; therefore, the adsorption of a polyelectrolyte with -COOH or -NH_3 on the powder surface is usually conducted. In this case, electrosteric stabilization is expected owing to the surface charge of the electrolyte and the adsorption of the polymer (Cesarano J. et al., 1998; Zhu X.W. et al., 2003; Tang F.Q. et al., 2006). In general, fine particles tend to agglomerate and a redispersion treatment in a solvent is necessary.

For the redispersion of nanoparticles and heavily aggregated particles, bead milling using small beads with a size of 15–50 μm is effective (Inkyo M. et al., 2006; Suárez G. et al., 2009a,b; Ogi T. et al., 2017). **Fig. 2** shows fine particles of hydroxyapatite (HAP) with a mean size of 48 nm, heavily aggregated HAP particles with a mean size of 280 nm after ultrasonic irradiation, and HAP particles

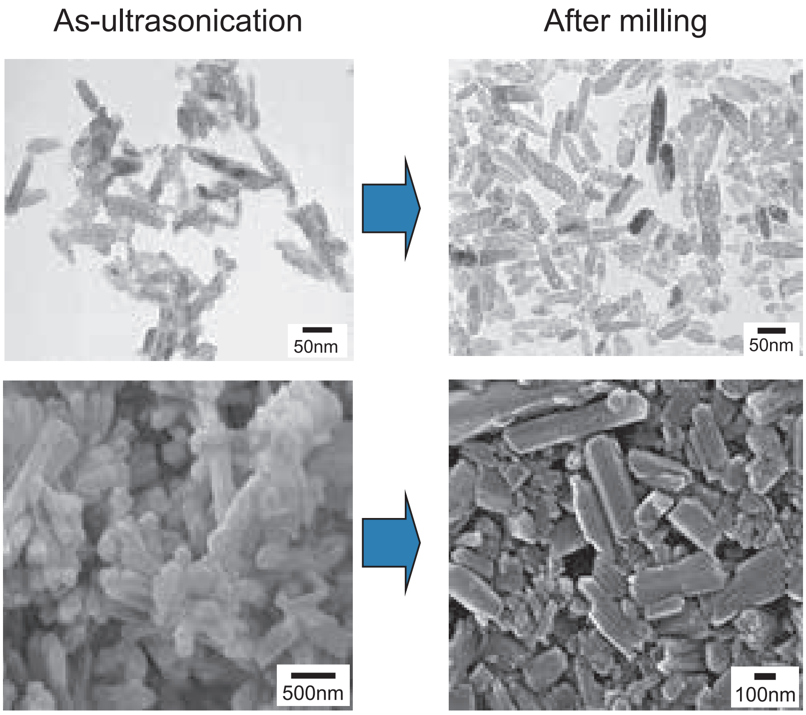

Fig. 2 HAP fine particles with a mean size of 48 nm (upper), heavily aggregated HAP particles with a mean size of 280 nm (lower) after ultrasonic irradiation (left), and those after bead milling (right).

with a mean size of 280 nm after milling using zirconia beads with a size of 50 μm. From the figure, it can be seen that the dispersion of the fine particles and heavily agglomerated particles by ultrasonic irradiation is difficult; however, it is possible by bead milling. A dense compact with a narrow distribution of pore size was fabricated by the pressure filtration of a suspension of fine HAP particles. After sintering at 1000 °C, dense and fine grained HAP with a mean grain size of 170 nm was successfully fabricated (**Fig. 3**).

In ceramic materials in which the grains are rigid, the combination of grain-boundary sliding, grain switching and grain rearrangement due to diffusion (Ashby M.F. and Verrall R.A., 1973; Gifkins R.C., 1978) can be regarded as the main mechanism of superplastic deformation. If this combination is ideally uniform and successive, then superplastic deformation is also uniform and successive without cavitation damage along grain boundaries or at multiple junctions. For such an ideal case, the stress–strain rate relationship is given by

$$\dot{\varepsilon} = \frac{A\sigma_0^n}{d^p}\exp\left(-\frac{Q}{RT}\right) \qquad (1)$$

Here, $\dot{\varepsilon}$ indicates the strain rate; A, a constant; σ_0, the stress; n, the stress index; d, the grain diameter; p, the grain diameter index; Q, the activation energy; R, the gas constant; and T, the temperature. For a fixed combination of stress and temperature, Eq. (1) implies that the strain rate can be increased by a reduction in the grain size. In

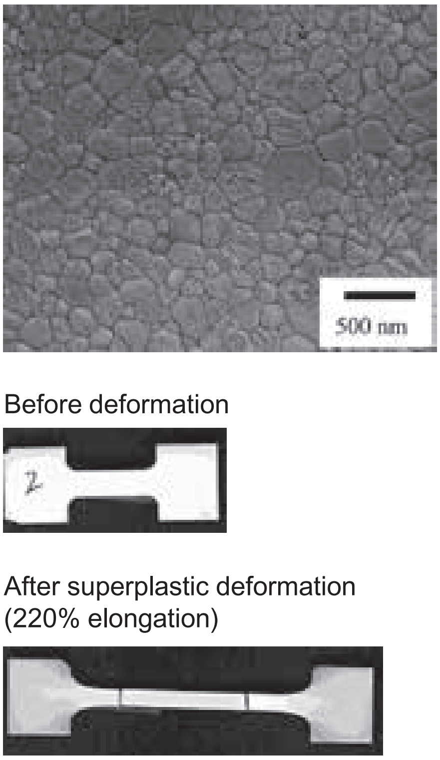

Fig. 3 SEM photo of fine grained HAP after sintering at 1000 °C, and photos before and after superplastic deformation.

actual ceramic materials, however, the combination of grain–boundary sliding, grain switching and grain rearrangement and accommodation is not ideal. Also note that Eq. (1) does not consider any microstructural changes during deformation. Experimental studies have shown that superplastic deformation is inherently accompanied by accelerated grain growth (dynamic grain growth) and intergranular cavitation. The former increases the level of flow stress for a given strain rate and enhances the latter. Since cavitation damage leads to premature failure or degrades the post deformation strength, consideration of these dynamic phenomena is indispensable for attaining superplastic deformation (Hiraga K. et al., 2002, 2005, 2007).

Therefore, the factors contributing to the superplastic deformation in monolithic ceramics are the refinement of the grain size, the decrease in the initial defect density, and a homogeneous microstructure (Sakka Y. et al., 2001; Hiraga K. et al., 2007). These are the merits of colloidal processing using fine particles.

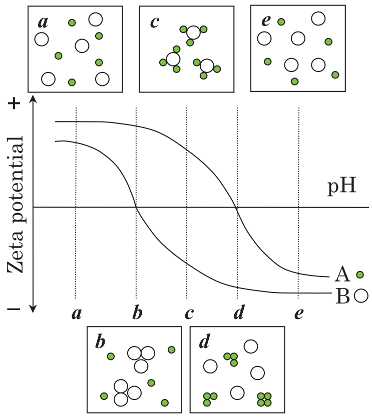

Fig. 4 pH and zeta potential of two components of A and B, and the dispersion state of both components.

When the strain rate was 5.56×10^{-5}/s at 1100 °C, the tension extension of the fine-grained and dense HAP reached the maximum value of 220%, and the superplasticity (above 200% elongation) was achieved in HAP for the first time. **Fig. 3** also shows the shape of the test specimen before and after the tensile test.

3. Heterocoagulation method

Fig. 4 schematically shows the relationship between the pH and zeta potential of components A and B, and the dispersion state of both components. In regions b and d in the figure, the flocculation of one component occurs owing to a low zeta potential, and the dispersion state cannot be established, as schematically shown. In regions a and e, a well-dispersed suspension is obtained owing to the higher zeta potential of both components. In region c, both components are dispersed, but a heterocoagulated suspension is obtained owing to their opposite zeta potentials. In the multicomponent systems, either a well-dispersed suspension or a heterocoagulated suspension is used to obtain a homogeneous microstructure. For a dispersed suspension, segregation during colloidal filtration is a common problem owing to differences in the sedimentation rate, but it can be minimized by using a suspension with a high solid content.

3.1 Ordered porous ceramics

The heterocoagulation method is also applicable to the preparation of porous materials as is schematically shown in **Fig. 5** (Tang F. et al., 2003a, b, 2004; Sakka Y. et al., 2005a). This is based on the templating-assisted approach of a core-shell composite, in which monodisperse polymer

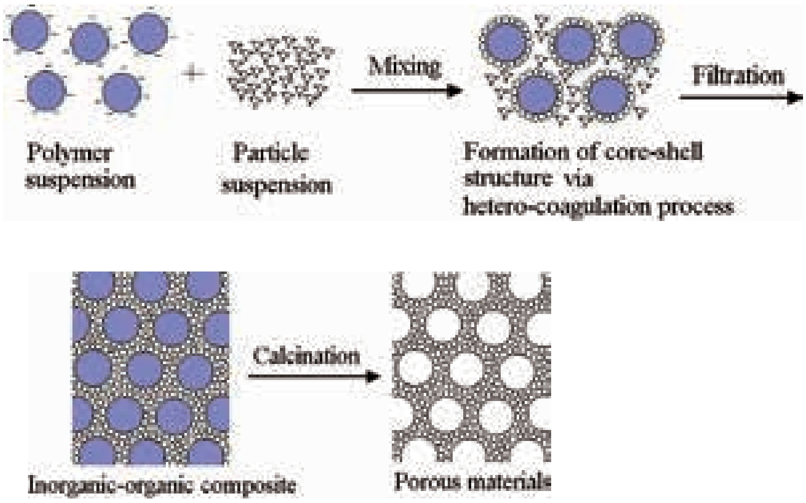

Fig. 5 Schematic of fabrication process of ordered porous ceramics. Reprinted with permission from Ref. (Tang et al., 2004). Copyright: (2004) Elsevier B.V.

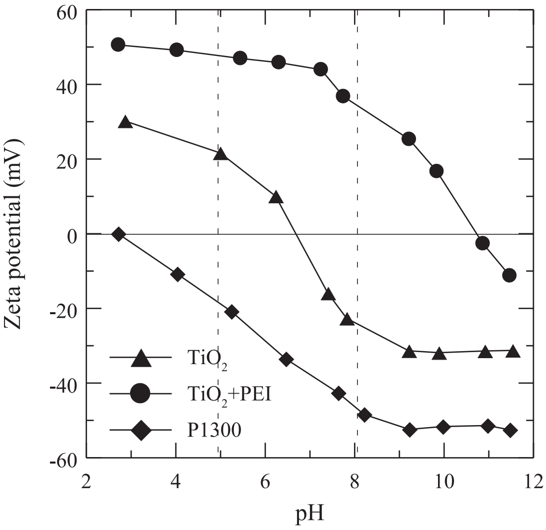

Fig. 6 Relationship between pH and zeta potential when PMMA, titania, or titania + PEI is added. Reprinted with permission from Ref. (Tang et al., 2003a). Copyright: (2003) Elsevier B.V.

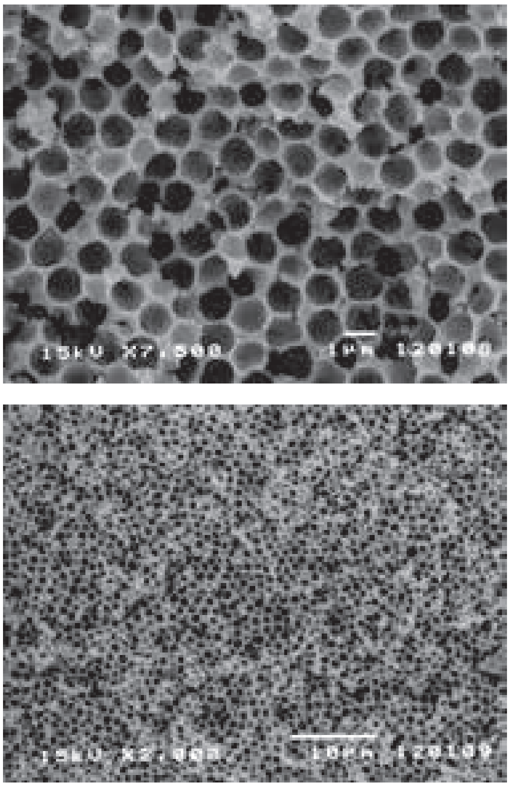

Fig. 7 SEM images of porous titania. High magnification (upper) and low magnification (lower). Reprinted with permission from Ref. (Tang et al., 2003a). Copyright: (2003) Elsevier B.V.

spheres are used as templates, and ceramic particles act as the target materials. By particle surface modification, well-dispersed suspensions of the polymer and ceramic particles with high opposite charges can be obtained at the same pH. When two suspensions are mixed, an electrostatic attractive force is induced between the polymer and ceramic particles, and the polymer particles are uniformly modified by the ceramic particles. After vacuum filtration of the suspension obtained by the heterocoagulation process, the composite is subjected to calcination at a predetermined temperature to remove the spherical polymer particles and loosely sinter the ceramic particles. Through these processes, ordered porous ceramics with regularly arranged pores having the same shape are obtained.

Fig. 6 shows the relationship between the pH and zeta potential of aqueous suspensions when (1) polymethylmethacrylate (PMMA) particles 1300 nm in size, (2) titania particles 30 nm in size, and (3) titania and polyethyleneimine (PEI) particles, were added (Tang F. et al., 2003a). Appropriate amount of PEI was added as a polyelectrolyte to the suspension containing titania to add positive charges to the titania particles, which are negative at pH = ~8, similarly to PMMA. Well-dispersed suspensions with PMMA and with titania and PEI were prepared at pH = ~8 and mixed to enable heterocoagulation. **Fig. 7** shows a scanning electron microscopy (SEM) image of a fractured surface of porous titania obtained by vacuum casting, calcinating for 4 h at 500 °C, and heating again at 850 °C (Tang F. et al., 2003a). It can be seen that three-dimensional porous titania with a uniform pore size was obtained.

Using this method, porous materials of different systems with different particle sizes may be easily fabricated by changing the type and size of the ceramic and polymer particles (Tang F. et al., 2004; Sakka Y. et al., 2005a).

3.2 Highly conductive carbon nanotube (CNT)-dispersed alumina

CNTs with excellent strength and elastic moduli as well as high chemical, thermal and electrical properties (Iijima S. et al., 1996; Falvo M.R. et al., 1997; Palaci I. et al., 2005) have been considered as an ultimate additive to improve the mechanical and electrical properties of conventional ceramics such as alumina. As a method of increasing its conductivity while maintaining its mechanical properties, large amount of multiwall carbon nanotubes (CNTs) is added to alumina. In fact, however, the ability of CNTs to directly improve the macroscopic mechanical properties of CNTs reinforced ceramics has been questioned and debated mainly owing to CNTs agglomeration, poor CNT/matrix interfacial compatibility, CNTs damage during processing (Estili M. and Sakka Y., 2014a). To this end, it is necessary to prepare a mixed powder in which CNTs and alumina are well dispersed and to fabricate a dense sintered material (Estili M. and Sakka Y., 2014a).

High-purity CNT (Bussan Nanotech), synthesized by a catalytic-CVD process and graphitized at about 2600 °C, was prepared and functionalized as follows. The CNT powder was treated with a mixture of H_2SO_4 and HNO_3 with a volume ratio of 3:1 at 110 °C for 20 min. The oxidative agent produced by the sulfonitric mixture was found that oxidation starts with the C-C and C-H bonds generating different oxidized groups from alcohol to carboxylic acid, following a sequential oxidation (Gomez S. et al., 2017). The mixtures were cooled with water and washed up to pH = 7. The hydrophilic CNT powder obtained was dispersed in water by ultrasonic irradiation at pH = 4.4, resulting in the surfactant-free and COOH-terminated CNT aqueous suspension.

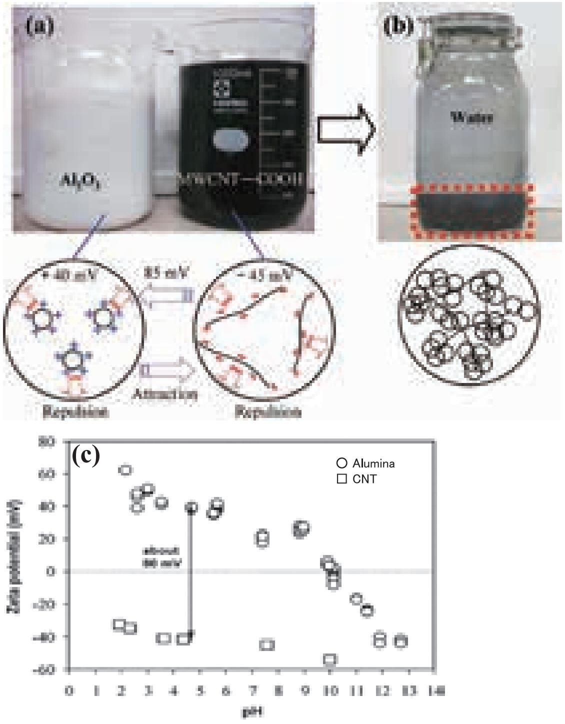

Fig. 8 Suspensions of alumina, CNT powder after hydrophilic treatment, and heterocoagulated suspension. Reprinted with permission from Ref. (Estili M., 2012). Copyright: (2012) Wiley-VCH Verlag GmbH & Co. KGaA, Weinheim.

Suspensions of the hydrophilically treated CNT powder and alumina powder were separately prepared (Estili M. and Kawasaki A., 2008; Estili M. et al., 2008, 2012, 2013). Considering the different surface potentials of CNTs and alumina under acidic conditions, the suspensions were mixed at pH = 4.4 and subjected to heterocoagulation to obtain a well-dispersed mixed powder (**Fig. 8**). By SPS of the CNT–alumina mixed powder (**Fig. 9**, upper) at 1300 °C, a dense nanocomposite of 20 vol% well-dispersed CNT dispersed alumina (**Fig. 9**, lower) was obtained. This sintered material exhibited an electrical conductivity of 5000 S/m, which is the highest reported for an alumina-based material (Estili M. et al., 2012, 2013). The bending strength and fracture toughness of the obtained sintered material with different amounts of CNTs increased up to a CNTconcentration of 10 vol%. It is seen in **Table 2** that the bending strength and fracture toughness obtained with the addition of 20 vol% CNTs were similar to those without the addition of CNTs (Estili M. et al., 2012).

This method has been attracting interest as a fabrication method for high-strength, high-conductivity oxide and non-oxide ceramics (Estili M. and Sakka Y., 2014a; Wu W.W. et al., 2017). This method is also applicable to the graphene dispersed ceramics (Estili M. et al., 2014b).

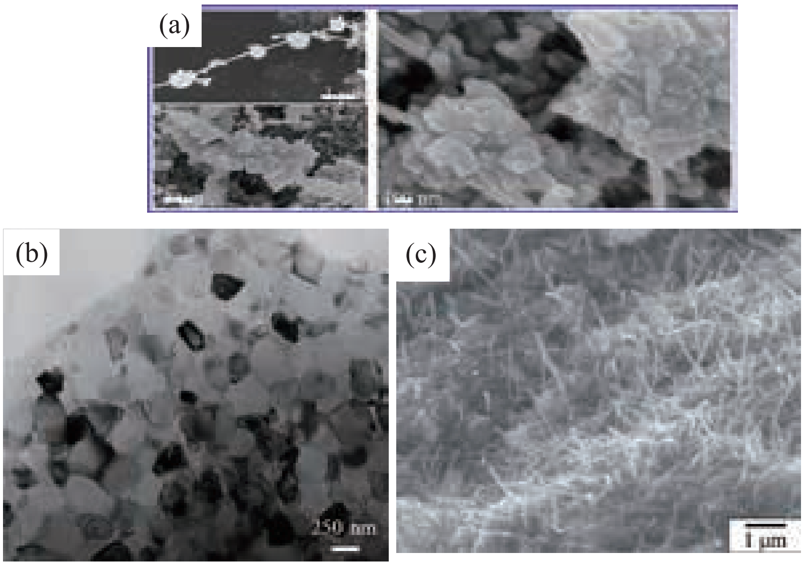

Fig. 9 SEM photos of the heterocoagulated mixed powders **(a)**, and TEM photo **(b)** and fractured SEM photo **(c)** of the dense nanocomposite of 20 vol%-CNT dispersed alumina after SPS at 1300 °C. Reprinted with permission from Ref. (Estili M., 2012). Copyright: (2012) Wiley-VCH Verlag GmbH & Co. KGaA, Weinheim.

Table 2 Comparison of mechanical properties of alumina and CNT dispersed alumina hybrid.

SPSed bulks	Density (g cm^{-3})	Strain to failure (%)	K_{1C}(MPa m$^{0.5}$) Three-point bending (SENB method)	Flexural strength (MPa) Four-point bending
α-Al_2O_3 (reference material)	3.960 (100%)	0.105	4.41	395.82
2.0 vol% hybrid	3.901 (99.44%)	0.11 (+8.2%)	5.78 (+31%)	413.46 (+4.5%)
10.0 vol% hybrid	3.733 (98.91%)	0.19 (+81%)	6.71 (+52.2%)	483.19 (+22%)
20.0 vol% hybrid	3.544 (98.8%)	0.21 (+98%)	4.62 (+4.7%)	403.72 (+2%)

4. Control of crystal orientation by colloidal processing in strong magnetic field

The rotation of particles in a magnetic field is caused by the generation of a magnetic torque due to magnetic anisotropy. If the crystal structure is asymmetrical, such as tetragonal or hexagonal, the magnetic susceptibility depends on the direction of the crystal axis and shows anisotropy. On the basis of the interaction between the anisotropy and the magnetic field, the magnetic torque given by Eq. (2) induces the rotation of particles (Suzuki T.S. et al., 2001; Sakka Y. and Suzuki T.S., 2005b).

$$T = -\Delta\chi V B^2 \sin 2\theta / 2\mu_0 \tag{2}$$

Here, T is the magnetic torque, μ_0 is the magnetic the permeability of vacuum, $\Delta\chi$ is the anisotropy of magnetic susceptibility, V is the volume of particles, B is the magnetic flux density, and θ is the angle between the easy axis of magnetization and the direction of the applied magnetic field. The magnetic torque is usually regarded as negligible because the magnetic susceptibilities of paramagnetic and diamagnetic materials are extremely small. However, with recent advances in the technology of superconductivity, strong magnetic fields exceeding 10 T are now more easily obtained without supplying liquid He, enabling orientation using magnetic torque. Our research group has demonstrated that it is possible to control the crystal orientation of alumina, titania, aluminum nitride, silicon carbide, zinc oxide, silicon nitride, HAP, and piezoelectric ceramics, all of which are diamagnetic and have extremely small magnetic susceptibility, by colloid processing in a strong magnetic field (Sakka Y. and Suzuki T.S., 2005b; Suzuki T.S., et al., 2006a). The uniaxial orientation of alumina and titania is possible by the application of a static magnetic field because their magnetic susceptibilities along the *c*-axis are higher than those along the *a*, *b*-axis (Sakka Y. and Suzuki T.S., 2005b; Suzuki T.S. et al., 2006b). In contrast, for aluminum nitride, silicon carbide, zinc oxide, silicon nitride, and HAP, only a *c*-plane-oriented material is obtained when a static magnetic field is applied because their magnetic susceptibilities along the *a*, *b*-axis are higher than those along the *c*-axis. In this case, uniaxially oriented materials are fabricated using a rotating magnetic field (Tanaka S. et al., 2006; Suzuki T.S., et al., 2009, 2010; Zhu X. and Sakka Y., 2008a; Zhu X. et al., 2010, 2014).

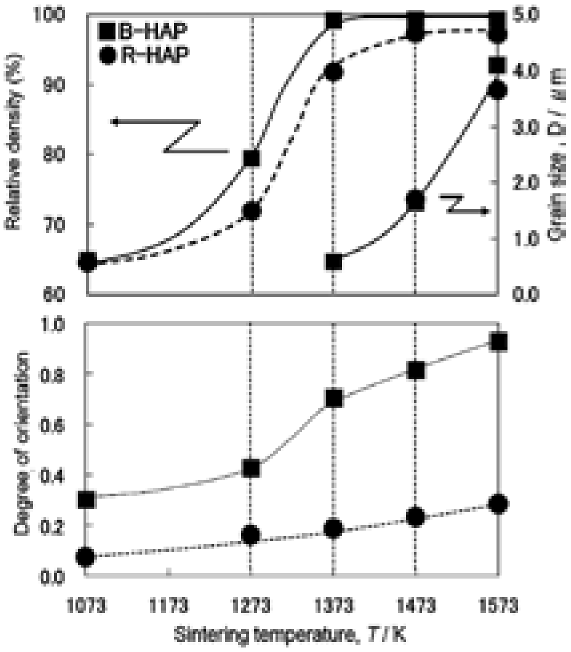

Fig. 10 Temperature dependences of relative density and the grain size (upper), and the Lotgering orientation factor (lower) of heavily agglomerated R-HAP as ultrasonic irradiation and de-agglomerated B-HAP after bead milling (shown in **Fig. 2**).

Fig. 10 compares the Lotgering orientation factor (Lotgering F.K., 1959), grain size, and relative density of heavily agglomerated HAP after ultrasonic irradiation (R-HAP) and redispersed HAP after bead milling treatment (B-HAP) after sintering at fixed temperatures. The higher degree of orientation for the B-HAP is mainly due to the deagglomeration by the milling procedure. It is well known that the slip casting of a well-dispersed suspension yields a dense green body with a narrow pore size distribution, which results in a dense and fine-grained microstructure characterized by low-temperature sintering. This colloidal processing technique is also useful for obtaining highly oriented ceramics.

It can be seen that the orientation factor is promoted by sintering at higher temperatures. The magnetic energy is proportional to the volume of the particle, the square of the magnetic field, and the difference between the crystal susceptibility of *a*, *b* and that of *c*. The orientation factor of HAP is basically determined by the particle size and the magnetic field when each particle is well dispersed. However, owing to thermal fluctuation, each particle tends to align in a specific direction with some distribution of the angle. Therefore, the orientation factor is not so large initially. Then the orientation factor increases with grain growth, where the oriented particles act as a template for the oriented grain growth. These features are confirmed by in situ observation (Hirota N. et al., 2008; Terada N. et al., 2008).

To obtain oriented materials with weak magnetic susceptibility, the following conditions are necessary (Sakka Y. and Suzuki T.S., 2005): (1) the particles should be single-crystal and well dispersed, (2) the crystal structure should be noncubic to yield an anisotropic magnetic susceptibility, (3) the magnetic energy should be larger than the thermal motion energy, (4) the viscosity of the suspension should be sufficiently low for the particles to be rotated with a low energy, and (5) grain growth is necessary to obtain a highly oriented structure, particularly when spherical particles are used. For colloidal processing, slip casting, gel-casting, and EPD have been conducted as will be shown later.

5. Ceramics with highly controlled microstructures

5.1 Highly oriented ceramics

As shown in the previous session, when the magnetic susceptibility along the *a*, *b*-axis is higher than that along the *c*-axis, uniaxially oriented materials can be fabricated using a rotating magnetic field. As an example of the merit of using a rotating magnetic field, the processing of textured β-Si_3N_4 is discussed (Zhu X.W. et al., 2006, 2008, 2010). α-Si_3N_4 (Ube Industry's SN-E10) was used as a raw powder, and 5 mol% Y_2O_3 and 5 mol% Al_2O_3 were added as sintering aids. As a seed, 5 mol% β-Si_3N_4 was added. Ethanol was used as a solvent, 1 wt% PEI was used as a dispersant, and a 30 vol% slurry was prepared. After slip casting under 12 T followed by consolidation, drying, cold isostatic pressing (392 MPa), and calcination (500 °C for 2 h in air), sintering was conducted in a graphite resistance furnace at 1800 °C in 0.2 MPa N_2.

As shown in **Table 3**, a static magnetic field leads to a large decrease in the intensity ratio between the (200) and (101) planes from the top surface to the side surface, indicating the orientation of the *a*, *b*-axis (Zhu X.W., et al., 2008b, 2010). On the other hand, the rotating magnetic field allows the intensity between the (002) and (200) planes to become zero on the side surface, indicating the successful orientation of the *c*-axis. Clearly, the addition of the β-Si_3N_4 seed leads to the substantially higher orientation of β-Si_3N_4 crystals in green bodies in both cases, as indicated by the larger intensity ratios on the top surfaces. **Fig. 11** schematically shows orientation mechanism of static and rotating magnetic fields. **Fig. 12** shows the microstructures of β-Si_3N_4 slip-cast in a static magnetic field of 12 T (left) and β-Si_3N_4 consolidated in a rotating magnetic field (right). Elongated β-Si_3N_4 grains were observed in random directions on an oriented c-plane in a static magnetic field. In contrast, elongated β-Si_3N_4 grains were oriented uniaxially along the c-axis in a rotating magnetic field.

Using Y_2O_3 and $MgSiN_2$ powders as sintering aids, the fabrication of β-Si_3N_4 with a high thermal conductivity of 176 $Wm^{-1}K^{-1}$ along the c-axis was successful (Zhu X.W. et al., 2014). When silicon nitride thus obtained is used as

Table 3 Orientation of β-Si_3N_4 grains in the green and sintered bodies using a static magnetic field (SMF) and rotation magnetic field (RMF).

Sample	Tested surface$^{\#}$	Texture in green body		Texture in sintered body			
		XRD Intensity ratio		Lotgering orientation factor (*f**)			
		SMF	RMF	SMF		RMF	
		$I_{(200)}/I_{(101)}$	$I_{(002)}/I_{(200)}$	15 min	6 h	1 h	3 h
Non-seeded	TS (⊥ B)	2.90	≈0.5	0.68	0.88	0.17	0.24
	SS (// B)	0.75	≈0				
Seeded	TS (// B)	12.4	5.07	0.86	0.97	0.49	0.51
	SS (⊥ B)	0.89	≈0				

$^{\#}$ TS = top surface, SS = side surface. * $f = (P - P_0)/(1 - P_0)$, for SMF, $P_0 = \Sigma I_{0(hk0)}/\Sigma I_{0(hkl)}$ (JCPDS card), $P = \Sigma I_{(hk0)}/\Sigma I_{(hkl)}$ (sample); for RMF, $P_0 = \Sigma I_{0(00l)}/\Sigma I_{0(hkl)}$, $P = \Sigma I_{(00l)}/\Sigma I_{(hkl)}$.

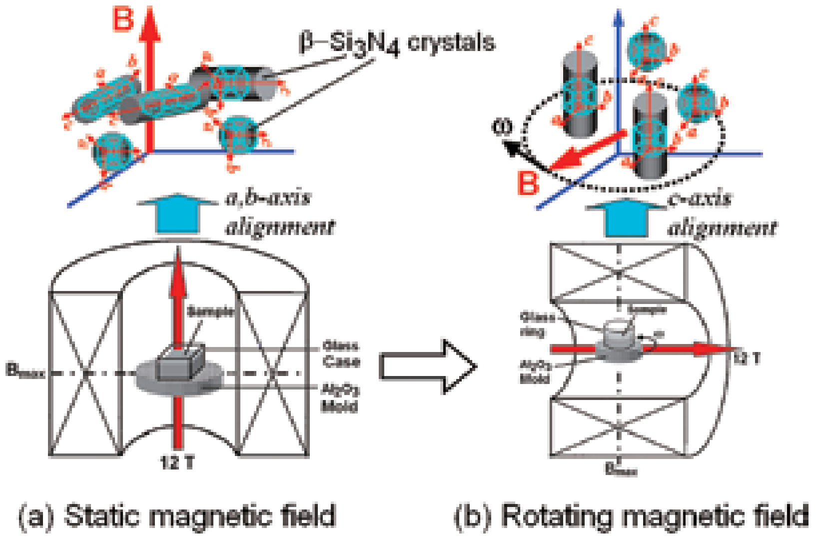

Fig. 11 Schematic of orientation mechanisms of β-Si_3N_4 crystals during slip casting in **(a)** static and **(b)** rotating magnetic fields.

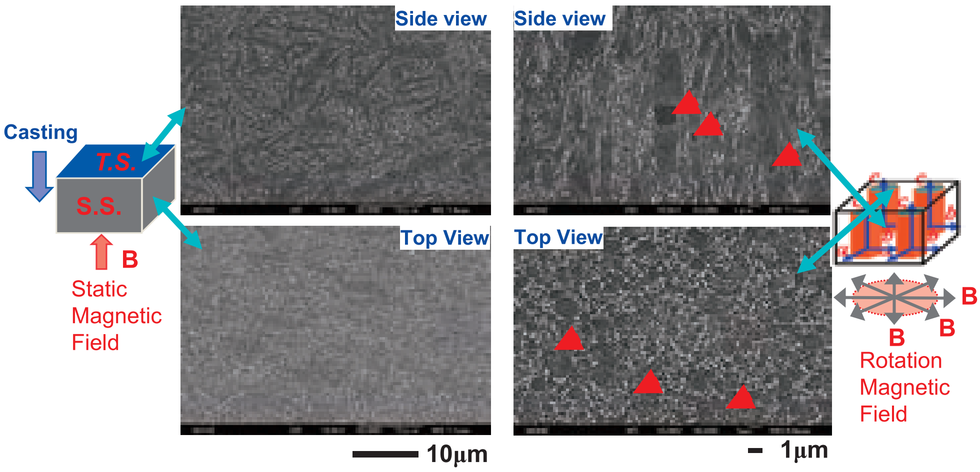

Fig. 12 SEM microstructures of β-Si_3N_4 slip-cast in a static magnetic field of 12 T (left) and β-Si_3N_4 consolidated in a rotating magnetic field (right) after sintering at 1800 °C for 5 h. Reprinted with permission from Ref. (Zhu et al., 2008b). Copyright: (2008) Trans Tech. Pub. LTD.

a heat-radiating substrate, the c-axis can correspond to the thickness direction. Thus, heat-sink substrates made of β-Si_3N_4 are expected to be used in power electronics.

To control the structure of high-functionality materials, biaxial or triaxial orientations are desired rather than a uniaxial orientation.

Bi_3TiNbO_9 planar particles with a biaxial orientation can be obtained by employing gravity and applying a magnetic field (Keskinbora K. et al., 2010; Suzuki T.S. et al., 2013; Gao Z.P. et al., 2015). For platelet particles with micron-order sizes, the largest energy in the dispersion state is the gravitational energy. Therefore, platelet particles are first oriented parallel to the bottom surface, and then they are oriented biaxially by applying a magnetic field. In this case, the lattice constants *a* and *b* are similar (Suzuki T.S. et al., 2013). To obtain a triaxially oriented ceramics, platelet $Bi_4Ti_4O_{15}$ particles, for which the lattice constants *a*, *b*, and *c* are different in the orthorhombic structure, were used and a two-step procedure involving the application of a magnetic field from two directions sequentially were employed (Suzuki T.S. et al., 2016). In addition, triaxially oriented $Y_2Ba_4Cu_7O_y$, which is paramagnetic at room temperature, was obtained in an epoxy resin by changing the rate of rotation of a magnetic field at a modulated rate (modulated rotating magnetic field) (Fukushima T. et al., 2008).

5.2 Nacre-like ceramics

In general, the strength and toughness of ceramics are very difficult to enhance simultaneously; these two factors usually show opposite tendencies. The intrinsic brittleness of ceramics also limits their wide application. The keys to improve material characteristics by controlling the microstructure can be found in nature (Lin A.Y.M. et al., 2006; Munch E. et al., 2008). Through the process of evolution over millions of years, plants and animals have selected the optimal structures to survive in harsh environments. For example, oriented tabular calcium carbonate layers with a thickness of ~100 nm are laminated in nacre. At the interfaces of the layers, a layer containing several percent of protein membranes is inserted to form an oriented laminated structure (hierarchical structure) in **Fig. 13(a)** (Lee S.W. et al., 2008; Meyers M.A. et al., 2008). Compared with sintered calcium carbonate, the hierarchical structure has much higher strength and toughness (fracture toughness). To improve both the strength and toughness simultaneously, the microstructure of the material must have (1) weak grain boundary interfaces and (2) rodlike particles and a tabular structure (Lawn B. R. et al., 1994; Tang Z. et al., 2003). Using these requirements as guidelines, $M_{n+1}AX_n$ (MAX; M, transition metal; A, group A element; X, C or N) phase ceramics have attracted attention as nanolaminates, where ideally $n = 1$–3. MAX has a layered structure (**Fig. 14**) (Barsoum M.W. and El-Raghy T., 2001; Wang X.H. and Zhou Y.C., 2010; Sun Z.M., 2011).

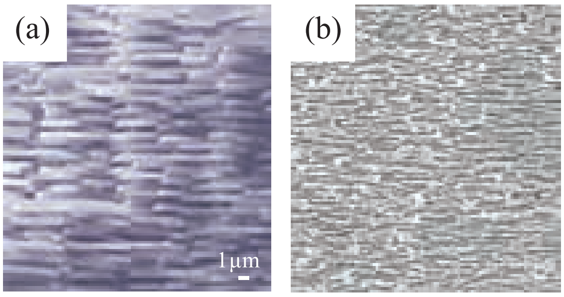

Fig. 13 Microstructures of **(a)** nacre-like layer and **(b)** textured Nb_4AlC_3 ceramic. Reprinted with permission from Ref. (Hu et al., 2011a). Copyright: (2011) Elsevier B.V.

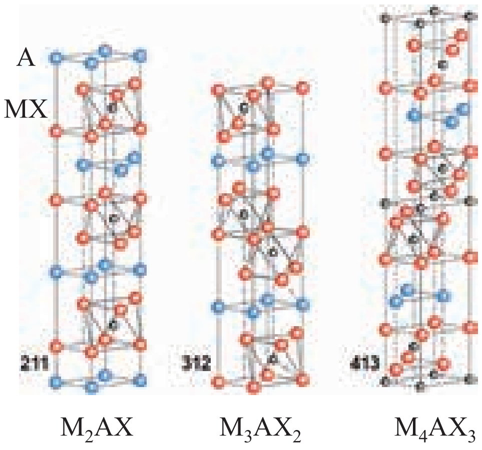

Fig. 14 Layered structures of three types of MAX phase ceramics.

As an example, the results of the microstructure and mechanical properties for the MAX phase ceramic Nb_4AlC_3 are shown (Hu C. et al., 2011a, b, c). The weak bonding between Al atom layers, and Nb and C atom layers contributes to the easy formation of dislocations and their slipping, which induce the development of kink bands in the grains exhibiting "quasi-plastic" behavior. To align Nb_4AlC_3 nanoparticles on a layer, a suspension of Nb_4AlC_3 particles is slip cast in a strong magnetic field and subjected to SPS to obtain a dense compact. From SEM and transmission electron microscopy (TEM) images, the obtained structure has a nacre-like microstructure with layer stacking from the nanoscale to the milliscale shown in **Fig. 13(b)**. Undoubtedly, the microstructure design explains the mechanical responses. Single-edge notched bending (SENB) samples tested along the c-axis direction exhibited the zigzag fracture mode. The zigzag fracture surface corresponds to a high surface energy transformed from the mechanical energy. Additionally, the investigation of the microscale zigzag fracture surface revealed pull-out grains distributed on the entire surface, which means that the toughening mechanisms may involve crack deflection, which increases the surface energy, and crack bridging, which lowers the stress intensity factor at the crack tip (Dericioglu A.F. and Kagawa Y., 2002)

Fig. 15 shows a diagram of the flexural strength and fracture toughness of the textured Nb_4AlC_3 ceramic in comparison with those of other advanced ceramics and other textured MAX phase ceramics (Zhang H.B. et al.,

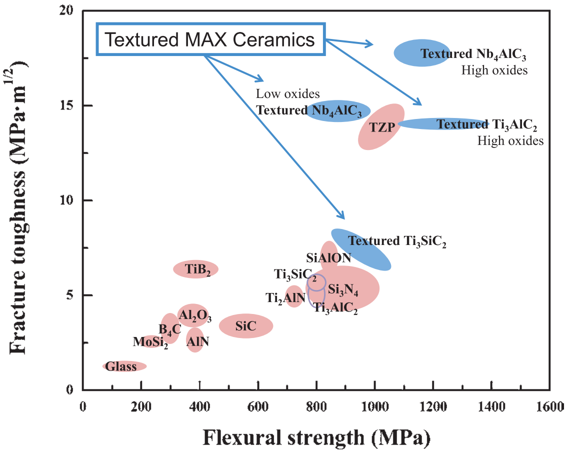

Fig. 15 Relationship between bending strength and fracture toughness of textured MAX phase ceramics and other ceramics, where oxide dispersed MAX phase ceramics was prepared by oxidation of MAX phase powder during powder processing. This figure is revised and added newly obtained data of the Ref. (Hu C. et al., 2011a).

2015). Here the oxide phase is introduced during the powder processing. Textured Nb_4AlC_3 ceramics have the highest bending strength and fracture toughness. The textured MAX phase ceramics are also expected to show anisotropic properties such as electric and thermal conductivities, oxidation resistance, and tribological properties (Xu L.D. et al., 2017). In addition, the processing of MAX phase ceramics is straightforward (Mishra M. et al., 2012a, b; Zhou T.L. et al., 2014; Sato K. et al., 2014a, b; Idzkowska A. et al., 2015). Therefore, structural components with a complicated shape can be easily formed, which is expected to lead to the development and design of high-performance layered ceramic materials.

5.3 Laminated composites

As shown in session 2, during the EPD in which particles themselves move, the deposition rate does not depend on the particle size and is extremely fast. Based on this point, EPD is a suitable method for consolidating nanoparticles and EPD has received a significant amount of attention for fabricating highly structured controlled ceramics resulting in advanced ceramics. As compared with tape casting, EPD is also suitable for the production of thickness-controlled laminates with good adherence between the layers (Uchikoshi T. et al., 2002). Therefore, recently EPD has recently been applied in many fields.

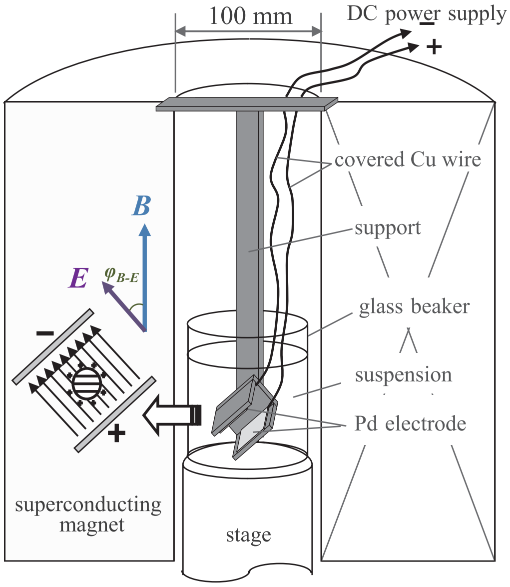

Fig. 16 Schematic of EPD in strong magnetic field.

We have demonstrated that EPD in a high magnetic field is an excellent method to fabricate thick crystalline textured ceramic bodies (Uchikoshi T. et al, 2003, 2004). **Fig. 16** shows a schematic of the experimental setup used for EPD in a strong magnetic field. By changing the angle between the magnetic field and the electric field (φ_{B-E}) during the superposed application of the two fields, the crystal orientation with respect to the substrate is controlled. In addition, by changing φ_{B-E} during EPD at predetermined intervals, layers with different crystal orientations can be deposited.

Fig. 17 shows an example of a crystalline textured alumina/alumina laminated composite deposited by alternately applying magnetic fields with (a) $\varphi_{B-E} = 0°$ and $90°$ and (b) $\varphi_{B-E} = 45°$ and $-45°$. It was possible to align the crystal orientations by controlling φ_{B-E}, regardless of the crystal orientation of the underlying layer, even when the oriented layers were laminated (Uchikoshi T. et al, 2003, 2004; Suzuki T.S. et al., 2006b).

The orientation and laminating technology is effective not only for controlling the mechanical properties but also for improving the functions and reliability of thermoelectric elements, photoelectrodes, ion conductors, piezoelectrics, and dielectrics (Horii S. et al., 2007; Okamoto T. et al., 2006; Kawakita M. et al., 2009; Yamada H. et al., 2013; Zhang C.N. et al., 2014; Miwa Y. et al., 2015; Matsuda M. et al., 2016).

6. Concluding remarks

Colloidal processing has been attracting attention as a consolidation process utilizing the advantages of fine par-

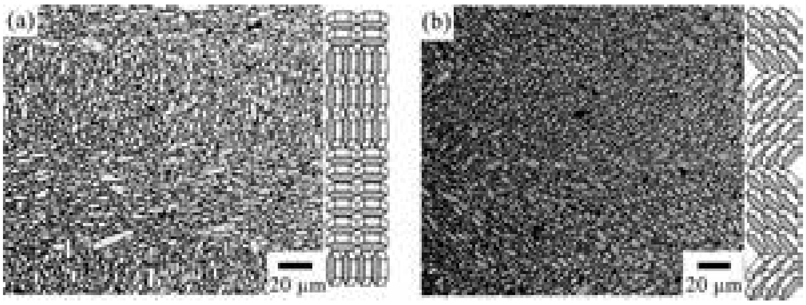

Fig. 17 Crystalline textured alumina/alumina laminated composites deposited by alternately applying magnetic fields with **(a)** $\varphi_{B-E} = 0°$ and $90°$ and **(b)** $\varphi_{B-E} = 45°$ and $-45°$. Reprinted with permission from Ref. (Suzuki et al., 2006b). Copyright: (2006) NIMS & Elsevier B.V.

ticles. Controlling the dispersion of fine particles will enable the fabrication of dense sintered materials, porous ceramics and CNTs-ceramic nanocomposites. In addition, applying electric and magnetic fields externally during consolidation is expected to enable the advanced control of the microstructure. In this review, examples of the fabrication of nacre-like ceramics with textured MAX phase ceramics and laminated composites were introduced. Various material properties, such as corrosion resistance, wear resistance, thermal conductivity, electric conductivity, piezoelectric properties, and transparency, depend on the crystal orientation. Therefore, the method outlined in this review is applicable to all ceramics except those with cubic crystals. In future studies, the characteristic structures and related properties will be analysed to optimize the material structure, which is expected to lead to the development of advanced functional ceramics.

Acknowledgements

This study was supported by many colleagues and postdoctoral researchers at the National Institute of Materials Science, and students at the University of Tsukuba, Tokyo University of Science, Hosei University, and Shibaura Institute of Technology. In particular, I would like to express my sincere thanks to Dr. T. Suzuki (senior researcher), Dr. T. Uchikoshi (group leader), Dr. F.Q. Tan, Dr. S. Grasso, Dr. C. F. Hu and Dr. K. Sato, Dr. X.W. Zhu, and Dr. M. Estille for the support in studies on magnetic field orientation, the EPD process, ordered porous materials, the SPS process, high-intensity MAX phase ceramics, the advances in silicon nitride, and the fabrication of CNT nanocomposites, respectively.

References

Akasay I.A., Molecular and colloidal engineering, Ceramics International, 17 (1991) 267–274.

Ashby M.F., Verrall R.A., Diffusion-accommodated flow and superplasticity, Acta Metallurgica, 21 (1973) 149–163.

Barsoum M.W., El-Raghy T., The MAX phases: Unique new carbide and nitride materials, American Scientist, 89 (2001) 334–343.

Bednarek P., Szafran M., Sakka Y., Mizerski T., Gelcasting of alumina with a new monomer synthesized from glucose, Journal of the European Ceramic Society, 30 (2010) 1795–1801.

Besra L., Liu M., A review on fundamentals and applications of electrophoretic deposition (EPD), Progress in Materials Science, 52 (2007) 1–61.

Cesarano J., Akasay I.A., Bleier A., Stability of aqueous α-Al_2O_3 suspensions with (methacrylic acid) poly-electrolyte, Journal of the American Ceramic Society, 71(1988) 250–255.

Dericioglu A.F., Kagawa Y., Fail-safe light transmitting SiC fiber-reinforced spinel matrix optomechanical composite, Journal of Materials Science, 37 (2002) 523–530.

Estili M., Kawasaki A., Sakamoto H., Mekuchi Y., Kuno M., Tsukada T., The homogeneous dispersion of surfactantless, slightly disordered, crystalline, multiwalled carbon nanotubes in α-alumina ceramics for structural reinforcement, Acta Materialia, 56 (2008) 4070–4079.

Estili M., Kawasaki A., An approach to mass-producing individually alumina-decorated multi-walled carbon nanotubes with optimized and controlled compositions, Scripta Materialia, 58 (2008) 906–909.

Estili M., Kawasaki A., Sakka Y., Highly concentrated 3D macrostructure of individual carbon nanotubes in a ceramic environment, Advanced Materials, 24 (2012) 4322–4326.

Estili M., Sakka Y., Kawasaki A., Unprecedented simultaneous enhancement in strain tolerance, toughness and strength of Al_2O_3 ceramic by multiwall-type failure of a high loading of carbon nanotubes, Nanotechnology, 24 (2013) 155702.

Estili M., Sakka Y., Recent advances in understanding the reinforcing ability and mechanism of carbon nanotubes in ceramic matrix composites, Science and Technology of Advanced Materials, 15 (2014a) 064902.

Estili M., Wu W.W., Khazaei M., Sakka Y., Mechanically reliable thermoelectric (TE) nanocomposites by dispersing and embedding TE-nanostructures inside a tetragonal ZrO_2 matrix: the concept and experimental demonstration in graphene oxide-3YSZ system, Science and Technology of Advanced Materials, 15 (2014b) 014201.

Falvo M.R., Clary G.J., Taylor R.M., Chi V., Brooks F.P., Washburn S., Superfine R., Bending and buckling of carbon nanotubes under large strain, Nature, 389 (1997) 582–584.

Fukushima T., Horii S., Ogino H., Uchikoshi T., Suzuki T.S., Sakka Y., Ishihara A., Shimoyama J.-I., Kishio, K., Triaxial grain orientation of $Y_2Ba_4Cu_7O_y$ achieved by the magneto-science method, Applied Physics Express, 1 (2008) 111701.

Gao Z., Suzuki T.S., Grasso S., Sakka Y., Reece M.J., Highly anisotropic single crystal-like $La_2Ti_2O_7$ ceramic produced by combined magnetic field alignment and templated grain growth, Journal of the European Ceramic Society, 35 (2015) 1771–1776.

Gifkins R.C., Grain rearrangement during superplastic deformation, Journal of Materials Science, 13 (1978) 1926–1936.

Gómez S., Rendtorff N.M., Aglietti E.F., Sakka Y., Suárez G., Intensity of sulfonitric treatment on multiwall carbon nanotubes, Chemical Physics Letters, 689 (2017) 135–141.

Grasso S., Sakka Y., Maizza G., Electric current activated/assisted sintering (ECAS): A review of patents 1906–2008, Science and Technology of Advanced Materials, 10 (2009) 53001.

Hiraga K., Nakano K., Suzuki T.S., Sakka Y., Processing-dependent microstructural factors affecting cavitation damage and tensile ductility in a superplastic alumina dispersed with zirconia, Journal of the American Ceramic Society, 85 (2002) 2763–2770.

Hiraga K., Kim B.-N., Morita K., Suzuki T.S., Sakka Y., Microstructural design for high-strain-rate superplastic oxide ceramics, Journal of the Ceramic Society of Japan, 113 (2005) 191–197.

Hiraga K., Kim B.N., Morita K., Yoshida H., Suzuki T.S., Sakka Y., High-strain-rate superplasticity in oxide ceramics, Science and Technology of Advanced Materials, 8 (2007) 578–587.

Hirota N., Ando T., Shimada T., Wada H., Sakka Y., In situ observation of magnetic orientation process of feeble magnetic materials under high magnetic fields, Science and Technology of Advanced Materials, 9 (2008) 24211.

Horii S., Kumagai T., Uchikoshi T., Suzuki T.S., Sakka Y., Shimoyama J.-i., Kishio K., Improvement of thermoelectric performance in magnetically *c*-axis-oriented bismuth-based cobaltites, Scripta Materialia, 57 (2007) 333–336.

Hu C., Sakka Y., Grasso S., Nishimura T., Guo S., Tanaka H., Shell-like nanolayered Nb_4AlC_3 ceramic with high strength and toughness, Scripta Materialia, 64 (2011a) 765–768.

Hu C., Sakka Y., Tanaka H., Nishimura T., Grasso S, Fabrication of textured Nb_4AlC_3 ceramic by slip casting in a strong magnetic field and spark plasma sintering, Journal of the American Ceramic Society, 94 (2011b) 410–415.

Hu C., Sakka Y., Nishimura T., Guo S., Grasso S., Tanaka H., Physical and mechanical properties of highly textured polycrystalline Nb_4AlC_3 ceramic, Science and Technology of Advanced Materials, 12 (2011c) 44603.

Iijima S., Brabec C., Maiti A., Bernholc J., Structural flexibility of carbon nanotubes, The Journal of Chemical Physics, 104 (1996) 2089–2092.

Inkyo M., Tahara T., Iwaki T., Iskandar F., Hogan C.J., Okuyama K., Experimental investigation of nanoparticle dispersion by beads milling with centrifugal bead separation, Journal of Colloid and Interface Science, 304 (2006) 535–540.

Idzkowska A., Sato K., Sakka Y., Szafran M., Deflocculation and stabilization of Ti_3SiC_2 ceramic powder in gelcasting process, Journal of the Ceramic Society of Japan, 123 (2015) 1010–1017.

Kawakita M., Uchikoshi T., Kawakita J., Sakka Y., Preparation of crystalline-oriented titania photoelectrodes on ITO glasses from a 2-propanol-2,4-pentanedione solvent by electrophoretic deposition in a strong magnetic field, Journal of the American Ceramic Society, 92 (2009) 984–989.

Kawakita M., Kawakita J., Uchikoshi T., Sakka Y., Photoanode characteristics of dye-sensitized solar cell containing TiO_2 layers with different crystalline orientations, Journal of Materials Research, 24 (2011) 1417–1421.

Keskinbora K., Suzuki T.S., Ozer I.Z., Sakka Y., Suvaci E., Hybrid processing and anisotropic sintering shrinkage in textured ZnO ceramics, Science and Technology of Advanced Materials, 11 (2010) 065006.

Lange F.F., Powder processing and technology for increased reliability, Journal of the American Ceramic Society, 72 (1989) 3–15.

Lawn B.R., Padture N.P., Cait H, Guiberteau F., Making ceramics “ductile”, Science, 263, (1994) 1114–1116.

Lee S.W., Kim G.H. Choi C.S., Characteristic crystal orientation of folia in oyster shell, Crassostrea gigas, Materials Science and Engineering: C, 28 (2008) 258–263.

Lin A.Y.M., Meyers M.A., Vecchio K.S., Mechanical properties and structure of Strombus gigas, Tridacna gigas, and Haliotis rufescens sea shells: A comparative study, Materials Science and Engineering: C, 26 (2006) 1380–1389.

Lotgering F.K., Topotactical reactions with ferrimagnetic oxides having hexagonal crystal structures—I, Journal of Inorganic and Nuclear Chemistry, 9 (1959) 113–123.

Maizza G., Grasso S., Sakka Y., Noda T., Ohashi O., Relation between microstructure, properties and spark plasma sintering (SPS) parameters of pure ultrafine WC powder, Science and Technology of Advanced Materials, 8 (2007) 644–654.

Maizza G., Grasso S., Sakka Y., Moving finite-element mesh model for aiding spark plasma sintering in current control mode of pure ultrafine WC powder, Journal of Materials Science, 44 (2009) 1219–1236.

Matsuda M., Hashimoto M., Matsunaga C., Suzuki T.S., Sakka Y. and Uchikoshi T., Electrophoretic fabrication of a-b plane oriented La_2NiO_4 cathode onto electrolyte in strong magnetic field for low-temperature operating solid oxide fuel cell, Journal of the European Ceramic Society, 36 (2016) 4077–4082.

Meyers M.A., Chen P.-Y., Lin A.Y.-M., Seki Y., Biological materials: Structure and mechanical properties, Progress in Materials Science, 53 (2008) 1–206.

Mishra M., Sakka Y., Szudarska A., Szafran M., Suzuki T.S., Uchikoshi T., Textured Ti_3SiC_2 by gelcasting in a strong magnetic field, Journal of the Ceramic Society of Japan, 120 (2012a) 544–547.

Mishra M., Sakka Y., Hu C.F., Suzuki T.S., Uchikoshi T., Besra L., Electrophoretic deposition of Ti_3SiC_2 and texture development in a strong magnetic field, Journal of the American Ceramic Society, 95 (2012b) 2857–2862.

Miwa Y., Kawada S., Kimura M., Omiya S., Kubodera N., Ando A., Suzuki T.S., Uchikoshi T., Sakka Y., Processing and enhanced piezoelectric properties of highly oriented compositionally modified $Pb(Zr,Ti)O_3$ ceramics fabricated by magnetic alignment, Applied Physics Express, 8 (2015) 041501.

Munch E., Launey M.E., Alsem D.H., Saiz E., Tomsia A.P., Ritchie R.O., Tough, Bio-Inspired Hybrid Materials, Science, 322 (2008) 1516–1520.

Nicholson P.S., Sarkar P., De D., Proc. Composites at Lake Louise’97 (1997) 54–66.

Ogi T., Zulhijah R., Iwaki T., Okuyama K., Recent progress in nanoparticle dispersion using bead mill, KONA Powder and Particle Journal, 34 (2017) 3–23.

Okamoto T., Horii S., Uchikoshi T., Suzuki T.S., Sakka Y., Funahashi R., Ando N., Sakurai M., Shimoyama J.-I., Kishio, K., Fabrication of multilayered oxide thermoelectric modules by electrophoretic deposition under high magnetic fields, Applied Physics Letters, 89 (2006) 081912.

Omatete O.O., Janney M.A., Nunn, S.D., Gelcasting: From laboratory development toward industrial production, Journal of the European Ceramic Society, 17 (1997) 407–413.

Palaci I., Fedrigo S., Brune H., Klinke C., Chen M., Riedo E., Radial elasticity of multiwalled carbon nanotubes, Physical Review Letters, 94 (2005) 175502.

Sakka Y., Suzuki T.S., Morita K., Nakano K., Hiraga K., Colloidal processing and superplastic properties of zirconia- and alumina-based nanocomposites, Scripta Materialia, 44 (2001) 2075–2078.

Sakka Y., Tang F., Fudouzi H., Uchikoshi T., Fabrication of porous ceramics with controlled pore size by colloidal processing, Science and Technology of Advanced Materials, 6 (2005a) 915–920.

Sakka Y., Suzuki T.S., Textured development of feeble magnetic ceramics by colloidal processing under high magnetic field, Journal of the Ceramic Society of Japan, 113 (2005b) 26–36.

Sakka Y., Fabrication of highly microstructure controlled ceramics by novel colloidal processing, Journal of the Ceramic Society of Japan, 114 (2006) 371–376.

Sakka Y., 4.5.7 Fabrication of nanoceramics by colloidal processing, in: Hosokawa M., Nogi K., Naito M., Yokoyama T. (Eds.), Nanoparticle Technology Handbook, Elsevier, Amsterdam, 2007, pp. 246–250.

Sakka Y., Suzuki T.S., Uchikoshi T., Fabrication and some properties of textured alumina-related compounds by colloidal processing in high-magnetic field and sintering, Journal of the European Ceramic Society, 28 (2008) 935–942.

Sakka Y. and Uchikoshi T., Forming and microstructure control of ceramics by electrophoretic deposition (EPD), KONA Powder and Particle Journal, 28 (2010) 74–90.

Santacruz I., Nieto M.I., Moreno R., Alumina bodies with near-to-theoretical density by aqueous gelcasting using concentrated agarose solutions, Ceramics International, 31 (2005) 439–445.

Sarkar P., Nicholson P.S., Electrophoretic deposition (EPD): Mechanisms, kinetics, and application to ceramics, Journal of the American Ceramic Society, 79 (1996) 1987–2002.

Sato K., Mishra M., Hirano H., Hu C.F., Sakka Y., Pressureless sintering and reaction mechanisms of Ti_3SiC_2 ceramics, Journal of the American Ceramic Society, 97 (2014a) 1407–1412.

Sato K., Mishra M., Hirano H., Suzuki T. S., Sakka Y., Fabrication of textured Ti_3SiC_2 ceramic by slip casting in a strong magnetic field and pressureless sintering, Journal of the Ceramic Society of Japan, 122 (2014b) 817–821.

Suárez G., Sakka Y., Suzuki T.S., Uchikoshi T., Aglietti E.F., Effect of bead-milling treatment on the dispersion of tetragonal zirconia nanopowder and improvements of two-step sintering, Journal of the Ceramic Society of Japan, 117 (2009a) 470–474.

Suárez G., Sakka Y., Suzuki T., Uchikoshi T., Aglietti E.F., Texture development in 3 mol% yttria-stabilized tetragonal zirconia, Materials Research Bulletin, 44 (2009b) 1802–1805.

Sun Z.M., Progress in research and development on MAX phases: a family of layered ternary compounds, International Materials Reviews, 56 (2011) 143–166.

Suzuki T.S., Sakka Y., Kitazawa K., Orientation amplification of alumina by colloidal filtration in a strong magnetic field and sintering, Advanced Engineering Materials, 3 (2001) 490–492.

Suzuki T.S., Kimura M., Shiratsuyu K., Ando A., Sakka Y., Sakabe Y., Highly controlled orientation of $CaBi_4Ti_4O_{15}$ using a strong magnetic field, Applied Physics Letters, 89 (2006a) 132902.

Suzuki T.S., Uchikoshi T., Sakka Y., Control of texture in alumina by colloidal processing in a strong magnetic field, Science and Technology of Advanced Materials, 7 (2006b) 356–364.

Suzuki T.S., Uchikoshi T., Sakka Y., Effect of sintering additive on crystallographic orientation in AlN prepared by slip casting in a strong magnetic field, Journal of the European Ceramic Society, 29 (2009) 2627–2633.

Suzuki T.S., Uchikoshi T., Sakka Y., Effect of sintering conditions on microstructure orientation in α-SiC prepared by slip casting in a strong magnetic field, Journal of the European Ceramic Society, 30 (2010) 2813–2817.

Suzuki T.S., Miwa Y., Kawada S., Kimura M., Uchikoshi T., Sakka Y., Two-dimensional orientation in $Bi_4Ti_3O_{12}$ prepared using platelet particles and a magnetic field, Journal of the American Ceramic Society, 96 (2013) 1085–1089.

Suzuki T.S., Suzuki Y., Uchikoshi T., Sakka Y., Jones J., Triaxial crystalline orientation of $MgTi_2O_5$ achieved using a strong magnetic field and geometric effect, Journal of the American Ceramic Society, 99 (2016) 1852–1854.

Tanaka S., Makiya A., Kato Z., Uchida N., Kimura T., Uematsu K., Fabrication of *c*-axis oriented polycrystalline ZnO by using a rotating magnetic field and following sintering, Journal of Materials Research, 21 (2006) 703–707.

Tang F., Fudouzi H., Zhang J., Sakka Y., Preparation of macroporous titania from nanoparticle building blocks and polymer templates, Scripta Materialia, 49 (2003a) 735–740.

Tang F., Fudouzi H., Sakka Y., Fabrication of macroporous alumina with tailored porosity, Journal of the American Ceramic Society, 86 (2003b) 2050–2054.

Tang F., Fudouzi H., Uchikoshi T., Sakka Y., Preparation of porous materials with controlled pore size and porosity, Journal of the European Ceramic Society, 24 (2004) 341–344.

Tang F., Uchikoshi T., Ozawa K., Sakka Y., Effect of polyethylenimine on the dispersion and electrophoretic deposition of nano-sized titania aqueous suspensions, Journal of the European Ceramic Society, 26 (2006) 1555–1560.

Tang Z., Kotov N.A., Magonov S., Ozturk B., Nanostructured artificial nacre, Nature Materials, 2 (2003) 413.

Terada N., Suzuki H.S., Suzuki T.S., Kitazawa H., Sakka Y., Kaneko K., Metoki N., In situ neutron diffraction study of aligning of crystal orientation in diamagnetic ceramics under magnetic fields, Applied Physics Letters, 92 (2008) 112507.

Uchikoshi T., Hatton B.D., Sakka Y., Nicholson P.S., Electrical conductivity of a 3Y-TZP/alumina laminate composite synthesized by electrophoretic deposition, Journal of the Ceramic Society of Japan, 110 (2002) 959–962.

Uchikoshi T., Suzuki T.S., Okuyama H., Sakka Y., Electrophoretic deposition of α-alumina particles in a strong magnetic field, Journal of Materials Research, 18 (2003) 254–256.

Uchikoshi, T., Suzuki, T.S., Okuyama, H., Sakka, Y., Nicholson, P.S., Electrophoretic deposition of alumina suspension in a strong magnetic field, Journal of the European Ceramic Society, 24 (2004) 225–229.

Wang X.H., Zhou Y.C., Layered machinable and electrically conductive Ti_2AlC and Ti_3AlC_2 ceramics: a review, Journal of Materials Science & Technology, 26 (2010) 385–416.

Wu W.W., Estili M., Zhang G.J., Sakka Y., Dispersion and structural evolution of multi-walled carbon nanotubes in ZrB_2 matrix, Ceramics International, 43 (2017) 10533–10539.

Xu L., Zhu D., Grasso S., Suzuki T.S., Kasahara A., Tosa M., Kim B.-N., Sakka Y., Zhu M., Hu C., Effect of texture microstructure on tribological properties of tailored Ti_3AlC_2 ceramic, Journal of Advanced Ceramics, 6 (2017) 120–128.

Yamada H., Suzuki T.S., Uchikoshi T., Hozumi M., Saito T., Sakka Y., Ideal design of textured $LiCoO_2$ sintered electrode for Li-ion secondary battery, APL Materials, 1 (2013) 042110.

Young A.C., Omatete O.O., Janney M. A., Menchioffer P.A., Gelcasting of alumina, Journal of the American Ceramic Society, 74 (1991) 612–618.

Zhang C., Uchikoshi T., Liu L., Sakka Y., Hirosaki N., Beta-sialon phosphor deposits fabricated by electrophoretic deposition (EPD) process in a magnetic field, Ceramics International, 40 (2014) 8369–8375.

Zhang H.B., Hu C.F., Sato K., Grasso S., Estili M., Guo S.Q., Morita K., Yoshida H., Nishimura T., Suzuki T.S., Barsoum M.W., Kim B.N., Sakka Y., Tailoring Ti_3AlC_2 ceramic with high anisotropic physical and mechanical properties, Journal of the European Ceramic Society, 35 (2015) 393–397.

Zhou T.L. Kim B., Sakka Y., Hu C.F., Huang Q., Microwave sintering of $Ti_3Si(Al)C_2$ ceramic, Journal of the American Ceramic Society, 97 (2014) 2731–2735.

Zhu X.W., Tang F.Q., Suzuki T.S., Sakka Y., Role of the initial degree of ionization of polyethylenimine in the dispersion of silicon carbide nanoparticles, Journal of the American Ceramic Society, 86 (2003) 189–191.

Zhu X.W., Suzuki T.S., Uchikoshi T., Nishimura T., Sakka, Y., Texture development in Si_3N_4 ceramics by magnetic field alignment during slip casting, Journal of the Ceramic Society of Japan, 114 (2006) 979–987.

Zhu X., Sakka Y., Textured silicon nitride: Processing and anisotropic properties, Science and Technology of Advanced Materials, 9 (2008a) 33001.

Zhu X.W., Suzuki T.S., Uchikoshi T., Sakka Y., Texturing of Si_3N_4 ceramics via strong magnetic field alignment, Key Engineering Materials, 368–372 (2008b) 871–874.

Zhu X.W., Sakka Y., Suzuki T.S., Uchikoshi T., Kikkawa S., The c-axis texturing of seeded Si_3N_4 with β-Si_3N_4 whiskers by slip casting in a rotating magnetic field, Acta Materialia, 58 (2010) 146–161.

Zhu X.W., Sakka Y., Zhou Y., Hirao, K., Itatani, K., A strategy for fabricating textured silicon nitride with enhanced thermal conductivity, Journal of the European Ceramic Society, 34 (2014) 2585–2589.

Author's Short Biography

Yoshio Sakka

Dr. Yoshio Sakka is a Senior Scientist and an advisor of Graduate Program Office at NIMS, Japan. He received his B.E. in 1978, M.E in 1980, and PhD in 1983 from Kyushu University. After receiving his PhD he joined the National Research Institute for Metals (present NIMS). He is the author or coauthor of 19 books, above 650 original referee's papers, above 100 review papers, and above 80 patents (including application). By the above establishment, he received many awards, such as Academy member of World Academy of Ceramics (2009), Richard Brook Award from European Ceramic Society (2011), KONA Award (2014).

KONA Powder and Particle Journal No. 36 (2019) 129–144/Doi:10.14356/kona.2019008 Review Paper

Challenges Associated with the Pulmonary Delivery of Therapeutic Dry Powders for Preclinical Testing[†]

Dominique N. Price[$], **Nitesh K. Kunda**[$] **and Pavan Muttil**[*]

[1] *Department of Pharmaceutical Sciences, College of Pharmacy, The University of New Mexico, Health Sciences Center, USA*

Abstract

Significant progress has been made over the last half-century in delivering therapeutics by the pulmonary route. Inhaled therapeutics are administered to humans using metered-dose inhalers, nebulizers, or dry powder inhalers, and each device requires a different formulation strategy for the therapeutic to be successfully delivered into the lung. In recent years, there has been a shift to the use of dry powder inhalers due to advantages in the consistency of the dose delivered, ease of administration, and formulation stability. Numerous preclinical studies, involving small and large animals, have evaluated dry powder drugs, vaccines, and immunotherapeutics delivered by the pulmonary route. These studies used different dry powder delivery devices including nose-only, whole-body, and intratracheal administration systems, each of which works with different aerosolization mechanisms. Unfortunately, these delivery platforms usually lead to variable powder deposition in the respiratory tract of animals. In this review, we will discuss obstacles and variables that affect successful pulmonary delivery and uniform powder deposition in the respiratory tract, such as the type of delivery device, dry powder formulation, and the animal model used. We will conclude by outlining factors that enhance the reproducible deposition of dry powders in the respiratory tract of preclinical animal models and identifying knowledge and technology gaps within the field. We will also outline the important factors necessary for successful translation of studies performed in preclinical models to humans.

Keywords: pulmonary delivery, dry powders, preclinical models, intratracheal, endotracheal, inhalation devices

1. Introduction

Inhaled therapies and medicines date back to 2000 B.C. in India, where datura roots were smoked for their bronchodilating properties (Anderson, 2012). The ancient Egyptians, the Greeks, and Native cultures in Central and South America all used different forms of inhalable medicines (Anderson, 2012). Even inhaled insulin, a therapy considered relatively recent, was first explored in 1925 by a German scientist named Gansslen (Ghosh and Collier, 2007; Patton and Byron, 2007).

However, the development of dry powders for inhalation by the pharmaceutical industry is a more recent development, with the first commercially available dry powder inhaler (DPI) patented in 1949 (Fields, 1949; Stein and Thiel, 2017). Dry powder therapeutics continue to be a popular pulmonary therapeutic option for patients because of the consistency in the lung dosing, ease of administration, short delivery time, and the excellent stability that is inherent to these formulations (Telko and Hickey, 2005; Vehring, 2008; Sou et al., 2011; Kunda et al., 2016). Since 1987, the number of commercially available DPIs has dramatically increased, and preclinical drug development using dry powders has grown rapidly (Stein and Thiel, 2017).

It is interesting, then, that pulmonary delivery of medicines often meets with resistance and pushback from the general medical community, and that the transition of successful preclinical drug and therapeutic candidates to the clinical trial stage, and finally to the market, has been difficult. A strong argument can be made that this is the result of a lack of the basic foundational tools and regulations which are required to make this transition smoother. This article will review the benefits of pulmonary drug administration, specifically dry powder aerosols, and follow up with an examination of several weak points of preclinical pulmonary delivery of dry powders and how these might be restricting successful translation to humans. Furthermore, the authors will propose areas in need of improvement and speculate on the directions that future dry powder pulmonary delivery in preclinical models needs to take.

[†] Received 24 August 2017; Accepted 21 November 2017
J-STAGE Advance published online 31 March 2018

[1] Albuquerque, New Mexico, 87131, USA
[$] Authors contributed equally to this publication
[*] Corresponding author: Pavan Muttil;
E-mail : pmuttil@salud.unm.edu
TEL: +1-505-272-2569

2. Pulmonary delivery in humans

2.1 Lung anatomy and physiology in the context of drug delivery

The human lung is an excellent platform to deliver drugs both locally and systemically. The large surface area, rapid absorption due to dense vasculature, minimal enzymatic activity (no hepatic first pass), and thin alveolar epithelium (0.1 µm to 0.2 µm) make the lungs an attractive, non-invasive site for delivering drugs (Patil and Sarasija, 2012).

The lungs are a highly structured tissue which resembles an inverted tree. In humans, the primary bronchi divide into the left and right lung, and each lobe further divides into three lobes on the right side and two lobes on the left (Kunda et al., 2013). Each lung branches into at least 23 generations with the first 16 generations made up of bronchi and bronchioles, and by the 17th generation alveoli begin to appear on the respiratory walls (Weibel, 1963). Each branch always divides into two smaller branches or bronchioles (dichotomous branching). By the 20th generation, alveolar ducts begin to appear and the entire lung wall is made up of alveoli. Toward the last generations, the alveolar ducts end in alveolar sacs (Effros, 2006; Kunda et al., 2013) (**Fig. 1**). Together, these lung branches result in a large surface area of approximately 140 square meters (Fernandes and Vanbever, 2009).

The physical, chemical, and physiological factors inherent to the inhaled particles of a particular drug affect the behavior of and ultimately the deposition of the drug in the lungs (Scheuch et al., 2006; Demoly et al., 2014). Proper consideration of the above factors allows for the development of an inhalation product that will deposit reproducible amounts of the drug into the lungs across patient populations. In addition to these factors, barriers to drug deposition and absorption presented by the diseased lung anatomy should be taken into consideration. Barriers such as mucus thickness, alveolar lining fluid, uptake by macrophages, and proteolytic degradation must be adequately incorporated in the design of a suitable formulation for inhalation (Scheuch et al., 2006).

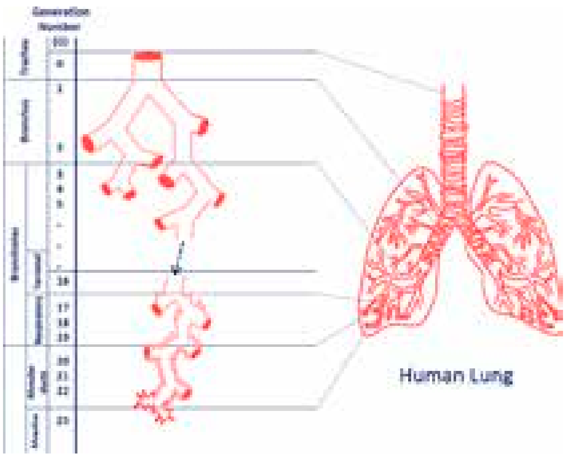

Fig. 1 Human lung with generations. (Adapted from (Kleinstreuer, Zhang and Donohue, 2008; Kunda et al., 2013))

2.2 Formulation and delivery of inhalation products

The formulation of a drug intended for pulmonary delivery together with an inhaler device constitutes an inhalation product (Hou et al., 2015). The compatibility between the inhalation device and the formulation, comprised of the active pharmaceutical ingredient (API) and the excipients, is essential to efficiently deliver the API to the target site. An ideal inhalation product must be easily operated, uncomplicated, handy, should deliver reproducible doses irrespective of temperature, humidity, and patient inspiratory flow rate (Bäckman et al., 2014).

An optimized formulation in a suitable inhaler is crucial for a successful inhalation product. The physico-chemical properties of the formulation such as particle size, morphology, size distribution, particle growth, and solid-state characteristics influence the deposition profile of the API in the lungs (Shaji and Shaikh, 2016). A review by Shaji and Shaikh discussed in detail the characterization techniques used to evaluate various aerosol drug delivery systems (Shaji and Shaikh, 2016). Currently, there are three main pulmonary drug delivery devices marketed: a) nebulizers, b) pressurized metered-dose inhalers (pMDIs), and c) dry powder inhalers (DPIs). The device employed for an inhalation product depends on the properties of the drug substance, choice of excipients, and patient compatibility. In addition, other factors that affect the choice of inhaler include device availability, clinical setting (inpatient, outpatient, emergency department, etc.), patient age, correct usage, device cost, administration duration, and patient convenience (especially during long-term use) (Dolovich et al., 2005).

Furthermore, the choice of drug state (aqueous vs solid), excipients, and device determine the inhalation product (nebulizer vs pMDI vs DPI). For example, albuterol sulfate is available as: a) Ventolin HFA (inhalation product), wherein the drug is a suspension (API in HFA 134a) and device is a pMDI, and b) ProAir Respiclick dry powder, wherein the drug is a dry powder (blend of API and lactose monohydrate) and device is a DPI.

2.3 Pulmonary drug delivery market

Over the last few decades, inhaled product development has seen huge success with hundreds of medications making it to the market (Forbes et al., 2011). Medications providing relief to local lung diseases such as asthma and chronic obstructive pulmonary disorder (COPD) are the major drivers for the inhalation market (Hickey, 2013). Inhalation product development, against cystic fibrosis (CF) (Garcia-Contreras and Hickey, 2003), chemotherapeutics, and macromolecules against lung cancer (Storti et al., 2015) have seen increased attention and are contributing to the continued interest in the development of new aerosol-based therapies. Furthermore, the ability to achieve rapid absorption of drugs from the lungs into the systemic circulation has initiated efforts to develop inhalable macromolecules. New macromolecule dry powder formulations are being designed for many diseases including diabetes, lung cancer, and alpha 1 antitrypsin deficiency. Most of the formulation testing in preclinical models begin with a liquid form of the macromolecule and subsequently transitions toward a dry powder formulation, probably due to the ease of delivery of liquid formulations in animals. However, this linear development process does not lead to novel dry powder inhalation products and the translational success of *de novo* dry powder products from preclinical studies to the clinic has been abysmal. The problems associated with this development process will be discussed later in detail in the "*Implementation of lessons learned from humans to animals*" section.

Table 1 lists a few of the different inhalation products that have been approved over the last few decades. The table shows the expansion of the inhalation market from the 1990's to date with pMDIs and nebulizers occupying the majority of the market compared to DPIs. Moreover, availability of more than one inhaler type per drug by different manufacturers shows the competition in the inhala-

Table 1 Selected inhalation products approved or in clinical trials.

Indication	API	Device	Product	Manufacturer	Approval Date
Asthma and COPD	Albuterol sulfate	pMDI	Proventil HFA	Merck	1999
		pMDI	Ventolin HFA	GlaxoSmithKline	2001
		Nebulizer	AccuNeb	Mylan	2001
		pMDI	ProAir HFA	Teva	2004
		DPI	ProAir Respiclick	Teva	2015
	Budesonide	DPI	Pulmicort Flexhaler	AstraZeneca	1998
		DPI	Pulmicort Turbuhaler	AstraZeneca	1998
		Nebulizer	Pulmicort Respules	AstraZeneca	2000
	Beclomethasone dipropionate + Formoterol fumarate	pMDI	Fostair	Chiesi	2007
		DPI	Fostair Nexthaler	Chiesi	2014
	Fluticasone furoate + vilanterol	DPI	Breo Ellipta	GlaxoSmithKline	2013
Cystic fibrosis	Tobramycin	Nebulizer	Tobi	Novartis	1997
		Nebulizer	Bethkis	Chiesi	2012
		DPI	TOBI Podhaler	Novartis	2013
	Itraconazole	DPI	PUR1900	Pulmatrix	Nonclinical Development
Diabetes	Insulin	Soft-mist	Dance-501	Dance Biopharm Inc	In Development
		DPI	Afrezza	Mannkind/Sanofi Aventis	2014
Idiopathic pulmonary fibrosis	A kinase inhibitor	DPI	PUR1800	Pulmatrix	Clinical Trial Phase II
Pulmonary arterial hypertension	Treprostinil	Nebulizer	Tyvaso	United Therap	2009
	Glycopyrrolate + Formoterol fumarate	pMDI	Bevespi Aerosphere	AstraZeneca	2016
	Budesonide, glycopyrronium, and formoterol (PT010)*	pMDI	NA	Pearl Therapeutics	Clinical Trial Phase III

tion market. Further, with recent advancements in dry powder formulation and inhaler technology, manufacturers have been developing DPI products for APIs currently available as pMDI/nebulizer products (shown as greyed area in the table). In 2015, MDIs accounted for 67 % of inhalation market; however, DPIs are forecasted to report an exceptional compound annual growth rate (CAGR) of 16.9 % over the next few years (Grand View Research, 2016). This shift toward developing DPI products is due to an increase in the physical and chemical stability of compounds formulated into solid-state; a DPI also simplifies the inhalation maneuver required by the patient compared to the other available inhaler technologies.

2.4 Problems associated with different inhaler devices

A major problem with current inhalers is the significant deposition of drug particles in the oropharyngeal region and upper airways (Ibrahim, Verma and Garcia-Contreras, 2015). In addition, lack of coordination between device actuation and patient inhalation (hand-breath coordination) increases the deposition in the upper airways leading to insufficient amounts of drug being delivered to the deep lungs (Scichilone, 2015). Fink and Rubin have estimated that improper inhaler maneuvers have a huge economic impact, with roughly $7–15.7 billion wasted, with no benefit to the health-care system or the patient population (Fink and Rubin, 2005).

pMDIs: For pMDIs, to overcome the hand-breath coordination problem, the use of add-on devices such as a spacer or valve-holding chamber is recommended, especially for children and the elderly (Kunda et al., 2017). These add-on devices increase the time between device actuation and inhalation allowing patients to inhale drug over longer periods of time thereby enhancing drug delivery to the deep lungs and decreasing deposition in the oropharyngeal regions and upper airways (Zhou et al., 2014; Kunda et al., 2017). More recently, pMDIs have been designed to operate on breath-activation rather than hand-breath coordination (Newman, 2005; Zhou et al., 2014).

Nebulizers: Nebulizers are recommended for patients who are unable to perform proper hand-breath coordination or perform a forceful inspiration; further, these devices work well for diseases which require higher inhalation doses (eg. CF patients). Three main types of nebulizers are available on the market and are differentiated by their aerosolization mechanism: Jet nebulizers, ultrasonic nebulizers, and vibrating mesh nebulizers. The vibrating mesh nebulizer overcomes some of the disadvantages observed with the first two nebulizer types, like lowering the total treatment time, minimal residual drug volumes, and better efficiency in drug delivery to the lung. However, the complicated operational procedures for nebulizers along with their high cost remains a barrier to better patience compliance (Ari and Fink, 2013; Chan et al., 2014; Ibrahim, Verma and Garcia-Contreras, 2015; Tashkin, 2016).

DPIs: For these devices, the properties of the dry powder formulation, the device design, and the patient inspiratory flow rate determine the efficiency of the inhalation product and the drug deposition to the deep lungs (Islam and Cleary, 2012). In addition, the inspiratory flow rate must be maintained for the duration of inhalation, with deep and forceful breaths, to de-aggregate drug/lactose carrier particles and facilitate drug deposition to the deep lung (Scichilone, 2015). Moreover, a ‘deep and forceful’ inspiration may be difficult to achieve for patients suffering from asthma or COPD, thereby limiting the use of passive DPIs. Passive DPIs require the patient’s inspiratory effort to first disperse the powder in the device and subsequently deliver the formulation to the deep lung. In addition, a rapid inspiration is likely to cause higher oropharyngeal deposition of the drug. Recent progress in the development of active DPIs that use an external energy source, such as compressed air or electrical vibration, may help in powder dispersion and de-agglomeration and thus increase drug deposition to the lungs. However, the major obstacle to the success of active DPIs is their high cost and portability (bulky devices) (Zhou et al., 2014). In addition, specific attention must be given to the pediatric and geriatric population since most DPI devices are designed for the adult population.

2.5 Progress in DPIs: The story of insulin

In recent years, the increasing worldwide diabetic population has motivated many pharmaceutical companies to focus on developing an inhalable insulin product that is fast-acting and can be administered without needles. In 2006, the FDA approved the first inhaled insulin, Exubera®, which was developed and marketed by Nektar Therapeutics and Pfizer laboratories, respectively (Mack, 2007). It is thought that Exubera® was withdrawn in 2007 because of poor patient compliance due to the cost and bulkiness of the device. Perhaps this may be explained by the reported lack of input from the physicians and patients on the design of the device before marketing Exubera®; most of the patients felt uncomfortable using the bulky device, which was almost the size of a flashlight (Mack, 2007).

With lessons learned from the failure of Exubera®, MannKind Corp. developed a smaller inhaled insulin product, Afrezza®, that could easily fit the palm of the patient (later marketed by Sanofi). Afrezza® was approved by the FDA in early 2015 for patients to help control their blood sugar levels during mealtime. The product reaches peak insulin levels in 12–15 min and remains active for up to 3 hours (Hoskins, 2017). However, Sanofi recently withdrew from marketing Afrezza® due to mediocre profits. Dance Pharmaceuticals is currently testing an inhalation insulin product, Dance-501, that delivers a gentle mist of recombinant human insulin using a vibrating mesh micropump technology (developed by Aerogen, Inc.). The story of insulin reflects the challenges associated with successful development of a DPI inhalation product which depends on the formulation, device, delivery, packaging, and proper marketing toward the physicians and patients. Despite the uncertainty observed with the development of an inhaled insulin product, there is renewed interest in exploring dry powder delivery of macromolecules for local and systemic delivery via inhalation.

3. Pulmonary delivery in preclinical models

3.1 Animal models

Animal models are crucial to evaluate the fate of inhaled material and providing valuable information for inhalation product development. When selecting the appropriate animal model, many parameters are considered, including cost, disease pathology, and immunological similarity to humans. Although the data obtained from preclinical studies is valuable in advancing inhalation drug delivery, extrapolation to humans is not straightforward due to the differences in the nasal, tracheobronchial, and the deep lung region across species (Phalen et al., 2008; Fernandes and Vanbever, 2009). For this reason, the similarity of the structure of the respiratory tract of the animal model to humans should be a significant parameter in choosing an appropriate animal model for preclinical studies (Phalen et al., 2008).

Human breathing differs from that of rodents. The latter, such as mice and rats, are obligatory nose breathers and are unable to perform mouth breathing, while adult humans can breathe through the nose and the mouth (**Fig. 2**). In contrast to adult humans, newly born human infants are obligate nose breathers during the first 2–6 months of life (**Fig. 2**) (Rubin and Williams, 2014; Amirav et al., 2015; McGregor, 2017).

The inability to inhale via the mouth limits the relevance of lung deposition data obtained through preclinical animal models that utilize whole-body and nose-only exposures. When using a nose-only or whole-body exposure systems, particles larger than a few microns are trapped in the nasal-pharyngeal region of the rodents and do not necessarily represent the true lung deposition profile observed in humans (Phalen et al., 2008). Another difference between humans and rodents is the presence or absence of respiratory bronchioles. The absence of respiratory bronchioles in the commonly used preclinical models results in different region-specific lung deposition data compared to humans. The clearance mechanism of inhaled insoluble particles also varies in the presence or absence of respiratory bronchioles (Phalen and Mendez, 2009).

In addition to the differences in the respiratory physiology and anatomy, cells present in the lung may also vary between humans and the animal model used. It is estimated that human alveolar macrophages are greater in number and are two-to-three fold larger in size than rodent alveolar macrophages (Stone et al., 1992). Additionally, humans have intravascular macrophages, cells that attack pathogens entering the lungs through the bloodstream, that are absent in rodents (Balhara and Gounni, 2012). These notable differences between humans and the most commonly employed rodent-based animal models call for a more cautious approach in extrapolating pulmonary drug delivery and disposition results from preclinical studies to humans.

3.2 Preclinical inhalation methodologies

One of the greatest obstacles to the successful transition of dry powder products from the research bench to the clinic is the lack of preclinical pulmonary delivery de-

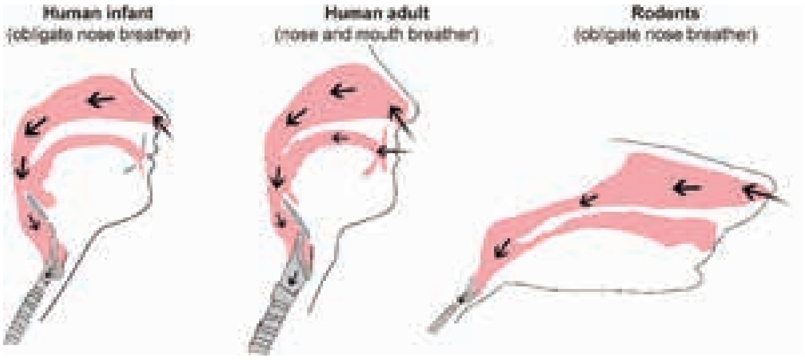

Fig. 2 Upper airway structural differences between human infants, adults, and rodents.

vices. Ideally, preclinical devices should work on similar mechanisms to that of human pulmonary delivery devices. Currently, inhaled medicines are delivered with three types of devices in humans: pMDIs, DPIs, and nebulizers, as discussed in a previous section (Hickey, 2013). However, human inhaler devices work on principles that differ from those used in preclinical models; this usually leads to variable deposition profiles of the agent in the respiratory tract.

The pulmonary delivery devices currently available for preclinical evaluation of aerosols can be categorized into passive and direct inhalation devices. Passive inhalation describes the ability of the animal to breathe an aerosol normally without anesthesia, whereas direct inhalation devices force the aerosol into the upper respiratory tract of the animal, usually under anesthesia. While both types of devices are widely used in the aerosol preclinical research field, the choice of device type, passive or direct, may be appropriate to certain experimental designs.

Passive inhalation delivery devices include whole-body inhalation chambers and head- and nose-only chambers (**Fig. 3A, B**). These devices do not require surgery or that the animal be anesthetized during the aerosol delivery. Further, passive aerosol delivery devices are considered more physiologically-relevant because the animal breathes in the aerosol normally with tidal breathing, and without any external force delivering the aerosol into the lungs. For small animals such as rabbits and rodents, the inhaled aerosol passes through the nasal cavity before reaching the lungs, as these animals are obligate nose breathers (**Fig. 2**) (Hoppentocht et al., 2014b). The passage of the aerosol via the nasal cavity will affect the amount, as well as the site, of aerosol deposition in the lung. Importantly, this deposition will be different compared to humans who inhale via the oral cavity using the existing oral inhalation devices. The fraction of dose deposited in the lung is further altered by the complex nasal turbinate anatomy of rodents, compared to a simple structure observed in humans (**Table 2**).

Whole-body chambers expose the whole animal to an aerosol atmosphere (**Fig. 3A**). These chambers have the advantage of housing several animals at once and the chambers can include food and water access. Commercially available devices include the Glas-Col® inhalation exposure systems and other units from TSE-systems and Shibata Biotechnology (Yi et al., 2013; Chung et al., 2015). Other advantages of whole-body exposure chambers include the ability to house animals for long periods if the experimental design requires long-term exposure, and repeated dosing is also possible. However, drawbacks of the whole-body exposure system include extra-pulmonary exposure through other administrations routes such as skin and oral/ GI tract, the requirement of large amounts of drug or dosing material, and difficulty quantifying and characterizing the dose delivered into the lung per animal (**Table 3**) (Cryan, Sivadas and Garcia-Contreras, 2007; Wong, 2007; Fernandes and Vanbever, 2009; Nahar et al., 2013). Ultimately, these chambers make excellent devices to study environmental exposures that require long-term dosing.

Head- and nose-only exposure chambers are like the whole-body chamber in that animals are not anesthetized during exposure and are able to breathe in a more physiologically-relevant environment. However, in contrast to the whole-body chamber, animals are held immobilized in an exposure tube with the animal's nose or head exposed to an airflow containing the dosing agent (**Fig. 3B**). Such an exposure chamber decreases extra-pulmonary exposure by other delivery routes and decreases the total amount of material needed for the experiment. However, several independent studies have shown that 80–90 % of inhaled aerosols are deposited into the nasopharynx and upper respiratory tract, despite the aerosols being in the respirable range (Society of Toxicology report, 1992; Kaur et al., 2008; Kuehl et al., 2012; Hoppentocht et al., 2014b). Very little of the aerosol reaches the deep lung, and therefore quantification of dose can be difficult. Other flaws of the system include stress on the animal, due to restraints and lack of access to food and water, as well as suffocation (rare occasion) if the animal moves around in the tube or the chamber generates heat (**Table 3**).

Direct inhalation devices include intratracheal methods of delivery and tracheostomy. These methods of aerosol delivery are considered less physiologically-relevant as the animal is anesthetized while the aerosol is forced directly into the trachea, rather than through normal inspiration. However, unlike passive inhalation methodologies, the quantification of the dose delivered into the lung is much easier with these devices because the nasopharynx is bypassed and the aerosol is forced directly into the trachea and upper lung airways (Hoppentocht et al., 2014b).

Intratracheal instillation (also called intratracheal/ endotracheal intubation or aerosolization) is the most utilized method of direct administration of therapeutics into the respiratory system of rodents. Several tools have been developed for this type of delivery; however, options become limited when delivering dry powders compared to liquid aerosols. Dry powder tools include the Penn Century Insufflator™ (**Fig. 3C**) and the BioLite Intubation System from Braintree Scientific, Inc (Walters et al., 2004; Morello et al., 2009). Using these devices an anesthetized rodent is intubated with an insufflator tube or catheter as far as the first bifurcation of the lungs (**Fig. 3C**). The dry powder is then aerosolized directly into the lung using a syringe or pipette bulb. The methodology is technically difficult and time intensive in smaller animals (i.e. mice and rats), however, repeated dosing and long-term studies are possible (**Table 3**).

Table 2 Pulmonary characteristics of different animal models.

Characteristics	Human	Rhesus monkey	Beagle dog	Rabbit	Guinea-pig	Rat	Mouse	Ref.
Body Weight (kg)	70	38	10–15	2.5–3.5	0.4	0.25–0.35	0.02–0.04	(Fernandes and Vanbever, 2009)
Nose and/or mouse breather	Nose and mouth breather	Nose and mouth breather	Nose and mouth breather	Obligate nose breather	Obligate nose breather	Obligate nose breather	Obligate nose breather	(Fernandes and Vanbever, 2009)
Nasal Anatomy								
Turbinate complexity	Simple	Simple scroll	Very complex	Complex scroll	Complex scroll	Complex scroll	Complex scroll	(Schreider and Raabe, 1981; Fernandes and Vanbever, 2009)
Pulmonary Anatomy								
Lung weight (g)	1000	—	100	18	3.2	1.5	0.12	(Brewer and Cruise, 1997; Fernandes and Vanbever, 2009)
Lung symmetry	dichotomous	dichotomous	monopodial	monopodial	monopodial	monopodial	monopodial	(Fernandes and Vanbever, 2009)
Trachea length/diameter (cm)	12/2	3/0.3	17/1.6	6/0.5	5.7/0.4	2.3/0.26	0.7/0.12	(Hoyt, Robert F. et al., 2007; Fernandes and Vanbever, 2009; Purser, 2010)
Lung volume (mL)	4341	204	736	79.2	13	8.6	0.74	(Fernandes and Vanbever, 2009; Asgharian et al., 2012)
Number of Alveoli ($\times 10^6$)	950	81.8	1040	135	69	43	18	(Fernandes and Vanbever, 2009; Asgharian et al., 2012)
Diameter of Alveoli (μm)	219	—	126	88	65	70	47	(Fernandes and Vanbever, 2009)
Alveolar macrophages ($\times 10^6$)	5990	—	3940	142	58.8	29.1	2.9	(Fernandes and Vanbever, 2009)
Respiratory parameters								
Respiratory rate (min^{-1})	12	38	23	51	90	85	163	(Fernandes and Vanbever, 2009)
Tidal volume (L/min)	400–616	20–21.2	11.4–16.6	15.8	1.72–1.75	0.87–2.08	0.15–0.18	(Fernandes and Vanbever, 2009)
Mucus clearance rate (mm/min)	3.6–21.5		7.5.21.6	3.2	2.7	1.9–5.9	—	(Fernandes and Vanbever, 2009)
Particle size for deep lung delivery (μm)	1–5	1–3	1–3	—	—	3.5	3	(Fernandes and Vanbever, 2009; Asgharian et al., 2012)

Modified from Fernandes et al. (Fernandes and Vanbever, 2009)

Major drawbacks of the intratracheal instillation technique include the requirement of anesthetization of the animal and a lack of universal availability of devices in the market. Repeated use of anesthesia can alter the physiology of animals (Balcombe et al., 2004; Hildebrandt et al., 2008), and makes intratracheal instillation a challenging method for long-term dosing studies. The lack of a universally accepted dry powder delivery device among different research laboratories leads to in-house fabrication of devices which result in variable delivery efficiency in published animal models. The Penn Century Insufflator™ was the most-published direct inhalation (for dry powders), until recently when the company closed. Now this device has become difficult to purchase and researchers are developing alternatives (Durham et al., 2017).

The insufflator was not without its problems however, and had been evaluated in several animal models using variable dosing parameters. Penn Century stated that the insufflator was designed to hold 1–4 mg of dry powder. However, Morello et al. showed that powder doses above 350 µg delivered with the Insufflator^{TM} could cause immediate death in mice (Morello et al., 2009). Furthermore, the same study showed that use of more than 250 µL of air (4–5x) resulted in mouse death. In contradiction to these studies, Duret et al. published an evaluation of the insufflator with powder doses ranging from 0.5 mg to 4.3 mg and suggested that dose recovery (drug amount that reached the lung lobe) was proportional to the amount insufflated into the lung (Duret et al., 2012). Hoppentocht and colleagues showed that powder aerosolized with less than 500–1000 µL of air led to significant powder remaining in the insufflator and had decreased lung deposition efficacy (Hoppentocht et al., 2014b). In rats, intubation with the insufflator alone (no drug delivered into the lung) was shown to cause lung trauma (Guillon et al., 2012).

Tracheal impaction and deposition is another problem associated with powder delivery using direct intubation strategies. The insufflator intubates the trachea up to the first bifurcation of the lungs. The powder is aerosolized through the firm depression of a syringe plunger attached to the insufflator (**Fig. 3C**). The force required to deagglomerate and aerosolize the powder from the insufflator results in an excessive force exerted on the particles, such that their momentum carries them directly into the walls of the trachea due to inertial impaction. Duret et al. and Tonnis et al. both showed independently that only about 65 % of the powder dose emitted from the insufflator reaches the lungs (Duret et al., 2012; Tonnis et al., 2014). Particles deposited onto the tracheal walls are rapidly cleared through mucociliary clearance and swallowed by the animal. In addition to the dose lost through tracheal impaction, a certain amount of powder is lost through exhalation due to the return airflow caused by overpressure within the lungs due to the sudden burst of air blown via the insufflator (Tonnis et al., 2014). Price et al. recently showed that poor lung deposition might also be associated with the humid lung environment in the rodent lung leading to powder agglomeration and retention in the insufflator (Price et al., 2017).

The only other methodology reported for direct delivery of dry powders is tracheostomy (Lombry et al., 2004; Wong, 2007; Fernandes and Vanbever, 2009). This method involves a surgical incision to expose the trachea and the placement of powders into a cannula that is inserted towards the lung or directly into the upper respiratory tract. The advantages of this method include efficient use of dosing material and easy characterization of deep lung dosing (Wong, 2007). However, this method has the drawback of invasiveness and cannot be used for long-term or repeated studies (**Table 3**) (Wong, 2007; Fernandes and Vanbever, 2009).

3.3 Dry powder formulation for preclinical pulmonary delivery

Dry powder flow properties and lung distribution patterns vary depending on the device with which they are delivered, the animal model used, and the formulation characteristics of the powder itself (**Fig. 4**) (Foster et al., 2001; Fernandes and Vanbever, 2009). Foster et al. showed that the mucociliary clearance of aerosolized insoluble colloidal particles and its distribution in a mouse lung were dependent on the delivery device (Foster et al., 2001). Nose-only administration delivered significantly fewer particles to the lung than intratracheal instillation and the deposited particles were cleared much more efficiently from the lung within 6- and 24-hour observational timepoints than particles delivered by intratracheal delivery. Further, small operational changes within a delivery technique using a particular delivery device can change the lung distribution patterns within the animal (Foster et al., 2001; Wong, 2007; Hasegawa-Baba et al., 2014). Hasegawa-Baba and colleagues showed a significant difference in pulmonary distribution patterns generated by intratracheal instillation depending on the angle at which the animal was intubated, the speed at which the drug

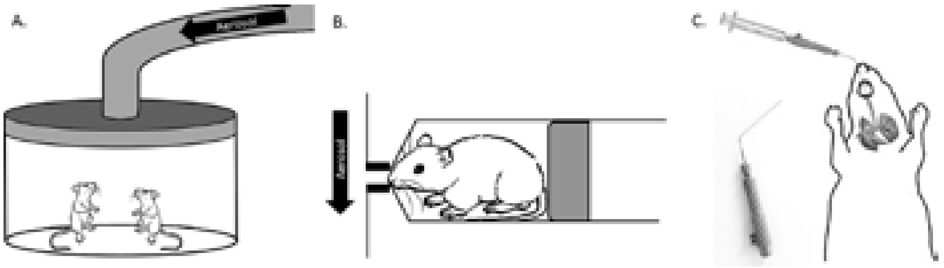

Fig. 3 Preclinical dry powder delivery devices. Passive inhalation devices include **A)** Whole body and **B)** Nose- and head-only devices. Direct inhalation methods require intubation of the rodent trachea. Shown in **C)** An intubated rodent with the Penn Century dry powder Insufflator^{TM} (inset: Insufflator^{TM}).

Table 3 Preclinical pulmonary delivery methodologies.

Methodology	Tissue Distribution	Tools required/ formulation	Benefits	Drawbacks	Ref.
Passive methodologies					
Whole body	Respiratory tract, GI tract, skin/fur, nasopharynx	Aerosol generator and exposure chamber,	Physiologically relevant, animals can be housed in chambers, long-term exposure capable, accommodates large group sizes	Other exposure routes, large amounts of material required, homogeneous air flow required, difficult to characterize deep lung dosing	(Cryan, Sivadas and Garcia-Contreras, 2007; Wong, 2007; Fernandes and Vanbever, 2009; Nahar et al., 2013)
Head Nose-only	Respiratory tract, GI tract, nasopharynx	Aerosol generator with compatible restraining tubes	Reduced extra-pulmonary exposure, reduced material requirements, suitable for repeated dosing	Animals are restrained, possible heat buildup, probable stress on animal and potential suffocation, labor intensive, difficult to characterize deep lung dosing	(Cryan, Sivadas and Garcia-Contreras, 2007; Wong, 2007; Fernandes and Vanbever, 2009; Nahar et al., 2013)
Direct methodologies					
Intratracheal Instillation	Trachea, Respiratory tract	Penn Century Insufflator^{TM} or Braintree Scientific Lung intubation system, plastic intubation needle	Direct dosing, Efficient dosing	Anesthesia, tracheal damage, technically difficult, time-intensive	(Cryan, Sivadas and Garcia-Contreras, 2007; Wong, 2007; Morello et al., 2009; Duret et al., 2012; Hoppentocht et al., 2014b)
Tracheostomy	Trachea, Respiratory tract (diffusion)	Surgery tools	Direct dosing, Efficient dosing	Anesthesia, surgery, not suitable for repeated or long-term dosing, labor intensive	(Lakatos et al., 2006; Fernandes and Vanbever, 2009)

Modified from Wong et al. (Wong, 2007)

was aerosolized into the lungs, and the volume of the dose delivered (Hasegawa-Baba et al., 2014). These differences in the operation of preclinical devices are inevitable based on individual operators working in different laboratories.

Historically, small and large animal models have been used for inhalation studies, and as mentioned earlier, these models differ greatly in their respiratory physiologies. The textbook definition of the optimal size range of particles delivered to the deep lung is 1–5 μm, without distinction between the animal models used. However, it is likely that the optimal pulmonary size range changes with the animal, the device used, and even by the device operator as mentioned above. Kuehl and colleagues delivered polydisperse powders (0.5 to 5 μm) to rats and mice using a nose-only inhalation system and observed different powder deposition patterns in the lung, as a function of particle size, within these two animal models (Kuehl et al., 2012). Phagocytosis and immune cell recruitment in response to pulmonary vaccines and therapeutics may also differ between animal models based on the macrophage numbers in the lung (Fernandes and Vanbever, 2009). Likewise, differing mucociliary clearance rates between animal species may affect drug retention in the

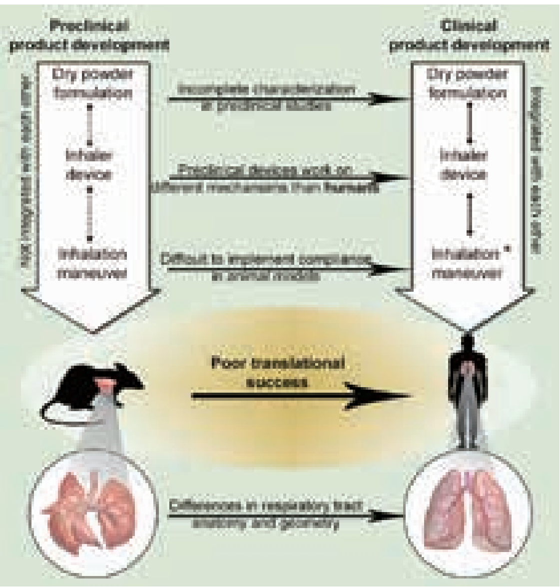

Fig. 4 The reasons for poor translational success of DPI products from preclinical studies to human. *Integration of inhalation maneuver remains a problem in infant and pediatric human populations.

lung and therefore efficacy, especially in long-term treatment studies (Fernandes and Vanbever, 2009).

Dry powders for pulmonary delivery may require different characterization for preclinical studies, separate from what goes into clinical trials. The lung distribution of the powder delivered by the insufflator^{TM} varies based on the powder properties and how it was formulated (Duret et al., 2012; Hoppentocht et al., 2014b). Powders with increased hygroscopicity may be difficult to deliver by intratracheal instillation, as the humid environment of the trachea may cause powder aggregation and clogging of the intubation tube (Price et al., 2017). Lastly, because dosing varies greatly between different methods of pulmonary delivery, i.e. passive and direct, it is critical to optimize the amount of powder delivered based on the device and the animal model used.

4. Innovations in the dry powder pulmonary delivery field

Significant progress has been made in the dry powder field (both in the formulation and device development) for humans since DPIs were first introduced almost half-century ago (**Table 1**). In this section, we will discuss some of the recent innovations in powder formulation, and inhaler devices that could improve not only drug deposition in the lung but patient adherence to treatment as well. We will end by discussing how these innovations can be applied toward animal inhalation studies.

4.1 Formulation innovations

Dry powders for pulmonary delivery were historically made using the ‘top-down’ approach of milling larger crystalline particles into a size appropriate for inhalation. This led to irregularly shaped particles that were cohesive and promoted particle aggregation. Although adding inert carrier particles such as lactose or mannitol to drug particles decreased particle cohesiveness to a variable extent, it also reduced delivery efficiency to the lung due to an increase in the total inhaled powder volume (Rubin and Williams, 2014). Newer formulation technologies have focused on engineering spherical particles in the respirable range where the active ingredient is encapsulated within an inert matrix, usually using a ‘bottom-up’ approach (precipitation and solvent evaporation techniques). Such an approach allows for greater control of particle size and polydispersity, morphology, porosity, density, and surface energy (Weers, Clark and Challoner, 2004). Lower contact points for spherical particles has helped in particle dispersion without the need for carrier particles; this has improved the delivery efficiency of the API by significantly decreasing the total volume of dry powder inhaled by the patient. Carrier-free spherical particles have been manufactured using techniques such as supercritical fluid, spray-freeze drying, and spray drying. These techniques can formulate liposomes and polymeric micro- and nanoparticles in the appropriate size range for pulmonary delivery. Liposomal formulations are usually well-tolerated and non-immunogenic when delivered into the lung since they can be prepared using surfactant phospholipids that are endogenous to the lung, for eg. dipalmitoylphosphatidylcholine (DPPC) (Cipolla et al., 2014).

Spray drying produces large porous particles in the respirable range with reduced particle aggregation during aerosolization (Edwards et al., 1997). Further, porous particles have achieved significantly higher drug loading; PulmoSpheres^{TM}, manufactured by an emulsion-based spray drying process, has achieved more than 90 % tobramycin loading by mass (Geller et al., 2011). PulmoSpheres^{TM} offer substantially improved lung deposition efficiency and more convenient administration over the nebulized delivery of tobramycin. Spray freeze-drying is used to produce dry powders for pulmonary delivery that have lower aggregation capability. However, due to their high porosity, spray-freeze-dried particles allow for low powder volumes to be loaded in DPIs (Saluja et al., 2010). Supercritical fluid technology is another bottom-up technology that generates uniformly sized particles for pulmonary delivery (Sacchetti and Van Oort, 2007). For reviews on dry powder formulation for pulmonary delivery, the readers are directed to articles that broadly cover these topics (Yang, Chan and Chan, 2014; Carvalho et al., 2015; Hickey, 2018).

4.2 Device innovation

Human DPI devices are categorized into passive and active inhalers as discussed earlier. Passive inhalers require the patient’s inspiration to deaggregate powders into the respirable range. Powders loaded in passive inhalers should, therefore, exhibit improved flow and dispersion properties based on the patient’s inspiratory strength. Conversely, active inhalers provide the energy for powder dispersion and are not dependent on the patient’s peak inspiratory flow rate. Newer passive inhaler devices enhance powder de-agglomeration and are less dependent on the patient’s inspiration. Such technologies include reverse flow cyclone technology (Harrison et al., 2011), mesh-sieving technology (Friebel et al., 2010), flutter-induced powder dispersion (Selvam et al., 2010). Although these device designs have minimized dependency on the patient inspiration to disperse powders in the inhaler device, low flow rates could still be a concern in patients with limited lung function or a reduced tidal volume, including children, the elderly, and patients suffering from cystic fibrosis. Current DPIs use carrier-based dry powders that worsen the above concerns, in addition to the significant deposition in the mouth and throat area observed with such powders, irrespective of the inhaler used. Carrier-free dry powders were evaluated using the HandiHaler® device and turbulence was shown to be their primary deaggregation mechanism (Longest et al., 2013). Highly effective passive inhalers may be required for carrier-free powders in order to improve the respirable fraction (10–70 %) currently achieved with the marketed DPIs (Islam and Cleary, 2012; Behara et al., 2014). Active inhaler devices disperse powders based on an external energy source such as compressed air, electrical vibration, and mechanical barriers. Although a few active dry powder inhalers have been clinically tested (Hoppentocht et al., 2014a), their widespread use in the future may be hindered due to their complexity, expense, failure due to the requirement for an external energy source, and most importantly, poor patient compliance due to the numerous operational steps required for inhalation (Smutney, Grant and Kinsey, 2013; Chan et al., 2014; de Boer et al., 2017).

Drug delivery efficiency to the lung has shown significant improvement when a powder inhaler is evaluated in combination with a specific formulation technology in human trials before being marketed (Frijlink and De Boer, 2004; Smutney, Grant and Kinsey, 2013). The TOBI Podhaler™, when tailored with tobramycin PulmoSpheres™, delivered up to 60 % of the total dose into the lung of healthy human subjects (Duddu et al., 2002); a significant increase from the usual 1–2 % delivery efficiency observed with earlier DPIs. Thus, the ability to characterize the inhaler device along with the formulation is critical for improving the amount of powder delivered into the lung (**Fig. 4 & 5**).

The ability to manipulate the patient's 'inhalation maneuver' while using a DPI has shown to improve the drug delivery efficiency to the lung. Conversely, incorrect inhaler use is a major factor in poor disease outcomes; up to 68 % of patients using DPIs do not use the device correctly (Fink and Rubin, 2005). Inhalation maneuver includes controlling the inhalation flow rate, holding breath for 10s or more, and varying the inhalation volume and inspiration time (Haidl et al., 2016). The patient's ability to hold their breath has shown to improve lung deposition efficiency by allowing the particles to settle in the deep lung region by diffusion (Horváth et al., 2017) and possibly leading to minimal exhalation of particles. Inhalation maneuver becomes even more critical for DPIs, compared to pMDIs and nebulizers, since the ability to vary the inspiration volume and time will dictate the amount of powder dispersed and ejected from an inhaler. However, manipulating the inhalation maneuver in human infants and rodents is challenging; both these groups are obligate nose-breathers compared to human adults (**Fig. 2**) and this results in significant powder deposition in the nasopharyngeal region rather than in the lower respiratory tract (DiBlasi, 2015).

4.3 Implementation of lessons learned from humans to animals

Many preclinical studies using dry powder pulmonary delivery for drugs, vaccines, and immunotherapies have been conducted in the last two decades. However, the translational success from these preclinical studies to human trials has been abysmal (**Fig. 5**). The poor success in clinical translation may be associated with the complexity of the pulmonary route of administration, especially when compared to the parenteral route of administration. For parenterally delivered products, similar formulation and devices are used across animals and humans. For exam-

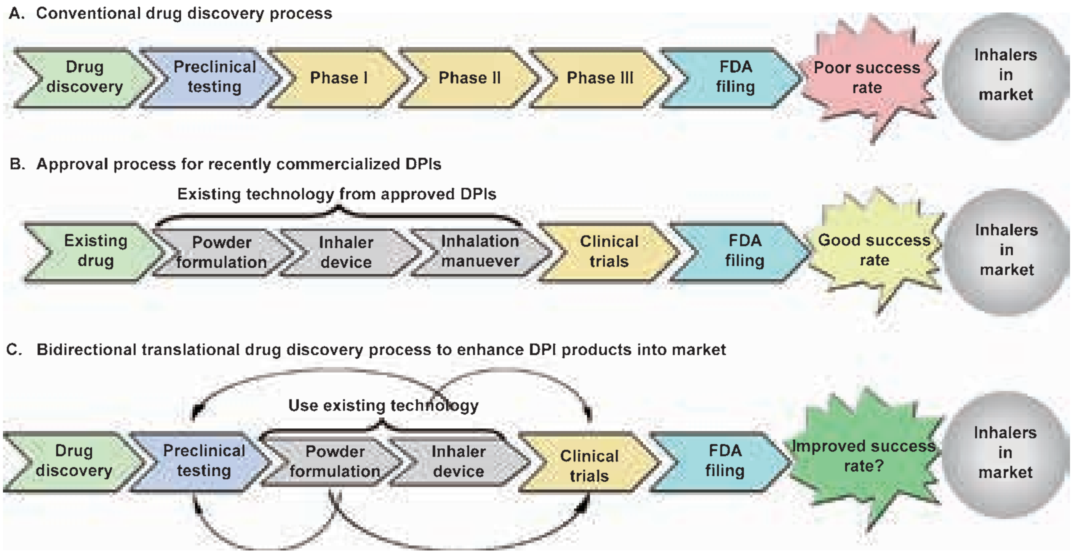

Fig. 5 Linear (conventional) drug discovery versus bidirectional drug discovery.

ple, a drug solution administered using a syringe and needle in preclinical studies will not require significant modifications to the formulation (solution) or device (syringes and needles) when subsequently evaluated in humans. However, for pulmonary delivery, differences in lung anatomy, respiratory physiology, formulation characteristics, and device type between preclinical and clinical studies could have significant implications for translation success (**Fig. 4**). Due to these differences, drug deposition patterns in the lung and drug clearance rates can vary between humans and animals (Cryan, Sivadas and Garcia-Contreras, 2007). In addition, variable drug losses are observed in the delivery device and in the host (both humans and animals). The complex nasal passage in rodents usually leads to significant powder deposition in the nasal passage, compared to the deposition observed in the oral passage in humans, when delivering dry powders to the lung. Furthermore, the compatibility of a powder formulation in combination with a specific inhalation device is not characterized in preclinical studies. This is due to the scarcity of inhalation devices available for preclinical studies (see *preclinical inhalation methodologies* section); in addition, as discussed previously, preclinical devices work on different mechanisms than that of human inhalers and do not take into account the lung anatomy and physiology of the preclinical model (see *animal models* section).

In the drug discovery process, preclinical studies precede human studies. However, recent drugs approved for DPI use were previously marketed as pMDIs and nebulizers, or utilized existing dry powder formulation technology and inhaler devices (**Fig. 5B**); very few of these DPIs went through the linear (conventional) drug discovery process involving preclinical studies (**Fig. 5A**). This shows that the translational success for pulmonary drug development can be significantly improved by including reverse- and forward-signaling loops (bidirectional) in the linear drug discovery process based on a feedback mechanism (**Fig. 5C**) (Wehling M., 2009). Although using such a feedback system cannot replace any of the steps required in the drug discovery cycle, it could increase the likelihood of a DPI product reaching the market.

The important and positive lessons learned from dry powder formulation and characterization, inhaler design, and subsequent evaluation in humans should be employed in preclinical studies to the extent possible (Lightfoot et at., 2017). In addition, a new drug can use the existing technology with regards to powder formulation and inhaler device in a forward-signaling loop in the discovery process (**Fig. 5C**). Such a feedback system will allow better collaboration between the basic scientist, industry partners, and clinicians working on preclinical inhalation studies, formulation and device development, and evaluating novel DPIs in humans, respectively. If possible, we need to develop preclinical inhaler devices that more closely mimic the devices being tested in humans. However, we need to also acknowledge the limitations of animal models with regards to their translational potential. This could be particularly true for drugs and biologics for pulmonary delivery.

5. Conclusion

Dry powder inhaled therapeutics have solved many problems associated with liquid therapeutics and their associated inhalers. However, drug development for dry powder formulations and inhalers have consistently faltered as they transition to the clinic, and *de novo* dry powder drug development is sparse when a linear drug discovery process is followed. The low success rate of these products may be due to the lack of innovation in other areas of preclinical pulmonary drug development. Current preclinical pulmonary delivery methodologies do not model human inspiration or current DPI mechanisms. Further, dry powder formulations are never modulated to fit preclinical models and devices; they are formulated with only human drug delivery in mind. Thus, innovation in dry powder therapeutics has become unidirectional in terms of development and very few products make it to market. To increase the success of dry powders in the pharmaceutical industry, efforts must be shifted to fix the current problems with preclinical development, and innovation must become bi-directional. This will create a system where novel research and discovery can inform preclinical and clinical drug development.

References

Amirav I., Borojeni A.A.T., Halamish A., Newhouse M.T., Golshahi L., Nasal versus oral aerosol delivery to the “lungs” in infants and toddlers, Pediatric Pulmonology, 50 (2015) 276–283.

Anderson P.J., History of aerosol therapy: Liquid nebulization to MDIs to DPIs, Respiratory Care, 50 (2012) 1139–1150.

Ari A., Fink J.B., Aerosol therapy in children: challenges and solutions, Expert Review of Respiratory Medicine, 7 (2013) 665–672.

Asgharian B., Price O., McClellan G., Corley R., Einstein D.R., Jacob R.E., Harkema J., Carey S.A., Schelegle E., Hyde D., Kimbell J.S., Miller F.J., Development of a rhesus monkey lung geometry model and application to particle deposition in comparison to humans, Inhalation Toxicology, 24 (2012) 869–899.

Bäckman P., Adelmann H., Petersson G., Jones C.B., Advances in inhaled technologies: understanding the therapeutic challenge, predicting clinical performance, and designing the optimal inhaled product, Clinical Pharmacology &

Therapeutics, 95 (2014) 509–520.

Balcombe J.P., Barnard N.D., Sandusky C., Laboratory routines cause animal stress, Journal of the American Association for Laboratory Animal Science, 43,6 (2004) 42–51.

Balhara J., Gounni A.S., The alveolar macrophages in asthma: a double-edged sword, Mucosal Immunology, 5 (2012) 605–609.

Behara S.R.B., Worth Longest P., Farkas D.R., Hindle M., Development and comparison of new high-efficiency dry powder inhalers for carrier-free formulations, Journal of Pharmaceutical Sciences, 103 (2014) 465–477.

Brewer N.R., Cruise L.J., The respiratory system of the guinea pig: Emphasis on species differences, Journal of the American Association for Laboratory Animal Science, 36,1 (1997) 100–108.

Carvalho S.R., Watts A.B., Peters J.I., Williams R.O., Dry Powder Inhalation for Pulmonary Delivery: Recent Advances and Continuing Challenges, John Wiley & Sons, Ltd, Chichester (2015) pp. 35–62.

Chan J.G.Y., Wong J., Zhou Q.T., Leung S.S.Y., Chan H.-k., Advances in device and formulation technologies for pulmonary drug delivery, AAPS PharmSciTech, 15 (2014) 882–897.

Chung Y.H., Han J.H., Lee Y.-H., A study on subchronic inhalation toxicity of 1-chloropropane, Toxicological Research, 31 (2015) 393–402.

Cipolla D., Shekunov B., Blanchard J., Hickey A., Lipid-based carriers for pulmonary products: Preclinical development and case studies in humans, Advanced Drug Delivery Reviews, 75 (2014) 53–80.

Cryan S.-A., Sivadas N., Garcia-Contreras L., In vivo animal models for drug delivery across the lung mucosal barrier, Advanced drug delivery reviews, 59 (2007) 1133–1151.

de Boer A.H., Hagedoorn P., Hoppentocht M., Buttini F., Grasmeijer F., Frijlink H.W., Dry powder inhalation: past, present and future, Expert Opinion on Drug Delivery, 14 (2017) 499–512.

Demoly P., Hagedoorn P., de Boer A.H., Frijlink H.W., The clinical relevance of dry powder inhaler performance for drug delivery, Respiratory Medicine, 108 (2014) 1195–1203.

DiBlasi R.M., Clinical controversies in aerosol therapy for infants and children, Respiratory Care, 60 (2015) 894–916.

Dolovich M.B., Ahrens R.C., Hess D.R., Anderson P., Dhand R., Rau J.L., Smaldone G.C., Guyatt G., Device selection and outcomes of aerosol therapy: Evidence-based guidelines, CHEST, 127 (2005) 335–371.

Duddu S.P., Sisk S.A., Walter Y.H., Tarara T.E., Trimble K.R., Clark A.R., Eldon M.A., Elton R.C., Pickford M., Hirst P.H., Newman S.P., Weers J.G., Improved lung delivery from a passive dry powder inhaler using an engineered PulmoSphere® powder, Pharmaceutical research, 19 (2002) 689–695.

Duret C., Wauthoz N., Merlos R., Goole J., Maris C., Roland I., Sebti T., Vanderbist F., Amighi K., In vitro and in vivo evaluation of a dry powder endotracheal insufflator device for use in dose-dependent preclinical studies in mice, European journal of pharmaceutics and biopharmaceutics: official journal of Arbeitsgemeinschaft für Pharmazeutische Verfahrenstechnik eV, 81 (2012) 627–634.

Durham P.G., Hanif S.N., Garcia-Contreras L., Young E.F., Braunstein M.S., Hickey A.J., Disposable dosators for pulmonary insufflation of therapeutic agents to small animals, Journal of Visualized Experiments, 121 (2017) e55356. DOI: 10.3791/55356.

Edwards D.A., Hanes J., Caponetti G., Hrkach J., Ben-Jebria A., Eskew M.L., Mintzes J., Deaver D., Lotan N., Langer R., Large porous particles for pulmonary drug delivery, Science (New York, NY), 276 (1997) 1868–1871.

Effros R.M., Anatomy, development, and physiology of the lungs, GI Motility online, 1 (2006) doi:10.1038/gimo73

Fernandes C.A., Vanbever R., Preclinical models for pulmonary drug delivery, Expert Opinion on Drug Delivery, 6 (2009) 1231–1245.

Fields M.R., Inhalator, US Patent, (1949) US2470297A.

Fink J.B., Rubin B.K., Problems with inhaler use: a call for improved clinician and patient education, Respiratory care, 50 (2005) 1360–1365.

Forbes B., Asgharian B., Dailey L.A., Ferguson D., Gerde P., Gumbleton M., Gustavsson L., Hardy C., Hassall D., Jones R., Lock R., Maas J., McGovern T., Pitcairn G.R., Somers G., Wolff R.K., Challenges in inhaled product development and opportunities for open innovation, Advanced Drug Delivery Reviews, 63 (2011) 69–87.

Foster W.M., Walters D.M., Longphre M., Macri K., Miller L.M., Methodology for the measurement of mucociliary function in the mouse by scintigraphy, Journal of Applied Physiology, 90 (2001) 1111–1118.

Friebel C., Stolte S., Steckel H., Solomon I., Performance of a new single-use disposable dry powder inhaler prototype, Respiratory Drug Delivery, 2 (2010) 517–522.

Frijlink H.W., De Boer A.H., Dry powder inhalers for pulmonary drug delivery, Expert Opinion on Drug Delivery, 1 (2004) 67–86.

Garcia-Contreras L., Hickey A.J., Aerosol treatment of cystic fibrosis, Critical Reviews™ in Therapeutic Drug Carrier Systems, 20 (2003) 317–356. DOI: 10.1615/CritRevTherDrugCarrierSyst.v20.i5.10

Geller D.E., Weers J., Heuerding S., Development of an inhaled dry-powder formulation of tobramycin using PulmoSphere™ technology, Journal of Aerosol Medicine and Pulmonary Drug Delivery, 24 (2011) 175–182.

Ghosh S., Collier A., Inhaled insulins, Postgraduate Medical Journal, 83 (2007) 178–181.

Grand View Research, 2016, *Digital Dose Inhaler Market Analysis By Product (Metered Dose Inhaler, Dry Powder Inhaler), By Type (Branded Medication, Generics Medication) And Segment Forecasts to 2024,* Available at: http://www.grandviewresearch.com/industry-analysis/digital-dose-inhaler-market, accessed 15.02.2018.

Guillon A., Montharu J., Vecellio L., Schubnel V., Roseau G., Guillemain J., Diot P., de Monte M., Pulmonary delivery of dry powders to rats: Tolerability limits of an intra-tracheal administration model, International Journal of Pharmaceutics, 434 (2012) 481–487.

Haidl P., Heindl S., Siemon K., Bernacka M., Cloes R.M., Inhalation device requirements for patients' inhalation maneuvers, Respiratory Medicine, 118 (2016) 65–75.

Harrison L.I., Novak C.C., Needham M.J., Ratner P., Comparative pulmonary function and pharmacokinetics of fluticasone propionate and salmeterol xinafoate delivered by two dry powder inhalers to patients with asthma, Journal of Aerosol Medicine and Pulmonary Drug Delivery, 24 (2011) 245–252.

Hasegawa-Baba Y., Kubota H., Takata A., Miyagawa M., Intratracheal instillation methods and the distribution of administered material in the lung of the rat, Journal of Toxicologic Pathology, 27 (2014) 197–204.

Hickey A.J., Back to the future: Inhaled drug products, Journal of Pharmaceutical Sciences, 102 (2013) 1165–1172.

Hickey A.J., Complexity in pharmaceutical powders for inhalation: A perspective, KONA Powder and Particle Journal, 35 (2018) 3–13.

Hildebrandt I.J., Su H., Weber W.A., Newport D.F., Cherry S.R., Rooney W., Pratte J.F., Junnarkar S., Stoll S., Master Z., Purschke M., Park S.J., Southekal S., Kriplani A., Krishnamoorthy S., Maramraju S., O'Connor P., Radeka V., Vaska P., Villanueva A., Yu B., Gershenson D.M., Kundra V., Lopez-Berestein G., Lutgendorf S.K., Cole S.W., Sood A.K., Anesthesia and other considerations for in vivo imaging of small animals, ILAR Journal, 49 (2008) 17–26.

Hoppentocht M., Hagedoorn P., Frijlink H.W., de Boer A.H., Technological and practical challenges of dry powder inhalers and formulations, Advanced Drug Delivery Reviews, 75 (2014a) 18–31.

Hoppentocht M., Hoste C., Hagedoorn P., Frijlink H.W.W., de Boer A.H.H., In vitro evaluation of the DP-4M PennCentury insufflator, European Journal of Pharmaceutics and Biopharmaceutics, 88 (2014b) 153–159.

Horváth A., Balásházy I., Tomisa G., Farkas Á., Significance of breath-hold time in dry powder aerosol drug therapy of COPD patients, European Journal of Pharmaceutical Sciences, 104 (2017) 145–149.

Hoskins M., Afrezza Updates: Upcoming TV Ads and Possibly 'The Uber of Diabetes'?, February 2017, Available at: http://www.healthline.com/diabetesmine/afrezza-updates-february-2017#1 (Accessed: 28 June 2017).

Hou S., Wu J., Li X., Shu H., Practical, regulatory and clinical considerations for development of inhalation drug products, Asian Journal of Pharmaceutical Sciences, 10 (2015) 490–500.

Hoyt Jr R.F., Hawkins J.V., St. Clair M.B., Kennett M.J., Mouse Physiology, in: Fox J.G., Barthold S.W., Davisson M.T. et al. (Eds.), Academic Press, Burlington, 2007, pp. 23–90, ISBN: 9780123694577.

Ibrahim M., Verma R., Garcia-Contreras L., Inhalation drug delivery devices: technology update, Medical Devices (Auckland, NZ), 8 (2015) 131–139.

Islam N., Cleary M.J., Developing an efficient and reliable dry powder inhaler for pulmonary drug delivery – A review for multidisciplinary researchers, Medical Engineering & Physics, 34 (2012) 409–427.

Kaur J., Muttil P., Verma R.K., Kumar K., Yadav A.B., Sharma R., Misra A., A hand-held apparatus for "nose-only" exposure of mice to inhalable microparticles as a dry powder inhalation targeting lung and airway macrophages, European Journal of Pharmaceutical Sciences, 34 (2008) 56–65.

Kleinstreuer C., Zhang Z., Donohue J.F., Targeted drug-aerosol delivery in the human respiratory system, Annual Review of Biomedical Engineering, 10 (2008) 195–220.

Kuehl P.J., Anderson T.L., Candelaria G., Gershman B., Harlin K., Hesterman J.Y., Holmes T., Hoppin J., Lackas C., Norenberg J.P., Yu H., McDonald J.D., Regional particle size dependent deposition of inhaled aerosols in rats and mice, Inhalation Toxicology, 24 (2012) 27–35.

Kunda N.K., Hautmann J., Godoy S.E., Marshik P., Chand R., Krishna S., Muttil P., A novel approach to study the pMDI plume using an infrared camera and to evaluate the aerodynamic properties after varying the time between actuations, International Journal of Pharmaceutics, 526:1 (2017) 41–49.

Kunda N.K., Somavarapu S., Gordon S.B., Hutcheon G.A., Saleem I.Y., Nanocarriers targeting dendritic cells for pulmonary vaccine delivery, Pharmaceutical Research, 30 (2013) 325–341.

Labiris N.R., Dolovich M.B., Pulmonary drug delivery. Part I: Physiological factors affecting therapeutic effectiveness of aerosolized medications, British Journal of Clinical Pharmacology, 56 (2003) 588–599.

Lakatos H.F., Burgess H.A., Thatcher T.H., Redonnet M.R., Hernady E., Williams J.P., Sime P.J., Oropharyngeal aspiration of a silica suspension produces a superior model of silicosis in the mouse when compared to intratracheal instillation, Experimental Lung Research, 32 (2006) 181–199.

Lightfoot J.T., Bamman M.M., Booth F.W., Translation goes both ways: The power of reverse translation from human trials into animal models, Translational Journal of the American College of Sports Medicine, 2 (2017) 29–31.

Lombry C., Marteleur A., Arras M., Lison D., Louahed J., Renauld J.-C., Préat V., Vanbever R., Local and systemic immune responses to intratracheal instillation of antigen and DNA vaccines in mice, Pharmaceutical Research, 21 (2004) 127–135.

Longest P.W., Son Y.-J., Holbrook L., Hindle M., Aerodynamic factors responsible for the deaggregation of carrier-free drug powders to form micrometer and submicrometer aerosols, Pharmaceutical Research, 30 (2013) 1608–1627.

Mack G.S., Pfizer dumps Exubera, Nature Biotechnology, 25 (2007) 1331–1332.

McGregor K., Principles of anaesthesia for term neonates, Anaesthesia & Intensive Care Medicine, 18 (2017) 75–78.

Nahar K., Gupta N., Gauvin R., Absar S., Patel B., Gupta V., Khademhosseini A., Ahsan F., In vitro, in vivo and ex vivo models for studying particle deposition and drug absorption of inhaled pharmaceuticals, European Journal of Pharmaceutical Sciences, 49 (2013) 805–818.

Newman S.P., Principles of metered-dose inhaler design, Respiratory Care, 50 (2005) 1177–1190.

Patil J., Sarasija S., Pulmonary drug delivery strategies: A concise, systematic review, Lung India, 29 (2012) 44–49.

Patton J.S., Byron P.R., Inhaling medicines: delivering drugs to the body through the lungs, Nature Reviews Drug Discovery, 6 (2007) 67–74.

Phalen R.F., Mendez L.B., Dosimetry considerations for animal aerosol inhalation studies, Biomarkers : biochemical indicators of exposure, response, and susceptibility to chemicals, 14 Suppl 1 (2009) 63–66.

Phalen R.F., Oldham M.J., Wolff R.K., The relevance of animal models for aerosol studies, Journal of Aerosol Medicine and Pulmonary Drug Delivery, 21 (2008) 113–124.

Price D.N., Stromberg L.R., Kunda N.K., Muttil P., In vivo pulmonary delivery and magnetic-targeting of dry powder nano-in-microparticles, Molecular Pharmaceutics, 14:12 (2017) 4741–4750.

Purser D.A., Similarities and differences between animal species in relation to the effect of irritants, in: Stec A., Hull R. (Eds.), CRC Press, Florida, 2010, pp. 75–83, ISBN: 9781845698072.

Rubin B.K., Williams R.W., Emerging aerosol drug delivery strategies: From bench to clinic, Advanced Drug Delivery Reviews, 75 (2014) 141–148.

Sacchetti M., Van Oort M.M., Spray drying and supercritical fluid particle generation techniques in inhalation aerosols, in: Anthony J.H. (Ed.), Informa Healthcare, New York, 2007, pp. 307–346.

Sakagami M., Systemic delivery of biotherapeutics through the lung: opportunities and challenges for improved lung absorption, Therapeutic Delivery, 4 (2013) 1511–1525, DOI: 10.4155/tde.13.119.

Saluja V., Amorij J.P., Kapteyn J.C., de Boer A.H., Frijlink H.W., Hinrichs W.L.J., A comparison between spray drying and spray freeze drying to produce an influenza subunit vaccine powder for inhalation, Journal of Controlled Release, 144 (2010) 127–133.

Scheuch G., Kohlhaeufl M.J., Brand P., Siekmeier R., Clinical perspectives on pulmonary systemic and macromolecular delivery, Advanced Drug Delivery Reviews, 58 (2006) 996–1008.

Schreider J.P., Raabe O.G., Anatomy of the nasal-pharyngeal airway of experimental animals, The Anatomical Record, 200 (1981) 195–205.

Scichilone N., Asthma control: the right inhaler for the right patient, Advances in Therapy, 32 (2015) 285–292.

Selvam P., McNair D., Truman R., Smyth H.D.C., A novel dry powder inhaler: Effect of device design on dispersion performance, International Journal of Pharmaceutics, 401 (2010) 1–6.

Shaji J., Shaikh M., Current development in the evaluation methods of pulmonary drug delivery system, Indian Journal of Pharmaceutical Sciences, 78 (2016) 294–306, DOI: 10.4172/pharmaceutical-sciences.1000118.

Smutney C.C., Grant M., Kinsey P.S., Device factors affecting pulmonary delivery of dry powders, Therapeutic Delivery, 4 (2013) 939–949.

Society of Toxicology report, Recommendations for the conduct of acute inhalation limit tests, Toxicological Sciences, 18 (1992) 321–327. DOI: 10.1016/0272-0590(92)90130-A.

Stein S.W., Thiel C.G., The history of therapeutic aerosols: A chronological review, Journal of Aerosol Medicine and Pulmonary Drug Delivery, 30 (2017) 20–41.

Stone K.C., Mercer R.R., Gehr P., Stockstill B., Crapo J.D., Allometric relationships of cell numbers and size in the mammalian lung, American Journal of Respiratory Cell and Molecular Biology, 6 (1992) 235–243.

Storti C., Le Noci V., Sommariva M., Tagliabue E., Balsari A., Sfondrini L., Aerosol delivery in the treatment of lung cancer, Current Cancer Drug Targets, 15 (2015) 604–612.

Tashkin D., A review of nebulized drug delivery in COPD, International Journal of Chronic Obstructive Pulmonary Disease, Volume 11 (2016) 2585–2596.

Telko M.J., Hickey A.J., Dry powder inhaler formulation, Respiratory Care, 50 (2005) 1209–1227.

Tonnis W.F., Bagerman M., Weij M., Sjollema J., Frijlink H.W., Hinrichs W.L.J., de Boer A.H., A novel aerosol generator for homogenous distribution of powder over the lungs after pulmonary administration to small laboratory animals, European Journal of Pharmaceutics and Biopharmaceutics, 88 (2014) 1056–1063.

Vehring R., Pharmaceutical particle engineering via spray drying, Pharmaceutical Research, 25 (2008) 999–1022. DOI: 10.1007/s11095-007-9475-1

Walters E.B., Panda K., Bankson J.A., Brown E., Cody D.D., Improved method of in vivo respiratory-gated micro-CT imaging, Physics in Medicine and Biology, 49 (2004) 4163–4172.

Weers J.G., Clark A.R., Challoner P., High dose inhaled powder delivery: challenges and techniques, Respiratory Drug Delivery IX, 1 (2004) 281–288.

Wehling M., Assessing the translatability of drug projects: what needs to be scored to predict success?, Nature Reviews Drug Discovery, 8 (2009) 541–546.

Weibel E.R., Geometric and dimensional airway models of conductive, transitory and respiratory zones of the human lung, in: Weibel E.R. (Ed.), Morphometry of the Human Lung, Springer Berlin Heidelberg, Berlin, 1963, pp. 136–142, ISBN 978-1-4832-0076-7.

Wong B.A., Inhalation exposure systems: design, methods and operation, Toxicologic Pathology, 35 (2007) 3–14.

Yang M.Y., Chan J.G.Y., Chan H.-K., Pulmonary drug delivery by powder aerosols, Journal of Controlled Release, 193 (2014) 228–240.

Yi J., Chen B.T., Schwegler-Berry D., Frazer D., Castranova V., McBride C., Knuckles T.L., Stapleton P.A., Minarchick V.C., Nurkiewicz T.R., Whole-body nanoparticle aerosol inhalation exposures, Journal of visualized experiments: JoVE, (2013) e50263. DOI: 10.3791/50263

Zhou Q., Tang P., Leung S.S.Y., Chan J.G.Y., Chan H.-K., Emerging inhalation aerosol devices and strategies: Where are we headed?, Advanced Drug Delivery Reviews, 75 (2014) 3–17.

Authors' Short Biographies

Dominique N. Price

Dominique Price is a medical student at the University of New Mexico Health Science Center, USA. She received her Ph.D. in Biomedical Sciences in 2016 from the University of New Mexico, USA. She has a broad research background in pulmonary delivery and infectious disease, especially diseases of the lung. She is continues to be an active researcher in laboratory of Dr. Pavan Muttil in the College of Pharmacy, University of New Mexico, USA. Her publications and research interests include a wide variety of research topics including localized delivery of pulmonary therapeutics, stabilization of bacterial vaccines and biologics, and interactions of environmental bacterial with immunization efficacy in tuberculosis.

Nitesh K. Kunda

Nitesh Kunda is a Post-doctoral fellow in the Department of Pharmaceutical Sciences at the College of Pharmacy, University of New Mexico, USA. He received his Ph.D. in Formulation and Drug Delivery in 2014 from Liverpool John Moores University, UK. He has extensive research experience in drug formulation, as well as drug and vaccine delivery, specifically pulmonary delivery. His research interests lie in nanotechnology in drug delivery, design and development of vaccine delivery systems, proteins and gene formulations, microneedle formulations, synthesizing polymeric nanoparticles and attaching targeting moieties for site specific delivery. His publications include a wide variety of research topics including formulation and delivery of drugs and vaccines, lung delivery, and stabilization of bacterial-based and viral-based vaccines. He is an active member of professional organizations such as the Royal Society of Chemistry, the Aerosol Society, American Association of Pharmaceutical Scientists, and the British Society of Nanomedicine amongst others.

Pavan Muttil

Dr. Muttil is an Associate Professor in the Department of Pharmaceutical Sciences at the University of New Mexico, NM, USA. He obtained his Ph.D. in aerosol drug delivery from Central Drug Research Institute, Lucknow, India. Dr. Muttil did his postdoctoral research in aerosol drug and vaccine delivery at the Eshelman School of Pharmacy, University of North Carolina, Chapel Hill. He was the recipient of a Bill and Melinda Gates Grand Challenges Exploration grant in 2012. Research in the Muttil Laboratory is focused on developing drug and vaccine formulations for inhaled, oral, and transdermal delivery systems for infectious diseases and cancers. These novel formulations are evaluated in animal models for their efficacy as a needle-free delivery strategy.

KONA Powder and Particle Journal No. 36 (2019) 145–155/Doi:10.14356/kona.2019011 Review Paper

Progress in the Preparation of Magnetite Nanoparticles through the Electrochemical Method [†]

Heru Setyawan* and **W. Widiyastuti**

[1] *Department of Chemical Engineering, Faculty of Industrial Technology, Institut Teknologi Sepuluh Nopember, Indonesia*

Abstract

Magnetite (Fe_3O_4) is one of the most important iron oxides due to its extensive range of application in various fields. The characteristics of magnetite can be considerably enhanced by reducing the particle size to the nanometer scale. When novel functions of nanoparticles are desired, it is necessary to have monodispersed or nearly monodispersed nanoparticles. Many synthesis methods have been proposed to produce monodispersed magnetite nanoparticles, including co-precipitation, sol-gel, hydrothermal and electrochemical methods. In this review, progress in the preparation of magnetite nanoparticles and their composites through the electrochemical method and the scale-up method are discussed.

Keywords: magnetite nanoparticles, electrosynthesis, scale-up, monopolar, particle formation, precipitation

1. Introduction

Magnetite (Fe_3O_4) is one of the most important iron oxides, a common compound that is widespread in nature and readily synthesized in the laboratory and is widely used in industry. Magnetite is a black, ferrimagnetic mineral containing both Fe(II) and Fe(III). Other names are recognized for magnetite, including black iron oxide, magnetic iron ore, iron(II, III) oxide, loadstone (when natural polarity is present), tri-iron tetroxide, ferrous ferrite and Hercules Stone. Although several of the names are not recognized as mineral names, they are in current use. The names reflect the diversity of disciplines for which this mineral is of interest.

Magnetite is a magnetic material and contains many exciting properties and potential for various applications. Magnetite particles have been used in data storage and improved electronic devices (Sharrock M.P. and Bodnar R.E., 1985). These particles also have considerable potential for use in the biomedical industry, such as targeted drug delivery, hyperthermia treatment, cell separation, magnetic resonance imaging, immunoassays and the separation of biomedical products (Jain T.K. et al., 2005; Mahmoudi M. et al., 2011; Qiao R. et al., 2009). Magnetite particles are also used as active catalysts for several oxidation/reduction and acid/base reactions and as an efficient candidate in environmental catalysis (Jin X. et al., 2012; Moghanian H. et al., 2014). The catalytic activity of magnetite can be considerably enhanced by reducing the particle size to the nanometer scale. It has been demonstrated that magnetite nanoparticles exhibit high catalytic activity for the esterification of oleic acid with methanol in the production of methyl oleate (biodiesel) (El-Nahas A.M. et al., 2017). These particles can also be used as promising electrode materials for electrochemical energy storage systems, such as Li-ion batteries and supercapacitors (Cheng J. et al., 2012; Liu J. et al., 2013).

Magnetite is naturally found in the form of an iron ore containing a significant amount of impurities. The iron ore must be processed to obtain higher purity of magnetite having specific properties suitable for various applications. The synthesis of magnetite nanoparticles is complicated because of their natural colloidal behavior. The most common method to synthesize magnetite nanoparticles is the co-precipitation of ferric and ferrous ions in highly basic conditions (Petcharoen K. and Sirivat A., 2012; Shen L. et al., 2014). The formation of magnetite is in favor in the pH range of 8 to 14 along with a Fe^{3+}/Fe^{2+} ratio of 2:1 under non-oxidizing conditions (Ramimoghadam D. et al., 2014). The advantage of this technique is its capability for a high production rate of magnetite nanoparticles. Controlling particle size distribution is, however, inconvenient due to the immediate reactions in the mixture that make it difficult to control the crystallization process.

Hydrothermal and sol-gel methods are among the most well-known techniques, as well as co-precipitation, for

---

[†] Received 2 April 2018; Accepted 22 May 2018

[1] Kampus ITS Sukolilo, Surabaya 60111, Indonesia

* Corresponding author: Heru Setyawan;
E-mail: sheru@chem-eng.its.ac.id
TEL: +62-31-5946240 FAX: +62-31-5999282

the production of magnetite nanoparticles with controlled morphology and chemical composition (Daou T.J. et al., 2006; Han C. et al., 2012; Haw C.Y. et al., 2010; Lemine O.M. et al., 2012; Xu J. et al., 2007). In the hydrothermal technique, reactions are carried out in aqueous media at high pressure and temperature. The size and shape of the nanoparticles can be controlled by manipulating the reaction time, temperature, reactant composition, solvent type and surfactant (Daou T.J. et al., 2006; Han C. et al., 2012).

Depending on the synthesis method and conditions, synthetic magnetite may have different morphologies and crystal structures. The hydrothermal method usually produces magnetite with octahedral crystals, but it grows to have a combination of rhombic dodecahedral crystals in the presence of mineralizers (Qu X. et al., 2010). Synthesis in aqueous systems at temperatures less than 100 °C produces rounded magnetite having cubic or octahedral crystals. For example, octahedral and spheres are obtained by oxidizing green rust with KNO_3 at 90 °C and pH 6–10. Spheres are formed when $Fe^{2+} > OH^-$, but they change into cubic crystals in excess OH^- (Thapa D. et al., 2004). Divalent iron may be partly or entirely substituted by a broad range of other divalent ions because of the availability of tetrahedral and octahedral positions. The substitution ions can be fitted well into the structure due to the flexibility of the oxygen framework, which can accommodate the cations of different sizes. The ion is accompanied by changes in the length of unit cell edge. The products in which the Fe(II) is fully substituted by another divalent ion M(II) to form MFe_2O_4 are known as ferrites. There has been considerable interest in ferrites themselves, owing to their applications in, for instance, electrical appliances and as catalysts (Galindo R. et al., 2012; Mazario E. et al., 2013).

2. Magnetite properties

2.1 Bulk properties

The general properties of magnetite are presented in **Table 1** (Cornell R.M. and Schwertmann U., 2003). The naturally occurring and synthesized magnetite crystals exhibit metallic luster and opaque black color. The density is approximately 5.18 g/cm^3, lighter than pure iron (α-Fe; 7.87 g/cm^3). The hardness is approximately 5.5, identical to glass. Magnetite particles are non-porous with surface areas that vary according to synthesis method. Different methods generate different particle sizes, and in turn, different surface areas. The standard free energy of formation is –1012.6 kJ mol^{-1}, indicating that magnetite formation is thermodynamically favorable. Magnetite is soluble under acid conditions (Setyawan H. et al., 2012). The solubility product is dependent on the appropriate dissolution reaction.

Table 1 General properties of magnetite.

Properties	
Crystal structure	cubic
Cell dimension (nm)	$a = 0.8396$
Formula units, per unit cell, Z	8
Density (g cm^{-1})	5.18
Color	black
Hardness	5 ½
Type of magnetism	ferrimagnetic
Curie temperature (K)	850
Std. free energy of formation (kJ mol^{-1})	–1012.6
Solubility product (pFe + 3 pOH)	35.7
Melting point (°C)	1583–1597
Boiling point (°C)	2623
Heat of fusion (kJ mol^{-1})	138.16
Heat of decomposition (kJ mol^{-1})	605.0
Heat of vaporization (kJ mol^{-1})	298

The crystal structure of magnetite follows an inverse spinel pattern with a face-centered cubic cell based on 32 O^{2-} ions, which are regularly cubic close-packed along the [111]. The unit cell has eight formula units per unit cell with a length edge of 0.839 nm. Magnetite contains both divalent and trivalent iron and is frequently non-stoichiometric, i.e., it has a cation-deficient Fe(III) sublattice. The divalent iron species occupy half of the octahedral lattice sites due to higher crystal field stabilization energy. Conversely, the trivalent iron species occupy the other octahedral lattice sites and all tetrahedral lattice sites. The octahedral and mixed tetrahedral/octahedral layers stacked along [111] (Cornell R.M. and Schwertmann U., 2003).

The melting point of magnetite ranges from 1583 to 1597 °C, and its boiling point is 2623 °C. The heat of fusion, decomposition, and vaporization are, respectively, 138.16, 605.0 and 298 kJ mol^{-1}.

The Curie temperature of magnetite is 850 K. Below that temperature, magnetite possesses ferrimagnetic behavior. In this case, magnetic moments on tetrahedral sites, occupied by Fe(III), are ferromagnetically aligned, while magnetic moments on octahedral sites, occupied by Fe(III) and Fe(II), are antiferromagnetic and cancel each other out. When the Curie temperature is attained, net magnetization is zero, and magnetite possesses superparamagnetic behavior.

Table 2 General properties of magnetite.

Material	Lattice parameter (Å)	Unit cell volume (Å)
Bulk magnetite	8.39	590.6
6.4 nm magnetite	8.40	592.7

2.2 Nano-sized properties

The effective surface area of magnetite particles should increase with decreasing particle size. The effective surface area of 0.2 μm-magnetite particles is approximately 6 $m^2 g^{-1}$ and increases considerably to 100 $m^2 g^{-1}$ when the size is down to ~50 nm. The change in surface area due to the change in size does not change the crystal structure of magnetite (Li Q. et al., 2017). Nano-sized magnetite still exhibits black color, having a face-centered cubic unit cell of the same lattice parameter and unit cell volume, as shown in **Table 2** (Cornell R.M. and Schwertmann U., 2003; Thapa D. et al., 2004).

As discussed above, bulk magnetite is ferrimagnetic at room temperature and has a Curie temperature of 850 K. The magnetic property changes with the change of particle size. The ferrimagnetic behavior of magnetite tends to change towards paramagnetic or superparamagnetic behavior when the particle size is below 6 nm. Superparamagnetic behavior is indicated by a zero remanence and a negligible coercivity in the absence of an external magnetic field. In the size range of 1 to 10 nm, each particle becomes a single magnetic domain, and the energy barrier for its spin reversal is easily overcome by thermal vibrations (Iglesias O. and Labarta A., 2004). Coercivity builds slowly as the particle size increases (Thapa D. et al., 2004).

3. Electrochemical synthesis of magnetite nanoparticles

An electrochemical synthesis is primarily conducted by passing an electric current through two or more electrodes, which consist of an anode and a cathode, in an electrolyte solution. The production of nanoparticles using this method involves the reduction and oxidation (redox) reactions at electrodes that induce precipitation from the solution phase. The reduction process is a reaction where a species in solution accepts an electron from the cathode, and the oxidation process is a reaction where a species in solution releases an electron to the anode. Thus, the redox process is a chemical phenomenon associated with charge transfer to or from an electrode. The amount of electron transfer at the cathode and the anode must be equal.

Electrode reactions are heterogeneous and occur in the interfacial region between electrode and solution. The reactions produce a slight unbalance in the electric charges of the electrode and the solution. Hence, the electrode reactions can be controlled by manipulating the interfacial potential difference through the potential difference between pairs of electrodes in an electrochemical cell.

The kinetic limitation in an electrochemical system at low temperature can be easily overcome by an applied potential or electric field (Bard J.B. and Faulkner L.R., 2001). Therefore, this method can be conducted at a low temperature below the boiling point of the electrolyte. The electrochemical reaction is also sensitive to the characteristics of the electrode surface and the electrolyte composition. The method represents a means of obtaining products that are not possible to gain from conventional chemical synthesis (Fajaroh F. et al., 2012).

3.1 Operation mode

A typical electrochemical cell is illustrated in **Fig. 1**, which consists of an anode, a cathode, and an electrolyte. During the electrosynthesis, the electrode reactions induce precipitation from the solution phase. Therefore, it appears that the key factors to control the reactions are the applied current and the applied potential. **Table 3** presents selected studies on synthesis of magnetite nanoparticles by the electrochemical method. For most studies, the electrochemical synthesis of magnetite nanoparticles is mostly performed under galvanostatic or potentiostatic mode although other modes such as cyclic voltammetry, pulsed potential, and pulsed current are also used. The magnetite nanoparticles produced by the electrochemical method are mainly spherical, although other morphologies, such as nanorod and cubic, can also be produced.

In the galvanostatic mode, the current is controlled to remain constant during the electrosynthesis. Since current is related to the number of materials reacted, it implies

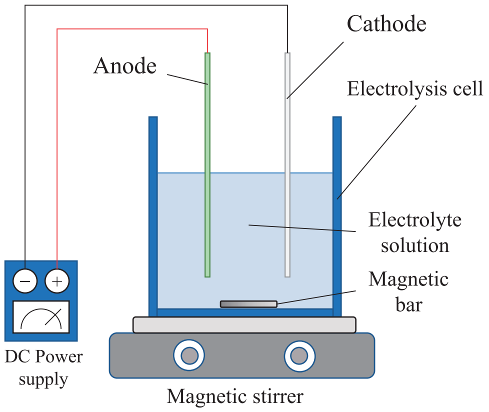

Fig. 1 Typical electrochemical cell.

Table 3 Selected studies on synthesis of magnetite nanoparticles by electrochemical method.

Precursor	Electrode	Electrolyte	Operation mode	Time	Particle size (nm)	Reference
Fe anode + $Fe(ClO_4)_2$	Fe sheet for both anode and cathode	0.0–1 M $Fe(ClO_4)_2$ (*aq*)	Galvanostat: 40–60 mA cm^{-2}	30 and 45 min	15–35 (cubic)	(Gopi D. et al., 2016)
Fe anode	Carbon steel plates for both anode and cathode	0.04 M NaCl (*aq*) bubbled with air	Galvanostat: 62.5 and 125 mA cm^2	20 and 30 min (room temp. and 70 °C)	30.5–45.2 (spherical)	(Weng, Y.C. et al., 2005)
Fe anode	Fe sheet for both anode and cathode	0.04 M Me_4NCl (*aq*)	Potentiostat: 1–15 V; Galvanostat: 10–200 mA cm^{-1}	1800 s (60 °C)	23–33 (spherical)	(Cabrera L. et al., 2008)
$Fe(NO_3)_3$	Three electrodes: carbon disk (WE), Ag/AgCl (RE), Pt rod (CE)	0.01–0.16 M $Fe(NO_3)_3.9H_2O$ in ethanol	Cyclic voltammetry (potential 20–60 V; current 30 mA cm^{-2})	NA	6.2 (spherical)	(Ibrahim M. et al., 2009)
Fe anode	Three electrodes: Stainless steel pellets (WE), SCE (RE), Pt wire (CE)	0.04 M NaCl; 0.02 M $NaSO_4$; 0.02 M NaSCN; 0.02 M NaS_2O_3 Dissolved in water at pH 10	Galvanostat 12.5 mA cm^{-1}	30 min	45–80 (spherical)	(Franger S. et al., 2004)
Fe anode	Fe sheet for both anode and cathode	0.25 M Na_2SO_4 and 0.04 M stabilizing agent (TU, PA, BU, HMTA, β-CD, or TBA)$^{(a)}$	Potentiostat 5 V (60 °C)	30 min	25–90 (primary); β-CD: agglomerate, fusiform structures; TBA: sheet-like;	(Mosivand S. et al., 2013)
Fe anode	Three electrodes: Fe foil (WE & CE), SSE (RE)	0.5 M KCl (*aq*)	Pulsed potential	60 min	27–32 (spherical)	(Rodríguez-López A. et al., 2012)
Fe anode	Fe sheet for both anode and cathode	2 M KOH with CTAB	Pulsed current (A = 18 mA cm^{-2}; f = 8 Hz)	24 h	~67 (nanorods)	(Karami H. and Chidar E., 2012)
Fe anode	Fe plate for both anode and cathode	Deionized water	Galvanostat: 205–415 µA cm^{-2}	20 h	10–30 (spherical)	(Fajaroh F. et al., 2012)
$Fe(NO_3)_3$	Carbon cylinders (anode and cathode)	0.01 – 0.016 M $Fe(NO_3)_3{\cdot}9H_2O$ in ethanol	Potentiostat: 62 V	12 h	4.4–9 (spherical)	(Marques R.F.C et al., 2008)

(a)TU = thiourea; PA = propylamine; BU = sodium butanoate; HMTA = hexamethylene-tetra-amine; β-CD = β-cyclodextrine; TBA = tetrabutylammonium bromide.

that the reaction kinetics are kept constant. The cell potential deviates during the process, which causes a decrease in the reactant activity. Conversely, the potential is kept constant during the electrosynthesis in potentiostatic mode. A suitable potential window must be appropriately selected to yield a desirable reaction using a certain type of electrode and chemical composition of the electrolyte. For example, in an aqueous system, water can undergo both oxidation (Eqn. 1) and reduction (Eqn. 2).

$$2H_2O \rightarrow O_2(g) + 4H^+ + 4e^- \quad E° = -1.23\ V \qquad (1)$$

$$2H_2O + 2e^- \rightarrow H_2(g) + 2OH^- \quad E° = -0.828\ V \qquad (2)$$

Thus, if an aqueous solution is electrolyzed, one or both reactions may compete with the electrolysis of the dissolved substances. The reaction depends on the value of the potential standard $E°$ of the substance relative to that of water.

As an illustration, suppose an aqueous $NiCl_2$ solution is electrolyzed using a Pt electrode. For this case, reactions of Eqns. 3 and 4 occur.

$$Ni^{2+} + 2e^- \rightarrow 2Ni(s) \quad E° = -0.24\ V\ \text{(anode)} \qquad (3)$$

$$2Cl^- \rightarrow Cl_2(g) + 2e^- \quad E° = -1.36\ V\ \text{(cathode)} \qquad (4)$$

Comparison of the $E°$ of reactions 1 and 3 and of reactions 2 and 4 would lead us to predict that the oxidation 3 would be favored over that of 1, and the reduction 4 would be favored over that of 2. When $NiCl_2$ is replaced with NaCl, H_2 will be generated at the cathode, not Na. At the cathode, reaction 1 will occur, and at the anode, $Cl^- \rightarrow 1/2\ Cl_2(g) + e^-$ ($E° = –1.36$ V). The value of $E°$ for the Na^+/Na pair is –2.714 V, and that for the H_2O/H_2 pair is –0.828 V. Because $E°_{Na^+/Na}$ is more negative than $E°_{H_2O/H^+}$, reduction of Na^+ is more difficult than the reduction of water, meaning that the latter will occur. If Cl^- ion is replaced by an anion that is more difficult to oxidize, such as NO_3^- or SO_4^-, water will oxidize.

In a galvanostatic operation, a low current density significantly influences the particle size of magnetite nanoparticles (Fajaroh F. et al., 2012). The particles size increases with the increase in current density. Conversely, the current density has no significant effect on the particle size at high current density, i.e., the particle size is constant even if the current density is varied (Cabrera L. et al., 2008). At high current density, the effects of the diffusion rate and the Helmholtz layer can be ignored during the reaction. In contrast, these effects cannot be neglected at low current density. As a result, both charge transfer and diffusion rate have a significant effect on the overall reaction of magnetite formation at low current density, i.e., low reaction rate.

Alternatively, pulsed potential or pulsed current has been used to produce magnetite nanoparticles (Setyawan H. et al., 2014). The use of pulsed potential or pulsed current can effectively prevent the particle aggregation and bubble formation that occur during synthesis due to the electrolysis of water. Particles dispersed in an electrolyte carry electrical charges due to the attachment of ions surrounding the particles. In the presence of the electrical field, especially near the electrode surface, the motion of charged particles is influenced by electrophoretic and electroosmosis forces (Naim M.N. et al., 2010). Hence, the charged particles are accelerated towards the electrode surface and tend to collide with each other to form an aggregate. Under pulsed potential or pulsed current, the motion of particles due to the two forces are stopped at the off-condition that prevents particles collision and, in turn, particles agglomeration (Rodríguez-López A. et al., 2012).

The potentials of the pulses must be appropriately selected to ensure the formation of magnetite. The applied minimum and maximum values of the potential pulses must cover the potential reductions of ferric to ferrous ions, of water to hydroxyl ions and of ferrous ion to metallic iron, and the oxidation of iron to ferric species. Using a dissymmetric pattern of potential pulses, i.e., changing the polarity of the electrodes, ferrous and ferric ions are generated when the iron acts as an anode and later generates hydroxyl ions to form chemically ferric hydroxide while simultaneously reducing that hydroxide to magnetite, when it acts as a cathode (Karami H. and Chidar E., 2012). In this way, the energy related to the mass transfer of hydroxyl ions generated at the cathode to the anode can be saved because they are no longer traveling to the other electrode.

The particle morphology can be controlled to become nanorods under pulsed current mode with the addition of surfactant (Karami H. and Chidar E., 2012). The nanorod structures in the pulsed-electrochemical synthesis may be formed as the result of the directional growth of initial magnetite formed on the electrode surface. The pulsed current slows the chemical reaction rate and may influence the nucleation process and growth. The electric field created during the pulsed current may interact with chemical reaction systems since it contains charged ions such as Fe^{3+}, Fe^{2+} and OH^- that form Fe_3O_4 cluster with a structural motif. If the electrostatic force is parallel to or far greater than the composition of forces in the structural motif and the nucleation process and growth are prolonged, structural motifs are likely to follow the minimum energy principle and growth along the easy electric field axis occurs to build single-crystal rod-like structures (Zhang W. et al., 2011).

Based on the above descriptions of various modes of operation to synthesize magnetite nanoparticles by an electrochemical method, the advantages and disadvantages can be understood. The applied potential to the electrochemical cell is constantly controlled using the potentiostat mode. This approach ensures that the electrochemical reactions taking place in the system can be maintained during the synthesis. Using the galvanostatic mode, the current supplied to the cell is set constant. The mode ensures the kinetics of reaction can be maintained over the period of synthesis. The potential may change, however, during the synthesis, influencing the electrochemical reactions in the system. It seems that the potential mode can give the desirable electrochemical reactions. As the precipitation is strongly influenced by the concentration of the reactants, however, the current mode is likely to be a better choice. If it is desired to have monodispersed, uniformly sized, stable magnetite nanoparticles, the pulsed mode may become the most suitable choice, but it requires considerably more time to obtain the desired amount of product.

3.2 Precursors and electrolytes

The most common method to prepare magnetite nanoparticles by electrochemical synthesis is electro-oxidation of iron (see **Table 3**). Typically, the iron source acts as an anode in an electrochemical cell. When the current/voltage is imposed on the cell, the iron is oxidized to become Fe^{2+} ions that are dissolved in the electrolyte solution. The ions subsequently interact with other ions to form iron oxide nanoparticles, either in the anode or cathode regions. In this case, the particles are generated by a primary nucleation and growth process. The continuous supply of Fe^{2+} ions generated by anodic dissolution causes a high concentration of Fe^{2+} ions, and when the concentration reaches supersaturation, homogeneous nucleation begins. The nuclei start colliding with each other and coagulation occurs to form larger particles.

The formation of magnetite nanoparticles using the sacrificial iron anode is influenced by certain parameters, the most critical one is the distance between electrodes. If the distance between electrodes is far away, the region close to anode will not reach a pH value necessary to form iron hydroxide. Although the hydroxide ion is formed, it would not reduce at the cathode, at least not in an appreciable amount. Thus, there is a critical distance in which magnetite nanoparticles can be formed (Fajaroh F. et al., 2012). It is apparent that pH is also a critical factor in the formation of magnetite nanoparticles. The formation of magnetite is favored in basic condition, typically at a pH between 9 and 11 (Ramimoghadam D. et al., 2014).

The supporting electrolyte solution is often necessary to enhance the electrical conductivity of solution during the electrochemical synthesis. The electrolyte must be appropriately selected for the magnetite nanoparticles to be formed. For example, magnetite can be formed in NaCl solution in the presence of Mg^{2+} and Ca^{2+} ions, while it is formed only slightly in the presence of Cu^{2+} ions (Ying T.Y. et al., 2002). The presence of Mg^{2+} and Ca^{2+} ions hinders the formation of magnetite particles because both ions tend to precipitate or incorporate in the particles. This problem can be overcome, however, by adding a strong electrolyte such as NaCl that significantly increases the conductivity and, in turn, increases the current density. On the other hand, the presence of Cu^{2+} ions interfere with the formation of magnetite particles. In this case, the Cu^{2+} ions make the pH of the solution lower due to the formation of Cu_2O. When Cu_2O is formed, hydrogen ions are produced, decreasing the pH, which leads to unfavorable condition for magnetite formation.

In addition to enhancing the conductivity, the electrolyte may also act as a surfactant or complexing agent. For example, amines are surfactants that acts as a supporting electrolyte and coating agent to control particle size and aggregation during synthesis (Cabrera L. et al., 2008). The magnetite nanoparticles produced using this surfactant have sizes between 20 and 30 nm. Various compounds may be used to serve as a complexing or stabilizing agent such as salts, e.g., NaCl, Na_2SO_4, NaSCN and $Na_2S_2O_3$ (Franger S. et al., 2004) and organics, e.g., thiourea, propylamine, sodium butanoate, hexamethylene-tetra-amine, β-cyclodextrin and tetrabutylammonium bromide (Mosivand S. et al., 2013), and $CH_4H_{12}NCl$ (Cabrera L. et al., 2008).

The role of the complexing entities in the electrolytes is purely kinetic. The elementary charge transfer process at an iron electrode is prolonged. Therefore, complexing agents are added to the electrolytes to enhance this electrochemical step by decreasing overpotential. The complexing species must have a lower affinity for iron(III) ions than hydroxide entities for an efficient process (i.e., $pKd < 11$). Otherwise, the formation of iron oxides in aqueous solution is not possible because of competitive reactions; this is the case with citrate, the complexing constant of which is much too high, being $pKd = 25$ (Franger S. et al., 2004).

Combining an iron anode precursor and an aqueous solution of $Fe(ClO_4)_2$ to produce magnetite nanoparticles by the electrochemical method changes the particle morphology from spherical to cubic (Gopi D. et al., 2016) giving particle size was in the range of 15 to 35 nm. Another precursor to synthesize magnetite nanoparticles by the electrochemical method is $Fe(NO_3)_3$ in ethanol medium (Ibrahim M. et al., 2009; Marques R.F.C. et al., 2008). The magnetite nanoparticles produced using this precursor have sizes ranging from 4.4 to 9 nm. The purity of the product is quite vulnerable to the iron concentration and current density. Moreover, this method requires a relatively water-free bath to obtain pure magnetite nanoparticles. The presence of water tends to favor the formation of $Fe(OH)_2$, which contaminates the magnetite nanoparticles.

It is well-known that the chemical co-precipitation method of iron salts is the most common technique to produce magnetite nanoparticles. This method is a straightforward and efficient wet chemical route. Magnetite is precipitated from an aqueous solution of Fe(II) and/or Fe(III) salts with alkali along with suitable aging time. The reaction in this system is very fast, making it difficult to control the precipitation process, and in turn, monodispersed nanoparticles are difficult to obtain. Since the precipitation is mainly governed by adjusting the solution pH by adding OH^-, this ion can be supplied with well-controlled rate by water reduction in an aqueous electrochemical cell (Aghazadeh M. et al., 2017; Karimzadeh I. et al., 2017a). It can be performed by electrolyzing an aqueous solution of Fe(II) and Fe(III) with a molar ratio of 1:2 using a stainless steel cathode and graphite anode. During the electrolysis, OH^- ions are produced by water reduction at the cathode (Eqn. 2). The OH^- ions later induce magnetite formation through the chemical reaction:

$$Fe^{2+} + 2Fe^{3+} + 8OH^- \rightarrow Fe_3O_4 + 4H_2O \tag{5}$$

As in the conventional co-precipitation method, when the Fe^{3+}/Fe^{2+} ratio is 2:1, magnetite can be generated when the pH is in the range of 8 to 14 (Franger S. et al., 2004; Manrique-Julio J. et al., 2016; Melnig V. and Ursu L., 2011).

3.3 Mechanism of particle formation

There are several different proposed mechanisms for the electrochemical formation of magnetite nanoparticles. The proposed mechanisms have been compiled and discussed thoroughly by Lozano I. et al. (2017). In general, the proposed mechanisms can be divided into four groups although the detail steps for each group may be different. They are (i) iron hydroxide reduction at the cathode (Cabrera L. et al., 2008; Ibrahim M. et al., 2009; Rodríguez-López A. et al., 2012; Ying T.Y. et al., 2002), (ii) hydrogen gas as a reducing agent of iron hydroxide (Franger S. et al., 2004; Manrique-Julio J. et al., 2016; Melnig V. and Ursu L., 2011), (iii) direct reaction between Fe^{2+} and Fe^{3+} (Karami H. and Chidar E., 2012; Ying T.Y. et al., 2002), and (iv) oxygen as oxidant agent and subsequent in-solution precipitation (Fajaroh F. et al., 2012; Gopi D. et al., 2016; Lozano I. et al., 2017; Pascal C. et al., 1999; Starowicz M. et al., 2011).

The first step for all of the proposed mechanisms involves the production of Fe^{2+} ions by the oxidation of a sacrificial iron anode and OH^- ions by the reduction of water at the cathode. The iron oxidation at the anode and water reduction at the cathode can be written, respectively, as

$$Fe \rightarrow Fe^{2+} + 2e^- \qquad (6)$$

$$H_2O + e^- \rightarrow 1/2\ H_2 + OH^- \qquad (7)$$

The subsequent mechanism steps are different for the four proposed mechanisms as will be discussed in the following. In the first and second mechanisms, Fe^{2+} ions are further oxidized to Fe^{3+} and in the presence of an OH^- ions leads to the formation of $Fe(OH)_3$. The Fe^{3+} ion is later reduced at the cathode to produce Fe_3O_4. The difference between the two mechanisms is the reducing agent. The reduction of the first mechanism occurs on the cathode surface via Faradaic reaction (Eqn. 8) and the second one by hydrogen produced on the cathode (Eqn. 9).

$$3\gamma\text{–}FeOOH(s) + e^- \rightarrow Fe_3O_4(s) + H_2O + OH^- \qquad (8)$$

$$3\gamma\text{–}FeOOH(s) + 1/2\ H_2 \rightarrow Fe_3O_4(s) + 2H_2O \qquad (9)$$

As noted by Lozano I. et al. (2017), however, it is unlikely that solid species such as $Fe(OH)_3$ can reach the cathode to undergo reduction. Additionally, due to its high propensity to escape from the reacting medium, it is almost impossible for hydrogen gas to react with iron hydroxide (Eqn. 9).

In the direct reaction mechanism, in addition to Fe^{2+} ions, Fe^{3+} ions are also produced on the anode surface. The two ions then react to form Fe_3O_4 in the presence of OH^- ions following the reaction

$$Fe^{2+} + 2Fe^{3+} + 8OH^- \rightarrow Fe_3O_4(s) + 4H_2O \qquad (10)$$

This mechanism has, however, a lack of further explanation.

The last mechanism which involves dissolved oxygen as an oxidizing agent for $Fe(OH)_2$ in solution to produce magnetite seems to be the most likely appropriate to describe the electrochemical formation of magnetite nanoparticles. This mechanism was first proposed by Fajaroh F. et al. (2012), and the validity was confirmed by Lozano I. et al. (2017) through experimental strategies to provide relevant information to prove the mechanisms. In brief, Fe^{2+} ions produced by iron dissolution (Eqn. 6) in the presence of OH^- ions precipitate to $Fe(OH)_2$. In the presence of oxygen, $Fe(OH)_2$ can be partially oxidized to form FeOOH, and they transform into magnetite when an appropriate proportion of the two substances is achieved. They can be summarized as, after Eqns. 6 and 7,

$$3Fe(OH)_2 + 1/2\ O_2 \rightarrow Fe(OH)_2 + 2FeOOH + H_2O \qquad (11)$$

$$Fe(OH)_2 + 2FeOOH \rightarrow Fe_3O_4 + 2H_2O \qquad (12)$$

Reaction 11 represents partial oxidation of ferrous hydroxide in the presence of oxygen to form FeOOH. Magnetite is formed when an appropriate proportion of $Fe(OH)_2$ and FeOOH is created by reaction 12.

4. Electrochemical synthesis of functional magnetite nanoparticles

The magnetite nanoparticles may be modified at their surface to have functional properties and applications. These functional nanoparticles are also be obtained by the combination of two or more constituents. The surface modification or the combination of more than one material may give rise to many varieties of properties that lead to various applications. For example, bare magnetite nanoparticles are susceptible to degradation in some environments, e.g., dissolve in an acidic environment (Setyawan H. et al., 2012) and susceptible to air oxidation (Fajaroh F. et al., 2013; Setyawan H. et al., 2012; Vatta L.L. et al., 2007). One way to protect magnetite nanoparticles from possible acid dissolution or air oxidation is by coating the particles with a more inert material, such as silica (Fajaroh F. et al., 2013; Setyawan H. et al., 2012). The electrochemical method seems to be effective and efficient to produce functional magnetite nanoparticles.

When an electrochemical route using a sacrificial iron anode coupled with an appropriate electrolyte, two metal oxide nanoparticles may be produced. For example, nickel ferrite ($NiFe_2O_4$) nanoparticles can be produced using two sheets of iron and nickel as sacrificial anodes in a three-electrode electrochemical cell (Galindo R. et al., 2012). Cobalt ferrite ($CoFe_2O_4$) nanoparticles having a size of approximately 20 nm are produced when the nickel sheet is replaced by cobalt (Mazario E. et al., 2012, 2013). The nickel ferrite nanoparticles have a cubic spinel structure and are spherical with sizes in the range of 5-45 nm. The same crystal structure and particle shape can be obtained for cobalt ferrite nanoparticles, but with a particle size of approximately 20 nm. Both kinds of ferrite particles have soft ferromagnetic behavior with a saturation magnetization of 48 emu/g (bulk 55 emu/g) and coercivity 31 Oe for nickel ferrite, and 71 emu/g (bulk 80 emu/g) and 442 Oe for cobalt ferrite.

When the electrolyte solution is dilute aqueous sodium silicate, silica-coated magnetite nanoparticles are produced (Setyawan H. et al., 2012). The silica-magnetite nanoparticles produced by this system are spherical, with a mean size ranging from 6 to 10 nm. They exhibit superparamagnetic properties with a saturation magnetization of approximately 20 emu/g. The superparamagnetic behavior of the silica-coated magnetite nanoparticles which is different from that of magnetite nanoparticles synthesized by the same electrochemical approach is probably caused by the smaller size of particles (< 10 nm). For very small particles, the energy barrier for its spin reversal is easily overcome by thermal vibrations because each particle becomes a single magnetic domain (Iglesias O. and Labarta A., 2004). The silica layer formed by this method is stable and can serve as a protective layer against an acidic environment and high temperature (Fajaroh F. et al., 2013; Setyawan H. et al., 2012).

Magnetite nanoparticles coated with polydopamine can be obtained when the electrochemical oxidation of iron is performed in the presence of dopamine (Mazario E. et al., 2014). The polydopamine-coated magnetite nanoparticles are spherical with the size varying between a few nanometers and 25 nm. The polymer coating makes the nanoparticles suitable for use in biomedical applications due to their excellent physicochemical and magnetic properties, excellent biocompatibility and nontoxicity. Polyvinyl alcohol (PVA)-coated magnetite nanoparticles of size 64 nm can also be obtained by electrodeposition using an iron chloride/nitrate solution in the presence of PVA (Karimzadeh I. et al., 2017a). Other organics such as vitamin C and sucrose have also been successfully used to coat magnetite nanoparticles by electrodeposition (Aghazadeh M. et al., 2017).

It appears that the electrochemical method is an efficient and facile route to synthesize functional magnetite nanoparticles. The substitution of iron in the magnetite or coating magnetite nanoparticles can be performed in one single step by merely changing the electrode or electrolyte composition.

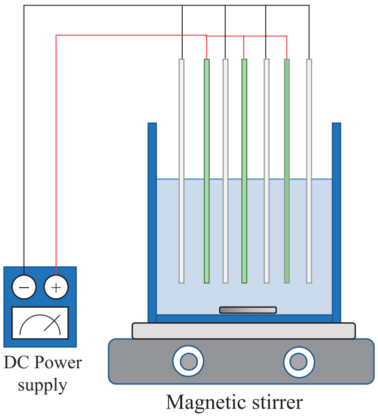

Fig. 2 Monopolar arrangement of an electrochemical cell for scaling up of magnetite nanoparticles production.

5. Scale-up

As discussed above, the electrochemical cell can be scaled up easily by enlarging the current density/potential and electrode size. The electrochemical cell used for the production of magnetite nanoparticles discussed above primarily consists of two electrodes, with one acting as the sacrificial anode for the iron precursor. The production rate of nanoparticles using such an electrode arrangement is very lacking in quantity. At a current density of 0.3 mA/cm^2, it takes 20 h to produce approximately 0.7 g of magnetite nanoparticles. The production rate can be increased significantly by enlarging the electrode size with the same reactor volume using many electrodes with the monopolar arrangement as shown in **Fig. 2**, in which each electrode is connected individually (Manrique-Julio J. et al., 2016).

6. Summary

The methods for the preparation of magnetite nanoparticles by electrochemical technique are briefly reviewed. The electrochemical method has emerged as an option for the preparation of magnetite nanoparticles and their composites. This method offers many advantages over other techniques. One advantage is that this method can easily control particle size by adjusting the imposed current and potential to the system. Additionally, the system is scalable to mass production by merely increasing the current or potential and enlarging the size of the electrode.

Acknowledgments

This scientific work was partly financed by the Ministry of Research and Technology—Indonesia for Fundamental Research Incentive in the years 2012–2014 as

Research Project No. 15300/IT2.11/HK.00.02/2016 and was also supported by JICA-Predict ITS.

References

Aghazadeh M., Karimzadeh I., Ganjali M.R., Mohebi Morad M., A novel preparation method for surface coated superparamagnetic Fe_3O_4 nanoparticles with vitamin C and sucrose, Materials Letters, 196 (2017) 392–395. DOI: 10.1016/j.matlet.2017.03.064

Bard J.B., Faulkner L.R., Electrochemical Methods: Fundamentals and Applications, John Wiley & Sons, Inc., New York, 2001.

Cabrera L., Gutierrez S., Menendez N., Morales M.P., Herrasti P., Magnetite nanoparticles: Electrochemical synthesis and characterization, Electrochimica Acta, 53 (2008) 3436–3441. DOI: 10.1016/j.electacta.2007.12.006

Cheng J., Yu J., Shi D., Wang D., Liu Y., Liu F., Zhang X., Li J., Controllable one-step synthesis of magnetite / carbon nanotubes composite and its electrochemical properties, Applied Physics A, 106 (2012) 837–842. DOI: 10.1007/s00339-012-6786-9

Cornell R.M., Schwertmann U., The Iron Oxides: Structure, Properties, Reaction, Occurences and Uses, first ed., Wiley-VCH Verlag GmbH & Co. KGaA, Weinheim, FRG. 2003. DOI: 10.1002/3527602097

Daou T.J., Pourroy G., Bégin-Colin S., Grenèche J.M., Ulhaq-Bouillet C., Legaré P., Bernhardt P., Leuvrey C., Rogez G., Hydrothermal synthesis of monodisperse magnetite nanoparticles, Chemistry of Materials, 18 (2006) 4399–4404. DOI: 10.1021/cm060805r

El-Nahas A.M., Salaheldin T.A., Zaki T., El-Maghrabi H.H., Marie A.M., Morsy S.M., Allam N.K., Functionalized cellulose-magnetite nanocomposite catalysts for efficient biodiesel production, Chemical Engineering Journal, 322 (2017) 167–180. DOI: 10.1016/j.cej.2017.04.031

Fajaroh F., Setyawan H., Nur A., Lenggoro I.W., Thermal stability of silica-coated magnetite nanoparticles prepared by an electrochemical method, Advanced Powder Technology, 24 (2013) 507–511. DOI: 10.1016/j.apt.2012.09.008

Fajaroh F., Setyawan H., Widiyastuti W., Winardi S., Synthesis of magnetite nanoparticles by surfactant-free electrochemical method in an aqueous system, Advanced Powder Technology, 23 (2012) 328–333. DOI: 10.1016/j.apt.2011.04.007

Franger S., Berthet P., Berthon J., Electrochemical synthesis of Fe_3O_4 nanoparticles in alkaline aqueous solutions containing complexing agents, Journal of Solid State Electrochemistry, 8 (2004) 218–223. DOI: 10.1007/s10008-003-0469-6

Galindo R., Mazario E., Gutiérrez S., Morales M.P., Herrasti P., Electrochemical synthesis of $NiFe_2O_4$ nanoparticles: Characterization and their catalytic applications, Journal of Alloys and Compounds, 536 (2012) S241–S244. DOI: 10.1016/j.jallcom.2011.12.061

Gopi D., Thameem Ansari M., Kavitha L., Electrochemical synthesis and characterization of cubic magnetite nanoparticle in aqueous ferrous perchlorate medium, Arabian Journal of Chemistry, 9 (2016) S829–S834. DOI: 10.1016/j.arabjc.2011.08.005

Han C., Zhao D., Deng C., Hu K., A facile hydrothermal synthesis of porous magnetite microspheres, Materials Letters, 70 (2012) 70–72. DOI: 10.1016/j.matlet.2011.11.115

Haw C.Y., Mohamed F., Chia C.H., Radiman S., Zakaria S., Huang N.M., Lim H.N., Hydrothermal synthesis of magnetite nanoparticles as MRI contrast agents, Ceramics International, 36 (2010) 1417–1422. DOI:10.1016/j.ceramint.2010.02.005

Ibrahim M., Serrano K.G., Noe L., Garcia C., Verelst M., Electro-precipitation of magnetite nanoparticles: An electrochemical study, Electrochimica Acta, 55 (2009) 155–158. DOI: 10.1016/j.electacta.2009.08.026

Iglesias Ò., Labarta A., Role of surface disorder on the magnetic properties and hysteresis of nanoparticles, Physica B: Condensed Matter, 343 (2004) 286–292. DOI: 10.1016/j.physb.2003.08.109

Jain T.K., Morales M.A., Sahoo S.K., Leslie-Pelecky D.L., Labhasetwar V., Iron oxide nanoparticles for sustained delivery of anticancer agents, Molecular Pharmaceutics, 2 (2005) 194–205. DOI: 10.1021/mp0500014

Jin X., Zhang K., Sun J., Wang J., Dong Z., Li R., Magnetite nanoparticles immobilized Salen Pd (II) as a green catalyst for Suzuki reaction, Catalysis Communications, 26 (2012) 199–203. DOI: 10.1016/j.catcom.2012.05.026

Karami H., Chidar E., Pulsed-electrochemical synthesis and characterizations of magnetite nanorods, International Journal of Electrochemical Science, 7 (2012) 2077–2090.

Karimzadeh I., Aghazadeh M., Dalvand A., Doroudi T., Kolivand P.H., Ganjali M.R., Norouzi P., Effective electrosynthesis and in situ surface coating of Fe_3O_4 nanoparticles with polyvinyl alcohol for biomedical applications, Materials Research Innovations, 8917 (2017a) 1–8. DOI: 10.1080/14328917.2017.1343968

Karimzadeh I., Aghazadeh M., Ganjali M.R., Doroudi T., Kolivand P.H., Preparation and characterization of iron oxide (Fe_3O_4) nanoparticles coated with polyvinylpyrrolidone/polyethylenimine through a facile one-pot deposition route, Journal of Magnetism and Magnetic Materials, 433 (2017b) 148–154. DOI: 10.1016/j.jmmm.2017.02.048

Lemine O.M., Omri K., Zhang B., El Mir L., Sajieddine M., Alyamani A., Bououdina M., Sol-gel synthesis of 8 nm magnetite (Fe_3O_4) nanoparticles and their magnetic properties, Superlattices and Microstructures, 52 (2012) 793–799. DOI:10.1016/j.spmi.2012.07.009

Li Q., Kartikowati C.W., Horie S., Ogi T., Iwaki T., Okuyama K., Correlation between particle size/domain structure and magnetic properties of highly crystalline Fe_3O_4 nanoparticles, Scientific Reports, 7 (2017) 1–4. DOI: 10.1038/s41598-017-09897-5

Liu J., Liu S., Zhuang S., Wang X., Tu F., Synthesis of carbon-coated Fe_3O_4 nanorods as electrode material for supercapacitor, Ionics, 19 (2013) 1255–1261. DOI: 10.1007/s11581-013-0857-6

Lozano I., Casillas N., de León C.P., Walsh F.C., Herrasti P., New insights into the electrochemical formation of magnetite nanoparticles, Journal of The Electrochemical Society, 164 (2017) D184–D191. DOI: 10.1149/2.1091704jes

Mahmoudi M., Sant S., Wang B., Laurent S., Sen T., Superparamagnetic iron oxide nanoparticles (SPIONs): Development, surface modification and applications in chemotherapy, Advanced Drug Delivery Reviews, 63 (2011) 24–46. DOI: 10.1016/j.addr.2010.05.006

Manrique-Julio J., MacHuca-Martinez F., Marriaga-Cabrales N., Pinzon-Cardenas M., Production of magnetite by electrolytic reduction of ferric oxyhydroxide, Journal of Magnetism and Magnetic Materials, 401 (2016) 81–85. DOI: 10.1016/j.jmmm.2015.10.018

Marques R.F.C., Garcia C., Lecante P., Ribeiro S.J.L., Noé L., Silva N.J.O., Amaral V.S., Millán A., Verelst M., Electro-precipitation of Fe_3O_4 nanoparticles in ethanol, Journal of Magnetism and Magnetic Materials, 320 (2008) 2311–2315. DOI: 10.1016/j.jmmm.2008.04.165

Mazario E., Menéndez N., Herrasti P., Cañete M., Connord V., Carrey J., Magnetic hyperthermia properties of electrosynthesized cobalt ferrite nanoparticles, Journal of Physical Chemistry C, 117 (2013) 11405–11411. DOI: 10.1021/jp4023025

Mazario E., Morales M.P., Galindo R., Herrasti P., Menendez N., Influence of the temperature in the electrochemical synthesis of cobalt ferrites nanoparticles, Journal of Alloys and Compounds, 536 (2012) S222–S225. DOI: 10.1016/j.jallcom.2011.10.073

Mazario E., Sánchez-Marcos J., Menéndez N., Herrasti P., García-Hernández M., Muñoz-Bonilla A., One-pot electrochemical synthesis of polydopamine coated magnetite nanoparticles, RSC Advances, 4 (2014) 48353–48361. DOI: 10.1039/C4RA08065C

Melnig V., Ursu L., Poly(amidehydroxyurethane) template magnetite nanoparticles electrosynthesis: I. Electrochemical aspects and identification, Journal of Nanoparticle Research, 13 (2011) 2509–2523. DOI: 10.1007/s11051-010-0144-7

Moghanian H., Mobinikhaledi A., Blackman A.G., Sarough-Farahani E., Sulfanilic acid-functionalized silica-coated magnetite nanoparticles as an efficient, reusable and magnetically separable catalyst for the solvent-free synthesis of 1-amido- and 1-aminoalkyl-2-naphthols, RSC Advances, 4 (2014) 28176–28185. DOI: 10.1039/C4RA03676J

Mosivand S., Monzon L.M.A., Ackland K., Kazeminezhad I., Coey J.M.D., The effect of organics on the structure and magnetization of electro-synthesised magnetite nanoparticles, Journal of Nanoparticle Research, 15 (2013) 1795. DOI: 10.1007/s11051-013-1795-y.

Naim M.N., Iijima M., Sasaki K., Kuwata M., Kamiya H., Lenggoro I.W., Electrical-driven disaggregation of the two-dimensional assembly of colloidal polymer particles under pulse DC charging, Advanced Powder Technology, 21 (2010) 534–541. DOI: 10.1016/j.apt.2010.02.004

Pascal C., Pascal J.L., Favier F., Elidrissi Moubtassim M.L., Payen C., Electrochemical synthesis for the control of γ-Fe_2O_3 nanoparticle size. Morphology, microstructure, and magnetic behavior, Chemistry of Materials, 11 (1999) 141–147. DOI: 10.1021/cm980742f

Petcharoen K., Sirivat A., Synthesis and characterization of magnetite nanoparticles via the chemical co-precipitation method, Materials Science and Engineering B: Solid-State Materials for Advanced Technology, 177 (2012) 421–427. DOI: 10.1016/j.mseb.2012.01.003

Qiao R., Yang C., Gao M., Superparamagnetic iron oxide nanoparticles: from preparations to in vivo MRI applications, Journal of Materials Chemistry, 19 (2009) 6274-6293. DOI: 10.1039/b902394a

Qu X., Zhou G., Yao Q., Fu S., Aspartic-acid-assisted hydrothermal growth and properties of magnetite octahedrons, The Journal of Physical Chemistry C, 114 (2010) 284–289. DOI: 10.1021/jp909175s

Ramimoghadam D., Bagheri S., Hamid S.B.A., Progress in electrochemical synthesis of magnetic iron oxide nanoparticles, Journal of Magnetism and Magnetic Materials, 368 (2014) 207-229. DOI: 10.1016/j.jmmm.2014.05.015

Rodríguez-López A., Paredes-Arroyo A., Mojica-Gomez J., Estrada-Arteaga C., Cruz-Rivera J.J., Elías Alfaro C.G., Antaño-López R., Electrochemical synthesis of magnetite and maghemite nanoparticles using dissymmetric potential pulses, Journal of Nanoparticle Research, 14 (2012) 993. DOI: 10.1007/s11051-012-0993-3

Setyawan H., Fajaroh F., Pusfitasari M.D., Yuwana M., Affandi S., A facile method to prepare high-purity magnetite nanoparticles by electro-oxidation of iron in water using pulsed direct current, Asia-pacific Journal of Chemical Engineering, 9 (2014) 258–261. DOI: 10.1002/apj.1828

Setyawan H., Fajaroh F., Widiyastuti W., Winardi S., Lenggoro I.W., Mufti N., One-step synthesis of silica-coated magnetite nanoparticles by electrooxidation of iron in sodium silicate solution, Journal of Nanoparticle Research, 14 (2012) 807. DOI: 10.1007/s11051-012-0807-7

Sharrock M.P., Bodnar R.E., Magnetic materials for recording: An overview with special emphasis on particles (invited). Journal of Applied Physics, 57 (1985) 3919–3924. DOI: 10.1063/1.334917

Shen L., Qiao Y., Guo Y., Meng S., Yang G., Wu M., Zhao J., Facile co-precipitation synthesis of shape-controlled magnetite nanoparticles, Ceramics International, 40 (2014) 1519–1524. DOI: 10.1016/j.ceramint.2013.07.037

Starowicz M., Starowicz P., Żukrowski J., Przewoźnik J., Lemański A., Kapusta C., Banaś J., Electrochemical synthesis of magnetic iron oxide nanoparticles with controlled size, Journal of Nanoparticle Research, 13 (2011) 7167–7176. DOI: 10.1007/s11051-011-0631-5

Thapa D., Palkar V.R., Kurup M.B., Malik S.K., Properties of magnetite nanoparticles synthesized through a novel chemical route, Materials Letters, 58 (2004) 2692–2694. DOI: 10.1016/j.matlet.2004.03.045

Vatta L.L., Kramer J., Koch K.R., Diethylenetriamine functionalized silica coated magnetite nanoparticles for selective palladium ion extraction from aqueous solutions, Separation Science and Technology, 42 (2007) 1985–2002. DOI: 10.1080/01496390701401402

Weng Y.C., Rusakova I.A., Baikalov A., Chen J.W., Wu N.L., Microstructural evolution of nanocrystalline magnetite synthesized by electrocoagulation, Journal of Materials Research, 20 (2005) 75–80. DOI: 10.1557/JMR.2005.0003

Xu J., Yang H., Fu W., Du K., Sui Y., Chen J., Zeng Y., Li M., Zou G., Preparation and magnetic properties of magnetite nanoparticles by sol-gel method, Journal of Magnetism and Magnetic Materials, 309 (2007) 307–311. DOI: 10.1016/j.

jmmm.2006.07.037

Ying T.Y., Yiacoumi S., Tsouris C., An electrochemical method for the formation of magnetite particles, Journal of Dispersion Science and Technology, 23 (2002) 569–576. DOI: 10.1081/DIS-120014025

Zhang W., Jia S., Wu Q., Ran J., Wu S., Convenient synthesis of anisotropic Fe_3O_4 nanorods by reverse co-precipitation method with magnetic field-assisted, Materials Letter, 65 (2011) 1973–1975. DOI: 10.1016/j.matlet.2011.03.101

Authors' Short Biographies

Heru Setyawan

Heru Setyawan is a Professor in the Department of Chemical Engineering at Institut Teknologi Sepuluh Nopember, Surabaya Indonesia. He is also the Vice Rector for Academic and Student Affairs. He got his bachelor degree from Institut Teknologi Sepuluh Nopember in 1990, master degree from Tokyo Institute of Technology in 1996, and doctoral degree from Hiroshima University in 2003. All are in chemical engineering. He was a researcher at Japan Science and Technology Agency from 2003 to 2004. Currently, he leads several research projects in the area of functional materials for use in energy storage and conversion, environmental and biomedical.

W. Widiyastuti

Widiyastuti is an Associate Professor in the Department of Chemical Engineering at Institut Teknologi Sepuluh Nopember, Surabaya Indonesia. She is also secretary of graduate program and head of electrochemical and corrosion laboratory in Chemical Engineering Department, Institut Teknologi Sepuluh Nopember. She got her bachelor and master degrees in chemical engineering from Institut Teknologi Sepuluh Nopember in 1998 and 2000. She received her doctoral degree in chemical engineering from Hiroshima University in 2008. She was a research assistant in Graduate School of Engineering, Hiroshima University in 2009. Her research interests are functional nanomaterials, aerosol and wet material processing, and modeling and simulation using computational fluid dynamics.

Comprehensive Characterization of Nano- and Microparticles by In-Situ Visualization of Particle Movement Using Advanced Sedimentation Techniques[†]

Dietmar Lerche*

[1] LUM GmbH, Germany

Abstract

The state of a suspension is crucial with regard to processing pathways, functionality and performance of the end product. In the past decade, substantial progress has been made in designing highly specialized and functionalized particles. In current particle technology, besides classic particle properties such as particle size distribution, shape and density, surface properties play an essential role for processing, product specification and use. For example, in medical therapy, analytical diagnostic applications, as well as in separation processing and harvesting of high-valued materials, magnetic micro- and nanoparticles play an increasing role. In addition to traditional parameters such as size, the particle magnetization has to be quantified here.

Sedimentation techniques have been used for hundreds of years to determine the geometrical characteristics of dispersed particles. Numerous national and international standards regarding these techniques have been published. Mainly due to the fast growing market share of laser scattering techniques over the past two decades, most customers these days are not aware of some advantageous features of particle characterization via a first-principle fractionating approach such as sedimentation. This is unfortunate as sedimentation techniques have made huge technological leaps forward regarding electronics, sensors and computing abilities.

This paper aims to give a short review about different cumulative and incremental sedimentation approaches to measure the particle size distribution. It focuses mainly on the in-situ visualization (STEP-Technology®) of particle migration in gravitational and centrifugal fields. It describes the basics of the new multi-sample measuring approaches to quantify the separation kinetics by spatial and time-resolved particle concentration over the entire sample height. Based on these data, the sedimentation velocity and particle size distribution are elucidated and estimates of accuracy, precision and experimental uncertainties are discussed. Multi-wavelength approaches, correction of higher concentration, and the influence of rheological behavior of continuous phase will also be discussed. Applications beyond the traditional scope of sedimentation analysis are presented. This concerns the in-situ determination of hydrodynamic particle density and of magnetophoretic velocity distributions for magnetic particulate objects.

Keywords: STEP-Technology, sedimentation velocity distribution, particle sizing, particle optical properties, particle density, magnetic particle velocity

1. Introduction

Particles were ubiquitous on our and on other planets all across the galaxy long before mankind. Regarding particle separation methods, winnowing grain in ancient Egypt is perhaps one of the oldest approaches to separating/classifying particles by their mass. Sir George G. Stokes' work about the resistance of a particle moving relative to a viscous incompressible liquid marks the milestone of "modern" sedimentation analysis. He linearized the corresponding general equation of motion, arrived at the time-dependent equation of creeping motion and applied it to the frictional damping of a spherical pendulum bob (Stokes, 1851). The obtained relationship between the resistance and the movement of such a spherical body at constant slow velocity is today known as Stokes' law and forms the basis of all sedimentation techniques. Since the days of Stokes, additional other techniques were developed to measure the particle size. The

---

[†] Received 1 July 2017; Accepted 18 August 2017

[1] Justus-von-Liebig-Str. 3, 12489 Berlin, Germany
E-mail: info@lum-gmbh.de
TEL: +49-30-67806030 FAX: +49-30-67806058

[*] This review is devoted to my teacher, thesis supervisor and promotor Prof. Dr. habil. Roland Glaser. I am very grateful for his help, encouragement, constructive criticism and guidance for more than 10 years.

ISO Technical Committee ISO/TC24/SC4 “Particle Characterization” alone counts 13 active working groups dealing with numerous different physical principles to determine particle size distributions (ISO, 2017). There are plenty of articles and numerous books dealing with size measuring techniques and approaches focusing on the needs of academia, regulatory administration or industry. We restrict ourselves to referencing several books of the last 10 to 20 years (Leschonski, 1988), (Allen, 1999), (Babick, 2016), (Masuda et al., 2006), (Merkus et al., 2014), (Schärtl, 2007). It should be emphasized that most commercial sizing analyzers feature high repeatability. But the reproducibility of these techniques depends in large part on representative sampling, sample size and sample preparation (e.g. (Sommer, 1986), (ISO 14887:2000), (Jillavenkatesa et al., 2001)).

General principles: Any measurand depending directly or implicitly on particle size can be used for size determination. Due to the various dependencies, developed different measuring techniques “see” a particle with different eyes. Particle sizing techniques may be grouped based on particle characteristics such as geometrical properties, mobility in external force fields, and signals due to interaction responses with externally applied fields. Most straightforward is the visual analysis of geometrical parameters by light, scanning electron or transmission electron microscopy. These techniques have the advantage that they can evaluate each individual particle. But even for this relatively simple technique, the primary measuring information is not the size but the 2D contour of the particle. It depends on the orientation of the particle with regard to the imaging focus plane. Image analysis of falling particles reduces orientation effects, but is limited to particles of micrometer scale. Other single particle analyzing techniques are based on counting principles. Particle detection is made by electrical or optical means. Well known is the Coulter Counter principle (electrical detection, (Coulter, 1953)) famous for blood cell counting. These instruments allow precise size and count determinations for narrow particle size distributions. Special single particle optical sizing detectors (White, 2002) enlarge the dynamic range and are widely used for tail detections of droplet size distributions of emulsion (USP-788, 2012), (USP-729, 2016). Measuring techniques with hydrodynamic focusing allow for an especially high size resolution (Shuler et al., 1972). Lichtenfeld was able to discriminate between 600 nm and 610 nm particles as well as to measure changes in thickness of individual layers of about 0.5 nm of LBL-coated particles by means of an optical detection system (Buske et al., 1980), (Lichtenfeld et al., 2004). Due to the latest EU regulations regarding the classification of nanomaterials (European Union, 2011), (Linsinger et al., 2012) improved methods are needed for providing direct number-weighted size distributions for nanoparticles.

Today, most laboratories employ ensemble methods such as static (SLS) or dynamic (DLS) light scattering as their standard analysis methods, (Allen, 1999), (Schärtl, 2007), (Merkus, 2009), (ISO 13320:2009), (ISO 22412:2017). Classic SLS analysis is based on the Fraunhofer diffraction theory, stating that the intensity of light forward-scattered by a particle bigger than the wavelength is directly proportional to the particle size (Ward-Smith et al., 2013). Size distribution is specified volume-weighted despite the fact that primary measurement data is area-weighted. Fraunhofer-based size analysis should only be used for micron-sized particles. For submicron particles, the Mie scattering theory has to be employed (Mie, 1908), (van de Hulst, 1981). However, since most real-world particles are non-spherical, any analytical results should be viewed with caution. Furthermore, the results are influenced by the deconvolution algorithms used by individual manufacturers. For additional details, refer to (Kuchenbecker et al., 2012), (Kelly et al., 2013).

In contrast, DLS is based on the temporal fluctuation of scattered laser light (speckle pattern) reflecting temporal fluctuations of the particle position due to Brownian motion (Schärtl, 2007). The autocorrelation function allows determination of the mean travel distance, and based on this, the diffusion coefficients of particles. This information can be converted by the Stokes-Einstein relation to a hydrodynamic equivalent spherical particle size distribution. Obtained distributions are intensity-weighted. The dynamic range is from about 1 nm to 1 μm. Review in nanoparticle sizing using DLS were very recently given by (Zhou et al., 2017).

Particle tracking analysis (PTA) is another emerging technique based on tracking the stochastic movement (trajectories) of individual dispersed particles due to Brownian motion (diffusion) by light scattering microscopy (ISO 19430:2016). Similar to DLS, hydrodynamic spherical equivalent diameters are obtained. Distribution is number-weighted and covers a size range from about 50 nm to 1 μm. Estimation of particle concentration can be given but has to be treated with care (Filipe et al., 2010), (Chenouard et al., 2014).

Finally, acoustic spectroscopy is another measurement principle to obtain particle size information based on interaction with externally applied fields. It is based on measuring the attenuation of ultrasound at a range of MHz frequencies. The attenuation at these different frequencies (raw data) is used for calculating a particle size distribution. In contrast to optical methods, the material parameters and acoustic properties such as sound speed, density and heat conductivity have to be known to come up with a particle size. Particle sizes can be measured in the range of 10 nm to 3 mm. In contrast to, e.g. SLS techniques, the volume concentration of particles should meet a given critical concentration. On the other hand, developed theories take into account particle-particle interactions, and particle size distributions can be extracted from attenuation spectra in concentrated systems (ISO 20998-1:2006), (Dukhin et al., 2010), (Zhou et al., 2017).

In our review, we aim to give an overview regarding different sedimentation approaches to measuring particle size distribution (ISO 13317-3:2001), (ISO 13318-2:2007), (ISO 13318-3:2004). In addition, we would like to point out to the reader the analytical ultracentrifugation (AUC) method. Numerous publications regarding particle characterization (see, e.g. (Mächtle et al., 2006), (Planken et al., 2010), (Uchiyama et al., 2016)) were published over nearly the last 100 years since its invention by (Svedberg et al., 1924).

Classic sedimentation techniques can be classified according to particle distribution at the beginning (line start or homogeneous sedimentation), to the measuring principle (incremental/differential or cumulative/integral) and to the driving force field (earth gravity or high gravity by centrifugation) (e.g. (Allen, 1999), (ISO 13317-1:2001), (ISO 13318-1:2001)).

This article focuses on the most recent and advanced sedimentation techniques. In particular on one using STEP-Technology®, which allows the direct and in-situ observation of particle migration in gravitational and centrifugal fields. The primary experimental data obtained by this technique are terminal particle sedimentation velocities (first-principle measurement) obtained from the kinetics of spatial concentration changes within the sample over time due to gravity fields. Particle velocity distributions allow detailed characterization of dispersed particles such as size and/or density modalities, and broadness and kind of distribution. Based on experimental particle velocities, which demand neither prior assumptions nor particle and liquid material constants, the size distribution of particles can be derived via Stokes' law (Stokes, 1851). It results in an extinction-based size distribution according to the transmission measurement principle. Volume (number)-based particle size distribution calculation demands optical particle properties such as the refractive particle index and particle shape. The Mie theory derived for spherical particles (Mie, 1908), (van de Hulst, 1981) is commonly used for taking into account the refractive contrast between particles and liquid. With regard to volume- and number-weighted particle size calculations based on extinction-weighted distribution, we restrict ourselves to a short overview, as this part is fairly standardized (ISO series 13317 and 13318).

There are numerous references and books dealing with various aspects of particle characterization but in general they all center on particle sizing. The third part of this paper reports on the extension of the traditional scope of sedimentation size analysis towards particle characterization in a more general sense. This includes in-situ determination of the density of particles dispersed into liquids (ISO 18747-1:2018), magnetization and magnet responsiveness of particles.

While this article is about the current state of sedimentation research, it centers somewhat on our own research and experience.

2. In-situ visualization of particle migration—STEP-Technology®

Conventional cumulative sedimentation techniques record the amount of settled particles. The reader may think of the weight-balance approach, where the weight of settled particles is recorded on a special tray (ISO 13317-4:2014). Another example is the time-dependent detection of the hydrostatic pressure at a given position in the lower part of the cell (Bickert, 1997). On the other hand, incremental methods determine the change of particle concentration in a small measuring zone of known position by optical or X-ray measuring systems. The latter techniques provide concentration data of the sample only from a small fixed volume at a time *t*. Scanning sensors (Mächtle et al., 2006) typical for AUC, provide more information but do not allow for the capture of fast concentration profile changes.

Initially, particle settling was analyzed at gravity (e.g. Ladal photosedimentometer, Paar Lumosed). An early centrifugal field application was invented by (Whitby, 1955). Known is the start line incremental disc rotor technique and was first used by (Kaye, 1962), and today is marketed by CPS Instruments Inc., Stuart, Florida, and Brookhaven Instruments Corp., Holtsville, New York. Homogeneous incremental methods were also available using cuvette-based photocentrifuges up to the turn of the last century from Japanese manufacturers such as Horiba Scientific Ltd. (e.g. CAPA 500), and Shimadzu Corp. (e.g. SA-CP3). All of these techniques pass a more or less parallel, focused light beam (ROI about 0.2 mm up to 1 mm) through the sample and measure at a single given position *p* the changes of transmission over time due to settling or creaming of particles (**Fig. 1a, b**). These techniques therefore provide the concentration only at a distinct small fixed data-point at a time t_i in the sample. Scanning sensors are typical for AUC and provide more information but do not allow recording an entire concentration profile over sample height at selected points of time.

As **Fig. 1c** displays, more comprehensive information can be obtained illuminating the entire sample by means of a narrow line beam of parallel light I_0 and recording the transmitted light intensity I_t instantaneously for any position *p* and any set time *t* by multiple sensors. This measuring technique allows the user to record concentration

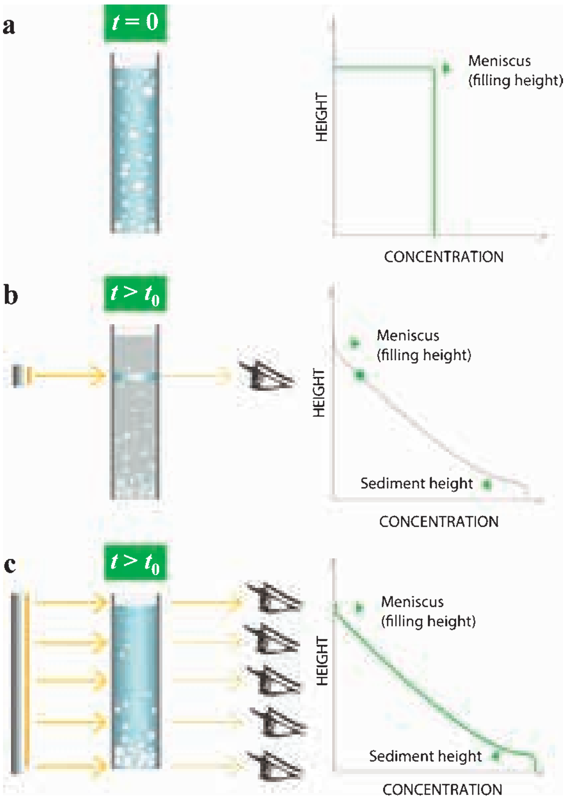

Fig. 1 Schematic drawing (© by LUM GmbH, Berlin) of homogeneously distributed particles in a sample cell at the start of the experiment ($t = 0$) and the corresponding constant particle concentration over the entire height of the sample (**a**). Classic techniques monitor changes of particle concentration due to sedimentation or creaming at a small volume with no information of spatial concentration (**b**). STEP-Technology® quantifies the concentration profile over the entire sample at selected points of time (**c**).

changes across the entire sample height due to the migration of particles or droplets driven by earth gravity or centrifugal fields, respectively, as well as, e.g. magnetic fields (Mykhaylyk et al., 2015).

Fig. 2 displays the main features of patented STEP-Technology® (Space- and Time-resolved Extinction Profiles) schematically in more detail as implemented in the multi-sample analytical photocentrifuge LUMiSizer® (AC-L, LUM GmbH, Germany). A linearly shaped parallel NIR or VIS light beam passes through the optical cells placed horizontally into one of the 12 channels of a disk rotor. The channel positions at the rotor are indicated by pale areas and numbering 11, 12, 1 and 2 in **Fig. 2**. Particles scatter the light, resulting in an attenuation of the forward beam. This forward intensity is recorded during centrifugation in real time as a function of the radial position p over the entire sample height with a space resolution of 13.7 µm. In the case of, e.g. a gravity sedimentometer LUMiReader® (GS-L, LUM GmbH, Germany), it amounts to 8.7 µm.

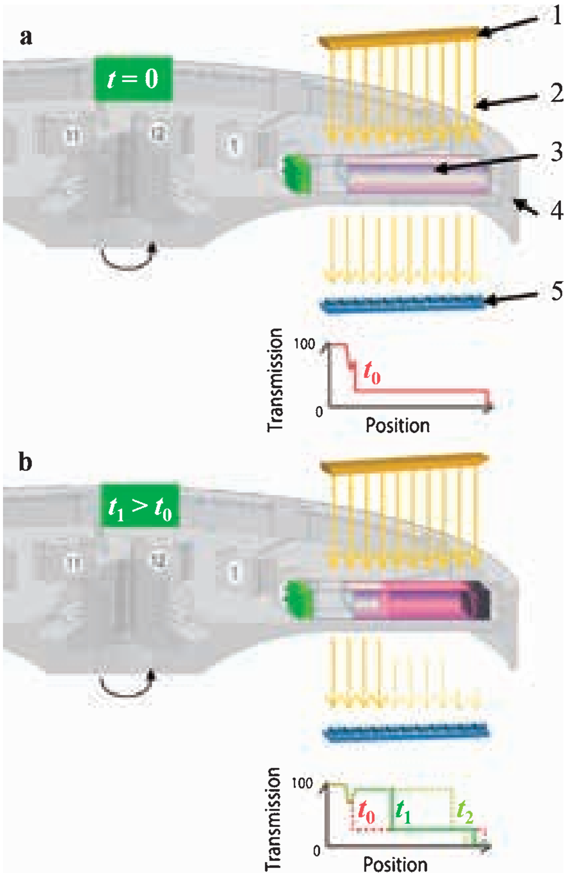

Fig. 2 Principle of measuring space- and time-resolved extinction profiles (displayed as transmission profiles) implemented in an analytical photocentrifuge (© by LUM GmbH, Berlin). (**a**) Transmission profile of an unseparated sample at t_0. (**b**) Transmission profile (green line) at t_1. Dotted lines indicate the situation at t_0 and t_2 for comparison. (1) light source(s); (2) parallel NIR or VIS light; (3) sample cell; (4) multi-sample rotor with indicated channel numbers 11, 12, 1 and 2; (5) line detector

In this way, space-resolved intensity profiles are obtained at adjustable time steps, monitoring concentration changes over time due to the sedimentation or creaming of dispersed particles. The recorded intensity at every position $I(r_i, t_j)$ is normalized by $I_0(r_i)$ measured with no cells (empty rotor) as is usually done in a photometer. The change of transmission and extinction profiles during centrifugation are calculated according to Eq. 1

$$\begin{aligned}\frac{I(r_i, t_j)}{I_0(r_i)} &= T(r_i, t_j)\\ &= \exp\left(-E(r_i, t_j)\right)\\ &= \exp(-A_{\mathrm{v}} \cdot \phi(r_i, t_j) \cdot L) \qquad (1)\end{aligned}$$

and displayed by the software package SEPView® as fingerprints of transmission or extinction (**Fig. 3a, b**).

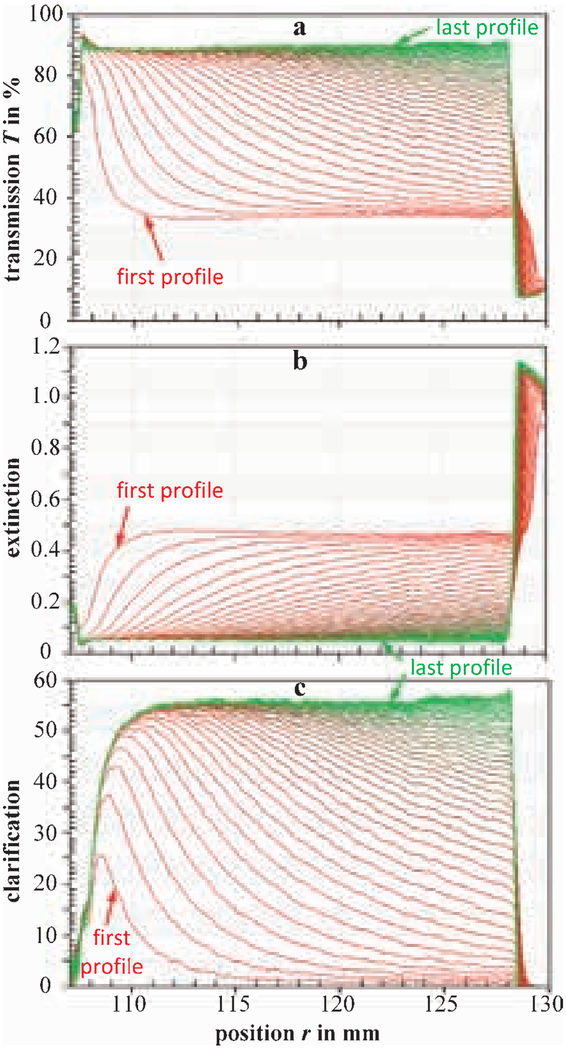

Fig. 3 Progress of separation over time visualized and recorded by STEP-Technology®. Fingerprints of particle separation can be quantified based on transmission (**a**), extinction (**b**) or clarification (**c**). The first recorded profile (red) displays the initial particle distribution of the sample just after centrifugation start (< 1 s). The green profiles visualize the final distribution of particles over sample height (position *r*) due to separation.

At the position of about 107 mm (distance from the center of revolution), the meniscus (filling height of sample) is identified as well as the bottom of the sample cell (130 mm). As indicated, the first red profile corresponds to the first recorded measurement, e.g. one second after start. The sharp decline **(a**, **c)** and increase **(b)** of green profiles at 107.4 mm indicates the interface between suspension and sediment at the end of the separation process (here by centrifugation). Clarification is another visualization approach. In this case, the initial transmission $I(r_i, t_0)$ is subtracted from any later recorded transmission profile $I(r_i, t_j)$ and the incremental change is displayed (**Fig. 3c**). For details refer to (Detloff et al., 2014). Visualization of the separation process by the change of transmission profiles at wavelengths of visible light gives similar information to an observation by the naked eye. Extinction profiles, on the other hand, are directly related to the corresponding concentration alterations within the sample according to Lambert-Beer-law (Eq. 1, 3rd line, right part). **Fig. 4** displays experimentally determined extinction for β-Methyl Orange solutions of different concentration (points) determined by the AC-L and a calibrated UV/VIS spectrophotometer Lambda 2 (Perkin Elmer). The correlation is very satisfying. The slight deviation from the ideal slope of unity is explained by the spectral line half-width of used LED as light source of AC-L which amounts to 25 nm compared to the monochromatic source (470 nm +/– 3 nm) of the calibrated spectrophotometer.

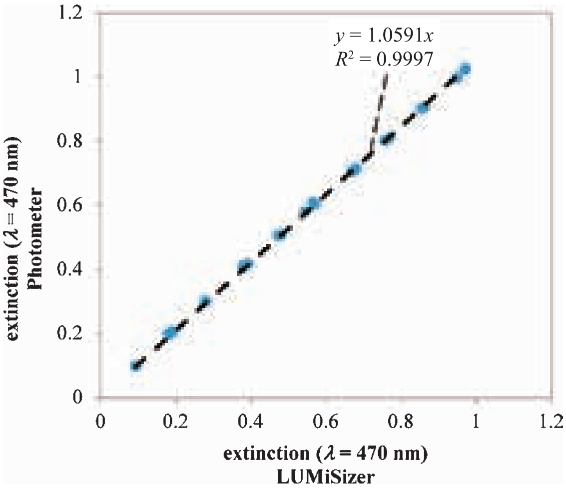

Fig. 4 Extinction of different concentrations of β-Methyl Orange (0.014 g/ml–0.142 g/ml, optical glass cells) measured by a calibrated photometer (*y*-axis) and an AC-L (*x*-axis). Points: Experimental data of different concentrations; Line: Linear fit.

The response (extinction) of the sensor systems of AC-L was also validated for a concentration range of more than 3 decades of different dispersed phases as shown in **Fig. 5** (Detloff, 2004). The theoretical extinction values were calculated by the Lambert-Beer law combined with a semi-empirical approach to account for multiple light scattering at higher particle volume concentrations. An error function was determined which is subtracted from the extinction values of the Lambert-Beer law. This function does not depend directly on the particle size *x*. The information about the differences in the particle sizes are delivered by the volumetric scattering cross-section A_V calculated by the Mie Theory. Only one set of parameters in the empirical part is required to calculate the extinction. The parameters were determined by fitting to experimental data (Detloff et al., 2007).

The light beam, penetrating the suspension or emulsion, interacts with both the particles (dispersed phase) and the continuous phase. The NIR-range of 850 nm–900 nm is advantageous to minimize the influence of optical properties of the continuous phase. For these wavelengths, most liquids and solutions are transparent independent of their color at visible light. **Fig. 6** displays the transmission changes monitored by STEP-Technology® at NIR (top) during centrifugation over the entire dispersion sample made of an organic pigment. No separation is detectable by the naked eye at visual light (photo middle). In contrast, recorded concentration changes could be also visualized by photographic means (**Fig. 6**, bottom), if the sample was illuminated in a special set-up with light in the NIR- range. Originally, this approach was invented to quantify the settling of red particles (red blood cells) in a continuous phase (blood plasma) of different color due to medication or surgery (Lerche et al., 1988), (Lerche et al., 1992).

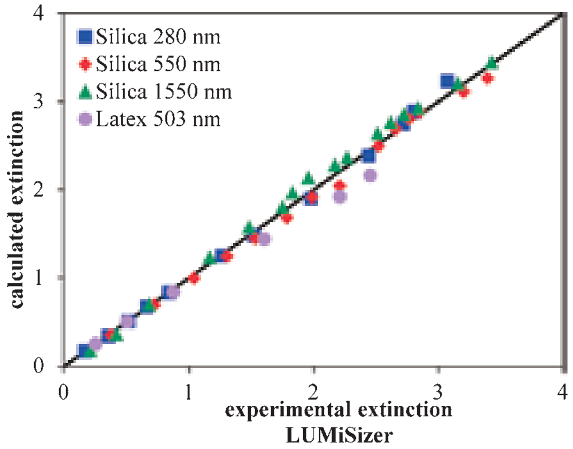

Fig. 5 Natural extinction of different silica and latex suspensions (280 nm to 1550 nm particle size, volume fractions from 0.014 % to 14.9 %) measured by an AC-L (x-axis) and theoretically calculated (y-axis) by the Lambert-Beer law extended by a semi-empirical approach for multiple scattering (Detloff et al., 2007).

Visible light on the other hand, e.g. blue wavelengths, has the advantage that it increases the sensitiveness towards much lower particle concentrations and nanoparticles as shown in **Fig. 7**. Scattering of non-adsorbing particles decreases with decreasing particle radius by $(x/2)^6$ according to Rayleigh, and correspondingly for NIR wavelengths, the dispersion sample is more transparent

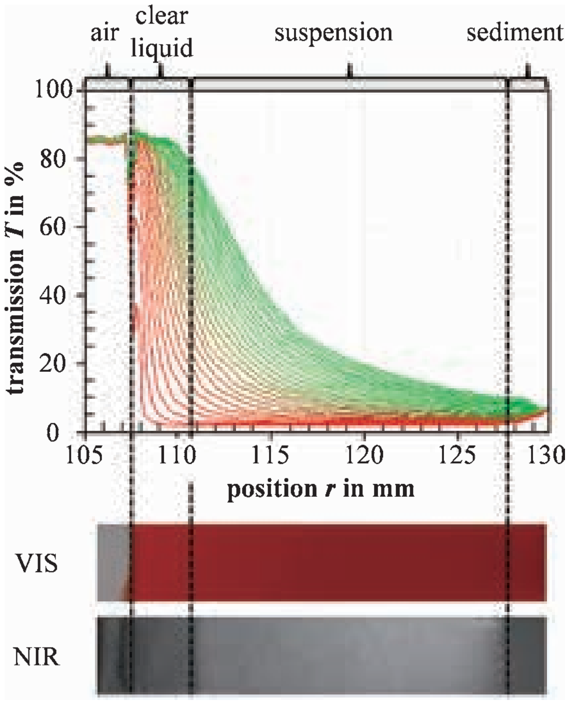

Fig. 6 Separation kinetics of a pigment recorded by STEP-Technology (NIR) and visual appearance of the sample cell at the end of centrifugation (last green profile) photographed by visible light (middle) and by a special NIR illumination set-up (bottom), respectively. Note that the sample cell is lying horizontally in the rotor with the applied centrifugal acceleration being from left to right.

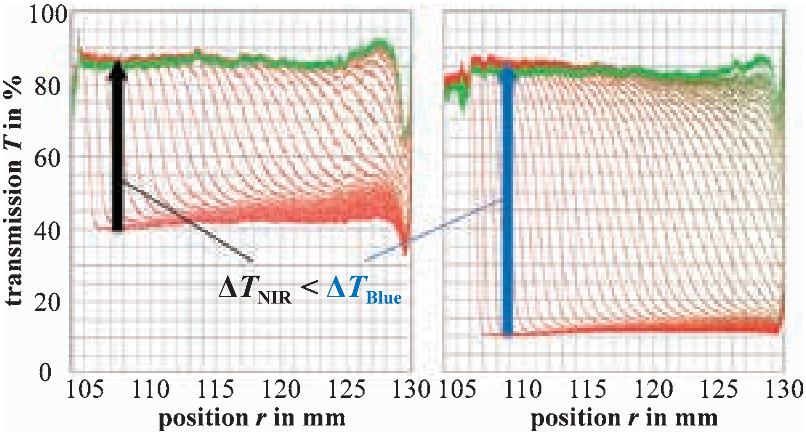

Fig. 7 Fingerprints of the separation behavior of the same silica nanoparticle suspension quantified by transmission changes recorded by NIR ($\lambda = 870$ nm) or blue light ($\lambda = 470$ nm) illumination. Arrow lengths indicate the difference between transmission of the initial sample and the particle-free supernatant, respectively.

compared to blue light as indicated by the first profile (red) of each fingerprint. Accordingly, the total transmission change amounts to 45 % and 75 %, respectively, for complete separation of particles (indicated by green profiles).

Eq. 1 obeys the linearity between extinction and particle concentration. In other words, multiple scattering of particles at higher particle concentration should be avoided. The applicability of the Lambert-Beer law regarding particle concentration can be broadened with no sample dilution by employing cells with shorter optical path (virtual dilution). As **Fig. 8** verifies, using sample cells of an optical path length as small as 1 mm allows working at 10-times higher volume concentrations with no sample dilution compared to 10-mm cells. (Luigjes et al., 2012), (Erne, 2012) reported on super thin made glass cells of 50 µm path length allowing the analysis of magnetic iron oxide particles dispersed in oleic acid-decalin of concentrations up to 300 g/l and measurement of osmotic pressures of strongly adsorbing and very concentrated dispersions.

Typical dispersion fingerprints—patterns of transmission profiles—visualizing the behavior of different types of suspensions and emulsions at original concentration (no dilution) are shown in **Fig. 9**. Sample fingerprints allow classification of the different types of dispersions based on their separation behavior over time. SEPView® provides the quantitative and direct evaluation of fingerprints by different analysis tools. The instability or separation index (Detloff et al., 2014), integral transmission and front tracking (Lerche et al. 2001), (Sobisch et al., 2010) or first derivative (Wiese, 2010) allow application-specific comparison

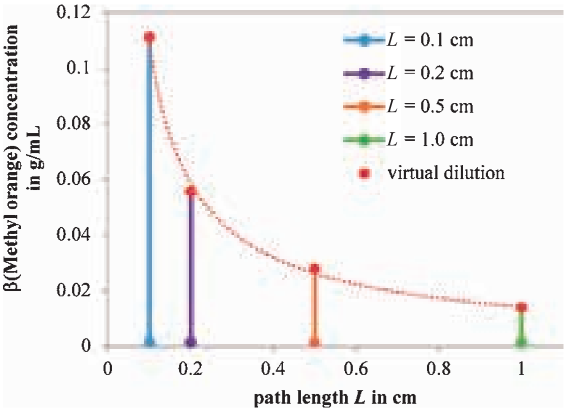

Fig. 8 Maximum concentration of β (Methyl Orange) accurately measured (linear range of detector) by AC-L using optical glass cells with path lengths from 0.1 cm to 1 cm.

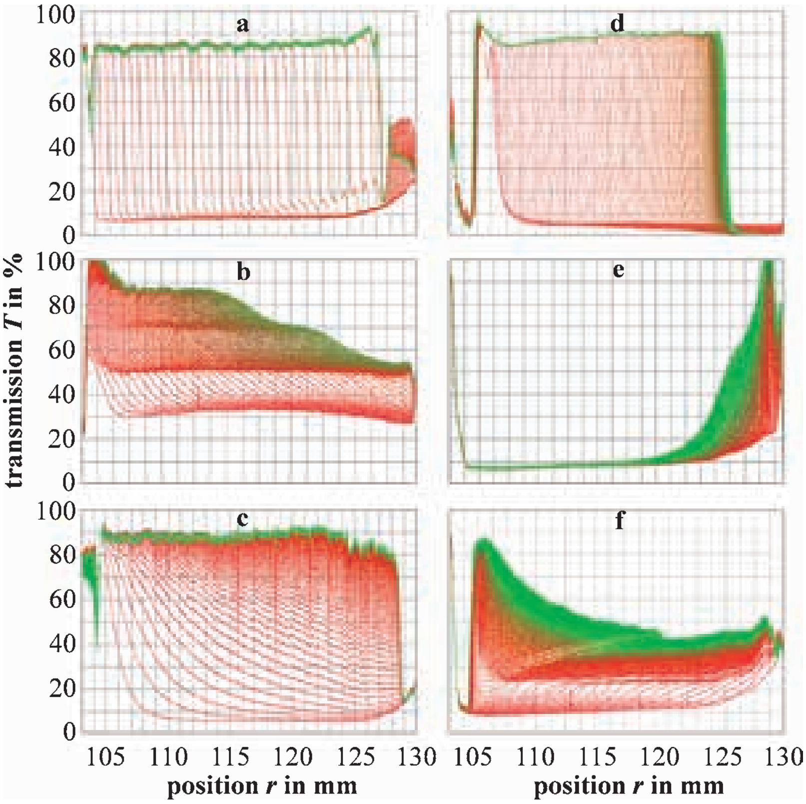

Fig. 9 Typical fingerprints of different types of dispersions recorded by an analytical space-resolving photocentrifuge (AC-L): (**a**) monomodal monodisperse suspension, (**b**) tetramodal monodisperse suspension (**c**) polydisperse suspension (**d**) particle-particle interaction, flocculated suspension (**e**) emulsion (**f**) suspo-emulsion (flotation and sedimentation).

and ranking of differently designed formulations and products and identification of destabilization phenomena as well as prediction of shelf life (Badolato et al., 2008), (Lerche et al., 2011), (Takeda, 2012), (Staudinger et al., 2014), (Lerche et al., 2014), (Cai et al., 2018). Nowadays, the use of AC-L gains also large interest in characterizing highly concentrated dispersions, especially in the field of centrifugal filtration and sediment consolidation (Usher et al., 2013), (Cao et al., 2014), (Loginov et al., 2017a, 2017b) as well as mechanical properties (rigidity, deformability) of e.g. hydrocolloid beads (Schuldt et al., 2018).

On the other hand, particle characteristics such as size, density and magnetic responsiveness can be quantified, upon which we focus in this paper.

3. Particle sizing in line with ISO 13317 and 13318

3.1 Particle velocity distribution

Any experimental set-up to analyze particle size must measure the terminal (stationary) velocity of particles (solid particles or droplets) due to gravity or centrifugal fields, respectively. If the density of dispersed particles is higher than that of the continuous phase, they settle. They cream or float in the opposite case. Conventionally, sedimentation velocity is determined by measuring the required time t for particles to settle from the filling height (meniscus) a fixed distance h (gravity sedimentation) or to a fixed radial position r (analytical centrifugation), respectively. This is the typical procedure in the case of line start centrifugal sedimentation techniques (Constant Position Approach, CPA) based on the time course of registered intensity of the emergent optical beam (ISO 13318-1:2001). Alternatively, the particle velocity can be determined by the "Constant Time approach (CTA)" (Detloff et al., 2006), (ISO 13318-2:2007) measuring the traveled distance of particles in a given time t by spatial resolving techniques.

$$v(r,\ t) = \frac{r - r_\mathrm{m}}{t} \tag{2}$$

Here, v denotes the particle velocity and r_m the position where the particles start to sediment/cream (sedimentation = position of the meniscus; creaming = position of the cell bottom). For a suspension of monodisperse particles, all profiles, independent of measurement time t_i, have a vertical transmission profile (horizontally placed sample cell) and therefore all particles have moved the same distance $h = r - r_\mathrm{m}$ (**Fig. 9a**). Accordingly, a unique velocity is obtained. For polydisperse particle systems, the profiles deviate from the vertical shape and become more and more skewed with increasing time $t_{i,}$ displaying the different traveling distances of the smaller and larger particles (**Fig. 9c**). The resolution of the particle velocity distribution improves with increasing sedimentation time (larger distances). It should be emphasized that the light intensity is merely recorded to determine the distance the particles move over a set time interval and is not used in itself to determine the particle size. This is in contrast to scattering methods, e.g. to laser diffraction, which uses the light intensity patterns to deduce the particle size based on applied algorithms.

In any case, the experimental determination of the particle velocity is a first-principle approach—measurands are time and distance and no assumptions have to be made, e.g. such as density, viscosity, refractive index, shape, and empirical models or fitting parameters. High accuracy (precision, trueness) as well as traceability can be achieved for the physical quantity "sedimentation velocity v_st", dividing the basic quantities settling distance h for a particle of size x and settling time t.

The hydrodynamics for a sphere slowly settling in a liquid due to gravity and the corresponding frictional coefficient were first described by (Stokes, 1851), and Eq. 3 was derived based on these considerations called Stokes law.

$$v = \frac{h}{t} = \frac{(\rho_\mathrm{p} - \rho_\mathrm{l}) \cdot x^2 \cdot g}{18 \cdot \eta} = K \cdot x^2 \cdot g \tag{3}$$

Fig. 10 displays as an example velocity distribution for a suspension consisting of a mixture of four quasi-monomodal PMMA particles (reference material (RM), same weight concentration) obtained by GS-L. Calculation of the sedimentation velocity was based on detection of the extinction changes at constant positions of 38.0 mm, 41.5 mm and 45.0 mm and thereafter averaged. The velocity of particles of the nominal size 15 and 20 µm can be differentiated easily (left two peaks).

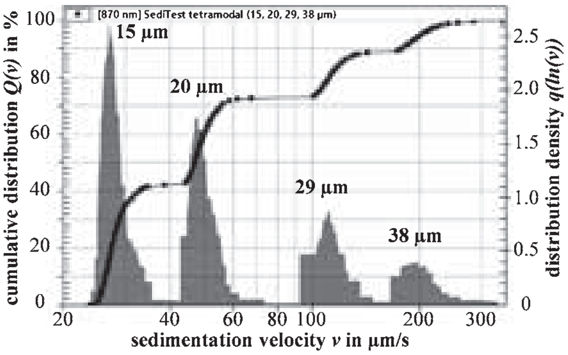

Fig. 10 Particle velocity distribution of a suspension made from batches of 4 monodisperse PMMA reference particles (nominal size indicated, LUMiReader PSA, 120 profiles, $\Delta t = 20$ s, $\vartheta = 30°\mathrm{C}$, $\lambda = 870$ nm). Particles were supplied by the company Dr. Lerche KG, Berlin, Germany.

The uncertainty of velocity measurement depends mainly on time resolution of the measuring system and, on the other hand, on distance resolution and precision of meniscus detection (r_m). Time resolutions that are technically easy to reach are in the order of less than a second (e.g. LUMiReader® PSA, 250 ms). The physical space resolution of sensors of GS-L was determined by calibrated mechanical references to be 8.7 µm and the expanded measurement uncertainty was determined for $k = 2$ to be 4.63 % (Rodriguez, 2017).

In a centrifugal field, the applied local gravity depends on angular velocity and the distance of the considered particle from the center of revolution r (Eq. 4)

$$a = (2 \cdot \pi \cdot n)^2 \cdot r = \omega^2 \cdot r \tag{4}$$

Where n equals the frequency of revolution (1/s = RPM/60s), ω equals the angular speed (radians/s) and r is the distance from the axis of rotation to be inserted in meters. According to (Svedberg et al., 1924), the earth acceleration g in Stokes' law (Eq. 3) is replaced by centrifugal acceleration a. Particle motion in this frame is a/g = RCA (relative centrifugal acceleration, also called separation factor G or Froude number F) times faster than Stokes' velocity under earth gravity g. Therefore, small nanoparticles and even molecules can be analyzed by high-speed AUC (Schuck et al., 2002), (Mächtle et al., 2006), (Mehn et al., 2017). Svedberg also introduced the so-called sedimentation coefficient:

$$s = \frac{v}{\omega^2 \cdot r} = \frac{\pi \cdot x^3 \cdot (\rho_\mathrm{p} - \rho_\mathrm{l})}{6 \cdot f} \tag{5}$$

where f describes the translational frictional coefficient well known from hydrodynamic theory (Ungarish, 1993), (Happel et al., 1983).

Svedberg's simplified approach of constant RCA fits well, if particles move only short distances within the measurement time. But in general, acceleration and therefore particle velocity depends also on the position within the sample cell (Eq. 4). Therefore, the velocity of dispersed particles increase as they move radially outward from the center of rotation. This can be seen in the dispersion fingerprint profiles where the distance between consecutive profiles taken at the same time interval increases (see **Fig. 9a**, monodisperse particles). To take this into account, acceleration and therefore particle velocity v has to be expressed in a differential way. Eq. 3 becomes

$$v(t) = \frac{\mathrm{d}r_p}{\mathrm{d}t} = K \cdot x^2 \cdot \omega^2 \cdot r \tag{6}$$

After integration we get:

$$t(r) = \frac{1}{K \cdot x^2 \cdot \omega^2} \cdot \ln\left(\frac{r}{r_\mathrm{m}}\right) \tag{7}$$

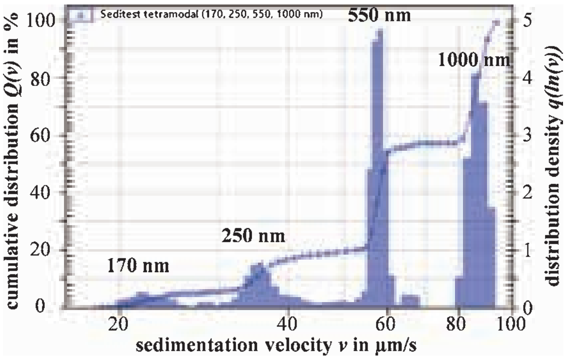

Fig. 11 Particle velocity distributions for a 4 modal monodisperse silica particle suspension (nominal size indicated, analytical photocentrifuge LUMiSizer, RCA ramp, $\vartheta = 25$°C, $\lambda = 470$ nm). RMs were supplied by the company Dr. Lerche KG, Berlin, Germany.

Fig. 11 displays extinction-based velocity distributions of a suspension consisting of a mixture of 4 quasi-monomodal silica particles (RM, same weight concentration) obtained by the AC-L (Uhl, 2015). The uncertainty of velocity measurement depends on the time resolution of the measuring system and on the distance resolution and precision of meniscus detection (r_m). Time resolution scales with applied RPM and amounts of 0.1 s (4000 RPM) to 0.3 s (200 RPM) for a typical analytical photocentrifuge (AC-L type). Space resolution is independent of RPM and was determined to be 13.9 µm by means of a calibrated physical reference. Determination of the meniscus position was evaluated by 3 different approaches (SEPView algorithm, direct boundary model (Walter et al., 2015b)) for 2-mm and 10-mm cells and 4 different RPMs of the rotor. The standard deviation for each approach ($n = 65$) was below 0.2 % (Boldt, 2017). The expanded measurement uncertainty was determined for $k = 2$ to be 4.29 % in the case of default settings by the manufacturer (Rodriguez, 2017).

The terminal sedimentation velocity demands a time-independent centrifugal acceleration. In other words, the final rotor speed has to be reached in a short time compared to the expected necessary sedimentation time and should not fluctuate. The above-described AC-L instruments reach a final RCA of 1000 at 8 s and of 2300 at 15 s and the RPM variation is below 0.75 % (RPM = 200) and 0.1% (RPM = 4000), respectively. To take into account the acceleration kinetics, the quantitative data obtained should be plotted against the so-called running time integral "$\int\omega^2\mathrm{d}t$" (Mächtle et al., 2006).

The velocity distribution is of great importance for the classification and separation of polydisperse fine particulate suspensions. Of practical interest is the flow of the main fraction as well as the particle size distribution of the fines in the centrate as a function of the residence time in a process unit (Leung, 2004). The composition of centrate can be simulated with velocity distributions of the sedimenting particles obtained by a laboratory analytical photocentrifuge using the “Constant Time Approach” (CTA) (Detloff et al., 2012). From **Fig. 12** it is obvious that with increasing time of centrifugation, the amount of coarser particles within the centrate decreases and that the distribution becomes narrower. The velocities for smaller particle fractions remain constant.

As the velocity determination is a primary method, the terminal sedimentation velocity can be determined experimentally for any particle shape, particle concentration, rheological behavior of liquid, laminar flow condition, etc.. But simulations or calculations based on Eq. 3 and Eq. 5 are only valid for dispersions of spherical particles of low concentration and settling in an unbounded Newtonian liquid at low Reynolds numbers.

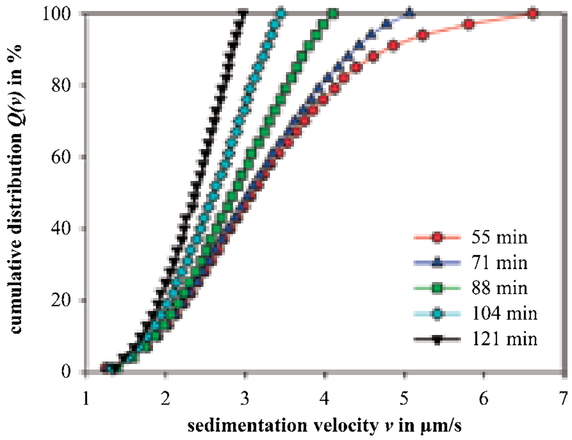

Fig. 12 Particle velocity distribution for an aqueous technical latex suspension within the centrate in dependency of the time of centrifugation (AC-L, RCA = 2325, (Detloff et al., 2012)).

Shape of particles: The geometry of particles can be taken into account by the so-called Stokes shape factor. As any non-spherical particle shape has a larger surface area than a sphere with the same volume, frictional coefficient *f* will consequently differ along with its terminal sedimentation velocity (Eq. 5). It was shown that sphericity can be used to predict the average resistance (Pettyjohn et al., 1948), (Happel et al., 1983). The sedimentation shape factor equals the ratio of corresponding sedimentation velocities. It is one for a sphere and smaller than one for non-spherical isotropic particles. For a cube, for example, it amounts to 0.921 according to the above authors. In the case of non-isotropic, non-spherical particles, the settling velocity depends in addition on particle orientation (Happel et al., 1983). The resistance of rod-like objects as, e.g. MWCNT were found to depend on the cross-section multiplied by the square root of its length in the case of disk centrifuge experiments (Nadler et al., 2008).

(Hogg, 2015) described in detail a spheroid model to account for the shape influence regarding different sizing methods. For different basic geometries, **Fig. 13** displays the settling (Stokes shape) factor in dependence of different height-to-diameter (cross-section) ratios (Happel et al., 1983).

The above considerations apply for rigid particles. In

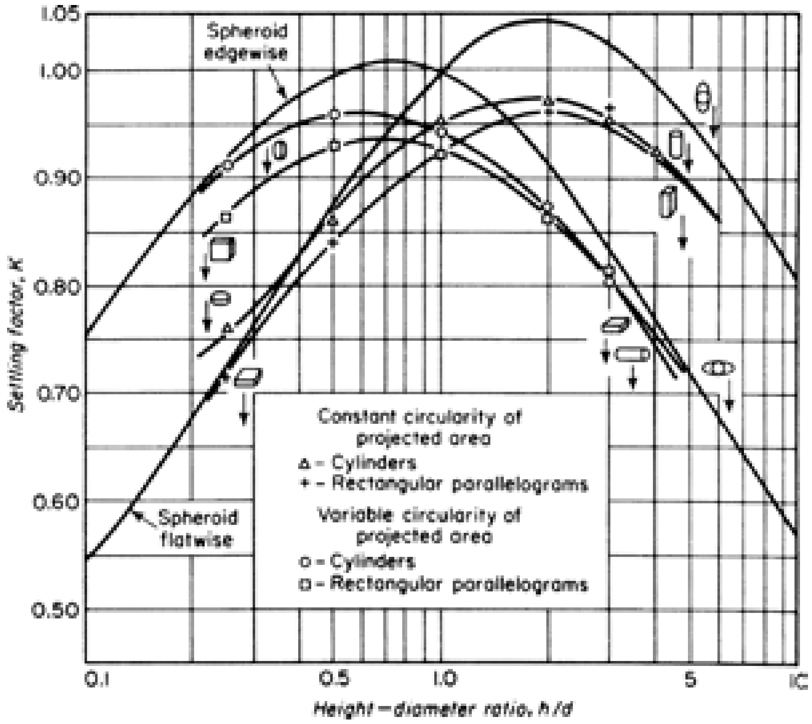

Fig. 13 Settling factor for cylinders, rectangular parallelepipeds, and spheroids calculated in dependence of the height-diameter ratio (Happel et al., 1983).

the case of deformable ones, the particle geometry and orientation depend on the flow conditions and may change depending on the applied shear stress. In general, shear-induced deformation decreases frictional resistance and enhances sedimentation. Pioneering work for emulsion droplets was published by (Taylor, 1932), relating the shear deformation to the ratio of inner viscosity of the droplet and the viscosity of the continuous phase (Kaur et al., 2010).

Lerche showed experimentally that rigidified human red blood cells settle at a slower rate compared to physiologically deforming ones (Lerche et al., 2001). The basics of this phenomenon are similar to the shear thinning effects of deformable particles and droplets (Pal, 2000).

There are also other definitions and approaches to take into account geometrical shapes (Arakawa et al., 1985), (Leith, 1987), (Luerkens, 1991), (Hölzer, 2007).

High particle concentration: Stokes' law was derived for a single particle settling in an unbounded (infinite) liquid. These requirements are never fulfilled by sedimentation methods. Let us first discuss concentration effects. In general, particles dispersed in liquid are separated by finite distances and mutually affect each other resulting in disturbed flow path trajectories around particles. This hydrodynamic interaction between particles reduces the settling velocity compared to their Stokes velocity. It is obvious that hydrodynamic hindrance depends on the number of particles dispersed in a given volume. In addition, hindrance depends on particle size distribution for the simple reason that the mean distance between two particles narrows with decreasing size of the dispersed phase for a given volume concentration. The retardation can be quantified by the so-called hindrance function $H(\phi)$, defined as the ratio of sedimentation velocity as a function of the volume concentration $v(\phi)$ to the Stokes velocity v of a single particle under otherwise identical settling conditions. Both (Steinour, 1944) and (Kynch, 1952) introduced the basic idea for the first time to describe sedimentation kinetics for virtually any particle volume concentration. The hindrance function is frequently used as given in Eq. 8,

$$H(\phi) = \frac{v}{v_0} = \frac{(1-\phi)^2}{\eta_{\text{rel}}} \tag{8}$$

where ϕ is the initial volume concentration of the dispersed phase and η_{rel} is the relative viscosity of the dispersion. Numerous empirical, semi-empirical and analytical models have been proposed since the pioneering work of Kynch (**Fig. 14**). The generic approach of Eq. 8 allows taking into account any apparent viscosity-concentration relationship $\eta(\phi)$ for dispersions, (Quemada, 1977, 1978a,b), (Bullard et al., 2009), (Brouwers, 2010).

Maude and Whitmore (Maude et al., 1958) proposed a two-parameter approach (Eq. 9) to describe hindered settling, where β depends on size, shape and *Re*.

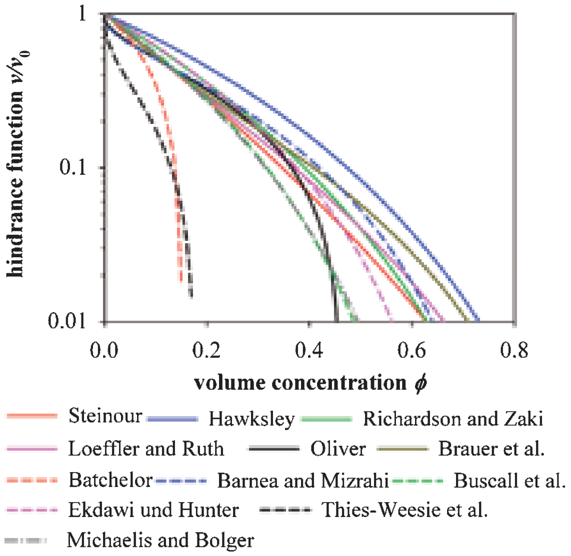

Fig. 14 Overview of the hydrodynamic interaction between particles in dependence of the volume concentration described by differently proposed hindrance functions.

$$H(\phi) = (1-\phi)^{\beta} \tag{9}$$

This relationship is very often used for solid micronized particles, and with $\beta = 4.65$, it is the well-known Richardson-Zaki-approach (Richardson et al., 1954). Eq. 9 does not take into account the experimental fact that separation velocities for suspensions go towards zero at volume concentrations of between 0.64–0.72. It also does not consider polydispersity. Michaels and Bolger (Michaelis et al., 1962) introduced a three-parameter approach for the relative viscosity of Eq. 8:

$$\eta_{\text{rel}}(\phi) = \left(1 - \frac{\phi}{\phi_{\max}}\right)^{-n} \tag{10}$$

The introduction of maximum packing concentration $\phi_{\max}$ enables accounting for particle shape and particle size distribution but not for particle size. Different exponents were proposed. (Quemada, 1977, 1978a,b) set $n = 2$. Eq. 10 is also known as the Krieger-Dougherty equation in the rheology community with a factorized exponent $n = [\eta]\phi_{\max}$, where $[\eta]$ is the intrinsic viscosity (Krieger et al., 1959). In the case of deformable particles such as blood cells or oil droplets, intrinsic viscosity $[\eta]$ quantifies the cell or droplet deformability (Dintenfass, 1980).

Fig. 15 shows as an example of the velocity distributions for an aqueous technical latex suspension at different volume concentrations. It can be seen that with increasing concentration, the distributions are shifted to smaller velocities. This occurs due to the increasing hindrance. The distance between the particles is smaller at higher concentrations and so the hydrodynamic interactions increase and result in slower settling.

If experimentally determined sedimentation velocity values are plotted against the volume concentration, the functional dependence of the hindrance function can be obtained easily by curve-fitting (Detloff et al., 2007). **Fig. 16** shows the particle sedimentation velocity dependence of monodisperse spherical silica particles on the volume concentration. The results show that the general shape of the hindrance function is independent of the particle size. Hindrance diminishes for particle volume concentrations lower than about 0.005. Interestingly, the exponent of the power law (Eq. 9) increases with decreasing size, and becomes more strongly pronounced in the lower nanometer size range. In addition to the particle-particle separation distance, both the immobilized water at the particle surface as well as the ionic double layer becomes increasingly important for smaller particle sizes (Salinas-Salas et al., 2007). In other words, the effective or apparent particle volume is larger than the geometrical one. On the other hand, it influences also the effective density of the particle (Hinderliter et al., 2010), (DeLoid et al., 2013). The hindrance also depends on particle shape. (He et al., 2010) demonstrated that for iso-volumetric platelet-like particles having different shapes, the hindrance function also depends on the aspect ratio. A single functional relationship over the whole concentration range for spherical particles was found. In contrast, the behavior of platelet-like-shaped particles show two different functional relationships with regard to volume concentration. Both slopes and critical onset concentration depend on the platelet shape aspect ratio.

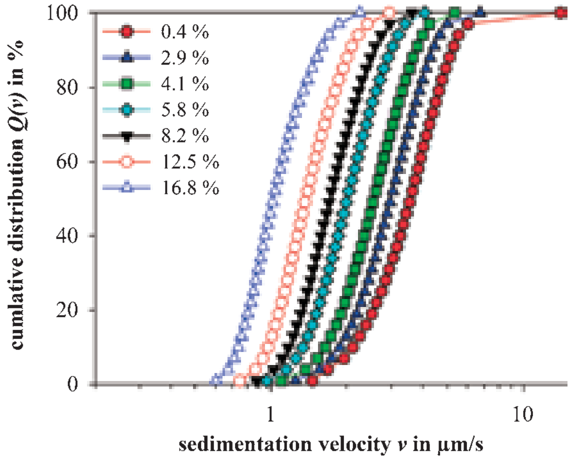

Fig. 15 Particle velocity cumulative distribution for an aqueous technical latex suspension ($x = 100$ nm–170 nm, density 1230 kg/m^3) in dependence of the mass ratio (AC-L data, RCA = 2325) (Detloff et al., 2012).

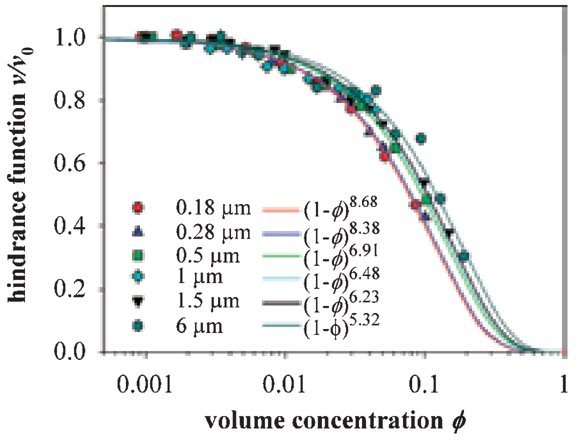

Fig. 16 Hindrance function in dependence of the size of monodisperse particles (see symbols) determined by means of an analytical centrifuge (LUMiFuge). Settling velocities (symbols) v were determined from the slope of the position of the interphase supernatant/dispersion versus time by Front Tracking. The given exponents were obtained by best-fitted curves (lines) based on Eq. 9.

Furthermore, the polydispersity of the dispersed phase has to be taken into account with respect to the hindrance function. The mean particle-particle separation distance depends on the size distribution of the dispersion. This is especially important since most applications involve broad distributions. The idea is supported by rheological references regarding the relative viscosity of dispersions made of a mixture of different-sized particles, e.g. (Horn et al., 2000).

Fig. 17 compares the hindrance of a suspension of monodisperse silica particles (0.18 µm) in dependence of the volume concentration (red line and red symbols) and binary suspensions containing 500-µm particles of increasing ratios (2/1 to 1/2) at the same total volume concentration. Hindrance is most pronounced for the small particles and decreases with increasing ratio of the large ones. Correspondingly, the exponent of Eq. 9 decreases. For a given total volume concentration, again, the hindrance

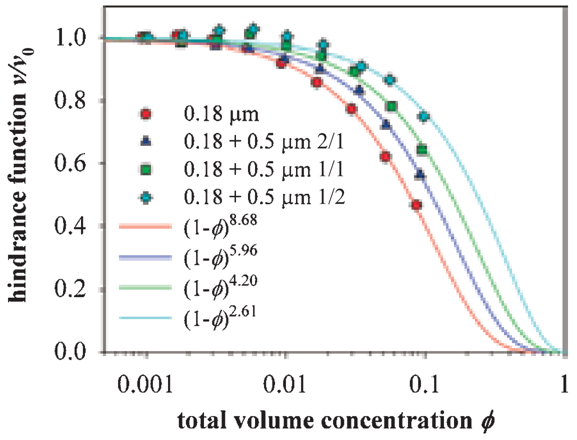

Fig. 17 Hindrance functions of binary mixtures (ratios as indicated) of differently sized monodisperse particles in dependence of the total volume concentration. Other details as **Fig. 16**.

for the monodisperse suspension of small particles (0.18 µm) is greater than for mixtures with the larger ones. This effect is also shown for the polydisperse technical latex dispersion (**Fig. 15**). The hindrance function determined based on different velocity quantiles showed that the exponent of Eq. 9 amounts to 6.5 and 8.2 for v_{10} and v_{90}, respectively.

Wall effects: In addition to the hydrodynamic particle-particle interaction, under real conditions, we also have to deal with a "bounded" liquid. Stokes' law did not account for the influence of cell walls (bounded liquid), where fluid streamlines are disturbed. Any container will influence the flow pattern around a settling particle causing increased drag for spheres. This applies to walls as well as to the top and bottom. In the early part of the last century, (Lorentz, 1907) and (Ladenburg, 1907) analyzed this phenomenon for single-ball viscometers. A correction term was added to the friction force taking into account the ratio of particle size x to the diameter of the circular cylinder-shaped container multiplied by a k-factor of 2.1044 (rectangular cross-section deviates only slightly). In the case of a 500 nm particle and a measuring cell of 1 mm optical path, the real settling velocity is about 0.11 % lower compared to Stokes velocity. If the size-container ratio amounts 1:100, the error is up to about 2 %. Regarding the influence of the bottom, the measurement position (e.g. for CPA) should be 50 particle diameters above the bottom to account for a friction error of less than 0.6 % (Allen, 1999). As shown recently, cylindrical particles may orient with regard to the wall and settle in narrow cylindrical cells even faster (Lau et al., 2010).

Reynolds number: It should be further underlined that Stokes' law (Eq. 3) was derived assuming the steady low-speed motion of a rigid spherical particle through a Newtonian liquid. A laminar flow condition is classified by the dimensionless Reynolds number defined as the characteristic flow speed multiplied by the characteristic flow length divided by the liquid kinematic viscosity. It reads ($Re = \rho_l \cdot v \cdot x/\eta = v \cdot x/\kappa$). The numerator characterizes the flow, whereas the denominator characterizes the liquid. Re increases with continuous phase density ρ_p and size x, faster sedimentation velocity v and lower liquid viscosity η. Re should be lower than $Re < 0.25$ for the application of Stokes' law (laminar Stokes regime). This critical Re would be reached if a particle of 1 µm in size settles in water at 20°C as fast as 0.25 m/s. In general, the drag coefficient decreases with increasing Re. If Re equals 0.25, the experimental terminal particle velocity will be about 3.5 % higher than that calculated by Stokes' law (Allen, 1999). Note that for particle sizing, this number is reduced by its square root (Eq. 12), and therefore amounts to 1.4 %.

In the case of high-gravity settling (centrifugation), the weight force and associated flow pattern around moving particles depends not only on particle mass and rheological behavior of the liquid but also on RCA, and the Re numbers may reach values above 0.25 (Stokes regime). For higher particle velocities ($Re > 0.25$), laminar flow ceases and two symmetrical recirculating eddies emerge near the rear stagnation point. For a Reynolds number at about $Re = 130$, these eddies already occupy a space larger than the particle and finally the flow around the particle becomes unstable and turbulent. Stokes' law underestimates the drag coefficient ($C_D = 24/Re$) as the Reynolds number increases, and the measured real velocity will be larger than that estimated for the Stokes regime. There are numerous papers dealing with extensions of Stokes' law for Re numbers up to turbulent flow, e.g. (Allen, 1999).

Non-Newtonian liquids: Eq. 3 and Eq. 5 hold only for slow particle movement in a Newtonian liquid. This means that shear viscosity does not vary with shear rate, and viscosity is a constant with respect to the time of shearing, respectively. Particle velocity is inversely proportional to the dynamic viscosity of the continuous phase and, in the case of analytical centrifugation, it scales linearly with centrifugal acceleration (Lerche et al., 2006), (Lerche et al., 2011), (ISO/TR 13097:2013). As far as that goes, sedimentation is very comparable to a vertical falling ball viscometer. Typical Newtonian liquids are those containing compounds of low molecular weight, as sugar in food, or low concentrations of dissolved polymers (e.g. starch, pectin, xanthan). Dynamic viscosities increase linearly with low solute concentration (Einstein equation) to become increasingly sloped upwards at higher concentrations. For Newtonian continuous phases, this concentration-dependent increase in viscosity can be taken into account according to Eq. 5.

Fig. 18 displays "normalized" sedimentation velocities of monodisperse polystyrene particles dispersed in different concentrated sucrose solutions normalized for dynamic viscosity and solution density (Werner, 1966). Despite the absolute solution viscosities differing by a factor of 5.4, a master curve is obtained after "normalization" of experimentally determined velocities by Stokes' law with respect to continuous phase density and dynamic viscosity, respectively.

Nowadays, research and dispersion formulators are dealing more and more with rheologically tuned continuous phases that exhibit non-Newtonian or gel-like behavior (Schulz et al., 1991), (Kuentz et al., 2003), (Arabi et al., 2016). Under such circumstances, dynamic viscosity is not a constant anymore and has to be described by means of a shear-stress versus shear-rate relationship (for details refer to (Macosko, 1994)). The dependence is non-linear and/or does not have its origin at zero. Another complication is often the time-dependent rheological behavior as a result of structural changes of the continuous phase due to

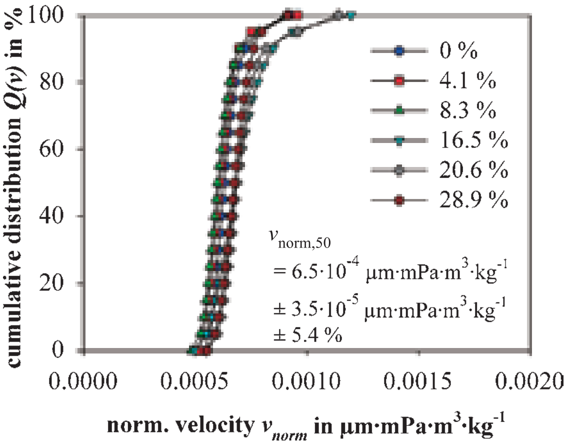

Fig. 18 Normalized sedimentation velocities of polystyrene particles (0.03 % m/m, 1.1 µm) in water and solutions of increasing mass fraction of sucrose up to 28.9 % (AC-L, $\vartheta = 4°C$, RCA = 580).

shearing. Shear-thinning, the decrease in viscosity with increasing shear rates, is the most common relevant behavior with respect to sedimentation (Quemada, 1977, 1978a,b). The question arises as to how the translational frictional coefficient f (Eq. 5) is influenced? During sedimentation, particles are driven by gravity fields through a stagnant liquid creating streamlines and shear rate gradients in the immediate vicinity of each particle. The qualitative and quantitative characteristics of this flow field in the neighborhood depend primarily on the velocity of the moving particle, as well as on the rheological behavior of the continuous phase. In addition, the flow pattern is influenced by particle shape and orientation of the settling particles. There are numerous papers dealing theoretically with the gravity settling of solid particles in rheologically well-defined continuous phases, e.g. (Deshpande et al., 2010). But there is no theoretical model to predict structural changes of the continuous phase due to forced particle movement or to deduce an apparent viscosity to be inserted into Eq. 3 and Eq. 5.

Interestingly, the apparent viscosity can be experimentally determined by monodisperse tracer particles. To this end, continuous phases of anionic polyacrylamide solutions (PAA, molecular mass 7 million Dalton, charge density 32 %, Praestol 2540 Ashland) of concentrations up to mass ratios of 0.1 % were prepared and the apparent viscosity in dependence of the shear rate was determined by means of a rheometer (LOW SHEAR 40, Contraves AG, Switzerland). The apparent viscosity rises with PAA concentration and, on the other hand, decreases with increasing shear rates (shear thinning behavior). Monodisperse silica tracer particles of about 1 µm in size were dispersed in these solutions and the settling velocities (CPA) of primary tracer particles were determined for increasing RCA of 33, 270, 740 and 1900. The apparent viscosities of the PAA solutions of different concentrations were calculated by Eq. 5 based on experimentally obtained velocities (first-principle approach), densities of the two phases and particle size. Concentration-dependent shear thinning behavior was detected with increasing centrifugal force. To compare the shear thinning behavior measured by a Couette rheometer and the sedimentation approach (multi-ball viscometer), the maximal shear rates created by gravity-driven falling balls (particles) in its neighborhood were approximated according to (Guyon et al., 2001) by:

$$\dot{\gamma}_{\max} = \frac{3}{2}\cdot\frac{v}{x} \tag{11}$$

Fig. 19 displays the results of both approaches. There is a very reasonable coincidence. Higher maximal shear rates result in a more pronounced shear thinning. Results can be interpreted in a way that the settling of polydisperse particles in a polymer solution (e.g. rheological thickener application) results in a broadening of the velocity distribution compared to Stokes' law prediction assuming a shear-rate-independent viscosity (Newtonian liquid).

In-situ visualization and quantification of the movement of tracer particles of known size can also be applied to study the time-dependent structuring and aging phenomena of polymeric liquids. Using a model polymer solution system, the sedimentation velocity of monosized silica particles was measured in continuous phases of increasing pectin concentrations and under different centrifugal forces (Sobisch et al., 2018).

Fig. 20 clearly demonstrates that the settling velocity of tracer particles slows down by about 2 decades with increasing pectin mass fraction up to 3 % (RCA = 2300).

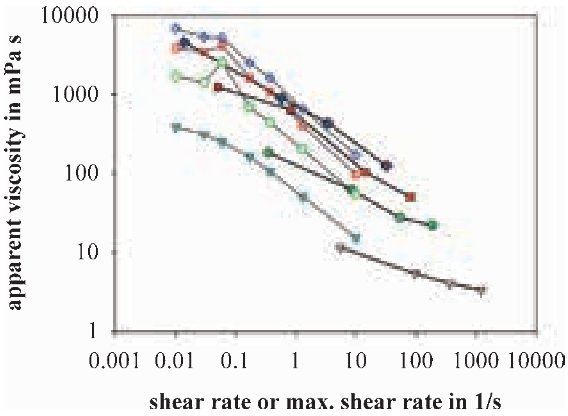

Fig. 19 Shear-dependent apparent viscosity of PAA solutions of different concentrations determined traditionally by a Low Shear 40 rheometer:
—▼— 0.01 % —○— 0.04 % —□— 0.07 % —◆— 0.10 %
and based on Stokes' law by sedimentation velocity of monodisperse tracer particles ("falling multi-ball viscometer"):
—▼— 0.01 % —■— 0.04 % —■— 0.075 % —◆— 0.10 %

The separation behavior of silica particles in pectin solutions (non-Newtonian continuous phases) does not depend linearly on RCA. In contrast, shear thinning-like behavior is observed and this behavior becomes more pronounced with increasing pectin concentration.

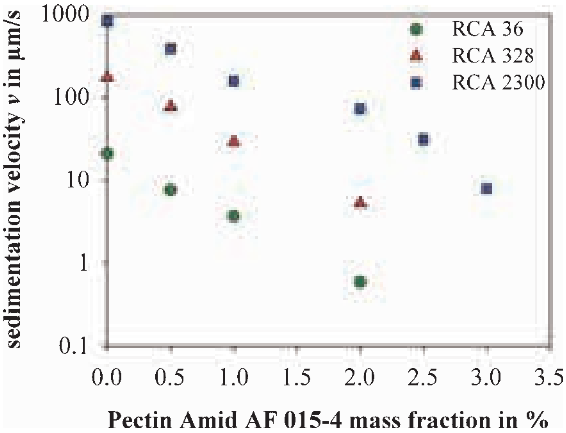

Fig. 20 Sedimentation velocity of silica tracer particles in dependence of the pectin concentration and RCA. Velocity determination by the slope of interface supernatant/suspension (front) tracking (threshold 10 % transmission). Data by AC-L, 2-mm cells, $\vartheta = 20°C$, mass fraction of 1-µm silica particles 5 % (Sobisch et al., 2018).

To investigate the aging of the pectin solution in situ, solutions of different pectin concentration, using silica tracers with a mass fraction of 2 %, were filled into sample vials immediately after preparation, and aged for up to 29 days at 4°C. Vials analyzed for structural changes after a set aging period (see indications in **Fig. 20**) were equilibrated at room temperature for about 30 minutes, carefully placed into the analytical centrifuge LUMiSizer, and then analyzed for any movement of the primary silica particles. In this way, the process of structure build-up can be investigated with no distortion by sampling quasi in-situ. **Fig. 21** displays the settling of the tracer particles for the freshly prepared sample (day 0, top). The red line represents the first transmission profile, green the last one taken. As can be seen, the area between transmission profiles for a sedimentation time of 230 minutes (quantifying clarification) decreases with increasing pectin concentration and aging. Interestingly, pectin solutions of 3 % and 3.5 % exhibit about the same aging alteration after 15 days and 1 day, respectively. No particle movement could be detected at RCA = 2300 after 29 days (3 %) and 15 days (3.5 %), respectively. This indicates that some kind of structure building occurred, resulting in a motion decrease of the tracer particles with aging time. The analytical

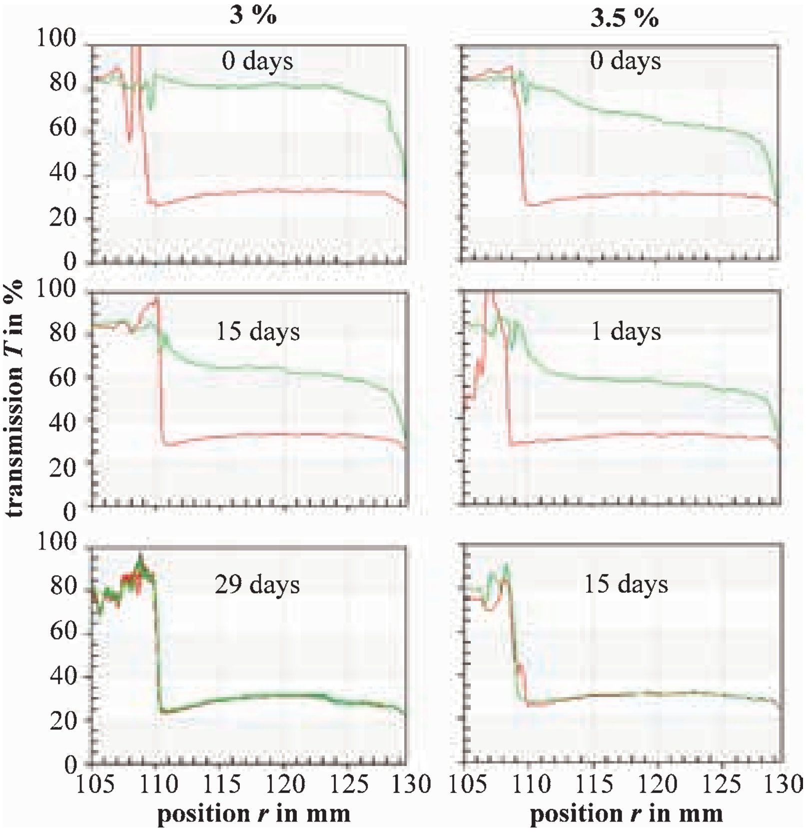

Fig. 21 Probing pectin gels at different concentrations and aging times by tracking the settling velocity of monodisperse tracer particles (AC-L, RCA = 2300, 230 min., 2-mm cells, $\vartheta = 20°C$). Only the first (red) and last (green) transmission profiles are displayed.

approach in this case tracks the particle movement directed by gravity fields, in contrast to particle tracking methods based on Brownian motion (Schuster et al., 2015)

Fig. 22 summarizes possible relationships between particle velocity and relative centrifugal/relative centrifugal force acceleration with regard to the rheological behavior of the continuous phase, as well as structural alterations due to shear stress acting on moving particles. In accordance with Stokes' law, the particle velocity is proportional to the centrifugal acceleration or RCA for a Newtonian continuous phase (line 1). In contrast, if the continuous phase exhibits shear thinning (line 2) or shear thickening (line 3), the particle velocity increases nonlinearly. On the other hand, non-linearity may indicate "changes" of the particles themselves due to hydrodynamics. Line 2 could be also provoked, e.g. by shear-stress-induced agglomeration (dilatancy), particle orientation, or deformation of emulsion droplets reducing the frictional coefficient. A behavior depicted schematically by line 3 may have its origin in a shear-stress-governed breakdown of agglomerates or flocs (Lerche et al., 2001). Created smaller particles settle at a slower rate compared to the initial size of the particles. The onset of consolidation of the disperse phase in the course of separation manifests itself earlier at a higher RCA (RCF) and also results in lowering the increase of the particles' settling velocity expected by Eq. 5 (Sobisch et al., 2006), (Usher et al., 2013). The depicted non-linearity can often be described by a simple power law. The exponents are greater than one for shear thinning (line 2) and less than one in the case of shear thickening (line 3) of the continuous phase. Finally, line 4 of **Fig. 22** demonstrates the effect of a continuous phase exhibiting a yield point. Particles start to move if the shear stress created by the particles due to centrifugal force destroys the polymer structure (Lerche et al., 2003). It should be underlined that a yield point does not always imply that particles do not settle (Kuentz et al., 2002). The fact that the rheological behavior of dispersion can be probed by sedimentation techniques was successfully demonstrated by (Kuentz et al., 2003), (Jacob, 2015).

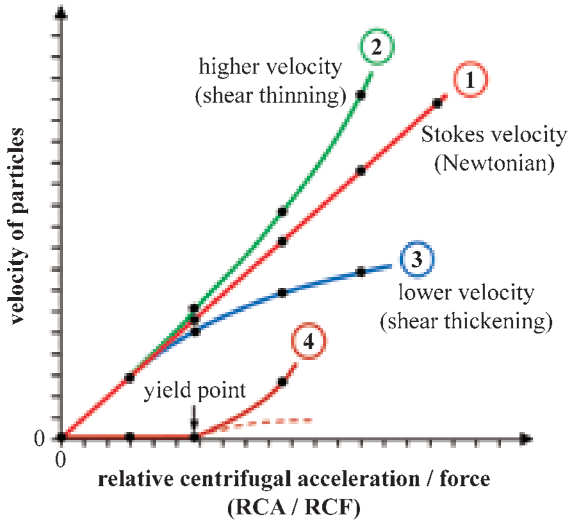

Fig. 22 Schematic drawing of particle (separation) velocity in dependence of the RCA for different classes of dispersions with respect to rheological behavior.

Kynch model: We now depart from the basic approach of Stokes and focus on moving particles in a bounded quiescent liquid. The law of volume continuity demands that settling particles displace the same volume of continuous phase as they occupy. In other words, the volume flux of particles creates a flux of continuous phase directed in the opposite direction. In literature, two major physicomathematical models are employed for the formulation of the governing equations of motion. The whole particle-liquid dispersion is assumed as a single flowing continuum—the "mixture" ("diffusion") model—or, the continuity and momentum balance are described separately for disperse phase and continuous phase—the "two-fluid (two-phase)" model (Ungarish, 1993). It was Kynch who proposed a kinematic theory of sedimentation based on the assumption that the suspension is a continuum and the sedimentation process is represented by the continuity equation (mixture model). The approach is governed by the local volume concentration of the dispersed phase as a function of space and time, and by the so-called flux density function (Kynch, 1952), (Concha et al., 2002). On the other hand, the approach assumes that the local solid-liquid relative velocity is a function of the total volume concentration of the dispersion only. For the first time, this basic framework allows the description of the complete "sedimentation" process, linking free-settling and consolidation by a unified theory. For details, industrial applications, progress and future work to be performed in this research field, refer to, e.g. (Fitch, 1983), (Buscall et al., 1987), (Schaflinger, 1990), (Ungarish, 1993), (Bustos et al., 1999), (Lerche et al., 2001), (Concha et al., 2002), (Frömer et al., 2002), (Berres et al., 2008), (Detloff et al., 2008), (Anestis et al., 2014).

3.2 Extinction-weighted size distribution

Particle velocity distributions are experimentally measured based on the primary principle with no assumptions regarding dispersions properties, models or algorithms. Experimentally determined velocities can be transformed to a particle size distribution for gravity sedimentation based on Eq. 3 and for centrifugal sedimentation based on Eq. 7, respectively (ISO 13317-1:2001), (ISO 13318-1:2001). The result is the Stokes diameter of a settling particle, more precisely an equivalent spherical Stokes diameter. If the particle shape is known, such a shape influence may be accounted for by introducing corresponding shape factors into the basic Stokes' law. In principle, particle size determination is merely a transformation of the calculated particle velocity distribution data. There is no change in the distribution pattern or modality. For the gravitational sedimentation transformation, this is given by Eq. 12:

$$x(h,t)=\sqrt{\frac{h}{K\cdot g\cdot t}} \tag{12}$$

and for centrifugal techniques by Eq. 13:

$$x(r,t)=\sqrt{\frac{1}{K\cdot\omega^2\cdot t}\cdot\ln\left(\frac{r}{r_\mathrm{m}}\right)} \tag{13}$$

Remember that the material constant K according to Eq. 3 depends on the density difference of the disperse and continuous phase as well as the viscosity of the continuous phase.

The amount of particles for each particle size class—cumulative distribution values $Q_\mathrm{ext}(x)$ (y-axis)—is calculated based on the determined extinction values at time t obtained by means of:

$$Q_\mathrm{ext}(x)=\frac{E(h,t)}{E(h,\mathrm{end})} \tag{14}$$

As the concentration of each particle class is physically based on an extinction measurement (Eq. 1), the obtained size distribution is extinction-weighted and cannot be directly compared with, e.g. intensity-weighted DLS or SLS or mass-weighted acoustic data, respectively.

In contrast to sedimentation under gravity, in a centrifugal field the initial concentration of dispersion decreases with increasing radial position r due to a radially outward higher acceleration acting upon the particles. The dilution is further elevated by particle motion on radial trajectories (**Fig. 23**). These so-called effects of radial dilution have to be taken into account calculating the distribution density data of velocity or particle size distribution (y-axis). It was shown that the concentration change of samples does not differ in the middle of the sample cell, regardless of whether rectangular or sector-shaped cells (**Fig. 23**) are employed (Detloff et al., 2008).

The mass balance

$$\phi(r,t)\cdot r^2(t)=m(r)=m(r_\mathrm{m})=\phi(r_\mathrm{m},0)\cdot r_\mathrm{m}^2 \tag{15}$$

states that the mass in any cross-sectional area is conserved when moving from the radial position r_m to $r(t)$ and is given by:

$$\phi(r,t)=\phi(r_\mathrm{m},0)\cdot\left(\frac{r_\mathrm{m}}{r(t)}\right)^2 \tag{16}$$

Here, $\phi(r, t)$ denotes the total concentration of all particles at position r at time t.

The distribution values (y-axis; $q_\mathrm{ext}(x)$) of the extinction-weighted particle size distribution in the centrifugal field are obtained by solving the following integral equation Eq. 17:

$$E(r,t)=E(r,0)\cdot L\cdot \int_{x_\mathrm{min}}^{x(t,r)}\exp\left(-2\cdot K\cdot x^2\cdot\omega^2\cdot t\right)\cdot q_\mathrm{ext}(x)\,\mathrm{d}x \tag{17}$$

This can be done in an analytic way for CTA by:

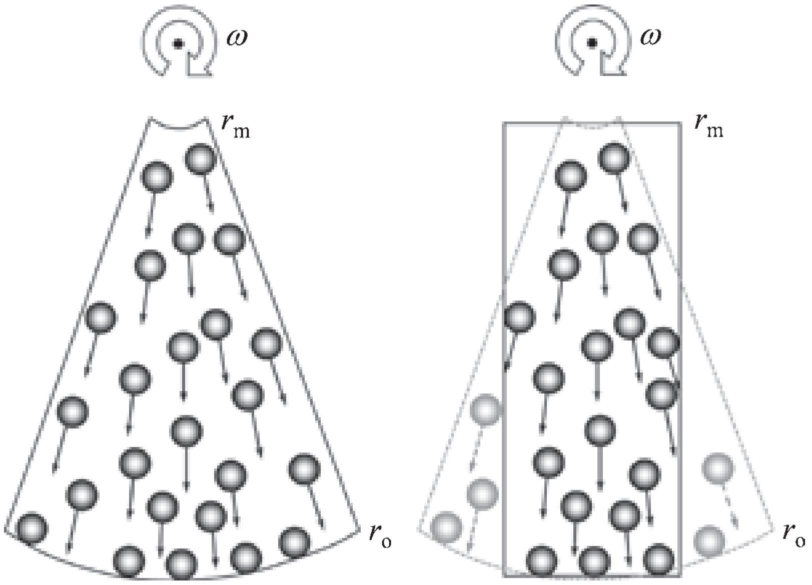

Fig. 23 Schematic illustration of centrifugal sedimentation with regard to the geometry of the sample cell shortly after the start of separation; left: sector-shaped AUC cell; right: AC-L rectangular cell.

$$Q_{\text{ext}}(x)=\frac{\int_{E_{\min}}^{E(r)} r^2 \mathrm{d}E(r)}{\int_{E_{\min}}^{E_{\max}} r^2 \mathrm{d}E(r)} \tag{18}$$

and for CPA in a numeric way by:

$$Q_{\text{ext}}(x_i)=\frac{1}{2}\cdot\left(y_i+y_{i-1,i}\right)\cdot E_i+ \sum_{j=1}^{i-1}\left(\frac{y_i+y_{i-1,i}}{y_{j+1,i}+y_{j,i}}-\frac{y_i+y_{i-1,i}}{y_{j,i}+y_{j-1,i}}\right)\cdot Q_{\text{ext},j} \tag{19}$$

with:

$$y_i=\left(\frac{r}{r_{\text{m}}}\right)^2,\ y_{i,j}=y_i^{\left(\frac{x_i}{x_j}\right)^2},\ for\ i,j = 1,2,3,\ldots,N, j\le i, y_{0,i}=1 \text{ and } y_{i,i}=y_i$$

It should be noted that in the case of centrifugal separation, in addition to buoyancy, the motion of the particles is driven by a second body force—the Coriolis force. Coriolis acceleration equals the particle velocity multiplied by the angular velocity of the rotor. Its direction is perpendicular to the radius (Ungarish, 1993), (Frömer et al., 2002), (Probstein, 2003). For an estimate let us assume the centrifugal separation of large and dense cement particles (x = 10 µm, ρ_{p} = 3150 kg/m^3) dispersed in isopropanol (η = 2.1 mPas). At an RCA = 4000 for a rotor speed of 5250 min^{-1}, computation of the ratio of Coriolis acceleration to centrifugal acceleration amounts to 0.9 %. Hence the Coriolis force for analytical centrifuges operating up to the above acceleration range can be neglected even for rather large and heavy particles.

Finally, we have to consider that the local concentration of particles at position r not only depends on directed body forces, as discussed so far, but also on particle diffusion. This becomes especially relevant for nanoparticles, as diffusion coefficients D increase inversely with particle size. A gravity-governed particle transport creates concentration gradients in the direction of the acting/applied gravity $\partial\phi/\partial r$, which causes a collective particle transport in the opposite direction of the concentration gradient by diffusion (Fick's law). Both transport terms were combined for the first time for AUC applications by (Lamm, 1929).

$$\frac{\partial\phi}{\partial t}=\frac{1}{r}\frac{\partial}{\partial r}\left[rD\left(\frac{\partial\phi}{\partial r}\right)-s\omega^2r^2\phi\right] \tag{20}$$

Eq. 20 describes the change of (particle) concentration $\partial\phi/\partial t$ due to the net transport by diffusion (first term) and sedimentation (second term) in the bracket. Above equation applies when both transport terms are independent of particle concentration. For details refer to (Fujita, 1962). It should be pointed out that even for nanoparticles, diffusion does not prevent particle sedimentation. It is broadening the separation created by concentration gradients. In other words, the mean particle velocity is not changed but the particle dispersity appears more polydisperse. Diffusion may be expected to be insignificant if the dimensionless Péclet number—relating the advective transport rate to the diffusive transport rate—is greater than one (Ungarish, 1993), (Probstein, 2003).

Recently, it was shown that primary sensor signals of AC-L saved by SEPView software can be imported into AUC software packages. This will allow users to tap into the existing AUC knowledge pool (Walter et al., 2015a).

3.3 Volume-weighted size distribution

Extinction-weighted particle size distribution does not account for the optical properties of the dispersion. Thus, the different particle classes contributing to the total recorded extinction intensity are not correctly weighted. To measure the correct amount of particles present in defined size distribution classes, the differences in the refractive index between particles and continuous phase, and the geometrical particle shape have to be accounted for. The volume-weighted particle size distribution is calculated by transforming the y-axis of the extinction-weighted size distribution by Eq. 21:

$$\Delta Q_{3,i}=\frac{\dfrac{\Delta Q_{\text{ext},i}}{A_{\text{v},i}}}{\sum_{j=0}^{N}\dfrac{\Delta Q_{\text{ext},j}}{A_{\text{v},j}}} \tag{21}$$

Here, A_{v} corresponds to the volume scattering cross-section which can be obtained by applying the Mie theory (Mie, 1908), (van de Hulst, 1981). **Fig. 24** compares exemplarily the extinction- and volume-weighted size distribution of polydisperse submicron silica particles. Polydispersity regarding size stays identical between the extinction- and volume-based results. However, fractions of size classes differ by about 10 %. The Mie correction assumes spherical particles. Therefore, strictly speaking, the calculated sizes should be called equivalent spherical particle sizes.

Of added interest is the fact that cuvette liquid centrifugal sedimentation methods are very flexible regarding different continuous phases (e.g. pH, ionic strength, solutions of different solutes, organic solvents, ionic liquids). It allows viscosity and density contrasts to be accounted for, as shown for the velocity in **Fig. 18**. The median size $x_{50,3}$ of the polystyrene particles dispersed in 8 different continuous phases amounts to $x_{50,3}$ = 1.081 µm ± 0.012 µm (Eq. 13 and Eq. 21). The accuracy (trueness, reproducibility) of sedimentation-based particle sizing (separation principle) is known to be on a very high level. An example is the round robin test (Lamberty et al., 2011), as well

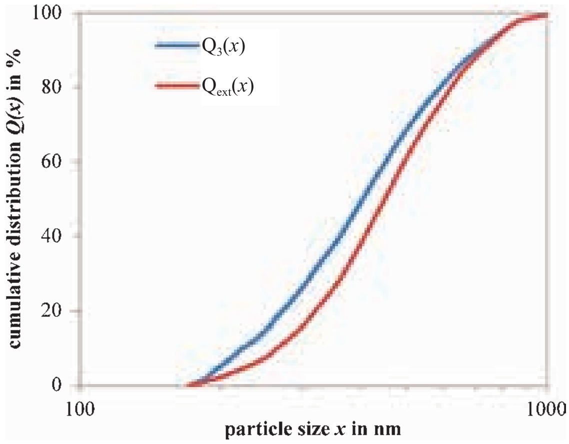

Fig. 24 Particle size distribution for polydisperse silica (SiO_2, 0.1 µm–1 µm) obtained by LUMiSizer, (RCA ramp, $\lambda = 470$ nm, $\vartheta = 25$°C, $\rho_p = 2200$ kg/m^3 $\rho_l = 997.3$ kg/m^3, $\eta = 0.899$ mPa s, $RI_p = 1.475\text{-}0i$, $RI_l = 1.3377\text{-}0i$); red: Extinction-weighted; blue: Volume-weighted.

as reports and publications issued by the European Research Project "Nanodefine" (NanoDefine, 2018).

3.4 Number-weighted size distribution

The number-weighted particle size distribution is obtained from the volume-weighted distribution by the method of moment-notation, as described in (Leschonski et al., 1974), (ISO 9276-2:2014). It is straightforward if the volume-weighted particle size distribution is correct and the particles are spherical. For non-spherical particles, the conversion situation is more difficult because different measurement principles derive an equivalent spherical size depending on the technique used.

This topic is intensively studied by the EU project "Nanodefine" (www.nanodefine.eu) inasmuch as the EU definition for the classification of products regarding "Nanomaterials" is going to be based on counting. The proposed definition states that a material (product) has to be classified a *nanomaterial* if for 50 % or more of particles in the number size distribution, one or more external dimensions is in the size range of 1 nm–100 nm (Bergeson et al., 2017). Recently, the performance of 12 different measurement techniques (microscopic, ensemble- and separation-based) was investigated regarding tier 1 classification, and compared to an SEM "reference." Altogether, 15 polydisperse RMs were included in this study. Number medians ranged from 5 nm to 2016 nm and the distributions were characterized as monomodal or polymodal for size, and spherical, non-spherical or fractal for shape, respectively. The use of liquid centrifugal sedimentation techniques was deemed appropriate for the tier 1 classification of nanomaterials. The deviation of median size values of the RM compared to SEM sizes was about 33.7 % (CPS disk centrifuge, 14 RMs measured), 28.8 % (LUMiSizer, 14 RMs) and 30.2 % (AUC, 10 RMs). For comparison, the deviation for DLS (14 RMs) amounts to 80.2 % (Babick et al., 2016a).

3.5 Multi-wavelength particle sizing

Besides wavelength, the extinction coefficient of particles at visible light depends on size and optical properties (refractive index difference with respect to the continuous phase, particle shape) at a given wavelength. If the complex refractive index is known, the scatter and absorption of light by spherical particles of different sizes can be taken into account by the Mie theory (Mie, 1908), (van de Hulst, 1981). Problems arise if the particle size or optical properties are not available.

The extinction values of dispersion depend on the wavelength. The ratio obtained at different wavelengths should provide information of the particle size. The Mie calculation shows that in general, for particles of submicron size, E_{NIR}/E_{VIS} is less than one, with the ratio depending on the particle size. The new LUMiReader® and LUMiSizer® models are equipped with multi-wavelength functionality, enabling the capture of extinction profiles across the entire sample height by multiple wavelengths de facto simultaneously. A decrease in the extinction ratio over time indicates, e.g. destabilization due to flocculation (Detloff et al., 2011). Note that particle size does not have to be determined directly.

Another way to circumvent the necessity of quantitative optical models consists in determining extinction-based particle size distributions at different wavelengths—as already proposed by (Weichert, 1981). The basic idea behind it is as follows. The wavelength dependency of turbidity for defined particle sizes is approximately equivalent to the size dependency of turbidity at fixed wavelengths. Hence, the multi-wavelength detection itself yields the required optical model. Extinction-weighted size distributions can be transferred into a volume-weighted distribution with no assumption regarding material parameter and particle shape. It relies on the assumptions that a) the extinction coefficient of a particle is a function of the dimensionless size x/λ, and b) extinction-weighted size distributions of different wavelengths give the same volume-weighted distribution (to be published). **Fig. 25** shows the results for colloidal Al_2O_3 particles obtained by the developed multi-wavelength LUMiSizer. (Babick et al., 2016b). The result of a cumulative weighted size distribution shows good conformity between the classic Mie approach and the newly developed analysis algorithm based on extinction-weighted distributions obtained by multi-wavelength experiments. Work is currently in progress to answer questions regarding detection limits for very fine and coarse particles on wavelength, and

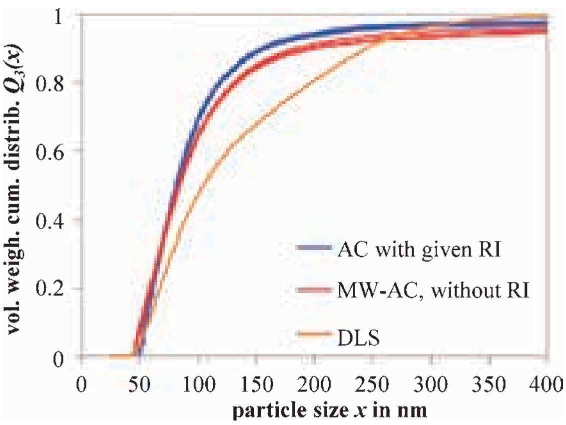

Fig. 25 Comparison of a cumulative volume-weighted size distribution of polydisperse colloidal Al_2O_3 determined by classic analysis (Mie approach, AC at 455 nm wavelength) and new Multi-Wavelength Particle Size Analysis obtained by an MW-LUMiSizer operating at 410 nm, 455 nm and 470 nm. In comparison, the results given are obtained by the DLS technique.

smoothing signal noise to derive high-quality optical models.

4. Beyond particle sizing

4.1 Hydrodynamic particle density

Density is an important material parameter. Its determination is a routine task for liquids and solids, but a challenge for nano- and microparticles such as biological cells, brushed, porous or hydrocolloid particles, core shell particles, particles stabilized by Pickering emulsification, droplets or fractals dispersed in a liquid. It is an important parameter for particle size determination based on sedimentation techniques by gravity or analytical centrifugation (ISO 13317-1:2001), (ISO 13318-1:2001), field flow fractionation (Kirkland et al., 1983) or acoustic techniques (Horváth-Szabó et al., 1996), (ISO 20998-1:2006). In addition, there are also many other application fields where density matters. Stabilization of dispersion is achieved by density matching (e.g. liquid food products (McClements, 2004)), optimization of solid-liquid separation, e.g. recycling, mining (Callahan, 1987), or to characterize the purity or composition of structured particles (e.g. internal phase of double emulsions, homogeneity of "hollow" particles or core/shell particles (Kirsch et al., 1999). Nowadays, there is an increasing interest in the particle density to enable estimation of the mass transfer of nanoparticles atop cell layers by sedimentation to calculate doses for in-vitro nanotoxicity assessment (Kato et al., 2009), (Hinderliter et al., 2010), (DeLoid et al., 2013).

Sedimentation techniques allow determining the density of dispersed particles in situ. The particle density can be calculated from experimentally determined velocities based on Stokes' law (Eq. 3), if the shape and particle size are known. But in most cases, especially for nanoparticles and surface-decorated particles, both material parameters are not available. In such cases, two different sedimentation approaches may be applied (Lerche, 2011), (Woehlecke et al., 2012). The first one—"isopycnic velocity interpolation approach" principally dates back to Archimedes of Syracuse (3rd century BC). The Archimedean principle or buoyancy principle states that a body or a particle stays suspended in a liquid if the densities of liquid and particle match. It sinks if the particle density is higher and it floats/creams, if the particle density is lower. There are different liquids and solutions available that allow for the density measurements of particles having a density from about 800 kg/m^3 to above 3000 kg/m^3. The measuring task simply consists of detecting the direction of particle migration in a series of liquids with appropriate densities—lower and higher as the expected particle density—and to interpolate the liquid density for zero migration velocity (ISO 18747-1:2018). This technique determines the buoyant density defined as the ratio of particle mass to particle volume including filled or closed pores as well as adjacent layers of liquid or other coating materials. Sedimentation methods are very attractive for detecting the direction of particle migration (sedimentation or creaming /flotation).

Fig. 26 displays as an example of the experimental data for RMs (PMMA) of different size supplied by the company Dr. Lerche KG, Berlin, Germany. The obtained particle velocities were multiplied by the corresponding continuous phase viscosity to normalize viscosity effects (Lerche et al., to be published). The density of the particles

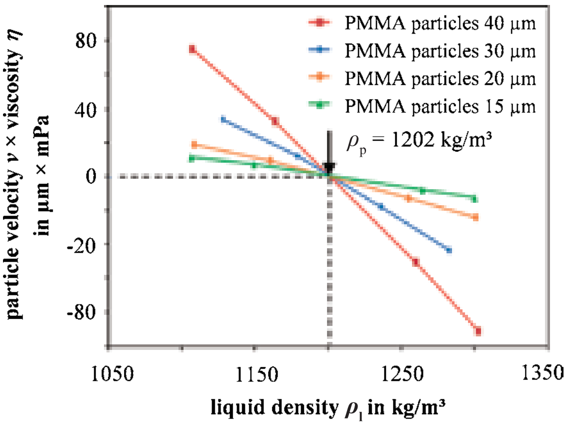

Fig. 26 Gravity sedimentation velocity of monodisperse PMMA particles of different size in dependence of the density of the continuous phase (polytungstate solutions of different concentration, particle mass fraction 0.2 % to 0.8 %, $\vartheta = 30°C$, LUMiReader PSA, $\lambda = 870$ nm, 10-mm PC cells).

then equals the liquid density corresponding to the zero number of the y-axis (dashed lines in **Fig. 26**) and the mean value of particle density amounts to 1201.5 kg/m^3. The density of the four particle size classes differs by only less than 0.1 %. This is to be expected, as size and shape do not enter into the equations of gravity and buoyancy forces. Therefore, reasonable agglomeration or flocculation during the experiment does not influence the density determination. The method is also robust for the chosen particle volume concentration over a wide range. On the other hand, accuracy depends on trueness of velocity determination, distance of interpolation points and precision of liquid density and viscosity data. Because of this, temperature changes during the experiment have to be avoided. Furthermore, the particles should not swell or shrink in the test solutions.

The second density determination approach—"multi-velocity approach"—is based on measurement of the mean sedimentation velocity or sedimentation velocity distribution of the particles in gravitational or centrifugal fields. It can be applied both for particles exhibiting sedimentation or flotation/creaming. This approach is already known from AUC (McCormick, 1964), (Mächtle, 1984). A draft ISO standard is currently available (ISO/DIS 18747-2, 2018). According to Stokes' law (Eq. 3, Eq. 5), the velocity v for a given particle size depends on liquid ρ_l and particle density ρ_p, respectively, and on liquid viscosity η. The multi-velocity approach is based on the velocity determination of particles dispersed in two different liquids having a different density. Based on Stokes' law applied to sedimentation in both dispersions, we get:

$$\rho_p = \frac{v_1 \cdot \eta_1 \cdot \rho_{l,2} - v_2 \cdot \eta_2 \cdot \rho_{l,1}}{v_1 \cdot \eta_1 - v_2 \cdot \eta_2} \tag{22}$$

where indices 1 and 2 correspond to the two different liquids.

Fig. 27 displays the cumulative velocity distribution of 1.1-µm spherical polystyrene particles. Particles from the same batch were dispersed at (mass fraction 0.03 % m/m) in continuous phases of different densities (water and solutions of different sucrose concentrations). At higher sucrose concentration, the particles float (negative velocity) as the density of the corresponding sucrose solution is higher than the particle density. For each possible combination of different continuous phases, the particle density was calculated according to Eq. 22 (Woehlecke et al., 2012). The mean density value amounts to 1053 kg/m^3 (standard deviation 0.4 %) based on all 9 liquid combinations. This value corresponds well to the known density of polystyrene (1055 kg/m^3). Often, normal water H_2O and D_2O are chosen as the continuous phase.

Fig. 28 displays exemplarily a cumulative velocity distribution of oil droplets dispersed in the two kinds of water. As the density difference is higher in the case of D_2O, the velocity distribution is shifted to the right. Based on the harmonic mean velocities of 26.72 µm/s and 53.64 µm/s, respectively, the density of rapeseed oil was calculated to amount to 923.6 kg/m^3. It differs only by 0.5 % from 918.5 kg/m^3 of the oil/emulsifier phase used to make the O/W emulsion. It should be mentioned that Eq. 22 can be applied to each percentile of the velocity distribution. Neglecting experimental uncertainties, the measured densities will be the same as long as all particles are of the same material or composition. On the other hand, the density differences for percentiles indicate that fast and slow particles have different densities and therefore differ in their composition. It has been shown that a destabilization by Ostwald ripening of density-matched

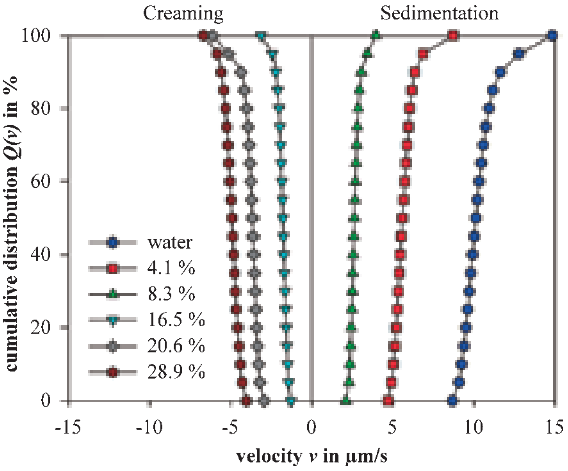

Fig. 27 Velocity distributions of monodisperse polystyrene particles dispersed in water and 5 different concentrations of sucrose solutions (sucrose/water mass fraction: 4.1 % to 28.9 %) measured by AC-L (RCA = 480, ϑ = 4°C, 2-mm PC cells, ROI 0.5 mm width at 20 mm (sedimentation), and 2 mm and 5 mm (creaming) above bottom.

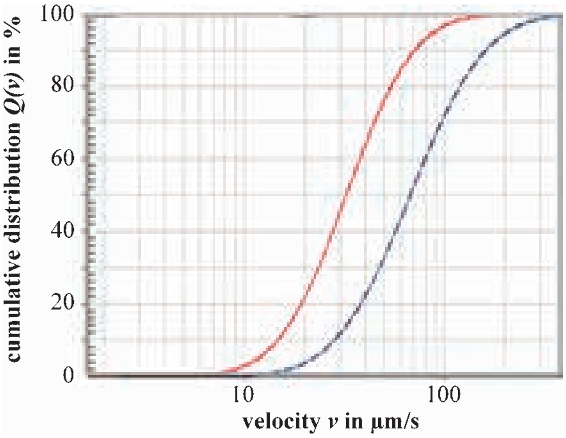

Fig. 28 Cumulative creaming droplet velocity of a rapeseed oil emulsion prepared in H_2O (ρ = 997 kg/m^3, left red line) and in D_2O (ρ = 1103 kg/m^3, right blue line). (AC-L, RCA = 2325, ϑ = 25°C, 2-mm PC cells).

emulsions leads to a density distribution of emulsion droplets (Sobisch et al., 2009). The density increase of slow (small) particles is due to the increase of the weighting agent concentration and vice versa for the faster (larger) particles. The described approach can also be employed for quality control of the homogeneity of "hollow" particles or core/shell particles, as well as for determining the internal phase of double emulsions. The multi-velocity approach relies metrologically on reliable determination of the particle velocity or velocity distribution. The smaller the difference in densities between the two continuous phases, the more accurately the particle velocity has to be determined. The chemical composition/density distribution of the particles themselves does not matter. Here too, the state of particles/dispersion should not change, e.g. the particles should neither swell nor shrink in the continuous phases, nor agglomerate or flocculate. Determination of the velocity distribution is preferably made at low volume concentrations.

A similar approach for line start sedimentation was published by (Kamiti et al., 2012), (Neumann et al., 2013). In contrast to the homogeneous sedimentation approach, it does not operate at constant continuous phase viscosity due to the built-up density gradient, and the density evaluation is more complex. Furthermore, the decane layer on top of the spinning liquid has to be taken into account.

4.2 Characterization of magnetic particles

Magnetic micro- and nanoparticles have increasingly wide applications in information technology, magnetic fluids, selective separation, and nanomedicine (Holschuh et al., 2014), (Anker et al., 2017). There are differently designed particles. Magnetic particles may be prepared by coating, i.e. uniform-sized core particles covered by a layer consisting of dispersed magnetite in a non-magnetic material (e.g. polystyrene). The magnetite content of these objects represents 10 % to 20 % and they are paramagnetic. Nanoparticles can also be built starting with a magnetite core of a few nanometers with a surrounding "isolating" non-magnetic layer of, e.g. silica carrying mostly polymers or macromolecules for functionalization. These particles are often supermagnetic. The magnetic behavior of these particles is very complex. Their susceptibility (responsiveness) and magnetization has to be analyzed during particle design, optimization of application and quality control of the production process (Wilhelm et al., 2002), (Mykhaylyk et al., 2008), (Eichholz et al., 2014).

As previously described, STEP-Technology® provides particle velocity as a primary experimental result. If an inhomogeneous magnetic field acts on magnetic particles, they start to move in the direction of the higher magnetic field strength in dependence of its magnetic properties (similar to manipulating particles in an inhomogeneous electrical field, dielectrophoresis (Pethig, 2017). In addition to gravity or centrifugal forces, the particles are additionally accelerated by the magnetic field and the terminal velocity depends on the directions of the corresponding force vectors (Wilhelm et al., 2002). As proposed by (Lerche et al., 2008), analytical centrifugation (e.g. of LUMiFuge / LUMiSizer-type) or earth-gravity-based separation analysis (e.g. LUMiReader) can be adapted with permanent magnets of field directions parallel or orthogonal regarding the gravity field (**Fig. 29a** and **Fig. 29b**). The strength of the magnetic field can be varied by the type of magnet and distance to the sample cell.

The first example of a "sedimentation-based technique" to analyze magnetic particles (Mykhaylyk et al., 2015) revolves around the analysis of magnetic lipoplexes formulated by different MNPs combined with liposomal enhancers for gene delivery to human corneal endothelium (Czugala et al., 2016). Complexes were assembled at a pDNA concentration of 10 µg/mL by 3 different MNPs but different Fe-to-pDNA w/w ratios (Tab. at **Fig. 30b**).

The size of magnetic objects was in the range of 0.83 µm to 1.1 µm. To confirm proper complexing and

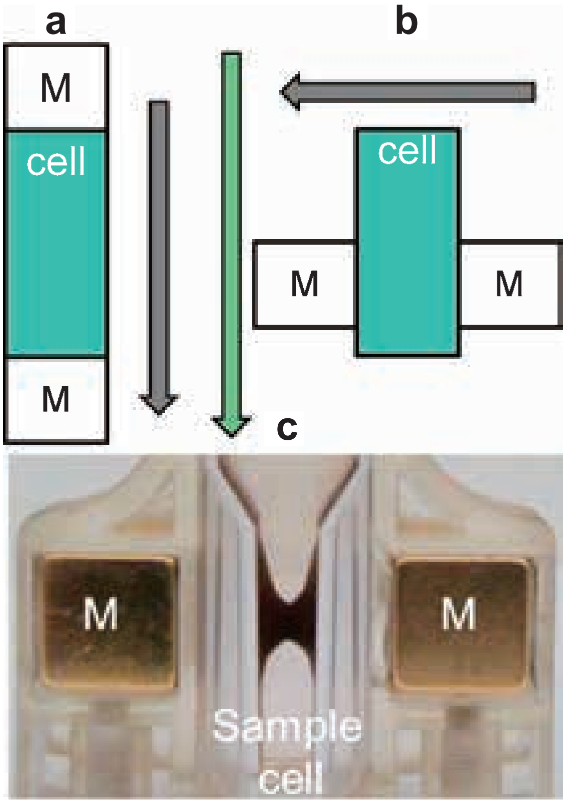

Fig. 29 Schematic drawing of vertical/radial **(a)** and orthogonal **(b)** magnet **(M)** arrangements (black arrow) with regard to earth gravity/centrifugal field (green arrow) and sample cell. Photo **(c)** shows the adapter to build an orthogonally directed magnet field and the sample cell with a formed bridge of magnet particles between magnets before centrifugation.

stability of these magnetic gene carriers, the magnetophoretic velocity was determined based on changes of space- and time-resolved extinction profiles both under gravity and superposed magnetic fields. The extinction profiles were registered along the vertical axis of the sample cell with a customized LUMiReader® device equipped with 2 disk Neodymium-iron-boron magnets positioned underneath an optical cell (**Fig. 30a**, right). This resulted in a magnetic flux density and gradient averaged over the vertical sample height of 0.16 T and 33.5 T/m, respectively. The magnetophoretic velocity v (**Fig. 30b**, right) was calculated based on an integral normalized extinction at 410 nm wavelength, E/E_0, versus time t (**Fig. 30b**, left). No sedimentation of the magnetic carriers was detected within 1500 s with no magnetic field application (horizontal lines at about 1.0 in **Fig. 30b**, left). With the magnetic field, a significant decline of the integral extinction (clarification) was observed indicating a decrease of magnetic particle concentration (magnetophoresis) depending on the type of lipoplexes (different MNPs and the amount per complex, Tab. of **Fig. 30b**). The calculated cumulative distribution of effective magnetophoretic velocity is shown in **Fig. 30b**, right). For details refer to (Mykhaylyk et al., 2015) and (Czugala et al., 2016).

Determination of magnetophoretic velocity by STEP-Technology® as a tool to characterize assembled objects

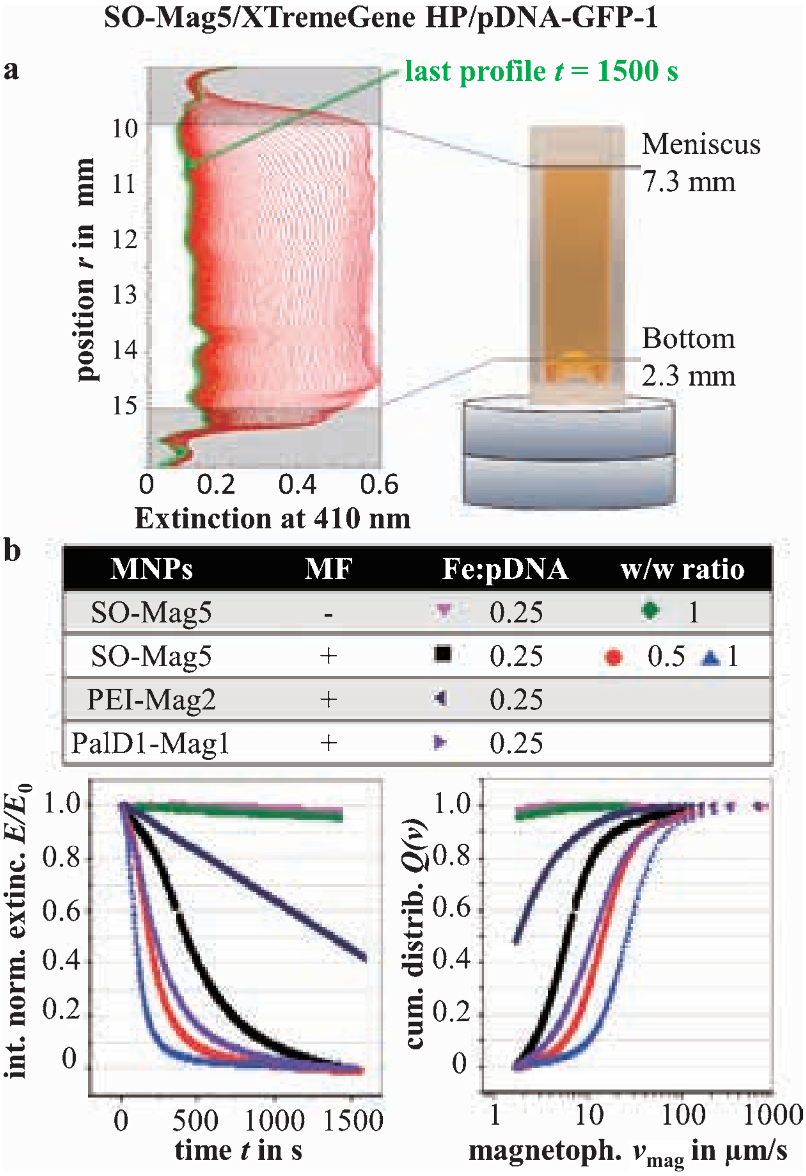

MNPs	MF	Fe:pDNA	w/w ratio
SO-Mag5	-	▼ 0.25	◆ 1
SO-Mag5	+	■ 0.25	● 0.5 ▲ 1
PEI-Mag2	+	◀ 0.25	
PalD1-Mag1	+	▶ 0.25	

Fig. 30 Principle of the determination of magnetophoretic velocity of different MNPs (Tab. (**b**)) by STEP-Technology® (customized LUMiReader, LUM GmbH, Berlin) (**a**, left). The magnetic field is applied from the bottom (**a**, right) parallel to the gravity field. The cumulative distribution of magnetophoretic velocity v_{mag} (**b**, bottom right) is determined based on the kinetics of the integral extinction profiles (**b**, bottom left) calculated between 2.3 mm and 7.3 mm (ROI) as indicated not greyed out in (**a**, left) (adopted from (Czugala et al., 2016)).

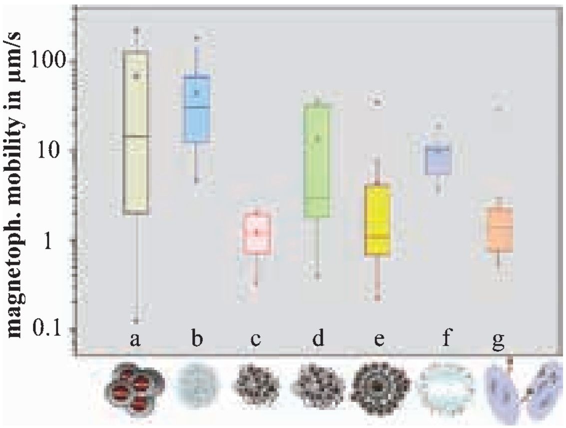

Fig. 31 Magnetophoretic velocities (orthogonal magnetic field with regard to earth gravity, **Fig. 29b**) of different MNPs and magnetic objects. (a) assemblies of MNPs; (b) micro particles; (c) siRNA-MNP; (d) pDNA-MNP; (e) virus-MNP; (f) micro bubbles; (g) labeled cells (Plank C. et al., 2011).

and determination of magnetic responsiveness can be applied to very different magnetic objects as depicted in **Fig. 31**. Magnetic fields cause magnetophoresis and change particle velocity compared to a gravity field. Mean magnetophoretic velocities amount to some tens of µm/s up to over 100 µm/s.

For the sake of completeness, besides magnetophoretic velocity distributions under gravity, analytical centrifugation can be employed to quantify the magnetization and magnetic forces between magnetic particles using magnetic fields directed orthogonally to the centrifugal field (**Fig. 29b**). The magnetic flux density (field strength) of different holders may vary up to 0.5 T in the middle of the sample cell and increases in the direction of the magnet surfaces. Holders are placed on the horizontal centrifuge rotor (**Fig. 2**). Due to the applied magnetic field, magnetic particles migrate in the direction of increasing magnetic strength and finally form a “bridge” between the magnets (**Fig. 29c**). If the “bridge” is exposed to an increasing centrifugal force, it slides down and starts to deform under the applied load like a two-end fixed rubber strap. Finally, at a critical centrifugal force, the magnetic interaction forces between particles are overcome and the “bridge” breaks (Lerche et al., 2008), (Eichholz et al., 2014).

5. Concluding remarks

In this review we discussed the in-situ visualization and quantification of particle movement in suspensions and emulsions using an advanced sedimentation measuring technique. STEP-Technology® can be applied for settling or creaming both at earth gravity or elevated centrifugal gravity, covering particle sizes from a few nm up to 100 µm. Although when talking about sedimentation measurement, first of all particle size comes to mind, it was demonstrated that the particle velocity distribution itself is a very powerful particle characteristic obtained based on a first-principle method. The influence of particle shape, particle concentration, rheological behavior of continuous phase on sedimentation or separation processes can be studied. Velocity can be analyzed in terms of particle size distribution in a straightforward manner and stands out with regard to sensitivity and accuracy. Advanced sedimentation measuring techniques can also be employed for additional particle characteristics such as the in-situ determination of density of dispersed particles in suspensions and emulsions or the magnetophoretic velocity (responsiveness) of MNPs and other magnetic objects.

Due to restricted space, we had to omit particle surface characterization which is gaining increasing attention in nanoparticle technology with respect to dispersion, polar-polar and hydrogen bond interaction (Hansen Dispersibility Parameters). This information is closely related to the dispersibility of particles in different liquids (Hansen et al., 2008), (Lerche et al., 2015), (Süß et al., 2018). Classification of stable and flocculated/agglomerated dispersed phases is another interesting application of the in-situ visualization of separation phenomena by analytical photocentrifugation (Lerche et al., 2007), (Paciejewska, 2011), (Bharti et al., 2011), (Lerche et al., 2014). The latter is applicable, in contrast to the Zeta potential, also for electrokinetically soft particles (Oshima, 2012) and does not need any dilution.

What could be the next steps in cuvette-based analytical photocentrifugation? It would be beneficial to increase the rotor speed to reduce the measurement time and to increase the pressure load for consolidation and filtration experiments (Loginov et al., 2017b). Higher flexibility with respect to the multi-wavelength approach would broaden application fields and allow 2-dimensional particle characterization. The determination of the volume-based particle size with no reference to particle shape and complex refractive index is also of great interest. From a theoretical point of view, a unified sedimentation theory based on the Kynch and Lamm approach is a very challenging goal.

Finally, I would like to underline that this review would not have been possible without the permanent communication, discussion and exchange of opinions with the academic and industrial communities, which has lasted now for about 25 years. Joint work in standardization organizations, especially WG 2 “Sedimentation, classification” of ISO TC24/SC4 has sharpened the understanding of the discussed matter.

Acknowledgements

Scientific work and instrument development was partly financed by grants from the European Union, Federal Ministry of Economics and Energy of Germany (Program ZIM) and Federal State of Berlin. The author gratefully acknowledges the contributions and support of all LUM team members, especially Dipl.-Ing. Torsten Detloff, Dean Dinair (PhD), Dr. Titus Sobisch, and Dr. Holger Woehlecke (company Dr. Lerche KG). The author acknowledges the support of Dr. O. Mykhaylyk regarding characterization and data of magnetic particles, and Dipl.-Ing. Torsten Detloff for providing unpublished results and great assistance in preparing the manuscript.

Nomenclature

AC-L	analytical photocentrifuge LUMiSizer®
Al_2O_3	aluminum oxide
AUC	analytical ultracentrifuge
CA	centrifugal acceleration
CPA	constant position approach
CTA	constant time approach
F	Froude number
G	separation number
GS-L	gravity sedimentometer LUMiReader®
D_2O	heavy water
DLS	dynamic light scattering
H_2O	water
ISO	International Organization for Standardization
MNP	magnetic nanoparticle
NIR	near infrared
O/W	oil/water
PA	polyamide
PC	polycarbonate
pDNA	plasmid-deoxyribonucleic acid
PMMA	poly(methyl methacrylate)
PTA	particle tracking analysis
RCA	relative centrifugal acceleration
Re	Reynolds number
RM	reference material
ROI	region of interest
SC	subcommittee
SEM	scanning electron microscope
SiO_2	silica, silicon dioxide
SLS	static light scattering
TC	technical committee
VIS	visible light
WG	working group
a	acceleration (m/s²)
A_V	volumetric scattering cross-section (1/m)
B	magnetic flux density (T)
C_D	drag coefficient
D	diffusion coefficient (m^2/s)
E	extinction
f	translational frictional coefficient
g	acceleration due to gravity (m/s²)
h	sedimentation distance (mm)
H	hindrance function
i	index
j	index
k	coverage factor of uncertainty equation
K	factor for material data in Stokes equation
L	optical path length (m)
m	mass (kg)
n	rotational speed (RPM)
N	end of index
$q_3(x)$	volume-weighted particle size distribution density
$Q_3(x)$	cumulative volume-weighted particle size distribution
$Q_{ext}(x)$	cumulative extinction-weighted particle size distribution
$Q(v)$	cumulative velocity distribution (%)
ΔQ	increment of cumulative distribution
r	position, distance from rotation center (mm)
r_m	meniscus position, filling height (mm)
r_o	outer position, position of cell bottom (mm)
r_p	position of the particle, distance of particle from rotation center (mm)
Re	Reynolds number
RI_l	fluid complex refractive index
RI_p	particle complex refractive index
p	particle position (mm)
s	sedimentation coefficient ($s = 10^{-13}$ s)
t	time (s)
Δt	time interval between transmission profiles (s)

T	transmission (%)
ΔT	change in transmission (%)
v	velocity (µm/s)
x	particle size (nm)
y	coefficient
η	viscosity (mPa s)
η_{rel}	relative dispersions viscosity
ϑ	temperature (°C)
λ	wavelength (nm)
κ	kinematic viscosity (m^2/s)
ρ_{l}	liquid density (kg m^{-3})
ρ_{p}	particle density (kg m^{-3})
ϕ	concentration (cm^3/cm^3, %)
$\Delta\phi$	change in concentration (cm^3/cm^3, %)
ω	angular speed (rad/s)

References

Allen T., Particle Size Measurement, Kluwer Academic Publishers, Dordrecht, The Netherlands, 1999.

Anestis G., Schneider W., Kinematic-wave analysis of particle settling in tube centrifuges, PAMM, Proceedings in Applied Mathematics and Mechanics, 14 (2014) 709–710.

Anker J.N., Mefford T., Biomedical Applications of Magnetic Particles, CRC Press, Boca Raton, 2017.

Arabi A.S., Sanders R.S., Particle terminal settling velocities in non-Newtonian viscoplastic fluids, The Canadian Journal of Chemical Engineering, 94 (2016) 1092–1101.

Arakawa M., Yokoyama T., Yamaguchi T., Minami T., Comparative data of particle size distribution on flake like particles by various methods, KONA Powder and Particle Journal, 3 (1985) 10–16.

Babick F., Suspensions of Colloidal Particles and Aggregates, Springer, Heidelberg New York Dordrecht London, 2016.

Babick F., Mielke J., Hodoroaba V.D., Weigel S., Wohlleben W., NanoDefine Technical Report D3.3: Critical review manuscript with real-world performance data for counting, ensemble and separating methods including in-build mathematical conversion to number distributions submitted for publiation, (2016a).

Babick F., Schmidt A., Stintz M., Detloff T., Lerche D., Obata K., Mori Y., Multi-wavelength photo-centrifugation for particle sizing without reference to models for the optical behavior, Intern Workshop Disp Anal & Mat Test 26th–27th September 2016, Berlin, Germany, (2016b).

Badolato G.G., Aguilar F., Schuchmann H.P., Sobisch T., Lerche D., Evaluation of long term stability of model emulsions by multisample analytical centrifugation, Progress in Colloid and Polymer Science, 134 (2008) 66–73.

Bergeson L.L., Hutton C.N., EC Begins Consultation on Revising Recommendation on Definition of Nanomaterial, 2017, Nano and Other Emerging Chemical Technologies Blog, <https://nanotech.lawbc.com/2017/09/ec-begins-consultation-on-revising-recommendation-on-definition-of-nanomaterial/> accessed 26.03.2018.

Berres S., Bürger R., On the settling of a bidisperse suspension with particles having different sizes and densities, Acta Mechanica, 201 (2008) 47–62.

Bharti B., Meissner G.H., Findenegg G.H., Aggregation of silica nanoparticles directed by adsorption of lysozyme, Langmuir, 27 (2011) 9823–9833.

Bickert G., Sedimentation feinster suspendierter Partikeln im Zentrifugalfeld, Institut für Mechanische Verfahrenstechnik und Mechanik (MVM), Fakultät für Chemieingenieurwesen (Fak. f. Chemieing.), Karlsruher Institut für Technologie, Karlsruhe, 1997.

Boldt S., Personal Communication, Beuth University of Applied Sciences, Applied Physics—Medical Engineering, Berlin, 2017.

Bonzel H.P., Bradshaw A.M., Ertl G., Physics and Chemistry of Alkali Metal Adsorption, Amsterdam New York : Elsevier, 1989.

Brouwers H.J.H., Viscosity of a concentrated suspension of rigid monosized particles, Physical Review E, 81 (2010) 1–11.

Bullard J.W., Pauli A.T., Garboczi E.J., Matys N.S., A comparison of viscosity–concentration relationships for emulsions, Journal of Colloid and Interface Science, 330 (2009) 186–193.

Buscall R., White L.R., The consolidation of concentrated suspensions. Part 1.—The theory of sedimentation, Journal of the Chemical Society, Faraday Transactions 1: Physical Chemistry in Condensed Phases, 1 (1987) 873–891.

Buske N., Gedan H., Lichtenfeld H., Katz W., Sonntag H., A method for measuring particle and aggregate size distribution in colloidal dispersions, Colloid and Polymer Science, (1980) 1303–1394.

Bustos M.C., Concha F., Bürger R., Tory E.M., Sedimentation and Thickening: Phenomenological Foundation and Mathematical Theory, Kluwer Academic Publishers, Dordrecht, 1999.

Cai Z., Wu J., Du B., Zhang H., Impact of distribution of carboxymethyl substituents in the stabilizer of carboxymethyl cellulose on the stability of acidified milk drinks, Food Hydrocolloids, 76 (2018) 150–157.

Callahan J., A non-toxic heavy liquid and inexpensive filters for separation of mineral grains, Journal of Sedimentary Research, 57 (1987) 765–766.

Cao D.Q., Iritani E., Katagiri N., Flotation and sedimentation properties in centrifugal separation of emulsion–slurry, Journal of Chemical Engineering of Japan, 47 (2014) 392–398.

Chenouard N., Smal I., de Chaumont F., Maska M., Sbalzarini I.F., Gong Y., Cardinale J., Carthel C., Coraluppi S., Winter M., Cohen A.R., Godinez W.J., Rohr K., Kalaidzidis Y., Liang L. et al., Objective comparison of particle tracking methods, Nature Methods, 11 (2014) 281–289.

Concha F., Bürger R., A century of research in sedimentation and thickening, KONA Powder and Particle Journal, 20 (2002) 38–70.

Coulter W.H., Means for counting particles suspended in a fluid, USA Patent, (1953) US2656508A.

Czugala M., Mykhaylyk O., Böhler P., Onderka J., Stork B., Wesselborg S., Kruse F.E., Plank C., Singer B.B., Fuchsluger T.A., Efficient and safe gene delivery to human corneal endothelium using magnetic nanoparticles, Nanomedicine (Lond), 11 (2016) 1787–1800.

DeLoid G., Cohen J.M., Darrah T., Derk R., Rojanasakul L., Pyrgiotakis G., Wohlleben W., Demokritou P., Estimating the effective density of engineered nanomaterials for in vitro dosimetry, Nature Communications, 5 (2014) 3514.

Deshpande A.P., Krishnan J.M., Kumar S., Rheology of Complex Fluids, Springer, New York, 2010.

Detloff T., Personal Communication, LUM GmbH, Berlin, Germany, 2004.

Detloff T., Küchler S., Sobisch T., Lerche D., Is it possible to reduce cost for pilot centrifuge testing by lab scale tests?, 11th World Filtration Congress, 16th–20th April 2012, Graz, Austria, Filtech Exhibitions Germany GmbH & Co. KG, 2012.

Detloff T., Lerche D., Centrifugal separation in tube and disc geometries: Experiments and theoretical models, Acta Mechanica, 201 (2008) 83–94.

Detloff T., Lerche D., Sobisch T., Particle size distribution by space or time dependent extinction profiles obtained by analytical centrifugation, Particle & Particle Systems Characterization, 23 (2006) 184–187.

Detloff T., Sobisch T., Lerche D., Particle size distribution by space or time dependent extinction profiles obtained by analytical centrifugation (concentrated systems), Powder Technology, 174 (2007) 50–55.

Detloff T., Sobisch T., Lerche D., Characterisation of separating dispersions by multi wavelength extinction profiles, Dispersion Letters, 2 (2011) 32–35.

Detloff T., Sobisch T., Lerche D., Instability index, Dispersion Letters Technical, T4 (2014) 1–4.

Dintenfass L., Internal Viscosity (Rigidity) of the Red Cell and Blood Viscosity Equation; Counteraction of Errors Due to Flow Instability of Plasma, Biofluid Mechanics, Plenum Publishing Corp., Boston, MA, 1980, pp. 401–416.

Dukhin A.S., Goetz P.J., Characterization of Liquids, Nano- and Microparticulates, and Porous Bodies Using Ultrasound, Elsevier, Amsterdam, 2010.

Eichholz C., Knoll J., Lerche D., Nirschl H., Investigations on the magnetization behavior of magnetic composite particles, Journal of Magnetism and Magnetic Materials, 368 (2014) 139–148.

Erne B., Sedimentation equilibria of colloidal dispersions in ultrathin glass capillaries, Dispersion Letters, 3 (2012) 16–17.

European Union, Commission recommendation of 18 October 2011 on the definition of nanomaterial, Official Journal of the European Union, 54 (2011) 38–40.

Filipe V., Hawe A., Jiskoot W., Critical evaluation of nanoparticle tracking analysis (NTA) by NanoSight for the measurement of nanoparticles and protein aggregates, Pharmaceutical Research, 27 (2010) 796–810.

Fitch B., Kynch theory and compression zones, AIChE Journal, 29 (1983) 940–947.

Frömer D., Lerche D., An experimental approach to the study of the sedimentation of dispersed particles in a centrifugal field, Archive of Applied Mechanics, 72 (2002) 85–95.

Fujita H., Mathematical Theory of Sedimentation Analysis, Academic Press Inc., New York, London, 1962.

Guyon E., Hulin J.P., Petit L., Mitescu C.D., Physical Hydrodynamics, Oxford University Press, Oxford, 2001.

Hansen C.M., Abbott S., Yamamoto H., Hansen Solubility Parameters: A User´s Handbook, fourth ed., www.Hansen-Solubility.com, 2008.

Happel J., Brenner H., Low Reynolds Number Hydrodynamics, Martinus Nijhoff Publishers, The Hague / Boston / Lancaster, 1983.

He P., Mejia A.F., Cheng Z., Sun D., Sue H.-J., Dinair D.S., Marquez M., Hindrance function for sedimentation and creaming of colloidal disks, Physical Review E, 81 (2010) 026310.

Hinderliter P.M., Minard K.R., Orr G., Chrisler W.B., Thrall B.D., Pounds J.G., Teeguarden J.G., ISDD: A computational model of particle sedimentation, diffusion and target cell dosimetry for in vitro toxicity studies, Particle and Fibre Toxicology, 7 (2010) 36.

Hogg R., A spheroid model for the role of shape in particle analysis, KONA Powder and Particle Journal, 32 (2015) 227–235.

Holschuh K., Bauer J., Industrial production, surface modification, and application of magnetic particles, in: Keller K. (Ed.) Upscaling of Bio-Nano-Processes, Springer, Berlin Heidelberg, 2014, pp. 117–128.

Hölzer A., Bestimmung des Widerstandes, Auftriebs und Drehmoments und Simulation der Bewegung nichtsphärischer Partikel in Laminaren und Turbulenten Strömungen Mit Dem Lattice-Boltzmann-Verfahren, Dissertation, 2007.

Horn F.M., Richtering W., Viscosity of bimodal charge-stabilized polymer dispersions, Journal of Rheology, 44 (2000) 1279–1292.

Horváth-Szabó G., Høiland H., Compressibility determination of silica particles by ultrasound velocity and density measurements on their suspensions, Journal of Colloid and Interface Science, 177 (1996) 568–578.

ISO 9276-2:2014, Representation of results of particle size analysis—Part 2: Calculation of average particle sizes/diameters and moments from particle size distributions, (2014).

ISO 13317-1:2001, Determination of particle size distribution by gravitational liquid sedimentation methods—Part 1: General principles and guidelines, (2001).

ISO 13317-3:2001, Determination of particle size distribution by gravitational liquid sedimentation methods—Part 3: X-ray gravitational technique, (2001).

ISO 13317-4:2014, Determination of particle size distribution by gravitational liquid sedimentation methods—Part 4: Balance method, (2014).

ISO 13318-1:2001, Determination of particle size distribution by centrifugal liquid sedimentation methods—Part 1: General principles and guidelines, (2001).

ISO 13318-2:2007, Determination of particle size distribution by centrifugal liquid sedimentation methods—Part 2: Photocentrifuge method, (2007).

ISO 13318-3:2004, Determination of particle size distribution by centrifugal liquid sedimentation methods—Part 3: Centrifugal X-ray method, (2004).

ISO 13320:2009, Particle size analysis—Laser diffraction methods, (2009).

ISO 14887:2000, Sample preparation—Dispersing procedures for powders in liquids, (2000).

ISO 19430:2016, Particle size analysis—Particle tracking analysis (PTA) method, (2016).

ISO 20998-1:2006, Measurement and characterization of particles by acoustic methods—Part 1: Concepts and procedures in ultrasonic attenuation spectroscopy, (2006).

ISO 22412:2017, Particle size analysis—Dynamic light scattering (DLS), (2017).

ISO, International Organization for Standardization, (2017).

ISO/DIS 18747-2, Determination of the particle density by sedimentation methods—Part 2: Multivelocity approach, (2018).

ISO 18747-1, Determination of particle density by sedimentation methods—Part 1: Isopycnic interpolation approach, (2018).

ISO/TR 13097:2013, Guidelines for the characterization of dispersion stability, (2013).

Jacob K.H., Prüfung der Entmischungsstabilität von Cremes, in: Miller R., Schäffler M. (Eds.), Dispersionseigenschaften: 2D-Rheologie, 3D-Rheologie, Stabilität, Self-Published, LUM GmbH, Berlin, Potsdam, 2015, pp. 191–202.

Jillavenkatesa A., Dapkunas S.J., Lum L.S.H., NIST Recommended Practice Guide: Particle Size Characterization, NIST, Washington, 2001.

Kamiti M., Boldridge D., Ndoping L.M., Remsen E.E., Simultaneous absolute determination of particle size and effective density of submicron colloids by disc centrifuge photosedimentometry, Analytical Chemistry, 84 (2012) 10526–10530.

Kato H., Suzuki M., Fujita, Horie M., Endoh S., Yoshida Y., Iwahashi H., Takahashi, Nakamura A., Kinugasa S., Reliable size determination of nanoparticles using dynamic light scattering method for in vitro toxicology assessment, Toxicology in Vitro, 23 (2009) 927–934.

Kaur S., Leal L.G., Drop deformation and break-up in concentrated suspensions, Journal of Rheology, 54 (2010) 981–1008.

Kaye B.H., UK Patent, (1962) 895 222, 320.

Kelly R., Etzler F.M., What is wrong with laser diffraction?, 2013, Donner Technologies <www.donner-tech.com/whats_wrong_with_ld.pdf> accessed 20.06.2018.

Kirkland J.J., Dilks Jr C.H., Yau Y.W.W., Sedimentation field flow fractionation at high force fields, Journal of Chromatography A, 255 (1983) 255–271.

Kirsch S., Doerk A., Bartsch E., Sillescu H., Landfester K., Spiess H.W., Maechtle W., Synthesis and characterization of highly cross-linked, monodisperse core−shell and inverted core−shell colloidal particles. polystyrene/poly(tert-butyl acrylate) core−shell and inverse core−shell particles, Macromolecules, 32 (1999) 4508–4518.

Krieger I.M., Dougherty T.J., A Mechanism for non-newtonian flow in suspensions of rigid spheres, Journal of Rheology, 3 (1959) 137–152.

Kuchenbecker P., Gemeinert M., Rabe T., Inter-laboratory study of particle size distribution measurements by laser diffraction, Particle & Particle Systems Characterization, 29 (2012) 304–310.

Kuentz M., Röthlisberger D., Sedimentation analysis of aqueous microsuspensions based on near infrared transmission measurements during centrifugation. Determination of a suitable amount of gelling agent to minimise settling in the gravitational field, STP Pharma Sciences, 12 (2002) 391–396.

Kuentz M., Röthlisberger D., Rapid assessment of sedimentation stability in dispersions using near infrared transmission measurements during centrifugation and oscillatory rheology, European Journal of Pharmaceutics and Biopharmaceutics, 56 (2003) 355–361.

Kynch G.J., A theory of sedimentation, Transactions of the Faraday Society, 48 (1952) 166–176.

Ladenburg R., Über den Einfluß von Wänden auf die Bewegung einer Kugel in einer reibenden Flüssigkeit, Annalen der Physik, 328 (1907) 447–458.

Lamberty A., Franks K., Braun A., Kestens V., Roebben G., Linsinger T., Interlaboratory comparison for the measurement of particle size and zeta potential of silica nanoparticles in an aqueous suspension, Journal of Nanoparticle Research, 13 (2011) 7317–7329.

Lamm O., Die Differentialgleichung der Ultrazentrifugierung, Arkiv för matematik, astronomi och fysik, 21B (1929) 1–4.

Lau R., Hassan M.S., Wong W., Chen T., Revisit of the wall effect on the settling of cylindrical particles in the inertial regime, Industrial & Engineering Chemistry Research, 49 (2010) 8870–8876.

Leith D., Drag on nonspherical objects, Aerospace Science and Technology, 6 (1987) 153–161.

Lerche D., Determination of hydrodynamic density of micro- and nano particles dispersed in liquids by migration velocities, Particulate Systems Analysis, Edinburgh UK, 2011.

Lerche D., Bilsing R., Separation of red blood cells at high volume concentration under low centrifugal acceleration, Biorheology, 25 (1988) 245–252.

Lerche D., Frömer D., Theoretical and experimental analysis of the sedimentation kinetics of concentrated red blood cell suspensions in centrifugal field: Determination of aggregation and deformation of RBC by flux density and viscosity function, Biorheology, 38 (2001) 249–262.

Lerche D., Hennicke G., The effect of different ionic and non-ionic X-ray contrast media on the morphological and rheological properties of human red blood cells, Clinical Hemorheology, 12 (1992) 341–355.

Lerche D., Horvat S., Sobisch T., Efficient instrument based determination of the Hansen Solubility Parameters for talc-based pigment particles by multisample analytical centrifugation: Zero to One Scoring, Dispersion Letters, 6 (2015) 13–18.

Lerche D., Mertens U., Sedimentationsverhalten von Teilchen unter Einwirkung überlagerter Magnetfelder, Jahrestreffen des Fachausschusses Mechanische Flüssigkeitsabtrennung, Würzburg, 2008.

Lerche D., Piesendel L., Senge B., Characterization of food quality and structural stability by analytical centrifugation, Proceedings of the 3rd International Symposium on Food Rheology and Structur, Zürich, Switzerland, ETH Zürich, 2003.

Lerche D., Sobisch T., Direct and accelerated characterization of formulation stability, Journal of Dispersion Science and Technology, 32 (2011) 1711–1811.

Lerche D., Sobisch T., Evaluation of particle interactions by in situ visualization of separation behaviour, Colloids and Surfaces A: Physicochemical and Engineering Aspects, 440 (2014) 122–130.

Lerche D., Sobisch T., Küchler S., Shelf life prediction of liquid food products based on multisample analytical centrifugation, Proc of 4th Int Symp on Food Rheology and Structure, Zürich, Switzerland, (2006).

Lerche T., Sobisch S., Consolidation of concentrated dispersions of nano- and microparticles determined by analytical centrifugation, Powder Technology, 174 (2007) 46–49.

Leschonski K., Grundlagen und moderne Verfahren der Partikelmesstechnik, Technische Universität Clausthal, Clausthal-Zellerfeld, 1988.

Leschonski K., Alex W., Koglin B., Teilchengrößenanalyse. 1. Darstellung und Auswertung von Teilchengrößenverteilungen, Chemie Ingenieur Technik, 46 (1974) 23–26.

Leung W., Separation of dispersed suspension in rotating tube, Separation and Purification Technology, 38 (2004) 99–119.

Leung W.W.F., Centrifugal Separations in Biotechnology, Oxford: Elsevier/Academic Press, 2007.

Lichtenfeld H., Stechemesser H.J., Möhwald H., Single particle light-scattering photometry—some fields of application, Journal of Colloid and Interface Science, 276 (2004) 97–105.

Linsinger T.P.J., Roebben G., Gilliland D., Calzolai L., Rossi F., Gibson N.K.C., Requirements on measurements for the implementation of the European Commission definition of the term “nanomaterial”, Geel, Belgium: Joint Research Centre of the European Commission, 2012.

Loginov M., Samper F., Gésan-Guiziou G., Sobisch T., Lerche D., Vorobiev E., Centrifugal ultrafiltration for determination of filter cake properties of colloids, Journal of Membrane Science, 536 (2017a) 59–75.

Loginov M., Zierau A., Kavianpour D., Lerche D., Vorobiev E., Gésan-Guiziou G., Mahnic-Kalamiza S., Sobisch T., Multistep centrifugal consolidation method for characterization of filterability of aggregated concentrated suspensions, Separation and Purification Technology, 183 (2017b) 304–317.

Lorentz H.A., Ein allgemeiner Satz, die Bewegung einer reibenden Flüssigkeit betreffend, nebst einigen Anwendungen derselben, Annalen der theoretischen Physik, 1 (1907) 28–42.

Luerkens D.W., Theory and Application of Morphological Analysis: Fine Particles and Surfaces, CRC Press, Boca Raton Ann Arbor Boston London, 1991.

Luigjes B., Thies-Weesie D.M.E., Erné B.H., Philipse A.P., Sedimentation equilibria of ferrofluids: I. Analytical centrifugation in ultrathin glass capillaries, Journal of Physics: Condensed Matter, 24 (2012) 245103 (8pp).

Mächtle W., Charakterisierung von disperisionen durch gekopplete H_2O/D_2O-ultrazentrifugenmessungen, Die Makromolekulare Chemie, 185 (1984) 1025–1039.

Mächtle W., Börger L., Analytical Ultracentrifugation of Polymers and Nanoparticles, Springer-Verlag GmbH, Berlin Heidelberg, 2006.

Macosko C.W., Rheology: Principles, Measurements, and Applications, VCH Publishers, Inc., New York, Weinheim, Cambridge, 1994.

Masuda H., Higashitani K., Yoshida Y., Powder Technology: Fundamentals of Particles, Powder Beds, and Particle Generation, CRC Press, Boca Raton London New York, 2006.

Maude A.D., Whitmore R.L., A generalized theory of sedimentation, British Journal of Applied Physics, 9 (1958) 477–482.

McClements D.J., Food Emulsions: Principles, Practices, and Techniques, second ed., CRC Press, Boca Raton, 2004.

McCormick H.W., Determination of latex particle size distribution by analytical ultracentrifugation, Journal of Colloid Science, 19 (1964) 173–184.

Mehn D., Iavicoli P., Cabaleiro N., E B.S., Caputo F., Geiss O., Calzolai L., Rossi F., Gilliland D., Analytical ultracentrifugation for analysis of doxorubicin loaded liposomes, International Journal of Pharmaceutics, 523 (2017) 320–326.

Merkus H.G., Particle Size Measurements: Fundamentals, Practice, Quality, Springer, Heidelberg New York Dordrecht London, 2009.

Merkus H.G., Meesters G.M.H., (Eds.) Particulate Products: Tailoring Properties for Optimal Performance, Springer, Cham, 2014.

Michaelis A.S., Bolger J.C., Settling rates and sediment volumes of flocculated kaolin suspensions, Industrial & Engineering Chemistry Fundamentals, 1 (1962) 24–33.

Mie G., Beiträge zur Optik trüber Medien, speziell kolloidaler Goldlösungen, Annals of Physics, 25 (1908) 377–452.

Mykhaylyk O., Lerche D., Vlaskou D., Schoemig V., Detloff T., Krause D., Wolff M., Joas T., Plank C., Magnetophoretic velocity determined by space- and time-resolved extinction profiles, IEEE Magnetics Letters, 6 (2015) 1–4.

Mykhaylyk O., Zelphat O., Hammerschmid E., Anton M., Rosenecker J., Plank C., Recent advances in magnetofection and its potential to deliver siRNAs in vitro, Methods in Molecular Biology, 487 (2008) 1–36.

Nadler M., Mahrholz T., Riedel U., Schilde C., Kwade A., Preparation of colloidal carbon nanotube dispersions and their characterisation using a disc centrifuge, Carbon, 46 (2008) 1384–1392.

NanoDefine, NanoDefine Publications, (2018) NanoDefine, 2018, NanoDefine Publications <www.nanodefine.eu/index.php/nanodefine-publications> accessed 26.03.2018.

Neumann A., Hoyera W., Wolff M.W., Reichl U., Pfitzner A., Rotha B., New methods for density determination of particles using CPS disc centrifuge, Colloids and Surfaces B: Biointerfaces, 104 (2013) 27–31.

Oshima H., Electrical phenomena in a suspension of soft particles, Soft matter, 8 (2012) 3511–3514.

Paciejewska K.M., 2011, Untersuchung des Stabilitätsverhalten von binären kolloidalen Suspensionen <http://nbn-resolving.de/urn:nbn:de:bsz:14-qucosa-65050> accessed 26.03.2018.

Pal R., Shear viscosity behavior of emulsions of two immiscible liquids, Journal of Colloid and Interface Science, 225 (2000) 359–366.

Pethig R., Dielectrophoresis: Theory, Methodology and Biological Applications, Wiley, Hoboken, West Sussex, 2017.

Pettyjohn E.S., Christiansen E.B., Effect of particle shape on free-settling rates of isometric particles, Chemical engineering progress, 44 (1948) 157–172.

Plank C., Zelphati O., Mykhaylyk O., Magnetically enhanced nucleic acid delivery. Ten years of magnetofection—Progress and prospects, Advanced Drug Delivery Reviews, 63 (2011) 1300–1331.

Planken K.L., Cölfen H., Analytical ultracentrifugation of colloids, Nanoscale, 2 (2010) 1849–1869.

Probstein R.F., Physicochemical Hydrodynamics. An Introduction, John While & Sons Inc., Hoboken, 2003.

Quemada D., Rheology of concentrated disperse systems and minimum energy dissipation principle. I. Viscosity-concentration relationship, Rheologica Acta, 16 (1977) 82–94.

Quemada D., Rheology of concentrated disperse systems II. A model for non-newtonian shear viscosity in steady flows, Rheologica Acta, 17 (1978a) 632–642.

Quemada D., Rheology of concentrated disperse systems III. General features of the proposed non-newtonian model. Comparison with experimental data, Rheologica Acta, 17 (1978b) 643–653.

Richardson J.F., Zaki W.N., Sedimentation and fluidisation. Part 1, Transactions Institution of Chemical Engineers, 32 (1954) 35–53.

Rodriguez L., Personal Communication, Dr. Lerche KG, Berlin, Germany, 2017.

Salinas-Salas G., Ruiz-Tagle-Gutiérrez I., Babick F., Análisis de la función de corrección de la velocidad de sedimentación para micro partículas / Analysis of the correction function for micro-particle sedimentation velocity, Ingeniare Revista Chilena de Ingeniería, 15 (2007) 283–290.

Schaflinger U., Centrifugal separation of a mixture, Fluid Dynamics Research, 6 (1990) 213–249.

Schärtl W., Light Scattering from Polymer Solutions and Nanoparticle Dispersions, Springer Verlag, Berlin Heidelberg, 2007.

Schuck P., Perugini M.A., Gonzales N.R., Howlett G.J., Schubert D., Size-distribution analysis of proteins by analytical ultracentrifugation: strategies and application to model systems, Biophysical Journal, 82 (2002) 1096–1111.

Schuldt U., Woehlecke H., Lerche D., Characterization of mechanical parameters of microbeads by means of analytical centrifugation, Food Hydrocolloids, (2018) in press. Doi:10.1016/j.foodhyd.2018.07.005

Schulz D.N., Glass J.E., Polymers as Rheology Modifiers, ACS Symposium Series, American Chemical Society, Washington, 1991.

Schuster B.S., Ensign L.M., Allan D.B., Suk J.S., Hanes J., Particle tracking in drug and gene delivery research: State-of-the-art applications and methods, Advanced Drug Delivery Reviews, 91 (2015) 70–91.

Shuler M.L., Aris R., Tsuchiya H.M., Hydrodynamic focusing and electronic cell-sizing techniques, Applied microbiology, 24 (1972) 384–388.

Sobisch T., Detloff T., Lerche D., Speeding up the evaluation of the physical stability of beverage dispersions, ISFRS 2009, Proceedings of the 5th International Symposium on Food Rheology and Structure, ed. P. Fischer, M. Pollard, E.J. Windhab, 2009, pp. 574–575.

Sobisch T., Küchler S., Uhl A., Comprehensive characterization of medical nutrition—accelerated stability analysis and creaming velocity distribution, Dispersion Letters, 1 (2010) 10–13.

Sobisch T., Lerche D., Separation behaviour of particles in biopolymer solutions in dependence on centrifugal acceleration: Investigation of slow structuring processes in formulations, Colloid Surface A: Physicochemical and Engineering Aspects, 536 (2018) 74–81.

Sobisch T., Lerche D., Detloff T., Beiser M., Erk A., Tracing the centrifugal separation of fine-particle slurries. Effect of centrifugal acceleration, particle interaction and concentration, Filtration, 6 (2006) 313–321.

Sommer K., Sampling of Powders and Bulk Materials, Springer-Verlag, Berlin Heidelberg, 1986.

Staudinger U., Krause B., Steinbach C., Pötschke P., Voigt B., Dispersability of multiwalled carbon nanotubes in polycarbonate-chloroform solutions, Polymer, 55 (2014) 6335–6344.

Steinour H.H., Rate of sedimentation. Nonflocculated suspensions of uniform spheres, Industrial & Engineering Chemistry, 36 (1944) 618–624.

Stokes G.G., On the effect of the internal friction of fluids on the motion of pendulums, Transactions of the Cambridge Philosophical Society, 9 (1851) 1–83.

Süß S., Sobisch T., Peukert W., Lerche D., Segets D., Determination of Hansen parameters for particles: A standardized routine based on analytical centrifugation, Advanced Powder Technology, 7 (2018) 1550–1561.

Svedberg T., Rinde H., The ultra-centrifuge, a new instrument for the determination of size and distribution of size of particle in amicroscopic colloids, Journal of the American Chemical Society, 46 (1924) 2677–2693.

Takeda S., Evaluation of stability of slurries by centrifugal sedimentation methods (in Japanese), Journal of the Society of Powder Technology, Japan, 49 (2012) 489–494.

Taylor G.I., The viscosity of a fluid containing small drops of another fluid, Proceedings of the Royal Society of London. Series A, 138 (1932) 41–48.

Uchiyama S., Arisaka F., Stafford W.F., Laue T., Analytical Ultracentrifugation: Instrumentation, Software, and Applications, Springer Japan, Tokyo, 2016.

Uhl A., Partikelgrößenverteilung von Kontrollpartikeln—Teil 1 SediTest Mikropartikel 1000 nm, Dispersion Letters Technical, T7 (2015) 1–5.

Ungarish, Hydrodynamics of Suspensions, Springer, Berlin, 1993.

Usher S.P., Studer L.J., Wall R.C., Scales P.J., Characterisation of dewaterability from equilibrium and transient centrifugation test data, Chemical Engineering Science, 93 (2013)

277–291.

USP-729, Injections and implanted drug products (parenterals)—Product quality tests, United States Pharmacopeial Convention, (2016).

USP-788, Particulate matters in injections, United States Pharmacopeial Convention, (2012).

van de Hulst H.C., Light Scattering by Small Particles, Dover Publications Inc., New York, 1981.

Walter J., Sherwood P.J., Lin W., Segets D., Stafford W.F., Peukert W., Simultaneous analysis of hydrodynamic and optical properties using analytical ultracentrifugation equipped with multiwavelength detection, Analytical Chemistry, 87 (2015a) 3396-3403.

Walter J., Thajudeen T., Süß S., Segets D., Peukert W., New possibilities of accurate particle characterisation by applying direct boundary models to analytical centrifugation, Nanoscale, 7 (2015b) 6574–6587.

Ward-Smith S., Rawle A., Validating laser diffraction particle sizing methods to maintain integrity, Scientist live, (2013).

Weichert R., Determination of extinction efficiency and particle size distribution by photosedimentation using light of different wavelengths, Poceed 4th Particle Size Analysis Conf Sept 21st–24th, 1981, Loughborough, Wiley, (1981).

Werner E., Zuckertechnik-Taschenbuch, Vol. 7. vollst. Neubearb. Aufl., Bartens, Berlin-Nikolassee, 1966.

Whitby K.T., A rapid general purpose centrifuge sedimentation method for measurement of size distribution of small particles, part I.—apparatus and method, Journal of the Air Pollution Control Association, 5 (1955) 120–132.

White D.J., The measurement of particle size distribution using the Single Particle Optical Sizing (SPOS) method, (2002).

Wiese B., Accelerated Sedimentation for the Prediction of Long-term Storage Stability, 3 Anwenderseminar 2D- und 3D-Rheologie, Potsdam, (2010).

Wilhelm C., Gazeau F., Bacri J.C., Magnetophoresis and ferromagnetic resonance of magnetically labeled cells, European Biophysics Journal, 32 (2002) 118–125.

Woehlecke H., Detloff T., Lerche D., Determination of hydrodynamic density of micro- and nano particles dispersed in liquids, Dispersion Letters, 3 (2012) 12–15.

Zhou W., Su M., Cai X., Advances in nanoparticle sizing in suspensions: dynamic light scattering and ultrasonic attenuation spectroscopy, KONA Powder and Particle Journal, 34 (2017) 168–182.

Author’s Short Biography

Dietmar Lerche

Professor Dr. D. Lerche studied biophysics at Lomonossow University in Moscow and received his PhD and Dr. of Sci. in biophysics from the Math and Natural Science Faculty at Humboldt University Berlin. From 1989 to 1994, he served as the director of the Institute of Medical Physics and Biophysics at the Medical School Charité at HUB and received a full professorship (medical physics and biophysics). He worked in fields such as dispersion analysis, colloid chemistry, blood rheology and fluid dynamics (> 250 papers). In 1994, he founded the independent LUM GmbH with the goal of providing innovative and unique instrumentation to advance the fields of suspension and emulsion sciences. He also chairs and directs subsidiary companies in the USA, China and Japan as well as the biotech company Dr. Lerche KG, and is an active member of the ISO-TC 24 / SC4—Committee “Particle Characterization” (convener of its WG2 (sedimentation methods) and WG16 (stability)). His achievements were rewarded with different prizes, among them the Innovation Prize 2012 of the states Berlin-Brandenburg (Germany).

KONA Powder and Particle Journal No. 36 (2019) 187–200/Doi:10.14356/kona.2019013 Review Paper

Direct Measurement of Interaction Forces between Surfaces in Liquids Using Atomic Force Microscopy[†]

Naoyuki Ishida[1*] **and Vincent S. J. Craig**[2]

[1] *Graduate School of Natural Science and Technology, Okayama University, Japan*
[2] *Department of Applied Mathematics, RSPE, Australian National University, Australia*

Abstract

The stability of particle suspensions, which is important in numerous industrial processes, is generally dominated by the interaction forces between the suspended particles. Understanding the interaction forces between surfaces in liquids is therefore fundamentally important in order to evaluate and control how particulates, including fluid droplets in emulsions and air bubbles in foams, behave in various systems. The invention of the surface force apparatus (SFA) enabled the direct measurement of interaction forces in liquids with molecular level resolution and it has led to remarkable progress in understanding surface forces in detail. Following the SFA, the application of atomic force microscopy (AFM) to force measurement has further extended the possibility of force measurements to a broad field of research, mainly due to the range of materials that can be employed. This review provides an overview of developments in the investigation of interaction forces between surfaces using AFM. The properties of various interaction forces, important in particle technology, revealed by the studies using AFM are described in detail.

Keywords: atomic force microscopy, interaction force, direct measurement, liquid phase, suspension stability

1. Introduction

As suspensions of particles play a role in numerous industrial processes, evaluating and controlling particle behavior in various processes is of utmost importance. Rapid developments in nanotechnology over recent years have led to the adaptation of these industrial processes to handle nanosized materials, including nanoparticles, in order to take advantage of their specific functions. Because such nanomaterials are often handled in liquids as colloidal dispersions, it has become significantly important to control the properties of nanoparticle suspensions properly and precisely, including their stability, sedimentation and rheology.

The stability of particle suspensions is generally dominated by the interaction forces between the surfaces of two opposing particles in suspension, which depend intricately on the properties of the liquid, the surfaces, solutes, and so on. Understanding of the interaction forces in liquids is therefore fundamental in many fields of science and engineering in order to evaluate and control how particulate matters (including two phase fluids such as emulsions and foams) behave in various systems.

The theoretical basis for analyzing surface forces between charged particles in aqueous solutions was provided by Derjaguin-Landau-Verwey-Overbeek (DLVO) theory in the 1940s (Derjaguin and Landau, 1941; Verwey and Overbeek, 1948), and is still used widely today. However, the detailed experimental analysis of surface forces had been impossible until the invention of the surface force apparatus (SFA) in the late 1960s. The SFA enabled the direct measurement of interaction forces both in air (Tabor and Winterton, 1968) and in liquid (Israelachvili and Tabor, 1972) with molecular level resolution, which led to remarkable progress in understanding surface forces in detail.

Following the SFA, the application of atomic force microscopy (AFM) to force measurement further extended the possibility of force measurements to new fields of research. AFM was invented as a new form of scanning probe microscope in 1986 (Binnig et al., 1986). Since its invention, the AFM has become a powerful tool in a wide range of research areas in science and engineering, including powder technology, as a technique to explore surface structures and properties. In addition to surface imaging, the introduction of the colloid probe technique (Butt, 1991; Ducker et al., 1991) enabled force measurements performed using the AFM to be compared to those

---

[†] Received 1 May 2018; Accepted 10 May 2018

[1] 3-1-1 Tsushima-naka, Kita-ku, Okayama 700-8530, Japan
[2] Canberra, ACT 2601, Australia
[*] Corresponding author: Naoyuki Ishida;
E-mail: n-ishida@okayama-u.ac.jp
TEL: +81-86-251-8201 FAX: +81-86-251-8201

performed with the SFA. In the colloid probe technique, a spherical particle is attached to the end of a probe tip and the force is measured between this particle and a flat surface, allowing quantitative evaluation of forces between macroscopic surfaces. This technique can utilize a much wider variety of materials than SFA and has therefore found applications in a wider variety of systems.

In this article, we review the development of investigating the interaction forces between surfaces, mainly focusing on studies using AFM. An overview of the various interaction forces important in particle technology is provided, as well as the principles of AFM and force measurements.

2. Principle of AFM and force measurement

The basic composition of an AFM instrument is illustrated in **Fig. 1**. The probe has a very sharp tip (the typical radius of commercial tips is 2–20 nm) attached to the end of a microfabricated cantilever, usually made either of Si or Si_3N_4. Scanning of the probe over the sample surface is carried out with the piezoelectric scanner, which expands or shrinks in response to applied voltages. A laser beam reflected from the back of the cantilever is detected with a four-segment photodiode detector. From the location of the incident beam at the detector, vertical deflections and lateral distortions of the cantilever can be evaluated. The controller evaluates the signals from the photodetector to adjust the z-displacement of the piezo scanner, i.e. moves the sample or the probe upward and downward, to keep the feedback control parameter constant. The mapping of the resulting z-piezo movements in the x and y dimensions provides the various images of the sample surface. By using a fluid cell, operation in liquid phase is possible.

In order to apply the AFM to force measurements, the probe or the sample substrate is moved vertically (z-direction) to alter the distance between the probe and the surface. For the colloid probe (**Fig. 2**), a spherical particle typically in the diameter range of 2–40 μm is attached to the probe with epoxy glue or hot-melt epoxy resin, using a micropositioning device such as a micromanipulator whilst observing with an optical microscope or a CCD camera. During scanning, the probe-substrate interaction force is determined from the vertical deflection of the probe cantilever. **Fig. 3(a)** shows a schematic representation of typical deflection versus piezo translation data one can obtain by a force measurement between surfaces in an aqueous solution. In most commercial AFMs, approaching the probe to the flat substrate, bringing the surfaces into contact and retracting the probe from the

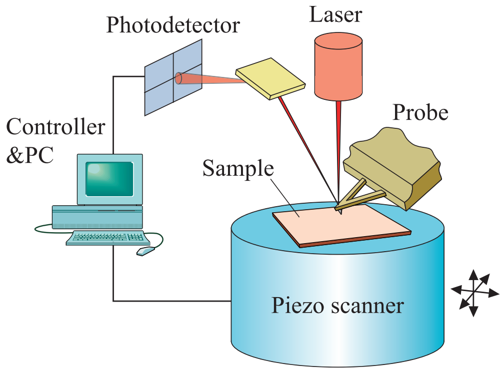

Fig. 1 Schematic drawing of the atomic force microscope.

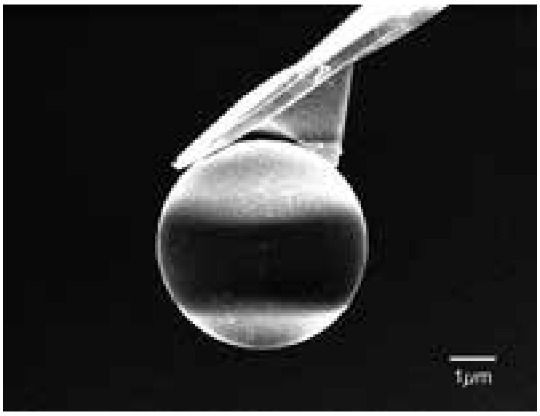

Fig. 2 Scanning electron microscope image of a colloid probe.

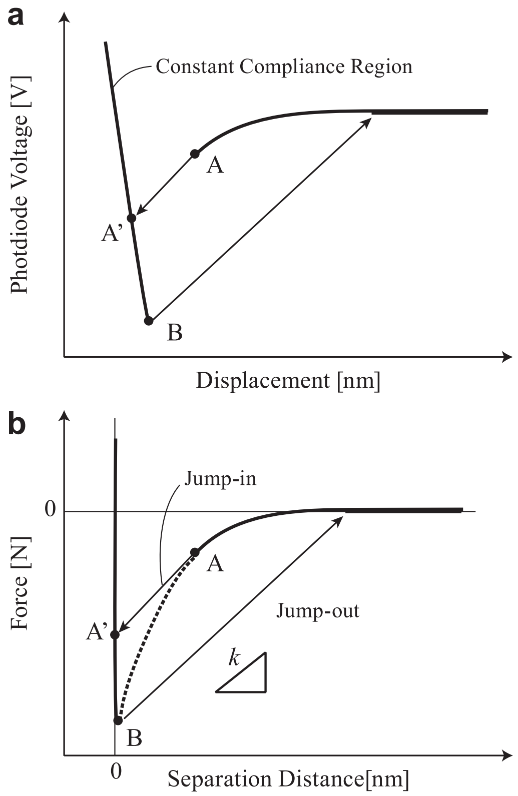

Fig. 3 Typical force data by AFM measurements. **(a)** The raw data and **(b)** the force-separation distance curve converted from **(a)**.

substrate constitutes one measurement cycle. A positive deflection (force) value usually indicates a repulsive force. During the measurement, the deflection of the cantilever is recorded by the photodetector output voltage as a function of the relative displacement of the sample or the probe. In the case of the force in **Fig. 3(a)**, an attractive force between the surfaces is detected. When the surfaces are in firm contact, the change in cantilever deflection equals the change in displacement as indicated by a linear region often called the "constant compliance region."

Unlike the SFA, the AFM usually contains no device or system to directly measure the separation distance between the interacting surfaces. Therefore, the force versus distance relationship has to be calculated from the photodiode voltage vs. piezo displacement curve, which is obtained directly from the AFM (Ducker et al., 1991). The cantilever deflection is calculated by dividing the photodiode voltage by the slope of the constant compliance region. By setting the separation distance to zero at the constant compliance region, the separation distance at each point of the data is simply calculated by adding the cantilever deflection to the piezo displacement at each point. Then, the force-distance relationship can be obtained by multiplying the cantilever deflection with the spring constant of the cantilever k as shown in **Fig. 3(b)**. When a colloid probe is used, the obtained force values are commonly divided by the particle radius R, because this value can be shown to be proportional to the interaction energy per unit area between parallel planes by the Derjaguin approximation.

If the attraction is a strong function of separation, the surfaces often "jump-in" to contact, due to the instability of the cantilever, which is denoted by point A and A' in **Fig. 3**. This occurs when the slope of the interaction force along the separation distance exceeds the spring constant of the cantilever. As the surfaces are separated, an adhesion force may be seen between the surfaces. In this case, the cantilever usually undergoes a jump-out to zero interaction force, which is marked by point B in the figure. This is the reverse effect of the jump-in.

It should be noted that an accurate zero distance cannot be guaranteed by this method, although it is the dominant means used to determine the separation distance in AFM measurements. In particular, if there is an adsorbed layer of any kind of molecules on the surfaces and if the molecules are not excluded when the surfaces are brought into contact, a certain offset of the distance should be expected. Therefore, the distance obtained with this method should be regarded as the relative distance from the point of closest approach in the AFM force measurements and this should be kept in mind when precise distances between the surfaces need to be considered. Additionally, most surfaces have some degree of roughness and this complicates both the definition of zero separation and the practical determination of zero separation in a force measurement. (Parsons et al., 2014)

3. Force measurements in liquid phase

3.1 DLVO force

As mentioned in the Introduction, the DLVO theory provides the theoretical basis for the surface forces between charged particles in aqueous solutions. In the DLVO theory, the total interaction force between two like particles is assumed simply to be the sum of the van der Waals attraction and an electrostatic double-layer repulsion. Force measurements with the SFA and the AFM were validated by the fact that the measurements between charged surfaces in aqueous electrolyte solutions were in broad agreement with the DLVO theory (**Fig. 4**). This in turn confirmed that DLVO theory describes real interaction forces quite accurately.

Since a variety of materials can be used for AFM force measurements, DLVO forces have been measured between many types of surfaces using AFM. The metals and their compounds that have been used include gold (Biggs et al., 1994), alumina (Larson et al., 1997), titania (Larson et al., 1995), zirconia (Biggs, 1995), zinc and lead sulphide (Toikka et al., 1997), iron oxide (Sander et al., 2004), tungsten (Andersson and Bergstrom, 2002) and cobalt (Andersson and Bergstrom, 2002). The forces between polymer particles have also been measured using polystyrene (Li et al., 1993), poly(etheretherketone) (Weidenhammer and Jacobasch, 1996) and Teflon

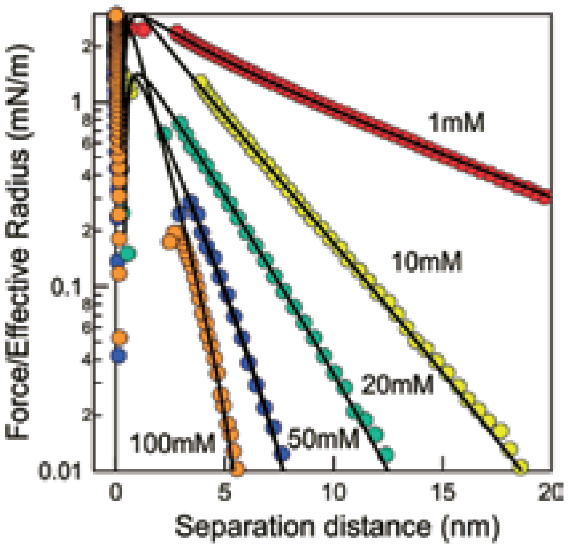

Fig. 4 Forces between carboxyl latex particles in aqueous KCl solutions at pH4. The solid lines represent the theoretical data calculated from DLVO theory. Adopted with permission from Montes et al., 2017. Copyright (2017) John Wiley and Sons.

(Drechsler et al., 2004). Not only the forces between identical surfaces, but those between different surfaces have also been analyzed (Larson et al., 1997; Toikka et al., 1997).

It is fundamentally important that the surfaces used in the measurement of interaction forces accurately represent the system of interest. Typically flat surfaces and spheres with an extremely low level of roughness are required in order to be able to interpret the data with confidence. In practice, however, this is not easily achieved as many materials are not available in such forms. In recent years, Atomic Layer Deposition (ALD) (George, 2010) has been applied to silicon and silica substrates to access a range of materials that are not available in a form suitable for surface force studies. This process involves a two-step gas phase chemical reaction that results in the production of a single conformal monolayer of material being grown on the surface during each cycle. By repeating the cycle a given number of times, a surface of controlled thickness can be grown on a substrate. The process can be performed with little or no increase in surface roughness, if the appropriate material and growth conditions are used (Walsh et al., 2012a). To date ALD films of alumina (Teh et al., 2010), titania (Walsh et al., 2012b), and hafnia (Eom et al., 2015) have successfully been used as substrates for force measurements.

In non-aqueous solvents, electrostatic double-layer forces are present when the dielectric constant is sufficiently high to allow the dissociation of surface groups which gives rise to a surface charge. The existence of double-layer forces have been confirmed practically in propylene carbonate (Christenson and Horn, 1983) and alcohol-water mixtures (Kanda et al., 1998). In apolar media such as hydrocarbons, the electrostatic forces can also be present when certain surfactants are added. The surfactants form reverse micelles in apolar solvents and dissolve free ions in the liquid and charge the surfaces at the same time. McNamee et al. (2004) measured the force between two silica surfaces in n-dodecane with the anionic surfactant AOT (bis(2-ethylhexyl)-sulfosuccinate) and observed electrostatic forces.

3.2 Hydration and solvation force

Developments in direct force measurements with the SFA and the AFM have not only provided an experimental basis for the DLVO paradigm, but have extended our understanding of the forces to those that lie outside of the DLVO paradigm. These are often called non-DLVO forces.

The hydration force is one of the most important non-DLVO forces. Although the force curves between charged surfaces in aqueous solutions measured with SFA and AFM fit well to the DLVO theory at surface separations down to several nanometers, the forces at shorter range usually deviate from the theory. This is because the DLVO theory assumes the liquid medium is a continuum, whereas the confined liquid can no longer be regarded as a continuum and the physical properties and the granularity of the liquid molecules are manifest at these small distances. Between charged surfaces in aqueous electrolyte solutions, particularly at high concentrations, monotonically repulsive forces with the range of about 1–5 nm are typically measured instead of the predicted van der Waals attraction, as indicted in **Fig. 4**. The repulsive force, called hydration force (Pashley, 1981), can be attributed to the energy required to remove water of hydration from surface functional groups (primary hydration) and hydrated ions from surfaces (secondary hydration) when they are brought into contact. The repulsive force can be empirically fitted with an exponential function, and its decay length is typically in the range of 0.6–1.1 nm for 1:1 electrolyte. Israelachvili and Pashley using the SFA found that the hydration force is not always monotonically repulsive but exhibits oscillations at separations below about 1.5 nm when the surfaces are molecularly smooth, like mica, and the salt concentration is low (Israelachvili and Pashley, 1983). In this case, the mean periodicity of the oscillatory force was found to be approximately equal to the diameter of a water molecule.

Hydration forces are inevitably influenced by the species of solute molecules. In experiments using SFA, the range of force between mica increased following the hydration enthalpy of the cations, in the order of $Li^+ \sim Na^+ > Cs^+$ (Pashley, 1981). This tendency was also confirmed with AFM (Higashitani and Ishimura, 1997) as shown in **Fig. 5**. On the other hand the addition of alcohol removes the hydration repulsion (Yoon and Vivek, 1998), which is likely due to the adsorption of alcohol molecules displacing the first layer of water on the hydroxylated silica surfaces.

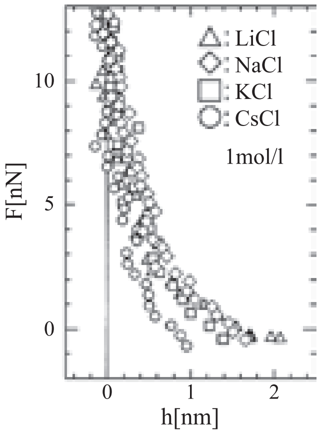

Fig. 5 Forces measured between an AFM tip and a mica surface in 1 M electrolyte solutions of monovalent cations. Reprinted with permission from Higashitani and Ishimura, 1997. Copyright (1997) The Society of Chemical Engineers, Japan.

Although the hydration force is a very short-ranged force, it has a significant influence on the bulk stability of suspensions, particularly in the case of nanoparticles. It has frequently been reported that the stability of particle dispersions disagrees with theoretical predictions at high salt concentration because the coagulation rate decreases when the size of the particle is less than several hundred nanometers (Kobayashi et al., 2005), whereas in the DLVO theory, the rate should be independent of particle size. This reduction is attributed to the hydration force or related structural forces. Recently, Higashitani et al. (2017) proposed a model that can successfully predict the reduction in the coagulation rate taking into account the effect of hydration layers.

In non-aqueous solvents, the force due to the solvation and structuring of liquid molecules adjacent to surfaces that gives rise to specific interactions, are referred to as solvation forces (Horn and Israelachvili, 1981). In most cases the force is an oscillatory function with a periodicity equal to the mean molecular diameter, decaying with distance. Using AFM, the solvation force has been observed in several solvents such as OMCTS (octamethylcyclotetrasiloxane) (Han and Lindsay, 1998) and n-alcohols (Franz and Butt, 2002) (**Fig. 6**).

3.3 Steric force

In various industrial processes, polymers are widely used as dispersants or flocculants to control the behavior of particle dispersions. The interactions of polymers with particle surfaces alter the interparticle forces in a manner that is dependent on the type and concentration of polymer and the interaction of the polymer with the particles, as schematically represented in **Fig. 7**.

When adsorbing polymers are added to a solution with particles, aggregation occurs when the polymer concentration is low, as mentioned in the next section. If the surface coverage of the adsorbed polymer becomes sufficiently high, a repulsive interaction arises from the overlapping of the polymer molecules on opposing surfaces as shown in **Fig. 7(b)**. This produces a repulsive force due to the unfavorable entropy of confining polymer chains between the surfaces. This repulsive force is well known as steric repulsion and is the controlling force when polymers act as dispersants in liquids. AFM measurements of steric repulsion have mainly been conducted between silica surfaces with polymers adsorbed from solution (Musoke and Luckham, 2004; McLean et al., 2005) or polymers grafted onto silica (McNamee et al., 2007).

Currently there is no simple, comprehensive theory available to describe experimentally measured steric forces, as steric forces are complex and are influenced significantly by many factors. The magnitude of the force between surfaces with polymers depends on the quantity and density of polymer on each surface and on whether they are physically adsorbed or irreversibly grafted onto the surfaces. The quality of the solvent also affects the force. For two brush-bearing surfaces, the Alexander-de Gennes (AdG) theory is usually used to approximate the steric force between them, while the theory has a limited validity for the steric force between physisorbed surfaces. McLean et al. (2005) reported that the Milner, Witten, and Cates (MWC) model (Milner et al., 1988) gives a better fitting than the AdG theory for the interaction between hydrophobic surfaces with adsorbed triblock copolymer layers, presumably because the segment density profile on the adsorbed polymer on the surfaces is in line with the assumptions of the MWC model. Further, it is theoretically and experimentally difficult to decouple steric forces from hydrodynamic forces associated with the expulsion of solvent during compression of a polymer brush or film (Wu et al., 2018).

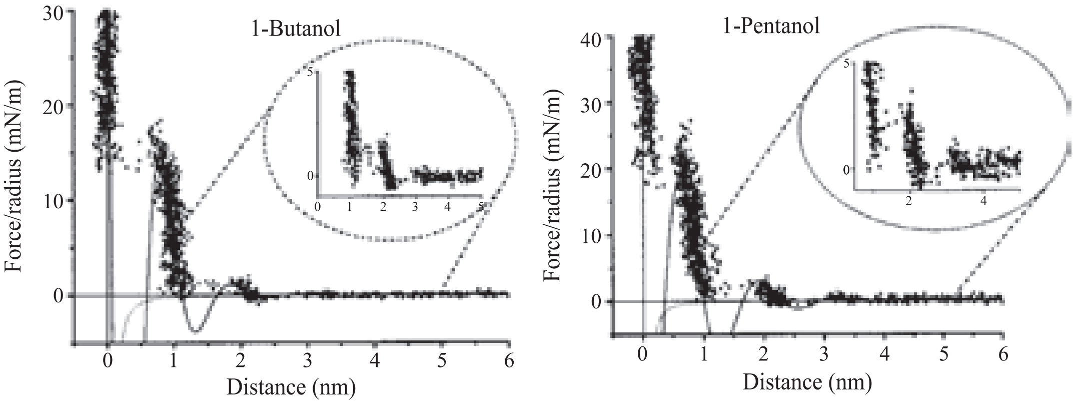

Fig. 6 Force curves for the interaction of a silicon nitride AFM-tip with mica in 1-butanol and 1-pentanol. The forces are normalized by radius of the tip. The solid and dotted lines show the fitting with an exponentially decaying periodic function and the calculated van der Waals forces, respectively. Adapted with permission from Franz and Butt, 2002. Copyright (2002) American Chemical Society.

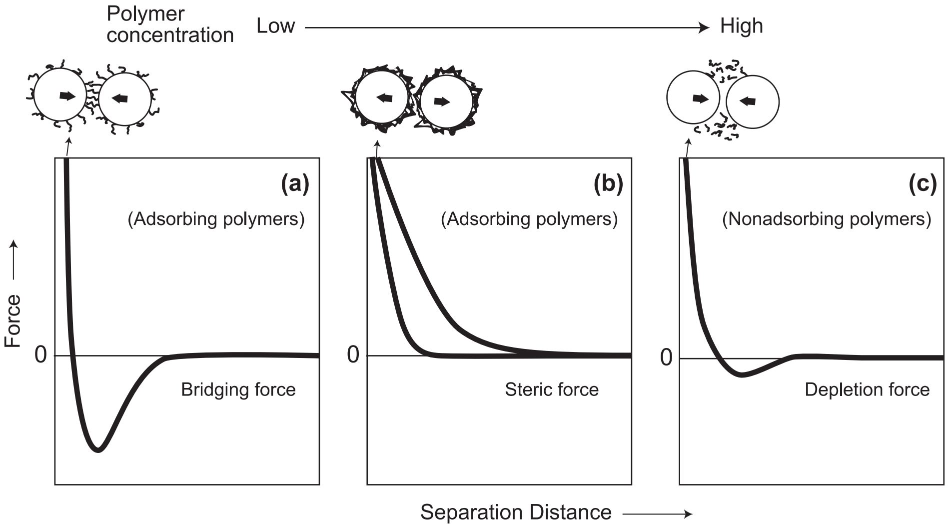

Fig. 7 Schematic drawing of the change in the interaction forces between surfaces depending on the polymer concentration. An attractive bridging force **(a)** is replaced with a repulsive steric force **(b)** in adsorbing polymer solutions when the concentration increases. The depletion force **(c)** acts in a solution of a nonadsorbing polymer at high concentration.

The steric force also acts between surfaces with adsorbed aggregate structures, such as micelles. The adsorption of charged surfactant micelles onto the surfaces gives strong steric repulsion at short range, along with electrostatic repulsion (Stiernstedt et al., 2005). Between silica surfaces in solutions of nonionic poly(oxyethylene) surfactants, a strong repulsive force was also observed at short range, at concentrations above the critical micelle concentration, due to the formation of surfactant bilayers (Rutland and Senden, 1993).

3.4 Bridging of polymers and depletion forces

As mentioned in the previous section, when adsorbing polymers are added to a dispersion of particles, aggregation occurs when the polymer concentration is low, as drawn in **Fig. 7(a)**. In this case the low surface coverage of the polymers allows the bridging of polymer molecules between particle surfaces, resulting in an attractive force evident at large separation distance. With the AFM, this attractive bridging force, with a range of several 10's of nanometers, was observed by Biggs (1995) between zirconia surfaces in polyacrylamide solutions and by Zhou et al. (2008) for cationic polymers between silica surface.

While polymers adsorbed at high concentration give rise to steric repulsion, the interaction is attractive in nonadsorbing polymer solutions at high concentration, as shown in **Fig. 7(c)**. Empirical knowledge of the ability of nonadsorbing polymers to promote particle flocculation has been long known. During the 1950s, Asakura and Oosawa presented a theory for an attractive force, referred to as a depletion force, as an explanation for this flocculation (Asakura and Oosawa, 1954). When solid surfaces are in a solution of a nonadsorbing polymer at high concentration, the polymer molecules are excluded from the region between the surfaces, when the distance between them is less than the effective diameter of the polymer. This reduces the osmotic pressure between the surfaces relative to the bulk solution, resulting in an attractive depletion force.

The existence of the depletion force was experimentally confirmed between stearylated silica surfaces in polydimethylsiloxane solutions in cyclohexane (Milling and Biggs, 1995). The depletion forces were observed not only in polymer solutions but in solutions containing surfactant micelles (Richetti and Kékicheff, 1992) and solid nanoparticles (Sharma and Walz, 1996), indicating that the depletion phenomenon is common in solutions containing nonadsorbing particulate matters at high concentration.

3.5 Hydrophobic attraction

It had been known empirically that there is a strong attractive force between hydrophobic particles in aqueous solutions as they aggregate quite rapidly. The first direct evidence that the force is of greater magnitude than the van der Waals force was obtained between mica surfaces bearing adsorbed cationic surfactant, by Israelachvili and Pashley with the SFA (Israelachvili and Pashley, 1982). Since then countless studies have been performed to elucidate the nature of the hydrophobic attraction. The origin of the hydrophobic attraction, however, was much disputed because the experimentally observed forces have sometimes shown an inconceivably long-range, that reaches up to several hundreds of nanometers (Kurihara

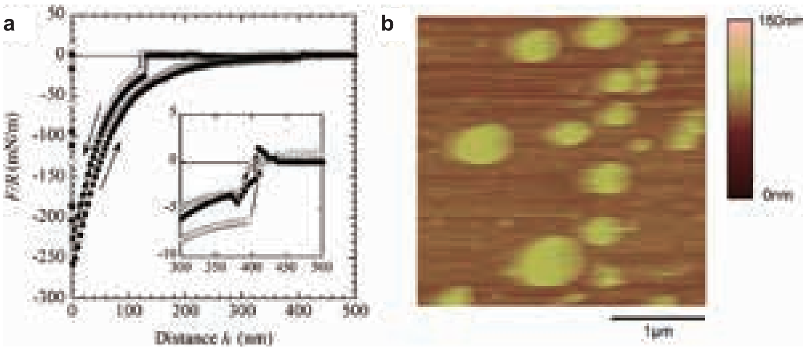

Fig. 8 Typical approaching and retracting force curves between silica surfaces hydrophobized with octadecyltrichlorosilane (OTS) measured in water **(a)** and a tapping-mode AFM image ($3 \times 3\ \mu m^2$) of the substrate hydrophobized with OTS obtained in water **(b)**. The steps that appear in the approaching and retracting force curves in **(a)** are considered to represent the force changes when a bridging of nanobubbles between the surfaces forms and disappears. The nanobubbles on the surface are observed as domain-like structures (bright regions) in the image in **(b)**.

and Kunitake, 1992), which no conventional thermodynamics can explain. In addition, the fact that the observed forces had a variety of ranges and magnitudes depending on the systems used (Christenson and Claesson, 2001) precluded a single theory from describing all the experimental results.

Gradually the contribution of numerous studies investigating the hydrophobic attraction, has revealed the origin of the measured force and multiple phenomena have been found to apply depending on the system. Bridging of nanobubbles is now recognized as the main cause of the very long-range forces. This mainly occurs when the surfaces are highly hydrophobic and robust, such as chemisorption of materials that produce hydrocarbon layers, as an example of the force data is shown in **Fig. 8(a)**. The existence of stable nanobubbles on surfaces in contact with an aqueous solution was first predicted in the mid-1990s (Parker et al., 1994) and was later experimentally confirmed by AFM observations (Ishida, et al., 2000a) (**Fig. 8(b)**) in relation to the hydrophobic attraction (Ishida et al., 2000b). On the other hand, when hydrophobic surfaces are prepared by physical adsorption of surfactants or amphiphiles, electrostatic forces can arise as they tend to form domains of aggregates on the surfaces (Zhang et al., 2005). Such aggregates can form as the surfaces approach (Meyer et al., 2005). Domains of these aggregates create patches with different charge properties. Upon interaction it is favorable for oppositely charged regions to align and this results in a long-range electrostatic attractive force that is dependent on the ionic strength of the solution.

Recent studies on the hydrophobic attraction are focusing on the "pure" component of the force, because the forces arising from the bubbles or charge domains are sometimes not regarded as that produced by the surface hydrophobicity itself. Indeed, the hydrophobic attraction has been found between highly hydrophobic surfaces in the absence of nanobubbles or electrostatic attraction (Ishida et al., 2012), as shown in **Fig. 9**. The general consensus thus far seems to be that such "pure" hydrophobic attraction has a short-range of less than 10–15 nm for all types of hydrophobic surfaces (Meyer et al., 2005). Although the origin of the force is still under intense scrutiny, this attraction seems to have an exponential form that decays with the surface separation. The experimentally obtained value of the decay length often lies in the range of 0.3–2.0 nm (Donaldson et al., 2015). On the other hand, Tabor et al. (2013) measured the forces between fluorocarbon oil droplets with the refractive index matched to that of solution, in order to minimize the effect of the

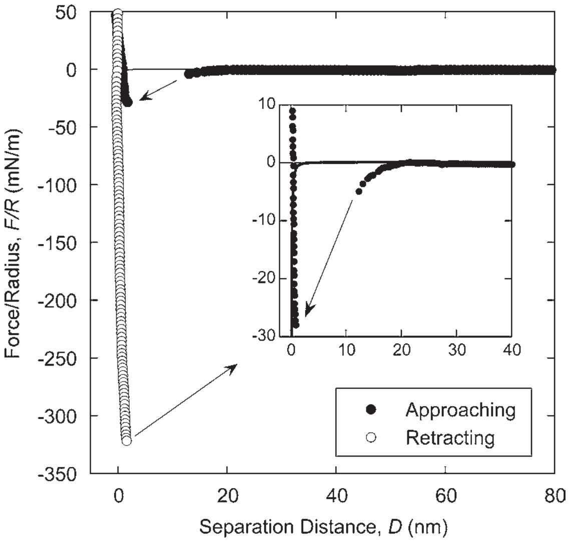

Fig. 9 Approaching and separating force curves between hydrophobic (OTS-coated) silica surfaces in 1 mM $NaNO_3$ solution obtained after the nanobubble-removing process. The inset shows a close-up plot of the short-range region of the approaching force. The solid line shows the calculated van der Waals attraction.

van der Waals attraction. They measured D_0 value to be 0.3 nm, shorter than that for solids. This difference in the decay length implies that the nature of the pure hydrophobic force could also vary depending on the system. Ishida et al. (2018) measured the interaction forces between silica surfaces modified to different degrees of hydrophobicity and found one surface is highly hydrophobic, this promotes the hydrophobic attraction such that it is observed even against a mildly hydrophobic surface. In this case, the contact angle of the other surface dominates the range and strength of the force and nanoscopic properties of the molecules on the surface play only a minor role. However, despite these contributions the mechanism responsible for this "pure" hydrophobic attraction remains unresolved and further studies are still necessary to reveal the origin of the force.

3.6 Capillary bridging

Capillary condensation of water vapor and bridging of condensed water films between surfaces is a well-established origin of a long-range and strongly attractive force between particles in the gas phase. Similarly, capillary-induced phase separation and bridging in a liquid phase often produces strong and complex interaction forces.

In several different cases it has been observed that confinement between surfaces has induced a phase separation, resulting in an attractive force. The best example of this would be water in nonpolar (water-insoluble) solvents. A trace amount of water present in cyclohexane was found to give rise to an extraordinary long-range force, the range of which was up to 250 nm, between silica surfaces (Kanda et al., 2001), as shown in **Fig. 10**. This force originates from the capillary condensation of water between the surfaces, due to its higher affinity with the silica surfaces than cyclohexane. The Laplace pressure associated with a bridge of the condensed water phase causes a long-range attraction. Similar phenomenon has also been observed in alcohol-cyclohexane mixtures (Mizukami et al., 2002), in which case the alcohol molecules are thought to form a network structure. Lee et al. (2011) found such capillary condensation occurs even in a mixture of miscible solvents. They found a long-range attractive force between a silica particle and a glass plate in mixtures of water and N-methyl-2-pyrrolidone (NMP), which are strongly heteroassociating liquids, when the NMP concentration range is within 30–50 vol%. In this case, it was also suggested that the bridging of macrocluster layers of water and NMP formed adjacent to hydrophilic surfaces.

Attractive forces also arise by the capillary condensation of solutes between surfaces. Solutions of polymer mixtures particularly have a strong tendency to phase separate and form two phases. Wennerström et al. (1998) observed a very long-range attractive force between mica surfaces in mixed aqueous systems of dextran and poly(ethyleneoxide) (PEO) using SFA. Further, Sprakel et al. (2007) found capillary condensation of polymer molecules from aqueous solutions, measuring a long-range force between hydrophobic surfaces in solutions of alkylchain-terminated PEO. They pointed out that in this case the interfacial tensions between the capillary bridge and the coexisting bulk phase is extremely low, on the order of 10 μN/m. Long range attractive forces between alumina surfaces in the presence of muconic acid were also attributed to capillary bridging due to the low solubility of the munconic acid (Teh et al., 2010).

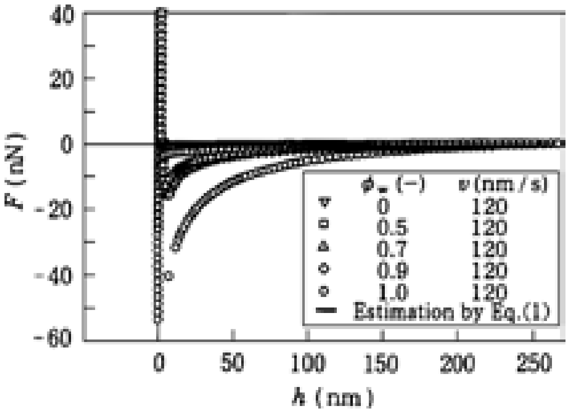

Fig. 10 Interaction forces between silica surfaces in cyclohexane with various amount of water. In the plot, ϕ_w denotes the mixing ratio of water-saturated cyclohexane (contains 68 ppm of water) to dried cyclohexane. Reprinted with permission from Kanda et al., 2001. Copyright (2002) The Society of Powder Technology, Japan.

3.7 Force between fluid interfaces

Interactions of particles with fluid interfaces such as air bubbles and oil droplets are found in many industrial processes, such as froth flotation. The interactions of a solid surface with fluid interfaces, therefore, should be as important as particle–particle interactions. Evaluation of the interactions between a particle and a bubble or oil droplet with the AFM or with AFM related setups, however, has not been as widely adopted as measurement of the solid-solid interactions. Whilst the measurements with the AFM can be readily performed by using the colloid probe technique in which the probe interacts with a small bubble or oil droplet attached to a hydrophobic plate in a liquid cell, interpretation of the obtained forces is often quite complex because of the deformation of fluid surfaces. The colloid probe, if hydrophobic, can even penetrate into the bubble or oil droplet.

Nevertheless, understanding of the interaction force between particles and fluid interfaces has progressed due to several studies. Fielden et al. (1996) confirmed that a monotonically repulsive force acted between a hydrophilic silica particle and an air bubble. The repulsive force fits to DLVO theory, indicating the water–gas interface is negatively charged at neutral pH as reported in previous measurements of bubble zeta potential (Li and Somasundaran, 1991).

The interactions of fluids with hydrophobic particles are more complicated to analyze because the attraction between a particle and an interface of the fluid, and the engulfment of the particle into the fluid happens almost simultaneously. In this case, the measured forces usually only reveal a single long-range jump and most of the detailed information on the attraction between the surface is lost. Ishida (2007) measured the forces between a hydrophobized silica particle and a bubble and estimated the separation of the surfaces just prior to the particle jumping in and being engulfed in the bubble by fitting the repulsive force before the jump to the DVLO theory. The thickness of the water film between the particle and the bubble surface when it ruptured was estimated to be 10–15 nm. Interestingly, this thickness is very close to the distance of the hydrophobic attraction, which is mentioned in the previous section.

The interaction between a particle and an oil droplet is similar to that between a particle and a bubble. As oil surfaces are usually negatively charged, a repulsive interaction has been found between a silica particle and a decane droplet with a decay length equal to the Debye length (Hartley et al., 1999).

Recently, an Australian group has successfully developed methods to measure and analyze forces between two fluid interfaces in solution (Dagastine et al., 2006; Clasohm et al., 2007; Vakarelski et al., 2010), such as bubble-bubble and oil-oil, as shown in **Fig. 11**. They attached a small bubble or an oil droplet on the top of a specially microfabricated cantilever and measured the forces of interaction with another bubble/oil droplet deposited on a hydrophobic plate. The separation distance of the surfaces and the deformation of the bubbles was calculated using mathematical models combining the surface forces, hydrodynamics and the deformation of the surfaces. One of the important findings they provided in the series of the experiments is that the coalescence of bubbles and oil droplets occurs within the paradigm of the DLVO force– no additional force was evident. This was surprising as a hydrophobic attraction had been expected based on earlier experiments on solid hydrophobic surfaces. Instead, hydrodynamic forces were influential, deforming the surfaces and inducing water drainage during the thinning of the water film between the surfaces.

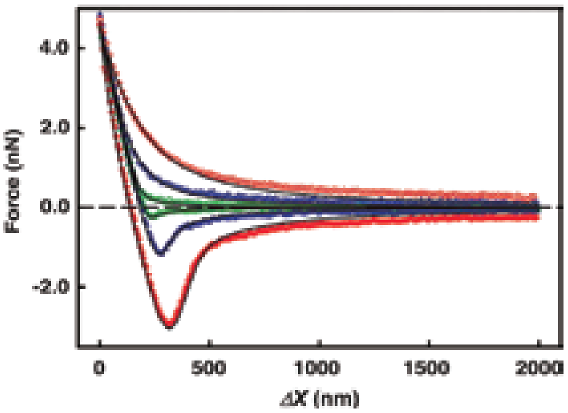

Fig. 11 The approaching (open symbols) and retracting (filled symbols) interaction force versus piezo drive motion ΔX between two decane droplets in 0.1 mM SDS solution in water measured at different probe velocities (green circles, 2 µm/s; blue triangles, 9.3 µm/s; red diamonds, 28 µm/s). The solid lines are the calculated force curves from a comprehensive model of the dynamic droplet interactions. Translated from Dagastine et al., 2006 with permission from AAAS.

3.8 Hydrodynamic force

In addition to “static” interactions described above, the hydrodynamic force is certainly an important issue in processing particles during stirring, separation, and transportation. Most AFM studies related to the hydrodynamic force seem to have focused on the boundary slip condition of Newtonian liquids over a solid wall. In classical fluid mechanics, the assumption was made that when a liquid flows over a solid surface, the liquid molecules adjacent to the solid have the same velocity as the solid (i.e. stationary relative to the solid), this is called the non-slip boundary condition. The boundary slip of liquid along a solid surface, however, has been observed at the micro-and nanoscale under certain conditions by sensitive experiments. The degree of boundary slip is characterized by the slip length, which is defined as the distance behind the interface at which the liquid velocity extrapolates to zero.

The first utilization of the AFM to measure the boundary slip in aqueous solutions was made by Craig et al (2001). They used the colloid probe technique to measure the hydrodynamic drag force between gold-coated silica and mica with a partially hydrophobic coating, in aqueous sucrose solutions. They observed slip occurring with a varying slip length of up to ~20 nm, depending on the liquid viscosity and the shear rate. As the result of numerous studies conducted following this report, it is now generally accepted that slip occurs for liquids on lyophobic surfaces, although a broad range of the observed slip length depends on the experimental conditions. On the other hand, when the surfaces are completely wetted and smooth, slip is not likely to occur (Maali et al., 2009), though surface roughness could induce slip (Bonaccurso et al., 2002).

3.9 Friction force

In circumstances where the flow of solutions with relatively high particle loadings occurs, not only normal forces but frictional forces between particles are important. In addition, the frictional forces play an important role in emerging technologies such as chemical mechanical planarization (CMP) and microelectromechanical systems (MEMS). As such, understanding of frictional phenomena at a nanoscale level has become one of the critical topics in various fields of technology.

The measurement of friction by AFM can be conducted by scanning a probe over a surface with a constant normal load and measuring the twisting of the cantilever using the photodiode output in the lateral direction. From the magnitude of the twist, the lateral force can be determined as a function of the normal load. Biggs et al. (2000) was the first to apply the colloid probe technique for friction measurements. They observed a difference in the friction properties depending on the surface hydrophobicity.

Higashitani's group has extensively investigated the friction between silica surfaces in aqueous electrolyte solutions. They found that the presence of salt ions has shown better lubrication between silica surfaces than pure water and the degree of lubrication has been found to follow the order of hydration of cations ($Li^+ > Na^+ > Cs^+$) (Donose et al., 2005), as shown in **Fig. 12**. This can be attributed to the lateral mobility of the water molecule in the hydration shell of adsorbed cations. The friction was found to increase linearly with the applied load without any dependence on pH in the range of pH 3.6 to 8.6, whereas the friction becomes extremely small and the dependence on the applied load became nonlinear at higher pH (Taran et al., 2007). They suggested that this transition is caused by the development of a gel layer composed of polymer-like segments of silicic acid anchored on the surface at high pH.

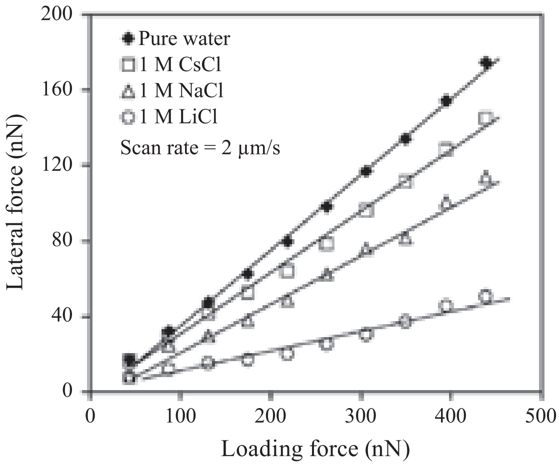

Fig. 12 Dependence of friction force on the applied load measured between a silica particle and a silica wafer in pure water and CsCl, NaCl, or LiCl solutions of 1 M. Adapted with permission from Donose et al., 2005. Copyright (2005) American Chemical Society.

Adsorption of surfactant also reduces the friction coefficient. Vakarelski et al. (2004) reported that the friction between silica surfaces in a cationic surfactant solution reduced with increasing concentration and became constant at concentrations higher than the CMC. An adsorbed layer of the weak polyelectrolyte (Notley et al., 2003) and hydrophilic polymer (Li et al., 2011) also reduced the friction between surfaces, implying that any form of hydrated layer will play an important role in friction reduction.

4. Conclusion

This review has presented an overview of how AFM has been employed for investigating the interaction forces between surfaces and interfaces. The studies introduced herein clearly show that AFM is arguably one of the best tools for gaining direct understanding of how the interaction forces change depending on the properties of the liquid, the surfaces, and solutes down to the nanometer scale.

There are some challenges in AFM force measurements that need to be resolved to allow the application of this technique to an even broader range of research problems. One of the issues is the application of the colloid probe method to interactions between nanoparticles. The rapid progress of nanotechnology has led to a demand for measurement of the interactions between nanoparticles directly. As the behavior of the particles is affected by the size and/or the shape of the particle, it is unclear whether the force data for spherical particles with a diameter of several micrometers could be directly applied to analyze the behavior of real nanoparticles. As nanoparticles are too small to be observed optically, effective methods are certainly necessary to attach a nanosized particle stably on the tip of an AFM. Even then for small nanoparticles the presence of tip itself will alter the interaction forces.

Correlation between the interaction forces measured by AFM and the behavior of real suspensions is another important challenge in the field of particle technology. The complicated behavior of concentrated slurries in particular, has scarcely been described in terms of particle interactions. Understanding of the effect of interaction forces on the precise rheological properties of suspensions remains limited. This requires that the surface forces measured between two surfaces be incorporated in understanding how this influences the larger scale structure of the dispersion and the forces between many particles. Further improvements in AFM force measurements in combination with other experimental methods and with other approaches such as computer simulation is expected to achieve a more comprehensive understanding of the behavior of particulate matters in liquids in the foreseeable future.

Acknowledgments

N.I. acknowledges financial support by KAKENHI (Grants 25420803 and 15KK0238) from the Japan Society for the Promotion of Science (JSPS) and by a research grant from Hosokawa Particle Technology Foundation. Partial financial support by Adaptable and Seamless Technology Transfer Program, Target-driven Research (A-STEP) Stage I from the Japan Science and Technology Agency (JST) is also gratefully acknowledged. V.S.J.C. acknowledges the support of the Australian Research Council (DP140102371).

References

Andersson K.M., Bergstrom L., DLVO interactions of tungsten oxide and cobalt oxide surfaces measured with the colloidal probe technique, Journal of Colloid and Interface Science, 246 (2002) 309–315.

Asakura S., Oosawa F., On interaction between two bodies immersed in a solution of macromolecules, The Journal of Chemical Physics, 22 (1954) 1255–1256.

Biggs S., Steric and bridging forces between surfaces bearing adsorbed polymer: An atomic force microscopy study, Langmuir, 11 (1995) 156–162.

Biggs S., Cain R., Page N.W., Lateral force microscopy study of the friction between silica surfaces, Journal of Colloid and Interface Science, 232 (2000) 133–140.

Biggs S., Mulvaney P., Zukoski C.F., Grieser F., Study of anion adsorption at the gold-aqueous solution interface by atomic force microscopy, Journal of the American Chemical Society, 116 (1994) 9150–9157.

Binnig G., Quate C.F., Gerber C., Atomic force microscope, Physical Review Letters, 56 (1986) 930–933.

Bonaccurso E., Kappl M., Butt H.J., Hydrodynamic force measurements: boundary slip of water on hydrophilic surfaces and electrokinetic effects, Physical Review Letters, 88 (2002) 076103 (4pp). DOI: 10.1103/PhysRevLett.88.076103

Butt H.-J., Measuring electrostatic, van der Waals, and hydration forces in electrolyte solutions with an atomic force microscope, Biophysical Journal, 60 (1991) 1438–1444.

Christenson H.K., Claesson P.M., Direct measurements of the force between hydrophobic surfaces in water, Advances in Colloid and Interface Science, 91 (2001) 391–436.

Christenson H.K., Horn R.G., Direct measurement of the force between solid surfaces in a polar liquid, Chemical Physics Letters, 98 (1983) 45–48.

Clasohm L.Y., Vakarelski I.U., Dagastine R.R., Chan D.Y.C., Stevens G.W., Grieser F., Anomalous pH dependent stability behavior of surfactant-free nonpolar oil drops in aqueous electrolyte solutions, Langmuir, 23 (2007) 9335–9340.

Craig V.S.J., Neto C., Williams D.R.M., Shear-dependent boundary slip in an aqueous newtonian liquid, Physical Review Letters, 87 (2001) 054504 (4pp). DOI: 10.1103/PhysRevLett.87.054504

Dagastine R.R., Manica R., Carnie S.L., Chan D.Y.C., Stevens G.W., Grieser F., Dynamic forces between two deformable oil droplets in water, Science, 313 (2006) 210–213.

Derjaguin B.V., Landau L.D., Theory of the stability of strongly charged lyophobic sols and of the adhesion of strongly charged particles in solution of electrolytes, Acta physicochimica U.S.S.R., 14 (1941) 633–662.

Donaldson S.H., Røyne A., Kristiansen K., Rapp M.V., Das S., Gebbie M.A., Lee D.W., Stock P., Valtiner M., Israelachvili J., Developing a general interaction potential for hydrophobic and hydrophilic interactions, Langmuir, 31 (2015) 2051–2064.

Donose B.C., Vakarelski I.U., Higashitani K., Silica surfaces lubrication by hydrated cations adsorption from electrolyte solutions, Langmuir, 21 (2005) 1834–1839.

Drechsler A., Petong N., Zhang J., Kwok D.Y., Grundke K., Force measurements between Teflon AF and colloidal silica particles in electrolyte solutions, Colloids and Surfaces A: Physicochemical and Engineering Aspects, 250 (2004) 357–366.

Ducker W.A., Senden T.J., Pashley R.M., Direct measurement of colloidal forces using an atomic force microscope, Nature, 353 (1991) 239–241.

Eom N., Walsh R.B., Liu G., Parsons D.F., Craig V.S.J., Surface forces in particle technology: Wet systems, Procedia Engineering, 102 (2015) 24–34.

Fielden M.L., Hayes R.A., Ralston J., Surface and capillary forces affecting air bubble−particle interactions in aqueous electrolyte, Langmuir, 12 (1996) 3721–3727.

Franz V., Butt H.-J., Confined liquids: Solvation forces in liquid alcohols between solid surfaces, The Journal of Physical Chemistry B, 106 (2002) 1703–1708.

George S.M., Atomic layer deposition: An overview, Chemical Reviews, 110 (2010) 111–131.

Han W., Lindsay S.M., Probing molecular ordering at a liquid-solid interface with a magnetically oscillated atomic force microscope, Applied Physics Letters, 72 (1998) 1656–1658.

Hartley P.G., Grieser F., Mulvaney P., Stevens G.W., Surface forces and deformation at the oil−water interface probed using AFM force measurement, Langmuir, 15 (1999) 7282–7289.

Higashitani K., Ishimura K., Evaluation of interaction forces between surfaces in electrolyte solutions by atomic force microscope, Journal of Chemical Engineering of Japan, 30 (1997) 52–58.

Higashitani K., Nakamura K., Shimamura T., Fukasawa T., Tsuchiya K., Mori Y., Orders of magnitude reduction of rapid coagulation rate with decreasing size of silica nanoparticles, Langmuir, 33 (2017) 5046–5051.

Horn R.G., Israelachvili J.N., Direct measurement of structural forces between two surfaces in a nonpolar liquid, The Journal of Chemical Physics, 75 (1981) 1400–1411.

Ishida N., Direct measurement of hydrophobic particle–bubble interactions in aqueous solutions by atomic force microscopy: Effect of particle hydrophobicity, Colloids and Surfaces A: Physicochemical and Engineering Aspects, 300 (2007) 293–299.

Ishida N., Inoue T., Miyahara M., Higashitani K., Nano bubbles on a hydrophobic surface in water observed by tapping-mode atomic force microscopy, Langmuir, 16 (2000a) 6377–6380.

Ishida N., Kusaka Y., Ushijima H., Hydrophobic attraction between silanated silica surfaces in the absence of bridging bubbles, Langmuir, 28 (2012) 13952–13959.

Ishida N., Matsuo K., Imamura K., Craig V.S.J., Hydrophobic attraction measured between asymmetric hydrophobic surfaces, Langmuir, 34 (2018) 3588–3596.

Ishida N., Sakamoto M., Miyahara M., Higashitani K., Attraction between hydrophobic surfaces with and without gas phase, Langmuir, 16 (2000b) 5681–5687.

Israelachvili J., Pashley R., The hydrophobic interaction is long range, decaying exponentially with distance, Nature, 300 (1982) 341–342.

Israelachvili J.N., Pashley R.M., Molecular layering of water at surfaces and origin of repulsive hydration forces, Nature, 306 (1983) 249–250.

Israelachvili J.N., Tabor D., The measurement of van der Waals dispersion forces in the range 1.5 to 130 nm, Proceedings of the Royal Society of London. A. Mathematical and Physical Sciences, 331 (1972) 19–38.

Kanda Y., Nakamura T., Higashitani K., AFM studies of interaction forces between surfaces in alcohol–water solutions, Colloids and Surfaces A: Physicochemical and Engineering Aspects, 139 (1998) 55–62.

Kanda Y., Nishimura T., Higashitani K., Interaction forces between silica surfaces in wet cyclohexane, Journal of the Society of Powder Technology, Japan, 38 (2001) 316–322.

Kobayashi M., Juillerat F., Galletto P., Bowen P., Borkovec M., Aggregation and charging of colloidal silica particles: Effect of particle size, Langmuir, 21 (2005) 5761–5769.

Kurihara K., Kunitake T., Submicron-range attraction between hydrophobic surfaces of monolayer-modified mica in water, Journal of the American Chemical Society, 114 (1992) 10927–10933.

Larson I., Drummond C.J., Chan D.Y.C., Grieser F., Direct force measurements between dissimilar metal oxides, The Journal of Physical Chemistry, 99 (1995) 2114–2118.

Larson I., Drummond C.J., Chan D.Y.C., Grieser F., Direct force measurements between silica and alumina, Langmuir, 13 (1997) 2109–2112.

Lee J.H., Gomez I., Meredith J.C., Non-DLVO silica interaction forces in NMP-water mixtures. I. A symmetric system, Langmuir, 27 (2011) 6897–6904.

Li C., Somasundaran P., Reversal of bubble charge in multivalent inorganic salt solutions—Effect of magnesium, Journal of Colloid and Interface Science, 146 (1991) 215–218.

Li Y., Liu H., Song J., Rojas O.J., Hinestroza J.P., Adsorption and association of a symmetric PEO-PPO-PEO triblock copolymer on polypropylene, Polyethylene, and Cellulose Surfaces, ACS Applied Materials & Interfaces, 3 (2011) 2349–2357.

Li Y.Q., Tao N.J., Pan J., Garcia A.A., Lindsay S.M., Direct measurement of interaction forces between colloidal particles using the scanning force microscope, Langmuir, 9 (1993) 637–641.

Maali A., Wang Y., Bhushan B., Evidence of the no-slip boundary condition of water flow between hydrophilic surfaces using atomic force microscopy, Langmuir, 25 (2009) 12002–12005.

McLean S.C., Lioe H., Meagher L., Craig V.S.J., Gee M.L., Atomic force microscopy study of the interaction between adsorbed poly(ethylene oxide) layers: Effects of surface modification and approach velocity, Langmuir, 21 (2005) 2199–2208.

McNamee C.E., Tsujii Y., Matsumoto M., Interaction forces between two silica surfaces in an apolar solvent containing an anionic surfactant, Langmuir, 20 (2004) 1791–1798.

McNamee C.E., Yamamoto S., Higashitani K., Preparation and characterization of pure and mixed monolayers of poly(ethylene glycol) brushes chemically adsorbed to silica surfaces, Langmuir, 23 (2007) 4389–4399.

Meyer E.E., Lin Q., Hassenkam T., Oroudjev E., Israelachvili J.N., Origin of the long-range attraction between surfactant-coated surfaces, Proceedings of the National Academy of Sciences of the United States of America, 102 (2005) 6839–6842.

Milling A., Biggs S., Direct measurement of the depletion force using an atomic force microscope, Journal of Colloid and Interface Science, 170 (1995) 604–606.

Milner S.T., Witten T.A., Cates M.E., Theory of the grafted polymer brush, Macromolecules, 21 (1988) 2610–2619.

Mizukami M., Moteki M., Kurihara K., Hydrogen-bonded macrocluster formation of ethanol on silica surfaces in cyclohexane, Journal of the American Chemical Society, 124 (2002) 12889–12897.

Montes R.-C.F.J., Mohsen M.-G., Magdalena E.-W., Plinio M., Forces between different latex particles in aqueous electrolyte solutions measured with the colloidal probe technique, Microscopy Research and Technique, 80 (2017) 144–152.

Musoke M., Luckham P.F., Interaction forces between polyethylene oxide-polypropylene oxide ABA copolymers adsorbed to hydrophobic surfaces, Journal of Colloid and Interface Science, 277 (2004) 62–70.

Notley S.M., Biggs S., Craig V.S.J., Application of a dynamic atomic force microscope for the measurement of lubrication forces and hydrodynamic thickness between surfaces bearing adsorbed polyelectrolyte layers, Macromolecules, 36 (2003) 2903–2906.

Parker J.L., Claesson P.M., Attard P., Bubbles, cavities, and the long-ranged attraction between hydrophobic surfaces, The Journal of Physical Chemistry, 98 (1994) 8468–8480.

Parsons D.F., Walsh R.B., Craig V.S.J., Surface forces: Surface roughness in theory and experiment, The Journal of Chemical Physics, 140 (2014) 164701 (10pp). DOI: 10.1063/1.

4871412

Pashley R.M., DLVO and hydration forces between mica surfaces in Li^+, Na^+, K^+, and Cs^+ electrolyte solutions: A correlation of double-layer and hydration forces with surface cation exchange properties, Journal of Colloid and Interface Science, 83 (1981) 531–546.

Richetti P., Kékicheff P., Direct measurement of depletion and structural forces in a micellar system, Physical Review Letters, 68 (1992) 1951–1954.

Rutland M.W., Senden T.J., Adsorption of the poly(oxyethylene) nonionic surfactant C12E5 to silica: A study using atomic force microscopy, Langmuir, 9 (1993) 412–418.

Sander S., Mosley L.M., Hunter K.A., Investigation of interparticle forces in natural waters: Effects of adsorbed humic acids on iron oxide and alumina surface properties, Environmental Science and Technology, 38 (2004) 4791–4796.

Sharma A., Walz J.Y., Direct measurement of the depletion interaction in a charged colloidal dispersion, Journal of the Chemical Society, Faraday Transactions, 92 (1996) 4997–5004.

Sprakel J., Besseling N.A., Leermakers F.A., Cohen Stuart M.A., Equilibrium capillary forces with atomic force microscopy, Physical Review Letters, 99 (2007) 104504.

Stiernstedt J., Fröberg J.C., Tiberg F., Rutland M.W., Forces between silica surfaces with adsorbed cationic surfactants: Influence of salt and added nonionic surfactants, Langmuir, 21 (2005) 1875–1883.

Tabor D., Winterton R.H.S., Surface forces: Direct measurement of normal and retarded van der Waals forces, Nature, 219 (1968) 1120–1121.

Tabor R.F., Wu C., Grieser F., Dagastine R.R., Chan D.Y.C., Measurement of the hydrophobic force in a soft matter system, The Journal of Physical Chemistry Letters, 4 (2013) 3872–3877.

Taran E., Kanda Y., Vakarelski I.U., Higashitani K., Nonlinear friction characteristics between silica surfaces in high pH solution, Journal of Colloid and Interface Science, 307 (2007) 425–432.

Teh E.J., Leong Y.-K., Liu Y., Craig V.S.J., Walsh R.B., Howard S.C., High yield stress associated with capillary attraction between alumina surfaces in the presence of low molecular weight dicarboxylic acids, Langmuir, 26 (2010) 3067–3076.

Toikka G., Hayes R.A., Ralston J., Evidence of charge reversal from direct force measurements involving dissimilar metal sulfides in aqueous electrolyte, Journal of the Chemical Society, Faraday Transactions, 93 (1997) 3523–3528.

Vakarelski I.U., Brown S.C., Rabinovich Y.I., Moudgil B.M., Lateral force microscopy investigation of surfactant-mediated lubrication from aqueous solution, Langmuir, 20 (2004) 1724–1731.

Vakarelski I.U., Manica R., Tang X., O'Shea S.J., Stevens G.W., Grieser F., Dagastine R.R., Chan D.Y.C., Dynamic interactions between microbubbles in water, Proceedings of the National Academy of Sciences of the United States of America, 107 (2010) 11177–11182.

Verwey E.J.W., Overbeek J.T.G., Theory of the Stability of Lyophobic Colloids, Elsevier Publishing Company, Amsterdam, 1948.

Walsh R.B., Howard S.C., Nelson A., Skinner W.M., Liu G., Craig V.S.J., Model surfaces produced by atomic layer deposition, Chemistry Letters, 41 (2012a) 1247–1249.

Walsh R.B., Nelson A., Skinner W.M., Parsons D., Craig V.S.J., Direct measurement of van der Waals and diffuse double-layer forces between titanium dioxide surfaces produced by atomic layer deposition, The Journal of Physical Chemistry C, 116 (2012b) 7838–7847.

Weidenhammer P., Jacobasch H.-J., Investigation of adhesion properties of polymer materials by atomic force microscopy and zeta potential measurements, Journal of Colloid and Interface Science, 180 (1996) 232–236.

Wennerström H., Thuresson K., Linse P., Freyssingeas E., Long range attractive surface forces due to capillary-induced polymer incompatibility, Langmuir, 14 (1998) 5664–5666.

Wu B., Liu G., Zhang G., Craig V.S.J., Polyelectrolyte multilayers under compression: concurrent osmotic stress and colloidal probe atomic force microscopy, Soft Matter, 14 (2018) 961–968.

Yoon R.-H., Vivek S., Effects of short-chain alcohols and pyridine on the hydration forces between silica surfaces, Journal of Colloid and Interface Science, 204 (1998) 179–186.

Zhang J., Yoon R.-H., Mao M., Ducker W.A., Effects of degassing and ionic strength on AFM force measurements in octadecyltrimethylammonium chloride solutions, Langmuir, 21 (2005) 5831–5841.

Zhou Y., Gan Y., Wanless E.J., Jameson G.J., Franks G.V., Interaction forces between silica surfaces in aqueous solutions of cationic polymeric flocculants: Effect of polymer charge, Langmuir, 24 (2008) 10920–10928.

Authors’ Short Biographies

Naoyuki Ishida

Naoyuki Ishida is an Associate Professor in the Department of Applied Chemistry and Biotechnology at Okayama University. After completing his Ph.D. degree at Kyoto University in 2000, he spent 12 years at the National Institute of Advanced Industrial Science and Technology (AIST) as a researcher, and then started an academic carrier at Okayama University in 2012. His research interests include the direct measurement of surface forces in liquids, the measurement of interaction forces between biomolecules, and the characterization of stimuli-responsive polymers.

Vincent S. J. Craig

Prof. Vincent Craig leads the colloids group in the Department of Applied Mathematics at the Australian National University. He completed both his B.Sc. (Honours in Chemistry in 1992) and Ph.D. degrees (jointly in Applied Maths and Chemistry in 1997) at the ANU before postdoctoral positions at UC Davis, California and the University of Newcastle, NSW.

He was awarded an ARC Postdoctoral fellowship in 1998, an ARC Research Fellowship in 2001 and an ARC Future Fellowship in 2009. His research interests include the measurement of surface forces both quasi-static and dynamic, adsorption of surfactants and polymers, specific ion effects and nanobubbles.

Rational Design of Efficient Semiconductor-based Photocatalysts via Microdroplets: A Review†

Xiang He and Wei-Ning Wang *

[1] *Department of Mechanical and Nuclear Engineering, Virginia Commonwealth University, US*

Abstract

Semiconductor-based photocatalysis is regarded as an effective approach to harness solar energy to address the critical energy and environmental issues, such as fossil fuel shortage and climate change. The overall efficiency of the semiconductor-based photocatalysts can be further improved by creating nanocomposites with the incorporation of other functional materials, including metals, graphene, and metal-organic frameworks (MOFs). This critical review highlights the recent progress on the rational design of semiconductor-based photocatalysts via microdroplets, where the synthesis can be completed in a fast and controlled manner. Particular emphasis is given to three typical semiconductor-based composites, including semiconductor heterojunctions, crumpled graphene oxide/semiconductor composites, and MOF/semiconductor composites. The rationale behind the nanocomposite design, photocatalytic performance, and fundamental mechanisms are systematically discussed.

Keywords: heterogeneous catalysis, heterojunction, spray pyrolysis, crumpled graphene oxide, MOFs, CO_2 photoreduction

1. Introduction

The Earth's surface (i.e., the land and oceans) receives about 89 petawatts (PW = 10^{15} W) of solar energy from the total incoming solar radiation (Tian Y. and Zhao C.Y., 2013). This enormous sustainable energy has stimulated numerous applications, such as solar desalination, solar thermal electricity, and photocatalysis, to mitigate environmental deterioration and energy crisis. Among these strategies, semiconductor-based heterogeneous catalysis by harnessing solar energy, that is, the so-called photocatalysis, has drawn extensive attention since the first demonstration of photocatalytic water splitting by Fujishima and Honda in 1972 (Fujishima A. and Honda K., 1972). The fundamental mechanisms of the semiconductor-based photocatalysis have been widely explored and established by prior studies (Fujishima A. et al., 2008; Hoffmann M.R. et al., 1995; Linsebigler A.L. et al., 1995; Schneider J. et al., 2014). As schematically illustrated in **Fig. 1** (Wang H. et al., 2014), a typical process of the semiconductor-based photocatalysis is composed of several steps, including light absorption, charge generation, separation and migration, and redox reactions. Initially, the photons, with energy equal to or exceeding the bandgap energy of the semiconductors, induce the generation and separation of electron-hole (e^--h^+) pairs, where electrons are excited to the conduction band (CB), leaving holes in the valence band (VB). Subsequently, the electrons and holes migrate to the semiconductor surface and act as reductants and oxidants, respectively. The whole process is completed at very short time scales. Taking TiO_2 as an example, the characteristic times for the charge carriers' generation, migration, and interfacial charge transfer are at the time scales of femtoseconds, femtoseconds to picoseconds, and picoseconds to microseconds, respectively (Schneider J. et al., 2014).

The photocatalysis, however, still suffers from low efficiencies, resulting from several factors, including limited light absorption, inefficient molecule adsorption, and fast recombination of photo-induced charge carriers. To enhance the efficiency, a myriad of efforts have been devoted, such as creating photocatalysts by combining semiconductors with other functional materials (e.g., metals, metal oxides, graphene, and metal-organic frameworks (MOFs)). For instance, the formation of semiconductor heterojunctions, such as CdS/WO_3 (Jin J. et al., 2015), Fe_2O_3/Cu_2O (Wang J.-C. et al., 2015), CdS/C_3N_4 (Cao S.-W. et al., 2013), ZnO/CuO (Wang W.N. et al., 2015), and TiO_2/Cu_2O (He X. and Wang W.N., 2018), can enhance the light absorption and facilitate the charge separation. The enhanced charge separation can also be achieved by creating the semiconductor/graphene composites (Jiang Y. et al.,

---

† Received 18 May 2018; Accepted 17 July 2018

[1] Richmond, Virginia 23219, US
* Corresponding author: Wei-Ning Wang;
E-mail: wnwang@vcu.edu
TEL: +1-(804) 827-4306 FAX: +1-(804) 827-7030

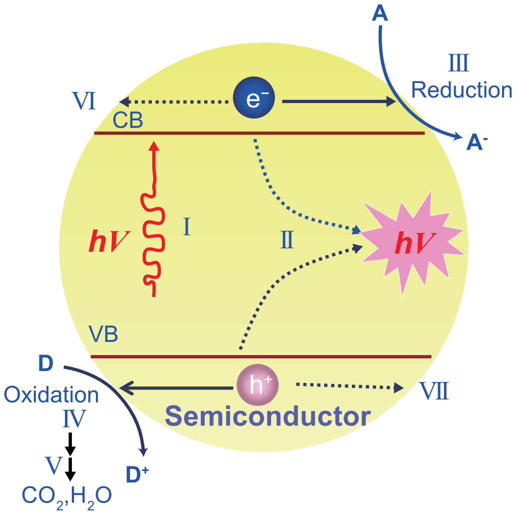

Fig. 1 Schematic illustration of the principle of semiconductor photocatalysis: (I) the formation of charge carriers by a photon; (II) the charge carrier recombination to liberate heat; (III) the initiation of a reductive pathway by a conduction-band electron; (IV) the initiation of an oxidative pathway by a valence-band hole; (V) the further thermal (e.g., hydrolysis or reaction with active oxygen species) and photocatalytic reactions to yield mineralization products; (VI) the trapping of a conduction band electron in a dangling surficial bond; (VII) the trapping of a valence-band hole at the surface of the semiconductor. Reprinted with permission from Ref. (Wang H. et al., 2014). Copyright: (2014) The Royal Society of Chemistry.

2014; Li N. et al., 2011; Nie Y. et al., 2016; Wang W.N. et al., 2014). While the incorporation of MOFs with semiconductors can improve the molecular adsorption (He X. et al., 2017a; He X. et al., 2017b). Given the aforementioned benefits of the formed semiconductor-based composite photocatalysts, a variety of methods have been applied, such as *in situ* growth (Cao S.-W. et al., 2013; He X. et al., 2017b; Wang D. et al., 2017), and chemical precipitation (Huang H. et al., 2015; Huang L. et al., 2009). It should be noted that, complicated steps and long reaction durations are inevitable in these methods.

On the other hand, a microdroplet-based aerosol process (i.e., the spray process, hereafter) is an alternative approach for the facile and fast synthesis of semiconductor-based photocatalysts. In a typical spray process, microdroplets serve as the reactors, which produce materials with controllable stoichiometry, tunable size, and high crystallinity in a fast manner (Okuyama K. and Wuled Lenggoro I., 2003; Wang W.N. et al., 2011a, 2013), offering lots of opportunities to improve the efficiency of catalysts. Given the growing studies regarding the design of semiconductor-based photocatalysts via microdroplets during the past years, it is of great importance to summarize the progress on this subject, which would promote the future development of photocatalysts and their applications to address energy and environmental issues. Therefore, a comprehensive review is provided here, covering the basics of the spray processes and the utilization of these processes for the rational design and facile synthesis of efficient photocatalysts, including semiconductor heterojunctions, graphene/semiconductor composites, and MOF/semiconductor composites.

2. Basics of the spray processes

A schematic illustration of a representative spray system for the synthesis of nanomaterials is shown in **Fig. 2**. The system generally comprises of an atomizer (or nebulizer), an aerosol reactor, and a sample collector. In a spray pyrolysis process, the atomizer produces microdroplets from the precursor solution. The microdroplets are then fed through the aerosol reactor (e.g., an electrical furnace, a flame reactor, or a plasma chamber) by the carrier gas, where the solvent evaporation, nucleation, pyrolysis, and crystallization occur to form the final products (Wang W.N. et al., 2011a). In a spray drying process, a colloidal suspension is used as the precursor and the evaporation-induced self-assembly (EISA) of the colloids inside the microdroplets (Boissiere C. et al., 2011; Iskandar F. et al., 2003; Lu Y.F. et al., 1999) is a major step to form the final particles. Finally, the products are collected by the collectors, such as filters and electrostatic precipitators.

Theoretical understanding of mass and heat transfer principles within the microdroplets is of paramount importance to guide the design and synthesis of materials by using the spray process. For example, great attention has been attracted to the design of functional materials via the EISA of nanoparticles within microdroplets by manipulating the solvent evaporation rate of the droplets (Boissiere C. et al., 2011; Iskandar F. et al., 2003; Lu Y.F. et al., 1999; Wang W.N. et al., 2011b). Practically, two key parameters, i.e., the size and temperature of the microdroplets play significant roles in the droplet-to-particle conversion process. Their dependence on time is governed by the equations as shown below:

In continuum regime (i.e., the Knudsen number, $Kn \ll 1$): (Xiong Y. and Kodas T.T., 1993)

$$\frac{\mathrm{d}R_\mathrm{d}}{\mathrm{d}t} = \frac{D_\mathrm{v} \cdot m}{R_\mathrm{d} \cdot \rho}(n_\infty - n_\mathrm{s}) \tag{1}$$

$$\frac{\mathrm{d}T_\mathrm{d}}{\mathrm{d}t} = \frac{3}{c_\mathrm{p} R_\mathrm{d}}[H_\mathrm{vap}\frac{\mathrm{d}R_\mathrm{d}}{\mathrm{d}t} + \frac{k_\mathrm{a}}{\rho R_\mathrm{d}}(T_\mathrm{c} - T_\mathrm{d})] \tag{2}$$

In free molecular regime (i.e., $Kn \gg 1$): (Fisenko S.P. et al., 2006)

$$\frac{\mathrm{d}R_\mathrm{d}}{\mathrm{d}t} = \frac{m}{\rho}[\frac{p_\mathrm{v}}{\sqrt{2\pi mkT_\mathrm{c}}} - \frac{p_\mathrm{s}}{\sqrt{2\pi mkT_\mathrm{d}}}] \tag{3}$$

where R_d is the radius of the microdroplet; t is time; D_v

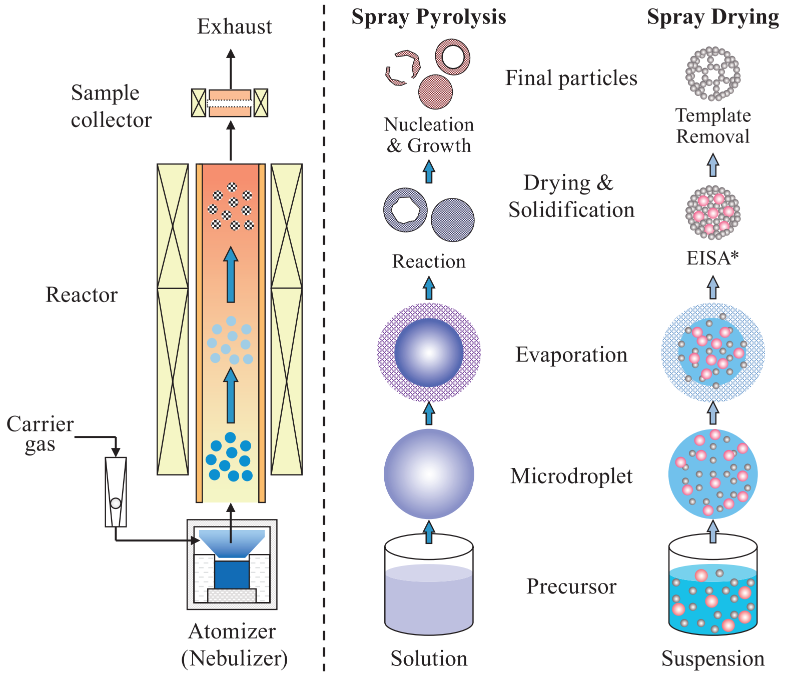

Fig. 2 Schematic illustration of particle synthesis by using the spray route. Left: an example of experimental setup; Right: typical particle formation pathways in spray pyrolysis and spray drying (EISA*: Evaporation-induced self-assembly).

$$\frac{\mathrm{d}T_\mathrm{d}}{\mathrm{d}t}=\frac{3\cdot\left[\frac{p_\mathrm{v}\left(c_\mathrm{p}T_\mathrm{c}+H_\mathrm{vap}+0.5kT_\mathrm{c}\right)}{\sqrt{mT_\mathrm{c}}}-\frac{p_\mathrm{s}\left(c_\mathrm{p}T_\mathrm{d}+H_\mathrm{vap}+0.5kT_\mathrm{d}\right)}{\sqrt{mT_\mathrm{d}}}+\frac{pT_\mathrm{c}\left(c_\mathrm{p}+0.5k\right)}{\sqrt{mT_\mathrm{c}}}-\frac{pT_\mathrm{d}\left(c_\mathrm{p}+0.5k\right)}{\sqrt{mT_\mathrm{d}}}\right]}{c_\mathrm{p}\rho R_\mathrm{d}\sqrt{2\pi k}}-\frac{3T_\mathrm{d}}{R_\mathrm{d}}\frac{\mathrm{d}R_\mathrm{d}}{\mathrm{d}t} \tag{4}$$

indicates the diffusion coefficient of solvent vapor in air; m is the molecule mass of the solvent; ρ represents the solvent density; n_∞ and n_s denote the number densities of solvent molecules at the infinite region and droplet surface, respectively; T_d and T_c are the temperatures of the droplet and the carrier gas, respectively; c_p and H_vap are the specific heat capacity and the specific latent heat of the solvent, respectively; k_a is the heat conductivity of air; k is the Boltzmann constant; p_v and p_s are the partial and saturated pressures of the solvent, respectively; p is the pressure of the carrier gas.

Several precursor and process parameters, including precursor concentration, viscosity, surface tension, droplet size, reactor pressure, temperature, and residence time, can be adjusted to control the properties of the final products (Hidayat D. et al., 2010; Wang W.N. et al., 2011a). For instance, the particle size is highly correlated with the concentration of the precursor solution (Nandiyanto A.B.D. et al., 2008). A governing equation describing this relationship has been developed based on the law of mass conservation (Iskandar F. et al., 2009; Wang W.N. et al., 2007; 2008; 2011b),

$$D_\mathrm{p}=D_\mathrm{d}\left(\frac{1}{(1-\varepsilon)}\sum\frac{M_iC_i}{\rho_i}\right)^{\frac{1}{3}} \tag{5}$$

where the D_p and D_d are the volume mean diameters of the particles and droplets, respectively; M, C and ρ indicate the molecular weight, concentration and density of components in the precursor solution, respectively; ε represents the porosity of the final particles. In a conventional spray process, a high precursor concentration usually results in a larger particle size.

The pressure also has a significant effect on the properties of the products. At ambient pressure, a conventional spray process follows a one-droplet-to-one-particle (ODOP) principle, which can only generate large particles (i.e., ~ micrometers) due to the limitation of the fine droplet formation (Wang W.N. et al., 2011a). On the other hand, reducing the gas pressure inside the tube furnace reactor (i.e., low-pressure spray process) can significantly fasten the evaporation of the solvents and thus the nucleation of the products (Ashgriz N., 2011; Wang W.N. et al., 2011c). Besides, the low-pressure environment can also limit the aggregation of the products. Therefore, the low-pressure spray process usually produces much smaller particles

(< 1 μm), following a one-droplet-to-multiple-particles (ODMP) principle (Ashgriz N., 2011; Hidayat D. et al., 2010; Wang W.N. et al., 2004; 2011a).

3. Design of photocatalysts via microdroplets

Based on the fundamental understanding of the spray process, various semiconductor-based photocatalysts have been designed via microdroplets, including semiconductor heterojunctions, graphene/semiconductor composites, and MOF/semiconductor composites.

3.1. Semiconductor heterojunctions

As mentioned above, the photocatalytic efficiency of semiconductors can be improved by combining the semiconductors with metals or other semiconductors to form heterojunctions, where the photoexcited charge carriers can be efficiently separated and migrated due to the built-in potential (Kittel C., 2005; Somorjai G.A. and Li Y., 2010; Wang D. et al., 2018). The doped metals typically have three functions in the enhancement, including (1) reducing the over-potential as cocatalysts, (2) promoting the separation of charge carriers by creating an electric field near the interface, and (3) increasing light absorption of semiconductors with plasmonic effect (Qu Y. and Duan X., 2013).

A large number of metal/semiconductor hybrid photocatalysts have been designed by using the spray pyrolysis process. In a typical synthesis procedure (**Fig. 3**), a mixture of metal ions and semiconductors are atomized to generate microdroplets. The microdroplets then pass through the reactor, where the metal ions are thermally reduced to metals and creating metal/semiconductor composite. For instance, a Pt/TiO_2 hybrid was directly synthesized by a single-step flame spray pyrolysis (Teoh W.Y. et al., 2005). The size of Pt can be adjusted by varying the concentration of the Pt precursor. The results show that the incorporation of Pt affects not only the crystallinity and surface area of TiO_2, but also the overall photocatalytic performance. The flame spray pyrolysis was also applied to synthesize noble metal/ZnO composites (e.g., Au/ZnO and Pt/ZnO) in one step (Pawinrat P. et al., 2009). The noble metals were homogeneously dispersed with average size between 3 and 7 nm. Species of the incorporated noble metals have significant effects on the photocatalytic activity. To be specific, the incorporation of Au can retard the recombination of charge carriers by modifying the Fermi level and trapping electrons. While, in the case of Pt, the electrons might be discharged into electrolytes. Similarly, Haugen et al. applied the spray pyrolysis technique to directly prepare metal (i.e., Ag and Au) doped TiO_2 photocatalysts (Haugen A.B. et al., 2011). The incorporated metals were found homogeneously distributed within the composite. The as-prepared composites exhibit promising performance in photodegradation of environmental pollutants. Zhao et al. designed Ag/TiO_2 composite photocatalysts by using an ultrasonic spray pyrolysis route (Zhao C. et al., 2012). The as-synthesized composite showed better dispersion of Ag, larger surface area, and thus a six-fold improvement in hydrogen production, in comparison to the one prepared by using the conventional wet-impregnation method. Recently, continuous spray pyrolysis was also applied to synthesize Au/CdS composite nanoparticles by using cadmium acetate, thiourea and chloroauric acid as the precursors (Kumar N. et al., 2014). The entire process is simple, fast and free of surfactants. The as-prepared hybrid nanoparticles exhibited enhanced photocatalytic efficiency as compared with bare CdS, which was mainly attributed to interfacial charge transfer as evidenced by the photoluminescence study. In addition, a Pt/WO_3 composite photocatalyst was designed by Okuyama's group (Widiyandari H. et al., 2012), where the existence of Pt could be indicated from the stacking-fault in the high resolution transmission electron microscopy (HR-TEM) image. The Pt in the composite acted as a capturer to snatch the photo-induced electrons and thus promotes the separation of the charge carriers. Another example of template-free synthesis of mesoporous Cu-TiO_2-SiO_2 nanocomposites by means of a spray route was demonstrated by Wang et al. (Wang W.N. et al., 2011b). As schematically shown in **Fig. 4A**, the nanocomposites were prepared from the aqueous suspensions of nanosized TiO_2 and SiO_2 colloids and copper nitrate via EISA. The particle size, composition, structure, and hence the catalytic performance were tailored by manipulating precursor properties and process parameters.

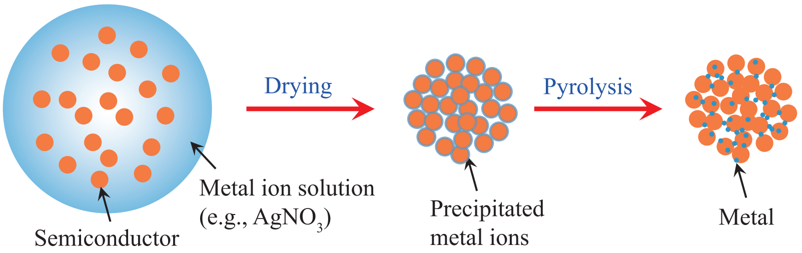

Fig. 3 Schematic illustration of the formation of metal/semiconductor composite.

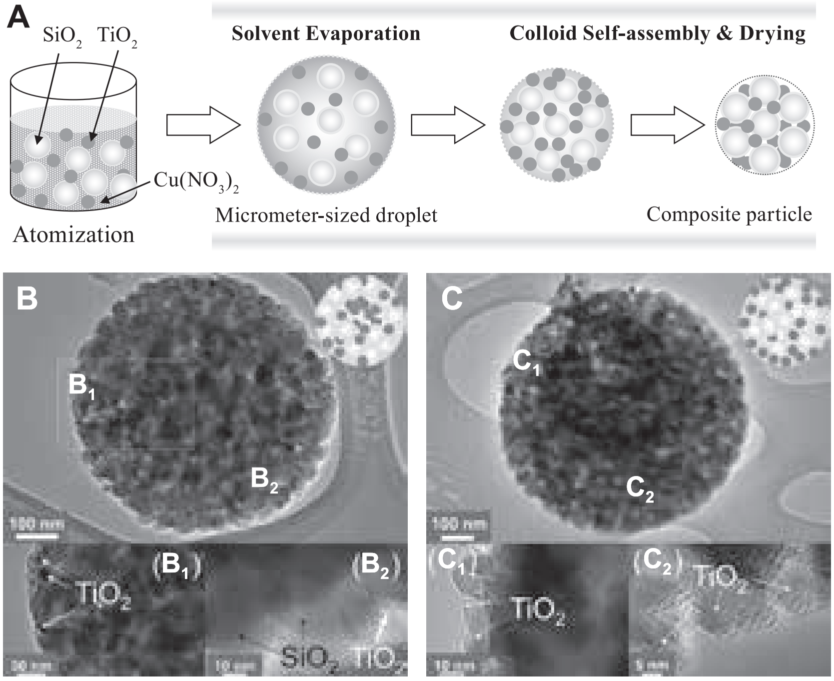

Fig. 4 (**A**) Possible formation mechanism of Cu-TiO_2-SiO_2 composites; (**B**) TEM and HR-TEM images of TiO_2–SiO_2 composite particles prepared at 400 (**B**) and 800 °C (**C**). Reprinted with permission from Ref. (Wang W.N. et al., 2011b). Copyright: (2011) The Royal Society of Chemistry.

For example, the reactor temperature was adjusted to control the solvent evaporation rate and hence the movement of TiO_2 nanocrystals within the microdroplets. As shown in **Figs. 4B** and **C**, more TiO_2 nanocrystals can be allocated on the surface of the nanocomposites by increasing the reactor temperature, resulting in enhanced catalytic performance. The self-assembly of the nanoparticles within the microdroplets was considered due to the thermophoretic force (Iskandar F. et al., 2003) and the Brownian motion (Hinds W.C., 1999). The thermophoretic force was created by the temperature gradient at the droplet surface, stemmed from the large heat transfer from droplet surface to gas stream due to the fast solvent evaporation.

Regarding the semiconductor/semiconductor (SS) heterojunctions, the photocatalytic efficiency is mainly facilitated by the migration of charge carriers. The migration pathways at the interfaces are highly dependent on the band structures of the components. Representative types of SS heterojunctions are summarized in **Fig. 5**, including type-II, p-n, and Z-scheme. Detailed discussion of the charge transfer with different heterojunctions has been comprehensively documented in a recent review (Low J. et al., 2017). Therefore, only a brief explanation for each heterojunction is presented here. In the case of type-II heterojunctions, with the staggered gap, the electrons are confined to the one component semiconductor, while the holes are confined to the other one (Zhou H. et al., 2012). This produces spatially localized charges and promotes separation of charge carriers and thus the photocatalytic efficiency. The migration of the charge carriers can be further accelerated with p-n heterojunctions created by p-type and n-type semiconductors. The accelerated charge separation is mainly due to the additional interfacial electric filed, generated by the initial diffusion of electrons and holes (He Z. et al., 2014). It should be noted that, the redox abilities of both type-II and p-n heterojunctions are decreased due to the migration of the charge carriers to lower redox potentials. One solution to this issue is to form Z-scheme heterojunctions, where the photogenerated electrons with lower reduction potential migrate to the other semiconductor and combine with the photogenerated holes with lower oxidation potential. Therefore, not only the separation of the charge carriers is enhanced, but also the charge carriers accumulate at higher redox potentials.

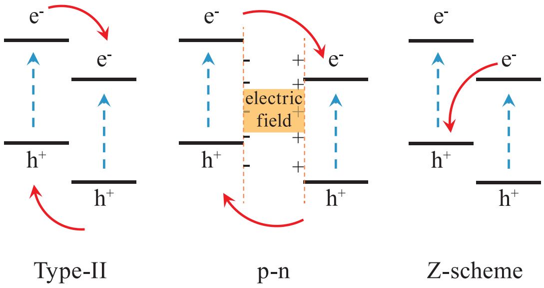

Fig. 5 Schematic illustration of the charge transfer patterns of typical semiconductor heterojunctions.

The synthesis of these heterojunctions is generally achieved by using wet-chemistry methods, involving complicated procedures and sometimes harsh chemicals (e.g., concentrated HNO_3) (Xu H. et al., 2012). In this regard, a spray process will be an excellent alternative for the fast and facile synthesis of such heterojunctions. For instance, ZnO/CeO_2 nanocomposites prepared by a flame spray pyrolysis were reported by Xiong et al. (Xiong Z. et al., 2017). The nanocomposites exhibited enhanced CO_2 photoreduction efficiency, mainly attributed to the existence of heterojunction and the co-existence of Ce^{4+}/Ce^{3+} pairs. A porous and spherical TiO_2/In_2O_3 composite photocatalyst was prepared by using an ultrasonic spray-assisted route (Li C. et al., 2014). The incorporation of small amount of In_2O_3 enhanced the light absorption and thus promoted the photocatalytic performance towards water treatment. The results also showed that excessive In_2O_3 would serve as the recombination center, which would undermine the photocatalytic performance (Li C. et al., 2014). Similarly, porous TiO_2/WO_3 microspheres were prepared by using a spray pyrolysis method, where the crystal phase of WO_3 played an important role in the photocatalytic efficiency (Arutanti O. et al., 2014; Yang J. et al., 2013). In addition to the particles, film composites can also be prepared. For example, Grbić et al. designed a TiO_2/WO_3 film composite with a thickness of ~ 1 μm on a stainless steel foil (Grbić B. et al., 2014). The increase of WO_3 contents induced positive shift of Ti_{2p} binding energy, suggesting the TiO_2/WO_3 interaction. More evidence about the interaction was obtained from Raman analysis, which demonstrated the minimal substitution of Ti by W in the crystal lattice. As a result, the photo-induced charge carriers can be effectively separated, leading to enhanced photocatalytic performance.

3.2. Crumpled graphene oxide/semiconductor composites

Graphene is two-dimensional (2D) nanosheet of sp^2-hybridized carbon atoms with an extended honeycomb network. The thickness of graphene is ultra-small (~ 0.35 nm) (Jiang Y. et al., 2016), while its mechanical, thermal and electrical properties are exceptional, stemming from the long-range π-conjugation (Allen M.J. et al., 2010; Wang W.N. and He X., 2016). Besides, the unique structure also grants graphene with huge specific surface area (~ 2600 m^2/g) (Stankovich S. et al., 2006), and extraordinary intrinsic electron mobility (~ 10^5 $cm^2/(Vs)$) (Novoselov K.S. et al., 2004), both of which are very appealing properties in photocatalysis processes. When combined with semiconductors, graphene promotes the adsorption of the reactants, and helps to increase the lifetime of charge carriers as sinks.

Typical semiconductors, which have been incorporated with graphene for photocatalysis, include TiO_2 (Liang Y. et al., 2010; Pan X. et al., 2012; Perera S.D. et al., 2012; Zhang Y. et al., 2011), Cu_2O (An X. et al., 2014; Tran P.D. et al., 2012; Zhang D. et al., 2016; Zou W. et al., 2016), $BiVO_4$ (Fu Y. et al., 2011; Ng Y.H. et al., 2010; Sun Y. et al., 2012), Fe_2O_3 (Han S. et al., 2014), CdS (Jia L. et al., 2011; Li Q. et al., 2011), CdSe (Oh W.-C. et al., 2011), MoS_2 (Chang K. et al., 2014; Min S. and Lu G., 2012), and C_3N_4 (Xiang Q. et al., 2011). With the incorporation of graphene, the overall photocatalytic efficiency has been significantly improved. For instance, Fe_2O_3/graphene composites were fabricated by Han et al. for the photodegradation of Rhodamine B (RhB) (Han S. et al., 2014), where the reaction rate of Fe_2O_3/graphene with an optimal ratio was found to be approximately four times higher than that of bare Fe_2O_3. The crucial factor for the improved efficiency is the enhanced charge transfer at the intimate and large contact interfaces.

Due to the hydrophobic nature and difficulties of handling of graphene nanosheets in solutions, the most commonly used precursor for graphene to fabricate graphene/semiconductor composites is the graphene oxide (GO) synthesized from the modified Hummers' method (Hummers Jr W.S. and Offeman R.E., 1958). Different from graphene, GO have massive oxygenated functional groups at the edges (e.g., carbonyl and carboxyl groups) and on the basal plan (e.g., epoxy and hydroxyl groups). These oxygenated groups enable GO dispersible in aqueous solution, which is a great feature for the further development of graphene-related composites. Whereas, these oxygenated groups also disrupt the electronic structure and break the π-conjugation of the pristine graphene sheets. As a result, the conductivity of the sheets decreased dramatically after the oxygenated functionalization. In order to restore to conductivity of the sheets, reduction process is necessary after the combination of GO and semiconductors. Thus, a more accurate term for the as-prepared composites should be reduced graphene oxide (RGO)/semiconductor photocatalysts.

Despite the remarkable properties, graphene or RGO sheets have an intrinsic problem, that is, they have a strong tendency to restack and aggregate due to the van der Waals attraction, which would significantly reduce the surface area and compromise the conductivity (Wang W.N. and He X., 2016). As pointed out by Yang et al. (Yang M.-Q. et al., 2014), because of the aggregation, the so-called semiconductor/graphene composites, under some circumstances, are essentially the same as the other semiconductor-carbon (e.g., fullerenes and carbon nanotubes) counterparts. Preventing the graphene or RGO sheets from aggregation is the key, which, however, is hardly achieved by using conventional methods. On the other hand, the spray process provides a promising strategy to address this issue by creating crumpled graphene balls (Chen Y. et al., 2018; El Rouby W.M.A., 2015; Gao

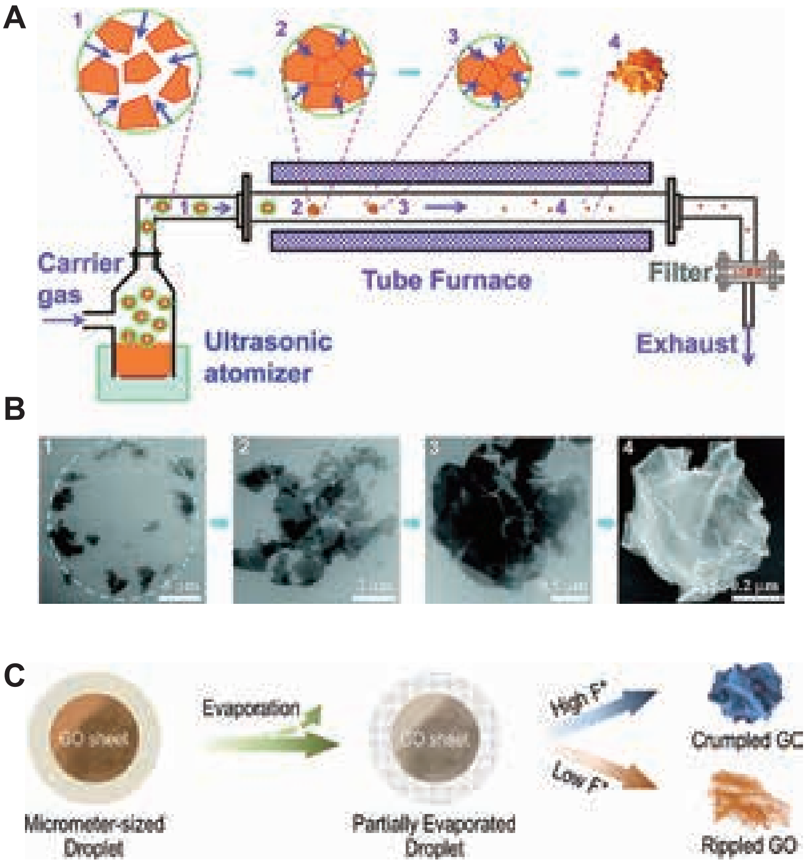

Fig. 6 Particles of crumpled GO sheets by rapid isotropic compression in evaporating aerosol droplets. (**A**) Schematic drawings illustrating the experimental setup and the evaporation-induced crumpling process. Aerosol droplets containing GO sheets were nebulized and rapidly evaporated by passing through a preheated tube furnace. (**B**) SEM images of four samples collected along the flying pathway from spots 1 to 4 showing the typical morphologies of deposited GO evolving from (**B1**) sparse sheets in a "coffee-ring" pattern, (**B2**) clustered and tiled sheets, (**B3**) aggregated sheets with extensive wrinkles, to (**B4**) the final 3D crumpled, ball-like particle. Reprinted with permission from Ref. (Luo J. et al., 2011). Copyright: (2011) American Chemical Society. (**C**) The possible formation mechanism of crumpled GO (F*: crumpling force). Reprinted with permission from Ref. (Wang W.N. et al., 2012). Copyright: (2012) American Chemical Society.

Z. et al., 2018; Luo J. et al., 2011; Ma X. et al., 2012; 2013; Mao B.S. et al., 2014; Mao S. et al., 2012; Wang W.N. et al., 2012; Zangmeister C.D. et al., 2012). During the solvent evaporation process, the 2D GO sheets inside the microdroplets will be crumpled into three dimensional (3D) spheres (i.e., crumpled graphene oxide, CGO) (**Figs. 6A and B**) by the confinement force resulting from the evaporation (**Fig. 6C**) (Wang W.N. et al., 2012). The unique crumpled structure enables CGO aggregation-resistant (Luo J. et al., 2011), while still maintains a high surface area (over 1500 m^2/g), 58.6 % of the original value (Cranford S.W. and Buehler M.J., 2011; El Rouby W.M.A., 2015), which offers stable anchoring sites for the semiconductor nanocrystals. One additional benefit of the spray process is that, the GO can simultaneously be thermally reduced during the spray process, providing CGO with desirable electrical conductivity.

Given all these advantages mentioned above, numerous studies have been carried out to synthesize the CGO/semiconductor composite photocatalysts (Carraro F. et al., 2015; Jiang Y. et al., 2014; Nie Y. et al., 2016; Wang W.N. et al., 2014). For instance, a spray approach was applied by Wang et al. to produce CGO/TiO_2 composites (**Fig. 7A**), where TiO_2 nanoparticles were encapsulated in the crumpled structure (Wang W.N. et al., 2014). The as-prepared composite demonstrated improved CO_2 photoreduction efficiency, and the mechanism was found to be the facilitated charge carrier separation induced by charge trapping ability of CGO. Besides, the CGO can also be amine functionalized to facilitate adsorption of CO_2, which would further enhance the CO_2 photoreduction efficiency (Nie Y. et al., 2016). In addition, a CGO/CoO hybrid catalyst (**Fig. 7B**) was designed with the similar strategy (Mao S. et al., 2014). Furthermore, Carraro et al. used a spray approach to fabricate an N-doped CGO/MoS_2 hybrid (**Fig. 7C**) in a fast and high-yield manner

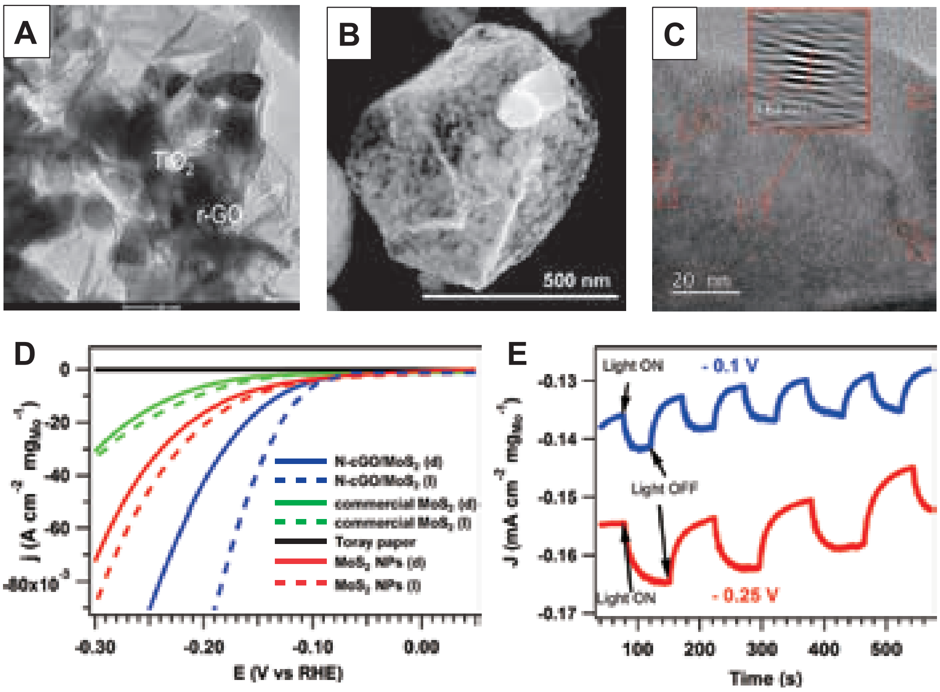

Fig. 7 (**A**) TEM images of a CGO/TiO_2 composite. Reprinted with permission from Ref. (Wang W.N. et al., 2014). Copyright: (2014) Mary Ann Liebert, Inc. (**B**) SEM image of a CGO–CoO nanocrystal. Reprinted with permission from Ref. (Mao S. et al., 2014). Copyright: (2014) The Royal Society of Chemistry. (**C**) HRTEM micrograph of N-CGO/MoS_2 nanohybrids presenting MoS_2 NPs highlighted by red squares. (**D**) Polarization curves (not iR corrected) in dark (**E**) J–t curves under light (ON) and dark (OFF) conditions at −0.1 and −0.25 V vs RHE and room temperature for N-CGO/MoS_2. Reprinted with permission from Ref. (Carraro F. et al., 2015). Copyright: (2015) American Chemical Society.

(Carraro F. et al., 2015), where the existence of N-doped CGO significantly enhanced photoelectrochemical production of hydrogen. The improved efficiency is mainly due to the enhanced charge carrier separation, as evidenced by the fact that N-doped CGO/MoS_2 hybrid has a much higher current density (**Figs. 7D and E**) compared with bare MoS_2 (Carraro F. et al., 2015). Materials, other than semiconductor photocatalysts, can also be supplemented in the crumpled structure to obtain additional functions. For example, Jiang et al. designed a ternary CGO/TiO_2/magnetite nanocomposite (Jiang Y. et al., 2014), which not only exhibited enhanced photocatalytic ability (20 times of the bare TiO_2), but also allowed easy recycle and reuse.

3.3. MOF/semiconductor composites

As a new class of porous materials, MOFs have attracted intense attention during recent years. MOFs are composed of metal cations and organic ligands (**Fig. 8A** (Lee Y.-R. et al., 2013)), and exhibit exceptional properties, including large surface area, high porosity and tunable structure. Schematic illustration of typical MOFs is shown in **Fig. 8B** (Dey C. et al., 2014), including HKUST-1 (HKUST: Hong Kong University of Science and Technology), MIL-101 (MIL: Material of Institute Lavoisier), and MOF-5. The occurrence of MOFs provides new opportunities to address the long-standing issues in semiconductor-based photocatalysis processes, including but not limited to the deficient gas adsorption, fast recombination of charge carriers, and poor molecule activation. To be specific, when incorporated with semiconductors, MOFs can help increase the adsorption of reactants, and provide more molecules to the surface of semiconductors (He X. et al., 2017a; He X. et al., 2017b). Besides, some MOFs possess coordinatively unsaturated metal sites (or simply called open metal sites), which could act as sinks for charge carriers or electron donors for molecule activation (He X. and Wang W.N., 2018).

Therefore, numerous efforts have been made to design MOF/semiconductor composites, including UiO-66/g-C_3N_4 (UiO: University of Oslo) (Wang R. et al., 2015), TiO_2/ZIF-8 (ZIF: zeolitic imidazolate framework) (Liu Q. et al., 2017; Zeng X. et al., 2016), and TiO_2/HKUST-1 (Li R. et al., 2014; Wang H. et al., 2016). For instance, UiO-66/g-C_3N_4 composite photocatalyst was designed for hydrogen production, and the composite shows significant enhancement in the production rate than that of the counterparts (Wang R. et al., 2015). The enhancement is found to be attributed to the effective separation of photo-induced charge carriers at the interface. Liu et al. integrated ZIF-8 onto the mesoporous TiO_2 nanobeads, and achieved pro-

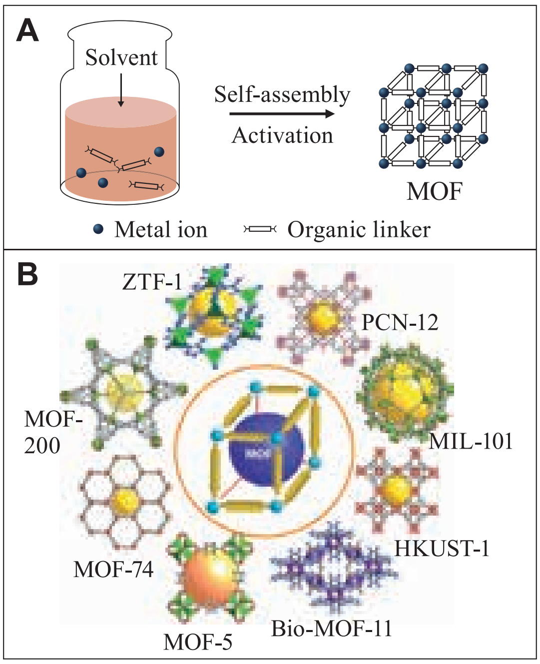

Fig. 8 (**A**) Conventional solvothermal synthesis of MOF structures. Reprinted with permission from Ref. (Lee Y.-R. et al., 2013). Copyright: (2013) Springer Nature. (**B**) Schematic representation of important reported MOFs which are known for high gas storage properties. Reprinted with permission from Ref. (Dey C. et al., 2014). Copyright: (2014) International Union of Crystallography.

moted performance for Cr(VI) reduction, which was attributed to not only the enhanced adsorption of Cr(VI), but also facilitated interfacial charge transfer (Liu Q. et al., 2017).

It should be noted that, the conventional synthesis of MOFs via wet-chemistry methods usually needs a long reaction duration, where the inefficient heat and mass transfer is inevitable. In this regard, the spray process is a promising alternate route for the rapid synthesis of MOFs (He X. et al., 2017a). As illustrated in **Fig. 9**, the rapid formation of MOFs within the microdroplets is primarily driven by the enhanced microscopic heat and mass transfer within the microdroplets. The theoretical calculations carried out by our group confirmed that the heat and mass transfer of the precursor within the microdroplets reaches equilibrium within milliseconds, which is much faster than that in bulk synthesis processes and benefits the subsequent nucleation and crystal growth (He X. et al., 2017a). In addition to the synthesis of pristine MOFs, the spray-drying process was applied to tune the properties of these porous materials or design MOF/semiconductor composite (Garcia Marquez A. et al., 2013; Garzón-Tovar L. et al., 2017; He X. et al., 2017a). For example, the spray-drying strategy was applied to produce 14 different discrete nanoMOFs, where the production time and cost were drastically reduced (Carné-Sánchez A. et al., 2013).

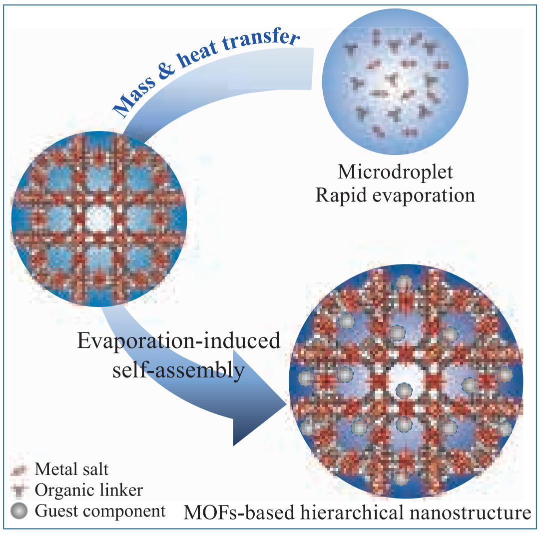

Fig. 9 Schematic illustration of the synthesis of MOFs-based hierarchical nanostructure via microdroplets. Reprinted with permission from Ref. (He X. et al., 2017a). Copyright: (2017) American Chemical Society.

Recently, $Cu_3(TMA)_2$ (or HKUST-1, TMA stands for trimesic acid) and $TiO_2/Cu_3(TMA)_2$ (or TiO_2/HKUST-1,) composite photocatalyst were designed by our group through the spray process (**Figs. 10A and B**) (He X. et al., 2017a). The precursor components were mixed within the microdroplets after the liquid atomization, which ensured the homogeneous distribution of TiO_2 in the matrix of HKUST-1 after the synthesis process (**Fig. 10B**). Besides, the incorporation of TiO_2 did not affect the crystallinity of MOF. While, the temperature played an important role in the properties of the as-prepared MOF/semiconductor composite, including crystallinity and surface chemistry. To be specific, the increased temperature (up to 300 °C) decreased the crystal size of the MOF due to the faster nucleation rate over growth rate. At higher temperatures (> 300 °C), the MOF turned amorphous as a result of the disintegration of the organic ligand, which is consistent with the changes in the color of the MOF. The surface chemistry of the MOF synthesized at various temperatures was evaluated by using Fourier transform infrared spectroscopy (FT-IR). At low synthesis temperature, the MOF has similar functional groups as the organic ligand (i.e., TMA). The slight difference in the FT-IR peaks between MOF and the ligand was due to the deprotonation and subsequent coordination of the organic ligand with the metal ions. When the temperature exceeded 300 °C, the adsorption bands weakened or disappeared because of the decomposition of the framework, which was in a good agreement with XRD analysis. The as-prepared HKUST-1/TiO_2 composite was applied for CO_2 photoreduction. The results revealed that HKUST-1 did not have the photocatalytic ability to reduce CO_2 but acted as a major adsorbent to capture CO_2 and H_2O molecules

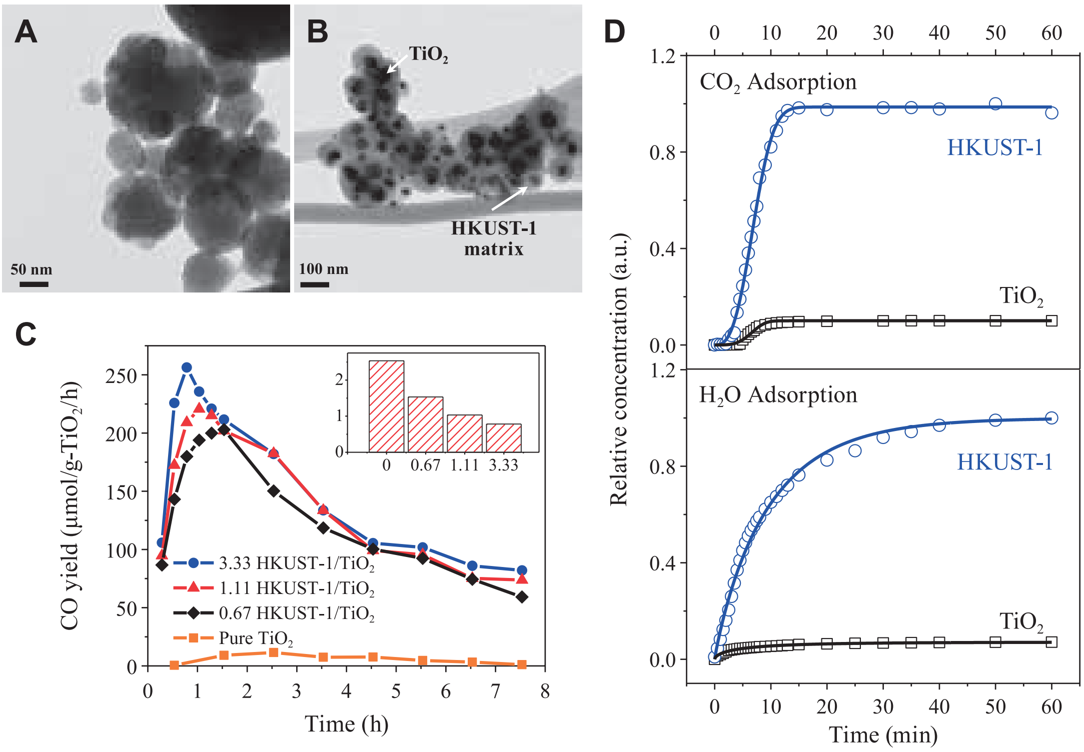

Fig. 10 TEM images of as-prepared (**A**) HKUST-1 and (**B**) HKUST-1/TiO_2; (**C**) CO_2 photoreduction analysis; (**D**) CO_2 and H_2O adsorption analysis. Reprinted with permission from Ref. (He X. et al., 2017a). Copyright: (2017) American Chemical Society.

(**Fig. 10D**), which subsequently improved the reaction rate and the production yield (**Fig. 10C**).

4. Conclusion and perspectives

In summary, a comprehensive review of recent development of semiconductor-based photocatalysts (i.e., semiconductor heterojunction, CGO/semiconductor and MOF/semiconductor nanocomposites) within microdroplets was provided. As being highlighted, the microdroplet-based process features simple procedure and rapid synthesis rate. The basics of the spray processes were discussed, and typical examples of the as-prepared semiconductor-based composite and their photocatalytic performance were presented. Despite the huge progress in photocatalyst design via microdroplets, further exploration is still needed. Taking the synthesis of MOF/semiconductor composite for an example, formation of the MOFs with high-nuclearity second-building units typically requires a long reaction time, which is a challenge for the rapid spray process and should be addressed in the prospective development. In terms of this, some techniques, such as computational and combinatorial chemistry as well as machine learning-based synthesis, might offer key assistance in the future.

Acknowledgements

The Donors of the American Chemical Society Petroleum Research Fund (ACS-PRF) (No. 57072-DNI10), the National Science Foundation (No. CMMI-1727553), and the Virginia Commonwealth University (VCU) Presidential Research Quest Fund (PeRQ) are greatly acknowledged for their financial support.

References

Allen M.J., Tung V.C., Kaner R.B., Honeycomb carbon: a review of graphene, Chemical Reviews, 110 (2010) 132–145.

An X., Li K., Tang J., Cu_2O/reduced graphene oxide composites for the photocatalytic conversion of CO_2, ChemSusChem, 7 (2014) 1086–1093.

Arutanti O., Nandiyanto A.B.D., Ogi T., Iskandar F., Kim T.O., Okuyama K., Synthesis of composite WO_3/TiO_2 nanoparticles by flame-assisted spray pyrolysis and their photocatalytic activity, Journal of Alloys and Compounds, 591 (2014) 121–126.

Ashgriz N., Handbook of atomization and sprays: theory and applications, Springer Science & Business Media, 2011, ISBN: 1441972641.

Boissiere C., Grosso D., Chaumonnot A., Nicole L., Sanchez C., Aerosol route to functional nanostructured inorganic and hybrid porous materials, Advanced Materials, 23 (2011)

599–623.

Cao S.-W., Yuan Y.-P., Fang J., Shahjamali M.M., Boey F.Y.C., Barber J., Joachim Loo S.C., Xue C., In-situ growth of CdS quantum dots on g-C_3N_4 nanosheets for highly efficient photocatalytic hydrogen generation under visible light irradiation, International Journal of Hydrogen Energy, 38 (2013) 1258–1266.

Carné-Sánchez A., Imaz I., Cano-Sarabia M., Maspoch D., A spray-drying strategy for synthesis of nanoscale metal–organic frameworks and their assembly into hollow superstructures, Nature Chemistry, 5 (2013) 203–211.

Carraro F., Calvillo L., Cattelan M., Favaro M., Righetto M., Nappini S., Píš I., Celorrio V., Fermín D.J., Martucci A., Agnoli S., Granozzi G., Fast one-pot synthesis of MoS_2/crumpled graphene p–n nanonjunctions for enhanced photoelectrochemical hydrogen production, ACS Applied Materials & Interfaces, 7 (2015) 25685–25692.

Chang K., Mei Z., Wang T., Kang Q., Ouyang S., Ye J., MoS_2/graphene cocatalyst for efficient photocatalytic H_2 evolution under visible light irradiation, ACS Nano, 8 (2014) 7078–7087.

Chen Y., Ren R., Wen Z., Ci S., Chang J., Mao S., Chen J., Superior electrocatalysis for hydrogen evolution with crumpled graphene/tungsten disulfide/tungsten trioxide ternary nanohybrids, Nano Energy, 47 (2018) 66–73.

Cranford S.W., Buehler M.J., Packing efficiency and accessible surface area of crumpled graphene, Physical Review B, 84 (2011) 205451(7pp). DOI: 10.1103/PhysRevB.84.205451

Dey C., Kundu T., Biswal B.P., Mallick A., Banerjee R., Crystalline metal-organic frameworks (MOFs): synthesis, structure and function, Acta Crystallographica Section B: Structural Science, Crystal Engineering and Materials, 70 (2014) 3–10.

El Rouby W.M.A., Crumpled graphene: preparation and applications, RSC Advances, 5 (2015) 66767–66796.

Fisenko S.P., Wang W.N., Wuled Lenggoro I., Okyuama K., Evaporative cooling of micron-sized droplets in a low-pressure aerosol reactor, Chemical Engineering Science, 61 (2006) 6029–6034.

Fu Y., Sun X., Wang X., $BiVO_4$–graphene catalyst and its high photocatalytic performance under visible light irradiation, Materials Chemistry and Physics, 131 (2011) 325–330.

Fujishima A., Honda K., Electrochemical photolysis of water at a semiconductor electrode, Nature, 238 (1972) 37–38.

Fujishima A., Zhang X., Tryk D.A., TiO_2 photocatalysis and related surface phenomena, Surface Science Reports, 63 (2008) 515–582.

Gao Z., Jin Z., Ji Q., Tang Y., Kong J., Zhang L., Li Y., Crumpled graphene prepared by a simple ultrasonic pyrolysis method for fast photodetection, Carbon, 128 (2018) 117–124.

Garcia Marquez A., Horcajada P., Grosso D., Ferey G., Serre C., Sanchez C., Boissiere C., Green scalable aerosol synthesis of porous metal-organic frameworks, Chemical Communications, 49 (2013) 3848–3850.

Garzón-Tovar L., Rodríguez-Hermida S., Imaz I., Maspoch D., Spray drying for making covalent chemistry: postsynthetic modification of metal–organic frameworks, Journal of the American Chemical Society, 139 (2017) 897–903.

Grbić B., Radić N., Stojadinović S., Vasilić R., Dohčević-Mitrović Z., Šaponjić Z., Stefanov P., TiO_2/WO_3 photocatalytic composite coatings prepared by spray pyrolysis, Surface and Coatings Technology, 258 (2014) 763–771.

Han S., Hu L., Liang Z., Wageh S., Al-Ghamdi A.A., Chen Y., Fang X., One-step hydrothermal synthesis of 2D hexagonal nanoplates of α-Fe_2O_3/graphene composites with enhanced photocatalytic activity, Advanced Functional Materials, 24 (2014) 5719–5727.

Haugen A.B., Kumakiri I., Simon C., Einarsrud M.-A., TiO_2, TiO_2/Ag and TiO_2/Au photocatalysts prepared by spray pyrolysis, Journal of the European Ceramic Society, 31 (2011) 291–298.

He X., Gan Z., Fisenko S., Wang D., El-Kaderi H.M., Wang W.N., Rapid formation of metal–organic frameworks (MOFs) based nanocomposites in microdroplets and their applications for CO_2 photoreduction, ACS Applied Materials & Interfaces, 9 (2017a) 9688–9698.

He X., Wang W.N., MOF-based ternary nanocomposites for better CO_2 photoreduction: roles of heterojunctions and coordinatively unsaturated metal sites, Journal of Materials Chemistry A, 6 (2018) 932–940.

He X., Yang C., Wang D., Gilliland Iii S.E., Chen D.-R., Wang W.N., Facile synthesis of ZnO@ZIF core-shell nanofibers: crystal growth and gas adsorption, CrystEngComm, 19 (2017b) 2445–2450.

He Z., Shi Y., Gao C., Wen L., Chen J., Song S., BiOCl/$BiVO_4$ p–n heterojunction with enhanced photocatalytic activity under visible-light irradiation, The Journal of Physical Chemistry C, 118 (2014) 389–398.

Hidayat D., Widiyastuti W., Ogi T., Okuyama K., Droplet generation and nanoparticle formation in low-pressure spray pyrolysis, Aerosol Science and Technology, 44 (2010) 692–705.

Hinds W.C., Aerosol Technology: Properties, Behavior, and Measurement of Airborne Particles, John Wiley & Sons, Inc., New York, 1999.

Hoffmann M.R., Martin S.T., Choi W., Bahnemann D.W., Environmental applications of semiconductor photocatalysis, Chemical Reviews, 95 (1995) 69–96.

Huang H., Han X., Li X., Wang S., Chu P.K., Zhang Y., Fabrication of multiple heterojunctions with tunable visible-light-active photocatalytic reactivity in BiOBr–BiOI full-range composites based on microstructure modulation and band structures, ACS Applied Materials & Interfaces, 7 (2015) 482–492.

Huang L., Peng F., Wang H., Yu H., Li Z., Preparation and characterization of Cu_2O/TiO_2 nano–nano heterostructure photocatalysts, Catalysis Communications, 10 (2009) 1839–1843.

Hummers Jr W.S., Offeman R.E., Preparation of graphitic oxide, Journal of the American Chemical Society, 80 (1958) 1339–1339.

Iskandar F., Gradon L., Okuyama K., Control of the morphology of nanostructured particles prepared by the spray drying of a nanoparticle sol, Journal of Colloid and Interface Science, 265 (2003) 296–303.

Iskandar F., Kim S.-G., Nandiyanto A.B.D., Kaihatsu Y., Ogi T., Okuyama K., Direct synthesis of hBN/MWCNT composite particles using spray pyrolysis, Journal of Alloys and Compounds, 471 (2009) 166–171.

Jia L., Wang D.-H., Huang Y.-X., Xu A.-W., Yu H.-Q., Highly durable n-doped graphene/CdS nanocomposites with enhanced photocatalytic hydrogen evolution from water under visible light irradiation, The Journal of Physical Chemistry C, 115 (2011) 11466–11473.

Jiang Y., Biswas P., Fortner J.D., A review of recent developments in graphene-enabled membranes for water treatment, Environmental Science: Water Research & Technology, 2 (2016) 915–922.

Jiang Y., Wang W.N., Biswas P., Fortner J.D., Facile aerosol synthesis and characterization of ternary crumpled graphene–TiO_2–magnetite nanocomposites for advanced water treatment, ACS Applied Materials & Interfaces, 6 (2014) 11766–11774.

Jin J., Yu J., Guo D., Cui C., Ho W., A hierarchical Z-scheme CdS–WO_3 photocatalyst with enhanced CO_2 reduction activity, Small, 11 (2015) 5262–5271.

Kittel C., Introduction to Solid State Physics, John Wiley & Sons, Inc., Hoboken, NJ, 2005.

Kumar N., Komarala V.K., Dutta V., In-situ synthesis of Au–CdS plasmonic photocatalyst by continuous spray pyrolysis and its visible light photocatalysis, Chemical Engineering Journal, 236 (2014) 66–74.

Lee Y.-R., Kim J., Ahn W.-S., Synthesis of metal-organic frameworks: a mini review, Korean Journal of Chemical Engineering, 30 (2013) 1667–1680.

Li C., Ming T., Wang J., Wang J., Yu J.C., Yu S.-h., Ultrasonic aerosol spray-assisted preparation of TiO_2/In_2O_3 composite for visible-light-driven photocatalysis, Journal of Catalysis, 310 (2014) 84–90.

Li N., Liu G., Zhen C., Li F., Zhang L., Cheng H.M., Battery performance and photocatalytic activity of mesoporous anatase tio_2 nanospheres/graphene composites by template-free self-assembly, Advanced Functional Materials, 21 (2011) 1717–1722.

Li Q., Guo B., Yu J., Ran J., Zhang B., Yan H., Gong J.R., Highly efficient visible-light-driven photocatalytic hydrogen production of CdS-cluster-decorated graphene nanosheets, Journal of the American Chemical Society, 133 (2011) 10878–10884.

Li R., Hu J., Deng M., Wang H., Wang X., Hu Y., Jiang H.-L., Jiang J., Zhang Q., Xie Y., Xiong Y., Integration of an inorganic semiconductor with a metal–organic framework: a platform for enhanced gaseous photocatalytic reactions, Advanced Materials, 26 (2014) 4783–4788.

Liang Y., Wang H., Sanchez Casalongue H., Chen Z., Dai H., TiO_2 nanocrystals grown on graphene as advanced photocatalytic hybrid materials, Nano Research, 3 (2010) 701–705.

Linsebigler A.L., Lu G.Q., Yates J.T., Photocatalysis on TiO_2 surfaces—principles, mechanisms, and selected results, Chemical Reviews, 95 (1995) 735–758.

Liu Q., Zhou B., Xu M., Mao G., Integration of nanosized ZIF-8 particles onto mesoporous TiO_2 nanobeads for enhanced photocatalytic activity, RSC Advances, 7 (2017) 8004–8010.

Low J., Yu J., Jaroniec M., Wageh S., Al-Ghamdi A.A., Heterojunction photocatalysts, Advanced Materials, 29 (2017) 1601694. DOI:10.1002/adma.201601694

Lu Y.F., Fan H.Y., Stump A., Ward T.L., Rieker T., Brinker C.J., Aerosol-assisted self-assembly of mesostructured spherical nanoparticles, Nature, 398 (1999) 223–226.

Luo J., Jang H.D., Sun T., Xiao L., He Z., Katsoulidis A.P., Kanatzidis M.G., Gibson J.M., Huang J., Compression and aggregation-resistant particles of crumpled soft sheets, ACS Nano, 5 (2011) 8943–8949.

Ma X., Zachariah M.R., Zangmeister C.D., Crumpled nanopaper from graphene oxide, Nano Letters, 12 (2012) 486–489.

Ma X., Zachariah M.R., Zangmeister C.D., Reduction of suspended graphene oxide single sheet nanopaper: the effect of crumpling, The Journal of Physical Chemistry C, 117 (2013) 3185–3191.

Mao B.S., Wen Z., Bo Z., Chang J., Huang X., Chen J., Hierarchical nanohybrids with porous CNT-networks decorated crumpled graphene balls for supercapacitors, ACS Applied Materials & Interfaces, 6 (2014) 9881–9889.

Mao S., Wen Z., Huang T., Hou Y., Chen J., High-performance bi-functional electrocatalysts of 3D crumpled graphene-cobalt oxide nanohybrids for oxygen reduction and evolution reactions, Energy & Environmental Science, 7 (2014) 609–616.

Mao S., Wen Z., Kim H., Lu G., Hurley P., Chen J., A general approach to one-pot fabrication of crumpled graphene-based nanohybrids for energy applications, ACS Nano, 6 (2012) 7505–7513.

Min S., Lu G., Sites for high efficient photocatalytic hydrogen evolution on a limited-layered MoS_2 cocatalyst confined on graphene sheets—the role of graphene, The Journal of Physical Chemistry C, 116 (2012) 25415–25424.

Nandiyanto A.B.D., Iskandar F., Okuyama K., Nanosized polymer particle-facilitated preparation of mesoporous silica particles using a spray method, Chemistry Letters, 37 (2008) 1040–1041.

Ng Y.H., Iwase A., Kudo A., Amal R., Reducing graphene oxide on a visible-light $BiVO_4$ photocatalyst for an enhanced photoelectrochemical water splitting, The Journal of Physical Chemistry Letters, 1 (2010) 2607–2612.

Nie Y., Wang W.N., Jiang Y., Fortner J., Biswas P., Crumpled reduced graphene oxide-amine-titanium dioxide nanocomposites for simultaneous carbon dioxide adsorption and photoreduction, Catalysis Science & Technology, 6 (2016) 6187–6196.

Novoselov K.S., Geim A.K., Morozov S.V., Jiang D., Zhang Y., Dubonos S.V., Grigorieva I.V., Firsov A.A., Electric field effect in atomically thin carbon films, Science, 306 (2004) 666–669.

Oh W.-C., Chen M., Cho K., Kim C., Meng Z., Zhu L., Synthesis of graphene-CdSe composite by a simple hydrothermal method and its photocatalytic degradation of organic dyes, Chinese Journal of Catalysis, 32 (2011) 1577–1583.

Okuyama K., Wuled Lenggoro I., Preparation of nanoparticles via spray route, Chemical Engineering Science, 58 (2003) 537–547.

Pan X., Zhao Y., Liu S., Korzeniewski C.L., Wang S., Fan Z., Comparing graphene-TiO_2 nanowire and graphene-TiO_2 nanoparticle composite photocatalysts, ACS Applied Materials & Interfaces, 4 (2012) 3944–3950.

Pawinrat P., Mekasuwandumrong O., Panpranot J., Synthesis of Au–ZnO and Pt–ZnO nanocomposites by one-step flame spray pyrolysis and its application for photocatalytic degradation of dyes, Catalysis Communications, 10 (2009) 1380–1385.

Perera S.D., Mariano R.G., Vu K., Nour N., Seitz O., Chabal Y., Balkus K.J., Hydrothermal synthesis of graphene-TiO_2 nanotube composites with enhanced photocatalytic activity, ACS Catalysis, 2 (2012) 949–956.

Qu Y., Duan X., Progress, challenge and perspective of heterogeneous photocatalysts, Chemical Society Reviews, 42 (2013) 2568–2580.

Schneider J., Matsuoka M., Takeuchi M., Zhang J., Horiuchi Y., Anpo M., Bahnemann D.W., Understanding TiO_2 photocatalysis: mechanisms and materials, Chemical Reviews, 114 (2014) 9919–9986.

Somorjai G.A., Li Y., Introduction to Surface Chemistry and Catalysis, Wiley, New York, 2010.

Stankovich S., Dikin D.A., Dommett G.H.B., Kohlhaas K.M., Zimney E.J., Stach E.A., Piner R.D., Nguyen S.T., Ruoff R.S., Graphene-based composite materials, Nature, 442 (2006) 282–286.

Sun Y., Qu B., Liu Q., Gao S., Yan Z., Yan W., Pan B., Wei S., Xie Y., Highly efficient visible-light-driven photocatalytic activities in synthetic ordered monoclinic $BiVO_4$ quantum tubes-graphene nanocomposites, Nanoscale, 4 (2012) 3761–3767.

Teoh W.Y., Mädler L., Beydoun D., Pratsinis S.E., Amal R., Direct (one-step) synthesis of TiO_2 and Pt/TiO_2 nanoparticles for photocatalytic mineralisation of sucrose, Chemical Engineering Science, 60 (2005) 5852–5861.

Tian Y., Zhao C.Y., A review of solar collectors and thermal energy storage in solar thermal applications, Applied Energy, 104 (2013) 538–553.

Tran P.D., Batabyal S.K., Pramana S.S., Barber J., Wong L.H., Loo S.C.J., A cuprous oxide-reduced graphene oxide (Cu_2O-rGO) composite photocatalyst for hydrogen generation: employing rGO as an electron acceptor to enhance the photocatalytic activity and stability of Cu_2O, Nanoscale, 4 (2012) 3875–3878.

Wang D., Li Z., Zhou J., Fang H., He X., Jena P., Zeng J.-B., Wang W.N., Simultaneous detection and removal of formaldehyde at room temperature: Janus Au@ZnO@ZIF-8 Nanoparticles, Nano-Micro Letters, 10 (2018) 4(11pp).

Wang D., Pillai S.C., Ho S.-H., Zeng J., Li Y., Dionysiou D.D., Plasmonic-based nanomaterials for environmental remediation, Applied Catalysis B: Environmental, 237 (2018) 721–741.

Wang H., Yu T., Tan X., Zhang H., Li P., Liu H., Shi L., Li X., Ye J., Enhanced photocatalytic oxidation of isopropanol by HKUST-1@TiO_2 core–shell structure with ultrathin anatase porous shell: toxic intermediate control, Industrial & Engineering Chemistry Research, 55 (2016) 8096–8103.

Wang H., Zhang L., Chen Z., Hu J., Li S., Wang Z., Liu J., Wang X., Semiconductor heterojunction photocatalysts: design, construction, and photocatalytic performances, Chemical Society Reviews, 43 (2014) 5234–5244.

Wang J.-C., Zhang L., Fang W.-X., Ren J., Li Y.-Y., Yao H.-C., Wang J.-S., Li Z.-J., Enhanced photoreduction CO_2 activity over direct Z-scheme α-Fe_2O_3/Cu_2O heterostructures under visible light irradiation, ACS Applied Materials & Interfaces, 7 (2015) 8631–8639.

Wang R., Gu L., Zhou J., Liu X., Teng F., Li C., Shen Y., Yuan Y., Quasi-polymeric metal–organic framework UiO-66/g-C_3N_4 heterojunctions for enhanced photocatalytic hydrogen evolution under visible light irradiation, Advanced Materials Interfaces, 2 (2015) 1500037(5pp). DOI: 10.1002/admi.201500037

Wang W.N., He X., Aerosol processing of crumpled graphene oxide-based nanocomposites for drug delivery, Current Pharmaceutical Design, 22 (2016) 2491–2500.

Wang W.N., Jiang Y., Biswas P., Evaporation-induced crumpling of graphene oxide nanosheets in aerosolized droplets: confinement force relationship, The Journal of Physical Chemistry Letters, 3 (2012) 3228–3233.

Wang W.N., Jiang Y., Fortner J.D., Biswas P., Nanostructured graphene-titanium dioxide composites synthesized by a single-step aerosol process for photoreduction of carbon dioxide, Environmental Engineering Science, 31 (2014) 428–434.

Wang W.N., Purwanto A., Lenggoro I.W., Okuyama K., Chang H., Jang H.D., Investigation on the correlations between droplet and particle size distribution in ultrasonic spray pyrolysis, Industrial & Engineering Chemistry Research, 47 (2008) 1650–1659.

Wang W.N., Tarafdar J.C., Biswas P., Nanoparticle synthesis and delivery by an aerosol route for watermelon plant foliar uptake, Journal of Nanoparticle Research, 15 (2013) 1417(13pp). DOI: 10.1007/s11051-013-1417-8

Wang W.N., Widiyastuti W., Lenggoro I.W., Kim T.O., Okuyama K., Photoluminescence optimization of luminescent nanocomposites fabricated by spray pyrolysis of a colloid-solution precursor, Journal of the Electrochemical Society, 154 (2007) J121–J128.

Wang W.N., Wu F., Myung Y., Niedzwiedzki D.M., Im H.S., Park J., Banerjee P., Biswas P., Surface engineered CuO nanowires with ZnO islands for CO_2 photoreduction, ACS Applied Materials & Interfaces, 7 (2015) 5685–5692.

Wang W.N., Itoh Y., Lenggoro I.W., Okuyama K., Nickel and nickel oxide nanoparticles prepared from nickel nitrate hexahydrate by a low pressure spray pyrolysis, Materials Science and Engineering B-Solid State Materials for Advanced Technology, 111 (2004) 69–76.

Wang W.N., Lenggoro I.W., Okuyama K., Preparation of nanoparticles by spray routes, in: Nalwa H.S. (Ed.) Encyclopedia of Nanoscience and Nanotechnology, American Scientific Publishers, 2011a, pp. 435–458.

Wang W.N., Park J., Biswas P., Rapid synthesis of nanostructured Cu-TiO_2-SiO_2 composites for CO_2 photoreduction by evaporation driven self-assembly, Catalysis Science & Technology, 1 (2011b) 593–600.

Wang W.N., Purwanto A., Okuyama K., Low-pressure spray pyrolysis, in: Ashgriz N. (Ed.) Handbook of Atomization and Sprays: Theory and Applications, Springer Science & Business Media, 2011, pp. 861–868.

Widiyandari H., Purwanto A., Balgis R., Ogi T., Okuyama K., CuO/WO_3 and Pt/WO_3 nanocatalysts for efficient pollutant degradation using visible light irradiation, Chemical Engineering Journal, 180 (2012) 323–329.

Xiang Q., Yu J., Jaroniec M., Preparation and enhanced visible-light photocatalytic H_2-production activity of graphene/C_3N_4 composites, The Journal of Physical Chemistry C, 115 (2011) 7355–7363.

Xiong Y., Kodas T.T., Droplet evaporation and solute precipitation during spray pyrolysis, Journal of Aerosol Science, 24 (1993) 893–908.

Xiong Z., Lei Z., Xu Z., Chen X., Gong B., Zhao Y., Zhao H., Zhang J., Zheng C., Flame spray pyrolysis synthesized ZnO/CeO_2 nanocomposites for enhanced CO_2 photocatalytic reduction under UV–Vis light irradiation, Journal of CO_2 Utilization, 18 (2017) 53–61.

Xu H., Xu Y., Li H., Xia J., Xiong J., Yin S., Huang C., Wan H., Synthesis, characterization and photocatalytic property of AgBr/$BiPO_4$ heterojunction photocatalyst, Dalton Transactions, 41 (2012) 3387–3394.

Yang J., Zhang X., Liu H., Wang C., Liu S., Sun P., Wang L., Liu Y., Heterostructured TiO_2/WO_3 porous microspheres: preparation, characterization and photocatalytic properties, Catalysis Today, 201 (2013) 195–202.

Yang M.-Q., Zhang N., Pagliaro M., Xu Y.-J., Artificial photosynthesis over graphene-semiconductor composites. Are we getting better?, Chemical Society Reviews, 43 (2014) 8240–8254.

Zangmeister C.D., Ma X., Zachariah M.R., Restructuring of graphene oxide sheets into monodisperse nanospheres, Chemistry of Materials, 24 (2012) 2554–2557.

Zeng X., Huang L., Wang C., Wang J., Li J., Luo X., Sonocrystallization of ZIF-8 on electrostatic spinning TiO_2 nanofibers surface with enhanced photocatalysis property through synergistic effect, ACS Applied Materials & Interfaces, 8 (2016) 20274–20282.

Zhang D., Hu B., Guan D., Luo Z., Essential roles of defects in pure graphene/Cu_2O photocatalyst, Catalysis Communications, 76 (2016) 7–12.

Zhang Y., Tang Z.-R., Fu X., Xu Y.-J., Engineering the unique 2D mat of graphene to achieve graphene-TiO_2 nanocomposite for photocatalytic selective transformation: what advantage does graphene have over its forebear carbon nanotube?, ACS Nano, 5 (2011) 7426–7435.

Zhao C., Krall A., Zhao H., Zhang Q., Li Y., Ultrasonic spray pyrolysis synthesis of Ag/TiO_2 nanocomposite photocatalysts for simultaneous H_2 production and CO_2 reduction, International Journal of Hydrogen Energy, 37 (2012) 9967–9976.

Zhou H., Qu Y., Zeid T., Duan X., Towards highly efficient photocatalysts using semiconductor nanoarchitectures, Energy & Environmental Science, 5 (2012) 6732–6743.

Zou W., Zhang L., Liu L., Wang X., Sun J., Wu S., Deng Y., Tang C., Gao F., Dong L., Engineering the Cu_2O–reduced graphene oxide interface to enhance photocatalytic degradation of organic pollutants under visible light, Applied Catalysis B: Environmental, 181 (2016) 495–503.

Authors' Short Biographies

Xiang He

Xiang He is a Ph.D. candidate in the Department of Mechanical and Nuclear Engineering at Virginia Commonwealth University, USA, under the supervision of Prof. Wei-Ning Wang since Fall 2015. He received his Master's and Bachelor's degrees in Environmental Engineering from Sun Yat-sen University, China, in 2015 and 2013, respectively. His research is focusing on the rational design of efficient photocatalysts for energy and environmental applications.

Wei-Ning Wang

Wei-Ning Wang is an Assistant Professor in the Department of Mechanical and Nuclear Engineering at Virginia Commonwealth University. He received Ph.D. degree in Chemistry and Chemical Engineering from Hiroshima University in 2006, and worked as a JSPS postdoctoral fellow from 2006 to 2007. He became an Assistant Professor at the same university from 2007 to 2009. He was a Postdoctoral Research Associate at Washington University in St. Louis from 2009 till 2012 and became Research Assistant Professor from 2013 to 2014. His research concerns functional materials design, synthesis and characterization, and their applications to address energy and environmental issues.

KONA Powder and Particle Journal No. 36 (2019) 215–223/Doi:10.14356/kona.2019017 Review Paper

Dense Discrete Phase Model Coupled with Kinetic Theory of Granular Flow to Improve Predictions of Bubbling Fluidized Bed Hydrodynamics †

Abolhasan Hashemisohi [1], Lijun Wang [2]* and Abolghasem Shahbazi [2]

[1] *Department of Computational Science and Engineering, North Carolina A&T State University, USA*
[2] *Department of Natural Resources and Environmental Design, North Carolina A&T State University, USA*

Abstract

Formation, expansion, and breakage of bubbles in single bubble and freely bubbling fluidized beds were studied using an improved hybrid Lagrangian-Eulerian computational fluid dynamics (CFD) approach. Dense Discrete Phase Model (DDPM) is a novel approach to simulate industrial scale fluidized bed reactors with polydispersed particles. The model uses a hybrid Lagrangian-Eulerian approach to track the particle parcels (lumping several particles in one computational cell) in a Lagrangian framework according to Newton's laws of motion. The interactions between particles are estimated by the gradient of solids stress solved in Eulerian grid. In this work, a single bubble fluidized bed and a freely bubbling fluidized bed were simulated using DDPM coupled with kinetic theory of granular flows (KTGF). The solid stress was improved to include both tangential and normal forces compared to current hybrid methods with the consideration of only normal stress or solid pressure. The results showed that solid pressure (normal forces) as the only contributor in solid stress would lead to overprediction of bubble size and overlooking of bubble breakage in a single bubble bed. Also, the results showed the improved model had a good prediction of bubble path in a freely bubbling bed compared to solid pressure-based model. It was shown that increasing the restitution coefficient increased the particle content of the bubbles and it lead to less breakage during the formation of the bubble. The probability of formation of bubbles was compared with experimental results and solid stress model showed less discrepancies compared to the solid pressure-based model.

Keywords: powder, particle, bubbling fluidized bed, hybrid Lagrangian-Eulerian, solid pressure, KTGF

---

1. Introduction

The vigorous mixing of powders and granules by means of a fluidization agent has introduced the fluidized beds as one of the best tools for powder processing specially when high heat and mass transfer rates are needed (Grace, 1990; Kunii and Levenspiel, 1991). However, design and scale up of fluidized beds are difficult due to the complex hydrodynamics for a bed charged with different particles and their interactions at different operating conditions (Cocco et al., 2017).

Mathematical modeling of fluidized beds can simplify the design procedure and scale up of the fluidized beds in a cost-effective approach (Cocco et al., 2017). Modeling of a fluidized bed was initially performed by fluidization models in which the bed is divided into two emulsion and bubble phases and semi-empirical correlations were used to predict the hydrodynamics properties such as bubble size and rising velocity, gas and solid volume fraction (Davidson and Harrison, 1966; Hashemi Sohi et al., 2012). These models are good to predict the outlet composition of the fluidized bed products, and can be integrated to the chemical plant process simulations (Singhal et al., 2017).

Recently, computational fluid dynamics (CFD) models attracted the attentions for the simulation of fluidized bed systems due to the progress in computational speed by the means of parallel computation in multiple CPUs and GPUs (Norouzi et al., 2017). There are two major CFD methods to simulate fluidized beds called Eulerian-Eulerian and Eulerian-Lagrangian. Eulerian-Eulerian methods consider both gas phase and solid phase as continuous phases and add the granular properties of the solid phase using with kinetic theory of granular flows (KTGF) (Ding and Gidaspow, 1990). These methods are good for the simulation of uniform particle systems in the reactors up to a pilot scale. Several researches have been conducted to reduce mesh dependency of these methods in a large scale using filter approaches and extending

---

† Received 25 April 2018; Accepted 17 July 2018
J-STAGE Advance published online 15 September 2018

[1,2] Greensboro, North Carolina 27411, USA
* Corresponding author: Lijun Wang
E-mail: lwang@ncat.edu
TEL: +1- 336-285-3833

application of these methods to polydisperse systems using mass balance equations (Igci et al., 2008; Radl and Sundaresan, 2014). On the other hand, Eulerian-Lagrangian methods consider a gas phase as a continuous phase and track the particles using newton laws. There are several ways to model the collisions between particles. Discrete element method (DEM) is the most accurate one in which spring dash soft sphere approach is used to model the particle collisions (Tsuji et al., 1993). However, it is impossible to simulate a large scale fluidized bed with billions of particle collisions. Therefore, different methods have been used to reduce the computational time (Benyahia and Galvin, 2010). Simplifying the collision between the particles and reducing the number of particles by grouping them into parcels are two major solutions. In the latter one, actual particles are grouped into computational parcels that are tracked in the Lagrangian framework. The event driven hard sphere and time driven hard sphere methods are simplified collision methods suffering from complex algorithm to search for particle-particle collisions in dense and polydisperse systems (Hoomans et al., 1996).

There is another approach to simplify the collisions using solid stress from Eulerian framework. In this method, the particle volume faction and velocity are mapped to the Eulerian grid and the solid stress tensor is calculated and mapped back to the particles. This approach has been used by several authors to study large scale fluidized beds for different applications due to their low computational cost. The most widely used method is called MP-PIC in which isotropic normal stress acting on each particle replaced the collisions (Fotovat et al., 2015; Snider, 2007).

$$\bar{\bar{\tau}}_{\mathrm{p}} = \frac{P_{\mathrm{s}}\theta_{\mathrm{p}}^{\beta}}{\max\left[\left(\theta_{\mathrm{cp}}-\theta_{\mathrm{p}}\right),\varepsilon\left(1-\theta_{\mathrm{p}}\right)\right]} \tag{1}$$

Where P_{s} is a positive constant with pressure unit, θ_{p} is the particle volume fraction, θ_{cp} is the particle volume fraction at close packing, β is a constant number arbitrarily specified with recommended values in the range 2 to 5, ε parameter is a small number to avoid singularity at close packing limits (Fotovat et al., 2015). Isotropic normal stress can avoid the particles from exceeding the maximum packing limit, but it does not consider the shear stresses. There are some studies in the literature reported that this approach caused weak prediction of the bubbling flow pattern in the bubbling fluidized beds (Liang et al., 2014; Lu et al., 2017).

On the other hand, Popoff and Braun (2007) introduced a dense discrete phase model in which, solid stress was calculated using kinetic theory of granular flows in Eulerian framework. However, the collision term in their work contained only the pressure like contributions (Normal pressure) of the complete stress tensor:

$$F_{\mathrm{collision}} = \frac{\nabla\cdot p_{\mathrm{p}}}{\rho} \tag{2}$$

Where p_{p} is the solid pressure, and ρ is the solid density.

This leads to unrealistic predictions at areas close to packing limit that occur in bubbling fluidized beds and high granular temperatures. Cloete et al. have studied the effect of shear and normal forces in a DDPM model on dilute systems with periodic boundary conditions (Cloete et al., 2012). However, the effect of shear and normal forces have not yet been studied in real physical systems specifically bubbling fluidized beds. Therefore, the tangential forces were added to the model to improve the DDPM model. Their effects on the formation of bubbles and hydrodynamics of bubbling beds were studied in this work.

2. Hybrid model equations

The mass and momentum conservation equations for the gas phase are given by:

$$\frac{\partial(\varepsilon_{\mathrm{g}}\rho_{\mathrm{g}})}{\partial t} + \nabla\cdot(\varepsilon_{\mathrm{g}}\rho_{\mathrm{g}}\vec{v}_{\mathrm{g}}) = 0 \tag{3}$$

and

$$\frac{\partial\left(\varepsilon_{\mathrm{g}}\rho_{\mathrm{g}}\vec{v}_{\mathrm{g}}\right)}{\partial t} + \nabla\cdot\left(\rho_{\mathrm{g}}\vec{v}_{\mathrm{g}}\vec{v}_{\mathrm{g}}\right) = -\varepsilon_{\mathrm{g}}\nabla p_{\mathrm{g}} + \nabla\cdot\bar{\bar{\tau}}_{\mathrm{g}}$$

$$+\varepsilon_{\mathrm{g}}\rho_{\mathrm{g}}\vec{g} + K_{\mathrm{DPM}}\left(\vec{v}_{\mathrm{DPM}} - \vec{v}_{\mathrm{g}}\right) \tag{4}$$

where ε_{g} is the volume fraction of gas phase, ρ_{g} is the density of gas phase, $\vec{v}_{\mathrm{g}}$ is the gas phase velocity, p_{g} is the pressure of gas phase, $\bar{\bar{\tau}}_{\mathrm{g}}$ is the shear tensor of the gas phase, K_{DPM} is the drag coefficient that can be calculated using a Gidaspow drag model (Ding and Gidaspow, 1990), $\vec{v}_{\mathrm{DPM}}$ is the particle averaged velocity of the discrete phase mapped to the cell center.

Particle velocity and position is calculated from Newton's law:

$$\frac{\mathrm{d}\vec{v}_{\mathrm{p}}}{\mathrm{d}t} = F_{\mathrm{D}}\left(\vec{v}_{\mathrm{g}} - \vec{v}_{\mathrm{p}}\right) + \frac{\vec{g}\left(\rho_{\mathrm{p}} - \rho_{\mathrm{g}}\right)}{\rho_{\mathrm{p}}} + \vec{F}_{\mathrm{interaction}} \tag{5}$$

Where $\vec{v}_{\mathrm{g}}$ is the gas velocity, $\vec{v}_{\mathrm{p}}$ is the particle velocity, F_{D} stands for drag force, and $\vec{F}_{\mathrm{interaction}}$ is the collision force between two particles calculated from:

$$\vec{F}_{\mathrm{interaction}} = \frac{1}{\rho_{\mathrm{p}}}\nabla\cdot\bar{\bar{\tau}}_{\mathrm{p}} \tag{6}$$

In the above equation, $\bar{\bar{\tau}}_{\mathrm{p}}$ is a solid stress including solid pressure, normal stress, and shear stress:

$$\bar{\bar{\tau}}_{\mathrm{p}} = -p_{\mathrm{p}}\bar{\bar{I}} + \varepsilon_{\mathrm{p}}\mu_{\mathrm{p}}\left(\nabla\vec{v}_{\mathrm{p}} + \nabla\vec{v}_{\mathrm{p}}^{T}\right)$$

$$+\varepsilon_{\mathrm{p}}\left(\lambda_{\mathrm{p}} - \frac{2}{3}\mu_{\mathrm{p}}\right)\nabla\cdot\vec{v}_{\mathrm{p}}\bar{\bar{I}} \tag{7}$$

where p_{p}, μ_{p}, and λ_{p} are solid pressure, shear viscosity, and bulk viscosity, respectively.

p_{p} is the solid pressure defined as:

$$p_{\mathrm{p}} = \varepsilon_{\mathrm{p}}\rho_{\mathrm{p}}\Theta + 2\rho_{\mathrm{p}}\left(1+e_{\mathrm{pp}}\right)\varepsilon_{\mathrm{p}}g_0\Theta \tag{8}$$

where first term is kinetic part and second term is collision part and g_0 is the radial distribution function that modifies the probability of collisions between particles in dense areas:

$$g_0 = \left[1 - \left(\frac{\varepsilon_{\mathrm{p}}}{\varepsilon_{\mathrm{p,max}}}\right)^{\frac{1}{3}}\right]^{-1} \tag{9}$$

The bulk viscosity is defined by (Lun et al., 1984):

$$\lambda_{\mathrm{p}} = \frac{4}{3}\varepsilon_{\mathrm{p}}\rho_{\mathrm{p}}d_{\mathrm{p}}g_0(1+e_{\mathrm{pp}})\left(\frac{\Theta}{\pi}\right)^{1/2} \tag{10}$$

The shear viscosity is defined by (Gidaspow, 1994):

$$\mu_{\mathrm{p}} = \frac{10\rho_{\mathrm{p}}d_{\mathrm{p}}\sqrt{\Theta\pi}}{96\varepsilon_{\mathrm{p}}g_0(1+e_{\mathrm{pp}})}\left[1 + \frac{4}{5}\varepsilon_{\mathrm{p}}g_0(1+e_{\mathrm{pp}})\right]^2$$

$$+\frac{4}{5}\varepsilon_{\mathrm{p}}\rho_{\mathrm{p}}d_{\mathrm{p}}g_0(1+e_{\mathrm{pp}})\left(\frac{\Theta}{\pi}\right)^{1/2} \tag{11}$$

where first term is kinetic part and second term is collisional part and Θ is granular temperature representing the kinetic energy of the fluctuating particles derived from kinetic theory model as:

$$\frac{3}{2}\left[\frac{\partial\left(\varepsilon_{\mathrm{p}}\rho_{\mathrm{p}}\Theta\right)}{\partial t} + \nabla\cdot\left(\varepsilon_{\mathrm{p}}\rho_{\mathrm{p}}\vec{v}_{\mathrm{p}}\Theta\right)\right]$$

$$= \bar{\bar{\tau}}_{\mathrm{p}} : \nabla\vec{v}_{\mathrm{p}} + \nabla\cdot\left(k_{\Theta}\nabla\Theta\right) - \gamma_{\Theta} + \phi_{\mathrm{pg}} \tag{12}$$

Equation (10) was solved algebraically by neglecting the convection and diffusion terms in the transport equation.

2.1 Simulation setup

The simulation setup has been created based on a single bubble injected by a jet in a fluidized bed at incipient fluidization conditions and a free bubbling fluidized bed with a uniform distributor to study the effect of solid stress on single and multiple bubbles. A fluidized bed of 0.57 m width, 0.005 m depth and 1.0 m height was initially filled with glass beads at a diameter of *500 μm* and a density of *2660 kg* m^{-3} up to a height of *0.5 m*. The background velocity for the whole bed was chosen to be 0.3 ms^{-1} to keep the bed close to its minimum fluidization velocity and a central jet with the velocity of 10 ms^{-1} was used to create the single bubble inside the bed (Kuipers, 1990). The computational column consists of 22903 quad cells. The second study was on a freely bubbling fluidized bed of 0.5 m width, 0.005 m depth and 1.0 m height filled with ballotini glass particles at a diameter of *700 μm* and density of *2500 kg* m^{-3} up to height of *0.3 m*. The superficial gas velocity for bubbling fluidization was 0.62 ms^{-1}, which equals to 1.75 times of the minimum fluidization velocity (Hernández, 2013). The computational column consists of 12600 cells. The rest of operating conditions can be found in the **Table 1**.

Table 1 Simulation parameters.

Quantity	Unit	Single bubble jet	Freely bubbling bed
Column dimensions	m	0.57 × 1 × 0.005	0.5 × 0.7 × 0.005
Static bed height	m	0.5	0.3
Gas density	$\frac{\mathrm{kg}}{\mathrm{m}^3}$	1.225	1.225
Gas Viscosity	$\frac{\mathrm{kg}}{\mathrm{m.s}}$	1.7894e−05	1.7894e−05
Particle diameter	µm	500	700
Particle Density	$\frac{\mathrm{kg}}{\mathrm{m}^3}$	2660	2500
Particle–particle restitution	—	0.9–0.99	0.9–99
Specularity coefficient	—	0.5	0.5
Number of parcel	—	400000	250000
Packing limit	—	0.6	0.6

The time averaged vertical velocity of particles, and averaged solid volume fraction were calculated by

$$V_{py}(x,y,z) = \sum_{i=1}^{N} C_i(x,y,z)V_{py,i}(x,y,z) \Big/ \sum_{i=1}^{N} C_i(x,y,z) \tag{13}$$

$$\varepsilon_p(x,y,z) = \sum_{i=1}^{N}\varepsilon_{p,i}(x,y,z)/N \tag{14}$$

where N is the number of snapshots, and C_i (0 inside the bubble and 1 in the emulsion phase) is an indicator defined by a threshold that separates bubbles from the dense phase which is recommended to be the arithmetic mean between the maximum and minimum solid volume fraction

(Hernández, 2013).

The probability of the formation of the bubbles were calculated according to:

$$\bar{B} = 1 - \sum_{i=1}^{N} C_i(x,y,z)/N \qquad (15)$$

The bed properties were averaged for 10 s from 20–30 s of the simulation with frequency of 10 frames/second.

3. Boundary condition and solver setup

Uniform gas velocity was selected at the inlet to represent the porous gas distributor coupled with a reflection boundary condition to prevent the tracking particles from draining out of the system. A pressure outlet was considered as the gas exit. No-slip boundary condition was selected for the gas phase on the bed wall and Johnson and Jackson boundary condition was used to calculate the granular phase shear force at the wall boundaries.

The commercial flow solver ANSYS Fluent 16 was used to complete the calculations. The phase coupled SIMPLE scheme was used for pressure–velocity coupling (Patankar, 1980). A second-order upwind scheme was used for momentum equation and QUICK method for the spatial discretization of volume fraction (Leonard and Mokhtari, 1990). The first order implicit transient formulation was used for temporal discretization.

4. Results and discussions

The particles were initially injected in the bed area by means of particle parcels. Since the sum of parcel diameters should be less than cell dimensions, the solid volume fraction can exceed the solid packing limit in a specific static bed height. Therefore, a minimum number of parcels should be injected to represent the static bed with a realistic volume fraction of particles and specific height.

Fig. 1 shows the mass of particle that should be injected to reach 0.6 solid volume fraction of 700-micron spherical particles in a static bed height of 0.3 m as a function of number parcels. It should be noticed that shapes of particles in this work were spherical according to spherical particles in the experimental data. The shapes of particle can affect minimum fluidization void fraction, mixing, and drag model. However, it was out scope of the current study, and we built our model with spherical assumption.

As it can be seen, at least 250,000 parcels were injected to achieve the same volume fraction of particles in the bed. In order to evaluate the effect of solid stress components on the predictions of DDPM model, single bubble fluidized and freely bubbling (multiple bubbles) fluidized beds were compared. As it is shown in **Fig. 2(b)** a single bubble like a mushroom is created when a solid normal pressure is responsible to simulate the particle collisions. Since there is no shear force, a single bubble without any breakage will continue to grow until it reaches the top of the bed. This approach is reasonable for the initial formation of a bubble using a high-speed jet because the normal forces imposed on the bubble are dominant. However, as the bubble rises in the bed, it will start to break in to three parts, and two bubbles will be formed as it can be seen in the experimental results **Fig. 2(a)**.

This can be explained by the fact that the shear forces will restrict the single bubble from further expansion and new bubbles will grow out of the original bubble. Therefore, the last two terms were added to the solid stress equation (5) to consider the shear stress generated by granular flow. As it can be seen in **Fig. 2(c)**, the bubble is broken into three parts which shows the effect of shear stresses on the bubble breakage. Moreover, a Eulerian-Eulerian simulation was performed using the same conditions and drag model as a control. The results showed the same trend of bubble breakage as the DDPM model with the consideration of a solid stress. However, the bubble breakage happens quickly in the bed compared to the experimental results, which can be related to the discontinuity in the drag model. After studying the effect of solid

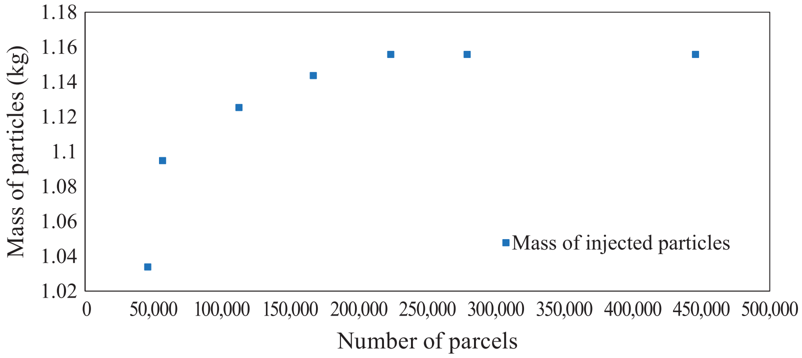

Fig. 1 Mass of particles as a function of number of parcels in a static bed at 0.3 m height.

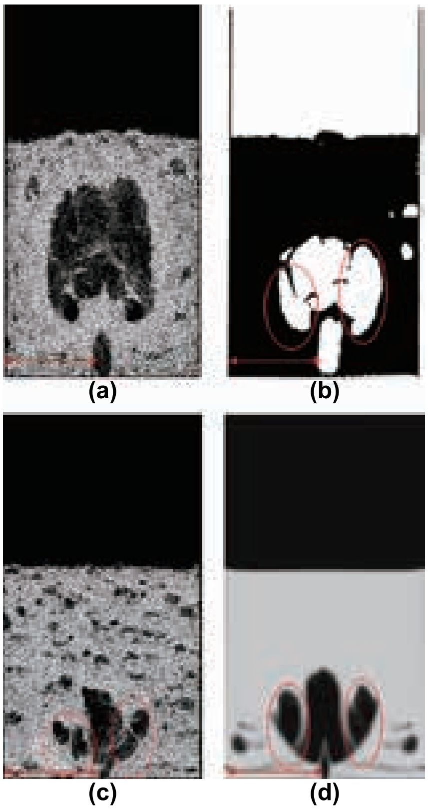

Fig. 2 Formation of single bubble in a thin fluidized bed after 0.4 s; (left to tight) (**a**) Solid pressure model (**b**) Experimental (Kuipers, 1990), (**c**) Complete solid stress (**d**) Euler-Euler model. Scale bar is 0.025 m.

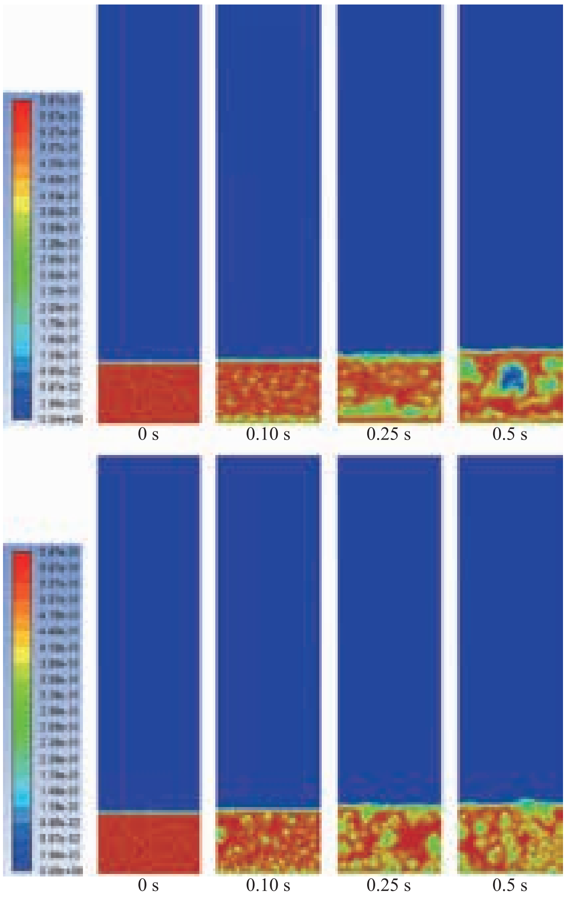

Fig. 3 The instantaneous solid volume fraction of freely bubbling bed at the initial condition simulated using complete solid stress (top) and solid pressure (bottom).

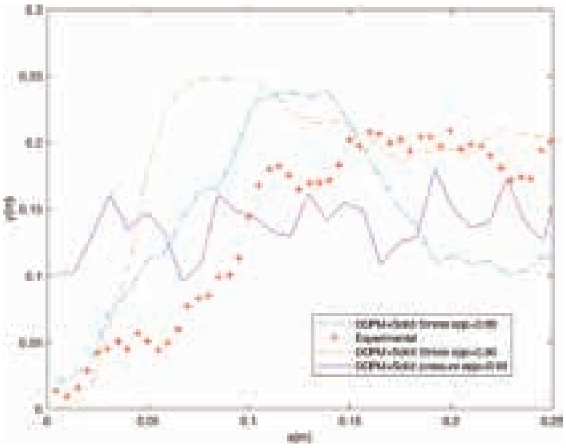

Fig. 4 Probability of formation bubbles at 0.25 m above the bed for model predictions and experimental from (Hernández, 2013).

stress on formation and expansion of a single bubble, a freely bubbling fluidized bed was simulated. The bubbling fluidized bed works at volume fractions close to packing limit which makes the tangential forces more important.

Fig. 3 shows the snapshots of a freely bubbling bed at the initial conditions using two different collision approaches. As it is shown, the large bubble is formed at the center of the bed as a result of breakage, expansion and coalescence of the bubbles when shear stress is included in the model. On the other hand, the bubbles are formed separately through the whole bed using the solid pressure approach. The number of bubbles and the solid volume fraction in the bubbles for the case with the solid pressure approach are higher. This means bubbles are initially formed but they cannot grow so much because the normal forces are smaller at lower velocities and shear forces are dominant.

On the other hand, after the first generation of bubbles is formed in the case with the solid stress approach, they are attached to each other to form a larger bubble and finally a central bubble passing through the bed is formed. **Fig. 4** shows the probability of the formation of bubble at the height of *0.25 m* above the bed. As it can be seen, the probability of the formation of bubble is fluctuating through the whole bed for the case that a solid pressure is used to represent the particle interactions. Coalescence and breakage of the bubbles are not observed in this case which confirms the previously reported results in the literature (Liang et al., 2014).

In addition, the performance of the model in prediction of the probability of formation bubbles was evaluated quantitatively using the root-mean-square deviation (RMSD), which is defined as follows:

$$RMSD = \sqrt{\frac{1}{N}\sum_{i=1}^{N}(Y_i - X_i)^2} \tag{16}$$

Where X_i and Y_i denote the experimental and predicted values respectively, and N is the number of observations. Also, coefficient of variation was used to calculate the relative discrepancy of the simulations:

$$CV = \frac{\sqrt{\frac{1}{N}\sum_{i=1}^{N}(Y_i - X_i)^2}}{\sqrt{\frac{1}{N}\sum_{i=1}^{N}(X_i)^2}} \tag{17}$$

Table 2 Discrepancy of simulations from experimental results using different collision models.

Quantity	Unit	Solid Stress, $e_{pp} = 0.90$	Solid Stress, $e_{pp} = 0.99$	Solid Pressure, $e_{pp} = 0.99$
RMSD	—	0.0031	0.0018	0.0224
CV	%	100	57.1	729

The calculated discrepancies between experimental and simulation results in the form of RMSD and CV are presented in the **Table 2**. As it can be seen in the table the model with solid pressure for prediction of particle collisions has several orders of magnitudes (729 %) deviation from the experimental results in prediction of bubble formation probability. The stress model results produce smaller discrepancies (100 and 57.1 %) which is in the same order of magnitude reported using Eulerian models in the literature (Hernández, 2013). The effect of front and back wall friction and the configuration of the distributor holes can be the reasons for current amount of discrepancies between simulation and experimental results.

When the tangential forces are involved in the solid stress in a DDPM model, the probability of the formation of the bubble is in a better agreement with experimental results and the predictions. It means that using a solid pressure to represent the collisions in the freely bubbling fluidized bed will not simulate the bubble pathways through the center of the bed and downward movement of particles. It should be noticed that in freely bubbling beds tangential forces are larger compared to a single bubble bed case formed by high velocity jet.

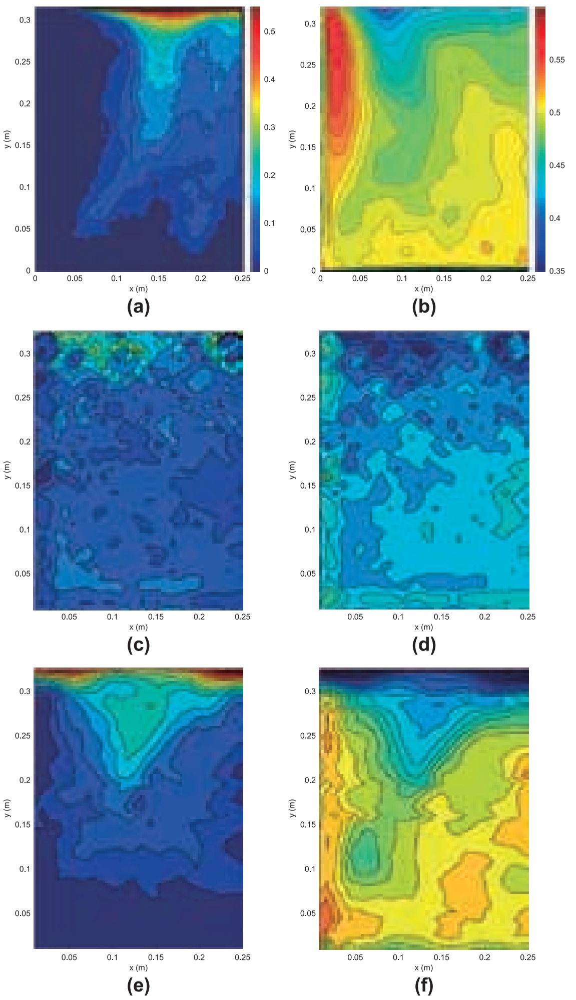

Fig. 5 Probability of formation of bubble $\overline{B}$ (left) and Solid volume fraction (right) (**a & b**) Experimental (Hernández, 2013) (**c & d**) Model with solid pressure (**e & f**) Model with solid stress.

Fig. 5(a, c, e) shows the contours of the bubble probability and the time averaged solid volume fraction in the bed for the experimental results and predictions. The bubbles are mostly formed in the center and close to the surface of the bed. The model with the solid stress approach was in a good agreement with the trend of experimental results, but the model with a solid pressure overpredicted the formation of bubbles at the bottom of the bed and underpredicts the formation of bubbles close to the surface of the bed. This is because tangential stresses are dominant in the case of bubbling fluidized beds and ignoring these terms would lead to unrealistic predictions in bubble formation which controls the bed hydrodynamics. The discrepancies between the model predictions and experimental results can be related to the non-ideal distribution of the air using a perforated distributor in the experiments. Moreover, the experimental time averaged solid volume fraction is compared with the model predictions in **Fig. 5(b, d, f)**. As it shows, the solids are close to packing limit beside the wall because the bubbles don't expand and rise in that region and their pathway is through the center of the bed. This is consistent with the well-known downward movements of particles beside the wall which inhabits the rising of bubbles.

One of the parameters in a solid stress is the coefficient

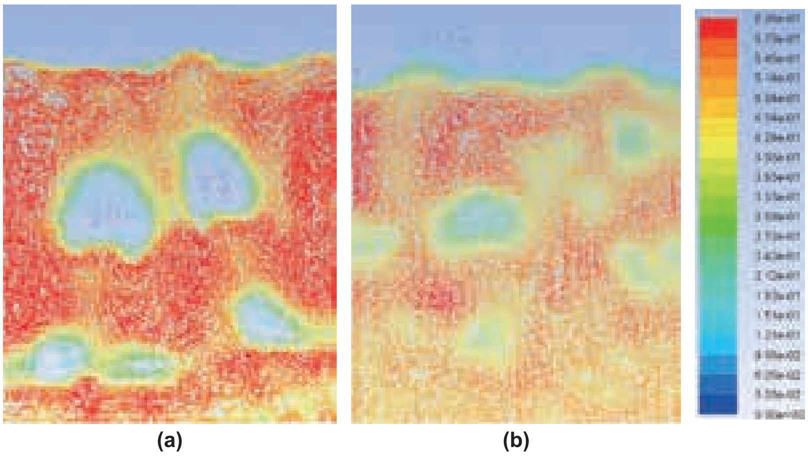

Fig. 6 DPM volume fraction as function of coefficient of restitution.

of restitution that can be determined by the elasticity of the particles. **Fig. 6** shows the effect of this parameter on hydrodynamics of bubbles. The particle volume fraction inside the bubbles was increased from 5 % to 30 % when coefficient of restitution was increased from 0.90 to 0.99. It means that fewer bubbles are formed when the coefficient of restitution is increased. As shown in **Fig. 6**, the formation of wake under the bubbles in the bubbling fluidized bed confirms the similar shapes of bubbles reported in the literature. High velocity of particles under a rising bubble creates low pressure under the bubble which leads to the deformation of the tracking bubbles. This is the main mechanism in formation of bubble path in bubbling fluidized beds.

The coefficient of restitution can be used as a controlling parameter to predict the fluidization of sticky particles using a DDPM model. It means that more segregation can happen between gas and solid phase when the coefficient of restitution is decreased.

5. Conclusion

Single bubble and freely bubbling fluidized beds were used to compare the ability of a modified hybrid Eulerian Lagrangian model for the prediction of single and multiple bubble behavior. Dense Discrete Phase Model coupled with kinetic theory of granular flows was used to build the model. Collision between particles were modeled by gradient of solid stress calculated from Eulerian grid and KTGF. The results showed that the predictions of bubbling hydrodynamics using hybrid Lagrangian Eulerian methods were improved using a solid stress compare to solid pressure-based model. It was found that eliminating the tangential forces in current state of the hybrid Lagrangian Eulerian method lead to discrepancies in predictions.

The results showed that a dense discrete phase model coupled with kinetic theory of a granular flow is a reliable approach if the solid stress is used in its complete form. It was shown that using a solid normal pressure instead of a solid stress will lead to the formation of round bubbles in a normal force dominant region in a fluidization bed. However, the formation of bubbles was underpredicted in the shear force dominant region. The probability of the formation of bubbles was deviating from experiments using the solid pressure approach in a freely bubbling fluidized bed.

Acknowledgements

This work was partially supported by the United States NSF-CREST Center for Bioenergy [Award No. HRD-1242152] and the United States Department of Energy [Award No. EE0003138].

References

Benyahia S., Galvin J.E., Estimation of numerical errors related to some basic assumptions in discrete particle methods, Industrial & Engineering Chemistry Research, 49 (2010) 10588-10605. DOI:10.1021/ie100662z

Cloete S., Johansen S.T., Amini S., Performance evaluation of a complete Lagrangian KTGF approach for dilute granular flow modelling, Powder Technology, 226 (2012) 43–52. DOI:10.1016/j.powtec.2012.04.010

Cocco R., Issangya A., Karri S.B.R., Freeman T., Jaeger H.M., Knowlton T.M., Small-scale particle interactions are having significant effects on global fluidized bed behavior, KONA Powder and Particle Journal, 34 (2017) 155–167. DOI:10.14356/kona.2017021

Cocco R., Fullmer W.D., Liu P., Hrenya C., CFD-DEM: Modeling the small to understand the large, Chemical Engineering Progress, 113 (2017) 38–45.

Davidson J.F., Harrison D., The behaviour of a continuously bubbling fluidised bed, Chemical Engineering Science, 21 (1966) 731–738. DOI:10.1016/0009-2509(66)87001-X

Ding J., Gidaspow D., A bubbling fluidization model using kinetic theory of granular flow, AIChE Journal, 36 (1990) 523–538. DOI:10.1002/aic.690360404

Fotovat F., Abbasi A., Spiteri R.J., de Lasa H., Chaouki J., A CPFD model for a bubbly biomass-sand fluidized bed, Powder Technology, 275 (2015) 39–50. DOI:10.1016/j.powtec.2015.01.005

Gidaspow D., Multiphase Flow and Fluidization: Continuum and Kinetic Theory Descriptions, 1 edition, Academic Press, Boston, 1994.

Grace J.R., High-velocity fluidized bed reactors, Chemical Engineering Science, 45 (1990) 1953–1966.

Hashemi Sohi A., Eslami A., Sheikhi A., Sotudeh-Gharebagh R., Sequential-based process modeling of natural gas combustion in a fluidized bed reactor, Energy & Fuels, 26 (2012) 2058–2067. DOI:10.1021/ef300204j

Hernández Jiménez F., Numerical and experimental investigations on pseudo-2D gas fluidized beds, Dissertation at the University Carlos III of Madrid, 2013.

Hoomans B.P.B., Kuipers J.A.M., Briels W.J., van Swaaij W.P.M., Discrete particle simulation of bubble and slug formation in a two-dimensional gas-fluidised bed: A hard-sphere approach, Chemical Engineering Science, 51 (1996) 99–118. DOI:10.1016/0009-2509(95)00271-5

Igci Y., Andrews IV A.T., Sundaresan S., Pannala S., & O'Brien T., Filtered two-fluid models for fluidized gas-particle suspensions, AIChE Journal, 54 (2008) 1431–1448. DOI:10.1002/aic.11481

Kuipers J.A.M., A two-fluid micro balance model for fluidized beds, Dissertation at the University of Twente, 1990.

Kunii D., Levenspiel O., Fluidization Engineering, Butterworth-Heinemann, 1991.

Leonard B., Mokhtari S., ULTRA-SHARP nonoscillatory convection schemes for high-speed steady multidimensional flow, NASA Technical Memorandum, (1990) 19900012254 (pp50).

Liang Y., Zhang Y., Li T., Lu C., A critical validation study on CPFD model in simulating gas – solid bubbling fluidized beds, Powder Technology, 263 (2014) 121–134. DOI:10.1016/j.powtec.2014.05.003

Lu L., Gopalan B., Benyahia S., Assessment of different discrete particle methods ability to predict gas-particle flow in a small-scale fluidized bed, Industrial and Engineering Chemistry Research, 56 (2017) 7865–7876. DOI:10.1021/acs.iecr.7b01862

Lun C.K.K., Savage S.B., Jeffrey D.J., Chepurniy N., Kinetic theories for granular flow: Inelastic particles in Couette flow and slightly inelastic particles in a general flowfield, Journal of Fluid Mechanics, 140 (1984) 223–256. DOI:10.1017/S0022112084000586

Norouzi H.R., Zarghami R., Mostoufi N., New hybrid CPU-GPU solver for CFD-DEM simulation of fluidized beds, Powder Technology, 316 (2017) 233–244. DOI:10.1016/j.powtec.2016.11.061

Patankar S., Numerical heat transfer and fluid flow, CRC Press, 1980. ISBN 9780891165224 - CAT# RT5223.

Popoff B., Braun M., A lagrangian approach to dense particulate flows, Proceedings of the ICMF 2007, 6th International Conference on Multiphase Flow, (2007) 11.

Radl S., Sundaresan S., A drag model for filtered Euler-Lagrange simulations of clustered gas-particle suspensions, Chemical Engineering Science, 117 (2014) 416–425. DOI:10.1016/j.ces.2014.07.011

Singhal A., Cloete S., Radl S., Quinta-Ferreira R., Amini S., Comparison of particle-resolved direct numerical simulation and 1D modelling of catalytic reactions in a packed bed, 12th International Conference on CFD in the Oil & Gas, Metallurgical and Process Industries (CFD2017), (2017).

Snider D.M., Three fundamental granular flow experiments and CPFD predictions, Powder Technology, 176 (2007) 36–46. DOI:10.1016/j.powtec.2007.01.032

Tsuji Y., Kawaguchi T., & Tanaka T., Discrete particle simulation of two-dimensional fluidized bed, Powder Technology, 77 (1993) 79–87. DOI:10.1016/0032-5910(93)85010-7

Authors' Short Biographies

Abolhasan Hashemisohi

Abolhasan Hashemisohi is a PhD candidate in Computational Science and Engineering at North Carolina Agricultural and Technical State University (NC A&T) under supervision of Dr. Lijun Wang and Dr. Abolghasem Shahbazi. He completed his Bachelor of science in Chemical Engineering (2009) University of Arak, Iran. He received his Master degree in Chemical Engineering with focus on Thermodynamics and Kinetics (2012). His research interests range from reaction engineering, heterogenous catalysis to simulation of fluidized bed reactors using computational fluid dynamics. He has been working on modelling and improvement of biomass gasification in fluidized beds since 2014 at NSF CREST Bioenergy Center.

Lijun Wang

Dr. Lijun Wang is a professor of biological engineering at NC A&T State University. Dr. Wang has 25 years of experience as a process engineer in advancing bioprocessing and biofuel research. He focuses his efforts on converting biomass into biofuels and bio-based products and improving energy efficiency in processing facilities. Wang is one of three thrust leaders of the interdisciplinary NSF CREST Bioenergy Center to lead the biomass gasification research. Dr. Wang is a licensed professional engineer in North Carolina and Nebraska and certified energy manager with the Association of Energy Engineers. He is a member of the American Institute of Chemical Engineers, and American Society of Agricultural and Biological Engineers.

Abolghasem Shahbazi

Abolghasem Shahbazi is a professor of Biological Engineering and the administrative director of CREST Center for Bioenergy. Dr. Shahbazi has over twenty-five years of experience with bioenergy and bioprocess engineering research. He has authored/co-authored more than 90 peer reviewed research publications and was the recipient of an interdisciplinary research award in 2014. He is a member of American Society for Agricultural and Biological Engineers. He has served as a member of Technical Advisory Committee for Biomass Research and Development Initiative for US Departments of Energy and Agriculture from April 2012 until December 2017. Dr. Shahbazi served as a co-chair of symposium on thermal and catalytic sciences for biofuels and bio-based products which was held at the Friday Center, UNC Chapel Hill, NC, November 2–4, 2016.

Uniform Spherical Graphene/Monocrystal-Copper Powder Fabricated by the Low Wettability of Liquid/Solid Interface †

Jimin Lyu, Ding-Bang Xiong*, Zhanqiu Tan, Genlian Fan, Qiang Guo, Cuiping Guo, Zhiqiang Li and Di Zhang

[1] *State Key Laboratory of Metal Matrix Composites, Shanghai Jiao Tong University, China*

Abstract

Uniform spherical graphene/monocrystal-copper powder is fabricated by melting bulk laminated composite. Graphene, in the form of reduced graphene oxide (rGO), is uniformly dispersed on the surface of monocrystal Cu particle. A mechanism is proposed based on liquid/solid interface interaction combining the surface energy minimization of liquid Cu and low wettability of molten Cu on graphene. The rGO/Cu composite powder exhibits good sphericity, and the size distribution could be controlled by the amount of rGO.

Keywords: graphene/copper, composite materials, powder technology, low wettability, liquid/solid interface

1. Introduction

Particle morphology control is fundamental in the processing of metal powders, such as 3-D printing, spraying, and injection moulding (Attia U.M. and Alcock J.R., 2011; Das S. et al., 2016; Lampke T. et al., 2011). Powders with good sphericity and controllable particle size are usually required. The most commonly methods used in fabricating metal powders are based on general surface tension principles at the liquid/gas or liquid/liquid interfaces, such as gas atomization (Ünal A., 1987), pressure-gas-atomization (Achelis L. and Uhlenwinkel V., 2008), water atomization (Seki Y. et al., 1990), and spark erosion in a dielectric fluid (Berkowitz A.E. et al., 2004). Recently, Lei et al. proposed a new method based on liquid/solid interface to prepare Cu-Zn powder (Lei C. et al., 2015). However, most of the methods mentioned above are developed for metal or alloy powders, and that for composite powder is still largely unexplored.

Graphene has attracted much attention owing to its excellent mechanical, electrical, and thermal properties. Graphene has shown a promising potential in improving the mechanical properties of metals (Cao M. et al., 2017; Kim Y. et al., 2013; Xiong D.B. et al., 2015), and also graphene wrapped micro-/nano-structures exhibit enhanced electrical and thermal conductivity (Goli P. et al., 2014; Mehta R. et al., 2015). Additionally, graphene encapsulated nanoparticles show a competitive advantage in lithium-ion batteries (Zhang J. et al., 2013). Therefore, graphene/metal composite powder may have great potential in the applications of metal materials processed by the technologies of 3-D printing, spraying, and injection molding. However, fabricating the composite powders is still a challenge. In this article, we proposed a new method based on liquid/solid interface interaction to fabricate graphene/copper composite powder with good sphericity and controlled size distribution.

2. Experimental

2.1 Preparation of rGO/Cu bulk laminated composite

The rGO/Cu bulk laminated composites were fabricated based on a modified flake powder metallurgy (Cao M. et al., 2017). Atomized pure copper powders (99.99 % purity, with an average particle size of 44 μm) were ball-milled to Cu flakes in pure ethanol in a stainless steel mixing jar. The mass ratio of the powder to milling balls (100 % stainless steel milling balls with diameter of 6 mm) is 1:20. The ball milling speed is 423 rpm and the ball milling time is 5 h. The as-prepared Cu flakes (30 g) were coated with polyvinyl alcohol (PVA) for surface modification by stirring them in 250 mL 1 wt% PVA aqueous solution and subsequent centrifugation and

---

† Received 26 September 2017; Accepted 18 December 2017

[1] 800 Dongchuan Road, Shanghai 200240, China

* Corresponding author: Ding-Bang Xiong;
E-mail : xiongdingbang@sjtu.edu.cn
TEL: +86-21-5474-2348 FAX: +86-21-3420-2749

washing with deionized water. Then the PVA modified Cu flakes were dispersed in 250 mL deionized water, and 18.0 mL (for 0.5 vol%) or 54.5 mL (for 1.5 vol%) GO aqueous suspension was added into the slurry. The GO suspension (1 mg/mL) with the lateral size of 400–500 nm and the thickness of 1 nm was prepared straight from ultrasound treating graphite oxide (Li Z. et al., 2014). The amount of GO added was calculated by characterizing the GO density to 1.06 g/cm^3 (Rafiee M.A. et al., 2009).

After stirred for 1 h, filtered and then dried in vacuum at 60 °C, the as-obtained GO/Cu composite flakes were reduced under 5 % H_2/Ar flow at 450 °C for 2 h. Finally, the bulk laminated composites were obtained by reducing the GO/Cu composite flakes (rGO/Cu) and assembling them in a graphite die (Φ30 mm), and then hot-pressed at 900 °C and 50 MPa for 20 min under Ar atmosphere.

2.2 Preparation of spherical rGO/Cu powder

The rGO/Cu bulk laminated composites were treated in a tube furnace in N_2 atmosphere at 1100 °C for 30 min with a heating rate of 10 °C/min. The rGO/Cu powder was obtained by natural cooling to room temperature under N_2 atmosphere.

2.3 Characterization of spherical rGO/Cu powder

The rGO/Cu powders were mounted in thermosetting resin and then polished by a vibratory polisher for microstructure and elemental analysis on cross section. Microstructure characterization was performed via field-emission scanning electron microscopy (FE-SEM, Sirion 200) equipped with an energy dispersive spectrometer (EDS, INCA X-Act) for compositional analysis. The electron backscatter diffraction (EBSD) was carried out in SEM (NOVA NanoSEM 230). The Raman spectra was performed at dispersive Raman microscope (Senterra R200-L) with a 532 nm laser excitation.

3. Results and discussions

Fig. 1 shows the SEM image of the GO/Cu composite powder flakes, where GO sheets are uniformly dispersed on the surface of Cu flakes. The white folds (black arrows) are signs of the wrinkling and existence of graphene. Usually, the GO sheets are very thin and almost transparent, but the transferred or absorbed graphene on substrates has line defects and disruptions such as wrinkles, ripples and foldings. And the surface roughness is also different with or without covered GO. The area with covered GO (black circle) is smoother than without covered GO. Combining the two aspects, we can identify the GO sheets and their uniform dispersion on the Cu surface.

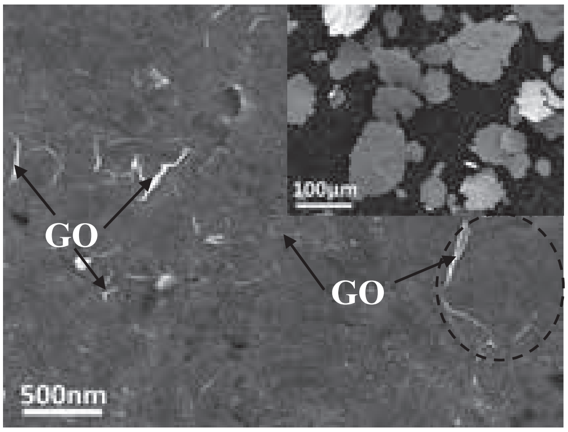

Fig. 1 SEM micrographs of GO/Cu composite flakes, showing GO was uniformly dispersed on the surface of Cu flakes.

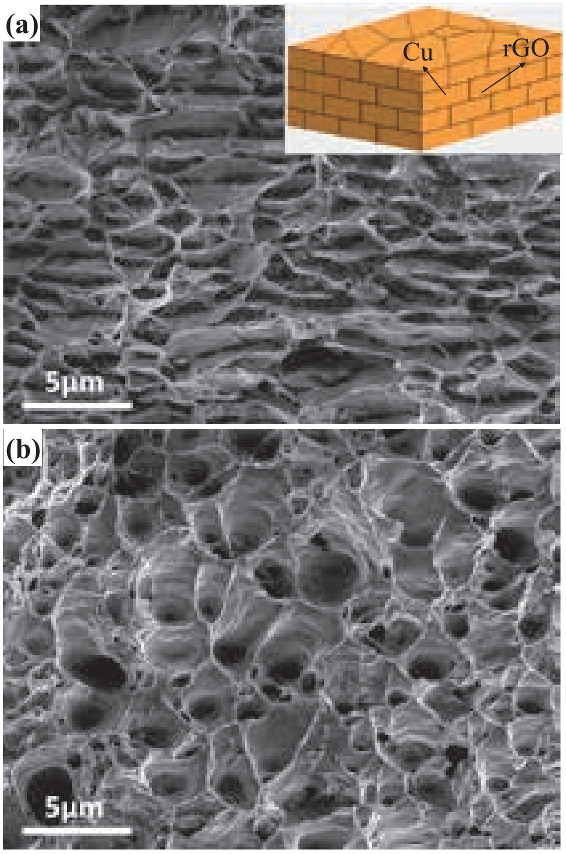

Fig. 2 **(a)** SEM micrograph of the fracture surface of bulk rGO/Cu composites fabricated by assembling the flakes, showing a laminated structure. **(b)** SEM micrograph of the fracture surface of pure copper fabricated by flake powder metallurgy.

The GO/Cu composite flakes have large aspect ratio (Lateral size and thickness ratio is about 200–400), which is beneficial for forming laminated structure, as shown in the fracture surface of the rGO/Cu bulk composite (**Fig. 2a**). The existence of rGO prevents the Cu flakes from growing up perpendicular to the lamella during the hot-pressing process. As revealed by the fracture surface of pure copper fabricated by flake powder metallurgy in **Fig. 2b**, the Cu flake cannot hold its laminated structure due to grain growth during heat treatment. The homogenous laminated structure is crucial for fabricating uniform spherical rGO/Cu composite powder. And the degree of the homogeneity of the laminated structure mainly characterized by the homogeneity of lamellar distance. The more uniform the lamellar distance is, the more conducive to the preparation of the uniform rGO/Cu powder. The lamellar distance in **Fig. 2a** is relatively uniform, which is about 0.5 μm.

Fig. 3 shows the SEM images of rGO/Cu powders fabricated via melting the bulk laminated composites with rGO content of 0.5 vol% (**Fig. 3a**) and 1.5 vol% (**Fig. 3b**). The rGO/Cu powders exhibit good sphericity, and the degree of sphericity computed by image processing is 0.9 ± 0.1 for both two rGO content. The rGO sheets are homogeneously dispersed on the particle surface and the coverage rate is about 50 %–60 % for 0.5 vol% and >100 % (Graphene sheets overlap with each other in some extent) for 1.5 vol%. The distributions of particle size scaled by the diameter of the powders are shown in **Fig. 3c** and **d**. The average particle sizes ($\bar{d}$) of the 0.5 vol%–powder ($\bar{d}_{0.5}$) and the 1.5 vol%–powder ($\bar{d}_{1.5}$) are 40.6 μm and 39.7 μm, respectively, and have no significant difference to each other. As discussed later, the particle size may depend on that of original Cu powder and thus the volume of Cu flake. It can be expected that a nanolaminated composite could lead to the formation of graphene/metal composite nanoparticles. Additionally, the size distribution of the rGO/Cu particles could be controlled by the rGO fraction in the bulk laminated composites. The standard deviation (σ) of diameter of the 1.5 vol%–powder ($\sigma_{1.5}$) is 10.9 μm, and is obviously smaller than that of the 0.5 vol%–powder ($\sigma_{0.5}$) of 17.5 μm. A possible explanation is that the rGO fraction of 0.5 vol% is too low to cover the whole surface of Cu flake, and some copper grains grow up at high temperature or liquid drops above melting point fuse together, resulting particles with larger sizes.

Raman spectroscopy was employed to characterize the original GO and the rGO on the surface of the composite powder (**Fig. 4**). It is predicted that the D/G intensity ratio (I_D/I_G) of GO decreased after reduction. However, I_D/I_G of rGO (0.95 in **Fig. 4b**) is found to be larger than that of original GO (0.75 in **Fig. 4a**). One possible reason is that new created graphitic domains in rGO are more numerous in number, but smaller in size comparing with integrated GO. So, the average size of the sp^2 domains decrease and the edge of sp^2 domains greatly increase after reduction, which leads to the increase appearing in I_D/I_G (Paredes J.I. et al., 2009; Ren P.G. et al., 2011). Besides, it is reported

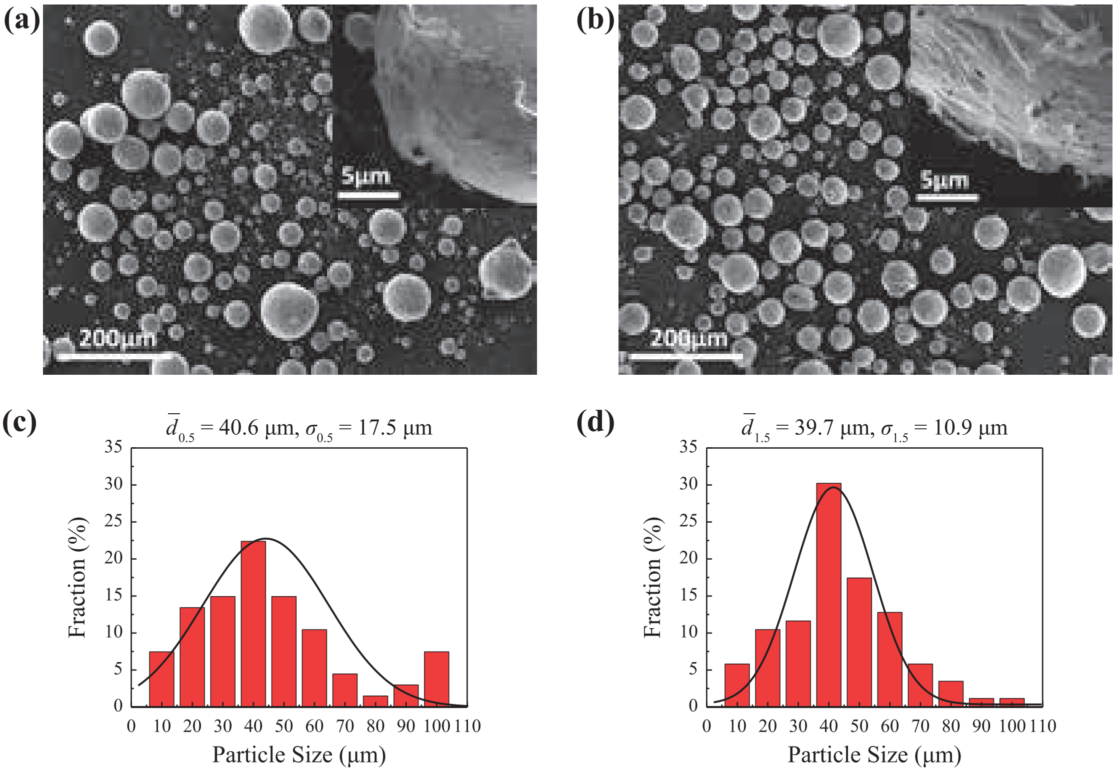

Fig. 3 **(a)(b)** SEM micrographs of the spherical rGO/Cu composite powders with GO fraction of **(a)** 0.5 vol% and **(b)** 1.5 vol%; **(c)(d)** particle size distribution of the spherical rGO/Cu composite powders with GO fraction of **(c)** 0.5 vol% and **(d)** 1.5 vol%.

that I_D/I_G firstly increases with increasing mean distance between defects (L_D) from 1 nm to about 3 nm and then decreases when L_D is larger than 3 nm (Cançado L.G. et al., 2011; Eigler S. et al., 2012). Thus, another possible explanation of I_D/I_G increase is that the L_D of our sample increases after reduction but still within 3 nm.

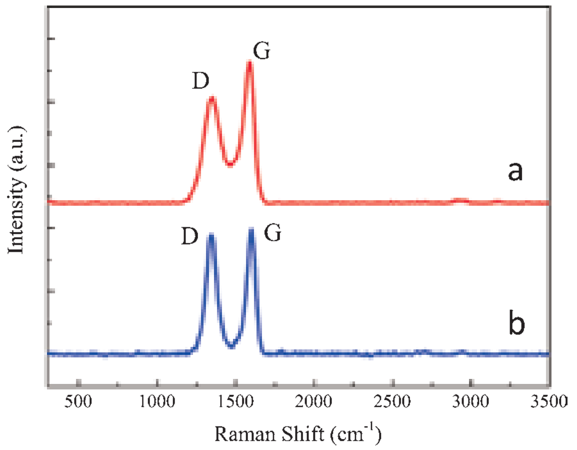

Fig. 4 Raman spectra of **(a)** original GO and **(b)** rGO on the surface of rGO/Cu composite powder.

Microstructure and elemental analyses were performed on the surface area and cross-section of the rGO/Cu powder. The EDS analysis in **Fig. 5(a)** shows that both carbon element and copper element are detected on the surface of the powder but carbon element is majority, showing most of the surface area is covered with carbon element. The EDS result in **Fig. 5(b)** shows that only copper is detected inside the rGO/Cu particle, indicating that graphene only disperses on the particle surface, which is consistent with the SEM results (**Fig. 3a, b**). As revealed by the EBSD result (**Fig. 6**), the Cu particle in the composite particle is monocrystal with the same orientation. Therefore, the composite powder is depicted as spherical monocrystal Cu core encapsulated with reduced graphene oxide.

The spherical rGO/Cu composite powder is formed after the bulk laminated rGO/Cu composites (**Fig. 7a**) go through over-melting point treatment and cooling process,

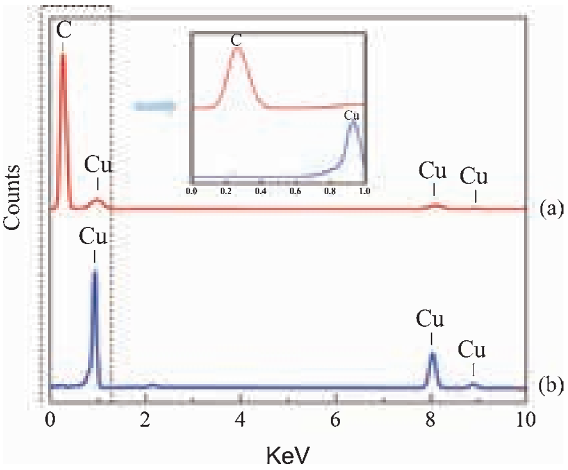

Fig. 5 EDS spectra of the element analysis of the **(a)** surface and **(b)** the cross-section of the rGO/Cu composite powder, showing the rGO dispersed on the surface of the powder and there only exists Cu element inside the powder.

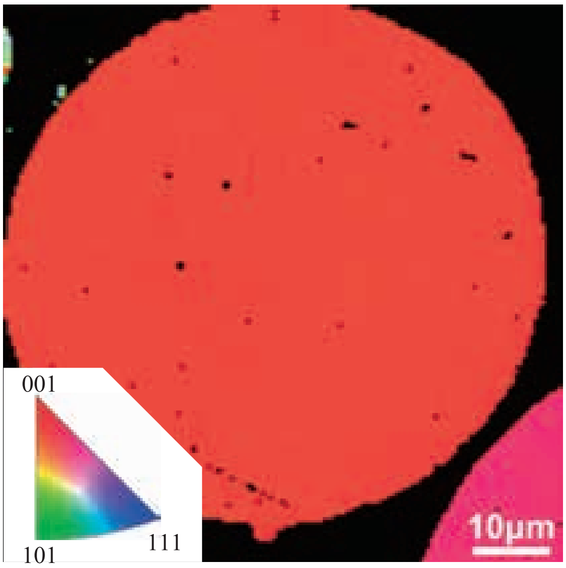

Fig. 6 An EBSD image of the cross-section of the rGO/Cu composite powder, showing the Cu phase is monocrystal.

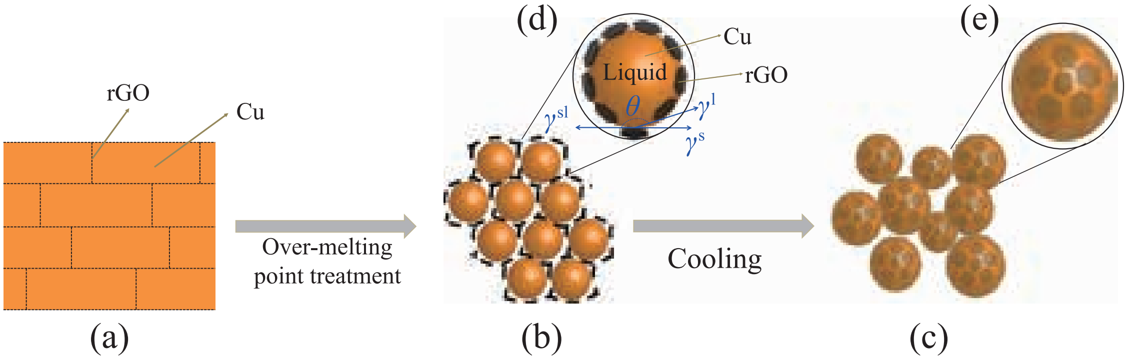

Fig. 7 Schematic illustration of the formation of spherical rGO/Cu composite powder.

and a possible formation mechanism is illustrated schematically in **Fig. 7**. Copper (with a melting point of 1083 °C) would melt at the temperature up to 1100 °C, while the rGO sheet remains unchanged because carbon has an ultrahigh melting point and carbon and copper are immiscible as well as no chemical reaction between them.

Further, spherical particles form because of a poor wettability of pure liquid Cu on carbon and surface energy minimization of a droplet. The wetting or de-wetting depends on the physical properties of the liquid and solid phases, especially the surface and interfacial energy. The wettability can be expressed using the equilibrium contact angle (θ) (**Fig. 7d**) of a metal droplet on the solid surface, and it can be described by the Young's equation:

$$\cos\theta = \frac{\gamma^{\mathrm{s}} - \gamma^{\mathrm{sl}}}{\gamma^{\mathrm{l}}} \tag{1}$$

where γ^{s} is the surface energy of solid phase, γ^{l} is the surface energy of liquid phase, and γ^{sl} is the interfacial energy between the solid phase and liquid phase. The surface energy γ^{s} of rGO is estimated to be between the surface energy of graphene (46.7 mJ/m^2) and GO (62.1 mJ/m^2), and closes to that of graphite (54.8 mJ/m^2) (Wang S. et al., 2009), but much lower than that of pure liquid Cu (1400 mJ/m^2 at the melting point) (Keene B.J., 1993). We assume that the equilibrium contact angle of rGO/Cu is similar to that of graphite/Cu (140° at 1150 °C) (Mortimer D.A. and Nicholas M., 1970), so the liquid Cu on rGO almost completely de-wets. Besides, surface energy minimization of a liquid Cu droplet drives the formation of spherical shape. After cooling down, the rGO sheets coat on the surface of the monocrystal Cu core. The contact between rGO and Cu should be dominated by a metallurgical bonding because graphene would not react with Cu even at high temperature under pressure (Cao M. et al., 2017).

4. Conclusions

In this work, we have fabricated spherical rGO/Cu composite powder based on the liquid/solid interface interaction, which takes advantage of low wettability of liquid Cu on solid rGO. The Cu phase of the composite powder is monocrystal and the rGO coats on its surface. The resulting composite powder exhibits good sphericity and narrow particle size distribution. Besides, it sheds light on fabricating other metal composite powders.

Acknowledgements

The authors would like to acknowledge the financial supports from the Ministry of Science & Technology of China (the National Key Research and Development Program of China 2017YFB0406200), and Shanghai Science & Technology Committee (Nos.14JC1403300, 14DZ2261204, 15JC1402100, 17520712400).

Nomenclature

$\bar{d}$	Average particle sizes
EBSD	Electron backscatter diffraction
EDS	Energy dispersive spectrometer
FE-SEM	Field-emission scanning electron microscopy
GO	Graphene oxide
I_{D}	Intensity of D-band
I_{G}	Intensity of G-band
L_{D}	Mean distance between defects (nm)
PVA	Polyvinyl alcohol
rGO	Reduced graphene oxide
σ	Standard deviation of diameter (µm)
θ	Equilibrium contact angle
γ^{s}	Surface energy of solid phase (mJ/m^2)
γ^{l}	Surface energy of liquid phase (mJ/m^2)
γ^{sl}	Interfacial energy between the solid phase and liquid phase (mJ/m^2)

References

Achelis L., Uhlenwinkel V., Characterisation of metal powders generated by a pressure-gas-atomiser, Materials Science and Engineering: A, 477 (2008) 15–20.

Attia U.M., Alcock J.R., A review of micro-powder injection moulding as a microfabrication technique, Journal of Micromechanics and Microengineering, 21 (2011) 043001.

Berkowitz A.E., Harper H., Smith D.J., Hu H., Jiang Q., Solomon V.C., Radousky H.B., Hollow metallic microspheres produced by spark erosion, Applied Physics Letters, 85 (2004) 940–942.

Cançado L.G., Jorio A., Ferreira E.H., Stavale F., Achete C.A., Capaz R.B., Moutinho M.V., Lombardo A., Kulmala T.S., Ferrari A.C., Quantifying defects in graphene via Raman spectroscopy at different excitation energies, Nano Letters, 11 (2011) 3190.

Cao M., Xiong D.B., Tan Z., Ji G., Amin-Ahmadi B., Guo Q., Fan G., Guo C., Li Z., Zhang D., Aligning graphene in bulk copper: Nacre-inspired nanolaminated architecture coupled with in-situ processing for enhanced mechanical properties and high electrical conductivity, Carbon, 117 (2017) 65–74.

Das S., Bourell D.L., Babu S.S., Metallic materials for 3D printing, MRS Bulletin, 41 (2016) 729–741.

Eigler S., Dotzer C., Hirsch A., Visualization of defect densities in reduced graphene oxide, Carbon, 50 (2012) 3666–3673.

Goli P., Ning H., Li X., Lu C.Y., Novoselov K.S., Balandin A.A., Thermal properties of graphene-copper-graphene heterogeneous films, Nano Letters, 14 (2014) 1497.

Keene B.J., Review of data for the surface tension of pure metals, International Materials Reviews, 38 (1993) 157–192.

Kim Y., Lee J., Yeom M.S., Shin J.W., Kim H., Cui Y., Kysar J.W., Hone J., Jung Y., Jeon S., Strengthening effect of single-atomic-layer graphene in metal-graphene nanolayered composites, Nature Communications, 4 (2013) 2114.

Lampke T., Wielage B., Pokhmurska H., Rupprecht C., Schuberth S., Drehmann R., Schreiber F., Development of particle-reinforced nanostructured iron-based composite alloys for thermal spraying, Surface and Coatings Technology, 205 (2011) 3671–3676.

Lei C., Huang H., Cheng Z., Tang S., Du Y., Mono-disperse spherical Cu–Zn powder fabricated via the low wettability of liquid/solid interface, Applied Surface Science, 357 (2015) 167–171.

Li Z., Fan G., Tan Z., Guo Q., Xiong D., Su Y., Li Z., Zhang D., Uniform dispersion of graphene oxide in aluminum powder by direct electrostatic adsorption for fabrication of graphene/aluminum composites, Nanotechnology, 25 (2014) 325601.

Mehta R., Chugh S., Chen Z., Enhanced electrical and thermal conduction in graphene-encapsulated copper nanowires, Nano Letters, 15 (2015) 2024.

Mortimer D.A., Nicholas M., The wetting of carbon by copper and copper alloys, Journal of Materials Science, 5 (1970) 149–155.

Paredes J.I., Villarrodil S., Solísfernández P., Martínezalonso A., Tascón J.M.D., Atomic force and scanning tunneling microscopy imaging of graphene nanosheets derived from graphite oxide, Langmuir: The ACS Journal of Surfaces and Colloids, 25 (2009) 5957–5968.

Rafiee M.A., Rafiee J., Wang Z., Song H., Yu Z.Z., Koratkar N., Enhanced mechanical properties of nanocomposites at low graphene content, ACS Nano, 3 (2009) 3884.

Ren P.G., Yan D.X., Ji X., Chen T., Li Z.M., Temperature dependence of graphene oxide reduced by hydrazine hydrate, Nanotechnology, 22 (2011) 055705.

Seki Y., Okamoto S., Takigawa H., Kawai N., Effect of atomization variables on powder characteristics in the high-pressured water atomization process, Metal Powder Report, 45 (1990) 38–40.

Ünal A., Effect of processing variables on particle size in gas atomization of rapidly solidified aluminium powders, Materials Science and Technology, 3 (1987) 1029–1039.

Wang S., Zhang Y., Abidi N., Cabrales L., Wettability and surface free energy of graphene films, Langmuir: The ACS Journal of Surfaces and Colloids, 25 (2009) 11078.

Xiong D.B., Cao M., Guo Q., Tan Z., Fan G., Li Z., Zhang D., Graphene-and-copper artificial nacre fabricated by a preform impregnation process: Bioinspired strategy for strengthening-toughening of metal matrix composite, ACS Nano, 9 (2015) 6934–6943.

Zhang J., Wan S., Yan B., Wang L., Qian Y., Graphene encapsulated Fe_3O_4 nanospindles as a superior anode material for lithium-ion batteries, Journal of Nanoscience and Nanotechnology, 13 (2013) 4364.

Authors' Short Biographies

Jimin Lyu

Jimin Lyu received her Bachelor degree in Materials Science and Engineering from Shanghai Jiao Tong University in 2015 and currently is a master student at State Key Laboratory of Metal Matrix Composites, Shanghai Jiao Tong University. Her current research focuses on the fabrication and characterization of graphene reinforced copper matrix composites.

Ding-Bang Xiong

Ding-Bang Xiong is an Associate Professor in the State Key Lab of Metal Matrix Composites, in Shanghai Jiao Tong University, China since 2012. He received Ph.D. degree in material physics and chemistry from Shanghai Institute of Ceramics in 2007. Between 2007–2010, he carried out his postdoctoral research as Alexander von Humboldt fellow in Marburg University, Germany, and between 2010–2012, he did collaboration research in Kyoto University supported by the Japan Society for the Promotion of Science. His current research focuses on fabrication and properties of metal matrix composite materials.

Zhanqiu Tan

Zhanqiu Tan is an Assistant Researcher at State Key Laboratory of Metal Matrix Composites, Shanghai Jiao Tong University since 2016. He received his Ph.D. degree in Materials Science and Engineering from Shanghai Jiao Tong University (2014), where he studied particulates reinforced aluminum matrix composites with high thermal conductivity for thermal management applications. He completed his postdoctoral research on interface control and performance of Carbon/Aluminum composites in 2014–2016 at Shanghai Jiao Tong University. His current research focuses on high performance nano-Carbon (carbon nanotubes, graphene et al.) reinforced metal matrix composites.

Genlian Fan

Genlian Fan is an Assistant Professor at State Key Laboratory of Metal Matrix Composites, Shanghai Jiao Tong University since 2011. She received her Bachelor degree and Ph.D. degree in Materials Science and Engineering from Xi'an Jiaotong University. Between 2009–2011, she completed her postdoctoral research in Shanghai Jiao Tong University. Her current research focuses on smart powder metallurgy processing for fabrication of advanced metal matrix composites, carbon nanotube & graphene reinforced metal matrix composites, and defect relaxation & energy dissipation of metal matrix composites.

Authors’ Short Biographies

Qiang Guo

Qiang Guo is an Associate Professor in the School of Materials Science & Engineering and the State Key Lab of Metal Matrix Composites, in Shanghai Jiao Tong University, China since 2012. He received the B.Sc. degree in microelectronics from Peking University, China in 2005, and received the M.Eng. degree in materials science and engineering from Massachusetts Institute of Technology (MIT), in 2006. He obtained the PhD degree in advanced materials in 2010 from National University of Singapore, under the Singapore-MIT Alliance (SMA) program. Between 2010–2012, he was a postdoc in the Department of Applied Physics and Materials Science in California Institute of Technology (Caltech). His current research focuses on the mechanical behavior of advanced metal matrix composites.

Cuiping Guo

Cuiping Guo is an Assistant Engineer at State Key Laboratory of Metal Matrix Composites, Shanghai Jiao Tong University since 2009. She received her Bachelor degree in Mineral Processing Engineering from Central South University, China in 2006 and received Master Degree on research on the preparation and property of bio-sorbent made from agricultural residues in 2009 at Shanghai Jiao Tong University. Her Current research focuses on materials characterization.

Zhiqiang Li

Zhiqiang Li is a Professor at State Key Laboratory of Metal Matrix Composites, Shanghai Jiao Tong University. He received his Bachelor degree in 1996, Master degree in 1998 and Ph.D. degree in 2001 from Harbin Institute of Technology. Between 2002–2003, he completed his postdoctoral research in Shanghai Jiao Tong University and later worked in Shanghai Jiao Tong University. During 2011–2012, he did visiting research in Osaka University. His current research focuses on fabrication and mechanism of bionic composite materials, deformation of metal matrix composites, and powder metallurgy composite technology & principles.

Di Zhang

Di Zhang is a Professor in Shanghai Jiao Tong University and is the director of State Key Laboratory of Metal Matrix Composites. He is awarded by Ministry of Education in China as “Cheung Kong Scholars Program” Distinguished Professor in material subject. He started to teach at Shanghai Jiao Tong University in 1988 and became a Professor in 1994. He was a visiting scholar or visiting professor in Japan Yuasa Central Research Institute, Osaka University, Kyoto University, Germany Max-Plank Institute of Metals and Saga University, successively. His research focuses on metal matrix composites and genetic materials template from nature species.

KONA Powder and Particle Journal No. 36 (2019) 232–240/Doi:10.14356/kona.2019003 Original Research Paper

Modified Ergun Equation for Airflow through Packed Bed of Loblolly Pine Grinds [†]

Gbenga Olatunde [1] **and Oladiran Fasina** [2*]

[1] *Glanbia Nutritionals, Inc., USA*
[2] *Department of Biosystems Engineering, Auburn University, USA*

Abstract

Biomass grinds are typically non-spherical and are composed of particles with wide range of sizes that may vary up to 10× between the smallest and largest particle. Since fluidized bed system is often used to convert biomass into fuels, chemicals and products, the viscous and kinetic energy losses' coefficients in the Ergun equation were determined to incorporate these unique characteristics of biomass grinds. The revised Ergun's equation, validated using loblolly pine wood grinds, and data from other published work resulted in estimated Ergun's K_1 and K_2 coefficients of 201 and 2.7 respectively. In addition, the relative mean deviation between experimental and predicted pressure drop was in general better with the modified Ergun's equation when compared to the original Ergun's equation.

Keywords: biomass, fluidization, physical properties, Ergun equation, pressure drop

1. Introduction

United States has the capacity to produce over one billion tonnes of biomass annually (DOE, 2016). These vast quantities of biomass feedstock can be processed into fuels, chemicals and products thereby reducing the dependency of the country on fossil fuels. One of the common reactors used for converting biomass to fuel and products is the fluidized bed system (FBS) because of relative uniformity in rate of heat transfer between biomass particles and fluidizing gases (Oliveira et al., 2013). Biomass materials properties such as moisture content (MC), density, particle shape and particle size distribution are needed to estimate the parameters (reactor pressure drop and minimum fluidization velocity—U_{mf}) needed to design, size, and operate FBS systems (Olatunde et al., 2017). There has been substantial progress made in quantifying the properties of biomass feedstock (Oginni et al, 2016; Olatunde et al., 2016) but the pressure drop and minimum fluidization velocity correlations developed for non-biomass materials are still currently used for biomass feedstocks. This has resulted in difficulties in sizing and designing equipment and reactors for fluidizing biomass feedstocks (Allen et al., 2013; Koekemoer and Luckos, 2015; Kunii and Levenspiel, 1991). Therefore the main focus of this study is to develop reactor pressure drop and U_{mf} equations that utilize the properties of and are suitable for biomass feedstocks.

Reynolds et al. (1901) developed the first relationship between pressure loss and velocity of the fluid flowing through a packed bed using the Darcy concept.

$$\frac{\Delta P}{LU} = a + b\rho U \tag{1}$$

Ergun (1952) suggested that energy losses as fluid flows through a bed of particulate material is a function of fractional bed porosity (void) which are embedded in the coefficients '*a*' and '*b*' (Eqn. 1). Coefficients '*a*' and '*b*' were respectively regarded as the kinetic energy loss and viscous energy loss, and were related to the void space (ε) by Eqns. 2 and 3 (Ergun, 1952).

$$a = \alpha\frac{(1-\varepsilon)^2}{\varepsilon^3} \tag{2}$$

$$b = \alpha\frac{(1-\varepsilon)}{\varepsilon^3} \tag{3}$$

Combining Eqns. 1, 2 and 3 and further modification of Eqn. 1 to include average particle size resulted in the most widely used equation (Ergun's equation) for predicting packed bed pressure drop as a function of fluid velocity (Eqn. 4). The first term on the right-hand side of Eqn. 4 represents viscous energy loss at low fluid flow rate while

---

[†] Received 18 July 2017; Accepted 14 November 2017

[1] 450 Falls Ave # 255, Twin Falls, ID 83301, USA
[2] Auburn, AL 36830, USA
[*] Corresponding author: Oladiran Fasina;
E-mail: fasinoo@auburn.edu
TEL: +1-334-844-3574 FAX: +1-334-844-3530

the second term on the right hand side represent inertial energy loss due to high fluid flow rate. The values of the coefficient K_1 and K_2 in Eqn. 4 were estimated to be 150 and 1.75 for mono-sized spherical and nearly spherical particles (such as crushed coke, sand, glass) (Ergun, 1952).

$$\frac{\Delta P}{L} = K_1 \frac{(1-\varepsilon)^2}{\varepsilon^3} \frac{\mu U}{\bar{d}^2} + K_2 \frac{1-\varepsilon}{\varepsilon^3} \frac{\rho U^2}{\bar{d}} \tag{4}$$

As expected, Ergun equation (Eqn. 4) performs satisfactorily in predicting pressure drop in packed bed that contains uniform and spherical particles (Cloete et al., 2015; Mawatari et al., 2003; Nemec et al., 2001). Several authors have however documented that this equation does not satisfactorily predict the pressure drop of bed consisting of non-uniform and non-spherical particles. For example, Kunii and Levenspiel (1991) reported that Ergun equation resulted in under-prediction (greater than 25 % error) of pressure drop in packed bed that contains particles with sizes ranging between 4.75 mm and 37.5 mm. Similarly, Koekemoer and Luckos (2015) obtained 29 % pressure drop prediction error for a bed that contains coal, char and ash particles. Dolejs and Machac (1995) obtained 72.6 % and 24.9 % pressure drop prediction error for packed beds of polyhedral and cubes respectively while Gunarathne et al. (2014) obtained 35 % error from predicting pressure drop in biomass pellet (cylindrical) packed bed. Therefore there is a need to modify Ergun's equation in order to improve the accuracy of predicted pressure drops (subsequently U_{mf}) in beds that consist of non-uniform and non-spherical particles such as biomass grinds (Olatunde et al., 2016).

There have been attempts to revise Ergun's equation for non-spherical and non-uniform particles size bed (Dolejs and Machac, 1995; Gunarathne et al., 2014; Innocentini et al., 1999). Some of the authors refitted Ergun's equation for a specific material and obtain new values for constant (K_1 and K_2) but retained the overall structure (the porosity correlation—Eqns. 2 and 3). For instance, Cloete et al. (2015) proposed $K_1 = 250$ and $K_2 = 2.5$ for cylindrical particle of γ-Al_2O_3. Quinn (2014) proposed a value of 267 for K_1 while K_2 was found to be 2.14, 2.51, 4.02 for leadshot, glass beads and white sand, respectively. Also, Ozahi et al. (2008) proposed a constant of $K_1 = 160$ and $K_2 = 1.61$ for zeolite and chickpeas. It is important to note that these samples have porosity less than 0.5. The porosity for biomass grinds is significantly higher (typically 0.8 and above) (Olatunde et al., 2016; Fasina, 2006). We hypothesize that the porosity correlations (Eqns. 2 and 3) may not be suitable for materials such as biomass grinds with high void space, and that improvements in the porosity correlations may improve the predictions of pressure drop in packed beds containing non-uniform and non-spherical particles.

2. Methodology

Clean loblolly pine wood chips were obtained from trees harvested in Alabama, U.S. Using standard E871-82 (ASTM, 2006), the moisture content of the chips was 8.5 %. The chips were ground through a hammer mill (Model No. 10HBLPK, Sheldon Manufacturing, Tiffin, OH) fitted with one of the following screens sizes: size 22.23 mm, 19.05 mm, 15.88 mm, 12.7 mm, 9.53 mm, 6.35 mm, or 3.18 mm. This resulted in seven samples with different bulk densities and porosities. The physical properties of each sample were determined as described below.

2.1 Particle size distribution and shape

Particle size distribution of each sample was determined with a digital image-based particle size analyzer (Camsizer®, Retsch Technology, Haan, Germany). An example of the image obtained from the particle size analyzer is shown in **Fig. 1**. For this analysis, about 100 g of a sample was poured into the hopper of the analyzer from where the sample was conveyed through a vibratory feeder to the measurement chamber of the system. The chamber is equipped with two cameras that capture pictures of the particles of the samples falling through the measurement field of the chamber. The software provided by the manufacturer of the analyzer was used to read, store and process the captured images. The size parameters that were retrieved from the software for these studies were: sphericity (φ), x_{84}, x_{16}, x_{50} and coefficient of variation (γ), and are defined below.

$$\varphi = \frac{4\pi A}{P^2} \tag{5}$$

$$\gamma = 50 \frac{x_{84} - x_{16}}{x_{50}} \tag{6}$$

where P is measured perimeter or circumference of a projected particle (mm), A is measured surface area covered by the projected particle (mm^2), and x_{84}, x_{16} and x_{50} are diameters (mm) at which 84 %, 16 % and 50 % of particles in a sample is comprised of smaller particles respectively.

2.2 Particle size distribution and shape

Particle density of each sample was measured with a gas pycnometer (Accupyc 1330, Micromeritics Instrument Corp., Norcross, Ga.) that uses helium to estimate the pressure difference between a reference cell and a cell containing the sample. The pressure difference was used by the pycnometer to estimate the volume of a known mass of sample. A digital weighing scale (Model AR3130, Ohaus Corp, Pinebrook, NJ) was used to measure the sample mass. Particle density was estimated as the ratio

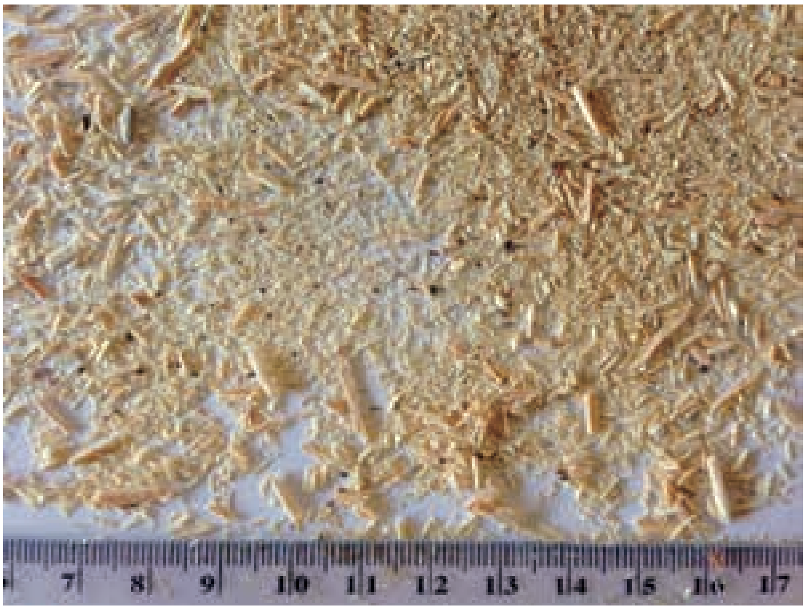

Fig. 1 Image showing the variation in particle size and shape of biomass grinds.

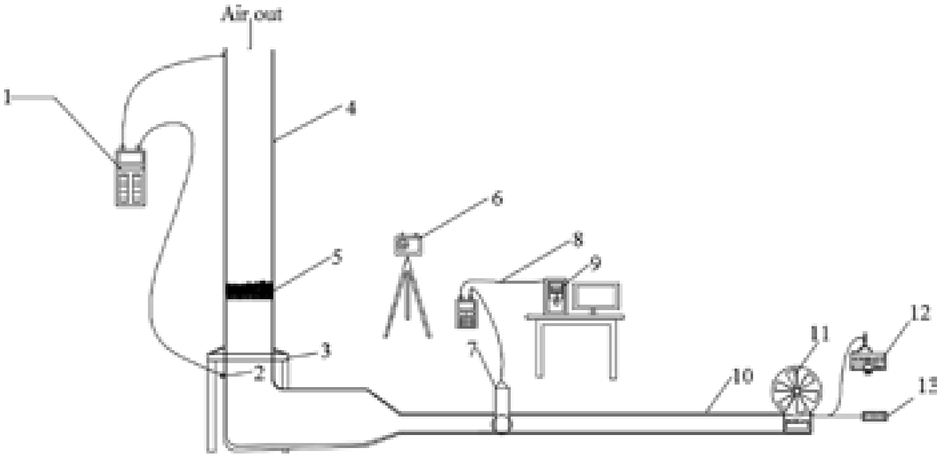

Fig. 2 Schematic diagram of experimental setup: (1)—Manometer, (2)—Lower pressure tap, (3) Bed support, (4)—Fluidization test chamber having 101.6 mm diameter pipe, (5)—Bed material on distributor plate, (6)—Nikon digital camera (7)—Flow rate probe, (8)—RS232 cable, (9)—Computer system, (10)—50.4 mm (D) PVC pipe, (11)—Air blower, (12) Air blower controller, (13) Power source.

of the mass of the sample in the cell and the volume estimated by the pycnometer.

Sample bulk density was determined using an apparatus that consists of a funnel through which the sample freely falls onto 1137 mm^3 cup. The ratio of the mass of the sample in the container to the volume of the container was used to compute the estimated bulk density. The inter-granular porosity (ε) of the ground wood sample was calculated from the measured values of bulk density and particle density as follows:

$$\varepsilon = 1 - \frac{\rho_\mathrm{b}}{\rho_\mathrm{p}} \quad (7)$$

2.3 Pressure drop test

The experimental setup (**Fig. 2**) utilized for the pressure drop measurements consists an acrylic cylindrical pipe with 0.1 m diameter and 1.0 m bed height. A perforated-plate having 100 µm holes (Purolator, Model UNS 530403, Sacramento, CA 95828) that serves as the distributor is located at the base end bed. The amount of ambient air supplied by a blower (Black and Decker, Model LH5000, Antioch, CA 94509) to the experimental unit was varied by means of a fan speed controller (Lutron electronic, MFG part S2-LFSQH-WH Monroe, NJ) and was measured by a vane anemometer (model 407113, Extech Instruments, Nashua, NH 03063). The pressure drop across the bed was measured by connecting a U-tube manometer into the upper (800 mm above the distributor) and lower pressure taps (200 mm below the distributor).

Fluidization experiments were conducted by adding 2 kg sample into the fluidization chamber. The blower was turned on and the fan speed controller was used to gradually increase airflow rate through the bed. At least, 10 airflow data (pressure drop and air velocity) were recorded for each sample before the onset of entrainment of the bed material. At each airflow velocity, 60 seconds was allowed for stabilization before the pressure drop across the chamber and the corresponding air velocity through the bed were recorded. The pressure drop across the chamber was determined for each superficial gas velocity starting from fixed bed condition until complete bed mixing was achieved.

2.4 Data analysis

All experiments were conducted in triplicates and results are presented in the relevant sections as mean values and standard deviation. Statistical significance of the following variables—screen size, porosity, particle and bulk density, particle size, sphericity and coefficient of variation was tested using the analysis of variance (ANOVA) procedures (SAS, 2011). Tukey multiple range test was used to compare means. Differences were considered to be statistically significant when $p < 0.05$. Mean Relative Deviation (MRD) (Eqn. 8) was used as statistical indicator to compare the predictive ability of the original Ergun and the modified Ergun (developed in this study) equations

$$MRD\,(\%) = \frac{1}{N} 100 \sum_{i=1}^{N} \frac{\left|\Delta P_{i.\mathrm{calc}} - \Delta P_{i.\exp}\right|}{\Delta P_{i.\exp}} \tag{8}$$

3. Results and discussion

3.1 Physical properties

The size, density, porosity and shape of the seven loblolly pine grind samples are summarized in **Table 1**. Coefficients of variation for all the samples were higher than 60 % thus further confirming that size of particles in each sample varied widely. The results in **Table 1** also affirm the high porosity and the non-spherical nature of biomass grinds (> 0.80) as earlier discussed in the introductory section. The particle density did not significantly vary with increase in particle size but bulk densities significantly decreased ($p < 0.05$) as particle size increased thereby indicating that the amount of inter-particle space (void or pore space) increased with increase in particle size. However, the increase in porosity was not significantly influenced by screen (or particle) size.

3.2 Pressure drop and airflow rate

The plots of ratio of pressure gradient to velocity against air mass flow rate (Eqn. 1) for s samples of loblolly pine wood grinds are presented in **Fig. 3**. It can be deduced from the plots that reduction in particle size resulted in higher pressure losses because there were less pore spaces for the air to flow through thereby confirming the bulk density, particle density and porosity results presented in **Table 1**.

The slopes, intercepts and the corresponding R^2 value of each of the plot in **Fig. 3** are summarized in **Table 2**. When the nominal screen size reduced by 89.8 %, the slope and intercept increased by 67.7 and 38.2 % respectively. Increase in the value of intercept or slope indicate

Table 1 Physical properties of loblolly pine wood grinds ground through different screen sizes.

Screen size (mm)	Particle size (mm)	Sphericity	Bulk density (kg/m^3)	Particle density (kg/m^3)	Porosity	γ*
6.35	1.64^{b} (0.10)	0.37^{c} (0.10)	250.9^{b} (2.40)	1453.3^{ab} (44.10)	0.83^{b} (0.01)	72.6^{bc} (0.01)
9.53	1.95^{a} (0.10)	0.37^{a} (0.10)	242.8^{b} (2.80)	1420.4^{b} (12.10)	0.84^{ab} (0.01)	72.8^{c} (0.1)
15.88	2.09^{a} (0.30)	0.39^{b} (0.10)	229.9^{d} (1.60)	1448.2^{ab} (3.03)	0.84^{ab} (0.01)	72.5^{abc} (0.1)
19.05	2.02^{a} (0.02)	0.42^{a} (0.10)	228.8^{d} (2.90)	1424.9^{b} (12.15)	0.84^{ab} (0.01)	67.9^{c} (0.06)
22.23	2.10^{a} (0.10)	0.41^{a} (0.01)	222.7^{e} (3.30)	1438.8^{ab} (11.70)	0.85^{a} (0.01)	64.0^{c} (0.02)

Values are means of triplicates experimental runs and are based on d_{50} from the particle size distribution data
Numbers in parentheses are standard deviation
Means with the different superscript (alphabet) in a column are significantly different ($p < 0.05$)
*coefficient of variation (calculated using Eqn. 6)

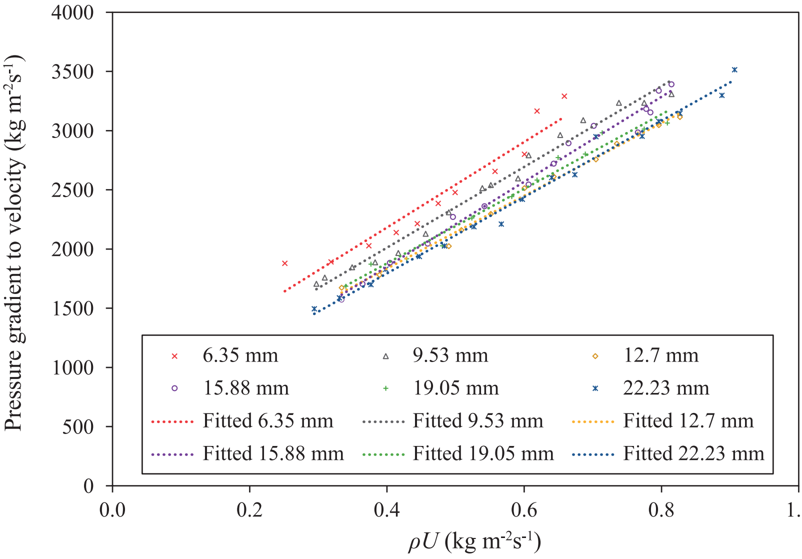

Fig. 3 Linear form of pressure–drop equation (Eqn. 1) using loblolly pine wood grind through different screen sizes.

Table 2 Estimation of slope and intercept parameters for loblolly pine wood at different particle sizes.

Screen size (mm)	Bulk density (kg/m^3)	$^+$Intercept (a)	$^+$Slope (b)	$^+R^2$	Void correlations based on (Eqn. 2)	(Eqn. 3)
6.35	250.89	883.2	3346.2	0.90	0.053	0.31
9.53	242.80	811.1	3248.3	0.95	0.046	0.28
15.88	229.93	687.7	3053.4	0.93	0.042	0.27
19.05	228.27	670.5	3071.1	0.98	0.041	0.26
22.23	222.72	633.1	2999.8	0.97	0.039	0.25

$^+$Values of (a), (b) and R^2 were obtained from **Fig. 4** and based on Eqn. 1

that resistance of the bed material to stress-shear deformation at viscous level and bed entropy (particle-particle collision per unit area due to kinetic energy) increased with reduction in size (Ergun, 1952). The last two columns in **Table 2** were calculated from the fraction correlation (kinetic energy loss (Eqn. 2) and viscous energy loss (Eqn. 3)) as proposed by Ergun (1952). The values were determined by substituting the experimentally determined porosity (values presented in **Table 1**) for each of the screen size into the corresponding Eqns. 2 and 3. The result showed that void fraction for kinetic energy loss were higher than viscous energy losses. This implies that energy losses due to particle-particle movement dominated the system.

Fig. 4 shows the plot of slope versus kinetic fractional correlation (Eqn. 2) on the primary axis and the plot of intercept values versus viscous void fractional correlation (Eqn. 3) on the secondary axis. The result shows a good fit of R^2 values of 0.95 for viscous energy loss but a weak R^2 values of 0.61 kinetic energy loss—an indication that the kinetic energy expression in the Ergun equation does not appear to be adequate for pressure drop-airflow relationship of irregular shape typical of biomass grinds.

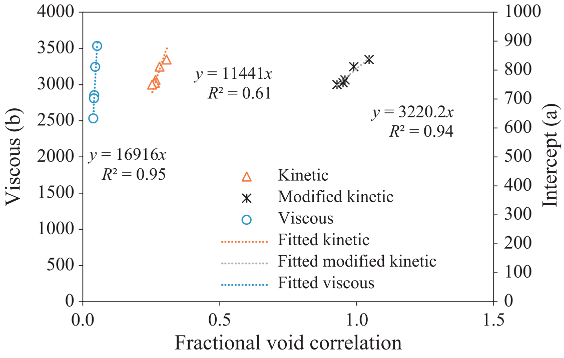

Fig. 4 Influence of kinetic and viscous energy losses on fractional void volume.

To improve the void fraction correlation for kinetic energy losses, the void fraction was modified into the expression below.

$$kinetic = \frac{(1-\varepsilon)^n}{\varepsilon^k} \tag{9}$$

The values of parameters '*n*' and '*k*' were obtained by using the Microsoft Excel® nonlinear solver based on generalized reduced gradient algorithm such that the error sum of square between kinetic void fraction correlation data and the corresponding slope data (**Table 2**) was minimized. The plot of slope versus modified kinetic fractional correlation (Eqn. 9) using the new values of '*n*' (0.3) and '*k*' (3.4) resulted in improved R^2 value of 0.94 (a 35 % improvement). These values of '*n*' and '*k*' indicate that other factors (in addition to turbulent flow) such as particle-to-particle cohesive force, particle-wall interactions, variations in the minimum fluidization velocity may be contributing to pressure drop during fluidization of bed that is composed of non-spherical and non-uniform particles. (Srivastava and Sundaresan, 2002; Olatunde et al., 2016)

3.3 Model development

As mentioned in the introductory section, the most common form of predicting packed bed pressure drop is the Ergun equation (Eqn. 4). The Ergun equation was modified by incorporating sphericity (φ) and coefficient of variation (γ) expression (Eqn. 10) below (Anderson and Warburton, 1949) and the kinetic energy loss expression developed in the previous section thereby extending the use of the Ergun equation to packed beds containing particles that are non-spherical and have wide particle size distribution (Eqn. 11).

$$d \cong \bar{d}\varphi(1+\gamma^2) \tag{10}$$

$$\frac{\Delta P}{L} = K_1 \frac{(1-\varepsilon)^2}{\varepsilon^3\left[\bar{d}\varphi(1+\gamma^2)\right]^2}\mu U + K_2 \frac{(1-\varepsilon)^{0.3}}{\varepsilon^{3.4}\bar{d}\varphi(1+\gamma^2)}\rho U^2 \tag{11}$$

$$\frac{\Delta P}{LU}\frac{\varepsilon^3 d^2}{\mu(1-\varepsilon)^2} = K_1 + K_2 \frac{N_{\mathrm{Re}}}{\varepsilon^{0.4}(1-\varepsilon)^{1.7}} \tag{12}$$

where

$$N_{\mathrm{Re}} = \frac{\rho U d}{\mu}$$

If

$$f_{\mathrm{v}} = \frac{\Delta P}{LU}\frac{\varepsilon^3 d^2}{\mu(1-\varepsilon)^2} \tag{13}$$

then

$$f_{\mathrm{v}} = K_1 + K_2 \frac{N_{\mathrm{Re}}}{\varepsilon^{0.4}(1-\varepsilon)^{1.7}} \tag{14}$$

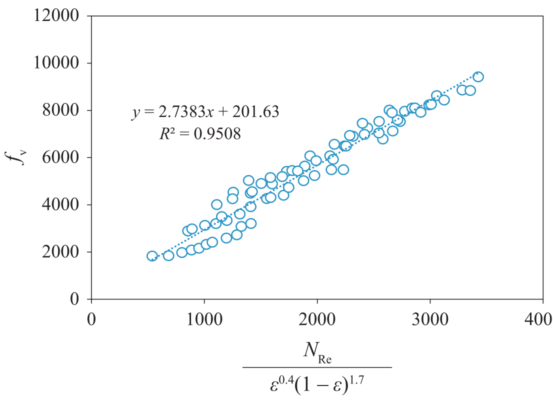

Fig. 5 A general plot for a single system having different void fraction using Ergun's concept using chord diameter scheme.

Based on the linear plot (**Fig. 5**) of

$$f_{\mathrm{v}} \text{ versus, } \frac{N_{\mathrm{Re}}}{\varepsilon^{0.4}(1-\varepsilon)^{1.7}}$$

coefficients K_1 and K_2 were estimated to be 201.6 and 2.7 for loblolly pine grinds, and are similar to values that have been reported in literature for non-spherical materials (K_1 varying from 160 to 267, and K_2 varying from 1.6 to 4.0; Quinn, 2004; Nemec and Levec, 2005; Ozahi et al., 2008; Cloete et al., 2015; Koekemoer and Luckos, 2015). Therefore, the modified Ergun equation for loblolly pine grinds is:

$$\frac{\Delta P}{L} = 201.6 \times \frac{(1-\varepsilon)^2}{\varepsilon^3\left(d\varphi(1+\gamma^2)\right)^2}\mu U + 2.7 \times \frac{(1-\varepsilon)^{0.3}}{\varepsilon^{3.4}d\varphi(1+\gamma^2)}\rho U^2 \tag{15}$$

3.4 Model validation

Validation of the modified equation (Eqn. 15) was achieved by comparing the pressure drop prediction from this equation to the values obtained from the Ergun equation of Eqn. 16 (a version of Ergun equation that has sphericity factor).

$$\frac{\Delta P}{L} = K_1 \frac{(1-\varepsilon)^2}{\varepsilon^3}\frac{\mu U}{\varphi^2 \bar{d}^2} + K_2 \frac{1-\varepsilon}{\varepsilon^3}\frac{\rho U^2}{\varphi \bar{d}} \tag{16}$$

A new set of loblolly pine wood chips were prepared with hammer screen sizes that were different from those used to prepare the samples utilized in the above model development. The physical attributes of the new samples are presented in **Table 3**. Similar effects of particle size on particle density, bulk density, and porosity were obtained as described earlier on. The MRD values from the predicted pressure drop values using the modified Ergun equation (Eqn. 16) and the original Ergun equation (Eqn. 4) are summarized in **Table 4**. The lower MRD values for the modified Ergun equation for all the hammer mill screen sizes provide proof that the modified Ergun equation is more suitable for predicting pressure drop in

Table 3 Physical properties of loblolly pine wood grinds used for validation.

Screen size (mm)	Particle size (mm)	Sphericity	Bulk density (kg/m^3)	Particle density (kg/m^3)	Porosity	γ*
22.40	2.90^{a} (0.20)	0.45^{a} (0.01)	222.7^{e} (2.2)	1438.5^{a} (3.1)	0.85^{a} (0.003)	66.1^{a} (2.6)
19.00	2.20^{b} (0.10)	0.45^{a} (0.01)	232.1^{d} (2.1)	1438.1^{a} (2.3)	0.84^{a} (0.003)	67.0^{a} (3.0)
15.80	2.09^{b} (0.30)	0.45^{a} (0.01)	275.4^{c} (2.62)	1437.7^{a} (4.9)	0.81^{a} (0.001)	60.0^{a} (4.4)
12.70	2.02^{b} (0.20)	0.46^{a} (0.01)	282.4^{c} (4.25)	1436.4^{a} (9.0)	0.80^{a} (0.001)	60.5^{a} (2.7)
6.35	0.82^{d} (0.03)	0.38^{cb} (0.02)	311.1^{ab} (1.57)	1422.3^{ba} (2.4)	0.78^{c} (0.001)	65.5^{a} (11.9)

Values are means of triplicates experimental runs and are based on x_{50} from the particle size distribution data
Numbers in parentheses are standard deviation
Means with the different superscript (alphabet) in a column are significantly different ($p < 0.05$)
*coefficient of variation (calculated using Eqn. 6)

Table 4 Comparison of the overall MRD (%) between predicted and the experimental data.

Screen size (mm)	Modified Ergun (Eqn. 16)	Original Ergun (Eqn. 4)
6.35	18.4	56.7
12.70	25.5	44.1
15.80	49.1	81.8
19.00	31.2	76.6
22.40	32.8	76.9

packed beds containing loblolly pine grinds in comparison to the original Ergun equation. The MRD values of the modified Ergun equation were about 2× lower than that of the original Ergun equation, and are similar to the values reported by others that have attempted to customize the Ergun equation for a particular material. For instance, Nemec and Levec (2005) used neutral network approach to modify Ergun using material shaped into various geometry sphere (size ranged between 1.66 mm and 3.50 mm, porosity 0.40 to 0.44), cylinder (size ranged between 2.62 and 3.50 mm, porosity 0.32 to 0.68) and quadralobes (size 2.13 porosity 0.47–0.50) and obtained MRD of 42.2, 20.6 and 60.0 %. Harrison et al. (2013) refitted Ergun's expression and obtained 119.8 for K_1 and K_2 to be 4.63 and author validated the equation over a wide range of Reynolds number and tube-diameter to particle diameter ratio. The author reported an absolute mean relative deviation of up to 50.7 %. Despite the significant improvement in the prediction of pressure drop during fluidization of biomass grinds suing the modified Ergun equation developed in this study, there is the need to continue to conduct studies that will lead to further improvement and development of equations for predicting the fluidization behavior of non-spherical and non-uniform particles.

4. Conclusions

Ergun's equation has attracted the attention of several researchers since it was first developed. Some of the authors showed that the equation is best suited for uniformly sized particles while others concluded that the void fraction correlation, the coefficients (K_1 and K_2) and a term of introducing the effect of size distribution need to be carefully determined before Ergun's equation can be used for a bed consisting of non-uniform particles having non-spherical shape. In this study, we introduced a new concept of determining the void fraction correlation suitable for non-uniform particle size distribution. We also incorporated coefficient of variation to capture the effect of particle distribution. Accordingly, we estimated a new coefficient K_1 and K_2 to be 201.6 and 2.7 respectively. We also proposed new frictional loss equation using ground loblolly pine wood. The result showed that the new equation resulted in lower overall mean relative deviation of pressure drop data compared with original Ergun equation.

Acknowledgements

We gratefully acknowledge funding support from Alabama Agricultural Experiment Station (AAES), and from USDA National Institute of Food and Agriculture (under S1041 multi-state project) and from the Southeast

Partnership for Integrated Biomass Supply Systems (IBSS). The IBSS partnership is supported by Agriculture and Food Research Initiative Competitive Grant no. 2011-68005-30410 from the USDA National Institute of Food and Agriculture.

Nomenclature

FBS	fluidized bed system
MRD	mean relative deviation (%)
a, b	constants
A	surface area (m^2)
d	particle diameter (m)
$\bar{d}$	average particle diameter (m)
P	perimeter (m)
ΔP	pressure drop (Pa)
g	acceleration due to gravity (m^2/s)
L	height of packed bed (m)
N_{Re}	Reynolds number
U_{mf}	minimum fluidization velocity (m/s)
k, n	constants
K_1, K_2	constants
x_{84}	particle diameter 84 % percentile
x_{50}	particle diameter 50 % percentile
x_{16}	particle diameter 16 % percentile
ρ	fluid density (kg/m^3)
ρ_{b}	bulk density (kg/m^3)
ρ_{p}	particle density (kg/m^3)
μ	fluid viscosity (Pa s)
φ	sphericity factor
ε	porosity
f_{v}	friction factor
γ	coefficient of variation

References

Allen K.G., von Backstrom T.W., Kroger D.G., Packed bed pressure drop dependence on particle shape, size distribution, packing arrangement and roughness, Powder Technology, 246 (2013) 590–600.

ASTM 2006, Standard E871-82—Moisture analysis for particulate wood fuels, ASTM International, West Conshohocken, PA (2009).

Cloete S., Johansen S.T., Amini S., Grid independence behavior of fluidized bed reactor simulations using the two fluid model: effect of particle size, Powder Technology, 269 (2015) 153–165.

DOE (U.S. Department of Energy), 2016 Billion-Ton Report: Advancing Domestic Resources for a Thriving Bioeconomy, Volume 1: Economic Availability of Feedstocks. Langholtz M.H., Stokes B.J., Eaton L.M. (Leads), ORNL/TM-2016/160. Oak Ridge National Laboratory, Oak Ridge, TN. 4480. DOI: 10.2172/1271651 <http://energy.gov/eere/bioenergy/2016-billion-ton-report> accessed 15.02.2018.

Dolejs V., Machac I., Pressure drop during the flow of a Newtonian fluid through a fixed bed of particulates, Chemical Engineering and Processing: Process Intensification, 34 (1995) 1–8.

Ergun S., Fluid flow through packed columns, Chemical Engineering Progress, 48 (1952) 89–94.

Fasina O.O., Flow and physical properties of switchgrass, peanut hull and poultry litter, Transactions ASAE, 49 (2006) 721–728.

Gunarathne D.S., Chmielewski J.K., Yang W., Pressure drop prediction of a gasifier bed with cylindrical biomass pellets, Applied Energy, 113 (2014) 258–266. DOI: https://doi.org/10.1016/j.apenergy.2013.07.032

Harrison L.D., Brunner K.M., Hecker W.C., A combined packed-bed friction factor equation: Extension to higher Reynolds number with wall effects, AIChE Journal, 59 (2013) 703–706.

Innocentini M.D., Salvini V.R., Macedo A., Pandolfelli V.C., Prediction of ceramic foams permeability using Ergun's equation, Materials Research, 2 (1999) 283–289.

Koekemoer A., Luckos A., Effect of material type and particle size distribution on pressure drop in packed beds of large particles: extending the Ergun equation, Fuel, 158 (2015) 232–238.

Kunii D., Levenspiel O., Fluidization Engineering. 2nd ed. Butterworth-Heinemann, Boston, 1991, 491 pp.

Mawatari Y., Tatemoto Y., Noda K., Prediction of minimum fluidization velocity for vibrated fluidized bed, Powder Technology, 131 (2003) 66–70.

Nemec D., Levec J., Flow through packed bed reactors: 1. Single-phase flow, Chemical Engineering Science, 60 (2005) 6947–6957.

Nemec D., Bercic G., Levec J., The hydrodynamics of trickling flow in packed beds operating at high pressures. The relative permeability concept, Chemical Engineering Science, 56 (2001) 5955–5962.

Oginni O., Fasina O., Adhikari S., Fulton J., Physical and flow properties of fractionated loblolly pine grinds, Transactions ASABE, 59 (2016) 999–1008.

Olatunde G., Fasina O., Adhikari S., McDonald T., Duke S.R., Size measurement method for loblolly pine grinds and influence on predictability of fluidization, Canadian Biosystems Engineering, 58 (2016) 4.1–4.10.

Olatunde G., Fasina O., Adhikari S., McDonald T., Duke S.R., Moisture effect on fluidization behavior of loblolly pine wood grinds, Biomass Conversion and Biorefinery, 7 (2017) 207–220.

Oliveira T.J.P., Cardoso C.R., Ataíde C.H., Bubbling fluidization of biomass and sand binary mixtures: Minimum fluidization velocity and particle segregation, Chemical Engineering and Processing: Process Intensification, 72 (2013) 113–121.

Ozahi E., Gundogud M.Y., Carpinlioglu M.O., A modification on Ergun's correlation for use in cylindrical packed beds with non-spherical particles, Advanced Powder Technology, 19 (2008) 369–381.

Quinn H.M., A reconciliation of packed column permeability data: Deconvoluting the Ergun papers, Journal of Materials, Article ID 548482 (2014) 24 pages.

Reynolds O., Brightmore A.W., Morroby W.H., Papers on Mechanical and Physical Subjects, Volume 2. Cambridge University Press, 1901, 780 pp.

SAS (The SAS System for Windows), Version 9.2., SAS Institute, Cary, NC, 2011.

Srivastava A., Sundaresan S., Role of wall friction in fluidization and standpipe flow, Powder Technology, 124 (2002) 45–54.

Authors' Short Biographies

Gbenga A Olatunde

Gbenga A Olatunde received his B.Sc., M.Sc., degrees from Obafemi Awolowo University, Nigeria in 2007 and 2011, respectively in Agricultural Engineering. He proceeded to Auburn University where he earned his PhD in Biosystems Engineering, in 2015.

He is currently a R&D scientist at Glanbia Nutritionals, Twin Falls, ID. His main areas of research interest are modeling biological system, drying of biological material and development of novel techniques for detection and detoxification of harmful grain molds and mycotoxins. He is a member American Society of Agricultural & Biological Engineering.

Oladiran Fasina

Oladiran Fasina is Professor and Head, Department of Biosystems Engineering at Auburn University, Auburn, USA. He received his PhD degree in 1994 in agricultural and bioresoruce engineering from University of Saskatchewan, Saskatoon, Canada. His research focus is in preprocessing, preparation, storage and handling of biological materials, food engineering and renewable energy. Dr. Oladiran Fasina has received many awards including the ASABE Evelyn E. Rosentreter Award. He is one of the editors of the journals published by ASABE and also a fellow of ASABE. Dr. Fasina has published 90 peer-reviewed papers and given over 100 presentations at national and international conferences.

KONA Powder and Particle Journal No. 36 (2019) 241–251/Doi:10.14356/kona.2019009 Original Research Paper

Effect of Moisture Content and Hammer Mill Screen Size on the Briquetting Characteristics of Woody and Herbaceous Biomass [†]

Jaya Shankar Tumuluru

[1] *Biofuels Department, Idaho National Laboratory, USA*

Abstract

Briquetting tests were conducted on lodgepole pine, switchgrass, and corn stover biomass. Three moisture levels (12, 15, and 18 % [w.b.]) and three-hammer mill screen sizes (4.8, 12.7, and 19.05 mm) were used to understand the impact of these variables on briquette-quality attributes such as unit and bulk density, durability rating, and briquetting energy consumption. A pilot-scale hydraulic continuous briquetting system was used in the present study. The briquette-quality attributes were measured after five days of storage. The hammer mill screen size of 4.8 and 12.7 mm and biomass moisture content of 12 and 15 % (w.b.) resulted in a higher unit and bulk density and durability rating. For the three biomasses tested, corn stover and lodgepole pine resulted in briquettes with bulk density > 480 kg/m^3 whereas durability rating of corn stover was > 97.5 and lodgepole pine was about 92–93 %. A larger screen size of the hammer mill (12.7 mm) and higher moisture content of 18 % (w.b.) increased the briquetting energy consumption for both the woody and herbaceous biomass. Larger hammer mill screen size (19.05 mm) and moisture content of 15 % (w.b.) resulted in lower density and durability rating of the briquettes produced.

Keywords: woody and herbaceous biomass, moisture content, hammer mill screen size, briquette press, briquette physical properties, energy consumption

1. Introduction

Energy from biomass has greater potential because it is renewable, unlike fossil fuels. Use of biomass for burning offers economic, social, and environmental benefits such as conservation of fossil-fuel resources, financial net savings, CO_2 and NOx emissions reduction, and job opportunities (Saidur et al., 2011). Variable moisture content, low bulk density, and irregular size and shape create feeding, handling, and transportation issues that limit the biomass application at commercial scale for biofuels and biopower generation. Typically, herbaceous biomass after harvesting has a bulk density of 112 to 160 kg/m^3 (Atchison and Hettenhaus, 2004), whereas woody biomass has a bulk density of 220 to 265 kg/m^3 (Tumuluru et al., 2015a). Tumuluru et al. (2016) indicated that densification helps to convert the raw biomass resources into an aerobically stable, high-density, tradable, and aggregatable commodity-like product. Common densification systems that are typically used in the biomass industry are pellet mill and briquette press (Tumuluru et al., 2011). A pellet mill typically produces a densified product with a bulk density of 650 to 750 kg/m^3, whereas a briquette press produces a densified product with a bulk density of 350 to 450 kg/m^3 and unit densities of 600–850 kg/m^3 (Tumuluru et al., 2011; Urbanovičová et al., 2017; Mani et al., 2006; Ndindeng et al., 2015). The quality of the densified product produced using pellet mill and briquette press depends on process conditions such as length-to-diameter ratio or compression ratio of the pellet die, die diameter, and biomass properties (particle size of the grind, biomass moisture content, and biomass composition). Various authors have done experiments to understand the impact of biomass type and process variables on the briquetting process.

Rajaseenivasan et al. (2016) studied the effect of binder (neem powder) on sawdust briquettes. Their studies indicated that blending neem powder with sawdust resulted in higher strength but lowered the calorific value (CV) compared to a briquette of sawdust alone. Also, the addition of neem powder to sawdust improved handling and water-resistance properties of briquettes. Water boiling tests on briquettes indicated that increasing the neem content re-

---

[†] Received 14 January 2018; Accepted 14 May 2018
J-STAGE Advance published online 30 June 2018

[1] 750 University Blvd, Idaho Falls, ID 3750 83415, USA
E-mail: JayaShankar.Tumuluru@inl.gov
TEL: +1-208-526-0529

duced the burning rate and increased time required for boiling.

Tumuluru et al. (2015b) worked on understanding the impact of briquetting pressure, hammer mill size, and moisture content on briquette quality attributes of wheat, barley, oat, and canola straws. Their study indicated that canola-straw briquettes had higher unit density and durability ratings. The high quality of the briquettes was produced at low-to-medium feedstock moisture content of 9 to 12 % (w.b.), high die temperature (130 °C), and compression pressure (12.5 MPa). Their results also indicated that a smaller screen size of 19.05 mm resulted in better quality briquettes in terms of density and durability rating compared to the briquettes made using 31.75 mm screen-size material.

Ndindeng et al. (2015) worked on optimizing the quality of briquettes made from rice-milling byproducts. The focus of their study was to produce briquettes that meet the needs of consumers. These authors tested different combinations of raw material, particle size, husk–bran ratio, drying method, and water temperature and concluded that these process variables influenced the hardness of rice-husk briquettes at constant pressure. They also concluded that the briquetting process increased bulk density of the raw material from 120 to 600 kg/m^3.

Rahaman and Salam (2017) worked on using sawdust as a binder for briquetting rice straw. These authors investigated the effect of particle size, pressure, and mold diameter on the physical characteristics of rice-straw briquettes. Adding sawdust as a binding material at 3:1 and 1:1 mixing ratios increased the briquettes stable density to 600 kg/m^3, improved shatter index significantly, increased heating value by 6–7.2 %, and reduced ash content from 13.61 to 10.3 and 6.93 %, respectively.

Lela et al. (2016) investigated physical–mechanical and thermal characteristics of cardboard/sawdust briquettes. Their results indicated that compression force did not have a significant influence on heating value or briquette moisture content, but slightly influenced ash content. Their study concluded that cardboard/sawdust briquettes showed potential for application as viable biomass fuel in terms of properties and cost.

Thabuot et al. (2015) worked on understanding the effect of applied pressure on the binder proportion of the fuel properties of holey bio-briquettes produced from selected biomass wastes such as bamboo sawdust, eucalyptus sawdust, corn cobs, and palm fiber. Increasing applied pressure increased the density of the briquettes. The briquettes produced had a density in the range of 260–416 kg/m^3. High-density briquettes were obtained from bamboo sawdust with 20 wt% molasses at a pressure of 70 kg/cm^2. The heating value of the bamboo briquette was about 21.26 MJ/kg.

Prasityousil and Muenjina (2013) investigated the properties of briquettes produced from rejected material of municipal waste composting char and sawdust char. The results indicated that calorific value, compressive strength, water resistance, and bulk density increased with an increasing ratio of sawdust char and a higher percentage of binder. This study demonstrated that the municipal-waste composting could be used as a fuel because it not only promotes the reuse of waste material but will also reduce the use of landfill space.

Jittabut (2015) worked on understanding the physical and thermal properties of briquette fuels from rice straw and sugarcane leaves in the ratios of 100:0, 80:20, 50:50, 20:80, and 0:100 using molasses as the binding agent. The physicochemical characteristics of the briquettes produced indicated that rice straw: sugarcane leaves (50:50) briquettes had low moisture content (4.22 %), high calorific value (17.83 MJ/kg), and low ash content (9.07 %). Analysis of sulphur and nitrogen also indicated that they are environmentally friendly as they are low in sulfur (0.02 %) and nitrogen (0.27 %) content.

Shuma and Madyira (2017) worked on production of loose biomass briquettes from agricultural and forestry residues and used cow dung and cactus as binders by varying compacting pressures (6, 12, and 19 MPa). The studies indicated that cactus binder was insensitive to compaction pressure due to its composition.

Zhang and Guo (2014) investigated the influence of pressure, temperature, moisture content, and particle size on physical properties such as density, durability, compressive strength, and impact resistance of solid fuel briquettes made from Caragana korshinskii Kom. These authors concluded that particle size most influenced briquettes' physical properties, followed by moisture content and temperature. Smaller particle size, lower moisture content, and high temperature produced good quality briquettes whereas pressure had a marginal impact. For the different material tested, an optimum moisture content of 8 % (w.b.), and temperatures and pressures in the range of 90–150 °C and 50–110 MPa are desirable to produce good quality briquettes.

Muazu and Stegemann (2015) investigated the effects of operating variables such as biomass source, material ratio (rice husks to corn cobs), the addition of a binder (starch and water mixture), and compaction pressure on the durability of fuel briquettes. The briquettes produced had a unit density of up to 1.9 times the loose-biomass bulk density. The durability of the briquettes was high as they lost only four percent mass during abrasion and ten percent during shattering tests. Also, storage properties of these briquettes were better because they absorbed 36 % less water than loose corn cobs.

Yank et al. (2016) investigated the impact of low-pressure densification on the physical properties of rice husk for rural applications. These authors studied the influence of the briquette formulation binders such as cassava wastewater, rice dust, and okra stem gum on the quality of the briquette produced. Physical properties (density, moisture content, calorific value, durability, and compressive strength) were tested to identify briquettes with the highest quality, i.e., greatest physical integrity. Briquettes made with rice dust had the highest durability (91.9 %) and compressive strength (2.54 kN) while the briquettes made with cassava starch had the greatest density (441.18 kg/m^3). Addition of water to the rice husk before densification had a positive influence on briquette quality; addition of bran influenced density the most, but not other briquette properties such as durability. The measured higher heating value of rice-husk briquettes was about 16.08 MJ/kg.

Antwi-Boasiako and Acheampong (2016) worked on understanding the strength and calorific values (CVs) of sawdust briquettes produced from tropical hardwoods such as Cylicodiscus gabunensis (heavy), Antiaris toxicaria (medium), and Ceiba pentandra (light), as well as a mixed composite that had different densities. These authors found that the initial wood density influenced all briquette properties and positively correlated with their CVs as C. gabunensis > A. toxicaria > mixed type > C. pentandra. The briquettes made from light-timber briquettes had greater compressive strength, and swelling values (i.e., less resistance to humidity). This study indicated that higher density of the raw material significantly influences briquette properties and correlates well with heating value (i.e., the CV), but inversely relates with shatter index, water/humidity resistance, and compression strength.

Most of the earlier research reported on briquetting was conducted on agricultural straws, sawdust, and some tropical woods, using a laboratory-scale single briquette press. Briquetting data on physical properties and energy consumption and the models describing the process for a pilot-scale continuous briquette press are not available. A significant advantage of a pilot-scale continuous briquetting process is ease of scale-up to commercial-scale systems. Also, models that are developed for the pilot-scale system can be translated to a commercial-scale system. The overall objective of the present research is to understand the briquetting characteristics of lodgepole-pine, switchgrass, and corn-stover biomass in a continuous pilot-scale briquette press. The specific objective is to understand the impact of hammer mill screen size (4.8, 12.7, and 19.05 mm) and biomass moisture content (12, 15, and 18 % [w.b.]) on such briquette properties as unit and bulk density, durability rating, and briquetting energy consumption, and to develop mathematical models of moisture content and hammer mill screen size for the briquette properties and briquetting energy consumption.

2. Materials and methods

2.1 Biomass

Switchgrass, which is an energy crop, was harvested in 2012 from Tulsa County, Oklahoma. Corn stover was harvested in 2014 from Palo Alto County, Iowa. Both switchgrass and corn stover were procured in bales. Lodgepole pine was harvested in 2014 from Fremont County, Idaho, and procured in the form of wood chips. The wood chips and corn stover and switchgrass bales were first ground in a stage-1 grinder (Vermeer Model HG200 grinder) fitted with a 50.8 mm screen. A commercial-scale rotary drum dryer was used to dry the ground biomass to about 10 % (w.b.). The dried material was further ground using an eliminator hammer mill (Bliss Model E-4424-TF) fitted with 4.8, 12.7, and 19.05 mm screens. The ground samples were measured for moisture content and further stored in super sacks.

3. Pilot-scale briquette press

A WEIMA C150 model briquette press was used in the present briquetting studies. The C150 briquette press (**Fig. 1**) is a pilot-scale machine that can produce about 50–80 kg of briquettes per hour. The briquetting press is a heavy-duty hydraulic press. The throughput of the press depends on the type of the biomass processed and its properties. This unit has a stainless steel hopper and chute. Details of the equipment include a) power: 460 V/60 Hz/3 Phase/16 A; b) hopper opening: (1040 × 1040 mm, 1346.2 mm above the floor); c) hopper configuration: four sides straight, 1040 mm high; d) hopper volume: 1.1 m^3;

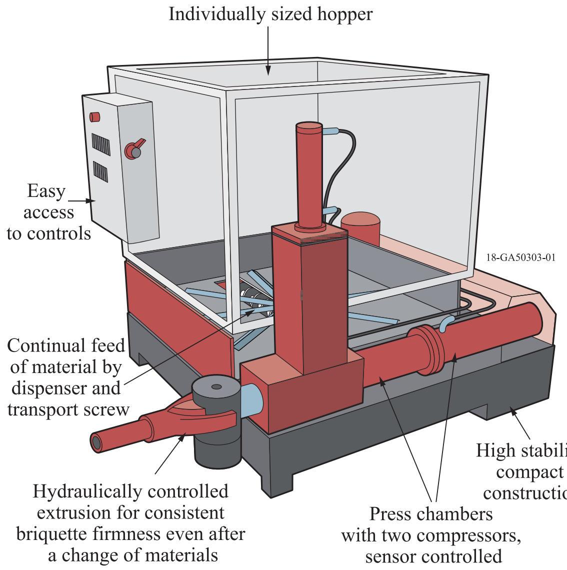

Fig. 1 Position of various parts in WEIMA C150 briquette press.

e) auger feed on hopper to hydraulic press; f) hydraulic motor: 9 hp; g) worm motor: 0.75 hp (0.55 kW); h) hydraulic oil volume: 26.4 gals (100 L); and g) briquette diameter: 2 in. (50.8 mm).

3.1 Briquetting process

Raw biomass processed using stage-1 and 2 grinders and a rotary dryer was used for briquetting tests. Lodgepole pine, corn stover, and switchgrass biomasses were ground in a hammer mill. The ground biomass was further reconditioned to different levels of moisture content. The reconditioned material was left overnight at room temperature (20 °C) for moisture to equilibrate. The reconditioned biomass was densified using the pilot-scale WEIMA briquette press. There are four different stages of briquette production (**Fig. 2**). Initially, the material underwent pre-pressing in the auger below the hopper. In the second stage, the material was pressed with a load pusher. In the third stage, a briquette was produced by applied pressure from a hydraulic ram. Finally, the briquette was discharged from the press. The briquettes produced had a diameter of 50 mm. About 10–12 kg of raw material was used for each test.

In the present study, the properties of the briquettes (unit and bulk density and durability rating) were measured after five days of storage at room temperature of 20 °C. According to Rahaman and Salam (2017), briquettes after 24 hours of storage tend to relax and attain more stability. Tumuluru et al. (2015b) also observed similar findings where the relaxed density of the wheat-, oat-, and canola-straw briquettes after five days of storage were more stable compared to density measured immediately after briquette production.

4. Experimental plan

The experimental plan was designed to understand the impact of biomass moisture content and hammer mill screen size on physical attributes (unit and bulk density and durability rating) and briquette energy consumption. Briquetting tests were conducted at two different hammer mill screen sizes (4.8 and 12.7 mm) and three levels of biomass moisture content (12, 15, and 18 % [w.b.]). Based on results, the moisture content—which can help to produce good quality briquettes in terms of bulk density and durability rating for the two hammer mill screen sizes—was further used to do briquetting tests using a larger hammer mill screen size (19.05 mm) material.

5. Raw material and briquette properties and energy consumption measurement

5.1 Geometric mean particle length (X_{gm})

The geometric mean particle length (X_{gm}) of the hammer milled corn stover, switchgrass, and lodgepole pine was determined using ASAE Standard S424 (1993). This standard is compatible with existing ASTM and ISO standards for particle-size-distribution measurement (ASAE Standard S424, 1993). Five square-hole screens and pans having a width of 406 mm and a length of 565 mm were used in the present tests. The nominal opening sizes of the screens were 19.0, 12.7, 6.3, 3.96, and 1.17 mm. These screens were stacked over each other where the largest opening size screen was placed on top, followed by other screens in decreasing opening size. As the bulk density of the ground material was low, only 750 g of material was used in the study. As per the standard, the screen shaker was set to shake the screens for five minutes. The mass of

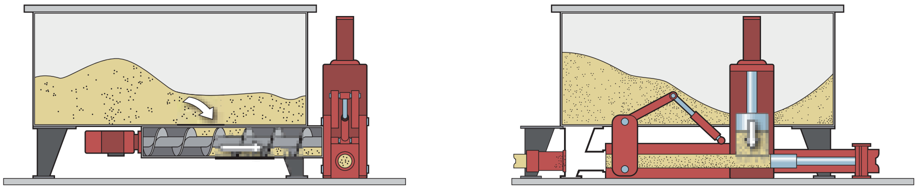

1. Material infeed and preprocessing stage

2. Prepressing with the load feeder

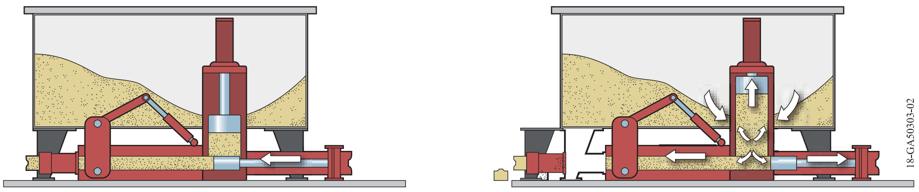

3. Briquette production, subject to pressure

4. Briquette discharge

Fig. 2 Different stages in briquetting of biomass in C 150 Briquette press.

biomass left over in each screen was determined and is further used to calculate X_{gm}. The tests were performed in replicates of three to understand the variability in the measured data.

5.2 Durability rating, moisture content, and loose bulk density

Durability-rating measurement helps in understanding the shear and impact forces the briquettes could withstand during handling, storage, and transportation processes (Tumuluru et al., 2015b). A briquette-durability rating was measured based on ASABE Standard S269.4, where ten briquettes (representing the ten replicates of each combination) were tumbled in a cube-durability tester for 3 minutes at 40 rpm. The dimensions of the durability box are 300 × 300 × 430 mm (12 × 12 × 17 in.) on each end. The axis of rotation of the box is horizontal. After tumbling, the briquette fragments with a mass of more than 20 % of the average original briquette fragment mass is designated "cylindrical size material" (CSM). In case the sample did not produce any CSM in the output sample, the durability rating is considered as zero. Eqn. 1 indicates the method to determine durability rating. The raw material and briquette moisture content were determined based on ASABE Standard S358.2. The unit and bulk density of the briquettes was measured based on ASABE Standard S269.4. As the variability in the measured values of the unit density values is high, the data reported were an average of 10 measurements. In case of bulk density, the observed variability in the data measured was lower, and the data reported are an average of three measurements.

$$DR = \frac{M_{\mathrm{CSM}}}{M_{\mathrm{INPUT}}} \times 100 \tag{1}$$

DR = Durability rating; M_{CSM} = Weight of cube-sized material (particles weighing more than 20 % of the average initial briquette weight); and M_{INPUT} = Weight of input material.

5.3 Energy consumption of the briquetting process

An APT power monitor meter was connected to the briquette press to log power data in kilowatts. LabVIEW software was used to log data during briquetting. Energy consumption for the briquetting process is calculated using Eqn. 2.

Briquetting energy consumption

$$= \frac{(\text{Full load power}\,(\text{kW}))*\text{time}\,(\text{h})}{\text{Weight of the briquettes}\,(\text{kg})} = \frac{\text{kWh}}{\text{kg}} \tag{2}$$

5.4 Data analysis

Experimental data collected for physical properties such as unit density, bulk density, and durability rating were used to calculate the standard-deviation values. Experimental data were further used to develop mathematical models. A multivariable regression model was used to fit the experimental data in order to understand the impact of moisture content and screen size on the product properties (unit and bulk density and durability) and energy consumption. Also, multivariate models are computationally easy to use, and they are not dependent on the underlying metric (Box, 2007). Many researchers have used single and multivariate models to understand the impact of the process variables on biomass commination and pelleting (Miao et al., 2011; Tumuluru et al., 2014; Tumuluru et al., 2016).

$$f(y) = a + b_1 x_1 + b_2 x_2 \tag{3}$$

where x_1: moisture content (%, w.b.); x_2: hammer mill screen size (mm); y: briquette properties (unit and bulk density (kg/m^3), and durability rating (%)) and briquetting energy consumption (kWh/t).

6. Results and discussions

6.1 Raw material properties

The X_{gm} of lodgepole pine was the highest for both 4.8 and 12.7 mm hammer mill screen size (see **Table 1**). The measured X_{gm} for lodgepole pine was 1.13 mm for 4.8 mm hammer mill screen size. Among the herbaceous biomass, switchgrass has the highest X_{gm} value of 2.35 mm, whereas corn stover has the lowest of 1.05 mm for 12.7 mm hammer mill screen size grind.

Table 1 Particle size data for the different feedstock.

Hammer mill screen size (mm)	Geometric particle length (*Xgm*) (mm)	*SD* (mm)
Lodgepole pine		
4.8	1.13	0.27
12.7	1.64	0.05
Switchgrass		
4.8	0.75	0.08
12.7	2.35	0.24
Corn Stover		
4.8	0.85	0.12
12.7	1.05	0.03

Note: *SD* = standard deviation

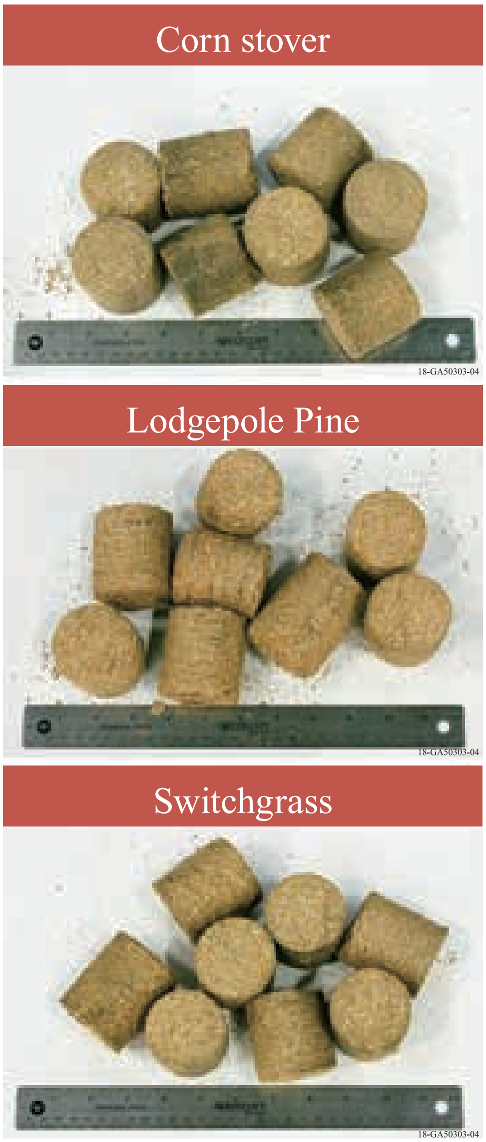

Fig. 3 Corn stover, lodgepole pine, and switchgrass briquettes produced using pilot-scale briquette press, moisture-15 % (w.b.), hammer mill screen size-4.8 mm.

6.2 Moisture content (%, w.b.)

Fig. 3 shows the corn stover, lodgepole pine, and switchgrass briquettes produced at 15 % (w.b.) moisture content using a 4.8 mm hammer mill screen grind. The moisture content of the briquettes after five days of storage at room temperature (20 °C) ranged from 8–11 % (w.b.).

6.3 Unit density (kg/m^3)

Fig. 4 shows the unit density of the lodgepole pine, switchgrass, and corn stover briquettes produced at three moisture contents and two hammer mill screen sizes. The data indicated that the smaller hammer mill screen size (4.8 mm) and lower moisture content (12 % [w.b.]) resulted in a higher unit density of 836 kg/m^3, whereas increasing the hammer mill screen size to 12.7 mm reduced the unit density to 771 kg/m^3 at the same moisture content for lodgepole-pine biomass. Increasing the moisture content of lodgepole pine to 18 % (w.b.) resulted in still lower unit density for both hammer mill screen sizes tested. In the case of herbaceous biomass (corn stover and switchgrass), lower and medium moisture content of 12 and 15 % (w.b.), and smaller hammer mill screen size of 4.8 mm resulted in a higher unit density of the briquettes. The maximum unit density of switchgrass briquettes was about 797 kg/m^3, whereas the corn stover was about 857 kg/m^3. Processed using a 12.7 mm hammer mill screen size at 18 % (w.b.) moisture content, corn-stover briquettes had a unit density of 826 kg/m^3, whereas the switchgrass briquettes had a unit density of 749 kg/m^3. Among the two herbaceous biomass feedstocks tested, switchgrass had a lower unit density compared to corn stover. The effect of biomass moisture content was found to be negligible at the 12.7 mm hammer mill screen size, but for the 4.8 mm hammer mill screen size, the moisture content did impact the unit density values.

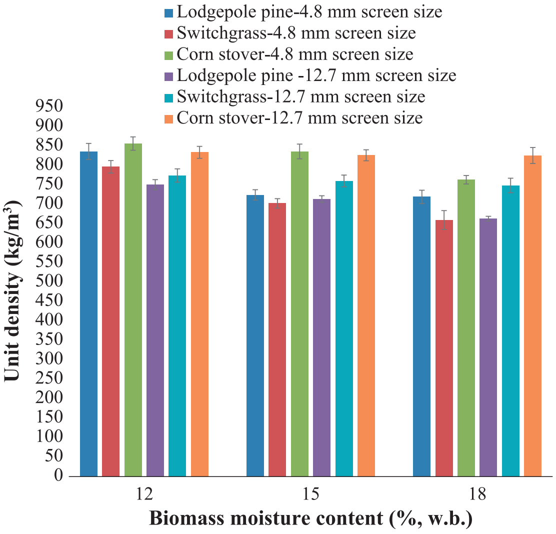

Fig. 4 Unit density of biomass briquettes produced at different process conditions.

6.4 Bulk density (kg/m^3)

The bulk density obtained for the three different biomass briquettes is given in **Fig. 5**. In the case of lodgepole-pine biomass at a lower moisture content of about 12 % (w.b.) and a 4.8 mm hammer mill screen size, the bulk density was about 489 kg/m^3, and increasing moisture content to 15 and 18 % (w.b.) lowered bulk density values to 422 and 420 kg/m^3. In the case of switchgrass, a maximum bulk density of about 446 kg/m^3 was observed at 15 % (w.b.) moisture content for a 4.8 mm hammer mill screen size, and increasing moisture content to 18 % (w.b.) reduced

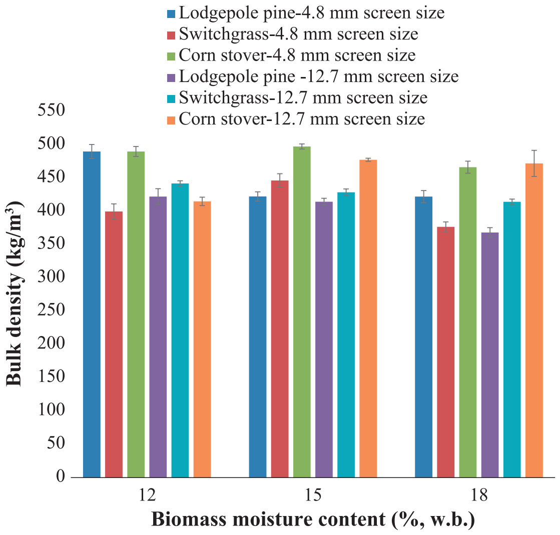

Fig. 5 Bulk density of biomass briquettes produced at different process conditions.

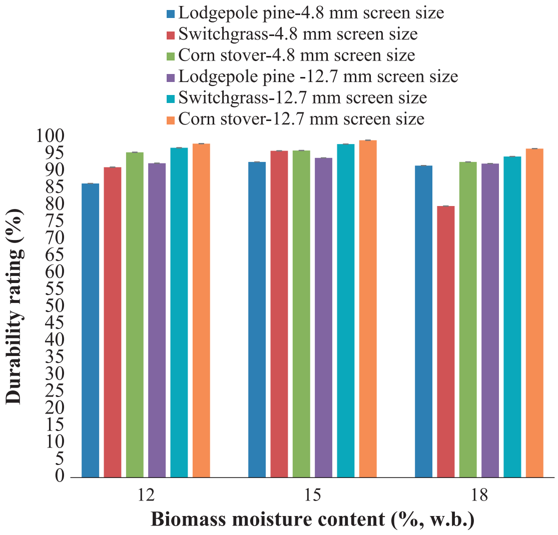

Fig. 6 Durability rating of biomass briquettes produced at different process conditions.

the bulk density values. The bulk density of the corn-stover briquettes followed a similar trend where the medium moisture content of 15 % (w.b.) produced briquettes with a bulk density of 497 kg/m^3 for a 4.8 mm hammer mill screen size grind and 477 kg/m^3 for a 12.7 mm hammer mill screen size. At 18 % (w.b.) moisture content and a 4.8 mm hammer mill screen size, the bulk density of the switchgrass and corn stover briquettes were about 376 and 466 kg/m^3, respectively. The results indicate that the density of the briquettes changes with biomass type, moisture content, and hammer mill screen size. It is also clear from the present results that the lower-to-medium moisture content and smaller screen size of 4.8 mm resulted in briquettes with a higher bulk density for both woody and herbaceous biomass. The unit and bulk density of corn stover briquettes are higher compared to switchgrass, which may be a result of better packing and interlocking of corn-stover particles compared to switchgrass.

6.5 Durability rating (%)

The durability rating measured for all briquettes produced under different process conditions is shown in **Fig. 6**. In the case of lodgepole pine, smaller hammer mill screen size (4.8 mm) and lower moisture content of 12 % (w.b.) resulted in the lowest durability rating of 86.5 %, whereas increasing the moisture content to 15 and 18 % (w.b.) resulted in higher durability ratings of 92 to 93 %. In the case of switchgrass and corn stover, the medium moisture content of 15 % (w.b.) resulted in higher durability-rating values (> 95 %) for a 4.8 mm hammer mill screen size. Increasing the screen size of the hammer mill to 12.7 mm resulted in higher durability ratings for both herbaceous and woody biomass. In the case of corn stover and switchgrass, a hammer mill screen size of 12.7 mm resulted in durability ratings of about 99 % and 98 %, respectively, whereas the durability rating for lodgepole pine was about 94 %.

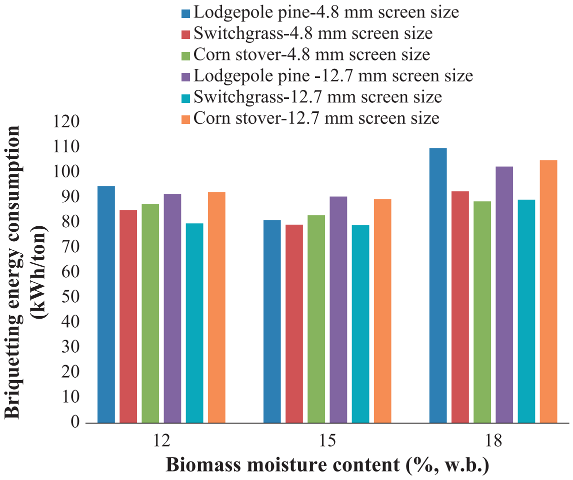

Fig. 7 Energy consumption of briquette production process at different process conditions.

6.6 Briquetting energy consumption (kWh/t)

Fig. 7 indicates energy consumption for the briquetting process. Briquetting energy increased with increased biomass moisture content. Also, increasing the hammer mill screen size resulted in increased energy consumption. For lodgepole pine biomass, the medium moisture content of 15 % (w.b.) and a 4.8 mm hammer mill screen size resulted in a lower energy-consumption value of 81 kWh/t, while increasing the moisture content to 18 % (w.b.) resulted in energy consumption of 110 kWh/t. In the case of switchgrass and corn stover, the lowest energy consumption was observed at 15 % (w.b.) moisture content for

4.8 mm hammer mill screen size (79 and 83 kWh/t for switchgrass and corn stover). When the hammer mill screen size was increased to 12.7 mm, the lowest energy consumption was again observed for 15 % (w.b.) moisture content. In the case of lodgepole-pine biomass at 15 % moisture content and a 12.7 mm hammer mill screen size, the energy consumption was about 90 kWh/t; for switchgrass and corn stover, the energy consumption was about 80 and 89 kWh/t. An increase in the screen size of the hammer mill had a slight impact on energy consumption for the herbaceous biomass. The present results indicate that moisture content of 15 % (w.b.) and a 12.7 mm hammer mill screen size could be the best conditions for producing durable corn-stover, switchgrass, and lodgepole-pine briquettes. To understand the impact of larger hammer mill screen size (19.05 mm) grind on the quality of woody and herbaceous biomass briquettes, tests were conducted at 15 % (w.b.) biomass moisture content.

6.7 Models

The experimental data generated for three different moisture contents (12, 15, and 18 % [w.b.]) and two hammer mill screen sizes (4.8 and 12.7 mm) were used to develop mathematical models to predict the quality of the briquettes made from wood and herbaceous biomass and energy consumption of the process. **Table 2** shows the multivariable linear-regression model fitted for the experimental data. Coefficients of determination (R^2) values for the fitted models are in the range of 0.5–0.8. The equation expresses the effect of moisture content and screen size of the hammer mill on quality (unit and bulk density and durability) and energy consumption.

The models indicated that corn stover, moisture content had a negative effect, while hammer mill screen size had a positive effect on unit density, whereas in the case of bulk density both hammer mill screen size and moisture content had a negative effect. In the case of lodgepole pine, hammer mill screen size and moisture content had a negative impact on both bulk and unit density. The models developed for switchgrass indicated that moisture content had a negative effect on unit density, while hammer mill screen size had a positive effect, whereas both hammer mill screen size and moisture content had a positive effect on bulk density. The durability rating of corn stover and switchgrass are negatively related to moisture content, but positively related to hammer mill screen size. In the case of lodgepole pine, both hammer mill screen size and moisture content had a positive impact on durability values. Energy consumption for briquetting corn stover is influenced positively by both moisture content and hammer mill screen size, whereas in the case of lodgepole pine and switchgrass, moisture content had a positive effect, but hammer mill screen size had a negative impact on energy consumption.

Table 2 Model to describe the effect of moisture content and screeen size on the physical properties and energy consumption.

Feedstock	Physical properties	Mathematical model	R^2
Lodgepole pine	Unit density (kg/m^3)	$y = 1046.93 - 17.045x_1 - 6.415x_2$	0.86
	Bulk density (kg/m^3)	$y = 623.24 - 10.143x_1 - 5.471x_2$	0.86
	Durability rating (%)	$y = 82.412 + 0.429x_1 + 0.326x_2$	0.50
	Energy consumption (kWh/t)	$y = 62.93 + 2.172x_1 - 0.0465x_2$	0.51
Switchgrass	Unit density (kg/m^3)	$y = 898.14 - 13.543x_1 + 5.246x_2$	0.72
	Bulk density (kg/m^3)	$y = 371.43 + 1.577x_1 + 2.615x_2$	0.45
	Durability rating (%)	$y = 102.12 - 1.166x_1 + 0.940x_2$	0.57
	Energy consumption (kWh/t)	$y = 66.340 + 1.413x_1 - 0.374x_2$	0.51
Corn stover	Unit density (kg/m^3)	$y = 939.62 - 8.432x_1 + 1.264x_2$	0.54
	Bulk density (kg/m^3)	$y = 619.66 - 7.80x_1 - 3.767x_2$	0.82
	Durability rating (%)	$y = 98.41 - 0.358x_1 + 0.400x_2$	0.79
	Energy consumption (kWh/t)	$y = 63.75 + 1.140x_1 + 1.169x_2$	0.61

Note: x_1 = moisture content (%, w.b.); x_2 = hammer mill screen size (mm); y = physical properties and briquetting energy consumption

Table 3 Physical properties and energy consumption of woody and herbaceous biomass briquettes produced using 19.05-mm screen size grind and 15 % (w.b.) moisture content.

Feedstock	Unit density (kg/m^3)	*SD*	Bulk density (kg/m^3)	*SD*	Durability rating (%)	*SD*	Energy consumption (kWh/t)
Lodgepole pine	712.04	11.21	393.53	5.26	90.73	0.002	97.84
Switchgrass	594.03	15.79	331.90	9.63	93.95	0.04	80.85
Corn stover	703.76	18.98	386.46	6.15	96.82	0.03	94.98

6.8 Physical properties and energy consumption of briquettes made using a 19.05 mm hammer mill screen size

Geometric mean particle length of corn stover and switchgrass ground in a hammer mill fitted with a 19.05 mm screen size was about 1.19 mm and 3.62 mm; lodgepole pine was about 4.37 mm. **Table 3** indicates the physical properties (unit and bulk densities and durability ratings) and energy consumption of the briquettes produced using a 19.05 mm hammer mill screen size and energy consumption of the process. It is clear from **Table 3** that briquette quality decreased when the hammer mill screen size was increased to 19.05 mm. Lodgepole pine, corn stover, and switchgrass had unit and bulk densities of 712 and 393 kg/m^3, 703 and 386 kg/m^3, and 594 and 331 kg/m^3, respectively. In the case of durability rating, corn stover had the highest value (of 96.82 %), followed by switchgrass (93.95 %), and lodgepole pine (90.73 %). In the case of energy consumption, lodgepole pine required higher energy to form the briquette (97.84 kWh/t), whereas switchgrass needed the lowest (80.85 kWh/t). Based on the present study, it can be concluded that increasing the screen size of the hammer mill to 19.05 mm reduced quality attributes and increased energy consumption.

7. Discussion

Tumuluru et al. (2011) indicated that both moisture and particle size have a significant impact on the quality of the briquettes produced. In general, smaller or finer particles in the grind, which have the higher contact-surface area, result in bringing the particles together, whereas smaller to medium particles rearrange in a way that forms a net by interlocking (Tumuluru et al., 2011). The presence of very large particles in the grind produces lower-quality briquettes due to a smaller contact-area among particles. Tumuluru et al. (2011), in their review of biomass densification systems, indicated that using a 8–12 mm screen size could result in high-quality briquettes in terms of durability and density. The results from the present study corroborate this observation where hammer mill screen size (12.7 mm) resulted in higher durability rating values. Experimental data from the current study also indicates that increasing the screen size of the hammer mill to 19.05 mm lowered unit- and bulk-density values for both woody and herbaceous biomass. The loss of density can be due to an increase in void spaces formed in the briquette. Tumuluru et al. (2011) indicated that larger grind size resulted in a lower bulk density due to increased porosity in the densified biomass. Ndindeng et al. (2015) found that particle size influenced the density, a larger grind size resulted in lower bulk density due to increased porosity, and smaller particles resulted in a more dense packing. Zhang and Guo (2014) studied the briquettes using a scanning electron microscope and found that briquettes formed using larger particles had a porous structure.

Another important parameter that impacts the physical properties of briquettes is moisture content. During cold densification (where there is no addition of heat), the binding is due to the formation of solid bridges due to elastic and plastic deformation and particle rearrangement resulting in particle interlocking bonds (Rumpf, 1962; Sastry and Fuerstenau, 1973). According to these authors, application of pressure can increase interfacial forces, capillary pressures, and cohesion among the biomass particles, resulting in the formation of solid and liquid bridges, which are formed due to hydrogen bonds, van der Waals' forces, attractive intermolecular force, and magnetic forces that result in particles adhering to each other. The other binding mechanism common in the briquetting process is the mechanical interlocking of the particles. Mechanical interlocking and solid bridges formed due to the presence of moisture and pressure determine briquette durability. In the present study, increasing the moisture content to 18 % (w.b.) and the screen size of the hammer mill to 19.05 mm resulted in lower density and durability ratings. Zhang and Guo's (2014) results corroborate with present research findings; increasing moisture content reduced the density of the solid fuels briquettes made from Caragana korshinskii Kom. In their study on pelleting of corn stover at higher moisture content using a 6 and 8 mm pellet die, Tumuluru (2014, 2015) indicated that high moisture content in the biomass lowers density, but durability and increases energy consumption. Tumuluru (2016) measured the expansion ratio of wood pellets produced using high-moisture lodgepole pine grind. The expansion ratio of pellets produced increased with an increase in moisture content. Higher expansion-ratio values lowered the pellet unit and bulk density and durability values. These observations corroborate with the present research, where increasing moisture content decreased unit and bulk density and durability of briquettes, which might be due to relaxation of the biomass fibers after extrusion from the die.

8. Conclusions

The present study indicates that good quality briquettes can be made using corn stover, switchgrass, and lodgepole pine. Maximum unit and bulk density of > 750 kg/m^3 and > 400 kg/m^3 were observed at 4.8 and 12.7 mm screen size and biomass moisture content of 12 and 15 % (w.b.) for both woody and herbaceous biomass. At 15 % (w.b.) moisture content and a hammer mill screen size of 12.7 mm, corn stover, switchgrass, and lodgepole pine resulted in briquettes with good durability ratings (> 94 %). Switchgrass and corn stover had maximum durability (> 97 %) compared to lodgepole pine, which recorded a maximum durability rating of about 94 %. The briquettes made using lodgepole pine were of lower quality when compared to herbaceous biomass briquettes. Briquetting energy consumption for switchgrass and corn stover ranged from 79 to 89 kWh/t for 4.8 and 12.7 mm screen size and 12 and 15 % moisture content. Multivariable linear regression models developed for the briquetting process with respect to moisture content and hammer mill screen size had coefficient of determination values in the range of 0.5–0.8. This study also indicated that going to a larger hammer mill screen size (of 19.05 mm) reduced the unit and bulk density and durability ratings of both woody and herbaceous biomass briquettes.

Acknowledgments

The author would like to acknowledge Craig C. Conner and Ty Dansie for support of experimental work. This work was supported by the Department of Energy, Office of Energy Efficiency and Renewable Energy under the Department of Energy Idaho Operations Office Contract DE-AC07-05ID14517. Accordingly, the publisher, by accepting the article for publication, acknowledges that the U.S. government retains a non-exclusive, paid-up, irrevocable, worldwide license to publish or reproduce the published form of this manuscript, or allow others to do so, for U.S. government purposes.

Author disclosure statement

No competing financial interests exist. This information was prepared as an account of work sponsored by an agency of the U.S. government. Neither the U.S. government nor any agency thereof, nor any of their employees, makes any warranty, express or implied, or assumes any legal liability or responsibility for the accuracy, completeness, or usefulness of any information, apparatus, product, or process disclosed, or represents that its use would not infringe privately owned rights. References herein to any specific commercial product, process, or service by trade name, trademark, manufacturer, or otherwise, do not necessarily constitute or imply its endorsement, recommendation, or favoring by the U.S. government or any agency thereof. The views and opinions of the authors expressed herein do not necessarily state or reflect those of the U.S. government or any agency thereof.

References

Antwi-Boasiako C., Acheampong B.B., Strength properties and calorific values of sawdust-briquettes as the wood-residue energy generation source from tropical hardwoods of different densities, Biomass and Bioenergy, 85 (2016) 144–152.

ASAE/ASABE Standards S269.4 (2008) Cubes, Pellets, and Crumbles—Definitions and Methods for Determining Density, Durability, and Moisture Content. American Society of Agricultural and Biological Engineers, St. Joseph, Michigan, USA, 2008.

ASAE/ASABE Standards S358.2 (1988) Moisture Measurement—Forages. American Society of Agricultural and Biological Engineers, St. Joseph, Michigan, USA, 1988.

ASAE/ASABE S424.1., Method of determining and expressing particle size of chopped forage materials by screening. March, 1992.

Atchison J.E., Hettenhaus J.R., Innovative Methods for Corn Stover Collecting, Handling, Storing and Transporting, NREL/SR-510-33893 (2004).

Box G.E.P., Draper N.R., Response Surfaces, Mixtures, and Ridge Analyses, second ed., John Wiley & Sons, Inc., New Jersey, 2007.

Jittabut P., Physical and thermal properties of briquette fuels from rice straw and sugarcane leaves by mixing molasses, Energy Procedia, 79 (2015) 2–9.

Lela B., Barišić M., Nižetić S., Cardboard/sawdust briquettes as biomass fuel: Physical–mechanical and thermal characteristics, Waste Management, 47 (2016) 236–245.

Mani S., Tabil L.G., Sokhansanj S., Specific energy requirement for compacting corn stover, Bioresource Technology, 97 (2006) 1420–1426.

Miao Z., Grift T.T., Hansen A.C., Energy requirement for comminution of biomass in relation to particle physical properties, Industrial Crops and Products, 33 (2011) 504–513.

Muazu R.I., Stegemann J.A., Effects of operating variables on durability of fuel briquettes from rice husks and corn cobs, Fuel Processing Technology, 133 (2015) 137–145.

Ndindeng S.A., Mbassi J.E.G., Mbacham W.F., Manful J., Graham-Acquaah S., Moreira J., Dossou J., Futakuchi K., Quality optimization in briquettes made from rice milling by-products, Energy for Sustainable Development, 29 (2015) 24–31.

Prasityousil J., Muenjina A., Properties of solid fuel briquettes produced from rejected material of municipal waste composting, Procedia Environmental Sciences, 17 (2013) 603–610.

Rahaman S.A., Salam P.A., Characterization of cold densified rice straw briquettes and the potential use of sawdust as binder, Fuel Processing Technology, 158 (2017) 9–19.

Rajaseenivasan T., Srinivasan V., Quadir G.S.M., Srithar K., An investigation on the performance of sawdust briquette blending with neem powder, Alexandria Engineering Journal, 55 (2016) 2833–2838.

Rumpf H., The strength of granules and agglomerates, in: Knepper W.A. (Ed.), Agglomeration, John Wiley, New York, 1962, pp. 379–418.

Saidur R., Abdelaziz E.A., Demirbas A., Hossain M.S., Mekhilef S., A review on biomass as a fuel for boilers, Renewable and Sustainable Energy Reviews, 15 (2011) 2262–2289.

Sastry K.V.S., Fuerstenau D.W., Mechanisms of agglomerate growth in green pelletization, Powder Technology, 7 (1973) 97–105.

Shuma R., Madyira D.M., Production of loose biomass briquettes from agricultural and forestry residues, Procedia Manufacturing, 7 (2017) 98–105.

Thabuot M., Pagketanang T., Panyacharoen K., Mongkut P., Wongwicha P., Effect of applied pressure and binder proportion on the fuel properties of holey bio-briquettes, Energy Procedia, 79 (2015) 890–895.

Tumuluru J.S., Wright C.T., Hess J.R., Kenney K.L., A review of biomass densification systems to develop uniform feedstock commodities for bioenergy application, Biofuels, Bioproducts, and Biorefining, 5 (2011) 683–707.

Tumuluru J.S., Effect of the process variables on the density and durability of the pellets made from high moisture corn stover, Biosystems Engineering, 119 (2014) 44–57.

Tumuluru J.S., High moisture corn stover pelleting in a flat die pellet mill fitted with a 6 mm die: physical properties and specific energy consumption, Energy Science & Engineering, 3 (2015) 327–341.

Tumuluru J.S., Specific energy consumption and quality of wood pellets produced using high-moisture lodgepole pine grind in a flat die pellet mill, Chemical Engineering Research and Design, 110 (2016) 82–97.

Tumuluru J.S., Lim C., Bi X., Kuang X., Melin S., Yazdanpanah F., Sokhansanj S., Analysis on storage off-gas emissions from woody, herbaceous, and torrefied biomass, Energies, 8 (2015a) 1745–1759.

Tumuluru J.S., Tabil L.G., Song Y., Iroba K.L., Meda V., Impact of process conditions on the density and durability of wheat, oat, canola, and barley straw briquettes, BioEnergy Research, 8 (2015b) 388–401.

Tumuluru J.S., Searcy E., Kenney K.L., Smith W.A., Gresham G.L., Yancey N.A., Impact of feedstock supply systems unit operations on feedstock cost and quality for bioenergy applications, in: Kumar R., Singh S., Balan V. (Eds.), Valorization of lignocellulosic biomass in a biorefinery: from logistic to environmental and performance impact, Nova Science Publishers, Inc., 2016, pp. 1–36.

Urbanovičová O., Krištof K., Findura P., Jobbágy J., Angelovič M., Physical and mechanical properties of briquettes produced from energy plants, Acta Universitatis Agriculturae et Silviculturae Mendelianae Brunensis, 65 (2017) 0219–0224.

Yank A., Ngadi M., Kok R., Physical properties of rice husk and bran briquettes under pressure densification for rural applications, Biomass and Bioenergy, 84 (2016) 22–30.

Zhang J., Guo Y., Physical properties of solid fuel briquettes made from Caragana korshinskii Kom, Powder Technology, 256 (2014) 293–299.

Author's Short Biography

Jaya Shankar Tumuluru

Dr. Tumuluru is a senior scientist in the Biofuels Department at Idaho National Laboratory (INL). He is the principal investigator for the Biomass Size Reduction, Drying, and Densification project for the U.S. Department of Energy Bioenergy Technologies Office. His research at INL is focused on mechanical and thermal preprocessing of biomass. He has published more than 100 papers in peer-reviewed journals and conference proceedings, and has received numerous awards, such as outstanding reviewer for the American Society of Agricultural and Biological Engineers, and INL's Outstanding Achievement in Scientific and Technical Publication, and the 2018 Asian American Engineer of the Year.

KONA Powder and Particle Journal No. 36 (2019) 252–263/Doi:10.14356/kona.2019010 Original Research Paper

Micromechanical Characterization of Particle-Particle Bond in Biomass Assemblies Formed at Different Applied Pressure and Temperature[†]

Apoorva Karamchandani, Hojae Yi* and Virendra M. Puri

[1] *Department of Agricultural and Biological Engineering, The Pennsylvania State University, USA*

Abstract

During biomass pelletization, the presence of activated natural binders is thought to promote the formation of solid bridges in a biomass assembly. To examine this hypothesis, bonded particles were extracted from the switchgrass compacts formed at different pressure and temperature. This study investigated the influence of these two factors on the resistance to dislocation of the particle-particle bond. The generated force-bond dislocation curves were used to calculate the slope from no load to failure from the assemblies formed at the treatments A (60 MPa and 75 °C), B (100 MPa at 75 °C), C (60 MPa and 90 °C), and D (100 MPa at 90 °C). Assemblies from the treatment B had the highest diametral tensile strength (60.9 ± 7.1 kPa) and densities (653.2 kg m^{-3}), whereas, assemblies formed from the treatment C had the lowest diametral strength (7.2 ± 1.4 kPa). The resistance to dislocation of particle-particle bonds at microscale was linearly correlated to the strength (R^2=0.838) and density (R^2=0.981) of the densified assemblies. High pressures are documented to form stronger compacts. However, the presence of sufficient moisture at low temperature can significantly improve the densified assembly properties by lowering the glass transition temperature of lignin to form stronger bonds.

Keywords: bond dislocation resistance, moisture content, diametral tensile strength, densification

---

1. Introduction

Ground biomass particles in pellets are brought together under high pressure and temperature to form bonds by inter-particle attraction forces and solid bridges by activation of natural binders present in biomass (Kaliyan N. and Morey R.V., 2010). Currently, biomass pelletization operation heavily relies on an empirical approach to ensure that biomass pellets maintain its integrity during subsequent handling and transport (Yi H. et al., 2018). Considering that the current empirical approach tends to focus on successful pelleting operation rather than optimizing energy input to achieve acceptable mechanical integrity, the biomass pelletization can be further engineered to produce pellets having acceptable durability with less than the current energy input. With the rapid growth in industrial production of biomass pellets (U.S. Department of Energy, 2016), it is expected that the efficient energy usage in the pelletization will result in the substantial production cost reduction in the respective industry.

Biomass pelletization process can be more energy and cost efficient by operating pellet mills with pressures that are close to the minimum threshold for achieving necessary interparticle bonding. Therefore, engineering biomass pelletization process requires a fundamental understanding of the basic mechanics of the pellet formation, i.e., how interparticle bonding develops under pressure and elevated temperature. To that end, this study aims to investigate how applied pressure and temperature during biomass compaction influence the resistance and strength of interparticle bonds by quantitatively measuring the mechanical response of formed bonds between and among particles.

Physical and chemical properties of biomass material have been studied actively (Adapa P. et al., 2009; Carroll J.P. and Finnan J. 2012; Colley Z. et al., 2006; Kaliyan N. and Morey R.V., 2009b; Karamchandani A. et al., 2015, 2016a; Mani S. et al., 2003; Mani S. et al., 2004, 2006; Poddar S. et al., 2014; Tumuluru J.S. et al., 2010). There are several factors such as moisture content, temperature, feedstock constituents, and physical properties of feedstocks, which play important roles in achieving the desired product quality. Many studies have been conducted

---

[†] Received 4 April 2018; Accepted 8 April 2018

[1] University Park, PA 16802, USA
* Corresponding author: Hojae Yi;
E-mail : huy1@psu.edu
TEL: +1-814-865-2807 FAX: +1-814-865-6178

to understand the effect of these factors on pellet qualities (Gilbert P. et al., 2009; Kaliyan N. and Morey R.V., 2006; Karamchandani A. et al., 2017; Mani S. et al., 2006; Tumuluru J.S., 2014). For example, a very wide optimal moisture content, ranging from 6 % to 20 %, has been reported for successful densification depending on the type of biomass and pelleting conditions. However, the optimum range of moisture content for pelletizing ground switchgrass, without adding any binders, has been reported to be between 17.5 % and 20 % (w.b.) (Karamchandani A. et al., 2015).

In addition to the moisture content, particle size also matters in the biomass pelletization. Several researchers observed that the optimal pellet quality is achieved with a mixture of particle sizes due to increased inter-particle bonding (mechanical interlocking) and the elimination of inter-particle spaces (attractive and adhesive and cohesive forces) (Kaliyan N. and Morey R.V., 2006; Payne J.D., 1978; Shaw M.D. and Tabil L.G., 2007). Finer particle sizes generally correspond with greater pellet strength and durability as larger particles serve as fissure points (MacBain R., 1966). Based on our previous studies (Karamchandani A. et al., 2015, 2016a), the pellet qualities were not significantly different for the two screen sizes, i.e., 3.175 mm and 6.35 mm. There is a trade-off between the energy required to produce finer particles, i.e., time and cost of grinding and the properties of pellets.

Therefore, the focus of this study is to examine, quantify, and explain the particle level bonding using a single screen size for particle size reduction. Kaliyan and Morey (Kaliyan N. and Morey R.V., 2010) showed that if the temperature rise of the biomass grinds due to frictional heating in the briquetting and pelleting machines is in the range of glass transition (i.e., softening) temperature of some of the constituents of biomass materials (i.e., ≥ 75 °C), then strong and durable briquettes and pellets could be produced without steam conditioning.

The applied pressure during densification process is another important parameter. Many studies have investigated the effect of the pressure (Adapa P. et al., 2007; Gilbert P. et al., 2009; Mani S. et al., 2006; Poddar S. et al., 2014; Rhén C. et al., 2005; Shaw M.D. and Tabil L.G., 2007). However, properties of bound biomass particles as a result of applied pressure to biomass particles, have yet to be sufficiently elucidated, which can impart critical information on the evolution of macroscopic densified structures and intricacies of the particle-particle binding mechanism.

Kaliyan N. and Morey R.V. (2010) and Stelte W. et al. (2011) attempted to examine the proposed binding mechanisms through microstructural imaging analyses. Due to biomass particles' small size, irregular shape, and rough surface, it has been difficult to study their mechanical response. Although there are numerous commonly used mechanical devices including universal testing machines or dynamic mechanical analyzer, they cannot be utilized directly in microscale experiments because of their unsuitable capability of manipulating test specimen with sub-millimeter size (Pantano M.F. et al., 2012).

To overcome the shortfalls of existing mechanical tests in characterizing the particle scale mechanics, quantitative properties of individual particles were studied by using a micromechanical device inspired by the microelectromechanical systems (MEMS) devices (Han J.H. and Saif, 2006; Karamchandani A. et al., 2016b; Zamil M.S. et al., 2014, 2015). A micromechanical device allowed tensile experiments to measure force-extension and, therefore, to determine the stress-strain response of single particles of ground biomass (Karamchandani A. et al., 2016b). From the dislocation testing of bonded particles, the bond resistance to dislocation and strength can be determined by decoupling particle and bond dislocation responses combining the previously reported single switchgrass particle mechanical properties. Using mechanical properties of particles, interparticle stiffness can be deduced to elucidate the mechanical properties of particles' binding mediated by natural binders present in the biomass.

Our previous study showed a relationship between mechanical properties of bulk ground material and strength of densified biomass products (Karamchandani A., 2013; Karamchandani A. et al., 2016a). Leveraging this finding, the strength of particle-particle bonds at the microscale can be linked to the strength of densified assemblies at the macroscale. The knowledge gap between the interparticle bond strength and a particulate assembly strength can be bridged with the microstructural tests that will enable a development of a multiscale theoretical framework during pelletization. Albeit few, the importance of understanding the thermo-mechanical binding mechanism of particles to engineer biomass densification has been qualitatively discussed (Kaliyan N. and Morey R.V., 2010; Stelte W. et al., 2011; Stelte W. et al., 2012). However, a quantitative measurement of mechanical responses of bound biomass particles had not been reported.

Therefore, the goal of this study is to determine the mechanical response including the strength of the bond formed due to natural binders present in the biomass particles. The objective of this study was to characterize the force-bond dislocation behavior of samples of two particles bonded together obtained from switchgrass compacts. We also tested the hypothesis that the resistance to a dislocation of two bonded particles is affected by the temperature and pressure applied to form the assemblies.

2. Material and methods

2.1 Test material

Switchgrass is a perennial warm-season grass, which was selected as the test material for this study. This grass can be grown on marginal land or rotated with other crops and has an advantage of lower ash and greater energy content over other crops (Parrish D.J. and Fike J.H., 2005; Sanderson M.A. et al., 2006). Pretreatment of biomass improves both its physical and chemical properties and makes the material easier to densify by facilitating the activation of natural binders for promoting better bond formation (Kaliyan N. and Morey R.V., 2010; Karamchandani A. et al., 2015; Mani S. et al., 2006; Stelte W. et al., 2011).

To obtain the optimal condition of pelletization, one screen size, 3.175 mm, was used for material size reduction task. Moisture content level of 17.5 % (w.b.) was considered for conditioning of ground switchgrass (Karamchandani A. et al., 2015, 2016b, 2016a). Switchgrass samples were conditioned in one batch of 25 g by adding required water and mixing with a manual Mini-Inversina (Bioengineering AG, Switzerland) that is capable of giving 360° motion (Karamchandani A. et al., 2015, 2016b). The conditioned material was kept in the humidity and temperature controlled chamber at 30 °C temperature and 60 % relative humidity for 24 h for moisture equilibration.

2.2 Biomass assembly

In our previous study, we reported the effect of moisture on the increased stiffness and modulus of elasticity of individual switchgrass particles (Karamchandani A. et al., 2016b). Water plays an important role in imparting strength to the individual particles, which is one of the critical preconditioning steps before the ground biomass is subjected to densification (Karamchandani A. et al., 2015; Lee S. et al., 2013; Mani S. et al., 2006; Tumuluru J.S., 2014).

Increase in the stiffness of switchgrass particles was thought to be contributed by the bundling of fibers promoted by the activation of binders due to increased moisture content. The addition of moisture generally increased failure stress but decreased failure strain, which can be attributed to the moisture's physiochemical interaction with and arrangement within switchgrass particles (Karamchandani A. et al., 2016b).

More importantly, conditioning the biomass with moisture reduces the glass-transition temperature of lignin from 120 °C–140 °C to 70 °C–90 °C (Irvine G.M., 1985). In particular, the glass transition temperature of switchgrass averaged at 75 °C and preheating the switchgrass grind from 75 °C to 100 °C increased the density of briquettes (Kaliyan N. and Morey R.V., 2009a).

Conditioned switchgrass at 17.5 % w.b. did not form stable assemblies at room temperature with the single die and punch system, which further affirmed the importance of temperature treatment during the densification process. Some initial runs were conducted at, and above 100 °C temperature, however, the moisture in the material was hypothesized to be expelled quickly, resulting in unstable crumbled densified assembly formation. Therefore, in this study, two temperatures, 75 °C, and 90 °C were selected to pretreat the material.

Compressive pressure is another important factor, which has been studied by several researchers (Adapa P. et al., 2007; Gilbert P. et al., 2009; Mani S. et al., 2006; Poddar S. et al., 2014; Rhén C. et al., 2005; Shaw M.D. and Tabil L.G., 2007). During densification, high pressures and temperatures may develop solid bridges by diffusion of molecules from one particle to another at the points of contact, which increases density (Tumuluru J.S. et al., 2011).

Conditioned switchgrass has been reported to form denser and more stable densified assemblies starting at 60 MPa as compared to 40 MPa, and the strength and density of pellets are documented to improve with an increase in compressive pressure (Mani S. et al., 2006). Because building higher pressure inside the pellet mill critically increases the energy consumption (Stelte W. et al., 2012), it is important to elucidate the particle binding mechanics under pressure levels near the on-set of stable assembly formation. Therefore, we chose two levels of pressure, namely 60 MPa and 100 MPa.

As explained above, based on initial trial runs and literature review, two temperatures (75 °C and 90 °C) and two pressure values (60 MPa and 100 MPa) were selected to form densified assemblies (**Table 1**). The assemblies were formed, at different applied pressure and temperature, in a single punch die attached to a universal testing machine (T-rex, Cooper Instruments and Systems, Warrenton, VA). The temperature of the die was controlled using a high-temperature barrel band heater (3671K151, McMaster-Carr, Aurora, OH). The die temperature was monitored using a thermocouple wire (Omega Engineering, TT-T-24-

Table 1 Design of experiment for densified assembly formation.*

Treatment	Temperature (°C)	Pressure (MPa)
A	75	60
B	75	100
C	90	60
D	90	100

*Number of replicates, $N = 5$

TCB, Norwalk, CT) attached to a temperature controller (Digi Sense temperature controller R/S, 89000-10, Cole Parmer, Vernon Hills, IL).

Temperatures of the top and die sleeve were checked before every run by inserting a thermocouple wire attached to a temperature sensor (2190 A Digital Thermometer, John Fluke Mfg. Co., Everett, Washington). The wire was removed during the compression process in order to avoid any foreign element interacting with the conditioned material and confounding effect on formed assemblies. Ground switchgrass compression was carried out by the top punch, whereas the bottom punch remained stationary at the bottom of the die during the densification process.

For each compact, approximately 0.7 g of switchgrass conditioned at 17.5 % w.b. moisture content was gravity filled in the cylindrical die and maintained at two temperature levels of 75 °C and 90 °C. After every run, both top and bottom punches and die contact surfaces were wiped with water to remove any binder that stuck on the surfaces. The top punch was inserted and kept in the cylindrical die to reach the same temperature as die sleeve and bottom punch after every run. The top punch was then retracted to fill the die with ground switchgrass and advanced to compress the material to form assemblies at desired pressure levels (**Fig. 1**).

Switchgrass assemblies (**Fig. 2**) were formed at pressure and temperature given in **Table 1**. The diametral tensile strength of the assemblies was measured using a universal testing device (Instron model 3345, Norwood, MA) at a compressive speed of 0.1 mm/min to maintain a quasi-static load application state. The strength of the assembly was correlated with the inter-particle binding strength at the microscale level. In addition, densities of individual assemblies were determined by measuring the weight (± 0.01 g) and calculating the volume. For volume calculation, the assembly shape was assumed to be a cylindrical disc; its volume was calculated using the measurement of its height (± 0.01 mm) and diameter (± 0.01 mm).

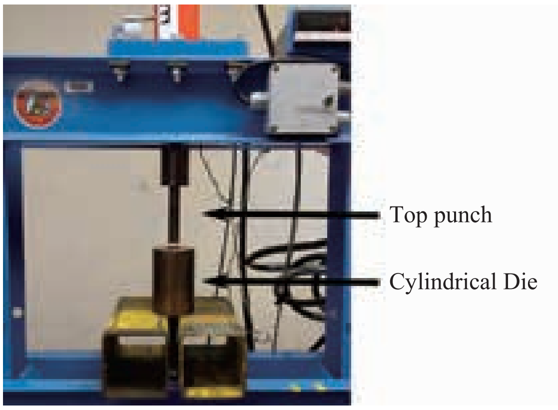

Fig. 1 Die punch system attached to a universal testing machine (T-rex Test Stand with two double action actuators, Coopers Instruments & Systems©) to form densified ground biomass assemblies.

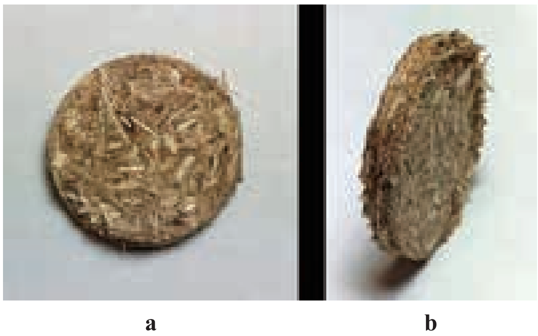

Fig. 2 Typical densified assembly formed at 60 MPa and 75 °C (**a**) top view and (**b**) side tilt view (Diameter = 21.8 mm and Height = 3.1 mm).

2.3 Bonded particle test

Bonded particles were extracted using a micromechanical device (Karamchandani A. et al., 2016b), which was inspired by MEMS chip design proposed by Zamil M.S. et al. (2014). This device consists of a piezoelectric motor-driven actuator (AG LS25, Newport, Bozeman, MT) and a 3D-printed force sensor beam (FSB) (Proto3000, Woodbridge, Ontario, Canada) (Karamchandani A. et al. (2016b).

Compliance of the device was verified by Karamchandani A. et al. (2016b) to avoid any error in the calculations. Formed assemblies were visually analyzed under a binocular 3.5x–90x zoom stereomicroscope (AmScope, SM-3BZ-80S, Irvine, CA) to identify and extract bonded particles formed due to the applied pressure. Selected bonded particles were gripped on the silicon chips attached to the fixed and moving ends of the micromechanical tester. The tests were carried out by applying stepwise incremental displacement loading, i.e., 0.45 μm displacement for each step, under a direct optical microscope (VanGuard 1242MM, Kirkland, WA) observation. A 10× objective lens and an additional eyepiece of magnification 4× were used for the optical observation.

The inherent nature of densification imparts the rearrangement of particles during the process, thereby, making it difficult to initially select two particles in the batch and extracting them out as a single bonded specimen after the process for experimental testing. Additionally, to form a local bond by selecting only two particles and pressing them in a die punch experiment in the presence of higher temperature to activate the natural binders is not documented in the literature and could not be achieved. Therefore, the limitation of this study was that the two bonded particle specimens were randomly selected from the densified assemblies with some selection criteria. For selected specimens, mechanical and chemical bonds formed between the particles were evaluated by holding one particle with the tweezer and slightly shaking the specimen to verify that particles did not fall apart. Two bonded particle samples that were thought not to establish mechanical and chemical interparticle bonds usually fell apart because of this shaking or moving from one petri dish.

There was a wide spectrum of particle sizes in the ground switchgrass ($D_{10} = 0.20$ mm, $D_{50} = 0.61$ mm, and $D_{90} = 1.4$ mm, where subscript numbers represent intercepts of 10 %, 50 %, and 90 % of the cumulative mass) (Karamchandani A. et al., 2015). When harvesting two bonded particle samples, it was ensured that the total length of the specimen, including the bond formed between two particles, should be less than 2 mm. This was considered in accordance to capture the dislocation in the bond and the extension in particles in the camera frame of 2048 × 1644 pixels throughout the experiment.

In addition, the specimens were selected on the basis of the angle formed between two particles. The two bonded particles with acute angle (less than 90°) assemblies were rejected in order to avoid the possible error due to extension (increase) of the angle during bond dislocation testing. In addition, it was verified that there was no angular movement between the particles during the stretching process by measuring the angles between two particles in selected images. Five replicates were performed for each treatment.

For gripping bonded particles on the silicon chips, glue (GPMR6008, Great planes, Champaign, IL) was applied on chip surfaces on the fixed and moving ends of the micromechanical tester. The bonded particles were picked up carefully using precision tweezers and placed on the glued portion on both sides (fixed arm and moving arm). The particles were gripped to the silicon chips on both sides so that the bonded area remains in the air without any support from the silicon chips. This process ensured that the glue did not wick onto the particle being tested. A glue accelerator (PT28, Zap Pacer Technology, Ontario, CA) was used to expedite the curing of applied glue. Silicon chip was attached to each side (fixed arm and moving arm) of the micromechanical device.

The loading was applied in the direction of increasing the distance between two particles. Resistance to this loading was assumed to come from mechanical interlocking and chemical bonding between two particles. The force required to move two particles away from each other was measured along with the increasing distance. These force and displacement data were subsequently analyzed as summarized in Karamchandani A. et al. (2016b). A typical sample of the particle-particle bond is shown in **Fig. 3**.

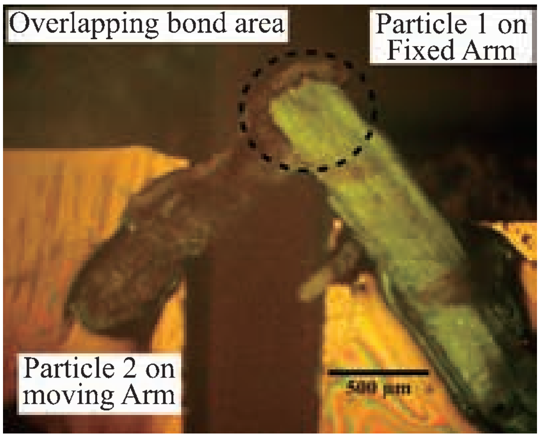

Fig. 3 A particle-particle bond sample on micromechanical tester. Left side is moving arm and the right side is the fixed arm.

3. Results and discussion

3.1 Force-dislocation curves

Fig. 4 shows force-dislocation curves for particle-particle bond at four different treatments, i.e., 75 °C and 90 °C temperature and 60 MPa and 100 MPa pressure, (number of replicates, $N = 5$) from no load to failure. The resistance value, the slope of force-bond dislocation response from no load to failure, of particle-particle bond extracted from the assemblies formed at treatment A (60 MPa pressure while maintaining the temperature of cylindrical die and punches at 75 °C) was 0.955 ± 0.368 kN m^{-1}. For treatments B (100 MPa at 75 °C), C (60 MPa and 90 °C), and D (100 MPa at 90 °C) resistance values were 0.986 ± 0.266 kN m^{-1}, 0.550 ± 0.248 kN m-1, and 0.703 ± 0.249 kN m^{-1}, respectively (**Table 2**). Because of the small sample size, a Mann-Whitney U test was performed (**Table 3**) to determine if there were differences in resistance of particle-particle bond between treatments (**Table 2**). The significance threshold was set at 0.05. None of the resistance to dislocation of particle-particle bond was significantly different ($p > 0.05$, **Table 3**). However, the trend of higher temperatures (Treatment C and D) producing higher bond resistance than lower temperatures (Treatment A and B) is clear. On the other hand, higher pressures (Treatment B and D) do not necessarily result in higher bond resistance (Treatment A and C).

The force-bond dislocation data was collected for the whole two bonded particle specimens, including the two particles and the bond formed between the particles. During the dislocation testing of bonded particles, the extension could manifest from the particles, and/or from the formed bond itself. Therefore, the proportion of binding strength, which is due to particle stretching and bond resistance, were deduced using the information from single

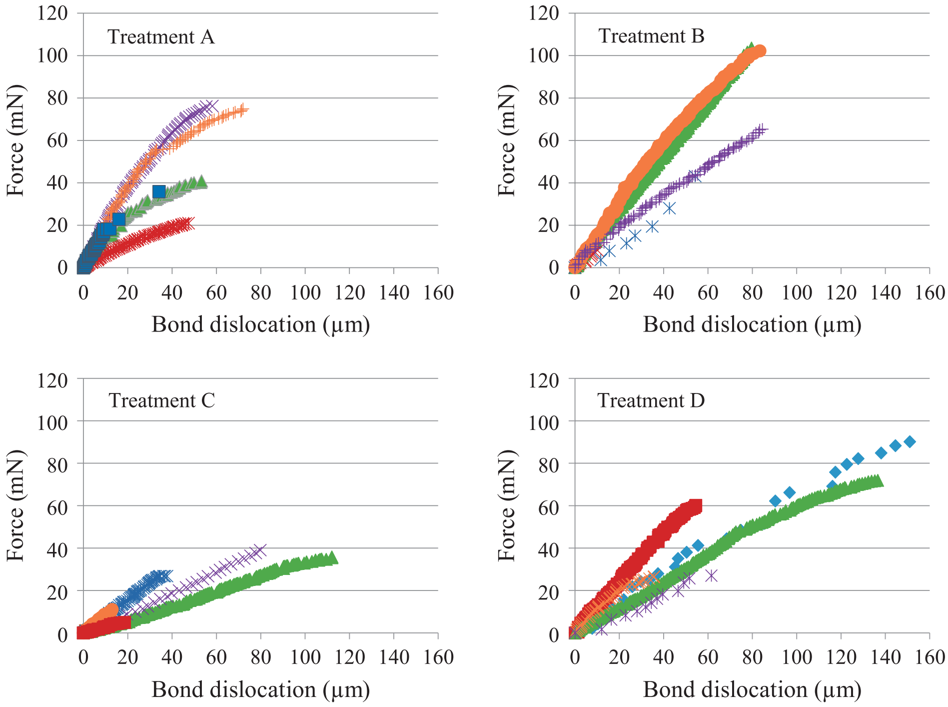

Fig. 4 Force-bond dislocation responses for **(a)** Treatment A (60 MPa and 75 °C), **(b)** Treatment B (100 MPa and 75 °C), **(c)** Treatment C (60 MPa and 90 °C), and **(d)** Treatment D (100 MPa and 90 °C) (Different marker represents different specimen).

Table 2 Resistance* of the particle-particle bond dislocation for five specimens at four different treatments**.

Specimen Number	Treatment A Pressure = 60 MPa Temperature = 75 °C	Treatment B Pressure = 100 MPa Temperature = 75 °C	Treatment C Pressure = 60 MPa Temperature = 90 °C	Treatment D Pressure = 100 MPa Temperature = 90 °C
1	0.445	0.784	0.346	0.497
2	0.754	0.784	0.289	0.570
3	1.026	0.809	0.498	0.604
4	1.153	1.273	0.791	0.719
5	1.399	1.280	0.825	1.125
Mean	0.955	0.986	0.550	0.703
SD	0.368	0.266	0.248	0.249

*Stiffness value is in kN m^{-1}

**P-values are included in Table 3 based on Mann Whitney U test

Table 3 P-value based on Mann-Whitney U tests.

Paired Treatments	Resistance of particle-particle bond (kN m^{-1})	Diametral Tensile Strength (kPa)	Assembly Density (kg m^{-3})
A and B	0.834	0.0122	0.2963
A and C	0.144	0.0122	0.0122
A and D	0.296	0.0122	0.0122
B and C	0.142	0.0122	0.0122
B and D	0.059	0.0122	0.0122
C and D	0.531	0.0216	0.1437

particle tests of switchgrass (Karamchandani A. et al., 2016b).

The calculations for particle-particle bond resistance were performed assuming that the bond due to natural binders and two particles formed a three-spring assembly (Eq. 1), where k is the resistance of each component.

$$\frac{1}{k_{\mathrm{eq}}} = \frac{1}{k_{\mathrm{particle1}}} + \frac{1}{k_{\mathrm{bond}}} + \frac{1}{k_{\mathrm{particle2}}} \tag{1}$$

The resistance, i.e. stiffness, of single particle (Karamchandani A. et al. 2016b) was calculated for a perfectly aligned particle oriented perpendicular to the silicon chips on the micromechanical tester.

Extracted bonded particle specimens were bonded at an angle greater than 90° in their natural state. As a result, the bonded particle specimens were not perpendicularly aligned to the silicon chips (**Fig. 3**). For all treatments and replicates, the stretching from individual particles was less than 0.5 % of total stretching observed during the test of the particle-particle bond. Therefore, stretching due to individual particles was considered negligible (< 0.5 %) and the arrangement of these particles in the specimen did not significantly affect the calculation of springs in the series.

The average value of resistance for treatment B was highest among all four treatments, followed by treatment A. Both the treatments were temperature treated at 75 °C, which appears to be the factor of increased resistance for the bonded particles although the difference is not significantly different ($p > 0.05$). Bonded particle assemblies extracted from compacts formed under higher temperature (treatments C and D) resulted in less resistant particle-particle bond. More moisture escaped from the specimen extracted from the assemblies formed at a higher temperature as compared to assemblies formed at a lower temperature, which may have changed the chemical characteristics of the bond formed between the particles.

This result is in alignment with our previous study, where moisture played a crucial role in stiffness of the conditioned and unconditioned switchgrass particles (Karamchandani A. et al., 2016b). The bond dislocation for treatments A, B, C, and D was 53.0 ± 13.9 µm, 64.2 ± 33.2 µm, 52.2 ± 42.6 µm, and 89.4 ± 50.2 µm, respectively. It was also observed for the force-dislocation curves of bonded particles at different treatments that the force at the failure of the particles had large variation. The force at failure for treatment A, B, C, and D was 49.7 ± 24.7 mN, 66.7 ± 43.6 mN, 23.5 ± 15.0 mN, and 55.2 ± 28.0 mN, respectively.

In most cases, the specimen underwent small plastic deformation right before the failure, whereas some specimens were observed to have a brittle failure. This variation in particle-particle bond may appear due to the alignment of particles in the assembly and force experienced during the compression process in the single die punch system. To minimize this variation to some extent, selected specimens were randomly extracted from the bottom-most layers of the densified assemblies, which were exposed to the lower punch during the densification process.

Limitation of determining the exact bonding area (**Fig. 3**) between the two particles prevented us from performing stress-strain analysis on the collected force-bond dislocation data. Since there was no control in the sample preparation, i.e., forming or finding a particle-particle bond with regularly shaped particles with the known bond area, the higher uncertainties of assuming the bonding area produced large errors in subsequent calculations for modulus of elasticity. In addition to the limitation mentioned above, there was no control on the individual particle sizes and shapes of the samples constituting the two particles. This study aimed to develop a characterization protocol to determine mechanical response of a particle-particle bond at the microscale level, which are the building blocks of the assemblies. Accordingly, this section includes discussion on presented data as supporting evidence for this developed protocol. Information on the exact bond area between particle-particle will be necessary and insightful for further mechanical characterization at the microscopic scale in future studies in this field.

3.2 Macroscale properties of densified assemblies

Table 4 lists mean and standard deviation values of diametral tensile strength and density of densified assemblies formed at four different treatments. Assemblies formed at 75 °C temperature at 100 MPa had the highest diametral tensile strength (60.9 ± 7.1 kPa), whereas, assemblies formed at 90 °C temperature at 60 MPa had the lowest diametral strength (7.2 ± 1.4 kPa). A Mann-Whitney U test was run on five samples of each treatment to determine if there were differences in strength of assemblies (**Table 3** and **4**). All pairs of macroscale strength of assemblies produced with treatments A, B, C, and D were statistically different (**Table 4**, $p < 0.05$).

Table 4 Diametral tensile strength and density of densified assemblies* formed at four different treatments**.

Treatment	Temperature (°C)	Pressure (MPa)	Diametral Tensile Strength (kPa)	Assembly Density (kg m^{-3})
A	75	60	38.1 ± 2.3	619.5 ± 25.4
B	75	100	60.9 ± 7.1	655.7 ± 55.7
C	90	60	7.2 ± 1.4	421.7 ± 52.5
D	90	100	16.4 ± 6.4	472.5 ± 19.5

*Number of replicates, $N = 5$
p-values are included in **Table 3 based on Mann Whitney U test

The density of individual assemblies followed the similar trend as the strength of assemblies. Because of a limited sample size, a non-parametric statistical test was used instead of typical parametric statistical mean difference test such as the t-test. A non-parametric test, Mann-Whitney U tests were performed on five samples of each treatment to determine if there were differences in density of assemblies. Differences in the bulk densities of switchgrass assemblies were statistically significant ($p < 0.05$) except differences between treatments A and B as well as C and D ($p \geq 0.05$).

The increase in density due to increase in pressure aligned with studies conducted by other researchers (Gilbert P. et al., 2009; Mani S. et al., 2006). Gilbert P. et al. (2009) mentioned that the increase in pressure increases the compressive pellet strength and pellet density, whereas, increase in temperature up to 95 °C increases the pellet qualities. However, further addition of heat may have resulted in quality deterioration. A study conducted by Kaliyan N. and Morey R.V. (2009a) did not show any significant difference in densified biomass compressed at 100 MPa pressure at two different temperatures, i.e., 75 °C and 100 °C. The preheating of biomass grind was performed in a closed insulated chamber, which might have reduced the moisture escape from the densified material.

In contrast to this mentioned study, the density of densified assemblies formed at 75 °C (treatment B) and 90 °C (treatment D) were significantly different at 100 MPa pressure ($p < 0.05$). At higher temperature, the test sample dries out quickly during the compression process. For higher temperature (90 °C) treatment C and D, at 60 MPa and 100 MPa pressure respectively, the moisture loss during the process to form assemblies was 12.0 ± 0.2 % w.b. and 12.3 ± 0.2 % w.b., respectively. The moisture loss for treatment A and B (temperature 75 °C at 60 MPa and 100 MPa pressure) was 7.5 ± 0.5 % w.b. and 9.1 ± 0.5 % w.b., respectively, which was lower as compared to other two treatments. This moisture loss might have contributed to the lower densities of the assemblies formed at higher pressure. Since moisture is an essential component that behaves as both lubricant and binder (Kaliyan N. and Morey R.V., 2010), increased loss of moisture during the densification process could not assist in the activation of binders.

The assemblies formed at a lower temperature (75 °C) were on average 42.6 % denser compared to the assemblies formed at a higher temperature (90 °C). The set-up of these experiments conducted in this current study was different from the above mentioned previous studies conducted by various researchers. Therefore, a pronounced difference can be seen in the macroscale properties of assemblies as compared to data collected by several other researchers. In the next section, we correlated the microscale particle properties to the macroscale quality metrics of densified assemblies formed using the same material.

3.3 Correlation between the resistance of particle-particle bond at microscale and macroscale assembly quality properties

Fig. 5a presents the correlation between the resistance of particle-particle bond at microscale and strength of densified assemblies at the macroscale. The resistance values tend to show a larger standard deviation, there seemed to exist a clear trend of higher bond resistance produced by higher temperature. Although this finding is limited by the lack of statistical significance, presumably due to the small sample size, there exist a clear trend of bond resistance to dislocation affected by temperature and pressure. The strengths of densified assemblies at different temperature and pressure levels are significantly different each other and the trend is in line with bond resistance of particles. It is thought that several particle-particle bonds collectively form the assemblies at macroscale and strengthen the macrostructure to hold the shape.

Based on the correlation, the strength of assemblies was linearly correlated to the resistance of particle-particle bonds ($R^2 = 0.838$) that were the building blocks of these

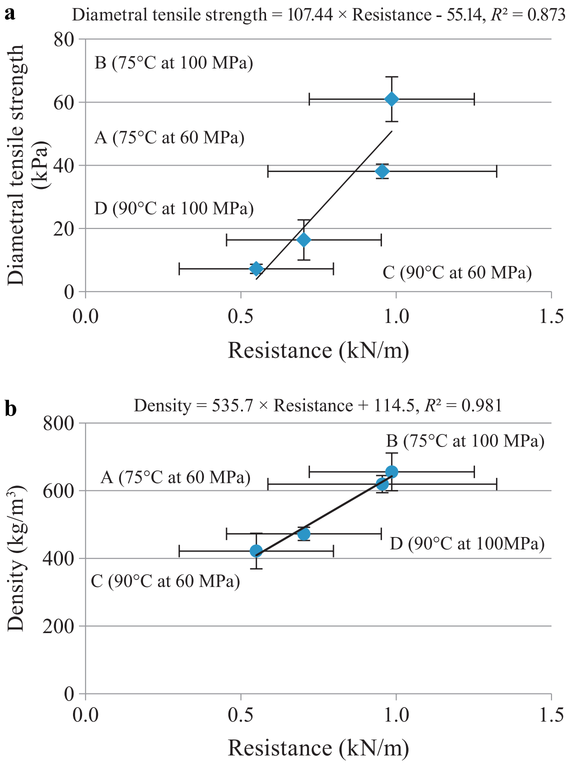

Fig. 5 Correlation between (**a**) particle-particle bond resistance at the microscale to the diametral tensile strength of switchgrass assembly at the macroscale and (**b**) particle-particle bond resistance at the microscale to the density of switchgrass assembly at the microscale.

assemblies. **Fig. 5b** presents the correlation between the resistance of particle-particle bond at microscale and density of densified assemblies at the macroscale. The trends of relationships of strength and density of assemblies to particle-particle bond resistance are similar. Based on the correlation, the density of assemblies highly correlated to the resistance of dislocation of particle-particle bonds ($R^2 = 0.981$).

The assemblies formed at lower temperature treatments (A and B–75 °C at 60 MPa and 100 MPa, respectively) were stronger than the assemblies formed at higher temperatures. Treatment B (75 °C at 100 MPa) formed strongest assemblies and had the highest resistance of particle-particle bonds, whereas the assemblies formed at 90 °C at 60 MPa (treatment C) were the weakest assemblies and had the most fragile particle-particle bond at the microscale. Although it is unknown, which chemical constituents contributed to the weakening of the bond at the higher temperature, the moisture loss and influence of moisture on the lignin could be the probable cause of these weak bonds.

The moisture loss at lower temperature was 5–7 %, whereas, moisture loss for assemblies formed at higher temperature was in the range of 9.6–12 %. At higher temperature, the moisture loss from the assemblies was substantially higher than for assemblies formed at a lower temperature. The lower moisture content, due to a higher rate of escape of moisture, in the formed assemblies resulted in a more brittle behavior at the particle-particle bond. In addition, lignin present in the switchgrass reaches glass transition temperature and gets activated in the presence of moisture at a temperature higher than 75 °C (Kaliyan N. and Morey R.V., 2009a). Higher moisture has been documented to decrease the glass transition temperature of the lignin. Although both temperatures in this study were in the lignin activation spectrum, a significant difference ($p < 0.05$) was observed in the densities and strength of the assemblies. The plasticizing effect of water on lignin is predominantly due to absorbed water at sites, and not the free volume of water, which significantly increases the molecular mobility that is accompanied by a decrease in thermal stability of lignin (Guigo N. et al., 2009).

In summary, we reasoned that the assemblies formed at higher temperature produced weaker bonds due to an insufficient amount of moisture at activation sites for lignin to undergo thermal softening. Presence of sufficient moisture at a low temperature can significantly improve the densified assembly properties. This observation provides strong evidence that stronger assemblies can be formed by modulating the amount of moisture for lignin activation without a large increase in temperature.

4. Conclusion

Force-dislocation curves were generated for particle-particle bonds extracted from assemblies formed at four different treatments; i.e., two pressure and two temperature values. Bonded particle assemblies extracted from compacts formed at higher pressure (at 100 MPa, temperature 75 °C and 90 °C) resulted in less resistant, i.e., more compliant, particle-particle bond. The resistance value of particle-particle bond extracted from the assemblies for treatments A (60 MPa and 75 °C), B (100 MPa at 75 °C), C (60 MPa and 90 °C), and D (100 MPa at 90 °C) were 0.955 ± 0.368 kN m^{-1}, 0.986 ± 0.266 kN m^{-1}, 0.550 ± 0.248 kN m^{-1}, and 0.703 ± 0.249 kN m^{-1}, respectively. At macroscale, the assemblies formed by applying same force at higher temperature were weaker as compared to assemblies formed at a lower temperature, although both temperatures were in the lignin activation spectrum. The diametral strength of formed assemblies at treatments A (60 MPa and 75 °C), B (100 MPa at 75 °C), C (60 MPa and 90 °C), and D (100 MPa at 90 °C) were 38.1 ± 2.3 kPa, 60.9 ± 7.1 kPa, 7.2 ± 1.4 kPa, and 16.4 ± 6.4 kPa, respectively. The densities of formed assemblies at treatments A (60 MPa and 75 °C), B (100 MPa at 75 °C), C (60 MPa and 90 °C), and D (100 MPa at 90 °C) were, 619.5 ± 25.4 kg m^{-3}, 655.7 ± 55.7 kg m^{-3}, 421.7 ± 52.5 kg m^{-3}, and 472.5 ± 19.5 kg m^{-3}, respectively.

Assemblies formed at the same temperature at higher pressure were stronger than assemblies formed at lower pressure. However, there was no significant difference between densities of the assemblies ($p > 0.05$). Increase in pressure was reasoned to bring immediate neighboring particles together, thus imparting more strength and higher density to the assembly. In this process, water supported the thermal softening of natural binders in the presence of heat. Therefore, the right combination of temperature, pressure, and moisture content should be achieved to form stable and stronger assemblies, which will further reduce the cost and energy of production of assemblies at a higher scale.

The microscale properties of particle-particle bonds were linearly correlated to the macroscale properties of densified assemblies. Diametral strength and densities of assemblies were linearly correlated to the resistance of particle-particle bonds (R^2=0.838 and R^2=0.981).

Acknowledgements

This scientific work was partly supported by USDA National Institute of Food and Agricultural Federal Appropriations under Project PEN04602 and Accession Number 1009850.

References

Adapa P., Schoenau G., Tabil L., Sokhansanj S., Singh A., Compression of fractionated sun-cured and dehydrated alfalfa chops into cubes—specific energy models, Bioresource Technology, 98 (2007) 38–45. DOI:10.1016/j.biortech.2005.11.032

Adapa P., Tabil L., Schoenau G., Compaction characteristics of barley, canola, oat and wheat straw, Biosystems Engineering, 104 (2009) 335–344. DOI:10.1016/j.biosystemseng.2009.06.022

Carroll J.P., Finnan J., Physical and chemical properties of pellets from energy crops and cereal straws, Biostystems Engineering, 112 (2012) 151–159. DOI:10.1016/j.biosystemseng.2012.03.012

Colley Z., Fasina O.O., Bransby D., Lee Y.Y., Moisture effect on the physical characteristics of switchgrass pellets, Transactions of the ASABE, 49 (2006) 1845–1852.

Gilbert P., Ryu C., Sharifi V., Swithenbank J., Effect of process parameters on pelletisation of herbaceous crops, Fuel, 88 (2009) 1491–1497. DOI:10.1016/j.fuel.2009.03.015

Guigo N., Mija A., Vincent L., Sbirrazzuoli N., Rodríguez F., Nadif A., Dam J.E.G. van, Molecular mobility and relaxation process of isolated lignin studied by multifrequency calorimetric experiments, Physical Chemistry Chemical Physics, 11 (2009) 1227. DOI:10.1039/b812512k

Han J.H., Saif M.T.A., In situ microtensile stage for electromechanical characterization of nanoscale freestanding films, Review of Scientific Instruments, 77 (2006) 45102. DOI:10.1063/1.2188368

Irvine G.M., The significance of the glass transition of lignin in thermomechanical pulping, Wood Science and Technology, 19 (1985) 139–149. DOI:10.1007/BF00353074

Kaliyan N., Morey R.V., Factors affecting strength and durability of densified products, 2006 ASABE Annual Meeting, (2006) 066077. DOI: 10.13031/2013.21754

Kaliyan N., Morey R.V, Densification characteristics of corn stover and switchgrass, Transactions of the ASABE, 52 (2009a) 907–920.

Kaliyan N., Morey V.R., Factors affecting strength and durability of densified biomass products, Biomass and Bioenergy, 33 (2009b) 337–359. DOI:10.1016/j.biombioe.2008.08.005

Kaliyan N., Morey V.R., Natural binders and solid bridge type binding mechanisms in briquettes and pellets made from corn stover and switchgrass, Bioresource Technology, 101 (2010) 1082–1090. DOI:10.1016/j.biortech.2009.08.064

Karamchandani A., Predictive relationships for quality assessment of densified biomass using fundamental mechanical properties of ground corn stover, switchgrass, and willow (Master of Science Dissertation), Pennsylvania State University, 2013.

Karamchandani A., Yi H., Puri V.M., Comparison of mechanical properties of ground corn stover, switchgrass, and willow and their pellet qualities, Particulate Science and Technology, 36 (2018) 447–456. DOI:10.1080/02726351.2017.1355860

Karamchandani A., Yi H., Puri V.M., Fundamental mechanical properties of ground switchgrass for quality assessment of pellets, Powder Technology, 283 (2015) 48–56. DOI:10.1016/j.powtec.2015.04.069

Karamchandani A., Yi H., Puri V.M., Comparison and explanation of predictive capability of pellet quality metrics based on fundamental mechanical properties of ground willow and switchgrass, Advanced Powder Technology, 27 (2016a) 1411–1417. DOI:10.1016/j.apt.2016.04.036

Karamchandani A., Yi H., Puri V.M., Single particle mechanical characterization of ground switchgrass in air dry and wet states using a microextensometer, Powder Technology, 301 (2016b) 568–574.

Lee S.M., Ahn B.J., Choi D.H., Han G.S., Jeong H.S., Ahn S.H., Yang I., Effects of densification variables on the durability of wood pellets fabricated with Larix kaempferi C. and Liriodendron tulipifera L. sawdust, Biomass and Bioenergy, 48 (2013) 1–9. DOI:10.1016/j.biombioe.2012.10.015

MacBain R., Pelleting Animal Feed, American Feed Manufacturers Associations, (1966).

Mani S, Tabil L.G., Sokhansanj S., An overview of compaction of biomass grinds, Powder Handling and Processing, 15 (2003) 160–168.

Mani S., Tabil L.G., Sokhansanj S., Grinding performance and physical properties of wheat and barley straws, corn stover and switchgrass, Biomass and Bioenergy, 27 (2004) 339–352. DOI:10.1016/j.biombioe.2004.03.007

Mani S., Tabil L.G., Sokhansanj S., Effects of compressive force, particle size and moisture content on mechanical properties of biomass pellets from grasses, Biomass and Bioenergy, 30 (2006) 648–654. DOI:10.1016/j.biombioe.2005.01.004

Pantano M.F., Espinosa H.D., Pagnotta L., Mechanical characterization of materials at small length scales, Journal of Mechanical Science, 26 (2012) 545–561. DOI:10.1007/s12206-011-1214-1.

Parrish D.J., Fike J.H., The biology and agronomy of switchgrass for biofuels, Critical Reviews in Plant Sciences, 24 (2005) 423–459. DOI:10.1080/07352680500316433.

Payne J.D., Improving quality of pellet feeds, Milling Feed and Fertilizer, 161 (1978) 34–41.

Poddar S., Kamruzzaman M., Sujan S.M.A., Hossain M., Jamal M.S., Gafur M.A., Khanam M., Effect of compression pressure on lignocellulosic biomass pellet to improve fuel properties: Higher heating value, Fuel, 131 (2014) 43–48. DOI:10.1016/j.fuel.2014.04.061

Rhén C., Gref R., Sjöström M., Wästerlund I., Effects of raw material moisture content, densification pressure and temperature on some properties of Norway spruce pellets, Fuel Processing Technology, 87 (2005) 11–16. DOI:10.1016/j.fuproc.2005.03.003

Sanderson M.A., Adler P.R., Boateng A.A., Casler M.D., Sarath G., Switchgrass as a biofuels feedstock in the USA, Canadian Journal of Plant Science, 86 (2006) 1315–1325. DOI: 10.4141/P06-136.

Shaw M.D., Tabil L.G., Compression and relaxation characteristics of selected biomass `grinds, 2007 ASAE Annual Meeting, (2007) 076183. DOI:10.13031/2013.23511

Stelte W., Holm J.K., Sanadi A.R., Barsberg S., Ahrenfeldt J., Henriksen U.B., A study of bonding and failure mechanisms in fuel pellets from different biomass resources, Biomass and Bioenergy, 35 (2011) 910–918. DOI:10.1016/j.biombioe.2010.11.003

Stelte W., Sanadi A.R., Shang L., Holm J.K., Ahrenfeldt J., Henriksen U.B., Recent developments in biomass pelletization—a review, BioResources, 7 (2012) 4451–4490.

Tumuluru J.S., Effect of process variables on the density and durability of the pellets made from high moisture corn stover, Biostystems Engineering, 119 (2014) 44–57. DOI:10.1016/j.biosystemseng.2013.11.012

Tumuluru J.S., Wright C.T., Hess J.R., Kenney K.L., National I., A review of biomass densification systems to develop uniform feedstock commodities for bioenergy application, Biofuels, Bioproducts and Biorefining, (2011) 683–707. DOI:10.1002/bbb

Tumuluru J.S., Wright C.T., Kenny K.L., Hess J R., A review on biomass densification technologies for energy application, Idaho National Laboratory (INL), (2010) INL/EXT-10-18420. DOI:10.2172/1016196

U.S. Department of Energy, 2016 Billion-Ton Report: Advancing Domestic Resources for a Thriving Bioeconomy, Volume 1: Economic Availability of Feedstocks, Oak Ridge, 2016.

Yi H., Pandeya A., Karamchandani A., Puri V.M., Critical review on engineering mechanical quality of green compacts using powder properties, KONA Powder and Particle Journal, 35 (2018) 32–48. DOI:10.14356/kona.2018006

Zamil M.S., Yi H., Puri V.M., Mechanical characterization of outer epidermal middle lamella of onion under tensile loading, American Journal of Botany, 101 (2014) 778–787. DOI:10.3732/ajb.1300416

Zamil M.S., Yi H., Puri V.M., The mechanical properties of plant cell walls soft material at the subcellular scale: the implications of water and of the intercellular boundaries, Journal of Materials Science, 50 (2015) 6608–6623. DOI:10.1007/s10853-015-9204-9

Authors’ Short Biographies

Apoorva Karamchandani

Apoorva Karamchandani is a doctoral candidate in the department of Agricultural and Biological Engineering at Pennsylvania State University, working under the supervision of distinguished professor Virendra Puri. She received a B. Tech. degree in agricultural engineering from G.B. Pant University, Uttrakhand, India and a master’s degree from Penn State in the same discipline. At Penn State, Apoorva is working in the field of powder mechanics including physical and mechanical characterization of particulates and compaction. Her research explores the ways to improve the efficiency of biomass densification process by developing a fundamental framework to predict end product quality.

Hojae Yi

Dr. Hojae Yi is a Research Associate at the Pennsylvania State University. He earned his Ph.D. degree from the Seoul National University in 2003. He joined the Pennsylvania State University as a visiting scholar in 2000 for one year where he started his researches on powder mechanics. Dr. Hojae Yi has been working at Department of Agricultural and Biological Engineering of the Pennsylvania State University since 2006. His current research interests include experimental studies and mathematical modeling on compaction and flow behavior of particulate materials with emphasis on the multiscale approach.

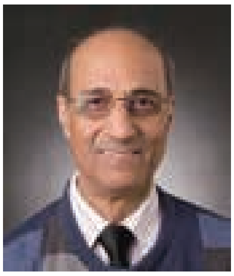

Virendra M. Puri

Dr. Virendra M. Puri, University Distinguished Professor, has researched in the field of powder mechanics for over three decades. He served as Acting Director of the Particulate Materials Center and co-authored numerous publications. He is co-inventor and holder of patents in powder flow, deposition, and compaction and has copyright for multi-purpose computational software on powder processing. Dr. Puri has served on several Editorial Boards, International Advisory Boards, and Chairpersons of bulk solids-related publications and professional activities. Professor Puri is member of KONA North Americas Editorial Board and Co-Editor-in-Chief of *Particulate Science and Technology*. He has received several teaching and research awards.

KONA Powder and Particle Journal No. 36 (2019) 264–270/Doi:10.14356/kona.2019016 Original Research Paper

The Swirl Reactor—a Reactor Concept for Continuous Gas-Solid Interactions[†]

Dag Øistein Eriksen [1*], Oddvar Gorset [2] and Håvar Gausemel [3]

[1] *Primus.inter.pares AS, Norway*
[2] *Aker Solutions AS, Norway*
[3] *Bayer AS, Norway*

Abstract

The Swirl reactor is an innovative concept for performing reactions in gas phases or solid and gas phase mixtures. It was developed during the initial boom of the solar cell industry, where the need for more energy- and cost-efficient means of producing high-purity solid silicon became important. The Swirl reactor was designed to fulfil the following requirements: continuous production of high-purity silicon; efficient energy transfer from the reactor to the gas; controlled transport of the Si-fines and the gas formed; the use of silane as feed for silicon. By employing a stainless steel tubular reactor honed on the inside and heated from the outside, and using argon as the carrier gas, the requirements were all shown to be fulfilled. The Swirl reactor throughput can be increased by having more than one injector introducing new swirls. Also, two swirls—each containing reacting agents—may form product where they mix, i.e. along the path where the swirls overlap. Thus, reactions can be controlled but still be run continuously. The possible uses of the Swirl reactor are numerous.

Keywords: silane, swirl flow, amorphous silicon, photovoltaic silicon, fines, cyclone, downer reactor

1. Background

In the first decade of this century, the photovoltaic industry had a growth of 10–30 % annually. Thus there was a strong incentive to produce high-purity silicon at a lower operating cost, e.g. at a lower energy consumption. For a comprehensive review of photovoltaic production at the time of development of the Swirl reactor, we refer to the Handbook of Photovoltaic Science and Engineering (Luque and Hegedus, 2003).

The standard method for the production of high-purity silicon was the use of the so-called Siemens reactor where trichlorosilane ($HSiCl_3$, called TCS) is thermally decomposed at silicon rods heated by electric current. This process is very energy-intensive and alternatives have been designed and tested. The Siemens reactors used to produce solid silicon from TCS are batch-operated and consume a huge amount of thermal and electric energy in addition to producing a very corrosive gas, HCl, at high temperatures: $HSiCl_3 + H_2 \rightarrow Si(s) + 3HCl$. The use of silane, SiH_4, instead is a much more attractive idea since $SiH_4 \rightarrow Si(s) + 2H_2$. Union Carbide Corp. had started the development of a fluidized bed reactor (FBR) based on silane, but were not successful. They sold their silicon facility to Komatsu Ltd. who formed the company Advanced Silicon Materials Inc. (ASiMI), which continued the development of the FBR. However, it was not until REC purchased the plant that this alternative finally became the process of choice for growing Si-crystals from the thermal decomposition of silane (Filtvedt et al., 2013; Du et al., 2014). The company REC Silicon is today the leading producer using this technology1). First, PV-quality silicon is produced, then the standard method of producing polycrystalline silicon wafers for PV-cells is applied, i.e. melting the silicon granules in a crucible, then performing a slow crystallization from the bottom creating what is called a bowl, and finally using a wire-saw to cut the bowl into ca 200-μm-thick sheets. This also turns almost half of the silicon into sawdust, called kerf. Since the saw uses glycol for cooling, the kerf is not easily regenerated. Today the Norwegian company ReSiTec is focusing on this part of PV production.

[†] Received 26 April 2018; Accepted 18 June 2018
J-STAGE Advance published online 31 August 2018

[1] Kongsberggata 20, 0468 Oslo, Norway
[2] Snarøyveien 20, 1360 Fornebu, PO Box 222, 1326 Lysaker, Norway
[3] Drammensveien 288, 0283 Oslo, Norway
[*] Corresponding author: Dag Øistein Eriksen;
E-mail: d.o.eriksen@kjemi.uio.no
TEL: +47-948-07-505

1) The company Renewable Energy Corporation (REC) was divided into REC Silicon and REC Solar. The latter is now a part of Elkem, while the former is an independent company.

However, during the competitive days, free-space reactors were tested for the decomposition of silane, but with minor success. The silicon formed was amorphous and of a very small particle size and high surface area. Such fines tend to stick to all kinds of surfaces and grow aggregates. This phenomenon is studied in the frames of homogeneous and heterogeneous nucleation of silane pyrolysis (Slootman and Parent, 1994; Onischuk et al., 2000). Attempts to develop free-space reactors stranded on the handling of the silicon fines. This was also the major obstacle to overcome in development of the FBR.

To meet the challenges of both energy transfer from a hot surface to the gas and to control the movement of the formed fines and agglomerates, the concept of a Swirl reactor was developed. Since the concept was also continuous, the succeeding production of wafers could also be included, but this part of the project was not initiated at the time when the Swirl reactor was developed. Later, a float-casting program was initiated in cooperation with a group at Carnegie-Mellon University in Pittsburgh, PA, USA (Ydstie et al., 2009).

The production of silicon was a case study, but the development of the reactor was in fact based on other kinds of powder and gases, and the technology is therefore not limited to the decomposition of silane.

1.1 The swirl concept

The Siemens reactor is a device where the gases to be decomposed are separated from air (to avoid the formation of SiO_2) and is operated at high temperature at the Si-rods (1100 °C), where the TCS is thermally reacted with hydrogen and decomposed to form polycrystalline silicon. To avoid reaction of the gas at other sites in the reactor than at the hot rod, the surface of the reactor must be cooled. Thus there is a huge heat loss in the process. In addition, the Siemens reactors must be operated in batch mode and involve manual interactions. To represent an attractive alternative, the Swirl reactor was designed to fulfil the following requirements:

i. Continuous production
ii. Efficient energy transfer from reactor to reagent
iii. Controlled transport of the fines and gas formed
iv. Use of silane as feed for Si

The concept can be expressed as: silane gas is swept along the inner surface of a tubular reactor being heated from the outside. The silane is diluted in an inert gas, e.g. argon or hydrogen, which acts as a carrier gas. The carrier gas will sweep the surface and bring the solid silicon formed to the end of the reactor for further processing. Of course, the Swirl reactor is not limited to silane, argon and hydrogen. In principle, it will be possible to use any kinds of fines and gases. Also, there is no reason why liquids cannot be used.

2. Experimental

2.1 Scope of work

The first test of the reactor was performed using simple tubular transparent reactors made of plastic or glass, using air as the gas and silica, SiO_2, or smoke as the solid particles. The particles' trajectories could then be measured by Laser Doppler Anemometry (LDA). (A primer of LDA can be found in Mathiesen et al. (1999)). In this way, we were able to easily make conical reactors to see how the swirl would be affected by a decreasing or increasing diameter. All reactors had smooth inner surfaces.

With LDA, the velocities' magnitude in the axial and tangential directions of the particles can be measured. It was shown that the path of the particles was a helix and that this was maintained even when the fluid mixture was heated, causing an expanded volume of fluid gas.

In the second part, the objective was to decompose silane. Then a reactor operating at temperatures up to at least 600 °C was needed. This is above the stability of glass. We therefore attempted to make a reactor based on a cylinder of quartz. However, we had to abandon the visibility due to technical problems with leaks in the connecting parts of the quartz reactor. This part therefore used a tubular stainless steel reactor. The challenge was then to prove that the swirl was maintained during the process.

2.2 Apparatus and chemicals

The LDA equipment was made by Dantec Dynamics who also supplied the lasers and control and analysis software. The gases used were argon and 5 % silane in argon, both supplied by AGA. The reactors were all produced exclusively for this project at the Institute for Energy Technology (IFE), Kjeller, Norway. IFE also constructed and manufactured the in- and outlet parts of the reactor according to our requirements. The injector part had a central inlet for measuring temperature and four peripheral inlets for gas and solid reactants or for other measuring devices. The outlet was too hot for standard filters and a water-cooled filter holder was therefore needed and constructed.

2.3 Reactors

For the initial LDA tests, cylindrical and conical reactors were made from transparent plastic and glass materials, and pressurized air was injected into the reactor with a lance injector through an inlet disc. Smoke was mixed with the air during low-temperature tests in order to make the flow patterns detectable by the LDA equipment, while SiO_2 dust particles were used during high-temperature tests.

In the high-temperature tests, the gas temperature inside the reactor was increased linearly along the reactor from room temperature (approx. 300 K) to 600 K, simulating an expanding gas flow as would be the case for a reaction where SiH_4-gas is decomposed completely to Si(s) and H_2(g). The increase in temperature was achieved by wrapping heating tape around the reactor on the outside and with decreasing space between neighboring tape windings along the reactor.

A cylindrical stainless steel (SS316) reactor was constructed, 500 mm long, with an inner diameter of 56.3 mm, and a wall thickness of 2.0 mm. The tube was honed inside to ensure a smooth reactor wall. At the ends, flanges were welded on, resulting in a neck of 40 mm on each side of the reactor. A separate injector piece was made and attached to the front flange. This was convenient when the injection angle or nozzle size were to be changed. At the back flange, a filtering piece was attached. As the gas exiting the reactor is hot and the dust particles to be collected are very small, we made a water-cooled filter housing. A steel mesh to support the glass-fiber filter also provided cooling to the filter.

Fig. 1 is a simplified Process Flow Diagram (PFD) of the set-up for a useful process including recycling of the carrier gas.

We have only tested the reactor at laboratory scale, producing a few grams per hour. One of the objectives in the project was to obtain design parameters for scaling-up the reactor. The reactants' length of trajectory along the inner surface of the reactor depends on the flow rate, the diameter, and the injection angle, whereas the heat transferred to the reaction is a function of the temperature of the reactor and the entering carrier gas, the nozzle size, the flow rate and the reactor length. A software package simulating this was planned as a part of the project, but this part had to be abandoned when the project was stopped.

2.4 Analyses

The silicon produced was analysed for structure by X-ray diffraction (XRD) using an INEL XRG 3000 diffractometer, with a multichannel curved position sensitive detector, recording all 2θ positions simultaneously. Particle size distributions were measured by a Malvern Mastersizer 2000, using laser scattering.

3. Results

3.1 LDA results

The particles' axial and tangential velocities were measured by LDA. The trajectories can then be extracted in various ways. **Figs. 2** and **3** show two possible representations. Both are real measurements of SiO_2-particles blowing in a conical reactor which is heated by a heating tape wound around the outside of the reactor wall. The laser was employed between the windings.

3.2 Particle analyses results

Fig. 4 shows an XRD spectrum of silicon produced by thermal decomposition in a small quartz tube reactor not used for the swirl measurements. The XRD measurements confirm that the bulk of the produced silicon is amorphous. The lack of crystalline structure gives the wide peak in the spectrum. The peak is possibly also wid-

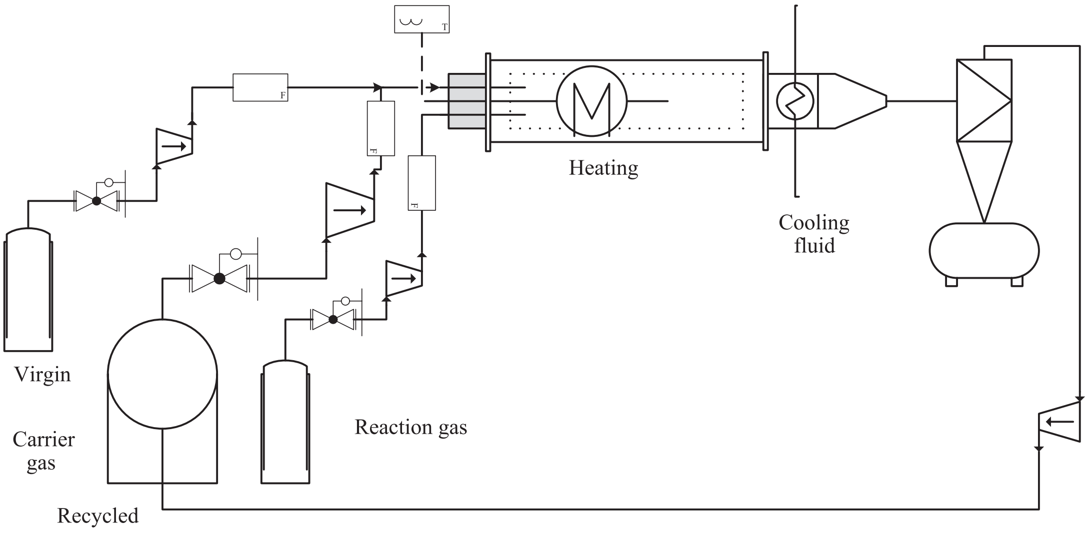

Fig. 1 Simplified Process Flow Diagram (PFD) of a Swirl reactor with pumps/compressors, valves and pressure flasks. The solid formed is separated and collected and the carrier gas is returned for reuse. This diagram is based on the thermal reduction of silane forming Si and H_2, which also is the carrier gas.

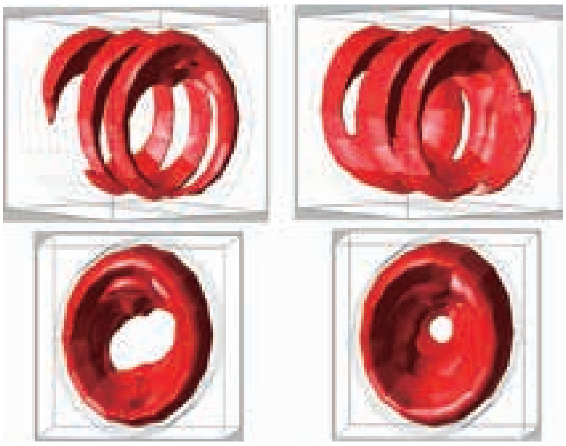

Fig. 2 Iso-surface plots for non-expanding (left panels) and expanding (right panels) swirling gas flows of SiO_2-particles. The expansion is due to heating.

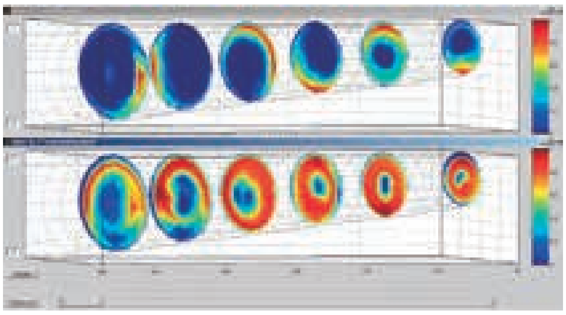

Fig. 3 Measured velocities in an isothermal, non-expanding conical swirl flow reactor. The upper panel shows the axial velocity, and the lower panel shows the tangential velocity.

ened by the small particle size and the small amount of silicon. The freshly made Si-particles tended to form aggregates. To enable particle size distribution measurement, the produced silicon was absorbed in glycol and the particle distribution measured a short time after (in the order of minutes) by laser scattering. This method was not qualified, but the best measurements gave a distribution ranging from 0.04 to 1 µm. If the particles were allowed to aggregate, the distribution would range from 200 to > 2000 µm. This gives an illustration of the property of Si-fines to form aggregates. The average particle sizes can be used for estimating the surface area, and simple calculations using the atomic distance of Si-Si bonds as the atomic diameter (235.2 pm; Winter, 2018)—assuming spherical Si-particles—gives estimates of > 100 000 m^2/g. Considering that the Si-atoms at the surface have non-saturated bonds, it is not surprising that agglomerates are formed.

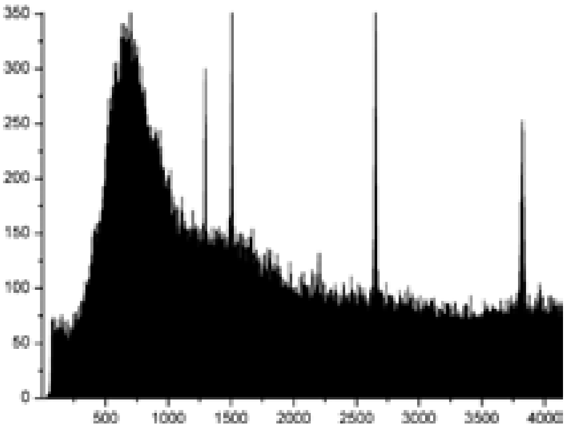

Fig. 4 XRD spectrum of silicon produced by the thermal decomposition of silane, SiH_4. The spectrum shows the intensity of reflections as a function of channel numbers, which is proportional to the scattering angle. The narrow peaks are reflections of elements in the backing of the silicon and have nothing to do with the Si.

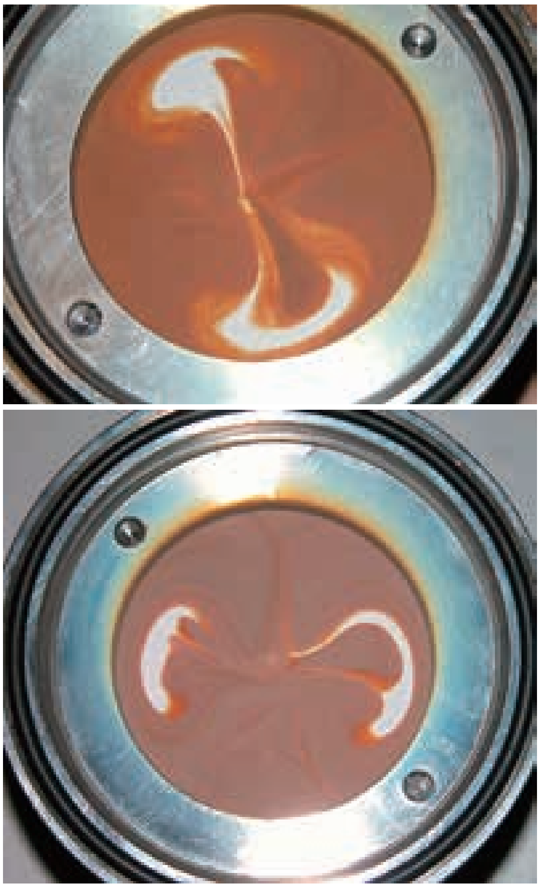

Fig. 5 Silicon produced in the Swirl reactor at one set of injection angle and flow. The difference in color is due to the different time of exposure in air before the picture was taken.

Fig. 5 shows the structure of the silicon absorbed on two filters. It is shown that applying the same conditions, i.e. mainly nozzle injection angle and flow, the flow conditions inside the reactor are then maintained and there can be no other cause than a swirl for creating such a complex pattern. The difference in color is believed to be dependent on the time the filter was exposed to air. The silicon particles have a high surface area, as explained,

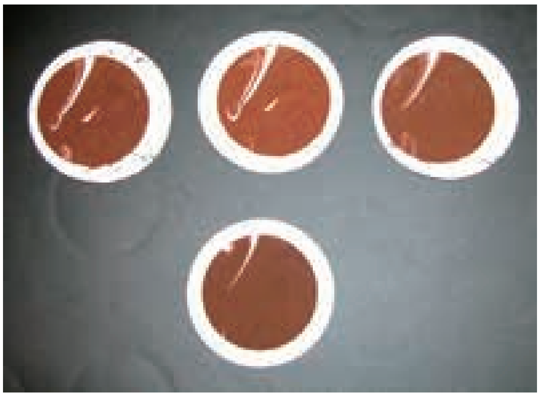

Fig. 6 Silicon produced in the Swirl reactor at a different set of injection angle and flow compared to **Fig. 4**. The same operational conditions were tested four times.

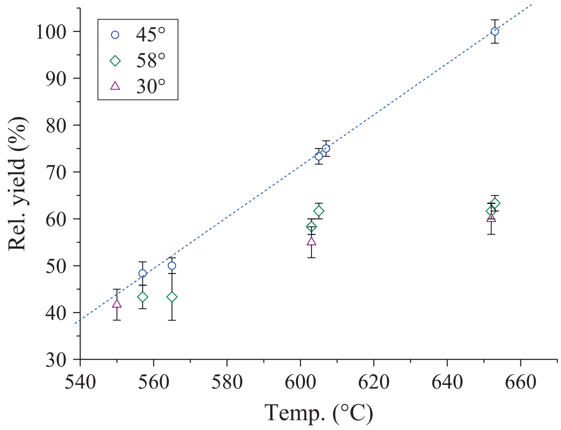

Fig. 7 Relative yields as a function of temperature and injection angle. Gas flow 2.0 L/min. The line is drawn to guide the eye.

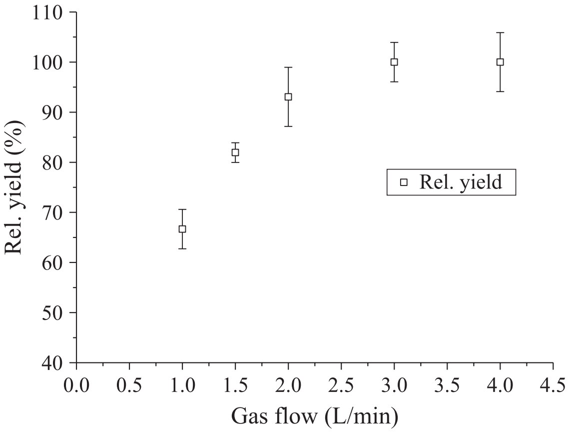

Fig. 8 Relative yields at 600 °C as a function of the carrier gas flow rate.

and can easily form oxides which will show up as white or gray.

Moreover, **Fig. 6** represents a different condition, but again it was shown that the flow pattern was maintained as four equivalent tests gave the same pattern.

3.3 Reaction results

With a fixed steel reactor length, the three parameters to vary were temperature, injection angle and flow. Nozzle size was not usually changed. **Figs. 7** and **8** show the relative variations in yield of silicon as a function of these three parameters. The yield in this case was unfortunately not a well-defined amount in this experimental set-up. It was determined as the amount of Si accumulated on the filter relative to the amount injected. But no Si outside the filter or unreacted silane was detected or included in the calculation of the yield reported. The fact that the yield approaches 100 % at the highest flow rate tested indicates that the highest flow rate brings out more Si from the reactor and therefore gives a more efficient swirl. The silicon not measured at the outlet for the lower flows is believed to stick to the interior of the reactor. The temperature reported is the one at the outside of the reactor. The temperature in the center of the reactor was monitored, but only to check that the gradient between the outside and inside was small.

4. Discussion and conclusion

The results presented in the foregoing paragraph clearly show that the swirl flow is maintained in the reactor. Moreover, finely grained, amorphous material with a high affinity for making agglomerates and a tendency to stick to any surface could be handled well.

When our work on the Swirl reactor was ongoing, the focus was primarily on the production of photovoltaic (PV) silicon. From the above results the optimum seems to be 45° injection angle, 3.0 L/min gas flow at a temperature of 650 °C (923 K). Both injection angles of 30° and 60° seem to give lower yields than 45°. Overly small angles may give too little force along the reactor and then lose solids to the central part of the reactor, whereas overly large angles will not wipe the whole surface effectively. These statements are hypotheses and need to be investigated further.

The Swirl reactor has similarities with the downer reactor, but that is based on cyclone technology. A downer reactor is vertical and uses gravitation for avoiding backmixing. Cheng Y. et al. (2008) have published a review of this reactor technology. Downer reactors utilize plug flow whereas the Swirl reactor—where the fluid is heated at the inner surface of the reactor—develops a radial kinetic energy gradient that causes turbulence. Estimates of the Reynolds number indicate figures well above the limit for a turbulent regime. This implies good mixing between solids and gas; important for reactions which comprise these.

Downer reactors were primarily developed for the same purposes as fluidized bed reactors are used for: reforming catalysis of natural gas, cracking of hydrocarbons, anaerobic combustion, etc. The solids employed in the downers, e.g. catalyst and absorbents, are usually recycled. The production of silicon is not a common theme, but Levin H. and Ford L.B. (1982) have patented a vertical cyclone reactor for transforming silicon gas directly into a melt of silicon. We believe the Swirl reactor may be operational in the same segments as the downer reactors.

The Swirl reactor throughput can be increased by having more than one injection point. As shown in **Fig. 2**, there is space without solids between the swirls. This can be utilized by another swirl. Also, two swirls containing reacting agents may then form product wherever they touch, i.e. along the path where the swirls overlap. Thus reactions can be controlled but still be run continuously.

By combining Swirl reactors in a “honeycomb” pattern, heat loss can be reduced and throughput increased. Increasing the diameter of the reactor increases the volume even more, but the central part of the Swirl reactor is of less use, so there is a possibility of turning the reactor into an annular reactor and thus saving space to be heated.

The concept of the Swirl reactor was patented (Eriksen D.O. and Gorset O., 2008) by the Institute for Energy Technology (IFE) where the authors were all once employed, but was later stopped and there is presently no patent hindering the use or development of this reactor concept. In the patent, means for separating the solids formed from the carrier gas, flow distributions inside different kinds of reactors and verification tests are described.

We believe the Swirl reactor may be useful also for liquids and for the treatment of ores such as carbo-chlorination reactions. Here, the oxidic mineral or solid feed can first be mixed with carbon and then in the Swirl reactor the solid mixture meets chlorine gas. The carbon binds the oxygen and the metal will form gaseous chlorides. Metals forming gaseous chlorides are iron, titanium, silicon, vanadium, zirconium, etc. This can also be used for removing such metals from other non-volatile metal chlorides like the rare earths.

A new segment for use may be the coating of solid particles. For example, combining finely ground graphite and silane may form Si-coated graphite which is of great interest as an electrode material for use in Li-ion batteries.

Acknowledgements

This scientific work was financed as a Strategic Institute Project at IFE by a grant from the Research Council of Norway. The authors are grateful to IFE for releasing the patent so that interested parties can develop the technology further.

Nomenclature

Abbreviations used in the text:

ASiMI	Advanced Silicon Materials Inc.
FBR	Fluidized Bed Reactor
IFE	Institute for Energy Technology, Kjeller, Norway
LDA	Laser Doppler Anemometry
PV	Photovoltaic
PFD	Process Flow Diagram
REC	Renewable Energy Corporation
TCS	Tri-Chlorosilane, $HSiCl_3$
XRD	X-Ray Diffraction

References

Cheng Y., Wu C., Zhu J., Wei F., Jin Y., Downer reactor: From fundamental study to industrial application, Powder Technology, 183 (2008) 364–384. DOI: 10.1016/j.powtec.2008.01.022

Du J., Dutta S., Ydstie B.E., Modeling and control of solar-grade silicon production in a fluidized bed reactor, AIChE Journal, 60(5) (2014) 1740–1751. DOI: 10.1002/aic.14378

Eriksen D.O., Gorset O., Method and reactor for continuous production of semiconductor grade silicon, US Patent, (2008) US20080292525A1.

Filtvedt W.O., Mongstad T., Holt A., Melaaen M., Klette H., Production of silicon from SiH_4 in a fluidized bed, operation and results, International Journal of Chemical Reactor Engineering, 11(1) (2013) 57–68. DOI: 10.1515/ijcre-2012-0027

Levin H., Ford L.B., Thermal Reactor, US Patent, (1982) US4343772A.

Luque A., and Hegedus S., Eds., Handbook of Photovoltaic Science and Engineering, John Wiley & Sons, 2003. DOI: 10.1002/0470014008

Mathiesen V., Solberg T., Arastoopour H., Hjertager B.H., Experimental and computational study of multiphase gas/particle flow in a CFB riser, AIChE Journal, 45(12) (1999) 2503–2518. DOI: 10.1002/aic.690451206

Onischuk A.A., Levykin A.I., Strunin V.P., Ushakova M.A., Samoilova R.I., Sabelfeld K.K., Panfilov V.N., Aerosol formation under heterogeneous/homogeneous thermal decomposition of silane: Experiment and numerical modeling, Journal of Aerosol Science, 31(8) (2000) 879–906. DOI: 10.1016/S0021-8502(99)00562-5

Slootman F., Parent J.-C., Homogeneous gas-phase nucleation in silane pyrolysis, Journal of Aerosol Science, 25(1) (1994) 15–21. DOI: 10.1016/0021-8502(94)90178-3

Winter M., WebElements <www.webelements.com>, WebElements Ltd., UK, 2018.

Ydstie B.E., Ranjan S., Sukumar B., Seetharaman S., Methods for casting by a float process and associated apparatuses, (2009) PCT/US2009/006114.

Authors' Short Biographies

Dag Øistein Eriksen

Dag Øistein Eriksen has a PhD degree in nuclear chemistry from the University of Oslo, 1976. He is currently the owner and CEO of Primus.inter.pares AS—a private consultancy company excelling in separation science and the use of radioactivity as tracers. Eriksen was eight years in the rare earth industry and 15 years as a senior scientist at the Institute for Energy Technology (IFE). He was appointed as a member of the Expert Group of Prometia and has for the last four years served as senior advisor to the Department of Chemistry, University of Oslo.

Oddvar Gorset

Oddvar Gorset has his MSc. degree in chemical engineering from the Physical Chemistry Department at NTNU (the Norwegian University of Science and Technology) in 1995. He has held positions as process engineer, researcher, project manager and senior process engineer in the engineering companies ABB Environmental, Alstom and Aker Clean Carbon, and the research institute IFE. Oddvar now works as Specialist Engineer and Project Manager in Aker Solutions, Fornebu, Norway, within Aker Solutions' CO_2 capture technology.

Håvar Gausemel

Håvar Gausemel has a Dr. scient. in nuclear chemistry from the University of Oslo, 2004. He is currently the Radionuclidic Sourcing Manager and Radiation Safety Expert at Bayer AS, a pharmaceuticals company. Gausemel held a post-doc. position at IFE while working on the swirl reactor and worked as a senior scientist at Renewable Energy Corporation AS for four years, focusing on the thermal decomposition of silane.

Hydrodynamic Study of a Circulating Fluidized Bed at High Temperatures: Application to Biomass Gasification[†]

Sébastien Pecate[1]*, Mathieu Morin[1], Sid Ahmed Kessas[1],
Mehrdji Hemati[1], Yilmaz Kara[2] and Sylvie Valin[3]

[1] *Laboratoire de Génie Chimique, Université de Toulouse, France*
[2] *ENGIE Lab - Centre de Recherche et d'Innovation Gaz et Energies Nouvelles (CRIGEN), France*
[3] *CEA (LITEN), France*

Abstract

Experimental data on the hydrodynamic behavior of dense and circulating fluidized beds at high temperatures are scarce in the literature. This work deals with the hydrodynamic study of a Fast Internally Circulating Fluidized Bed (FICFB) used for biomass gasification. The first part of this study investigates the influence of the bed temperature (between 20 and 950 °C) and the nature of fluidizing gas (air or steam) on the hydrodynamic parameters of a dense fluidized bed of olivine particles (i.e. minimum fluidization velocity and voidage as well as average voidage). Three olivine batches are used with a mean Sauter diameter of 282, 464 and 689 µm, respectively. Experimental results are compared with different empirical correlations from the literature to evaluate their validity under elevated temperature conditions. Besides, two dimensionless correlations calculating the minimum fluidization velocity and average bed voidage are proposed. The second part of this study focuses on the hydrodynamic behavior of an FICFB operating between 20 and 850 °C. The effect of different process parameters (i.e. bed material nature, air velocity, solids inventory, bed temperature) on the solids circulation flow rate is investigated. It was found that the transport velocity U_{tr} is not affected by the bed temperature and the bed material inventory. It mainly depends on the terminal settling velocity U_{t} of bed material particles. Besides, key parameters controlling solids flow rate are the combustor gas velocity and the solids inventory. An increase in these parameters leads to a higher circulation flow rate.

Keywords: circulating fluidized bed, transport velocity, hydrodynamic, olivine, biomass gasification

1. Introduction

High-temperature biomass gasification is a promising alternative to fossil fuel for power generation and the production of fuel via methanation or the Fisher-Tropsch process. The reactive system of biomass conversion is an endothermic process. To maintain a fixed temperature in the reactor, a contribution of energy is required. Two types of technology exist for biomass gasification depending on the method of heat transmission (Gómez-Barea and Leckner, 2010; Ruiz et al., 2013). On the one hand, the heat can be provided by "in-situ" combustion. This process includes the fixed bed gasifiers (up-draft and down-draft) and the "bubbling fluidized bed" gasifiers. In these types of reactors, the biomass undergoes drying, pyrolysis, partial combustion of volatile matters and char and finally gasification of char. On the other hand, the heat can be supplied by the "ex-situ" combustion of char. One of the most promising technologies using "ex-situ" combustion is the Fast Internally Circulating Fluidized Bed (FICFB) (Hofbauer et al., 2002). The facility used in this study is of FICFB type. Its principle relies on the circulation of a medium (sand, olivine or catalyst particles) acting as a heat carrier between an endothermic reactor and an exothermic reactor. In the first one (called gasifier), which operates at around 750 °C–850 °C, biomass is continuously fed into a dense fluidized bed containing the heat transfer medium (olivine particles) fluidized by superheated steam. The biomass thermochemical conversion leads to the production of synthesis gas and a solid carbonaceous residue called char. Bed material (olivine and unconverted char) is continuously discharged through a dump to a transported fluidized bed reactor called "Combustor" that is fed by preheated combustion air. In this reactor, which operates at around 850 °C–950 °C,

---

[†] Received 3 May 2018; Accepted 29 June 2018
J-STAGE Advance published online 15 September 2018

[1] CNRS, INPT, UPS, Toulouse, France
[2] 361, avenue du Président Wilson–BP33–93211 Saint Denis la Plaine Cedex, France
[3] 17, rue des Martyrs–38054 Grenoble cedex 9, France
* Corresponding author: Sébastien Pecate;
E-mail: sebastien.pecate@ensiacet.fr
TEL: +33(0)1-58-81-20-00

combustion of part of the char coming from the gasifier induces olivine particle heating. At the outlet of the combustor, olivine particles are separated from flue gas by a cyclone and are returned to the gasifier through a standpipe. Thus, the heat needed for endothermic steam-gasification is provided by the ex-situ combustion of residual char. The FICFB biomass gasification efficiency is strongly dependent on a thermal equilibrium between gasification zone and combustion zone. This equilibrium is controlled by the temperature difference and circulating solids flow rate between the two reaction zones. However, this last parameter also depends on the process operating conditions (i.e. bed inventory, gas velocity, bed temperature), and cannot be imposed. Thus, it appears essential to identify the process key parameters which enable control of the circulating medium flow rate.

Besides, it is well known that the hydrodynamic behavior of an FICFB affects heat and mass transfer and therefore the overall reaction rate. In the literature, current knowledge on the hydrodynamic behavior of dense and circulating fluidized beds was essentially acquired at ambient operating conditions and a lack of information is noticed on the effect of temperature.

1.1 Brief review on bubbling fluidized bed hydrodynamic study

Shabanian and Chaouki (2017) recently reviewed the effects of temperature, pressure and interparticle forces on the fluidization characteristics of gas-solid dense fluidized beds for a wide spectrum of particles belonging to group A, B and D of the Geldart classification (Geldart, 1973).

For Geldart class-B particles with no interparticle forces and at atmospheric pressure, the minimum fluidization velocity decreases as the temperature increases (Mii et al., 1973; Pattipati and Wen, 1981; Botterill et al., 1982a; Botterill et al., 1982b; Svoboda et al., 1983; Hartman and Svoboda, 1986; Grace and Sun, 1991; Llop et al., 1995; Formisani et al., 1998). The authors explain this trend by the fact that the increasing viscosity, with a rise in bed temperature, is the controlling factor for class-B particles. Some authors also investigated the effect of mean particle diameter on minimum fluidization velocity (Geldart, 1972; Stubington et al., 1984; Fatah, 1991; Tannous, 1993; Gauthier et al., 1999). The authors agreed to say that minimum fluidization velocity increases with mean particle size. Besides, many authors proposed correlations to estimate the minimum fluidization velocity (Wen and Yu, 1966; Bourgeois and Grenier, 1968; Richardson, 1971; Saxena and Vogel, 1977; Babu et al., 1978; McKay and McLain, 1980; Svoboda et al., 1983; Chitester et al., 1984; Thonglimp et al., 1984; Nakamura et al., 1985; Lucas et al., 1986; Chyang and Huang, 1988; Murachman, 1990; Fatah, 1991 and Tannous et al., 1994). They are listed in **Table 1**. The correlations proposed were often derived from the Ergun equation (Ergun, 1952) for pressure drop through a packed bed calculation (Equation 1):

$$\frac{\Delta P}{L} = \frac{150\cdot(1-\varepsilon)^2}{\varepsilon^3}\frac{\mu_f U}{(\varphi d_p)^2} + \frac{1.75\cdot(1-\varepsilon)}{\varepsilon^3}\frac{\rho_f U^2}{\varphi d_p} \tag{1}$$

where ΔP is the pressure drop (Pa), U is the fluid superficial velocity ($m \cdot s^{-1}$), ε is the bed average voidage (–), L is the bed height (m), μ_f is the fluid viscosity ($Pa \cdot s$), φ is the shape factor (–), d_p is the mean particle diameter (m) and ρ_f is the fluid density ($kg \cdot m^{-3}$).

Considering minimum fluidization as the transitional state between fixed bed and fluidized bed, the pressure drop through the fixed bed, defined in Equation 1, is equal to the bed weight per unit area. By using dimensionless Reynolds and Archimedes numbers, the Ergun equation at minimum fluidization leads to Equation 2:

$$Ar = \frac{150\cdot(1-\varepsilon_{mf})}{\varphi^2\cdot\varepsilon_{mf}^3}\cdot Re_{mf} + \frac{1.75}{\varphi\cdot\varepsilon_{mf}^3}\cdot Re_{mf}^2 \tag{2}$$

with:

$$Re_{mf} = \frac{\rho_f\cdot U_{mf}\cdot d_p}{\mu_f} \text{ and } Ar = \frac{g\cdot d_p^3\cdot\rho_f\cdot(\rho_p-\rho_f)}{\mu_f^2} \tag{3}$$

where Ar is the Archimedes number (–), Re_{mf} is the Reynolds number at minimum fluidization (–), ε_{mf} is the minimum fluidization voidage (–), U_{mf} is the minimum fluidization velocity ($m \cdot s^{-1}$), g is the acceleration due to gravity ($m \cdot s^{-2}$) and ρ_p is the particle apparent density ($kg \cdot m^{-3}$). Equation 2 may be rearranged to Equation 4, where K_1 and K_2 are constant numbers depending on the minimum fluidization voidage and shape factor.

$$Ar = K_1\cdot Re_{mf} + K_2\cdot Re_{mf}^2 \tag{4}$$

By solving Equation 4, Re_{mf} can be expressed as a function of Ar (Equation 5).

$$Re_{mf} = (C_1{}^2 + C_2\cdot Ar)^{0.5} - C_1 \tag{5}$$

where:

$$C_1 = \frac{K_1}{2\cdot K_2} \quad \text{and} \quad C_2 = \frac{1}{K_2} \tag{6}$$

Several authors attempted to estimate C_1 and C_2 through experimental data at various operating conditions (**Table 1**). However, studies performed at high temperatures are scarce in the literature. Most of the correlations were established at ambient temperature, as reported in **Table 1**. However, it is known that the bed temperature greatly influences viscosity and density of gas, thus making the use of these correlations a source of errors.

Regarding minimum fluidization voidage, it was found to slightly increase with bed temperature (Botterill et al., 1982a; Botterill et al., 1982c; Llop et al., 1995; Formisani

Table 1 Correlations in the literature for the prediction of minimum fluidization velocity.

Authors	Particle mean diameter (µm)	Particle apparent density ($kg \cdot m^{-3}$)	Shape factor φ (–)	Fluidizing agent	Bed temperature (°C)	Reactor pressure (bar)	Correlations
Tannous et al. (1994)	725–3900	1016–3950	0.62–1	Air	Ambient	1.013	$Re_{mf} = (25.83^2 + 0.043 \cdot Ar)^{0.5} - 25.83$
Wen and Yu (1966)	2050–6350	2360–7840	1	H_2O	Ambient	1.013	$Re_{mf} = (33.7^2 + 0.0408 \cdot Ar)^{0.5} - 33.7$
Bourgeois and Grenier (1968)	86–2510	1200–19300	1	Air and H_2O	Ambient	1.013	$Re_{mf} = (25.46^2 + 0.03824 \cdot Ar)^{0.5} - 25.46$
Richardson (1971)	Spherical and non-spherical particles						$Re_{mf} = (25.7^2 + 0.0365 \cdot Ar)^{0.5} - 25.7$
Saxena and Vogel (1977)	650–704	1900–2460	0.73–0.98	Air	18–427	1.79–8.34	$Re_{mf} = (25.28^2 + 0.0571 \cdot Ar)^{0.5} - 25.28$
Babu et al. (1978)	50–2870	2560–3924	0.63–0.74	Air–CO_2–N_2–H_2O–Chlorofluorocarbon	Ambient	1.013–69.914	$Re_{mf} = (25.25^2 + 0.0651 \cdot Ar)^{0.5} - 25.25$
McKay and McLain (1980)	9486–28690	1140–1490	0.387–0.417	H_2O	Ambient	1.013	$Re_{mf} = \left[(83.33 \cdot (1-\varepsilon_{mf}))^2 + \frac{\varepsilon_{mf}^3 \cdot \varphi \cdot Ar}{2.4}\right]^{0.5} - 83.33 \cdot (1-\varepsilon_{mf})$
Svoboda et al. (1983)	565–1125	1680–3330	0.524–0.819	Air	20–890	1.013	$Re_{mf} = \left[\left(\frac{28.407 \cdot (1-\varepsilon_{mf})}{\varphi}\right)^2 + \frac{\varepsilon_{mf}^3 \cdot \varphi \cdot Ar}{3.392}\right]^{0.5} - \frac{28.407 \cdot (1-\varepsilon_{mf})}{\varphi}$
Chitester et al. (1984)	88–374	1116–2472	n.r.	N_2	Ambient	1.013–6.306	$Re_{mf} = (28.7^2 + 0.0494 \cdot Ar)^{0.5} - 28.7$
Thonglimp et al. (1984)	180–2125	1607–7425	1	Air	Ambient	1.013	$Re_{mf} = (31.6^2 + 0.0425 \cdot Ar)^{0.5} - 31.6$
Nakamura et al. (1985)	200–4000	2500	1	N_2	7–527	1–50	$Re_{mf} = (33.95^2 + 0.0465 \cdot Ar)^{0.5} - 33.95$
Lucas et al. (1986)	Correlation from data in literature						$Re_{mf} = (29.5^2 + 0.0357 \cdot Ar)^{0.5} - 29.5$
Chyang and Huang (1988)	699–6062	910–6860		Air–Argon	15–830	1.013	$Re_{mf} = (33.3^2 + 0.0333 \cdot Ar)^{0.5} - 33.3$
Murachman (1990)	109–917	1480–3910	0.77–0.92	Air	20–900	1.013	$Re_{mf} = 0.0016 \cdot Ar^{0.9}$
Fatah (1991)	1000–3570	3950	0.48–0.89	Air	15–725	1.013	$Re_{mf} = \left(-7.987 \times 10^{-3} + \frac{16.058}{T}\right) \cdot Ar^{\left(0.5547 + \frac{2.084 \times 10^{-4}}{T}\right)}$

n.r.: non-reported

et al., 1998). Besides, the effect of mean particle size on this parameter is a source of controversy. Through experiments carried out with various bed materials belonging to group A and B of the Geldart classification (coal, sand, glass, coke, ceramic, carborundum, anthracite, cracking catalyst...), different trends were observed (Lewis et al., 1949; Matheson et al., 1949; Agarwal and Storrow, 1951; Van Heerden et al., 1951; Rowe, 1965; Geldart, 1972). When mean particle size increases, minimum fluidization voidage is found: to decrease according to Matheson et al. (1949), Agarwal and Storrow (1951), Rowe (1965), and Geldart (1972), to increase in the work of Van Heerden et al. (1951), and to remain unchanged for Lewis et al. (1949).

Finally, studies about average bed voidage showed that there is no influence of bed temperature for Geldart class-B particles (Botterill et al., 1982a; Botterill et al., 1982c). According to the authors, this parameter only depends on excess gas velocity (U-U_{mf}). The effect of mean particle size on average bed voidage was also investigated with various bed materials (ballotini crystal, cracking catalyst and sand particles) (Lewis et al., 1949; Rowe, 1965; Geldart, 1972). The authors found that the average bed voidage decreases as the mean particle size increases. Besides, several correlations were proposed in order to estimate the average bed voidage (Lewis et al., 1949; Matsen et al., 1969; Thonglimp et al., 1984; Chyang and Huang, 1988; Hilal and Gunn, 2002). These correlations are given in **Table 2**, and were established from experimental data obtained in gas-solid and liquid-solid reactors, or from the two-phase theory assuming that excess gas regarding minimum fluidization crosses the bed as bubbles.

1.2 Brief review on circulating fluidized bed hydrodynamic study

Circulating fluidized bed technologies have been used since 1940 for the Fuel Catalytic Cracking process (FCC) (Lim et al., 1995; Grace et al., 1997). In spite of this, the phenomena involved were not investigated until the 1970s (Yerushalmi et al., 1976). Lim et al. (1995) and Berruti et al. (1995) reported that circulating fluidized bed reactors offer several common advantages compared to conventional low-velocity bubbling and turbulent fluidized bed reactors. These advantages are: favorable gas-solids contact efficiency due to high slip between gas and solids, a more uniform distribution of solids due to reduced gas bypassing, reduced axial gas and solids back-mixing, higher gas throughput, independent gas and solids retention time control, improved turndown and possible separate gaseous reactant zones.

A large number of works in the literature are devoted to the identification of the fluidization regimes in risers. Yerushalmi et al. (1976) focused on the identification of transition velocities between bubbling, plugging and turbulent regimes at ambient temperature for class-A particles of the Geldart classification. The authors highlighted two characteristic velocities, U_{c} and U_{k}, which correspond to transition and complete turbulent fluidization velocities, respectively. For a gas velocity lower than U_{c}, bed pressure drop standard deviation increases to a peak as a result of a bubble coalescence phenomenon. Between U_{c} and U_{k}, internal solids circulation yields to bubbles breakup and decreases pressure drop standard deviation. Beyond U_{k}, the pressure drop standard deviation stabilizes and solid particles begin to be carried in the gaseous flow. These two velocities (i.e. U_{c} and U_{k}) are easily measurable for class-A particles but are not well-defined for other class particles. Chehbouni et al. (1994) denied the existence of turbulent velocity U_{k} for Geldart class-B particles. They concluded that the onset of turbulent fluidization is at U_{c}, and velocity U_{k} is an artefact due to the use of differential pressure transducers.

There is more than one technique for measuring the transport velocities of particles. Those recorded in the literature include determination of the flooding point (Yerushalmi and Cankurt, 1979), determination of the pressure drop at the bottom of the column as a function of the solids circulation flux at different gas velocities (Yerushalmi and Cankurt, 1979), determination of the maximum solids circulation flux at different gas velocities (Schnitzlein and Weinstein, 1988), and determination of the emptying times of a fast fluidization column (Han et al., 1985). According to Adanez et al. (1993), the last technique is the most attractive because the measurement is simple and quick to conduct.

By measuring the solids flow rate versus the gas velocity, Yerushalmi and Cankurt (1979) also reported the existence of a characteristic particle transport velocity U_{tr}, which corresponds to the onset of a fully transported bed flow.

Several authors attempted to estimate the influence of column diameter as well as solids properties and hold-up on the transition velocities U_{c}, U_{k} and U_{tr} at ambient temperature (Fan et al., 1983; Han et al., 1985; Mori et al., 1986; Lee and Kim, 1990; Perales et al., 1991b; Bi and Fan, 1992; Adanez et al., 1993; Tannous, 1993; Chehbouni et al., 1995). Most authors concluded that turbulent transition velocities increase with column diameter, for the same solids static height (Rhodes and Geldart, 1986; Grace and Sun, 1991; Chehbouni et al., 1995). This phenomenon is attributed to the effect of column diameter on bubble size. For a given gas velocity, an increase in column diameter leads to the formation of smaller bubbles which reduces internal solids circulation in the bed and delays the onset of the turbulent regime. Transport velocity U_{tr} also increases with column diameter. The solids static height was found to have a very low influence on turbulent transition and transport velocities (Werther,

Table 2 Correlations in the literature for the prediction of average bed voidage.

Authors	Particle mean diameter (μm)	Particle apparent density ($kg \cdot m^{-3}$)	Shape factor φ (–)	Fluidizing agent	Bed temperature (°C)	Reactor pressure (bar)	Correlations
Thonglimp et al. (1984)	180–2125	1600–7425	1	Air	Ambient	1.013	$\varepsilon = 1.57 \cdot Re^{0.29} \cdot Ar^{-0.19}$
Chyang and Huang (1988)	699–6062	910–6860	n.r.	Air–Argon	Ambient	1.013	$\varepsilon = 1.05 \cdot Re^{0.30} \cdot Ar^{-0.17}$
Lewis et al. (1949)	100–570	n.r.	n.r.	H_2O	Ambient	1.013	$\frac{H}{H_{mf}} = 1 + \frac{0.0034 \cdot (U - U_{mf})}{{d_p}^{0.5}}$
Matsen et al. (1969)	Two-phase theory						$\frac{H}{H_{mf}} = 1 + \frac{U - U_{mf}}{0.35 \cdot (g \cdot Dc)^{0.5}}$
Hilal and Gunn (2002)	50–1000	1228–11400	n.r.	Air	Ambient	1.013	$\frac{\rho_b}{\rho_{mf}} = \exp\left(-0.0052 \cdot U_t \cdot \left(\frac{\rho_f}{\mu_f \cdot g}\right)^{1/3} \cdot \left(\frac{U}{U_{mf}} - 1\right)\right)$

n.r.: non-reported

Table 3 Correlations in the literature for the prediction of characteristic U_{tr} velocity.

	Operating conditions at which the correlations were established					
Authors	Particle mean diameter (μm)	Particle apparent density ($kg \cdot m^{-3}$)	Fluidizing agent	Bed temperature	Class of particles	Correlations
Mori et al. (1986)	56–134	729–2400	—	—	**B**	$Re_{tr} = 1.41 \cdot Ar^{0.56}$
Lee and Kim (1990)	24–205	1250–2500	Air	Ambient	**B**	$Re_{tr} = 2.916 \cdot Ar^{0.354}$
Perales et al. (1991b)	325–975	2650	Air	Ambient	**B**	$Re_{tr} = 1.41 \cdot Ar^{0.483}$
Perales et al. (1991a)	n.r.	n.r.	Ambient	Ambient	**B**	$U_{tr} = 1.7 \cdot U_t$
Bi and Fan (1992)	325	660	Air	Ambient	**B**	$Re_{tr} = 2.28 \cdot Ar^{0.419}$
Adanez et al. (1993)	80–900	1400–2600	Air	Ambient	**B**	$Re_{tr} = 2.078 \cdot Ar^{0.463}$
Tannous (1993)	715–2800	1016–2650	Air	Ambient	**B**	$Re_{tr} = 1.834 \cdot Ar^{0.448}$
Ryu et al. (2003)	181	4080	Air	25–600	**B**	$Re_{tr} = 0.0428 \cdot Ar^{0.5866} \cdot \left(\frac{Dc}{d_p}\right)^{0.5208}$
Chehbouni et al. (1995)	23.6–5000	660–4510	Air	Ambient	**A, B, C and D**	$Re_{tr} = 0.169 \cdot Ar^{0.545} \cdot \left(\frac{Dc}{d_p}\right)^{0.3}$
Goo et al. (2010)	210–380	2500	Air	20–600	**B**	$Re_{tr} = 2.001 \cdot Ar^{0.405}$

1974; Satija and Fan, 1985; Chehbouni et al., 1995). Moreover, an increase in particle size and density leads to higher transition characteristic velocities U_c and U_k and transport velocity U_{tr} (Cai et al., 1990; Chehbouni et al., 1995). Lee and Kim (1990) showed that the transition turbulent fluidization velocity U_c is almost equal to the terminal settling velocity of single particles U_t for class-B particles. Furthermore, very recent studies have proved that the particle size distribution (PSD) has an influence on the transition velocity U_c, which was found to be higher for materials with a wider PSD (Chehbouni et al., 1995; Rim and Lee, 2016). Experimental data showing the influence of bed temperature on transition velocities are scarce in the literature. According to Bi and Grace (1996), a rise in temperature might cause a shift towards lower transition velocities. Besides, some correlations were proposed in the literature in order to estimate the transport velocity U_{tr} (Mori et al., 1986; Lee and Kim, 1990; Perales et al., 1991a; Perales et al., 1991b; Bi and Fan, 1992; Adanez et al., 1993; Tannous, 1993; Chehbouni et al., 1995; Ryu et al., 2003; Goo et al., 2010). These correlations are reported in **Table 3**, and were established at ambient temperature, for air as the fluidizing agent and for class-B particles.

By varying the gas velocity for a fixed circulating solids flow rate, Yates (1996) and Shamlou (2013) defined a characteristic velocity called choking velocity U_{ch}. It corresponds to the transition between dense phase flow and dilute phase flow. These authors showed that U_{ch} increases with particle size and circulating solids flow rate.

Basu and Cheng (2000) investigated the influence of operating parameters on the performance of a CFB equipped with a loop seal. This work was performed at ambient temperature with sand particles ($dp = 250$ μm). The authors showed that a rise in both the total weight of solid particles in the process (inventory) and the loop seal air velocity leads to an increase in the circulating solids flow rate. Besides, studies carried out by Bull (2008) and Detournay (2011) focused on the hydrodynamic of a circulating fluidized bed biomass gasifier at ambient temperature using olivine ($dp = 250$ μm) and sand particles ($dp = 316$ μm) as media. Results showed that gas velocity in the riser (combustor) and total inventory are the main parameters which influence the circulating solids flow rate.

The present work is divided into two parts. The first part aims to determine the influence of operating conditions such as bed temperature (ranging from 20 to 950 °C), mean particle size (between 282 and 689 μm) and fluidizing gas nature (air or steam) on the hydrodynamic parameters of a dense fluidized bed of olivine particles (i.e. minimum fluidization velocity and voidage as well as average voidage). The purpose of the second part is to identify the key parameters controlling the circulating solids flow rate, as well as their effect on solids circulation.

2. Materials

2.1 Description of the experimental rig

All the experiments were conducted in the FICFB presented below (**Fig. 1**). The process contains two reactors

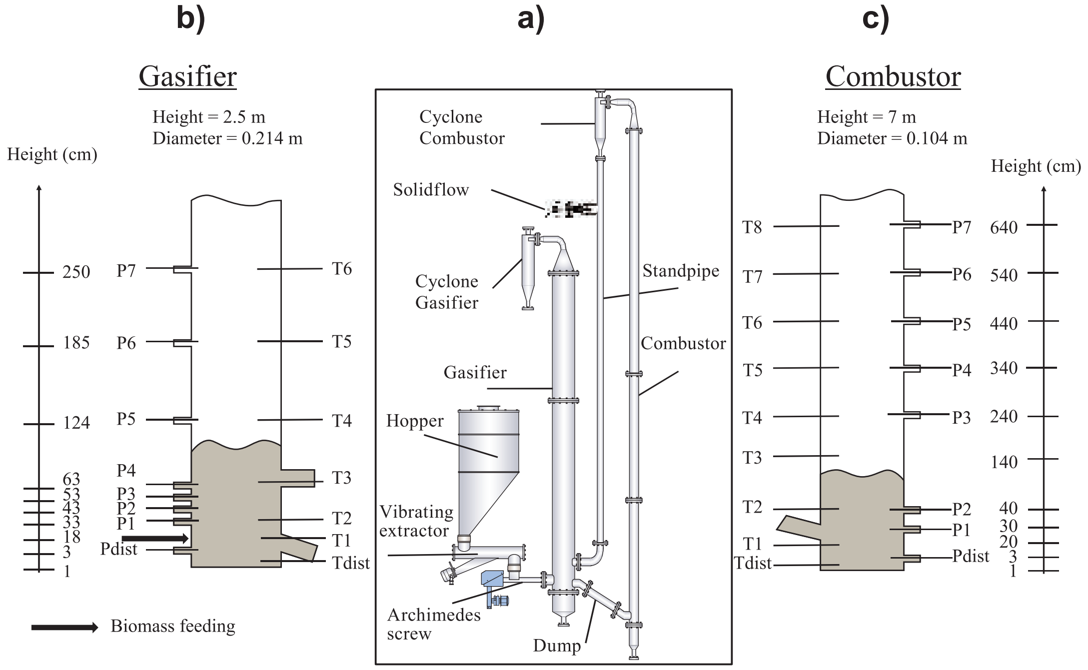

Fig. 1 Circulating fluidized bed biomass gasifier (**a**: pilot plant; **b** and **c**: pressure and temperature tap positions in the gasification section and in the combustion section, respectively).

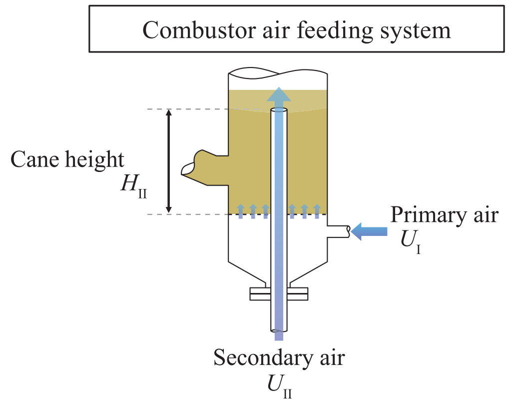

Fig. 2 Distribution of combustion air in the combustor.

whose connections enable an interchange of solids. The gasifier (internal diameter = 214 mm) is a dense fluidized bed of bed material particles. For this hydrodynamic study, it is fluidized either by super-heated steam or by air. The bed material is continuously discharged from the gasifier to the combustor through a dump. The combustor (internal diameter = 104 mm) is a transported fluidized bed, fed by preheated air separated into two streams (**Fig. 2**). The first one, named "primary air", ensures a dense fluidized bed at the bottom of the combustor. The second stream, called "secondary air", is used for particle transport. It is fed by an injection cane at an adjustable height. At the top of the combustor, a cyclone is used to separate transported particles from air. Then, solids are recycled back to the gasifier through the standpipe, equipped with an L-valve placed on the base and fluidized by steam or air.

Gasifier and combustor are surrounded by electric furnaces with 15 and 5.7 kW electric output, respectively. Gasifier and combustor temperatures can be controlled independently by two PID controllers. Nevertheless, carrying out tests at temperatures higher than 500 °C also requires the use of natural gas feeding in the combustor, precisely at 40 cm above the distributor.

The pilot plant is equipped with 23 pressure sensors and 20 temperature sensors (**Fig. 1**). The circulating solids mass flow rate is measured with a microwave probe (supplier: SWR Engineering, model: SolidFlow 2.0), previously calibrated, located in the standpipe, 50 cm below the base of the combustor cyclone (**Fig. 1**).

At the outlet of each reactor, a burner associated with a post-combustion chamber heated to 850 °C allows the burning of all combustible gas. Then, gas streams are mixed together in a cylindrical chamber and cooled down in a 5-m multitubular exchanger. A cyclone and a bag filter ensure the filtration of fine particles before rejecting gas into the atmosphere.

2.2 Bed material pretreatment and characterization

Most of the experiments presented in this study were carried out with olivine particles provided by the Austrian manufacturer Magnolithe GmbH as bed material. Nevertheless, some tests were also performed with sand particles. As shown in **Table 4**, olivine particles are essentially made of magnesium oxide, silicon oxide and iron oxide. The latter reaches 10.5 wt% in our case. Regarding sand particles, they are mainly made of silicon oxide. Before their use as bed material in the gasifier, the particles previously underwent:

- A fine elutriation step. In this step, the undesired fine particles are removed by elutriation, at ambient temperature during 20 hours;
- a calcination step, at 850 °C during 4 hours.

During these stages, carried out in the gasifier, the gas velocity was maintained at 8 times the minimum fluidization velocity ($U = 8 \cdot U_{\mathrm{mf}}$) at the considered temperature. After this treatment, the particle size distribution, particle density, skeletal density, aerated bulk density, packed bulk density, angle of repose, internal voidage, specific surface area and shape factor were measured using Laser Diffraction Particle Sizing MS2000, Mercury Porosimetry, Hosokawa analyzer, Helium Pycnometry, BET analyzer and G3 Morphology, respectively. Based on the values of the mean Sauter diameter and particle density reported in **Table 4** for both sand and olivine, it can be concluded that the particles used in this work belong to the Geldart class B. Besides, the particles have a low compressibility factor γ (lower than 15 %), meaning that they have an excellent flow. Otherwise, the particles employed are minimally porous, with internal voidage of 9 % and 7 % for sand and olivine particles, respectively.

In this work, Sauter diameter ($d_{3/2}$) is considered as the mean particle size.

3. Bubbling fluidized bed hydrodynamic study

This part of the study focusses on the effect of bed temperature, particle size distribution and fluidization gas nature (air or steam) on minimum fluidization velocity (U_{mf}) and bed voidage ($\varepsilon_{\mathrm{mf}}$), as well as on average voidage (ε) of the olivine particle dense fluidized bed. Experiments are performed in the gasifier, isolated from the combustor and the circulation loop. For each test, the total olivine particle inventory in the gasifier is 40 kg. In addition, some tests are carried out in the combustor, isolated from the gasifier and the circulation loop, in order to confirm the conclusions drawn in the gasifier for a reactor with a different diameter. For each test performed in the combustor, the total olivine inventory is 7 kg.

Table 4 Physical properties of olivine and sand particles.

Type of particle	Sand	Olivine batch [200–300 μm]	Olivine batch [300–400 μm]	Olivine batch [400–600 μm]
Chemical formula	SiO_2	$(Fe_x, Mg_{1-x})_2SiO_4$		
Composition	SiO_2: 98.34 % Fe_2O_3: 0.022 % Al_2O_3: 1.206 % TiO_2: 0.03 % CaO: 0.014 % K_2O: 0.745 %	MgO: 47.5–50.0 % SiO_2: 39.0–42.0 % CaO: max. 0.4 % Fe_2O_3: 8.0–10.5 %		
Skeletal density ρ_s ($kg \cdot m^{-3}$)	2,650	3,265		
Internal voidage χ (%)	9	7		
Particle density ρ_P ($kg \cdot m^{-3}$)	2,400	2,965		
Aerated bulk density ρ_{BA} ($kg \cdot m^{-3}$)	1,519	1,344	1,368	1,445
Packed bulk density ρ_{BP} ($kg \cdot m^{-3}$)	1,643	1,500	1,513	1,643
Mean aerated bulk bed voidage ε_{BA} (–)	0.49	0.53		
Mean packed bulk bed voidage ε_{BP} (–)	0.45	0.48		
Angle of repose (°)	33.2	29.6	—	—
Compressibility factor: $\gamma = 100 \cdot (\rho_{BP}\text{-}\rho_{BA})/\rho_{BP}$ (%)	8	10	10	12
Shape factor (–)	0.85	0.85	—	—
d_{10} (μm)	190	188	337	508
d_{50} (μm)	305	300	483	709
d_{90} (μm)	488	475	689	1,015
$d_{3/2}$ (μm)	285	282	464	689
$d_{4/3}$ (μm)	324	318	501	741
$C_v = (d_{90}\text{-}d_{10})/d_{50}$ (–)	0.98	0.96	0.73	0.72
Specific surface area ($m^2 \cdot g^{-1}$)	—	0.73	—	—

3.1 Determination methods

For each experiment, the bed was first vigorously fluidized and the pressures along the reactor were measured. Then, the gas velocity was decreased and the pressures were measured again. From the experimental results, the minimum fluidization velocity was estimated through (Botterill et al., 1982a; Murachman, 1990; Fatah, 1991; Tannous, 1993):

- the plot of the average total bed pressure against the superficial gas velocity (**Fig. 3a**). As long as the bed is in a fixed state, the total pressure increases with the gas velocity. When the minimum fluidization point is exceeded, the total pressure remains constant as the gas velocity increases. Thus, the intersection of the sloping fixed bed and horizontal fluidized bed pressure lines on the pressure drop versus gas velocity plot was considered as the minimum fluidization velocity;
- the plot of the partial pressure drop, measured between two pressure sensors, against the superficial gas velocity (**Fig. 3b**). For an increase in the gas velocity, the partial pressure drop first increases as long as the bed is fixed. Then, it slightly decreases as soon as the bed is fluidized. This decrease is related to the rise in the bubble volume fraction in the area considered. Thus, the minimum fluidization velocity can be defined as the peak on the partial pressure drop versus gas velocity plot;
- the plot of the total pressure standard deviation against the superficial gas velocity (**Fig. 3c**). In this study, the standard deviation of a given parameter is defined as below:

$$\sigma_Z = \frac{\left[\frac{1}{N_e - 1}\cdot\sum_{i=1}^{N_e}\left(Z_i-\bar{Z}\right)^2\right]^{0.5}}{\bar{Z}} \tag{7}$$

where σ_Z is the standard deviation of the parameter Z, N_e is the number of data, Z_i is the value of Z at a given time, and $\bar{Z}$ is the mean value of Z. For fixed

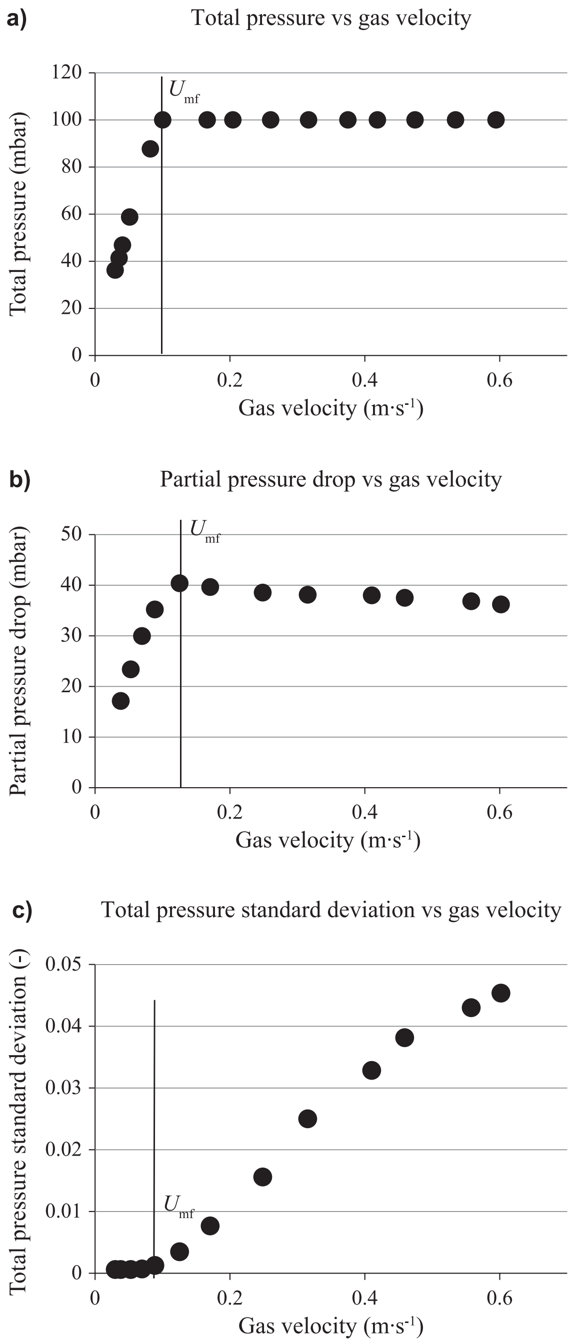

Fig. 3 Methods used for the determination of U_{mf}.

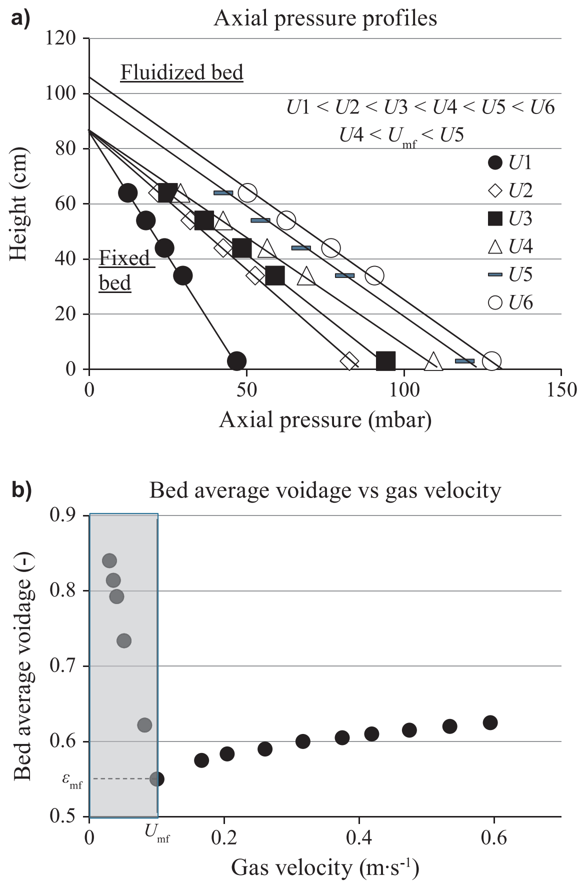

Fig. 4 Methods used for the determination of ε and ε_{mf}.

beds, the pressure standard deviation is zero. It only starts increasing with gas velocity when the bed is fluidized. Thus, the minimum fluidization velocity is considered as the intersection of the growing part of the curve and the gas velocities' axis.

These methods lead to similar results, with a relative error always under 10 %.

From the experimental results, the bed average voidage and minimum fluidization voidage can also be calculated. The bed average voidage is obtained by measuring and plotting the axial pressure profiles at several gas velocities (**Fig. 4a**). For gas velocities lower than the minimum fluidization velocity, the axial pressure profiles converge at the same height, i.e. the aerated fixed bed height. For gas velocities higher than the minimum fluidization velocity, the axial pressure profiles are parallels and lead to heights increasing with gas velocity. Thus, for a given weight of olivine particles, the average bed voidage is calculated as below:

$$\varepsilon = 1 - \frac{m_P}{A_c \cdot H \cdot \rho_P} \tag{8}$$

where ε, m_p, A_c, H and ρ_P are the bed average voidage, the solids inventory (kg), the cross-section of the gasifier (m^2), the dense fluidized bed height (m) and the particle density (kg·m^{-3}), respectively.

Regarding the minimum fluidization voidage, it is calculated using the bed height at minimum fluidization velocity (i.e. the aerated fixed bed height) and Equation 8. It is also determined from the method recommended by Botterill et al. (1982c) and Lucas et al. (1986). This method consists in plotting the bed average voidage, calculated through Equation 9, against the superficial gas velocity, and calculating the minimum fluidization voidage by extrapolating the results for $U = U_{mf}$. A typical example is illustrated in **Fig. 4b**. The blackened part of the curve, for gas velocities under the minimum fluidization velocity, corresponds to operating conditions where Equation 9 is not valid. The two methods lead to very close results.

$$\frac{\Delta P}{L} = (1-\varepsilon)\cdot\left(\rho_{\mathrm{P}} - \rho_{\mathrm{g}}\right)\cdot g \qquad (9)$$

3.2 Effect of operating parameters on minimum fluidization velocity (U_{mf})

Fig. 5a shows the effect of bed temperature on the minimum fluidization velocity of three olivine batches. For the same mean particle size, the minimum fluidization velocity decreases as temperature increases. Besides, minimum fluidization velocity increases with mean particle size for a fixed bed temperature. These trends are consistent with the results reported in the literature (Mii et al., 1973; Pattipati and Wen, 1981; Botterill et al., 1982a; Botterill et al., 1982b; Svoboda et al., 1983; Hartman and Svoboda, 1986; Grace and Sun, 1991; Llop et al., 1995; Formisani et al., 1998; Gauthier et al., 1999). In addition, the Re_{mf} range is between 0.07 and 14 in our operating conditions. However, the first term in Equation 1 on the right-hand side, representing the pressure loss through viscous effects, is the dominant term in the laminar flow region ($Re < 10$). This indicates that Equation 1 can be rearranged to Equation 10.

$$R_e < 10 \quad U_{\mathrm{mf}} = \frac{d_{\mathrm{p}}^2\cdot\varphi^2}{150}\cdot\left(\frac{\rho_{\mathrm{P}}-\rho_{\mathrm{f}}}{\mu_{\mathrm{f}}}\right)\cdot g\cdot\frac{\varepsilon_{\mathrm{mf}}^3}{\left(1-\varepsilon_{\mathrm{mf}}\right)} \qquad (10)$$

This equation shows that for fine particles, the viscous drag force (related to gas viscosity) has a major effect on the minimum fluidization velocity. Thus, an increase in gas viscosity with bed temperature leads to a rise in the viscous drag force which decreases the minimum fluidization velocity. Similarly, Equation 10 also shows that an increase in particle size yields a higher minimum fluidization velocity.

The nature of fluidizing gas (air or steam) also has an effect on the minimum fluidization velocity. **Fig. 5b** shows that the minimum fluidization velocity obtained with steam is higher than that obtained with air. These results are mainly explained by the low value of steam viscosity compared to air. The low value of steam density is also responsible for these trends. Values of density and viscosity for the two fluids are reported in **Table 5**.

Experimental results determined from about 40 tests carried out in the gasifier and in the combustor were compared to values predicted by 15 correlations of literature, given in **Table 1**. This comparison was based on the following statistical criteria, already defined in the work of Tannous et al. (1994):

- Relative error R_1:

$$R_1 = 100\cdot\frac{1}{N_{\mathrm{e}}}\cdot\sum_{1}^{N_{\mathrm{e}}}\frac{Z_{\exp}-Z_{\mathrm{predict}}}{Z_{\exp}} \qquad (11)$$

- Absolute relative error R_2:

$$R_2 = 100\cdot\frac{1}{N_{\mathrm{e}}}\cdot\sum_{1}^{N_{\mathrm{e}}}\frac{\left|Z_{\exp}-Z_{\mathrm{predict}}\right|}{Z_{\exp}} \qquad (12)$$

where $Z_{\exp}$ is the experimental value, Z_{predict} is the predicted value and N_{e} is the number of experimental results compared to predictions. Values of R_1 and R_2 are given in **Table 6**. It was found that the relationships proposed by Bourgeois and Grenier (1968), Richardson (1971), Thonglimp et al. (1984) and Nakamura et al. (1985) represent our results with an absolute relative error similar to the experimental uncertainty (lower than 10 %). The best one is the correlation of Bourgeois and Grenier (1968)

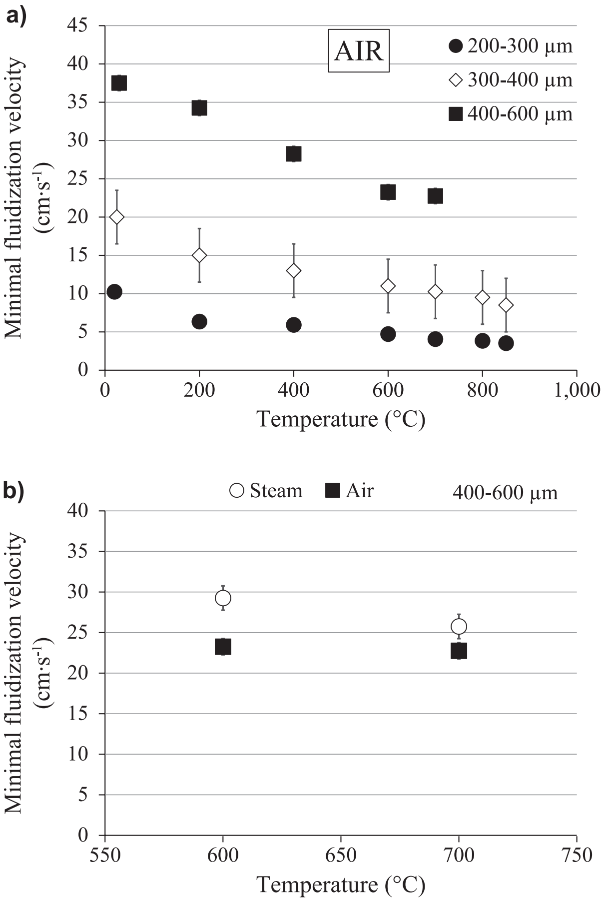

Fig. 5 Bed temperature effect on U_{mf} for different olivine batches (**a**) and for two fluidizing gases (**b**).

Table 5 Values of density and viscosity for steam and air at 600 and 700 °C.

Steam/Air	600 °C		700 °C	
Density ($\mathrm{kg\cdot m^{-3}}$)	0.25	0.40	0.22	0.36
Viscosity ($\mathrm{Pa\cdot s}$)	3.41×10^{-5}	4.04×10^{-5}	3.85×10^{-5}	4.31×10^{-5}

Table 6 Prediction of minimum fluidization velocity: comparison between experimental findings and literature correlations.

Authors	R_1	R_2
Tannous et al. (1994)	–13 %	14 %
Wen and Yu (1966)	17 %	17 %
Bourgeois and Grenier (1968)	–3 %	8 %
Richardson (1971)	3 %	9 %
Saxena and Vogel (1977)	–51 %	51 %
Babu et al. (1978)	–71 %	72 %
McKay and McLain (1980)	–23 %	25 %
Svoboda et al. (1983)	–134 %	134 %
Chitester et al. (1984)	–17 %	18 %
Thonglimp et al. (1984)	8 %	10 %
Nakamura et al. (1985)	6 %	9 %
Lucas et al. (1986)	17 %	17 %
Chyang and Huang (1988)	31 %	31 %
Murachman (1990)	–14 %	17 %
Fatah (1991)	–6 %	36 %

with a relative error equal to –3 %.

A new correlation is proposed (Equation 13) in order to estimate the minimum fluidization velocity of olivine particles as a function of bed temperature, particle size and fluidizing gas nature. This correlation was established between 20 and 950 °C, with olivine particles of mean Sauter diameter between 282 and 689 µm and for air and steam as fluidizing gas. It is intended to be used for the design of FICFB biomass gasifiers operating with olivine as the heat transfer medium.

$$Re_{\mathrm{mf}} = (20.32^2 + 0.031 \cdot Ar)^{0.5} - 20.32 \tag{13}$$

This correlation enables prediction of experimental U_{mf} with a relative error R_1 equal to –2 % and an absolute relative error of 8 % (**Fig. 6**).

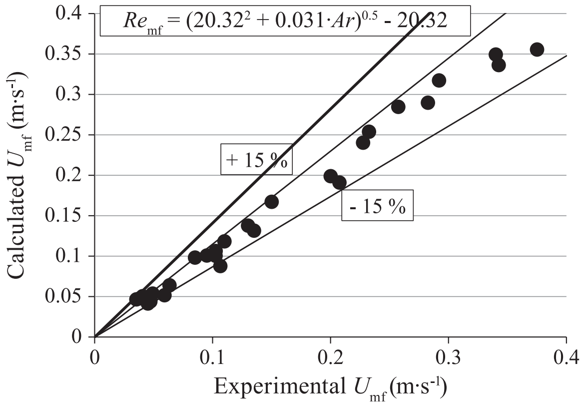

Fig. 6 Prediction of minimum fluidization velocity: comparison between experimental findings and proposed correlation.

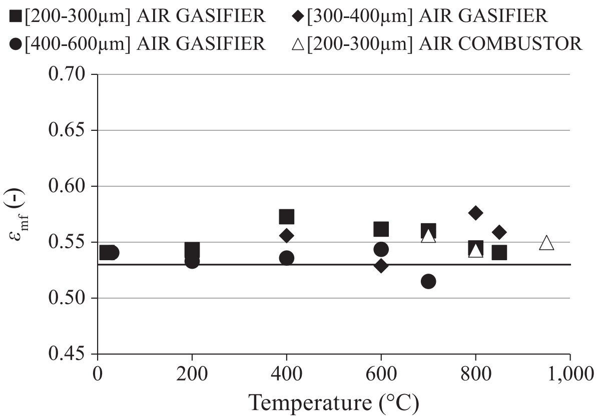

Fig. 7 Effect of bed temperature on minimum fluidization voidage for different olivine batches.

3.3 Effect of operating parameters on bed voidage

Fig. 7 shows that bed voidage at minimum fluidization conditions ($\varepsilon_{\mathrm{mf}}$) is independent of bed temperature and mean particle size. The estimated bed voidage is about 0.55, which is slightly higher than the mean voidage of an aerated fixed bed $\varepsilon_{\mathrm{BA}}$. Tests carried out in the combustor between 700 and 950 °C lead to the same conclusions. These results are likely explained by the fact that for class-B particles, the absence of interparticle force leads to an almost instantaneous transition between fixed bed and fluidized bed states (no deaeration phenomenon). Thus, for this class of particles, minimum fluidization voidage is almost equal to the fixed bed voidage.

Fig. 8a, **Fig. 8b** and **Fig. 8c** show the average bed voidage evolution vs excess gas velocity (U-U_{mf}), at different bed temperatures (between 20 °C and 850 °C), for 3 olivine batches. The average bed voidage increases with excess gas velocity, regardless of particle size and bed temperature. Besides, for the same excess gas velocity, bed voidage is slightly affected by bed temperature and particle size. Tests carried out in the combustor between 700 and 950 °C confirm these results (**Fig. 8d**). These trends are consistent with the experimental findings reported in the literature (Botterill et al., 1982a; Botterill et al., 1982c). They may be related to the fact that bed expansion is mainly caused by the presence of bubbles in the bed. Bed voidage can be estimated from Equation 14 (Kunii and Levenspiel, 1991), which strongly depends on bubble properties:

$$\varepsilon = \delta_{\mathrm{B}} + (1 - \delta_{\mathrm{B}}) \cdot \varepsilon_{\mathrm{mf}} \tag{14}$$

In Equation 14, the bubble volume fraction in the bed

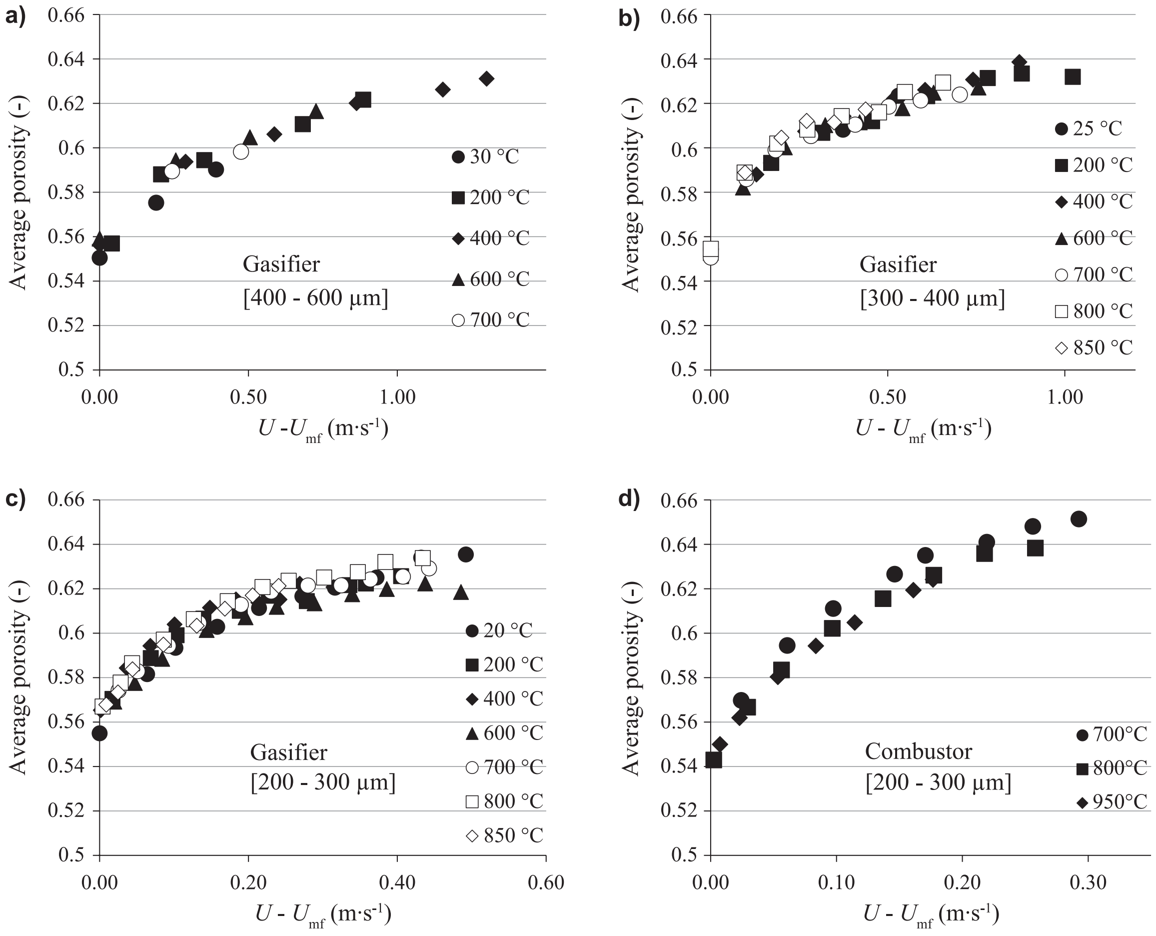

Fig. 8 Effect of excess gas velocity on the average fluidized bed voidage, for different bed temperatures and olivine batches in the gasifier (**a**, **b**, **c**) and the combustor (**d**).

δ_B mainly depends on excess gas velocity $U\text{-}U_{mf}$, as described in **Appendix A**. Thus, average bed voidage depends only on excess gas velocity, as observed in our experiments.

Experimental ε values determined from about forty tests in both gasifier and combustor were compared to values predicted from literature correlations, reported in **Table 2**. These correlations are usually used for fluidized bed reactor design, modeling and simulation. Relative error R_1 and absolute relative error R_2 were calculated and are presented in **Table 7**. For our operating conditions and olivine particles, the relationships proposed by Lewis et al. (1949), Matsen et al. (1969), and Thonglimp et al. (1984) are the most adapted. The best one is the correlation of Matsen et al. (1969) with a relative error of –10 % and an absolute relative error of 10 % (**Fig. 9**).

Table 7 Prediction of average bed voidage: comparison between experimental findings and literature correlations.

Authors	R_1	R_2
Thonglimp et al. (1984)	10 %	13 %
Chyang and Huang (1988)	30 %	30 %
Lewis et al. (1949)	–11 %	11 %
Matsen et al. (1969)	–10 %	10 %
Hilal and Gunn (2002)	–20 %	20 %

A new correlation (Equation 15) that takes into account fluidized bed temperature, mean particle size and fluidizing gas nature is proposed in order to estimate the average bed voidage of a bubbling fluidized bed of olivine particles. This correlation was established between 20 and 950 °C, with olivine particles of mean Sauter diameter between 282 and 689 µm and for air and steam as fluidizing gas. It is intended to be used for the design of FICFB biomass gasifiers which operate with olivine as the heat transfer medium.

$$\frac{\varepsilon}{\varepsilon_{mf}} = 1.0394 \cdot \left(\frac{U - U_{mf}}{U_{mf}} \right)^{0.026} \cdot Ar^{0.006} \tag{15}$$

This correlation enables the prediction of experimental ε with a relative error and an absolute relative error both equal to 1 % (**Fig. 10**). It is interesting to notice that despite the low coefficient applied to the Archimedes number, its contribution cannot be ignored. Indeed, for some

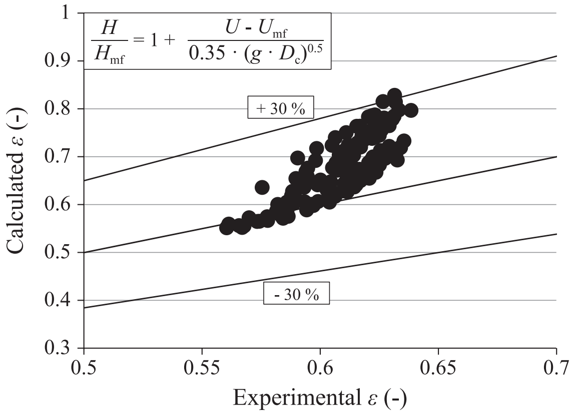

Fig. 9 Comparison between ε experimental findings and predictions of the Matsen et al. (1969) correlation.

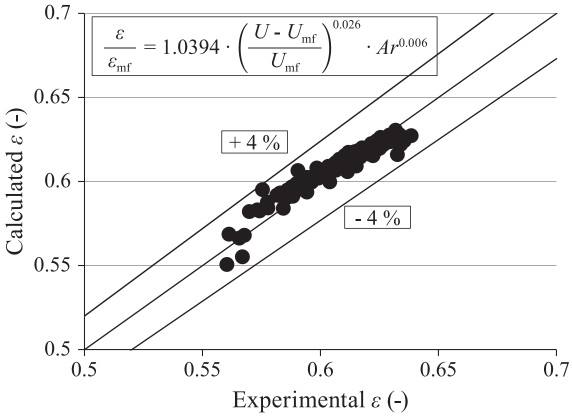

Fig. 10 Prediction of average bed voidage: Comparison between experimental findings and proposed correlation.

experiments ($T = 30$ °C and $d_p = [400–600\ \mu m]$), the Archimedes number is almost equal to 25,000. In these cases, the Archimedes number contribution is about 6 %.

4. Circulating fluidized bed hydrodynamic study

The biomass gasification efficiency in an FICFB mainly depends on heat transfer medium circulation flow rate. Thus, it appears essential to identify the key parameters influencing the circulation flow rate.

Process parameters are: gas velocity in the gasifier U_G, gas velocity in the standpipe U_S, particle inventory m_p, bed temperature T, secondary air injection position H_{II} and air average velocity in the combustor U_{comb}. The last parameter depends on primary and secondary air flow rates in the combustor. However, in order to ensure a good fluidization in the dense fluidized bed of the combustor, the primary air flow rate is set so that $U_I = 4 \cdot U_{mf}(T)$. Based on previous work (Detournay, 2011), the value of the secondary air injection position (injection cane height H_{II}) is set at 15 cm. Thus, only the secondary air flow rate, called "transport air", is varied in our experiments. For each experiment, temperatures in both gasifier and combustor were set at almost identical values.

Table 8 Operating conditions of circulation experiments.

	Reference	Range
m_p (kg)	35	35–60
U_G (U/U_{mf})	4	1–8
U_{comb} (U/U_t)	2.4	0.5–3
H_{II} (cm)	15	15
U_S (U/U_{mf})	8	1–9
T (°C)	500	20–850

Table 9 Effect of bed temperature on terminal settling velocity of single olivine and sand particles.

Temperature (°C)	20	300	500	800	850
U_t ($m \cdot s^{-1}$)–Olivine	2.05	2.10	2.03	1.90	1.88
U_t ($m \cdot s^{-1}$)–Sand	1.92	1.91	1.81	1.67	1.65

Most of the experiments were performed with the olivine batch [200–300 μm] as bed material, between 20 and 850 °C. However, some tests were also carried out with sand particles at ambient temperature, in order to investigate the effect of the bed material nature. The properties of these materials are reported in **Table 4**.

Table 8 indicates the variation range of the process parameters in this study. In this table, U_t is the terminal settling velocity of the particles used. It is given by:

$$U_t = \left[\frac{4 \cdot d_p \cdot (\rho_P - \rho_g) \cdot g}{3 \cdot C_d \cdot \rho_g}\right]^{1/2} \tag{16}$$

where C_d is the drag coefficient. The latter depends on the solids shape factor φ, and is estimated by (Haider and Levenspiel, 1989):

$$C_d = \frac{24}{Re_t} \cdot \left[1 + 8.17 \cdot e^{-4.0655 \cdot \varphi} \cdot Re_t^{(0.0964 + 0.5565 \cdot \varphi)} + \frac{73.69 \cdot e^{-5.0748 \cdot \varphi} \cdot Re_t}{Re_t + 5.378 \cdot e^{6.2122 \cdot \varphi}}\right] \tag{17}$$

where Re_t is the Reynolds number at $U = U_t$.

Besides, in **Table 9**, the values of U_t calculated for several temperatures between 20 and 850 °C are reported for both sand and olivine particles. It can be noticed that olivine and sand particles have close values of U_t, in particular at ambient temperature. Besides, U_t velocity only decreases by 8 and 13 % between 20 and 850 °C, for olivine and sand particles, respectively.

A previous study (Detournay, 2011) carried out at ambient temperature on the same pilot as the one used in this work showed that:

- Gas flow rate in both gasifier and standpipe do not have any effect on the solids circulation flow rate for gas velocities higher than 1.5 times the minimum fluidization velocity;
- key parameters are U_{comb} and solids inventory m_{p}.

Experiments carried out in this study for temperatures up to 850 °C confirm these trends.

4.1 Determination of transport velocity: Presentation of a typical example

Fig. 11 presents a typical example regarding the effect of gas velocity on solids circulation flow rate, using sand as bed material. Three regimes can be observed:

- For gas velocities lower than U_{t} ($1.9\ \mathrm{m \cdot s^{-1}}$): a very low solids circulation flow rate is measured (about $10–20\ \mathrm{kg \cdot h^{-1}}$). For these velocities, the combustor is a deep «dense fluidized bed», whose height can exceed 1 m. Thus, elutriation of the fine particles initially present in the solids batch explains the residual values of circulation flow rate;
- for gas velocities between 1.9 and $3.3\ \mathrm{m \cdot s^{-1}}$: a transitional regime is observed. Circulation mass flow rate is found to increase from 30 to $200\ \mathrm{kg \cdot h^{-1}}$. This is likely attributed to the fact that the kinetic energy contained in the bubbles during their eruption at the bed surface is enough to transport particles brought into its wake to the combustor outlet;
- for gas velocities higher than $3.3\ \mathrm{m \cdot s^{-1}}$ ($= 1.6 \cdot U_{\mathrm{t}}$): the solids mass flow rate sharply increases before reaching a plateau. According to the definition proposed by Yerushalmi and Cankurt (1979), this velocity is the transport velocity U_{tr} at which the solids traverses the column in a stable transported flow. Besides, according to Chehbouni et al. (1994), the transport velocity U_{tr} marks the onset of the circulating fluidization. To be more precise, beyond $4.0\ \mathrm{m \cdot s^{-1}}$, the circulation flow rate levels off on a stable plateau because the dense fluidized bed height at the bottom of the combustor reached its limit value (i.e. the secondary air injection cane height). Thus the difference between gasifier and combustor inventories, acting as the driving force on the solids circulation, cannot increase anymore. These inventories are calculated from total pressure drop measurement in gasifier and combustor.

In order to ascertain the appropriateness of the U_{tr} value measured in this study and presented above, the emptying time technique was employed (Han et al., 1985). This technique is based on measurements of the time required for all solids to leave the bed at different settings of the superficial gas velocity. No fresh solids are fed to the column and the dump is closed. As the gas velocity is increased, a point is reached where acceleration of the solids increases. In the absence of solids recycling, the bed empties in a short time. All experiments were performed at ambient temperature with samples of 7 kg of sand particles. For a fixed gas velocity, the emptying time is defined as the time necessary to reduce the total pressure in the combustor from its initial value to a residual value. The transport velocity, U_{tr}, is taken to be the intersection of the lines of low and high accelerations (**Fig. 12**). The value of U_{tr} measured by this method is $3.4\ \mathrm{m \cdot s^{-1}}$, which is consistent with the value obtained from **Fig. 11** (i.e. $3.3\ \mathrm{m \cdot s^{-1}}$).

In order to investigate the effect of the bed material nature on solids circulation, the results previously obtained with sand particles were compared with new ones obtained using olivine particles, for a bed material inventory of 35 kg (**Fig. 13**). It was found that the solids mass flow rate evolution vs gas velocity is not significantly affected

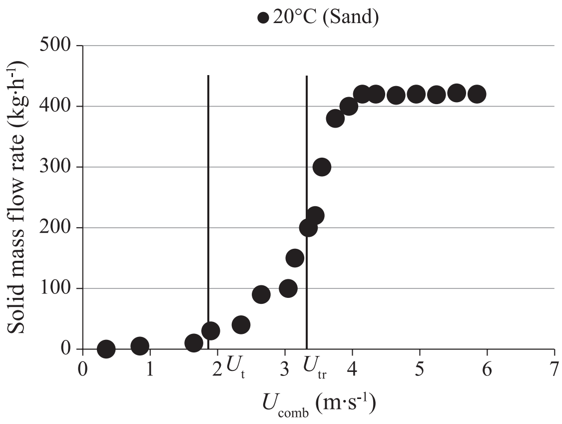

Fig. 11 Effect of combustor gas velocity on circulating solids mass flow rate (sand, $m_{\mathrm{p}} = 35$ kg, $U_{\mathrm{G}} = 4 \cdot U_{\mathrm{mf}}$, $U_{\mathrm{I}} = 4 \cdot U_{\mathrm{mf}}$, $H_{\mathrm{II}} = 15$ cm).

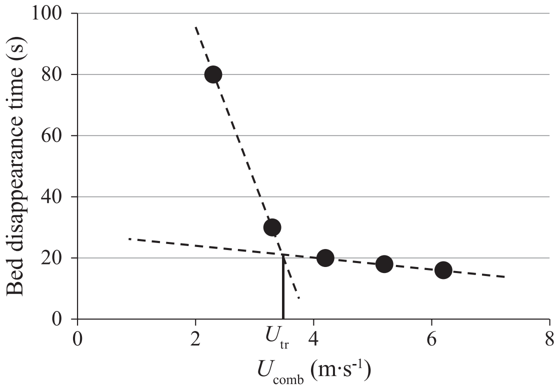

Fig. 12 Effect of combustor gas velocity on the disappearance time of solids (sand, $m_{\mathrm{p}} = 7$ kg, $T = 20$ °C).

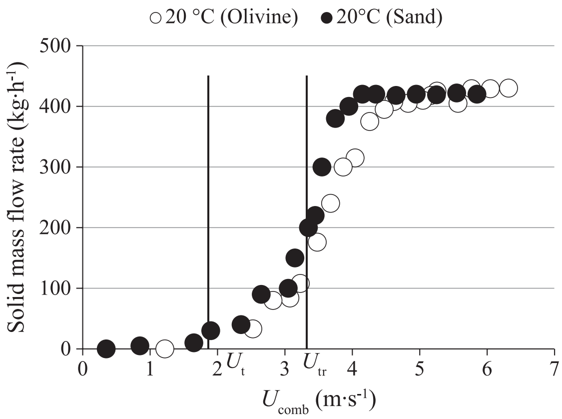

Fig. 13 Effect of bed material nature on circulating solids mass flow rate ($U_G = 4 \cdot U_{mf}$, $U_I = 4 \cdot U_{mf}$, $m_p = 35$ kg, $H_{II} = 15$ cm).

by the bed material nature when solids batches have similar U_t values. Results show that the same transport velocity U_{tr} and circulation mass flow rate on the plateau were found with olivine particles regarding the values obtained with sand.

According to Perales et al. (1991a), the transport velocity is directly proportional to the terminal settling velocity with a ratio between U_{tr} and U_t equal to 1.7. This value is close to the one presented above. Besides, **Fig. 14a** shows that for an increase in combustor gas velocity U_{comb}, the gasifier inventory increases almost linearly before reaching a plateau.

Regarding combustor inventory, it decreases as gas velocity rises, and also reaches a plateau. Thus, results show that the difference between gasifier and combustor inventories presented in **Fig. 14b** increases with combustor gas velocity before levelling off. This trend is similar to the one of solids mass flow rate vs. gas velocity.

This is consistent since the difference between gasifier and combustor inventories is directly related to the difference in pressures between these two reactors. However, the latter acts as the driving force on solids circulation. Thus a rise in combustor gas velocity produces an increase in pressure difference between gasifier and combustor, leading to higher solids circulation flow rates. These trends are consistent with the ones presented above for sand particles.

4.2 Effect of bed material inventory and temperature

Fig. 15 presents the effect of the bed material inventory, between 20 and 60 kg, on the solids circulation flow rate for a given combustor air velocity ($U_{comb} = 3.6 \text{ m} \cdot \text{s}^{-1}$), with sand particles as the bed material. Results show that a rise in bed material inventory leads to higher solids mass flow rates. Besides, **Fig. 16** presents the effect of bed temperature, between 20 and 850 °C, on olivine circulation flow rate vs. combustor gas velocity, for 35- and 60-kg bed inventories. It can be noticed that for each bed temperature and bed material inventory, the curves follow the same trends. Besides, results show that:

- For gas velocities lower than U_{tr}, the solids mass flow rate is not affected by the bed temperature or inventory;
- the solids circulation onset, at $U = U_{tr}$, was found to be reached for a gas velocity between 1.6 and $1.7 \cdot U_t$.

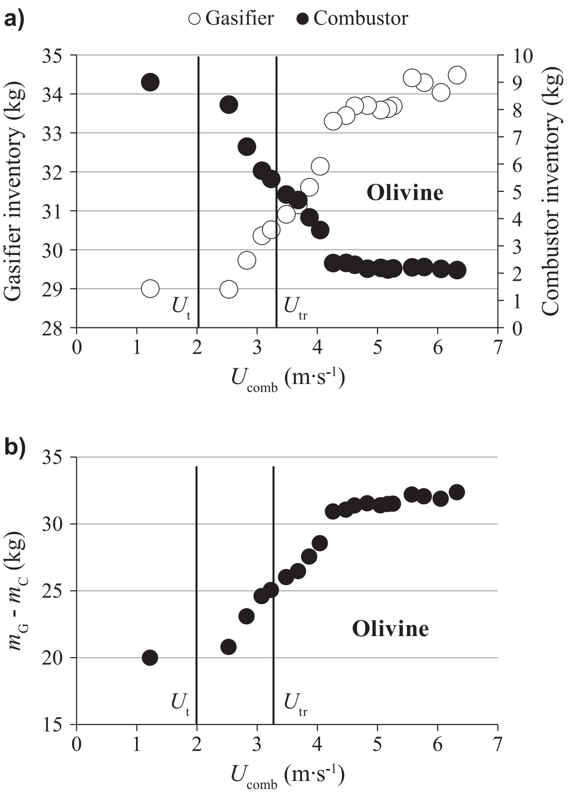

Fig. 14 Effect of gas velocity in the combustor on gasifier and combustor inventories (olivine, $U_G = 4 \cdot U_{mf}$, $U_I = 4 \cdot U_{mf}$, $m_p = 35$ kg, $H_{II} = 15$ cm).

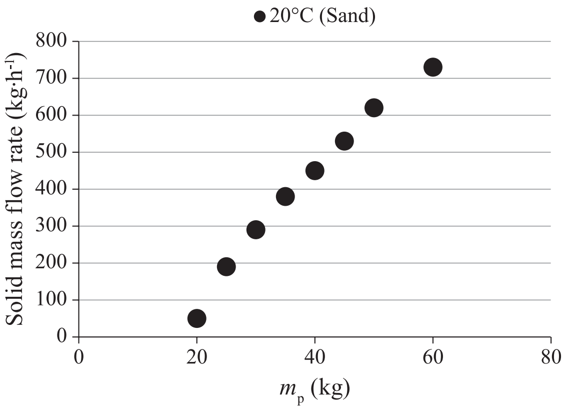

Fig. 15 Effect of bed material inventory on circulating solids mass flow rate (sand, $T = 20$ °C, $U_G = 4 \cdot U_{mf}$, $U_I = 4 \cdot U_{mf}$, $U_{II} = 3.3 \text{ m} \cdot \text{s}^{-1}$, $H_{II} = 15$ cm).

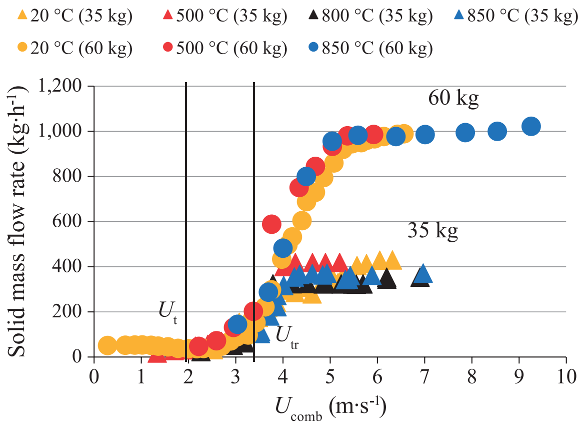

Fig. 16 Effect of gas velocity in the combustor on solids mass flow rate, for bed temperature between 20 and 850 °C, and bed inventory between 35 and 60 kg (olivine, $U_G = 4 \cdot U_{mf}$, $U_I = 4 \cdot U_{mf}$, $H_{II} = 15$ cm).

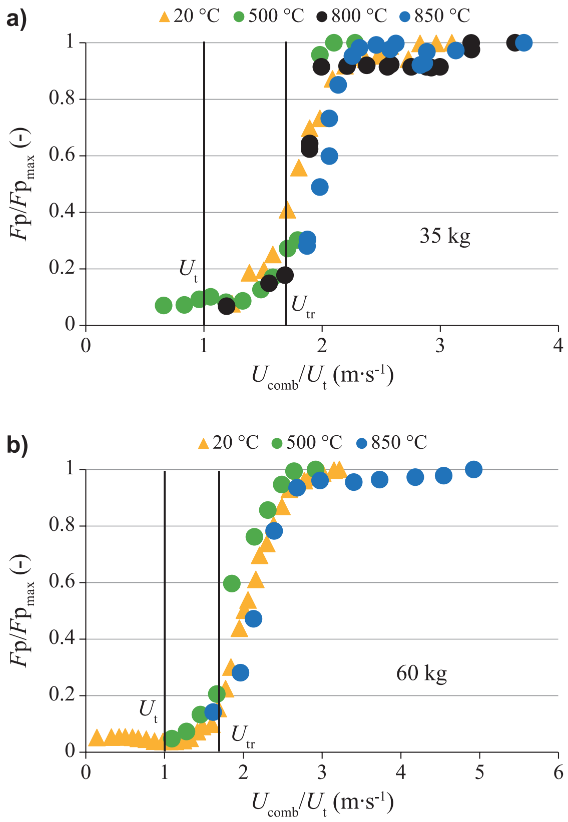

Fig. 17 Effect of bed temperature on normalized solids flow rate vs. normalized gas velocity for 35 **(a)** and 60 **(b)** bed material inventories (olivine, $U_G = 4 \cdot U_{mf}$, $U_I = 4 \cdot U_{mf}$, $H_{II} = 15$ cm).

Besides, it is independent of bed temperature and bed material inventory. Some correlations in literature (Perales et al., 1991a; Perales et al., 1991b; Bi and Fan, 1992; Tannous, 1993), reported in **Table 3**, allow estimating U_{tr} velocity at ambient temperature, with relative errors between −6 and 2 %. However, for bed temperatures higher than ambient temperature, only the correlation proposed by Perales et al. (1991a) properly estimates U_{tr} values;

- beyond U_{tr}, the solids mass flow rate increases as gas velocity rises until it reaches a plateau. The velocity at which this plateau is reached was found to increase with bed material inventory. For instance, it increases from $2.2 \cdot U_t$ to $2.7 \cdot U_t$ as the bed inventory rises from 35 to 60 kg. However, it is not affected by bed temperature. Besides, results show that the solids mass flow rate on this plateau only depends on the bed material inventory. The slight differences between each curve are likely explained by the uncertainty of the microwave probe (SolidFlow 2.0) as well as by experimental errors.

Besides, **Fig. 17a** and **Fig. 17b** illustrate the normalized solids mass flow rate (Fp/Fp_{max}) vs. the normalized gas velocity (U_{comb}/U_t), between 20 and 850 °C, for bed inventories of 35 and 60 kg, respectively. Results confirm that U_{tr} velocity is not affected by bed temperature or bed inventory.

4.3 Comments on the effect of combustor gas velocity on solids mass flow rate and total pressure drop fluctuations

An experiment was carried out at 500 °C for an olivine inventory of 35 kg. **Fig. 18** shows the influence of combustor air velocity U_{comb} on the normalized circulating solids mass flow rate Fp/Fp_{max}, total pressure in the combustor P_{comb}, pressure profiles along the combustor and distribution of solids inventory in both gasifier and combustor. Total pressure is considered as the pressure difference between two pressure taps, P_{dist} (3 cm above the distributor) and P_7 (2.5 m above the distributor). From the temporal fluctuations of solids flow rate and total pressure in the combustor, a standard deviation was determined for several velocities U_{comb}. Results show that the hydrodynamic regimes defined above, as well as the transport velocity, can be estimated from the plot of these standard deviations against gas velocity. For instance, it was found from results at 500 °C that:

- For velocities up to 2.4 $m \cdot s^{-1}$ (zone 1 in **Fig. 18**), solids inventories in both gasifier and combustor remain almost constant, which is in agreement with the constant total pressure of the combustor. Moreover, a very low solids circulation flow rate is measured. As mentioned above, the combustor is a deep «dense fluidized bed» with a height reaching 1.5 m (**Fig. 18c**). In this zone, the solids concentration in the free-board area is very small. Thus elutriation of fine particles initially present in the solids batch explains the residual values of the circulation flow rate. Besides, an increase in gas velocity leads to a peak in the combustor pressure standard deviation

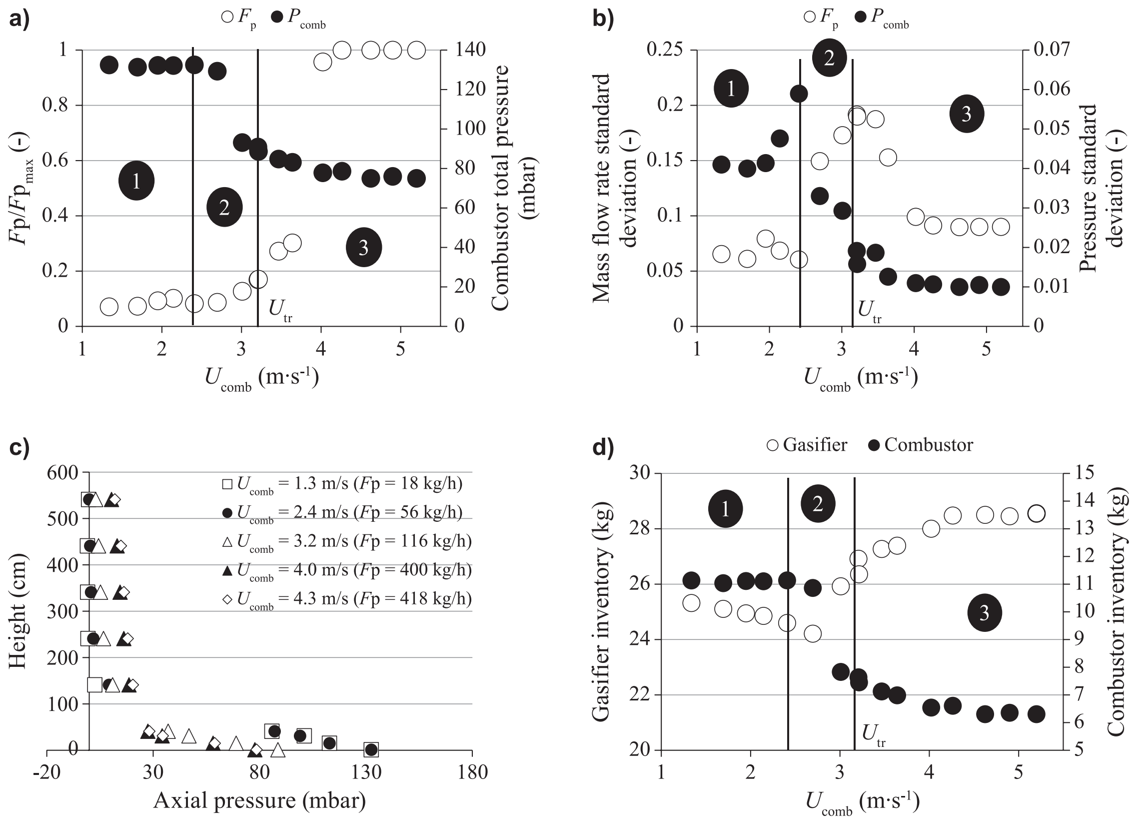

Fig. 18 Effect of combustor gas velocity on the solids mass flow rate, the combustor total pressure (**a**), its standard deviation (**b**), the axial pressure profiles (**c**) as well as on solids inventory in both gasifier and combustor (**d**) (olivine, $m_p = 35$ kg, $T = 500$ °C).

(**Fig. 18b**). According to many authors (Yerushalmi and Cankurt, 1979; Han et al., 1985; Mori et al., 1986; Chehbouni et al., 1994), this peak is explained by the slugging phenomenon due to an increase in bubble formation and coalescence. These authors defined this velocity as the onset of turbulent fluidization, U_c. It can be noticed that this velocity is slightly higher than the terminal settling velocity U_t (2.03 m·s^{-1} at 500 °C);

- for velocities between 2.4 and 3.2 m·s^{-1} (zone 2), an increase in the circulation mass flow rate from 50 to 120 kg·h^{-1} and an abrupt rise of its standard deviation are observed. As explained above, this is likely attributed to the fact that the kinetic energy contained in the bubbles during their eruption at the bed surface is enough to transport particles brought into its wake to the combustor outlet. This phenomenon, as shown in **Fig. 18d**, leads to an increase in the inventory difference between both reactors (i.e. the pressure difference on both sides of the dump). Consequently, a decrease in the total pressure of the combustor was observed (**Fig. 18a**). The total pressure standard deviation was also found to decrease (**Fig. 18b**). Some authors (Yerushalmi and Cankurt, 1979; Han et al., 1985; Satija and Fan, 1985; Mori et al., 1986; Perales et al., 1991a; Tannous, 1993) explain this trend by the breakup of bubbles and slugs due to internal solids circulation, and by the decrease in bubble formation and coalescence;
- for velocities beyond 3.2 m·s^{-1} (zone 3), the solids mass flow rate increases before reaching a plateau. Simultaneously, its standard deviation decreases to a stable stage. According to Chehbouni et al. (1994), these trends indicate that the velocity at which this third zone starts is the transport velocity, U_{tr}, which marks the onset of the circulating fluidization. Worthy of note is that the value of U_{tr} found from the evolution of solids mass flow rate standard deviation vs. gas velocity is close to the one determined above (3.3 m·s^{-1}). For velocities higher than 4.0 m·s^{-1}, the stabilization of the solids mass flow rate, combustor total pressure and inventory difference between both reactors is in agreement with the results of Yerushalmi and Cankurt (1979). These authors found that beyond the transport velocity U_{tr}, solid traverses the column in a stable transported flow.

However, supplementary studies have to be performed in order to ascertain the good reproducibility of circulation flow rate and total pressure standard deviation.

5. Conclusion

From experimental data obtained between 20 and 950 °C, correlations were proposed in order to estimate olivine minimum fluidization velocity and bed voidage. These relationships can be useful for industrial gasifier design. Moreover, hydrodynamic experiments were carried out in a circulating fluidized bed between 20 and 850 °C. Results showed that, under our operating conditions:

- The trend of solids mass flow rate vs. gas velocity is of S-shape type;
- the transport velocity U_{tr} is not significantly affected by bed temperature and bed material inventory. It only seems to be proportional to terminal settling velocity U_{t}. The correlation proposed by Perales et al. (1991a) enables a good estimate of this characteristic velocity;
- beyond U_{tr}, the circulation mass flow rate mainly depends on bed material inventory and gas velocity. For the same bed inventory and gas velocity, it is independent of bed temperature;
- beyond a certain gas velocity, the circulation mass flow rate levels off. The mass flow rate on this plateau is not affected by bed temperature but is strongly dependent on bed material inventory.

Besides, results showed that key parameters for the solids flow rate control are combustor gas velocity and solids inventory. An increase in these parameters leads to higher circulation flow rates. However, the bed temperature and bed material nature showed no influence, neither on the transport velocity nor on the solids flow rate.

Nomenclature

A_{c}: reactor section (m^2)

Ar: Archimedes number (–)

C_1, C_2: constant numbers relating to Ar and Re_{mf} (–)

C_{11}: constant number, $C_{11} = 0.64 \cdot A_c^{0.4}$ ($\mathrm{m}^{0.8}$)

C_{12}: constant number, $C_{12} = \dfrac{1.30}{g^{0.2} \cdot N_{\mathrm{or}}^{0.4}}$ ($\mathrm{m}^{-0.2} \cdot \mathrm{s}^{0.4}$)

C_{d}: drag coefficient (–)

C_{v}: diameter variation coefficient (–)

$\overline{d_{\mathrm{B}}}$: bubble mean diameter (m)

d_{B0}: initial bubble diameter, at the outlet of the gas distributor (m)

d_{Bm}: maximal bubble diameter (m)

d_{p}: Sauter mean particle diameter (m)

D_{C}: reactor diameter (m)

Fp: circulating solids mass flow rate ($\mathrm{kg} \cdot \mathrm{h}^{-1}$)

Fp_{max}: maximal circulating solids mass flow rate ($\mathrm{kg} \cdot \mathrm{h}^{-1}$)

g: acceleration due to gravity ($\mathrm{m} \cdot \mathrm{s}^{-2}$)

H: bed height (m)

H_{II}: secondary air injection cane height (m)

H_{mf}: bed height at minimum fluidization conditions (m)

K_1, K_2: constant numbers relating to Ar and Re_{mf} (–)

L: packed bed height in Ergun equation (m)

m_{p}: total weight of particles, inventory (kg)

m_{pC}: total weight of particles in the combustor (kg)

m_{pG}: total weight of particles in the gasifier (kg)

Mv: density number, $Mv = \dfrac{\rho_{\mathrm{P}} - \rho_{\mathrm{f}}}{\rho_{\mathrm{f}}}$ (–)

N_{e}: number of data (–)

N_{or}: orifice number in the gas distributor (–)

P_{comb}: total pressure drop in the combustor (mbar)

P_{dist}: pressure drop measured 3 cm above the distributor, in the combustor (mbar)

R_1: relative error (%)

R_2: absolute relative error (%)

Re_{mf}: Reynolds number at the minimum fluidization point (–)

Re_{tr}: Reynolds number at the gas velocity U_{tr} (–)

T: temperature (°C)

U: superficial gas velocity ($\mathrm{m} \cdot \mathrm{s}^{-1}$)

U_{b}: bubble rise velocity in the bed ($\mathrm{m} \cdot \mathrm{s}^{-1}$)

U_{c}: turbulent regime characteristic velocity ($\mathrm{m} \cdot \mathrm{s}^{-1}$)

U_{ch}: chocking velocity ($\mathrm{m} \cdot \mathrm{s}^{-1}$)

U_{comb}: total air velocity in the combustor ($\mathrm{m} \cdot \mathrm{s}^{-1}$)

U_{G}: gas velocity in the gasifier ($\mathrm{m} \cdot \mathrm{s}^{-1}$)

U_{I}: primary air velocity in the combustor ($\mathrm{m} \cdot \mathrm{s}^{-1}$)

U_{II}: secondary air velocity in the combustor ($\mathrm{m} \cdot \mathrm{s}^{-1}$)

U_{mf}: minimum fluidization velocity ($\mathrm{m} \cdot \mathrm{s}^{-1}$)

U_{s}: superficial gas velocity in the standpipe ($\mathrm{m} \cdot \mathrm{s}^{-1}$)

U_{t}: terminal settling velocity of single particle ($\mathrm{m} \cdot \mathrm{s}^{-1}$)

U_{tr}: transport velocity ($\mathrm{m} \cdot \mathrm{s}^{-1}$)

z: given height in the dense fluidized bed (m)

$\overline{Z}$: mean value of a given parameter (unit of the parameter)

Z_i: value of a given parameter (unit of the parameter)

Greek symbols

γ : compressibility factor (–)

δ_{B}: bubble volume fraction in the bed (–)

ΔP: pressure drop (Pa)

ε: average fluidized bed voidage (–)

$\varepsilon_{\mathrm{BA}}$: mean aerated bulk bed voidage (–)

$\varepsilon_{\mathrm{BP}}$: mean packed bulk bed voidage (–)

$\varepsilon_{\mathrm{mf}}$: minimum fluidization voidage (–)

μ_{f}: fluid viscosity ($\mathrm{kg \cdot m^{-1} \cdot s^{-1}}$)

ρ_{b}: bed density ($\mathrm{kg \cdot m^{-3}}$)

ρ_{BA}: aerated bulk density ($\mathrm{kg \cdot m^{-3}}$)

ρ_{BP}: packed bulk density ($\mathrm{kg \cdot m^{-3}}$)

ρ_{f}: fluid density ($\mathrm{kg \cdot m^{-3}}$)

ρ_{mf}: bed density at the minimum fluidization condition ($\mathrm{kg \cdot m^{-3}}$)

ρ_{p}: particle density ($\mathrm{kg \cdot m^{-3}}$)

ρ_{s}: skeletal density ($\mathrm{kg \cdot m^{-3}}$)

σ_{Z}: normalized standard deviation (–)

φ: shape (sphericity) factor (–)

χ: particle internal voidage (–)

References

Adanez J., De Diego L.F., Gayan P., Transport velocities of coal and sand particles, Powder Technology, 77 (1993) 61–68.

Agarwal O.P., Storrow J.A., Pressure drop in fluidization beds, Chemistry & Industry, 15 (1951) 278–286.

Babu S.P., Shah B., Talwalkar A., Fluidization correlations for coal gasification materials-minimum fluidization velocity and fluidized bed expansion ratio, AIChE Symposium Series, 74 (1978) 176–186.

Basu P., Cheng L., An analysis of loop seal operations in a circulating fluidized bed, Chemical Engineering Research and Design, 78 (2000) 991–998.

Berruti F., Pugsley T.S., Godfroy L., Chaouki J., Patience G.S., Hydrodynamics of circulating fluidized bed risers: a review, The Canadian Journal of Chemical Engineering, 73 (1995) 579–602.

Bi X., Fan L.-S., Existence of turbulent regime in gas-solid fluidization, AIChE journal, 38 (1992) 297–301.

Bi X., Grace J.R., Effects of pressure and temperature on flow regimes in gas-solid fluidization systems, The Canadian Journal of Chemical Engineering, 74 (1996) 1025–1027.

Botterill J.S.M., Teoman Y., Yuregir K.R., Comments on 'Minimum fluidization velocity at high temperature', Industrial & Engineering Chemistry Process Design and Development, 21 (1982a) 784–785.

Botterill J.S.M., Teoman Y., Yuregir K.R., The effect of operating temperature on the velocity of minimum fluidization, bed voidage and general behaviour, Powder Technology, 31 (1982b) 101–110.

Botterill J.S.M., Teoman Y., Yuregir K.R., The effect of temperature on fluidized bed behaviour, Chemical Engineering Communications, 15 (1982c) 227–238.

Bourgeois P., Grenier P., The ratio of terminal velocity to minimum fluidising velocity for spherical particles, The Canadian Journal of Chemical Engineering, 46 (1968) 325–328.

Bull D.R., Performance improvements to a fast internally circulating fluidised bed (FICFB) biomass gasifier for combined heat and power plants (Doctoral dissertation), University of Canterbury, 2008.

Cai P., Jin Y., Yu Z.-Q., Wang Z.-W., Mechanism of flow regime transition from bubbling to turbulent fluidization, AIChE journal, 36 (1990) 955–956.

Chehbouni A., Chaouki J., Guy C., Klvana D., Characterization of the flow transition between bubbling and turbulent fluidization, Industrial & Engineering Chemistry Research, 33 (1994) 1889–1896.

Chehbouni A., Chaouki J., Guy C., Klvana D., Effects of different parameters on the onset of fluidization in a turbulent regime, Canadian Journal of Chemical Engineering, 73 (1995) 41–50.

Chitester D., Kornosky R.M., Fan L.-S., Danko J.P., Characteristics of fluidization at high pressure, Chemical Engineering Science, 39 (1984) 253–261.

Chyang C.S., Huang W.C., Characteristics of large particle fluidization, Journal of The Chinese Institution of Chemical Engineers, 19 (1988) 81–89.

Davidson J.F., Harrison D., Fluidized Particles, Cambridge University Press, Cambridge, England, 1963.

Detournay M., Vapogazéification de la biomasse en Lit Fluidisé Circulant: Élaboration des outils théoriques et expérimentaux (Doctoral dissertation), Institut National Polytechnique de Toulouse, 2011.

Ergun S., Fluid flow through packed columns, Chemical Engineering Progress, 48 (1952) 89–94.

Fan L.T., Ho T.-C., Walawender W.P., Measurements of the rise velocities of bubbles, slugs and pressure waves in a gas-solid fluidized bed using pressure fluctuation signals, AIChE Journal, 29 (1983) 33–39.

Fatah N., Fluidisation des grosses particules à haute température hydrodynamique et transferts thermiques, Institut National Polytechnique de Toulouse, 1991.

Formisani B., Girimonte R., Mancuso L., Analysis of the fluidization process of particle beds at high temperature, Chemical Engineering Science, 53 (1998) 951–961.

Gauthier D., Zerguerras S., Flamant G., Influence of the particle size distribution of powders on the velocities of minimum and complete fluidization, Chemical Engineering Journal, 74 (1999) 181–196.

Geldart D., The effect of particle size and size distribution on the behaviour of gas-fluidised beds, Powder Technology, 6 (1972) 201–215.

Geldart D., Types of gas fluidization, Powder Technology, 7 (1973) 285–292.

Gómez-Barea A., Leckner B., Modeling of biomass gasification in fluidized bed, Progress in Energy and Combustion Science, 36 (2010) 444–509.

Goo J.H., Seo M.W., Kim S.D., Song B.H., Effects of temperature and particle size on minimum fluidization and transport velocities in a dual fluidized bed, Proceedings of the 20th International Conference on Fluidized Bed Combustion, Xian, 2009, pp. 305–309.

Grace J.R., Sun G., Influence of particle size distribution on the performance of fluidized bed reactors, The Canadian Journal of Chemical Engineering, 69 (1991) 1126–1134.

Grace J.R., Knowlton T.M., Avidan A.A., Circulating Fluidized Beds, 1st ed., Blackie Academic and Professional, London, UK, 1997.

Haider A., Levenspiel O., Drag coefficient and terminal velocity of spherical and nonspherical particles, Powder Technology, 58 (1989) 63–70.

Han G.Y., Lee G.S., Kim S.D., Hydrodynamic characteristics of a circulating fluidized bed, Korean Journal of Chemical Engineering, 2 (1985) 141–147.

Hartman M., Svoboda K., Predicting the effect of operating temperature on the minimum fluidization velocity, Industrial & Engineering Chemistry Process Design and Development, 25 (1986) 649–654.

Hilal N., Gunn D.J., Solid hold up in gas fluidised beds, Chemical Engineering and Processing: Process Intensification, 41 (2002) 373–379.

Hofbauer H., Rauch R., Löffler G., Kaiser S., Fercher E., Tremmel H., Six years of experience with the FICFB-gasification process, In: 12th European conference on biomass and bioenergy. Amsterdam, The Netherlands, 2002.

Kunii D., Levenspiel O., Fluidization Engineering, 2nd ed., Butterworth-Heinemann, Stoneham, USA, 1991.

Lee G.S., Kim S.D., Bed expansion characteristics and transition velocity in turbulent fluidized beds, Powder Technology, 62 (1990) 207–215.

Lewis W.K., Gilliland E.R., Bauer W.C., Characteristics of fluidized particles, Industrial & Engineering Chemistry, 41 (1949) 1104–1117.

Lim K.S., Zhu J.X., Grace J.R., Hydrodynamics of gas-solid fluidization, International Journal of Multiphase Flow, 21 (1995) 141–193.

Llop M.F., Casal J., Arnaldos J., Incipient fluidization and expansion in fluidized beds operated at high pressure and temperature, In: Large J.-F., Laguerie C. (Eds.), Fluidization VIII, Engineering Foundation, New York, 1995, pp. 131–138.

Lucas A., Arnaldos J., Casal J., Puigjaner L., High temperature incipient fluidization in mono and polydisperse systems, Chemical Engineering Communications, 41 (1986) 121–132.

Matheson G.L., Herbst W.A., Holt P.H., Characteristics of fluid-solid systems, Industrial & Engineering Chemistry, 41 (1949) 1098–1104.

Matsen J.M., Hovmand S., Davidson J.F., Expansion of fluidized beds in slug flow, Chemical Engineering Science, 24 (1969) 1743–1754.

McKay G., McLain H.D., Fluidization characteristics of cuboids, Industrial & Engineering Chemistry Process Design and Development, 19 (1980) 712–715.

Mii T., Yoshida K., Kunii D., Temperature-effects on the characteristics of fluidized beds, Journal of Chemical Engineering of Japan, 6 (1973) 100–102.

Mori S., Wen C.Y., Estimation of bubble diameter in gaseous fluidized beds, AIChE Journal, 21 (1975) 109–115.

Mori S., Hashimotot O., Haruta T., Mochizuki K., Matsutani W., Hiraoka S., Yamada I., Kojima T., Tuji K., Turbulent fluidization phenomena. In: Basu P., Large J.F. (Eds.), Circulating Fluidized Bed Technology II, Pergamon Press, Oxford, 1986, 75–87.

Murachman B., Hydrodynamique et transferts thermiques dans les lits fluidisés par les gaz, Institut National Polytechnique de Toulouse, 1990.

Nakamura M., Hamada Y., Toyama S., Fouda A.E., Capes C.E., An experimental investigation of minimum fluidization velocity at elevated temperatures and pressures, The Canadian Journal of Chemical Engineering, 63 (1985) 8–13.

Pattipati R.R., Wen C.Y., Minimum fluidization velocity at high temperatures, Industrial & Engineering Chemistry Process Design and Development, 20 (1981) 705–707.

Perales J.F., Coll T., Llop M.F., Arnaldos J., Casal J., The prediction of transport velocity in fast fluidized beds, Récents Progrès en Génie des Procédés: La Fluidisation, 1991a, pp. 47–53.

Perales J.F., Coll T., Llop M.F., Puigjaner L., Arnaldos J., Casal J., On the transition from bubbling to fast fluidization regimes. In: Basu P., Horio M., Hasatani M. (Eds.), Circulating Fluidized Bed Technology III, Pergamon Press, Oxford, 1991b, pp. 73–78.

Rhodes M.J., Geldart D., Transition to turbulence?. In: Ostegaard K., Sorensen A. (Eds.), Fluidization, vol. V, Engineering Foundation, New-York, 1986, pp. 281–288.

Richardson J.F., Incipient fluidization and particulate systems, In: Davidson J.F., Harrison D. (Eds.), Fluidization, Academic Press, New York, 1971, p. 26.

Rim G., Lee D., Bubbling to turbulent bed regime transition of ternary particles in a gas–solid fluidized bed, Powder Technology, 290 (2016) 45–52.

Rowe P.N., An X-ray study of bubbles in fluidized beds, Transactions of the Institution of Chemical Engineers, 43 (1965) 157–175.

Ruiz J.A., Juárez M.C., Morales M.P., Muñoz P., Mendívil M.A., Biomass gasification for electricity generation: review of current technology barriers, Renewable and Sustainable Energy Reviews, 18 (2013) 174–183.

Ryu H.-J., Lim N.-Y., Bae D.-H., Jin G.-T., Minimum fluidization velocity and transition velocity to fast fluidization of oxygen carrier particle for chemical-looping combustor, Korean Institute of Chemical Engineers, 41 (2003) 624–631.

Satija S., Fan L.-S., Characteristics of slugging regime and transition to turbulent regime for fluidized beds of large coarse particles, AIChE Journal, 31 (1985) 1554–1562.

Saxena S.C., Vogel G.J., The measurement of incipient fluidization velocities in a bed of coarse dolomite at temperature and pressure, Transactions of the Institution of Chemical Engineers, 55 (1977) 184–189.

Schnitzlein M.G., Weinstein H., Flow characterization in high-velocity fluidized beds using pressure fluctuations, Chemical Engineering Science, 43 (1988) 2605–2614.

Shabanian J., Chaouki J., Effects of temperature, pressure, and interparticle forces on the hydrodynamics of a gas-solid fluidized bed, Chemical Engineering Journal, 313 (2017) 580–590.

Shamlou P.A., Handling of Bulk Solids: Theory and Practice, Butterworths, 1988, pp. 20–50.

Stubington J.F., Barrett D., Lowry G., On the minimum fluidizing velocity of coal-derived chars at elevated temperatures, Chemical Engineering Science, 39 (1984) 1516–1518.

Svoboda K., Cermak J., Hartman M., Drahos J., Selucky K., Pressure fluctuations in gas-fluidized beds at elevated temperatures, Industrial & Engineering Chemistry Process Design and Development, 22 (1983) 514–520.

Tannous K., Contribution à l'étude hydrodynamique des lits fluidisés de grosses particules, Institut National Polytechnique de Toulouse, 1993.

Tannous K., Hemati M., Laguerie C., Characteristics of incipient fluidization and expansion of fluidized-beds of particles of Geldart category-D, Powder Technology, 80 (1994) 55–72.

Thonglimp V., Hiquily N., Laguerie C., Vitesse minimale de fluidisation et expansion des couches fluidisées par un gaz, Powder Technology, 38 (1984) 233–253.

Van Heerden C., Nobel A.P.P., Van Krevelen D.W., Studies on fluidization. I—the critical mass velocity, Chemical Engineering Science, 1 (1951) 37–49.

Wen C.Y., Yu Y., Mechanics of fluidization, Chemical Engineering Progress Symposium Series, 62 (1966) 100–101.

Werther J., Influence of the bed diameter on the hydrodynamics of gas fluidized beds, AIChE Symposium Series, 70 (1974) 53–62.

Yates J.G., Effects of temperature and pressure on gas-solid fluidization, Chemical Engineering Science, 51 (1996) 167–205.

Yerushalmi J., Turner D.H., Squires A.M., The fast fluidized bed, Industrial & Engineering Chemistry Process Design and Development, 15 (1976) 47–53.

Yerushalmi J., Cankurt N.T., Further studies of the regimes of fluidization, Powder Technology, 24 (1979) 187–205.

Appendix A: Bubble fraction estimation

The bubble fraction in the bed δ_{B} can be estimated from the following equations (Davidson and Harrison, 1963; Mori and Wen, 1975):

$$\delta_{\mathrm{B}} = \frac{U - U_{\mathrm{mf}}}{U_{\mathrm{b}}} \tag{A1}$$

$$U_{\mathrm{b}} = (U - U_{\mathrm{mf}}) + 0.711 \cdot \left(g \cdot \overline{d_{\mathrm{B}}}\right)^{1/2} \tag{A2}$$

$$\overline{d_{\mathrm{B}}} = d_{\mathrm{Bm}} - (d_{\mathrm{Bm}} - d_{\mathrm{B0}}) \cdot \exp\left(-0.3 \cdot \frac{\frac{H}{2}}{D_t}\right) \tag{A3}$$

$$d_{\mathrm{Bm}} = 0.64 \cdot [A_{\mathrm{c}} \cdot (U - U_{\mathrm{mf}})]^{0.4} = C_{11} \cdot (U - U_{\mathrm{mf}})^{0.4} \tag{A4}$$

$$d_{\mathrm{B0}} = \frac{1.30}{g^{0.2}} \cdot \left(\frac{U - U_{\mathrm{mf}}}{N_{\mathrm{or}}}\right)^{0.4} = C_{12} \cdot (U - U_{\mathrm{mf}})^{0.4} \tag{A5}$$

where C_{11} and C_{12} are numbers depending on reactor and gas distributor geometry. Combining Equations A3 to A5 gives the bubble mean diameter, dependent only on the excess gas velocity, as:

$$\overline{d_{\mathrm{B}}} = (U - U_{\mathrm{mf}})^{0.4} \cdot \left[C_{11} - (C_{11} - C_{12}) \cdot \exp\left(-0.3 \cdot \frac{\frac{H}{2}}{D_{\mathrm{C}}}\right)\right] \tag{A6}$$

Then, a combination of Equations A1, A2 and A6 shows that average bed voidage depends only on excess gas velocity.

Authors' Short Biographies

Sébastien Pecate

Sébastien Pecate holds a PhD (2017) in process engineering, and more precisely on "Biomass Gasification in an FICFB". He worked as a research engineer on biomass and sludge gasification at LGC from 2014 to 2018. He is now working on solid waste thermal treatment (incineration, pyrolysis, gasification, combustion) for waste to energy, waste to fuels and waste to chemicals applications.

Mathieu Morin

Dr. Mathieu Morin studied chemical engineering processes at the University of Toulouse, France, where he received his PhD degree on "Biomass Gasification in Circulating Fluidized Bed" in 2017. During his PhD thesis, he particularly developed experimental and modeling tools in order to study the chemical reactions occurring during biomass conversion (pyrolysis, gasification, combustion, catalytic cracking and reforming of tar). Currently, Dr. Mathieu Morin is working at IFPEN in Lyon, France, at the Department of Process Design and Modeling. His main topics are the development of processes for the production of environmental fuels, chemical intermediates and energy from fossil and renewable resources.

Sid Ahmed Kessas

Sid Ahmed Kessas is a second-year PhD student who graduated in chemical engineering in 2016 and who worked on:

- Characterization of biomass.
- Reactivity and kinetics of steam gasification & combustion.
- Synthesis of catalyst in a fluidized bed.

Authors' Short Biographies

Mehrdji Hemati

Mehrdji Hemati is a professor in chemical engineering at the ENSIACET-INP in Toulouse. His research activities focus on three items:

- ➢ Hydrodynamics and transfers in dense and circulating fluidised beds. Two approaches were developed: the experimental approach and the theoretical approach.
- ➢ Application of fluidised beds in the field of chemical reaction gathering catalytic reactions, gas-solid reactions (biomass and sewage sludge pyrolysis, gasification and combustion).
- ➢ Processes for elaboration of materials gathering: drying, mixing, size enlargement by spray coating and granulation, dry impregnation in F.B.

He is author and co-author of more than 100 publications in international scientific journals.

Yilmaz Kara

Yilmaz Kara is a process engineer working on biomass gasification, fluidized beds, REFIOM vitrification and many other subjects related to energetic valorization. He is also an expert on green gas production and treatment, and flow assurance.

Sylvie Valin

Sylvie Valin holds a PhD (1999) in energetics from the Institut National Polytechnique de Grenoble (France). She has been working as a research engineer on biomass gasification at CEA since 2004. Her research activity mainly concerns biomass and waste pyrolysis and gasification for energy application, coupling experimental and modelling approaches from particle to reactor scale. She especially works on gasification in high-temperature reactors (fluidised bed, entrained flow reactor).

The 52nd Symposium on Powder Technology

The 52nd Symposium on Powder Technology organized by Hosokawa Powder Technology Foundation took place at Tokyo Garden Palace, in Japan on Monday, September 3, 2018. It was held by the planning of Council of Powder Technology, Japan and with the sponsorship of Hosokawa Micron Corporation. Over 160 people from the industries and universities attended this symposium. The theme of the symposium this year was “Powder Technology for Synthesis and Application of Power Materials”. There were six lectures including a special one given by the KONA Awardee with questions and answers after each lecture followed by a get-acquainted party for further free discussions.

At the beginning of the symposium, Mr. Yoshio Hosokawa, the president of the Foundation, gave the opening address mentioning that this symposium started in 1968, just 50 years ago and has been continued almost annually since then. Prior to the lectures, the KONA Award presentation ceremony was held and the plaque of KONA Award was handed from the president to Prof. Sotiris E. Pratsinis, who received this Award in the last fiscal year 2017. The KONA Award has been given to the researcher with excellent performance and contributions to the powder and particle science and technology since 1990. It was first started by Hosokawa Micron Corporation and taken over by Hosokawa Foundation after its establishment in 1991. Though it had been presented to Japanese researchers by the Foundation till two years ago, it was opened to worldwide and given to the overseas researcher by the Foundation last year for the first time.

The special lecture given by Prof. Pratsinis focusing on the scalable synthesis of sophisticated nanoparticles with controlled composition, size and morphology by flame spray pyrolysis putting new various high-value products such as single atom catalysts and chemoresistive sensors for breath analysis.

The contents of the symposium are shown below. In the second lecture, the technology of processing and evaluation of nano-carbon based sintered composites using graphene, which shows unique functional properties such as enhanced electrical conductivity, thermoelectric performance and improved mechanical properties.

The following lecture 3 was concerning the white LED application of sialon phosphors used as power luminescent materials and besides forthcoming phosphors applicable for high color rendering lighting or super high vision TV were summarized. In the lecture 4, it was explained about the innovation of sheeting technology of electrodes for on-board battery used for the automobiles based on the fundamental investigation on the rheological behavior and micro structures of colloidal dispersions with the objective of identifying rheological control guidelines for concentrated slurries.

On the other hand, as a spotlighted organic material was introduced in lecture 5 the cellulose nanofibers (CNFs) having unique properties such as high viscosities at low consistencies, characteristic thixotropy behavior by shear forces, high emulsifying and suspending capability, etc. and applied as thickening agent of the ink of the aqueous ball-point pen with unique rheological properties. In the final lecture, the worldwide trends and basic technology of the environment-friendly powder coating using no solvent were introduced together with the new development of the coating system and the related instruments.


KONA Award presentation

The 52nd Symposium on Powder Technology

Theme: "Powder Technology for Synthesis and Application of Power Materials"

Opening address Mr. Yoshio Hosokawa (President of Hosokawa Powder Technology Foundation, President of Hosokawa Micron Corporation)

- 2017 KONA Award presentation ceremony

Session 1 Chaired by Prof. Makio Naito (Osaka University)

- Lecture 1 (Special lecture by the KONA Awardee)
  "Material Synthesis by Aerosol Particle Technology: from Carbon Black to Breath Sensors"
  Prof. Sotiris E. Pratsinis (Swiss Federal Institute of Technology Zurich (ETH Zurich))
- Lecture 2
  "Processing and Evaluation of Nano-Carbon Based Sintered Composites"
  Prof. Akira Kawasaki (Graduate School of Engineering, Tohoku University)

Session 2 Chaired by Dr. Yoshio Sakka (Senior Scientist, NIMS)

- Lecture 3
  "White LED Application of Sialon Phosphors and their Forefront"
  Dr. Kohsei Takahashi (National Institute for Materials Science, JAPAN (NIMS))
- Lecture 4
  "Innovation of Sheeting Technology of Electrodes for On-Board Battery
  —Control of Shear-Thickening Behavior—"
  Mr. Hiroshi Nakamura (Principal Fellow, Toyota Central R&D Labs., Inc.)

Session 3 Chaired by Dr. Hisao Makino (Research advisor, Central Research Institute of Electric Power Industry (CRIEPI))

- Lecture 5
  "Characteristics of Cellulose Nanofibers as Additive"
  Mr. Yohsuke Goi (Specialist, Rheocrysta R&D Group, Life Sciences R&D Department, R&D Headquarters, DKS Co., Ltd.)
- Lecture 6
  "Trend of Latest Powder Coating Technology"
  Mr. Shoji Kimura (President, Wagner-Hosokawa Micron Ltd.)

Closing remarks Emeritus Prof. Fumio Saito (Tohoku University, President of Council of Powder Technology, Japan)

Symposium on Powder Technology

Get-acquainted Party

KONA Powder and Particle Journal No. 36 (2019) 296/Doi:10.14356/kona.2019022

The 25th KONA Award

Sotiris E. Pratsinis is professor of process engineering and materials science at the Swiss Federal Institute of Technology (ETH Zurich) since 1998. There he teaches Mass Transfer, Introduction to Nanoscale Engineering and Micro-Nano-Particle Technology. He received his Diploma in Chemical Engineering from Aristotle Univ. of Thessaloniki, Greece in 1977. He served in the Greek Navy and worked in a textile company before receiving his MSc (1982) and PhD from University of California, Los Angeles in 1985. He was in the faculty of the Univ. of Cincinnati, USA from 1985 to 2000. He has graduated 40 PhD students, now at leading positions in industry and academia, worldwide. He has published 400+ refereed journal articles and has been awarded 20+ patents that are licensed to industry and have contributed to the creation of four spinoffs.

His research focuses on *multiscale* particle dynamics & aerosol reactor design. He has pioneered flame synthesis of nanostructured materials with closely controlled characteristics. This scalable process is practiced today in industrial units and academic labs. For example, in April 2017 the German National Science Foundation launched a 6-year, 6M Euro program funding about 20 PhDs in German universities on the fundamentals of flame spray pyrolysis (FSP) that was developed in his laboratories back in 2002. Also Harvard's School of Public Health is using extensively his FSP for synthesis of nanomaterials of various sizes and compositions to benchmark their toxicity under $5M funding by the U.S. National Institute of Health since 2016.

He first measured the oxidation rate of $TiCl_4$ for synthesis of TiO_2 that has been recognized as "… *a landmark contribution to … (pigment) industry…*". He has led the development of innovative algorithms for agglomerate formation and growth by 2-dimensional (mass and surface area) population balances for reaction, coagulation and sintering. These models along with his proof of the rapid attainment of both *self-preserving* size distribution and *fractal-like* structure during aerosol synthesis of materials enabled him to create simple, reliable, unimodal and even monodisperse particle dynamics models. These are interfaced readily with fluid mechanics greatly facilitating process design for particle manufacture and processing. For example, his model for production of optical fiber preforms was the first of its kind and it is still used in industry.

Motivated by this quantitative understanding, he showed experimentally, how to control flame-made particle size, crystallinity and, for the first time, morphology: from perfectly spherical particles to highly ramified agglomerates. Most notably, he developed the above FSP process for synthesis of sophisticate particle compositions, up to 5 kg/h in his labs, perhaps world's largest such facility for manufacture of nanoparticles at an academic institution. With FSP he prepared novel heterogeneous catalysts (primarily for environmental remediation) and gas sensors (primarily for breath analysis) and, for the first time, flame-made nutritional supplements, dental and theranostic materials. Also his FSP contributed decisively to environmental policy by identifying the origins of nanosilver toxicity and even developing processes for "curing" it.

His program has been funded by both Swiss and U.S. National Science Foundations, European Union as well as by DuPont, Dow, Degussa, Toyota, Nestle, Siemens, Millennium, Bühler, Clariant & others. His research has been recognized by the *1988 Kenneth T. Whitby Award* of the American Association of Aerosol Research, a *1989 Presidential Young Investigator Award* from the U.S. National Science Foundation, a *1995 Smoluchowski Award* by Gesellschaft für Aerosolforschung, the *2003 Thomas Baron Award* by the American Institute of Chemical Engineers (AIChE). In 2009 he won an *Advanced Investigator Grant* from the European Research Council, in 2011 a *Humboldt Research Award* (Germany) and in 2018 both a *Fuchs Memorial Award* from the International Aerosol Research Assembly and the *Lifetime Achievement Award in Particle Technology* from AIChE. He is member of the *Swiss Academy of Engineering* since 2012.

Mr. Y. Hosokawa (Left), the president of Hosokawa Foundation and Prof. Pratsinis, the KONA Awardee

KONA Powder and Particle Journal No. 36 (2019) 297/Doi:10.14356/kona.2019023 Infomation Article

General Information

History of the Journal

In the history of KONA Powder and Particle Journal, two organizations have been playing an important role. The one is the Council of Powder Technology, Japan (CPT) and the other is the Hosokawa Powder Technology Foundation (Hosokawa Foundation). The CPT was established in 1969 by Hosokawa Micron Corporation as a nonprofit organization to enhance the activities of research and development on powder science and technology. The Hosokawa Foundation was established in 1991 as a public-service corporation approved by the Ministry of Education, Culture, Sport, Science and Technology of Japan. The issues from No.1 (1983) to No.12 (1994) of KONA were published by CPT and the issues from No.13 (1995) by the Hosokawa Foundation.

The aim of KONA in the early days was to introduce excellent Japanese papers to the world and thus KONA consisted of papers recommended by some Japanese academic societies and translated from Japanese to English. From the issue of No.8, the CPT changed its editorial policy to internationalize the KONA and to incorporate papers by authors throughout the world in addition to translated papers. In response to this change, three editorial blocks have been organized in the world; Asian-Oceanian, American, and European. The policy and system have not changed even after the Hosokawa Foundation has taken over from the CPT. From the issue of No.27 (2009), publication of translated papers has been terminated and only original papers have been published. The CPT is still active today and is collaborating with the Hosokawa Foundation.

Aims and Scope

KONA publishes review and original research papers in a broad field of powder & particle science and technology, ranging from fundamental principles to practical applications. The papers on critical reviews of existing knowledge in special areas are very welcome.

The submitted papers are published only when they are judged by the Editor to contribute to the progress of powder science and technology, and approved by any of the three Editorial Committees.

The paper submitted to the Editorial Secretariat should not have been previously published.

Category of Papers

- Invited articles
  Review papers and feature articles invited by the KONA Editorial Committees.
- Contributed papers
  Original review papers and some limited number of original research papers of high quality submitted to the KONA Editorial Committees, and refereed by the reviewers and editors.

Submission of Papers

It is now possible to submit your paper online via Editorial Manager® for KONA Online Paper Submission and Peer Review **System**. For all further information, please go to the journal's homepage on http://www.kona.or.jp/jp/journal/info.html.

Publication in KONA is free of charge.

Publication Schedule

KONA is published annually. The publication date is around January 10th.

Subscription

KONA is distributed free of charge to senior researchers at universities and laboratories as well as to institutions and libraries in the field throughout the world. The publisher is always glad to consider the addition of names of those, who want to obtain this journal regularly, to the mailing list.

Instructions to Authors

(1) Language

All submissions should be written in good English. Authors may choose either British or American English, provided that the chosen style is used consistently. Authors from non-English-speaking countries are encouraged to use a professional English editing service to proofread their manuscript.

(2) Manuscript format

- Electric files should be submitted to the Editorial Secretariat by online. Authors' short biography with less than 100 words per person and color photographs of all the authors should be attached to the final version.
- The structure of manuscripts should follow the following order; title, authors, affiliations, abstract, graphical abstract, keywords, main text, (acknowledgement), (appendix), (nomenclature), references. The items with parentheses are not mandatory.
- Full postal addresses must be given for all the authors. Indicate the corresponding author by the asterisk mark"*" after the name. Telephone and fax numbers and e-mail address should be provided for the corresponding author.
- Abstract should not exceed 200 words.
- Graphical abstract should be a concise, visual summary of the article which will be displayed in the contents list both online and print.
- The appropriate number of keywords is 5 or 6.
- The maximum pages printed in KONA are supposed to be:
  15 for an original paper and 25 for a review paper.
- Symbols and units should be listed in alphabetical order with their definition and dimensions in SI units.
- The color figures will appear in color both on the KONA Website (http://www.kona.or.jp) and also in the paper version.
- Concerning references, the alphabetical system should be adopted. Please use reference management software such as Endnote to manage references as far as possible.
  List: References should be arranged first alphabetically and then further sorted chronologically if necessary. More than one reference from the same author(s) in the same year must be identified by the letters "a", "b", "c", etc., placed after the year of publication.
  Examples:
  - Reference to a book:
    Strunk Jr. W., White E.B., The Elements of Style, fourth ed., Longman, New York, 2000.
  - Reference to a chapter in an edited book:
    Mettam G.R., Adams L.B., How to prepare an electronic version of your article, in: Jones B.S., Smith R.Z. (Eds.), Introduction to the Electronic Age, E-Publishing Inc., New York, 2009, pp.281–304.
  - Reference to a journal publication:
    Tsuji Y., Tanaka T., Ishida T., Lagrangian numerical simulation of plug flow of cohesionless particles in a horizontal pipe, Powder Technology, 71 (1992) 239–250. DOI: 10.1016/0032-5910(92)88030-L

  Text: All citations in the text should refer to:
  1. Single author: the author's name (without initials, unless there is ambiguity) and the year of publication;
  2. Two authors: both authors' names and the year of publication;
  3. Three or more authors: first author's name followed by "et al." and the year of publication.

  Citations may be made directly (or parenthetically). Groups of references should be listed first alphabetically, then chronologically.
  Examples:
  "as demonstrated (Hidaka J. et al., 1995; Tsuji Y., 1992a, 1992b, 1993). Mori Y. and Fukumoto Y. (2002) have recently shown ...."

(3) Copyright and permission

- The original paper to be submitted to KONA has not been published before in any language or in any journals or media; it is not submitted and not under consideration for publication in whole or in part elsewhere.
- Authors are responsible for obtaining permission from the copyright holders to reproduce any figures, tables and photos for which copyright exists.
- The KONA Journal applies the Creative Commons Attribution License to all works published by the Journal. Copyright stays with the agreed copyright owner, and the Hosokawa Powder Technology Foundation is granted the exclusive right to publish and distribute the work, and to provide the work in all forms and media.
- Users of the journal will be able to reuse the contents in any way they like, provided they are accurately attributed. No permission is required from either the authors or the publisher.

Free electronic publication of KONA is available at http://www.kona.or.jp


picoline
HOSOKAWA ALPINE
Start out small and hit it really big.


Mixing, Drying &
Agglomeration Solutions


MAJSx²
MIKRO AIR JET SIEVE
HOSOKAWA MICRON
START


COSTS
SPEED
EFFICIENCY
QUALITY

HOSOKAWA MICRON GROUP

The Hosokawa Micron Group will always be the leading global company covering the mountain range of Powder Technologies. The Group has been a pioneer in the filed of powder and particle processing and blown film processing. We provide R&D, engineering, manufacturing and services in various fields of the world's major industrial markets.

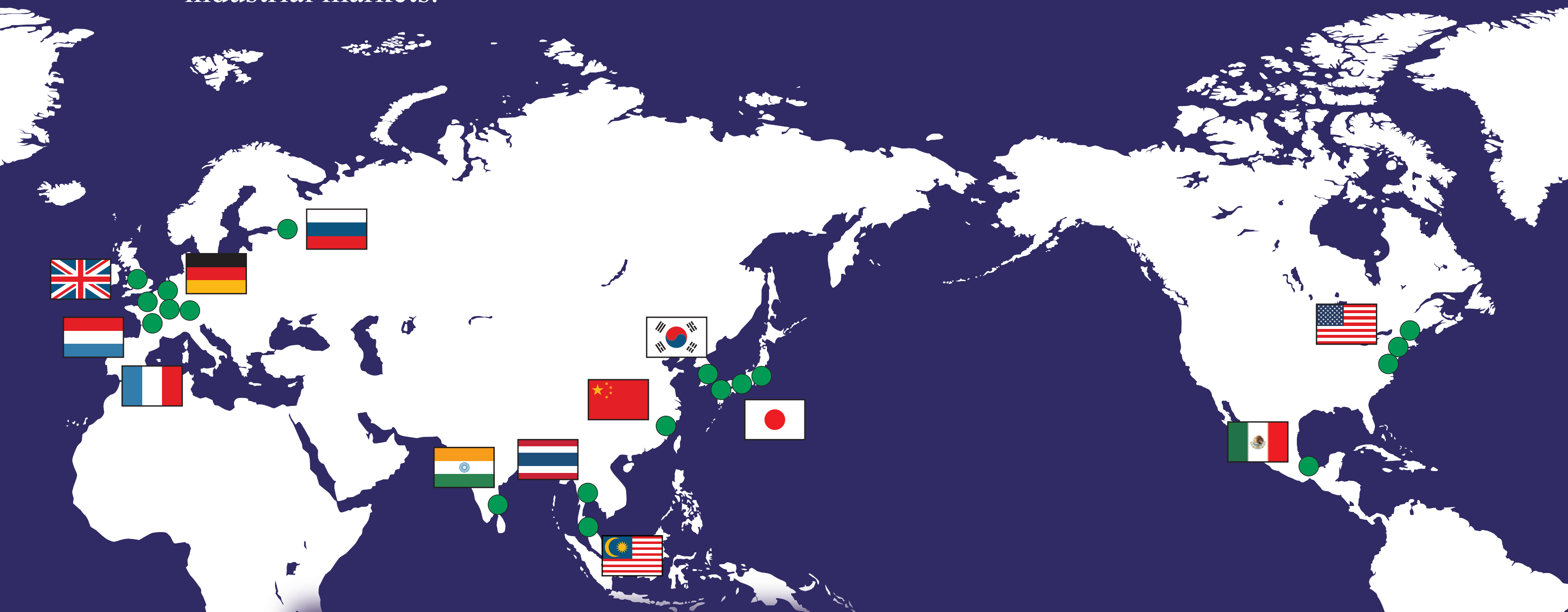

Measuring instruments for developing the powder science & engineering

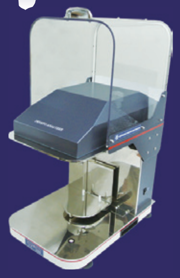

Penetration speed

Peneto Analyzer, PNT-N

Carr's indicies

Powder characteristics tester, PT-X

Wet sieving

Viblette, VBL-F

Process Technologies for Tomorrow

HOSOKAWA MICRON CORPORATION

Headquaters Location :

HOSOKAWA MICRON CORPORATION

https://www.hosokawamicron.com/